Lecture Notes in Physics 926

Miguel Onorato
Stefania Residori
Fabio Baronio *Editors*

Rogue and Shock Waves in Nonlinear Dispersive Media

Springer

Lecture Notes in Physics

Volume 926

The Lecture Notes in Physics

The series Lecture Notes in Physics (LNP), founded in 1969, reports new developments in physics research and teaching-quickly and informally, but with a high quality and the explicit aim to summarize and communicate current knowledge in an accessible way. Books published in this series are conceived as bridging material between advanced graduate textbooks and the forefront of research and to serve three purposes:

- to be a compact and modern up-to-date source of reference on a well-defined topic
- to serve as an accessible introduction to the field to postgraduate students and nonspecialist researchers from related areas
- to be a source of advanced teaching material for specialized seminars, courses and schools

Both monographs and multi-author volumes will be considered for publication. Edited volumes should, however, consist of a very limited number of contributions only. Proceedings will not be considered for LNP.

Volumes published in LNP are disseminated both in print and in electronic formats, the electronic archive being available at springerlink.com. The series content is indexed, abstracted and referenced by many abstracting and information services, bibliographic networks, subscription agencies, library networks, and consortia.

Proposals should be sent to a member of the Editorial Board, or directly to the managing editor at Springer:

Christian Caron
Springer Heidelberg
Physics Editorial Department I
Tiergartenstrasse 17
69121 Heidelberg/Germany
christian.caron@springer.com

More information about this series at http://www.springer.com/series/5304

Miguel Onorato • Stefania Residori • Fabio Baronio
Editors

Rogue and Shock Waves in Nonlinear Dispersive Media

Springer

Editors
Miguel Onorato
Dipartimento di Fisica
Università di Torino
Torino, Italy

Stefania Residori
Institut Non Linéaire de Nice
Centre National de la Recherche Scientifique, CNRS
Université de Nice-Sophia Antipolis
Valbonne, France

Fabio Baronio
Dipartimento di Ingegneria dell'Informazione
Università di Brescia
Brescia, Italy

ISSN 0075-8450 ISSN 1616-6361 (electronic)
Lecture Notes in Physics
ISBN 978-3-319-39212-7 ISBN 978-3-319-39214-1 (eBook)
DOI 10.1007/978-3-319-39214-1

Library of Congress Control Number: 2016950208

Printed on acid-free paper

This Springer imprint is published by Springer Nature
The registered company is Springer International Publishing AG Switzerland

Preface

Rogue and dispersive shock waves are phenomena that occur in nonlinear dispersive media. They have been studied in different fields of physics, including ocean waves, nonlinear optics, Bose-Einstein condensates, plasma physics, etc. They are apparently very different phenomena; however, they are both characterised by the development of extremes: while the amplitude of a rogue wave reaches large values, shock waves develop extreme gradients. The presence of rogue and shock waves in an incoherent wave system drastically influences its statistical properties.

During the last 15 years, the field of "rogue waves" has experienced a very quick development. The original motivation of the research was related mostly to the occasional measurement of extreme waves on the surface of the ocean and to the occurrence of various accidents caused by the impact of large amplitude waves on ships. Only more recently, it has been shown that extreme light fluctuations could be observed in an optical fibre; the research activity has now broadened up to the creation of a new field in its own.

A rogue wave is the manifestation of a process of focussing of energy. One of the most accredited explanations of the formation of rogue waves (at least in an idealised case) is the modulational instability process by which a small perturbation of a plane wave can grow exponentially fast in time. This mechanism has been known from the late sixties, but only at the beginning of the new century, it has been associated to rogue waves. The nonlinear stages of the modulational instability are described by exact solutions of the nonlinear Schrödinger equation. Those solutions, named breathers, have been considered as the prototypes of rogue waves in the ocean.

The development of an infinite gradient in finite time (gradient catastrophe) with consequent wave-breaking is probably a less baleful phenomenon, nonetheless of extreme nature. Mathematically, a classical shock wave is a discontinuous (weak) solution describing propagation beyond a breaking point where an infinite derivative develops. Starting from the last century, in several branches of physics, it has been recognised that the dissipation plays an important role in regularising the jump leading to physical shock waves characterised by strong but finite gradients. A completely different non-trivial dynamics may result when dispersion dominates.

In the latter case, after wave-breaking, the infinite gradient is regularised by the spontaneous onset of fast non-stationary oscillations that progressively fill an extended region. The effect of dispersion on the regularisation of shock waves is very intriguing, leading to a complex strongly non-stationary dynamics. Optics has provided only recently the opportunity to observe these dynamics that appear to be similar to those produced in hydrodynamics under specific conditions involving, for examples, strong tidal bores propagating upstream in river estuaries. Shock waves have impact on many practical situations ranging from photonics to hydraulic dam-breaking to traffic or gas dynamics problems, for which the dispersive effects, which are normally neglected, may determine a qualitative change of the system behaviour.

In the summer of 2015, we have organised a school on rogue and dispersive shock waves in the beautiful village of Cargese, Corsica (France). The idea was to bring together top-level theoretical physicists, mathematicians and experimentalists working mainly in ocean waves and nonlinear optics with the aim of presenting to students and young researchers a unifying concept of rogue and dispersive shock waves. The school lasted for 2 weeks: the first one was characterised by a set of 3-h lectures whose goal was to introduce the students to the deterministic and statistical approach to the subject in the various fields. During the second week, shorter talks, in the workshop format, were given in which more advanced topics were discussed. It turned out that the event was very successful with about 70 (including students and lecturers) participants and many useful discussions. The present book can be considered as a collection of notes from some of the 3-h lectures. It includes a first chapter "Hydrodynamic and Optical Waves: A Common Approach for Unidimensional Propagation" in which a close analogy between optics and hydrodynamic waves is made. The chapter introduces the reader to the nonlinear Schrödinger (NLS) equation which has played a major role in the understanding of rogue waves. A second chapter "Integrability in Action: Solitons, Instability and RogueWaves" is devoted to the role played by integrable equations in the development of the field; the chapter explains how to construct solutions that describe coherent structures such as solitons and rogue waves or how to investigate patterns as those caused by shock waves or instabilities. The third chapter "Hydrodynamic Envelope Solitons and Breathers" and fourth chapter "Experiments on Breathers in Nonlinear Fibre Optics" describe experiments in hydrodynamics and nonlinear optics where exact breather solutions of the NLS equation have been reproduced experimentally. The following three chapters are devoted to a statistical description of rogue waves in water waves: in chapter "Hamiltonian Description of Ocean Waves and Freak Waves" a theory for estimating the kurtosis and the skewness of the surface elevation from wave spectra is explained. The theory has a major relevance in the forecasting of rogue waves in operational systems. Its validation with field measurements is also reported. In chapter "Modelling Transient Sea States with the Generalised Kinetic Equation" an extension of the theory presented in chapter "Hamiltonian Description of Ocean Waves and Freak Waves" is discussed: in particular, the role of sharp changes of wind in the generation of rogue waves is highlighted. Chapter "Rogue Waves in Random Sea States: An Experimental Perspective" describes the results from a number of experiments performed in wave

tanks with the aim of establishing the probability of formation of rogue waves in different sea states; experiments including currents under the waves are also described. In chapters "Introduction to Wave Turbulence Formalisms for Incoherent Optical Waves" and "Integrable Turbulence with Nonlinear Random Optical Waves" the attention is turned to the description of incoherent optical waves. The reader is brought to the construction of statistical tools for describing a system of a large number of interacting optical waves; issues related to condensation, thermalisation, incoherent modulational instability and wave turbulence are discussed. Chapter "Integrable Turbulence with Nonlinear Random Optical Waves" is related to the emerging field of integrable turbulence, i.e. the nonlinear state generated by a large number of incoherent waves described by integrable equations. Experiments in optical fibres ruled by NLS equation and numerical simulations revealing the formation of heavy tails in the probability density function of the wave amplitude are described. The last two chapters deal with dispersive shock waves: the first of the two includes a pedagogical introduction to the Whitham modulation equation that plays a major role in the understanding of dispersive shock waves. The last chapter includes experimental results in optics and hydrodynamics displaying dispersive shock waves.

Our idea was to create a book accessible to graduate students and researchers working in various fields of physics and applied mathematics. Moreover, we hope that this work might be useful to students by bringing to their attention problems of fundamental nature that are often neglected in graduate courses. The book cannot be considered as exhaustive; the reason is that the field on rogue and dispersive shock waves is rapidly evolving, and every month, new interesting ideas appear in the literature. We have made a selection of the topics, giving priorities to what we believe are the results described by a common and interdisciplinary language. Each chapter is self-consistent and it does not require the reading of the previous one.

We would like to thank all the authors of the chapters of the book and, more generally, all the speakers of the school in Cargese with whom we have exchanged many fruitful and interesting discussions on rogue and dispersive shock waves. Finally, we would also like to acknowledge the CNRS, the Università di Torino, the Università di Brescia and the European Geophysical Union for their financial support to the school.

Torino, Italy
Brescia, Italy
Valbonne, France
February 2016

Miguel Onorato
Fabio Baronio
Stefania Residori

Contents

Hydrodynamic and Optical Waves: A Common Approach for Unidimensional Propagation

Miguel Onorato, Fabio Baronio, Matteo Conforti, Amin Chabchoub, Pierre Suret, and Stephane Randoux

Abstract The aim of this chapter is to build a bridge between water and optical waves. After a brief introduction on the role played by the so-called *normal variable* in the D'Alembert equation and a short description of the Hamiltonian formulation of water waves, we introduce a similar formalism for describing optical waves. We restrict our analysis to one-dimensional propagation. Under a number of assumptions, we rewrite the Maxwell equations in a very general form that account for three- and four-wave interactions. Those equations are very similar to the one describing water waves. Analogies and differences between hydrodynamic and optical waves are also discussed.

M. Onorato (✉)
Dipartimento di Fisica, Università degli Studi di Torino, IT-10125 Torino, Italy

Istituto Nazionale di Fisica Nucleare, INFN, Sezione di Torino, IT-10125 Torino, Italy
e-mail: miguel.onorato@unito.it

F. Baronio
INO CNR and Dipartimento di Ingegneria dell'Informazione, Università di Brescia, Via Branze 38, 25123 Brescia, Italy
e-mail: fabio.baronio@unibs.it

M. Conforti
Univ. Lille, CNRS, UMR 8523 - PhLAM - Physique des Lasers Atomes et Molécules, F-59000 Lille, France
e-mail: matteo.conforti@univ-lille1.fr

A. Chabchoub
Department of Ocean Technology Policy and Environment, Graduate School of Frontier Sciences, The University of Tokyo, Kashiwa, Chiba 277-8563, Japan

Department of Mechanical Engineering, School of Engineering, Aalto University, FI-02150 Espoo, Finland
e-mail: amin.chabchoub@isea.k.u-tokyo.ac.jp

P. Suret • S. Randoux
Laboratoire de Physique des Lasers, Atomes et Molecules, UMR-CNRS 8523, Université de Lille I, Sciences et Technologies, France Centre d'Etudes et de Recherches Lasers et Applications (CERLA), 59655 Villeneuve d'Ascq, France
e-mail: Pierre.Suret@univ-lille1.fr; stephane.randoux@univ-lille1.fr

M. Onorato et al. (eds.), *Rogue and Shock Waves in Nonlinear Dispersive Media*,
Lecture Notes in Physics 926, DOI 10.1007/978-3-319-39214-1_1

1 Introduction

It is well known that the spatio-temporal dynamics of narrow-banded wave packets in nonlinear dispersive media can be modeled by the nonlinear Schrödinger (NLS) equation [1–4]. One important feature of such equation is that analogies between surface waves, optical waves, Bose-Einstein condensates, plasma physics, etc. can be drawn. For example, recently a detailed comparison between the NLS equation for surface gravity waves and optical waves in a fiber has been reported in [5], see also [6].

Here, our aim is to present a more general framework in which analogies between hydrodynamics and optics can be established beyond the NLS equation. The key ingredient is the so-called *normal* or *wave action* variable. While such variable has been widely used in hydrodynamics [3, 7–11], it appears that in nonlinear optics it is not as common and only recently it has been exploited to propose an Hamiltonian structure of the equations describing the propagation of ultrashort optical pulses [12, 13]. Within this variable, the evolution equations for water and optical waves can be written in a similar fashion: a linear term which accounts for full dispersion is followed by integral terms that include quadratic, cubic and, in the most general case, higher-order nonlinearities; these integral terms are responsible for the transfer of energy between modes. In nonlinear optics the strength of the nonlinear interaction depends on the medium: $\chi^{(2)}$ and $\chi^{(3)}$ correspond to quadratic and cubic nonlinearity, respectively. For water waves the nonlinear terms are the results of a integral power series expansion for which the small parameter is the wave steepness, i.e. the product of wave amplitude times and wave number.

In this chapter we will first introduce the normal variable in the linear wave equation; this part is purely pedagogical and it should help the reader to familiarise with the formalism before introducing the nonlinear terms. Then, water, i.e. gravity and capillary, waves will be discussed very briefly by presenting the equations written in the normal variable. The discussion on optical waves will be more detailed: the formalism adopted here, especially for the three-wave interaction and the use of the canonical transformation to remove non-resonant terms, is somehow less discussed in the optical literature. We will also show that using the normal variable, it is also straightforward to derive simple models; just to give examples, we show a quick derivation of the Second-Harmonic Generation model and the Three-Wave Interaction system. Conclusions are presented in the last Section.

2 Normal Variables in the Wave Equation

Let us consider the D'Alembert equation for wave propagating along the x-direction:

$$\frac{\partial^2 q}{\partial t^2} - c^2 \frac{\partial^2 q}{\partial x^2} = 0, \tag{1}$$

where $q = q(x,t)$ is some displacement with respect to an equilibrium position and c is the wave velocity. The approach presented here is developed in Fourier space, therefore, the following definition of inverse and forward Fourier Transform in the spatial variable is given:

$$q(k,t) = \int_{-\infty}^{+\infty} q(x,t)e^{ikx}dk, \tag{2}$$

$$q(x,t) = \frac{1}{2\pi}\int_{-\infty}^{+\infty} q(k,t)e^{-ikx}dx. \tag{3}$$

The Dirac Delta function plays a crucial role and its definition here follows:

$$\delta(k_1 - k_2) = \frac{1}{2\pi}\int_{-\infty}^{+\infty} e^{i(k_1-k_2)x}dx. \tag{4}$$

We now plug the definitions of the Fourier Transform into Eq. (1) to obtain the following set of infinite decoupled harmonic oscillators, each oscillating with angular frequency $\tilde{\omega}_k^2 = \tilde{\omega}(k)^2 = c^2k^2$:

$$\frac{\partial^2 q_k}{\partial t^2} + \tilde{\omega}_k^2 q_k = 0, \tag{5}$$

where we have used the short notation $q_k = q(k,t)$. We now introduce the momentum $p_k = \partial q_k/\partial t$ and the following *normal variable* $a_k = a(k,t)$, defined as follows:

$$a_k = \sqrt{\frac{\omega_k}{2}}\left(q_k + \frac{i}{\omega_k}p_k\right). \tag{6}$$

It is important to underline that in the definition (6) ω_k has been chosen as the positive root, i.e. $\omega_k = c|k|$, with c positive. It is then straightforward to show that Eq. (5) for the variable a_k reduces to the simple *universal* equation:

$$i\frac{\partial a_k}{\partial t} = \omega_k a_k. \tag{7}$$

A few remarks are needed:

1. Equation (7) is equivalent to the D'Alembert equation (1) in the sense that no approximations have been made (apart from the assumption that the Fourier Transform can be applied).
2. Starting from a second-order partial differential equation, we have reduced the system to a first-order partial differential equation for a complex variable a_k (note that $a(x,t)$ is not real, thus, $a_k \neq a^*_{-k}$).

3. The equation has some degree of universality in the sense that extending the D'Alembert equation by including dispersion, it can still be expressed in the form of (7). Just to give an example, let us consider the following dispersive equation:

$$\frac{\partial^2 q}{\partial t^2} - c^2 \frac{\partial^2 q}{\partial x^2} = \beta \frac{\partial^4 q}{\partial x^4}, \tag{8}$$

with β constant. Then, it is trivial to show that by introducing the *normal variable* as in (6), Eq. (8) reduces to (7), with the only attention that now $\omega_k = +\sqrt{c^2k^2 - \beta k^4}$, i.e. waves are dispersive.
4. In the dispersive case (see point 3), it is trivial to derive a linear Schrödinger equation (without external potential) from Eq. (7): the dispersion relation needs to be expanded to second-order around a specific wave number k_0; a rotation is then performed to eliminate the phase term (details for the nonlinear case will be given in the following sections) and the last step consists in writing the equation in physical space.
5. Equation (7) still describes waves travelling into different directions (positive and negative x). Indeed, it turns out that for positive values of k, waves travel in the positive x direction, while for negative values of k, they travel in the opposite direction.
6. Equation (7) has a Hamiltonian structure:

$$i\frac{\partial a_k}{\partial t} = \frac{\delta H}{\delta a_k^*}, \tag{9}$$

where δ now is a functional derivative and

$$H = \int_{-\infty}^{+\infty} \omega_k |a_k|^2 dk = \frac{1}{2}\int_{-\infty}^{+\infty} (|p_k|^2 + \omega_k^2 |q_k|^2) dk, \tag{10}$$

is the Hamiltonian, i.e. the kinetic plus the potential energy. Moreover, if $h_k = \omega_k |a_k|^2$ is an energy density, then $|a_k|^2$ plays the role of wave action; in slowly varying environments (for example the nonhomogeneity due to the presence of an ocean current under the waves), while the energy changes, the wave action is preserved. This is another good reason for using the a_k variable instead of the q_k and p_k variables.
7. If experimental data from optical fibers or wave tank experiments need to be compared with numerical simulations, it can be convenient to deal with an evolution equation in space rather than in time. For the D'Alembert equation, this result is achieved by taking the Fourier Transform in time of Eq. (1) using

the following definitions:

$$q(x,\omega) = \int_{-\infty}^{+\infty} q(x,t)e^{i\omega t}dt, \tag{11}$$

$$a_\omega = \sqrt{\frac{k_\omega}{2}}\left(q_\omega + \frac{i}{k_\omega}p_\omega\right), \tag{12}$$

with $k_\omega = k(\omega) = +|\omega|/c$ and $a_\omega = a(\omega, x)$. The evolution (in space) equation can be written as follows:

$$i\frac{\partial a_\omega}{\partial x} = k_\omega a_\omega. \tag{13}$$

Again, no approximations have been made at this stage. For $\omega > 0$ waves travel in the positive direction, while for $\omega < 0$ waves travel in the opposite direction. The corresponding Hamiltonian is

$$H = \int_{-\infty}^{+\infty} k_\omega |a_\omega|^2 d\omega. \tag{14}$$

In dispersive nonlinear systems, the transformation from an evolution equation in time to one in space is in general not exact and one has to assume that the dispersion and nonlinearity are small, see for example Sect. 3.2.1.

In the following Sections we will introduce in the surface and optical wave systems the same formalism as the one described for the D'Alembert equation, with the *only* addition that nonlinearity will be taken into account; the structure of Eq. (7) or Eq. (13) will remain the same except for the fact that some integral terms, that are the results of wave-wave interactions, will appear on the right hand side of the equations.

3 Water Waves in One Horizontal Dimension and Their Hamiltonian Formulation

Here we give a brief overview of the Hamiltonian formulation of surface gravity waves; for more details the reader can look at the contribution of P.A.E.M. Janssen in the same volume. We consider waves propagating along the x-coordinate in a water depth h; we assume the fluid to be inviscid, incompressible and irrotational. Under the last hypothesis, the velocity potential $\phi(x, z, t)$, related to the velocity field as $\mathbf{u} = \nabla\phi$, can be introduced.

Under these conditions the equations of motions, known as the Euler equations for surface waves, take the following form:

$$\begin{aligned}
&\frac{\partial^2\phi}{\partial x^2}+\frac{\partial^2\phi}{\partial z^2}=0 && -h<z<\eta(x,t)\\
&\frac{\partial\eta}{\partial t}+\frac{\partial\phi}{\partial x}\frac{\partial\eta}{\partial x}=\frac{\partial\phi}{\partial z} && z=\eta(x,t)\\
&\frac{\partial\phi}{\partial t}+\frac{1}{2}\left[\left(\frac{\partial\phi}{\partial x}\right)^2+\left(\frac{\partial\phi}{\partial z}\right)^2\right]+g\eta-\gamma w=0 && z=\eta(x,t)\\
&\frac{\partial\phi}{\partial z}=0 && z=-h
\end{aligned} \tag{15}$$

g is the gravity acceleration, γ is the ratio between the surface tension coefficient and the fluid density and w is the surface curvature:

$$w=\frac{\partial\eta/\partial x}{\sqrt{1+(\partial\eta/\partial x)^2}}. \tag{16}$$

The equations appear, at first sight, rather complicated: the Laplace equation has to be solved in a domain that changes as a function of space and time and depends on the potential as well. In [3] it has been shown that the surface elevation, $\eta(x,t)$, and the velocity potential evaluated at the free surface, $\psi(x,t)=\phi(x,z=\eta(x,t),t)$, are canonically conjugate variables and the Hamiltonian is the total (kinetic plus potential) energy of the system. The formulation is made in wave number space and the Hamiltonian is then expanded for small steepness, i.e. small amplitude with respect to the wave length, in such a way that it will be the sum of an unperturbed Hamiltonian plus terms related to wave-wave interactions. Here, we consider the expansion truncated to cubic nonlinearity in the evolution equation, therefore three- and four-wave interactions are included (for five-wave interactions, the reader should refer to [7]). The action density normal variable is then introduced as follows:

$$a(k,t)=\sqrt{\frac{g}{2\omega(k)}}\eta(k,t)+i\sqrt{\frac{\omega(k)}{2g}}\psi(k,t), \tag{17}$$

$\omega(k)$ is the frequency associated to wave number k and is taken as the positive root of the dispersion relation in arbitrary depth h:

$$\omega(k)=\sqrt{(g|k|+\gamma|k|^3)\tanh(|k|h)}. \tag{18}$$

The evolution equation for the action variable, up to cubic nonlinearity, takes the following form:

$$
\begin{aligned}
i\frac{\partial a_1}{\partial t} = \omega_1 a_1 &+ \int V^{(1)}_{1,2,3} a_2 a_3 \delta_{1-2-3} dk_{23} + 2\int V^{(2)}_{2,1,0} a_2^* a_3 \delta_{1+2-3} dk_{23} \\
&+ \int V^{(3)}_{0,1,2} a_2^* a_3^* \delta_{1+2+3} dk_{23} + \int T^{(2)}_{1,2,3,4} a_2^* a_3 a_4 \delta_{1+2-3-4} dk_{234} \\
&+ \int T^{(1)}_{1,2,3,4} a_2 a_3 a_4 \delta_{1-2-3-4} dk_{234} + 3\int T^{(1)}_{3,2,1,0} a_2^* a_3^* a_4 \delta_{1+2+3-4} dk_{234} \\
&+ \int T^{(4)}_{1,2,3,4} a_2^* a_3^* a_4^* \delta_{1+2+3+4} dk_{234}.
\end{aligned}
\tag{19}
$$

The notation, taken directly from [7], is the following: the argument k_j in a, ω, $V^{(n)}$, $T^{(n)}$ and δ-functions are replaced directly by subscripts j; for example $a_j = a(k_j, t)$, $\omega_j = \omega(k_j)$, $V^{(n)}_{1,2,3} = V^{(n)}(k_1, k_2, k_3)$ and $\delta_{1-2-3} = \delta(k_1 - k_2 - k_3)$.

The equation is valid for both gravity and capillary waves; however, there is a substantial difference between the two dynamics. For capillary waves three-wave interactions can be resonant: this is exactly the same as considering a $\chi^{(2)}$ medium in which the phase-matching condition is satisfied, see Sect. 4.1. As described in the following section, for surface gravity waves exact three-wave resonant interactions are forbidden. Despite this, Eq. (19) without cubic nonlinearity is the starting point for the derivation of many important physical models in shallow water such as the Korteweg de Vries (KdV) equation or the Boussinesq model (or in two horizontal dimensions the Kadomtsev-Petviashvili equation); all the above equations are derived assuming that waves are long; the dispersion relation for gravity waves is $\omega = \sqrt{g|k|\tanh(|k|h)}$ so that the Taylor expansion around $k = 0$ leads to first and third derivatives of the surface elevation, i.e. the linear terms in the KdV equation.

3.1 Surface Gravity Waves: The Canonical Transformation

For surface gravity waves in arbitrary depth h the dispersion relation simplifies to $\omega^2(k) = g|k|\tanh(|k|h)$. Given the geometrical form of the dispersion relation, it can be shown (see for example [14]) that three-wave resonant interactions are forbidden, i.e. none of the following pair of equations, related to the first, second and third integrals in (19),

$$
\begin{aligned}
k_1 - k_2 - k_3 = 0, &\quad \omega_1 - \omega_2 - \omega_3 = 0, \\
k_1 + k_2 - k_3 = 0, &\quad \omega_1 + \omega_2 - \omega_3 = 0, \\
k_1 + k_2 + k_3 = 0, &\quad \omega_1 + \omega_2 + \omega_3 = 0,
\end{aligned}
\tag{20}
$$

have solutions. This result implies that the main dynamical process is a four-wave interaction one and quadratic nonlinearities have the role of developing bound modes. Moreover, we mention that not all of the four-wave interactions are in general allowed. For surface gravity waves, it can be shown that none of the following processes is possible:

$$\begin{aligned} k_1 - k_2 - k_3 - k_4 = 0, \quad \omega_1 - \omega_2 - \omega_3 - \omega_4 = 0, \\ k_1 + k_2 + k_3 - k_4 = 0, \quad \omega_1 + \omega_2 + \omega_3 - \omega_4 = 0, \\ k_1 + k_2 + k_3 + k_4 = 0, \quad \omega_1 + \omega_2 + \omega_3 + \omega_4 = 0, \end{aligned} \tag{21}$$

and the only relevant process is the following:

$$k_1 + k_2 - k_3 - k_4 = 0, \quad \omega_1 + \omega_2 - \omega_3 - \omega_4 = 0. \tag{22}$$

All the integrals that cannot satisfy the resonant condition can be removed by an *ad hoc* canonical transformation from variable $\{a, a^*\}$ to $\{b, b^*\}$. This is expressed through an integral power series of the form:

$$\begin{aligned} a_1 = b_1 &+ \int A^{(1)}_{1,2,3} b_2 b_3 \delta_{1-2-3} dk_{2,3} + \int A^{(2)}_{1,2,3} b_2^* b_3 \delta_{1+2-3} dk_{2,3} \\ &+ \int A^{(3)}_{1,2,3} b_2^* b_3^* \delta_{1+2+3} dk_{2,3} + \int B^{(1)}_{1,2,3,4} b_2 b_3 b_4 \delta_{1-2-3-4} dk_{2,3,4} \\ &+ \int B^{(2)}_{1,2,3,4} b_2^* b_3 b_4 \delta_{1+2-3-4} dk_{2,3,4} + \int B^{(3)}_{1,2,3,4} b_2^* b_3^* b_4 \delta_{1+2+3-4} dk_{2,3,4} \\ &+ \int B^{(4)}_{1,2,3,4} b_2^* b_3^* b_4^* \delta_{1+2+3+4} dk_{2,3,4}. \end{aligned} \tag{23}$$

The coefficients $A^{(i)}_{1,2,3}$ and $B^{(i)}_{1,2,3,4}$ are selected in order to remove the non-resonant quadratic and cubic terms in Eq. (19). The equation for the new variable takes the following simpler form:

$$i \frac{\partial b_1}{\partial t} = \omega_1 b_1 + \int \tilde{T}^{(2)}_{1,2,3,4} b_2^* b_3 b_4 \delta_{1+2-3-4} dk_{234}, \tag{24}$$

where $\tilde{T}^{(2)}_{1,2,3,4}$, reported for example in [15] for arbitrary depth, is the interaction coefficient that depends on $T^{(2)}_{1,2,3,4}$ and $A^{(i)}_{1,2,3}$. Equation (24) is known in the field of water waves as the *Zakharov equation* [3] and it is the starting point for both deterministic and statistical studies on water waves. As we will see in the next Section, the Zakharov equation is also suitable for deriving envelope equations such as the Nonlinear Schrödinger and higher-order equations. The Hamiltonian takes

the following form:

$$H = \int \omega_1 |b_1|^2 dk_1 + \frac{1}{2} \int \tilde{T}^{(2)}_{1,2,3,4} b_1^* b_2^* b_3 b_4 \delta_{1+2-3-4} dk_{1234}. \tag{25}$$

We recall that $\tilde{T}^{(2)}_{1,2,3,4}$ is real and, in order the system to be Hamiltonian, the following symmetries $\tilde{T}^{(2)}_{1,2,3,4} = \tilde{T}^{(2)}_{2,1,3,4} = \tilde{T}^{(2)}_{3,4,1,2}$ need to be satisfied.

3.2 The NLS Equation for Surface Gravity Waves in Infinite Water Depth

In order to derive the NLS equation, it is sufficient to take the narrow-band approximation of the Zakharov equation. Before doing that, we should note that, in terms of nondimensional variables, the nonlinear term in the Zakhaorv equation is smaller than the linear one; more precisely, because of the presence of the cubic nonlinearity, the integral is of the order of ϵ^2, with ϵ is the wave steepness. In taking the narrow-band limit, such information is important in order to balance properly the nonlinearity and the dispersion. We introduce the variable $K = k - k_0$ and, after Taylor expanding the dispersion relation around k_0 to second-order, we get:

$$\omega(k) \simeq \omega_0 + K \frac{d\omega(k)}{dk}\bigg|_{k=k_0} + \frac{1}{2} K^2 \frac{d^2\omega(k)}{dk^2}\bigg|_{k=k_0}, \tag{26}$$

where $\omega_0 = \omega(k_0)$. The interaction coefficient is also Taylor expanded around k_0 to the leading order,

$$\tilde{T}^{(2)}_{k_1,k_2,k_3,k_4} \simeq \tilde{T}^{(2)}_{k_0,k_0,k_0,k_0} = k_0^3, \tag{27}$$

so that the nonlinearity is balanced by the K^2 dispersive term. Introducing the variable $b(K,t) = A(K,t) \exp(-i\omega_0 t)$ in order to remove a phase and after taking the Fourier Transform, the NLS equation is obtained:

$$i\left(\frac{\partial A}{\partial t} + c_g \frac{\partial A}{\partial x}\right) - \beta_2 \frac{\partial^2 A}{\partial x^2} - \gamma |A|^2 A = 0, \tag{28}$$

with

$$
\begin{aligned}
c_g &= \frac{d\omega(k)}{dk} = \frac{1}{2}\frac{\omega_0}{k_0}, \\
\beta_2 &= -\frac{1}{2}\frac{d^2\omega(k)}{dk^2}\bigg|_{k_0} = \frac{\omega_0}{8k_0^2}, \\
\gamma &= k_0^3.
\end{aligned}
\tag{29}
$$

Using a Galilean transformation of the form $x' = x - c_g t$, it is always possible to remove the term containing the group velocity. Note that usually the NLS equation is written for a variable that has the dimensions of the surface elevation and not of the wave action as in Eq. (28); the reason of our choice is related to the fact that, as noted in [16], the higher-order envelope equations keep the Hamiltonian structure in the wave action variable.

3.2.1 The NLS Equation as an Evolution Equation in Space

The nonlinear and the dispersive terms in Eq. (28) are of higher-order with respect to the terms inside the parenthesis. This fact can be used to write the NLS equation as an evolution equation in space rather than in time; indeed, at leading order we have:

$$
\frac{\partial A}{\partial x} = -\frac{1}{C_g}\frac{\partial A}{\partial t} + h.o.t, \tag{30}
$$

where *h.o.t* means higher-order terms. We use such solution in order to build the second-order derivative operator contained in the NLS equation by taking the x derivative of Eq. (30)

$$
\begin{aligned}
\frac{\partial^2 A}{\partial x^2} &= -\frac{1}{c_g}\frac{\partial}{\partial x}\left(\frac{\partial A}{\partial t}\right) + h.o.t \\
&= -\frac{1}{c_g}\frac{\partial}{\partial t}\left(\frac{\partial A}{\partial x}\right) + h.o.t = \frac{1}{c_g^2}\frac{\partial^2 A}{\partial t^2} + h.o.t.,
\end{aligned}
\tag{31}
$$

where we have used the fact that derivatives in t and x commute. We plug our result in Eq. (28) to get:

$$
i\left(\frac{\partial A}{\partial x} + \frac{1}{c_g}\frac{\partial A}{\partial t}\right) - \frac{\beta_2}{c_g^3}\frac{\partial^2 A}{\partial t^2} - \frac{\gamma}{c_g}|A|^2 A \simeq 0. \tag{32}
$$

The evolution equation in time is only asymptotically equivalent to the evolution equation in space [higher-order terms are omitted in Eq. (32)] and there is no

exact transformation that can map one into the other. The term containing the first derivative of the amplitude can always be removed by the transformation $t' = t - x/c_g$.

4 Optical Waves in Normal Variables

We now consider optical waves described by the Maxwell equation in a medium characterized by quadratic and cubic nonlinearity. We suppose that the optical wave field is linearly polarized along the x transverse direction, $E = (E, 0, 0)$ with $E = E(z, t)$ and assume that the material acquires a polarization $\mathbf{P} = P\mathbf{e_x} = P(z, t)\mathbf{e_x}$, oriented along the x direction. It is not difficult from the Maxwell equations to write the following second-order partial differential equation for the electric field E:

$$\frac{\partial^2 E}{\partial z^2} - \frac{1}{c^2}\frac{\partial^2 E}{\partial t^2} - \frac{1}{\epsilon_0 c^2}\frac{\partial^2 P_L}{\partial t^2} = \frac{1}{\epsilon_0 c^2}\frac{\partial^2 P_{NL}}{\partial t^2}, \tag{33}$$

where P has been split as a sum of a linear and a nonlinear contribution, $P = P_L + P_{NL}$. The above equation can be written in Fourier frequency space as:

$$\frac{\partial^2 E(\omega)}{\partial z^2} + \frac{\omega^2}{c^2}E(\omega) + \frac{\omega^2}{\epsilon_0 c^2}P_L(\omega) = -\frac{\omega^2}{\epsilon_0 c^2}P_{NL}(\omega), \tag{34}$$

where

$$\begin{aligned} P_L(\omega) &= \epsilon_0 \chi^{(1)} E(\omega) \\ P_{NL}(\omega) &= \epsilon_0 \int \chi^{(2)}(\omega, \omega_1, \omega_2) E(\omega_1) E(\omega_2) \delta(\omega - \omega_1 - \omega_2) d\omega_{1,2} \\ &\quad + \epsilon_0 \int \chi^{(3)}(\omega, \omega_1, \omega_2, \omega_3) E(\omega_1) E(\omega_2) E(\omega_3) \delta(\omega - \omega_1 - \omega_2 - \omega_3) d\omega_{1,2,3}. \end{aligned} \tag{35}$$

The linear dispersion relation has the following form:

$$\tilde{k}(\omega)^2 = \frac{\omega^2}{c^2}(1 + \chi^{(1)}(\omega)). \tag{36}$$

We assume that $\chi^{(1)}(\omega)$ has also a negligible imaginary component (losses are neglected), so that $\chi^{(1)}(-\omega) = \chi^{(1)}(\omega)$; $\chi^{(2)}$ and $\chi^{(3)}$ are also assumed real. For simplicity of notation we rewrite Eq. (34) as follows:

$$\frac{\partial^2 E_1}{\partial z^2} + \tilde{k}_1^2 E_1 = -\frac{\omega_1^2}{c^2}\int \chi^{(2)}_{1,2,3} E_2 E_3 \delta_1^{2,3} d\omega_{2,3} - \frac{\omega_1^2}{c^2}\int \chi^{(3)}_{1,2,3,4} E_2 E_3 E_4 \delta_1^{2,3,4} d\omega_{2,3,4} \tag{37}$$

with

$$E_i = E(\omega_i), \quad \tilde{k}_i^2 = \tilde{k}(\omega_i)^2 \tag{38}$$

and introduce the *normal* variable:

$$a(\omega, z) = \frac{1}{2}\frac{\sqrt{2k(\omega)}}{|\omega|}\left[E(\omega, z) + i\frac{1}{k(\omega)}\frac{E(\omega, z)}{\partial z}\right] \tag{39}$$

where

$$k(\omega) = \sqrt{\frac{\omega^2}{c^2}(1 + \chi^{(1)}(\omega))} \tag{40}$$

is the positive branch of the dispersion relation (note that $k(\omega) = k(-\omega)$). Because of the reality of $E(z, t)$, it follows that

$$a(-\omega, z)^* = \frac{1}{2}\frac{\sqrt{2k(\omega)}}{|\omega|}\left[E(\omega, z) - i\frac{1}{k(\omega)}\frac{E(\omega, z)}{\partial z}\right]; \tag{41}$$

therefore, the electric field can be expressed in terms of the normal variable as follows:

$$E(\omega, z) = \frac{|\omega|}{\sqrt{2k(\omega)}}[a(\omega, z) + a(-\omega, z)^*]. \tag{42}$$

Taking the derivative in z of Eq. (41) and using (37), we get after some algebra:

$$\begin{aligned} i\frac{\partial a_1}{\partial z} = {} & k_1 a_1 + \int V_{1,2,3}\Big(a_2 a_3 \delta_{1-2-3} + 2a_2^* a_3 \delta_{1+2-3} + a_2^* a_3^* \delta_{1+2+3}\Big) d\omega_{2,3} \\ & + \int T_{1,2,3,4}\Big(\frac{1}{3}a_2 a_3 a_4 \delta_{1-2-3-4} + a_2^* a_3 a_4 \delta_{1+2-3-4} \\ & + a_2^* a_3^* a_4 \delta_{1+2-3-4} + \frac{1}{3}a_2^* a_3^* a_4^* \delta_{1+2+3+4}\Big) d\omega_{2,3,4}, \end{aligned} \tag{43}$$

where

$$V_{1,2,3} = \frac{1}{c^2}\frac{|\omega_1\omega_2\omega_3|}{\sqrt{8k_1k_2k_3}}\chi^{(2)}_{1,2,3}, \quad T_{1,2,3,4} = \frac{3}{c^2}\frac{|\omega_1\omega_2\omega_3\omega_4|}{\sqrt{16k_1k_2k_3k_4}}\chi^{(3)}_{1,2,3,4}. \tag{44}$$

We have assumed the following symmetries on $\chi^{(2)}_{1,2,3}$ and $\chi^{(3)}_{1,2,3,4}$:

$$\begin{aligned}\chi^{(2)}_{1,2,3} &= \chi^{(2)}_{1,-2,3} = \chi^{(2)}_{1,2,-3}\\ \chi^{(3)}_{1,2,3,4} &= \chi^{(3)}_{1,-2,3,4} = \chi^{(3)}_{1,2,-3,4} = \chi^{(3)}_{1,2,3,-4}.\end{aligned} \tag{45}$$

Without such assumptions, the structure of the equation remains the same apart from the fact that each term inside the integral has a different coefficient in front [just like in the water wave problem, see Eq. (19)].

In the following we will consider separately the following cases:
(1) $\chi^{(3)} = 0$ and $\chi^{(2)} \neq 0$, (2) $\chi^{(2)} = 0$ and $\chi^{(3)} \neq 0$, (3) $\chi^{(2)} \neq \chi^{(3)} \neq 0$.

4.1 Three-Wave Interactions: $\chi^{(2)}$ Media

Here, we neglect four-wave interactions and consider the following equation:

$$i\frac{\partial a_1}{\partial z} = k_1 a_1 + \int V_{1,2,3}\Big(a_2 a_3 \delta_{1-2-3} + 2a_2^* a_3 \delta_{1+2-3} + a_2^* a_3^* \delta_{1+2+3}\Big) d\omega_{2,3}. \tag{46}$$

Once more, we emphasise that the above equation does not have any restriction on the spectral width of the optical pulse: no paraxial approximation has been used to neglect the second-order derivative of the electric field; moreover, it still describes waves propagating into two directions and it is as exact as Eq. (33) for a pure χ^2 media. The presence of the three Dirac Delta functions in Eq. (46) implies that transfer of energy can take place if one of the following conditions is satisfies:

$$\omega_1 = \omega_2 + \omega_3, \quad \omega_1 = \omega_3 - \omega_2, \quad \omega_1 = -\omega_3 - \omega_2. \tag{47}$$

Such transfer can be efficient or not depending if the associated conservation of momentum takes place. Indeed, by applying the following rotation, $A(\omega, z) = a(\omega, z)e^{ik(\omega)z}$, it is straightforward to write the equation in the so-called *interaction representation*:

$$\begin{aligned}i\frac{\partial A_1}{\partial z} = \int V_{1,2,3}\Big(&A_2 A_3 e^{i(k_1-k_2-k_3)z}\delta_{1-2-3} + 2A_2^* A_3 e^{i(k_1+k_2-k_3)z}\delta_{1+2-3}\\ &+ A_2^* A_3^* e^{i(k_1+k_2+k_3)z}\delta_{1+2+3}\Big) d\omega_{2,3};\end{aligned} \tag{48}$$

the presence of the complex exponentials on the right hand side implies a quasi-periodic transfer of energy. An efficient transfer is achieved if the so-called *phase*

matching or *resonant* condition takes place:

$$k_1 = k_2 + k_3, \quad k_1 = k_3 - k_2, \quad k_1 = -k_3 - k_2. \tag{49}$$

As mentioned, three frequencies satisfying one of the equations in (47) and the associated equations in (49) are said to be in *resonance*.

Equation (48) describes some of the well known physical phenomena of optical wave propagation such as Sum-Frequency Generation, Difference-Frequency Generation, Second-Harmonic Generation, Optical Rectification, and the Three-Wave Resonant Interaction system. Just to give an example, in the next section we will give a straightforward derivation of the equations for Second Harmonic Generation and for the Three-Wave Resonant Interaction (3WRI) system, see [17, 18].

4.1.1 Second-Harmonic Generation Model

Let us assume that the variable $A(\omega, z)$ is the sum of a wave whose frequency is ω_p and a second one with frequency $\omega = 2\omega_p$ as follows:

$$A(\omega, z) = A_{\omega_p}(z)\delta(\omega - \omega_p) + A_{2\omega_p}(z)\delta(\omega - 2\omega_p). \tag{50}$$

Plugging such expression in (48), we get immediately the following two equations:

$$\begin{aligned} i\frac{dA_{2\omega_p}(z)}{dz} &= V_{2\omega_p,\omega_p,\omega_p} A_{\omega_p}(z)^2 e^{-i[2k_{\omega_p} - k_{2\omega_p}]z} \\ i\frac{dA_{\omega_p}(z)}{dz} &= 2V_{\omega_p,\omega_p,2\omega_p} A_{\omega_p}(z)^* A_{2\omega_p}(z) e^{i[2k_{\omega_p} - k_{2\omega_p}]z} \end{aligned} \tag{51}$$

with

$$V_{2\omega_p,\omega_p,\omega_p} = V_{\omega_p,\omega_p,2\omega_p} = \frac{1}{\sqrt{2}c^2} \frac{\omega_p^3}{\sqrt{k_{\omega_p}^2 k_{2\omega_p}}} \chi^{(2)}_{2\omega_p,\omega_p,\omega_p}, \tag{52}$$

where the first equality results from the fact that $\chi^{(2)}_{2\omega_p,\omega_p,\omega_p} = \chi^{(2)}_{\omega_p,\omega_p,2\omega_p}$. It should be noted, once more, that in order to derive such set of equations, using the electric field as a variable, one needs to assume that the variation of its amplitude over one wave length is small, i.e. $|\partial^2 E(\omega, z)/\partial z^2| \ll k|\partial E(\omega, z)/\partial z|$; within the new normal variable, such hypothesis is not needed. In the case of phase matching condition, $2k(\omega_p) = k(2\omega_p)$, the equations can be further simplified.

In general the Second-Harmonic Generation model can be derived also for surface waves with the particular attention that, while for capillary-gravity or pure capillary waves, the phase matching condition can be satisfied, this is not possible for pure gravity waves.

4.1.2 The Three-Wave Resonant Interaction System

Here, we will derive from Eq. (46) the 3WRI system for which recently rogue wave solutions have been found [19]. The idea is to assume that the wave field is the result of the following superposition of narrow band fields centred in ω_A, ω_B, ω_C:

$$a(\omega) = A(\omega - \omega_A)e^{-ik(\omega_A)z} + B(\omega - \omega_B)e^{-ik(\omega_B)z} + C(\omega - \omega_C)e^{-ik(\omega_C)z}. \tag{53}$$

We then assume that waves are in resonance according to the following process:

$$\omega_A = \omega_B + \omega_C \quad \text{and} \quad k(\omega_A) = k(\omega_B) + k(\omega_C); \tag{54}$$

The derivation consists in the following four straightforward steps:

1. Plug Eq. (53) in Eq. (46).
2. Taylor expand A, B and C around ω_A, ω_B, ω_C. Use the first-order expansion in the linear term and the leading order one in the nonlinear part of the equation.
3. Use Eq. (54) to neglect unimportant terms.
4. Write equations in physical space using the definition of the Fourier Transform.

The resulting equations are the following:

$$\begin{aligned}
\frac{\partial A}{\partial z} + \frac{1}{v_A}\frac{\partial A}{\partial t} &= +iqBC \\
\frac{\partial B}{\partial z} + \frac{1}{v_B}\frac{\partial B}{\partial t} &= +iqAC^* \\
\frac{\partial C}{\partial z} + \frac{1}{v_C}\frac{\partial C}{\partial t} &= +iqAB^*,
\end{aligned} \tag{55}$$

with

$$q = \frac{1}{\sqrt{2}} \frac{\omega_A \omega_B \omega_C}{\sqrt{k(\omega_A)k(\omega_B)k(\omega_C)}} \chi^{(2)}_{\omega_A,\omega_B,\omega_C}, \tag{56}$$

where v_A, v_B and v_C are the group velocities of the three wave systems. Note that the equation is written in physical variables. The system is integrable via the Inverse Scattering Theory [20]. The above system cannot be derived for pure surface gravity waves; however, it has been derived in hydrodynamics in the context of capillary-gravity waves, see for example [21].

4.2 Four-Wave Interactions in Pure $\chi^{(3)}$ Media

We now assume that the medium is ruled exactly by cubic nonlinearity or four-wave interactions. In other words we assume that $\chi^{(2)}_{1,2,3}$ is identically zero. Under this assumption, Eq. (43) reduces to the following one:

$$i\frac{\partial a_1}{\partial z} = k_1 a_1 + \int T_{1,2,3,4}\Big(\frac{1}{3}a_2 a_3 a_4 \delta_{1-2-3-4} + a_2^* a_3 a_4 \delta_{1+2-3-4} + a_2^* a_3^* a_4 \delta_{1+2-3-4} + \frac{1}{3}a_2^* a_3^* a_4^* \delta_{1+2+3+4}\Big).d\omega_{2,3,4} \tag{57}$$

Depending on the functional form of $\chi^{(1)}(\omega)$, some interactions may be resonant, i.e. some of the following conditions may be satisfied:

$$\begin{aligned} \omega_1 + \omega_2 - \omega_3 - \omega_4 = 0, \quad & k_1 + k_2 - k_3 - k_4 = 0, \\ \omega_1 - \omega_2 - \omega_3 - \omega_4 = 0, \quad & k_1 - k_2 - k_3 - k_4 = 0, \\ \omega_1 + \omega_2 + \omega_3 - \omega_4 = 0, \quad & k_1 + k_2 + k_3 - k_4 = 0, \\ \omega_1 + \omega_2 + \omega_3 + \omega_4 = 0, \quad & k_1 + k_2 + k_3 + k_4 = 0. \end{aligned} \tag{58}$$

If only the first of the above equations can be satisfied, as the case of surface gravity waves, then the second, third and fourth terms in the integral in (57) can be removed by an asymptotic transformation (see next section where non-resonant three-wave interactions are removed). The following equation is then obtained:

$$i\frac{\partial a_1}{\partial z} = k_1 a_1 + \int T_{1,2,3,4} a_2^* a_3 a_4 \delta_{1+2-3-4} d\omega_{2,3,4}, \tag{59}$$

where $T_{1,2,3,4}$ is

$$T_{1,2,3,4} = \frac{3}{4}\frac{\chi^{(3)}_{1,2,3,4}}{c^2}\frac{\omega_1\omega_2\omega_3\omega_4}{\sqrt{k_1 k_2 k_3 k_4}}, \tag{60}$$

The above equation has the same structure of the *Zakharov* equation derived for surface gravity waves, see Eq. (24). It is straightforward to show that the corresponding Hamiltonian is

$$H = \int k_1 |a_1|^2 d\omega_1 + \frac{1}{2}\int T_{1,2,3,4} a_1^* a_2^* a_3 a_4 \delta_{1+2-3-4} d\omega_{1,2,3,4}. \tag{61}$$

i.e. the same as the Hamiltonian (25) where space and time are interchanged.

4.2.1 The NLS Equation in Optical Waves

Let us consider the narrow band approximation of Eq. (59). Under such hypothesis, at the leading order, $T(\omega_1, \omega_2, \omega_3, \omega_4) = T(\omega_0, \omega_0, \omega_0, \omega_0) = T_{0,0,0,0} = const$; the linear dispersion relation can be expanded around $\omega = \omega_0$ as

$$k(\omega) = k_0 + \Omega \frac{\partial k}{\partial \omega}\bigg|_{\omega_0} + \Omega^2 \frac{1}{2} \frac{\partial^2 k}{\partial \omega^2}\bigg|_{\omega_0} + \ldots, \tag{62}$$

with $\Omega = \omega - \omega_0$ and $k_0 = k(\omega_0)$. Performing the rotation $a(z,t) = b(z,t)e^{-ik_0 z}$ and using the definition of the Fourier transform, the evolution equation can be written in physical space as:

$$i\left(\frac{\partial b}{\partial z} + \frac{1}{c_g}\frac{\partial b}{\partial t}\right) = \frac{\beta_2}{2}\frac{\partial^2 b}{\partial t^2} + \gamma |b|^2 b \tag{63}$$

with

$$\begin{aligned} &\frac{1}{c_g} = \frac{dk}{d\omega}\bigg|_{\omega_0}, \quad \beta_2 = -\frac{d^2 k}{d\omega^2}\bigg|_{\omega_0}, \\ &\gamma = T_{0,0,0,0} = \frac{3}{4}\frac{\chi^{(3)}_{0,0,0,0}}{c^2}\frac{\omega_0^4}{k_0^2} = \frac{3}{4}\frac{\chi^{(3)}_{0,0,0,0}\omega_0^2}{1+\chi^{(1)}}. \end{aligned} \tag{64}$$

We recall that $\chi^{(3)}$ is real. Note that if one is interested in an evolution equation for a variable that has the dimensions of the electric field, then one has to introduce the following variable A:

$$A = \frac{\sqrt{2}|\omega_0|}{\sqrt{k_0}} b \tag{65}$$

to get:

$$i\left(\frac{\partial A}{\partial z} + \frac{1}{c_g}\frac{\partial A}{\partial t}\right) = \frac{\beta_2}{2}\frac{\partial^2 A}{\partial t^2} + \frac{3}{8}\frac{\chi^{(3)}_{0,0,0,0} k_0}{1+\chi^{(1)}}|A|^2 A. \tag{66}$$

A detailed comparison of the NLS equation in an optical fiber and in one dimensional surface gravity waves is given in [5].

A generalised NLS equation can be derived from Eq. (59) if the dispersion relation is expanded to higher-order in both the linear (dispersive) and nonlinear terms.

4.3 Four-Wave Mixing in a $\chi^{(2)}$ and $\chi^{(3)}$ Medium

We now consider the case that three- and four-wave interactions are both not negligible; we also assume that three-wave resonant interactions are not allowed and the only possible phase-matched interaction is the following:

$$\omega_1 + \omega_2 - \omega_3 - \omega_4 = 0, \quad k_1 + k_2 - k_3 - k_4 = 0, \tag{67}$$

This is exactly the same situation encountered in the problem of surface gravity waves. As shown before in Sect. 3.1, all non-resonant interactions may be removed from the dynamics by a suitable near identity transformation of the form:

$$\begin{aligned} a_1 = b_1 &+ \int A^{(1)}_{1,2,3} b_2 b_3 \delta_{1-2-3} d\omega_{2,3} + \int A^{(2)}_{1,2,3} b_2^* b_3 \delta_{1+2-3} d\omega_{2,3} \\ &+ \int A^{(3)}_{1,2,3} b_2^* b_3^* \delta_{1+2+3} d\omega_{2,3} + \int B^{(1)}_{1,2,3,4} b_2 b_3 b_4 \delta_{1-2-3-4} d\omega_{2,3,4} \\ &+ \int B^{(2)}_{1,2,3,4} b_2^* b_3 b_4 \delta_{1+2-3-4} d\omega_{2,3,4} + \int B^{(3)}_{1,2,3,4} b_2^* b_3^* b_4 \delta_{1+2+3-4} d\omega_{2,3,4} \\ &+ \int B^{(4)}_{1,2,3,4} b_2^* b_3^* b_4^* \delta_{1+2+3+4} d\omega_{2,3,4}. \end{aligned} \tag{68}$$

$A^{(i)}$, $B^{(i)}$ are coefficients that are selected in order to remove the undesired terms. The algebra is quite lengthy and we refer to [7] and [8] for details. It can be shown that the transformation is canonical, see [7]. The coefficient $A^{(i)}_{1,2,3}$ turns out to be given by

$$A^{(1)}_{1,2,3} = -\frac{V_{1,2,3}}{k_1 - k_2 - k_3}, \; A^{(2)}_{1,2,3} = -\frac{2V_{1,2,3}}{k_1 + k_2 - k_3}, \; A^{(3)}_{1,2,3} = -\frac{V_{1,2,3}}{k_1 + k_2 + k_3}. \tag{69}$$

Clearly, if one of the three-wave phase-matched conditions is satisfied, then $A^{(i)}_{1,2,3}$ diverge and the transformation is not applicable. In the new canonical variables $\{b, b^*\}$ the evolution equation is given by:

$$i\frac{\partial b_1}{\partial z} = k_1 b_1 + \int \tilde{T}_{1,2,3,4} b_2^* b_3 b_4 \delta_{1+2-3-4} d\omega_2 d\omega_3 d\omega_4, \tag{70}$$

where the coupling coefficient takes the following form:

$$\tilde{T}_{1,2,3,4} = T_{1,2,3,4} + W_{1,2,3,4}, \tag{71}$$

with $W_{1,2,3,4}$ given in the appendix. Essentially, $\tilde{T}_{1,2,3,4}$ contains also some information about the non resonant three-wave interactions: physically speaking, it could be

said that the long time behaviour of non-resonant three-wave interactions leads to resonant four-wave interactions. Note once more that Eqs. (59) and (70) are written as evolution equations in space and not in time as Eq. (24). Nonetheless, it has been shown in [22] that also for surface gravity waves it is possible to derive a Zakharov equation that evolves in space.

Following the procedure explained in Sect. 4.2.1, the NLS equation can also be derived from Eq. (70); the only difference with respect the previous calculation is that now $\gamma = \tilde{T}_{0,0,0,0}$. Effect of three-wave interactions may be important: in surface gravity waves, such terms may reduce the strength of the nonlinearity and, below a critical value of the wave number (for a given water depth), the NLS equation becomes of defocusing type.

4.4 The Stokes Expansion in Optical Waves

The canonical transformation hides asymptotic nonlinear stationary solutions of the Maxwell equation for a non-resonant $\chi^{(2)}$ medium. In order to appreciate that, for simplicity, we consider the transformation up to second-order. Taking into account the relation (42) between the *normal* variable and the electric field, E, we can write

$$E(z,t) = \int E(z,\omega)e^{-i\omega t}d\omega = i\int \frac{|\omega|}{\sqrt{2k(\omega)}}\left[a(\omega,z) + a(-\omega,z)\right]e^{-i\omega t}d\omega + \ldots \tag{72}$$

We consider a monochromatic wave solution of the form:

$$b(\omega,z) = |b_0|\delta(\omega-\omega_0)e^{ik_0 z} \tag{73}$$

Introducing the solution in the canonical transformation, Eq. (68), up to second-order, after some lengthy algebra we get:

$$E(z,t) = \beta E_0^2 + E_0\cos(k_0 z - \omega_0 t) + \alpha E_0^2\cos(2(k_0 z - \omega_0 t)) \tag{74}$$

where

$$E_0 = \frac{2|\omega_0|}{\sqrt{2k_0}}|b_0|^2 \tag{75}$$

$$\begin{aligned}\alpha &= \left(A^{(1)}_{2\omega_0,\omega_0,\omega_0} + A^{(3)}_{-2\omega_0,\omega_0,\omega_0}\right)\frac{2k_0}{\sqrt{2k_{2\omega_0}}|\omega_0|}\\ \beta &= \lim_{\epsilon\to 0}\left(A^{(2)}_{\epsilon,\omega_0,\omega_0} + A^{(2)}_{-\epsilon,\omega_0,\omega_0}\right)\frac{k_0|\epsilon|}{\sqrt{2k_\epsilon}|\omega_0^2|}.\end{aligned} \tag{76}$$

Equation (74) is a stationary weakly nonlinear solution of the Maxwell equation in a $\chi^{(2)}$ medium. It corresponds to the second-order travelling wave solution found by Stokes [23], for the Euler equation for surface gravity waves. Note that the second-harmonic travels at the speed of the fundamental wave, i.e. it does not obey to the linear dispersion relation. A zero frequency contribution also appears in the solution: its value is related to the nonlinear response of the material as $\omega \to 0$. This delicate issue, related to optical rectification [17], will be addressed separately in the near future.

5 Discussion and Conclusions

Our aim has been to build a bridge between optics and hydrodynamics on a more general framework than the NLS equation. Indeed, in the past the latter has provided very interesting insights, especially in the field of rogue waves where it has been shown that its analytical solutions can be observed with some degree of accuracy both in hydrodynamics and in optics [24–27]. Here, the perspective discussed is more general and it is based on the similarity between the Maxwell equations in a medium and the Euler equations for surface waves once they are written in the so-called *normal* variables. Such variables, introduced by Zakharov [3] in the field of ocean waves, are very powerful and convenient for a number of reasons, see [28]. In our context, once the equations are written in such variables, they appear formally identical (the dispersion relation and the coefficient in front of the nonlinear terms are different), compare Eqs. (19) and (43). In general, in nonlinear optics there are some degrees of freedom in the dynamics because the dispersion relation can be changed and, according to it, different phenomena can be observed. For example, the dispersion relation can be chosen in such a way that three-wave interactions are in resonance (phase-matched condition). In this case we have shown that it is straightforward to derive simpler models such as the Second-Harmonic Generation model or the Three-Wave System. Three-wave resonant interactions, although accessible for capillary waves, are forbidden for surface gravity waves due to the concavity of the dispersion relation. In this regime, expanding the dispersion relation and the nonlinear coefficients in the nonlinear terms for long waves leads to equation of the Korteweg-De Vries type (see the contributions by T. Grava and the one by M. Conforti and S. Trillo in the present volume). The result is obtained when the dispersion relation is an odd function and becomes linear as $k \to 0$.

If three-wave resonances are absent, then the so-called Zakharov equation, very well known in the context of surface gravity waves, can be derived also in optics. This is a very general equation that has no limitation on the spectral bandwidth; moreover, it is a very good starting point for a statistical description of four-wave interactions [29], see also the contributions by P. Janssen, by Shrira and by Picozzi et al. in the present volume. The derivation of the NLS equation is then straightforward. Higher-order approximations, which includes terms of self-steepening and third-order dispersion, can be derived if the dispersion relation is

expanded to third-order. The canonical transformation adopted to remove the non resonant term has a very interesting physical meaning: indeed, it is possible to derive from it the so-called Stokes expansion.

Acknowledgements Miguel Onorato and Fabio Baronio were supported by MIUR Grant PRIN 2012BFNWZ2. Dr. B. Giulinico and F. Giardini are also acknowledged for discussions during the early stages of this work. Amin Chabchoub acknowledges support from the Burgundy Region, The Association of German Engineers (VDI) and the Japan Society for the Promotion of Science (JSPS).

Appendix

Coupling coefficient of the Zakharov equation (70) in optical waves in the presence of χ^2 and χ^3 media:

$$\tilde{T}_{1,2,3,4} = T_{1,2,3,4} + W_{1,2,3,4}, \tag{77}$$

with

$$\begin{aligned} W_{1,2,3,4} = &-V_{1,3,1-3}V_{4,2,4-2}\left[\frac{1}{k_3+k_{1-3}-k_1}+\frac{1}{k_2+k_{4-2}-k_4}\right] \\ &- V_{2,3,2-3}V_{4,1,4-1}\left[\frac{1}{k_3+k_{2-3}-k_2}+\frac{1}{k_1+k_{4-1}-k_4}\right] \\ &- V_{1,4,1-4}V_{3,2,3-2}\left[\frac{1}{k_4+k_{1-4}-k_1}+\frac{1}{k_2+k_{3-2}-k_3}\right] \\ &- V_{2,4,2-4}V_{3,1,3-1}\left[\frac{1}{k_4+k_{2-4}-k_2}+\frac{1}{k_1+k_{3-1}-k_3}\right] \\ &- V_{1+2,1,2}V_{3+4,3,4}\left[\frac{1}{k_{1+2}-k_1-k_2}+\frac{1}{k_{3+4}-k_3-k_4}\right] \\ &- V_{-1-2,1,2}V_{-3-4,3,4}\left[\frac{1}{k_{1+2}+k_1+k_2}+\frac{1}{k_{3+4}+k_3+k_4}\right]. \end{aligned} \tag{78}$$

References

1. Benney, D., Newell, A.: Propagation of nonlinear wave envelopes. J. Math. Phys. **46**(2), 133 (1967)
2. Hasimoto, H., Ono, H.: Nonlinear modulation of gravity waves. J. Phys. Soc. Jpn. **33**(3), 805–811 (1972)
3. Zakharov, V.: Stability of period waves of finite amplitude on surface of a deep fluid. J. Appl. Mech. Tech. Phys. **9**, 190–194 (1968)

4. Zakharov, V.: Instability of self-focusing of light. Sov. Phys. JETP **26**(5), 994 (1968)
5. Chabchoub, A., Kibler, B., Finot, C., Millot, G., Onorato, M., Dudley, J., Babanin, A.: The nonlinear schrödinger equation and the propagation of weakly nonlinear waves in optical fibers and on the water surface. Ann. Phys. **361**, 490–500 (2015)
6. Ablowitz, M.J.: Nonlinear Dispersive Waves: Asymptotic Analysis and Solitons, vol. 47. Cambridge University Press, Cambridge (2011)
7. Krasitskii, V.: On reduced equations in the Hamiltonian theory of weakly nonlinear surface waves. J. Fluid Mech. **272**, 1–20 (1994)
8. Janssen, P.: On some consequences of the canonical transformation in the hamiltonian theory of water waves. J. Fluid Mech. **637**(1), 1–44 (2009)
9. Janssen, P.A.E.M.: Nonlinear four–wave interaction and freak waves. J. Phys. Oceanogr. **33**(4), 863–884 (2003)
10. Annenkov, S.Y., Shrira, V.I.: Numerical modeling of water–wave evolution based on the Zakharov equation. J. Fluid. Mech. **449**, 341–371 (2001)
11. Annenkov, S.Y., Shrira, V.I.: Evolution of kurtosis for wind waves. Geophys. Res. Lett. **36**, L13603 (2009)
12. Amiranashvili, S., Demircan, A.: Hamiltonian structure of propagation equations for ultrashort optical pulses. Phys. Rev. A **82**(1), 013812 (2010)
13. Amiranashvili, S.: Hamiltonian framework for short optical pulses. In: New Approaches to Nonlinear Waves. Springer, Cham (2016), pp. 153–196
14. Janssen, P.A.E.M.: The Interaction of Ocean Waves and Wind. Cambridge University Press, Cambridge (2004)
15. Janssen, P.A.E.M., Onorato, M.: The intermediate water depth limit of the Zakharov equation and consequences for wave prediction. J. Phys. Oceanogr. **37**, 2389–2400 (2007)
16. Gramstad, O., Trulsen, K.: Hamiltonian form of the modified nonlinear schrödinger equation for gravity waves on arbitrary depth. J. Fluid Mech. **670**, 404–426 (2011)
17. Boyd, R.W.: Nonlinear Optics. Academic, London (2003)
18. Agrawal, G.P.: Nonlinear Fiber Optics. Academic, San Diego (2007)
19. Baronio, F., Conforti, M., Degasperis, A., Lombardo, S.: Rogue waves emerging from the resonant interaction of three waves. Phys. Rev. Lett. **111**(11), 114101 (2013)
20. Zakharov, V., Manakov, S.: Resonant interaction of wave packets in nonlinear media. Zh. Eksp. Teor. Fiz. Pisma Red **18**, 413 (1973)
21. Craik, A.D.: Wave Interactions and Fluid Flows. Cambridge University Press, Cambridge (1988)
22. Kit, E., Shemer, L.: Spatial versions of the Zakharov and Dysthe evolution equations for deep-water gravity waves. J. Fluid Mech. **450**, 201–205 (2002)
23. Stokes, G.G.: On the theory of oscillatory waves. Trans. Camb. Philos. Soc. **8**, 441–473 (1847)
24. Chabchoub, A., Hoffmann, N., Akhmediev, N.: Rogue wave observation in a water wave tank. Phys. Rev. Lett. **106**(20), 204502 (2011)
25. Kibler, B., Fatome, J., Finot, C., Millot, G., Genty, G., Wetzel, B., Akhmediev, N., Dias, F., Dudley, J.: Observation of Kuznetsov-Ma soliton dynamics in optical fibre. Sci. Rep. **2**, 463 (2012)
26. Kibler, B., Fatome, J., Finot, C., Millot, G., Dias, F., Genty, G., Akhmediev, N., Dudley, J.: The Peregrine soliton in nonlinear fibre optics. Nat. Phys. **6**(10), 790–795 (2010)
27. Kibler, B., Chabchoub, A., Gelash, A., Akhmediev, N., Zakharov, V.: Superregular breathers in optics and hydrodynamics: omnipresent modulation instability beyond simple periodicity. Phys. Rev. X **5**(4), 041026 (2015)
28. Zakharov, V.E., Kuznetsov, E.A.: Hamiltonian formalism for nonlinear waves. Physics-Uspekhi **40**(11), 1087–1116 (1997)
29. Nazarenko, S.: Wave Turbulence, vol. 825. Springer, Heidelberg (2011)

Integrability in Action: Solitons, Instability and Rogue Waves

Antonio Degasperis and Sara Lombardo

Abstract Integrable nonlinear equations modeling wave phenomena play an important role in understanding and predicting experimental observations. Indeed, even if approximate, they can capture important nonlinear effects because they can be derived, as amplitude modulation equations, by multiscale perturbation methods from various kind of wave equations, not necessarily integrable, under the assumption of weak dispersion and nonlinearity. Thanks to the mathematical property of being integrable, a number of powerful computational techniques is available to analytically construct special interesting solutions, describing coherent structures such as solitons and rogue waves, or to investigate patterns as those due to shock waves or behaviors caused by instability. This chapter illustrates a selection of these techniques, using first the ubiquitous Nonlinear Schrödinger (NLS) equation as a prototype integrable model, and moving then to the Vector Nonlinear Schrödinger (VNLS) equation as a natural extension to wave coupling.

1 Introduction to Integrability and Solitons

Many nonlinear partial differential equations which model dispersive wave propagation possess *solitary wave* solutions. In most physical contexts these special solutions describe the motion in one, two or three-dimensional space of a *bump*, possibly modulating a carrier plane-wave, whose profile depends on the particular nonlinear terms which appear in the wave equation itself. Among the nonlinear wave equations which have been derived in many physical applications, we consider here those special ones which prove to be *integrable* and model wave motion in 1-dimensional space. The solitary wave solutions of integrable equations, because of their exceptional mathematical properties, have been termed *solitons* [1]. The first

A. Degasperis
Dipartimento di Fisica, "Sapienza" Università degli Studi di Roma, Roma, Italy
e-mail: antonio.degasperis@uniroma1.it

S. Lombardo (✉)
Department of Mathematics and Information Sciences, Northumbria University, Newcastle upon Tyne, UK
e-mail: sara.lombardo@northumbria.ac.uk

M. Onorato et al. (eds.), *Rogue and Shock Waves in Nonlinear Dispersive Media*,
Lecture Notes in Physics 926, DOI 10.1007/978-3-319-39214-1_2

observation of a soliton dates back to 1834 (John Scott Russell's *wave of translation* [2]). Among the peculiar properties which are distinctive of integrability, we point out the following (see also Sect. 2):

- existence and explicit construction of infinitely many independent conservation laws;
- existence and explicit construction of N-soliton solutions, for any N;
- existence of a nonlinear generalization of the Fourier transform, the *Spectral transform*, which provides a tool to investigate the solution of special initial-boundary value problems.

Because of these properties, integrable nonlinear wave equations may be understood as the limit to *infinitely many* degrees of freedom of classical Liouville-integrable dynamical systems. Some of these integrable wave equations are relevant as approximate models in various physical contexts. In these cases one may say that Nature and Mathematics go well hand in hand as the powerful methods of integrability allow for analytical description/prediction of wave behaviors.

The reader who is not familiar with the theory of integrable systems, and, in particular, with the theory of solitons, may find it of interest to have a preliminary look at the following rather long, and yet partial, list of model equations of physical interest which have been proven to be integrable (t is the evolution variable and x is the space coordinate, while partial differentiation is indicated by a subscript)

- Korteweg-de Vries (KdV) equation:

$$u_t - u_{xxx} = 6uu_x \tag{1}$$

- Benjamin-Ono (BO) equation:

$$u_t - Hu_{xx} = uu_x \tag{2}$$

where the Hilbert operator H is defined as $Hf(x) = \frac{1}{\pi}\mathscr{P}\int_{-\infty}^{\infty} dy \frac{f(y)}{y-x}$

- complex modified Korteweg de Vries (cmKdV) equation:

$$u_t - u_{xxx} = 6s|u|^2 u_x\,, \quad s = \pm 1 \tag{3}$$

- Sine-Gordon (SG) equation:

$$u_{tt} - u_{xx} = -\sin u \tag{4}$$

- Nonlinear Schrödinger (NLS) equation:

$$iu_t + u_{xx} = 2s|u|^2 u\,, \quad s = \pm 1 \tag{5}$$

(continued)

- Long Wave-Short Wave (LWSW) equation:

$$iu_t + u_{xx} + vu = 0\,, \quad v_t = (|u|^2)_x \tag{6}$$

- Derivative Nonlinear Schrödinger (DNLS) equation:

$$iu_t + u_{xx} = is(|u|^2 u)_x\,, \quad s = \pm 1 \tag{7}$$

- Massive Thirring Model (MTM):

$$\begin{aligned} iu_{1t} + iu_{1x} - u_2 &= |u_2|^2 u_1 \\ iu_{2t} - iu_{2x} - u_1 &= |u_1|^2 u_2 \end{aligned} \tag{8}$$

- Vector Nonlinear Schrödinger (VNLS) equation:

$$iu_{jt} + u_{jxx} = 2\left(\sum_{n=1}^{N} s_n |u_n|^2\right) u_j\,, \quad j = 1, \cdots, N \tag{9}$$

  where $s_n = \pm 1$. For $N = 2$, $s_1 = s_2 = -1$ this is the Manakov model.
- Three Wave Resonant Interaction (3WRI) equations:

$$\begin{aligned} u_{1t} + V_1 u_{1x} &= u_2^* u_3^* \\ u_{2t} + V_2 u_{2x} &= -u_1^* u_3^* \\ u_{3t} + V_3 u_{3x} &= u_1^* u_2^* \end{aligned} \tag{10}$$

  where the asterisk denotes complex conjugation and where V_1, V_2 and V_3 are real constants.

All these nonlinear integrable equations have the common property of being the condition that two *linear* first order homogeneous ordinary differential equations, one with respect to the variable x and the other with respect to the variable t, be compatible with each other. This pair of linear equations is commonly referred to as *Lax pair*. In order to clarify and detail this scheme, we give here few examples, which may serve as well as guidelines for further computational exercises. In general a linear homogeneous ordinary differential equation with respect to the variable y takes the form

$$\psi_y = M(y)\psi\,, \quad \psi = \psi(y)\,, \tag{11}$$

where M is a $N \times N$ matrix whose entries are functions of the independent variable y, and $\psi(y)$ is a N-dimensional vector solution. Thus in this notation a Lax pair reads as

$$\psi_x = X\psi\,, \quad \psi_t = T\psi\,, \qquad \psi = \psi(x,t)\,, \tag{12}$$

where X and T are $N \times N$ matrices and the vector ψ is required to solve both equations. It is plain that, for a generic choice of $X(x,t)$ and $T(x,t)$, only the trivial solution $\psi = 0$ solves the pair of Eqs. (12), whereas a non vanishing solution ψ exists if the compatibility condition $\psi_{xt} = \psi_{tx}$ holds true, namely, as implied by (12), if the matrices X, T satisfy the equation

$$X_t + XT = T_x + TX, \quad \text{or} \quad X_t - T_x + [X,T] = O\,, \tag{13}$$

where $[A\,,\,B] = AB - BA$ and O stands for the zero matrix. It is moreover crucial for the integrability that the matrices X, T depend also on a complex variable λ, the so-called *spectral variable*, say $X = X(x,t,\lambda)$, $T = T(x,t,\lambda)$, with the additional strong requirement that the compatibility condition (13) holds for *any* value of λ. The following few explicit examples illustrate how indeed some of the integrable equations in the list above follow from compatibility conditions of the form (13). To this aim let X be the 2×2 traceless matrix

$$X = i\lambda\sigma_3 + Q(x,t)\,, \quad \sigma_3 = \begin{pmatrix} 1 & 0 \\ 0 & -1 \end{pmatrix}\,, \quad Q(x,t) = \begin{pmatrix} 0 & v(x,t) \\ u(x,t) & 0 \end{pmatrix}\,. \tag{14}$$

This is the simplest choice since $X(x,t,\lambda)$ is polynomial of first degree in the spectral variable λ while its dependence on x and t comes through the functions $u(x,t)$ and $v(x,t)$ which will eventually play the role of wave fields. As for the second equation of the Lax pair (12), the matrix $T(x,t,\lambda)$ may be taken as a third degree polynomial

$$T = \lambda^3 T_3 + \lambda^2 T_2 + \lambda T_1 + T_0\,. \tag{15}$$

In this case both sides of the compatibility equation (13) are fourth degree polynomials in λ so that Eq. (13) yields five matrix algebraic/differential equations which can be easily solved (this step being left to the diligent reader). The solution of these equations can be conveniently given as the following expression of the four

matrix coefficients T_j [see (15)]:

$$\begin{aligned} T_3 &= -4ic_3\sigma_3 \\ T_2 &= -4c_3Q + 2ic_2\sigma_3 \\ T_1 &= 2ic_3\sigma_3(Q_x - Q^2) + 2c_2Q \\ T_0 &= c_3([Q\,,\, Q_x] + Q_{xx} - 2Q^3) - ic_2\sigma_3(Q_x - Q^2) \end{aligned} \tag{16}$$

while the additional fifth equation

$$Q_t = c_3(Q_{xxx} - 6Q^2Q_x) - ic_2\sigma_3(Q_{xx} - 2Q^3) \tag{17}$$

yields the dispersive nonlinear wave equation for the matrix $Q(x, t)$, namely for its two entries $u(x, t)$, $v(x, t)$. The two parameters c_3 and c_2 are arbitrary. It is now left to the reader to verify that the KdV equation, the cmKdV equation and the NLS equation which appear in the list of integrable wave equations given above are just special cases of the evolution equation (17). Precisely, the choice $c_3 = 1$, $c_2 = 0$ and the reduction condition $v = -1$ yields the KdV equation (1), while setting again $c_3 = 1$, $c_2 = 0$ but with the condition $v = -su^*$, $s = \pm 1$, leads to the cmKdV equation (3), and finally the NLS equation (5) corresponds to the choice $c_3 = 0$, $c_2 = 1$ together with the reduction $v = su^*$, $s = \pm 1$.

Different choices of the two matrices X, T which appear in the Lax pair (12) generate, by the same scheme based on the compatibility equation (13), different integrable nonlinear (systems of) partial differential equations. For instance, if X and T are still 2×2 but their dependence on the spectral variable λ is rational rather than polynomial, one may obtain the SG equation (4) and the MTM (8). If instead X and T are higher rank $R > 2$, the 3WRI system (10), the LWSW (6) equations as well as the Manakov model [(9) for $N = 2$], are obtained for $R = 3$, while the rank $R = N + 1$ is required to derive the system of N coupled NLS equations (9).

Once a nonlinear wave equation has been associated to a Lax pair according to the method we have sketched here, what is this association good for?

The answer to this question is contained in the huge collection of research results which accumulated during the last half-century. Thus we conclude this section with a list of works on the subject which is neither exhaustive nor complete, but which may guide the interested reader in the vast land of integrability and its applications. A starting point for a reader with no previous exposure to integrability are the books [3, 4] which present an overview of solitons in applications. These are complemented by more classical (and at times more detailed) textbooks such as [5–13]. An overview on the origin of soliton theory and a fairly complete set of references of its origins can be found in [14]. A more mathematical introduction to the theory of integrable systems is presented in [15]. This text complements collections such as [16, 17] and classical textbooks such as [18, 19]. In [20] the *universality* of integrable systems is well explained, whereas the link with multiple scale analysis is given in [21] and reference therein. An introduction to the theory of

nonlinear waves can be found in the monographs [22–25]. As the NLS equation plays a central role in our exposition, we draw the reader's attention to a few monographs on this fundamental model [19, 26–28].

2 Integrability in Action: The NLS Equation as Study Case

The Nonlinear Schrödinger (NLS) equation

$$iu_t + u_{xx} = 2s|u|^2 u\,, \quad s = \pm 1\,, \tag{18}$$

has been first derived [29] in optics in the self-focusing case $s = -1$. However it arose again and again in different physical contexts, and it has been then recognized as a *universal* equation that models amplitude modulation of a quasi-monochromatic wave due to weak nonlinearities. Its universality stems from its derivation by multiscale perturbation theory [20, 21, 30, 31] from very large families of nonlinear dispersive wave equations (the nonlinear terms being treated as perturbation of the linear ones) which includes for instance Maxwell equations in Kerr and χ_2 media, Euler equations in ocean physics and Einstein gravitational field equations, among many others. In particular it can be derived by multiscale perturbation also from integrable equations, e.g. from the SG, KdV and cmKdV equations (see Sect. 1). Though its integrability has been discovered independently [32], from this very last fact one can predict that indeed the NLS equation should be integrable itself [20]. The aim of this section is to shortly illustrate a number of important consequences of the Lax pair associated to the NLS equation. In particular, we first show how to derive *infinitely many* local conservation laws. It is also shown here that the technique of transforming the Lax pair by a *Darboux transformation* leads to the algebraic construction, from a known solution, of a novel solution of the NLS equation.

2.1 Conservation Laws from the Lax Pair

Let us first consider how to obtain from the Lax pair an infinite sequence of local conservation laws,

$$\rho_t^{(n)} + f_x^{(n)} = 0\,, \quad n = 1, 2, \ldots, \tag{19}$$

where the functions $\rho^{(n)}(x,t)$ and $f^{(n)}(x,t)$ are the conserved densities and, respectively, the corresponding currents. The method we follow here is applicable to solutions of the NLS equation (18) which vanish sufficiently fast as the variable $|x|$ goes to infinity, namely $u(x,t) \to 0$ as $x \to \pm\infty$. The extension to different boundary conditions is possible with some extra technical efforts. The Lax pair

associated to the NLS equation is given by (12) where the matrices X and T are respectively given by (14), where $v = su^*$, and by (15) and (16) with $c_3 = 0$, $c_2 = 1$. Since it is convenient to proceed by performing our computation in the algebra of matrices, we consider now the 2×2 matrix $\Psi(x,t,\lambda)$ whose column vectors are two linearly independent solutions of the Lax pair, namely

$$\Psi_x = X\Psi\,, \quad \Psi_t = T\Psi\,. \tag{20}$$

When $x \to \pm\infty$ the matrix Q vanishes and the matrix solution Ψ goes to a solution $\Psi^{(\pm)}$ of the Lax pair with $Q = 0$. Just for mere sake of convenience, we choose the solution Ψ which satisfies the boundary condition

$$\Psi \to \Psi^{(-)} = \exp[i\lambda\sigma_3(x + 2\lambda t)]\,, \quad x \to -\infty\,. \tag{21}$$

It is also convenient to introduce the matrix $\Phi(x,t,\lambda) = \Psi(\Psi^{(-)})^{-1}$ which satisfies the pair of equations

$$\Phi_x = i\lambda[\sigma_3\,,\,\Phi] + Q\Phi\,, \quad \Phi_t = 2i\lambda^2[\sigma_3\,,\,\Phi] + (2\lambda Q + i\sigma_3 Q^2 - i\sigma_3 Q_x)\Phi\,. \tag{22}$$

More conveniently to our purposes, we rewrite these equations in the following form

$$\begin{cases} (\sigma_3\Phi)_x = i\lambda(\Phi - \sigma_3\Phi\sigma_3) + \sigma_3 Q\Phi \\ (\sigma_3\Phi)_t = 2i\lambda^2(\Phi - \sigma_3\Phi\sigma_3) + (2\lambda\sigma_3 Q + iQ^2 - iQ_x)\Phi \end{cases} \tag{23}$$

which shows that the two functions

$$R(x,t,\lambda) = \mathrm{tr}(\sigma_3 Q\Phi)\,, \quad F(x,t,\lambda) = -\mathrm{tr}[(2\lambda\sigma_3 Q + iQ^2 - iQ_x)\Phi]\,, \tag{24}$$

where $\mathrm{tr}(M)$ stands for the trace of the matrix M, satisfy, by cross-differentiating the two Eqs. (23), the conservation equation

$$R_t + F_x = 0\,. \tag{25}$$

Note that this continuity equation is direct consequence of the Lax pair (20) and that it depends on the spectral variable λ through the matrix Φ [see the definition (24)]. It now remains to extract from this last Eq. (25) conserved densities and currents whose expression contains only the solution $u(x,t)$ of the NLS equation (18). This step is done via the following theorem:

Theorem 1 *The matrix $\Phi(x,t,\lambda)$ which solves the system (22), with the boundary value $\Phi \to \boldsymbol{1}$ as $x \to -\infty$, has the following asymptotic expansion as $|\lambda|$ becomes very large, say around the point at infinity of the λ-plane,*

$$\Phi = \boldsymbol{1} + \frac{1}{\lambda}\Phi_1 + \frac{1}{\lambda^2}\Phi_2 + \frac{1}{\lambda^3}\Phi_3 + \ldots \tag{26}$$

where the matrix coefficients Φ_n depend only on x and t.

The computation of these coefficients Φ_n can be done recursively by inserting the expansion (26) into the first of the differential equations (22), and by splitting the matrix Φ into its diagonal part $\Phi^{(d)}$ and its off-diagonal part $\Phi^{(o)}$, namely $\Phi = \Phi^{(d)} + \Phi^{(o)}$. By taking into account the boundary condition $\Phi \to \mathbf{1}$ as $x \to -\infty$ [see (21)], the upshot of these computations is summarized by the following formulae (in self evident notation)

$$\begin{aligned} &\Phi_0^{(d)} = \mathbf{1}\,, \quad \Phi_0^{(o)} = 0\,, \quad \Phi_n^{(d)} = \textstyle\int_{-\infty}^{x} dy\, Q(y,t)\, \Phi_n^{(o)}(y,t)\,, \quad n \geq 1 \\ &\Phi_{n+1}^{(o)} = \tfrac{1}{2i}\sigma_3(\Phi_{nx}^{(o)} - Q\Phi_n^{(d)})\,, \quad n \geq 0\,. \end{aligned} \tag{27}$$

Note that this recursion equations generate the expression of all coefficients $\Phi_n^{(d)}$ and $\Phi_n^{(o)}$ in a way that is well suitable to symbolic computation. Equation (25) clearly yields infinitely many local conservation laws via the expansions

$$R = \frac{1}{\lambda}R_1 + \frac{1}{\lambda^2}R_2 + \frac{1}{\lambda^3}R_3 + \dots\,, \quad F = \frac{1}{\lambda}F_1 + \frac{1}{\lambda^2}F_2 + \frac{1}{\lambda^3}F_3 + \dots\,, \tag{28}$$

namely

$$R_{nt} + F_{nx} = 0\,, \quad n \geq 1\,. \tag{29}$$

Here we give the first three conserved quantities and leave the computation of the currents to the interested reader. It is convenient to define the conserved densities as

$$\rho_n = is\, 2^{n-1} R_n = is\, 2^{n-1} \mathrm{tr}(\sigma_3 Q\, \Phi_n^{(o)})\,, \quad n \geq 1\,, \tag{30}$$

and the time-independent quantities, i.e. the constants of the motion, as

$$C_n = \int_{-\infty}^{+\infty} dx\, \rho_n(x,t)\,, \quad n \geq 1\,, \tag{31}$$

to arrive at the well known expressions

$$C_1 = \int_{-\infty}^{+\infty} dx |u|^2\,, \quad C_2 = \int_{-\infty}^{+\infty} dx\, \mathrm{Im}(u u_x^*)\,, \quad C_3 = H - \frac{1}{6}C_1^3\,, \tag{32}$$

where the functional

$$H = \int_{-\infty}^{+\infty} dx (|u_x|^2 + s|u|^4)\,, \tag{33}$$

is the standard Hamiltonian which yields the NLS equation (18) via the Hamilton equation

$$u_t = -i\frac{\delta H}{\delta u^*}\,. \tag{34}$$

2.2 The Initial Value Problem and Particular Solutions

Before proceeding further we shortly comment on the way the Lax pair (20) gives the method of investigating the initial value problem $u(x,0) \to u(x,t)$ for the NLS equation (18). This method generalizes the well known Fourier analysis as applied to a linear equation with constant coefficients, for instance the linear Schrödinger equation $iu_t + u_{xx} = 0$. In the linear case, one introduces the Fourier Transform (*FT*) of the solution

$$\hat{u}(k,t) = \int_{-\infty}^{+\infty} dx\, e^{ikx} u(x,t) \tag{35}$$

together with its simple time dependence $\hat{u}(k,t) = \hat{u}(k,0)e^{-ik^2t}$ and then one performs the chain of steps

$$u(x,0) \;\to\; \hat{u}(k,0) \;\to\; \hat{u}(k,t) \;\to\; u(x,t).$$

Note that in the last step it is essential that the Fourier map $u(x,t) \to \hat{u}(k,t)$ (35) be invertible. Note also that we are dealing here with the class of solutions $u(x,t)$ which vanish as $|x| \to \infty$ sufficiently fast so that their Fourier integral is well defined. The initial value problem for the NLS equation (18) can be investigated in a similar way. In this case the Fourier transform has to be replaced by a new transform known as the *spectral transform* (or scattering transform) (*ST*). The map $u(x,t) \to ST$ which takes the solution $u(x,t)$ into its spectral transform *ST* is computed by considering the first equation of the Lax pair (20) as the eigenvalue problem [see (14)]

$$L\Psi = \lambda\Psi\,, \quad L \equiv -i\sigma_3\partial_x + i\sigma_3 Q\,, \tag{36}$$

for the differential operator L. While we refer the reader to textbooks, e.g. [6, 12], for details, we limit ourself to pinpoint here differences and similarities between the *ST* and the *FT*. In the *FT* (35) the spectral variable k takes its values on the real line, which is also the continuum spectrum of the differential operator L. In contrast, the *ST* is defined not only on the continuum spectrum of L but also, if it exists, on its discrete spectrum which consists of a finite number of complex values of k. The solutions of the NLS equation which correspond to these discrete eigenvalues are the soliton solutions. Like the *FT*, also the *ST* has the similarly simple and explicit exponential dependence on the time variable t, namely the nonlinear mapping

$u(x,t) \to ST(t)$ transforms the nonlinear dynamics of the NLS equation into a trivial linear dynamics. It is moreover easy to show that the approximate expression of the ST obtained by linearizing the nonlinear transformation $u(x,t) \to ST(t)$ reduces, on the continuum spectrum, to the FT. Similarly to the linear case, also for the NLS equation the solution of the initial value problem goes via the steps

$$u(x,0) \;\to\; ST(0) \;\to\; ST(t) \;\to\; u(x,t),$$

the last one requiring the (hard) task of reconstructing u from its ST. The problem of inverting the nonlinear map $u(x) \to ST$ is very important in many applications, e.g. in medical imaging techniques and earth's crust geophysics, and it is a research field on its own known as *inverse problem*. The application of the mathematical methods of the inverse problem to the solution of nonlinear integrable wave equations is a well established technique known as *IST*, namely Inverse Spectral Transform, see e.g. [12], or Inverse Scattering Transform, see e.g. [6, 13].

The physical significance of the solutions corresponding to the continuum spectrum is of dispersive wave packets in contrast with the solutions corresponding to the discrete spectrum which are instead multi-soliton solutions. In this respect we notice that in the defocusing case $s = 1$, the operator L [see (36)] is formally Hermitian, $L^\dagger = L$, with the implication that all eigenvalues are real; in this case therefore no discrete spectrum is possible and the defocusing NLS equation has no soliton solutions. This is not the case for the focusing NLS with $s = -1$ which possesses *bright* soliton solutions since $L^\dagger \neq L$. These conclusions drastically change if the solutions of the NLS equation do *not* vanish as $|x|$ goes to infinity. In the class of solutions which are required to behave as plane waves (see e.g. (47)) with $|u(x,t)| \to a =$ constant amplitude as $|x| \to \infty$, the ST of u has been as well defined and the method of solving the initial value problem has been extended to cover this class of solutions in both the defocusing case $s = 1$ [19, 33–35] and in the focusing case $s = -1$ [36]. In the defocusing case the NLS equation possesses soliton solutions which behave as plane waves at the boundary. These solutions are known as *dark* (grey or black) solitons. This occurs because the continuum spectrum is the real axis with the finite gap $-a < \lambda < a$ within which real discrete eigenvalues may exist (see e.g. Fig. 1, where $a = 1$). On the other hand, in the focusing case, in addition to the continuum spectrum, a complex discrete spectrum exists (see Sect. 3).

The spectral transform approach is able not only to deal with the initial value problem but also to explicitly construct those solutions which correspond to a purely discrete spectrum, namely the N-soliton solutions for any N. These special, yet important, solutions can be obtained also by a simpler direct algebraic technique which is known as the *Darboux transformation* (e.g. [37–40]), or *Dressing method* (e.g. [10, 41, 42]).

We conclude this section by shortly illustrating this method, and by providing the expression of the one soliton solution for solitons traveling in vacuum as well as over a continuous wave background.

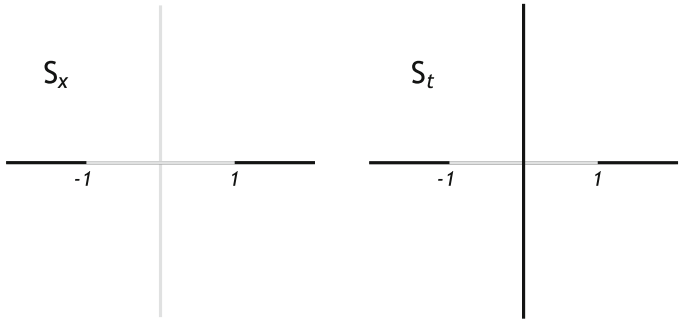

Fig. 1 Defocusing NLS: $S_x = x$-part spectrum/$S_t = t$-part spectrum of $u^{(0)} = \exp(-2it)$

Before doing this we point out that, as a general rule which applies to many other wave models, the analytic expression of any explicitly known wave solution depends not only on the variables x, t but also on a number of parameters which may be related to physically relevant properties and features. In the following however, we omit to show in the expression of the soliton solutions those arbitrary parameters which can be inserted by taking into account the symmetries of the wave equation. In the present case the following five symmetries, or transformations $u(x,t) \to u'(x,t)$ that leave the NLS equation unchanged, can serve this purpose:

1. x-translation $u'(x,t) = u(x+\xi, t)$
2. t-translation $u'(x,t) = u(x, t+\tau)$
3. phase factor $u'(x,t) = e^{i\theta}u(x,t)$
4. rescaling $u'(x,t) = pu(px, p^2t)$
5. Galilei change of frame $u'(x,t) = e^{i\frac{v}{2}(x-\frac{v}{2}t)}u(x-vt, t)$

The initial step of the Darboux approach consists in linearly transforming the matrix solution of the Lax pair (20). Precisely, if $\Psi^{(0)}$ is a solution of the Lax pair (20) with X, T replaced by $X^{(0)}$, $T^{(0)}$, and consequently Q replaced by $Q^{(0)}$, the Darboux transformation $\Psi^{(0)} \to \Psi$, reads

$$\Psi(x,t,\lambda) = D(x,t,\lambda)\Psi^{(0)}(x,t,\lambda)\,, \tag{37}$$

where D is a 2×2 matrix. We first observe that this linear transformation implies that also the new matrix Ψ satisfies a compatible Lax pair of equations, namely (20), where $X = DX^{(0)}D^{-1} + D_xD^{-1}$ and $T = DT^{(0)}D^{-1} + D_tD^{-1}$. Thus the new matrices X, T satisfy themselves the compatibility equation (13) as a consequence of the compatibility equation $X_t^{(0)} + X^{(0)}T^{(0)} = T_x^{(0)} + T^{(0)}X^{(0)}$ of the original Lax equations. Next one looks for a Darboux matrix $D(x,t,\lambda)$ which satisfies the following (strong) conditions: (1) the new matrices X, T and the original ones $X^{(0)}$, $T^{(0)}$ have the same structure (14) and (15) with (16); (2) the Darboux matrix has a polynomial dependence on the spectral variable λ. To our present purpose we

assume that this polynomial be first degree,

$$D(x,t,\lambda) = \lambda \mathbf{1} - M(x,t)\,, \tag{38}$$

where the matrix $M(x,t)$ has still to be found. To find it we use the symmetry condition

$$\Sigma D^{\dagger}(x,t,\lambda^*)\Sigma D(x,t,\lambda) = d_s(\lambda)\mathbf{1}\,, \tag{39}$$

where $\Sigma = \mathbf{1}$ if $s = -1$ and $\Sigma = \sigma_3$ if $s = 1$, and $d_s(\lambda)$ is a scalar x,t-independent second degree polynomial. This condition follows from the property $Q^{\dagger} = sQ$ [or, equivalently, $v = su^*$, see (14)], and the pair of differential equations

$$D_x + DX^{(0)} = XD\,, \quad D_t + DT^{(0)} = TD\,, \tag{40}$$

which are implied by the Lax equations (20) together with the Darboux transformation (37). Once the matrix M has been computed, inserting the Darboux matrix expression (38) into the first of the two Eqs. (40) yields the expression $Q = Q^{(0)} + i[\sigma_3\,, M]$, or more explicitly and in self-evident notation,

$$u = u^{(0)} - 2i\,M_{21}\,, \tag{41}$$

of the new solution $u(x,t)$ of the NLS equation. This expression can be given an alternative form of more practical use by involving the constant eigenvalues α and α^* of $M(x,t)$, together with their corresponding eigenvectors. While we skip detailing this computation, we limit our consideration here only to the focusing case $s = -1$. Thus, for the focusing NLS equation the Darboux matrix is

$$D(x,t,\lambda) = \lambda\mathbf{1} - \alpha^*\mathbf{1} - (\alpha - \alpha^*)P = \lambda\mathbf{1} - \alpha P - \alpha^*(\mathbf{1} - P)\,, \tag{42}$$

where $P(x,t)$ is the projection matrix

$$P(x,t) = \frac{1}{|z_1|^2 + |z_2|^2}\begin{pmatrix} |z_1|^2 & z_1 z_2^* \\ z_1^* z_2 & |z_2|^2 \end{pmatrix}\,, \tag{43}$$

which projects on the eigenvector $z(x,t)$ of the matrix M (corresponding to the eigenvalue α) with components $z_1(x,t)$ and $z_2(x,t)$. It turns out that this eigenvector z is a vector solution of the original Lax pair with $\lambda = \alpha$, namely

$$z_x = X^{(0)}(x,t,\alpha)z\,, \quad z_t = T^{(0)}(x,t,\alpha)z\,. \tag{44}$$

The expression (41) takes now the more explicit and standard form

$$u = u^{(0)} - 2i(\alpha - \alpha^*)\frac{z_2 z_1^*}{|z_1|^2 + |z_2|^2}\,. \tag{45}$$

Note that here the complex number α has to be strictly complex ($\mathrm{Im}\,\alpha \neq 0$) and that it is going to be an arbitrary parameter in the new solution $u(x,t)$. It should be also noticed that the applicability of the Darboux method obviously requires that the solution $u^{(0)}$ of the NLS equation, as well as the solution $\Psi^{(0)}$ of the corresponding Lax pair, be known. Before going into applications of the Darboux technique, let us summarize the computational scheme in the following steps: (1) fix the known solution $u^{(0)}(x,t)$ and $\Psi^{(0)}(x,t,\lambda)$, (2) give an arbitrary complex value α to the spectral variable, and fix an arbitrary constant vector γ, (3) compute the vector $z(x,t) = \Psi^{(0)}(x,t,\alpha)\gamma$, (4) apply the explicit formula (45). We also note that the constant vector γ in step (3) introduces an arbitrary complex parameter.

The simplest exercise now is the construction of the bright soliton solution. The starting known solution is the vacuum $u^{(0)} = 0$ and the solution obtained via the Darboux method is

$$u = e^{it}\mathrm{sech}(x) \tag{46}$$

for $\alpha = i/2$ and $\gamma = (1\ ,\ 1)$. Moreover, the corresponding operator L (36) possesses two discrete eigenvalues, $\lambda_1 = \alpha = i/2$, $\lambda_2 = \alpha^* = -i/2$ that are the roots of the polynomial $\det D = (\lambda - \alpha)(\lambda - \alpha^*)$, see (42). Consider now the Darboux construction of soliton solutions obtained when $u^{(0)}$ is the continuous wave solution of the focusing NLS equation:

$$u^{(0)}(x,t) = e^{2it}\,. \tag{47}$$

In this case the general formula (45) leads to the expression

$$u = e^{2it}\left[1 + \cosh(\eta)\frac{2\cosh(px) - e^{(\eta+iqt)} - e^{-(\eta+iqt)}}{\cos(qt) - \cosh(\eta)\cosh(px)}\right] \tag{48}$$

where $p = 2\sinh(\eta)$, $q = 2\sinh(2\eta)$. This is a one-parameter family of solutions, the parameter η taking both real values $0 \leq \eta < +\infty$ and imaginary values $\eta = i\mu\,,\ 0 < \mu < +\infty$. As in the previous case the discrete eigenvalues of the Lax equation (36) are on the imaginary axis of the λ-plane, $\lambda_1 = i\cosh(\eta)$, $\lambda_2 = -i\cosh(\eta)$, and are again the roots of $\det D$. Further observations on this solution will be reported in the next section. We finally note that the Darboux technique can be applied in a similar way (with some extra care [43–45]) to the defocusing case. As already mentioned above, in the defocusing regime no bounded solutions are found if $u^{(0)} = 0$, while if $u^{(0)} = \exp(-2it)$ the zeros of $\det D$ are required to be real. The Darboux method can be extended to polynomial Darboux matrices $D(x,t,\lambda)$ of higher degree in λ so as to construct solutions of the NLS

equation which describe the interaction of N solitons (e.g. [46, 47]). Moreover, this method applies as well to other Lax pairs and therefore to other integrable equations, f.i. to the VNLS equation (see Sect. 4) (e.g. [37, 40, 43–45, 48]).

3 NLS Equation: Linear Instability and Rogue Waves

Investigating the linear stability of a given solution $u^{(0)}(x,t)$ of a nonlinear partial differential equation goes via the following standard computational steps: (1) linearizing the given nonlinear equation in the neighborhood of the given solution, (2) finding a complete set of solutions of this linear equation which are everywhere bounded in the space variables, (3) checking the boundedness of all these solutions over the entire time evolution. It is sufficient that some of this complete set of solutions of the linearized equation grow in time with no bound to declare that given solution $u^{(0)}(x,t)$ of the nonlinear equation is linearly unstable. In particular, if the linearized equation is, or may be mapped into, an equation with constant coefficients, then the complete set of its solutions is the set of Fourier (continuous wave) exponentials of the type $\exp[i(kx-\omega t)]$. In such simple case the solution of the nonlinear equation is unstable if there exist real values of k such that the corresponding frequency $\omega(k)$ has a non vanishing and positive imaginary part.

Here we show how the linear stability analysis can be alternatively handled if the nonlinear partial differential equation is integrable. Consistently with the previous section, we consider the integrability properties of the NLS equation (18), in both the defocusing ($s=1$) and focusing ($s=-1$) regimes. Again the basic tool is the Lax pair (20) with (14). Let $u^{(0)}(x,t)$ be the given solution of the NLS equation (18) whose stability we aim to investigate. Then the linearized NLS equation around this solution reads

$$i(\delta u)_t + (\delta u)_{xx} - 2su^{(0)2}(\delta u)^* - 4s|u^{(0)}|^2(\delta u) = 0\,, \tag{49}$$

where the function $\delta u(x,t)$ is the small deviation from the given solution $u^{(0)}$, namely $u = u^{(0)} + \delta u$. Assume now that not only the solution $u^{(0)}(x,t)$ is known, but that it is also known the explicit expression of an invertible matrix solution $\Psi^{(0)}(x,t,\lambda)$,

$$\Psi^{(0)} = \begin{pmatrix} \psi_{11}^{(0)} & \psi_{12}^{(0)} \\ \psi_{21}^{(0)} & \psi_{22}^{(0)} \end{pmatrix}\,, \tag{50}$$

of the Lax pair (20) (with u replaced by $u^{(0)}$). Then the following result provides the link between the linearized equation (49) and the Lax pair.

Theorem 2 *For any value of the variable λ, the function $(\psi_{22}^{(0)}(x,t,\lambda))^2$ satisfies the linearized equation (49).*

Note that, for the vanishing solution $u^{(0)} = 0$, $(\psi_{22}^{(0)})^2 = \exp[-2i\lambda(x + 2\lambda t)]$ coincides with the Fourier mode $\exp[i(kx - \omega t)]$, with $\omega(k) = k^2$ and $k = -2\lambda$, of the linear Schrödinger equation [see (49)]. If $u^{(0)} \neq 0$, in analogy with the previous case, we learn that the solutions $(\psi_{22}^{(0)}(x, t, \lambda))^2$ of the linearized equation (49) play the role of generalized Fourier modes. In this generic case the spectral variable λ runs over the entire spectrum, both continuum and discrete (if any), of the x-part differential equation of the Lax pair [see (36)]. If the solution $u^{(0)}$ is such that its corresponding functions $(\psi_{22}^{(0)}(x, t, \lambda))^2$, for some value of λ in the spectrum, grows with time with no bound, then this solution $u^{(0)}$ is linearly unstable. In general the computations required by this procedure may not be explicitly doable. However for $u^{(0)} = 0$ and $u^{(0)} = \exp(-2ist)$, i.e. for the vacuum and the continuous wave solution, the method can be carried out in explicit form. The linear stability of the vanishing solution is easily established for $s = \pm 1$. As for the continuous wave solution, in both the defocusing $s = 1$ and focusing $s = -1$ regimes, the discrete spectrum is empty and so it remains to compute the continuum spectrum. For the purpose of establishing the stability, it is convenient to compute the spectrum associated to both equations of the Lax pair (20). The x-part spectrum S_x is defined as the set of values of the spectral variable λ such that the corresponding solution $\Psi^{(0)}$ of the Lax equation $\Psi_x^{(0)} = X^{(0)}\Psi^{(0)}$ is bounded on the entire x-axis at any fixed time, and the t-part spectrum S_t is defined via the Lax equation $\Psi_t^{(0)} = T^{(0)}\Psi^{(0)}$ in just the similar way. More explicitly, the Lax pair of equations for the matrix solution (50) reads

$$\begin{cases} \Psi_x^{(0)} = \begin{pmatrix} i\lambda & su^{(0)*} \\ u^{(0)} & -i\lambda \end{pmatrix} \Psi^{(0)} \\ \Psi_t^{(0)} = \begin{pmatrix} 2i\lambda^2 + is|u^{(0)}|^2 & 2\lambda su^{(0)*} - isu_x^{(0)*} \\ 2\lambda u^{(0)} + iu_x^{(0)} & -2i\lambda^2 - is|u^{(0)}|^2 \end{pmatrix} \Psi^{(0)} . \end{cases} \tag{51}$$

The solution of these equations with $u^{(0)} = \exp(-2ist)$ can be conveniently written as

$$\Psi^{(0)}(x, t, \lambda) = \begin{pmatrix} e^{ist} & 0 \\ 0 & e^{-ist} \end{pmatrix} e^{i(xW - tF)} , \tag{52}$$

where the two matrices

$$W = \begin{pmatrix} \lambda & -is \\ -i & -\lambda \end{pmatrix} , \quad F = \begin{pmatrix} -2\lambda^2 & 2is\lambda \\ 2i\lambda & 2\lambda^2 \end{pmatrix} = -2\lambda W \tag{53}$$

depend only on λ. Next we compute the eigenvalues $\pm w$ and $\pm f$ of the matrices W and F, respectively. If $g_\pm$ are their corresponding common eigenvectors, it follows

that $Wg_\pm = \pm w g_\pm$, $Fg_\pm = \pm f g_\pm$ with

$$w = \sqrt{\lambda^2 - s}\,, \quad f = -2\lambda\sqrt{\lambda^2 - s}\,. \tag{54}$$

The implication is that the Fourier modes take the vector expression

$$\Psi^{(0)}(x,t,\lambda)g_\pm = e^{\pm i(wx - ft)} \begin{pmatrix} e^{ist} & 0 \\ 0 & e^{-ist} \end{pmatrix} g_\pm\,, \tag{55}$$

which clearly show the spectra S_x and S_t. Indeed, in the defocusing case $s = 1$, the "wave number" w is real if and only if λ is real but off the forbidden gap $-1 < \lambda < 1$.

So the spectrum $S_x = \{-\infty < \lambda \le -1\} \oplus \{1 \le \lambda < +\infty\}$. On the t-side, f is real if and only if $\lambda \in S_t$ where $S_t = S_x \oplus \{\lambda = i\nu, -\infty < \nu < +\infty\}$, see Fig. 1. Since whenever w is real also f is real, we conclude that in this case the continuum wave solution $u^{(o)} = \exp(-2it)$ is linearly stable.

Considering now the focusing case $s = -1$; by reasoning in a similar way one derives from the expression (55), with (54), the x-spectrum, $S_x = \{-\infty < \lambda < +\infty\} \oplus \{\lambda = i\nu, -1 \le \nu \le +1\}$ while the t-spectrum is $S_t = \{-\infty < \lambda < +\infty\} \oplus \{\lambda = i\nu, -\infty < \nu \le -1\} \oplus \{\lambda = i\nu, +1 \le \nu < +\infty\}$, see Fig. 2.

In this case the imaginary values of λ in the interval $-1 < \mathrm{Im}\lambda < +1$ belong to S_x but not to S_t, and therefore the solution $u^{(0)} = \exp(2it)$ is linearly unstable. This result is known for water waves as Benjamin-Feir instability [49], and as modulational instability in optics [50] (see also [51]). It is common and convenient to characterize these wave phenomena by plotting the imaginary part of the wave frequency versus the wave number. To this purpose we consider again the Fourier-like mode (see above) $(\psi_{22}^{(0)})^2 = e^{2it}\exp[i(kx - \omega t)]$ with

$$k = -2w = -2\sqrt{\lambda^2 + 1}\,, \quad \omega(k) = -k\sqrt{k^2 - 4}\,. \tag{56}$$

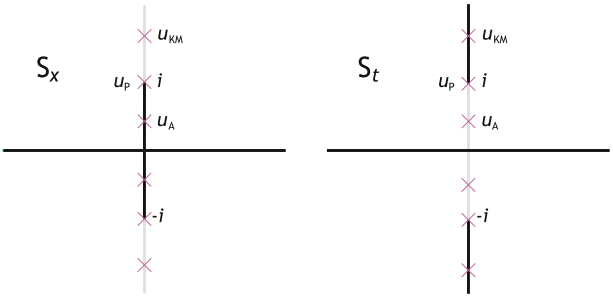

Fig. 2 Focusing NLS: S_x = x-part spectrum/S_t = t-part spectrum of $u^{(0)} = \exp(2it)$; the crosses indicate examples of solutions in the one parameter family (48)

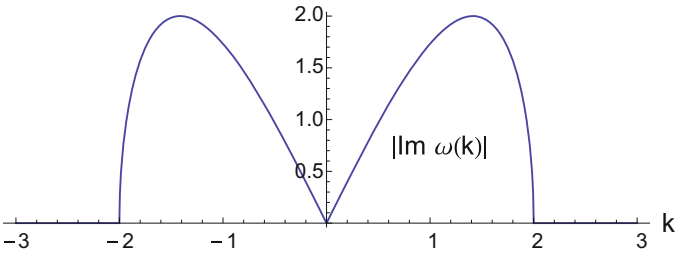

Fig. 3 NLS instability of $u^{(0)} = \exp(2it)$: imaginary part of frequency $\omega(k)$ versus wave number k, see (56)

The resulting instability plot is shown in Fig. 3.

The linear stability analysis can tell that a solution is unstable by showing an exponential (or, in marginal cases, polynomial, see below) growth of that solution as time goes by. However, it is not able to tell the long time evolution. Depending on the perturbing deviation $\delta u(x,t)$, it may well happen that the growing perturbation eventually develop into a finite, likely soliton, solution of the NLS equation. Candidates to playing such role are indeed solutions with a simple spectral characterization such as those corresponding to discrete eigenvalues. One example of this type of solutions of the focusing NLS equation can be computed by means of one of the tool provided by its integrability, namely by the Darboux transformation. This construction has been done in the previous section, the outcome being the family of solutions (48). This is a one-parameter family, the parameter η being real if the corresponding pair of discrete eigenvalues, $\lambda_1 = i\cosh(\eta)$, $\lambda_2 = \lambda_1^* = -i\cosh(\eta)$ lie off the spectrum S_x, while η has to be imaginary, i.e. $\eta = i\theta$, $0 \le \theta \le \pi/2$, if on the contrary the discrete eigenvalues $\lambda_1 = i\cos(\theta)$, $\lambda_2 = \lambda_1^* = -i\cos(\theta)$, are required to be in the spectrum S_x, see Fig. 2. The corresponding solutions of the NLS equation, $u_{KM}(x,t)$ if η is real, and $u_A(x,t)$ if instead η is imaginary, have been separately found in [52, 53] and, respectively, in [54]. Here the subscript $_{KM}$ indicates the Kuznetsov-Ma solution u_{KM} [52, 53] while the subscript $_A$ indicates the Akhmediev solution u_A [54]. The x and t dependence of these two different types of solutions may be understood by looking at the position of their corresponding eigenvalues in the λ-plane. Indeed, $u_{KM}(x,t)$ is localized in x and periodic in t since its corresponding eigenvalues are in S_t and off S_x while the opposite occurs for $u_A(x,t)$ which is instead periodic in x. In order to show that indeed this last solution $u_A(x,t)$ describes the fate of a small perturbation of the unstable continuum wave $u^{(0)} = \exp(2it)$, we first give this solution the more convenient expression

$$u = e^{2i(t-\theta)}[1 + i\sin(\theta)\frac{e^{i(\theta+iqt)} - e^{-i(\theta+iqt)}}{\cosh(qt) - \cos(\theta)\cos(px)}], \quad p = 2\sin(\theta)\,,\ q = 2\sin(2\theta) \tag{57}$$

and then we note that its asymptotic behavior

$$u(x,t) = e^{2it}[1 + \delta u(x,t) + \mathrm{O}(e^{2qt})]\,, \tag{58}$$

as $t \to -\infty$, is that of the background continuum wave perturbed by the small exponential tail

$$\delta u(x,t) = i\sin(2\theta)e^{-i\theta}e^{2it}\cos(px)e^{qt}\,, \tag{59}$$

which satisfies the linearized equation (49).

Let us finally consider the marginal case of the solution family (48) which corresponds to the parameter value $\eta = 0$, or equivalently, to the border value $\lambda = \pm i$ of the corresponding eigenvalue, see Fig. 2. By performing this limit, the final expression has no more exponential functions in it since it features only a rational dependence on the variables x, t, which reads

$$u_P(x,t) = e^{2it}\left[1 - \frac{4(1+4it)}{1+4x^2+16t^2}\right]. \tag{60}$$

In this solution the subscript $_P$ stands for Peregrine and this is indeed the well known Peregrine soliton [55]; it gained relevance as model of water rogue waves [56–61], and later in other physical contexts [62–66]. Its peculiarity is that of appearing and disappearing over an unstable background while its amplitude reaches a maximum value which is three times that of the surrounding periodic wave. The suggestion that rogue waves, as they appear in nature, may be described by rational solutions has given a strong impulse in this direction, particularly to the mathematical side of this subject. Various extensions [45, 67–78] of the Peregrine soliton to other integrable wave models have soon been available and investigated, and still are to a considerable extent. Some of these developments are discussed in the next section.

4 Wave Coupling: Integrability and Rogue Waves

The dynamics of waves frequently requires that more than just one field propagates. For instance dealing with polarized light beams in a nonlinear (Kerr) medium naturally leads to consider both self interaction, as in the NLS equation, and cross interaction among the two different polarization fields. As a different mechanism causing similar wave-wave coupling, one may consider two different quasi-monochromatic waves with wave-numbers k_1, k_2 propagating in the same medium with cubic nonlinearity. Then a multiscale analysis shows that, if the weak resonance condition $v_g(k_1) = v_g(k_2)$ is satisfied, $v_g(k)$ being the group velocity, the two waves interact with each other. In both these examples the resulting system of equations reads

$$\begin{cases} iu_{1t} + \gamma_1 u_{1xx} + (g_1|u_1|^2 + g_{12}|u_2|^2)u_1 = 0 \\ iu_{2t} + \gamma_2 u_{2xx} + (g_2|u_2|^2 + g_{21}|u_1|^2)u_2 = 0 \end{cases} \tag{61}$$

where the constant coefficients γ's and g's depend on the particular physical process. Integrable methods apply also to this system of equations provided the coefficients satisfy the conditions $\gamma_1 = \gamma_2$, $g_1 = g_{21}$, $g_2 = g_{12}$. Indeed, if these relations do not hold true, the system (61) is not integrable, and no Lax pair is associated to it. Thus there exist only three different integrable cases which, by appropriate cosmetic rescaling, see Sect. 2, take the form

$$\begin{cases} iu_{1t} + u_{1xx} - 2(s_1|u_1|^2 + s_2|u_2|^2)u_1 = 0 \\ iu_{2t} + u_{2xx} - 2(s_1|u_1|^2 + s_2|u_2|^2)u_2 = 0 \end{cases}, \quad s_1^2 = s_2^2 = 1 \,. \tag{62}$$

Depending on the two signs s_1, s_2, we have the focusing case (Manakov model [79]), $s_1 = s_2 = -1$, the defocusing case $s_1 = s_2 = 1$ and the mixed case $s_1 = -s_2 = 1$ which models self-defocusing for the wave amplitude u_1 and self-focusing for u_2. All of these cases have applications in fluid dynamics [80–82], optics [83–87] and Bose-Einstein condensates [88]. The system (62) clearly generalizes the NLS equation (18) and it is known as Vector Nonlinear Schrödinger (VNLS) equation since the two-component vector $(u_1\,,\,u_2)$ can be easily generalized to a N-component vector for any N, see (9). As expected, it shares with the NLS equation several properties but it also differs under various aspects. Its Lax pair formally looks like (20) but now the matrices X and T are 3×3 with

$$X = i\lambda\Sigma + Q(x,t)\,, \quad \Sigma = \begin{pmatrix} 1 & 0 & 0 \\ 0 & -1 & 0 \\ 0 & 0 & -1 \end{pmatrix}, \quad Q = \begin{pmatrix} 0 & s_1 u_1^* & s_2 u_2^* \\ u_1 & 0 & 0 \\ u_2 & 0 & 0 \end{pmatrix}, \tag{63}$$

and

$$T = 2i\lambda^2\Sigma + 2\lambda Q + i\Sigma(Q^2 - Q_x). \tag{64}$$

Starting from these expressions, and similarly to what has been done for the NLS equation, one can find an infinite number of local conservation laws of the form (29) [89], and can construct soliton solutions by means of the Darboux transformation (e.g. [43, 44]). Also the inverse spectral method can be extended to solve the initial value problem when the boundary values, as $x \to \pm\infty$, vanish, say $u_1(x,t)$ and $u_2(x,t) \to 0$ (see e.g. [79]), and also when $u_1(x,t)$ and $u_2(x,t)$ go, in the same limit of x, to a continuous wave solution (see e.g. [90]).

Here our discussion focuses on the construction of bounded rational solutions of (62) whose interest is well motivated by their application as rogue wave models. In analogy with the NLS equation, and according to a general common understanding of this phenomenon, the existence of rogue waves requires that they are superimposed to an unstable continuous background. However we do not address here the problem of determining the stability of the background solution, as done in the previous section for the NLS equation. We rather limit ourselves to point out that, quite differently from the NLS equation, instability occurs not only

in the focusing regime $s_1 = s_2 = -1$, but also in the defocusing and mixed cases (e.g. [45, 91, 92]). In the previous section we obtained the rational (alias Peregrine) solution (60) by taking the limit $\eta \to 0$ of the η-dependent family (48). The analytic construction of rational solutions of multicomponent wave equations, as the VNLS system (62), by taking such limit is no longer convenient, if at all doable. In the following we show a direct way to solve this problem with no need to take this limit operation. We begin by observing that the solution (48) of the NLS equation is made out of exponential functions which come in, through the Darboux formula (45), from the exponential solution (52) of the Lax pair (with $s = -1$). Thus, to our purpose, the main task is to change the exponential matrix function $\exp[i(xW - tF)]$, see (52), into a polynomial function. This is not possible if the matrix $W(\lambda)$ (and therefore $F(\lambda)$) is diagonalizable. It is instead possible if, for a special value of the spectral variable λ, the matrices W, F are not diagonalizable. If such value of λ exists, it is called *critical* and denoted λ_c. The expressions (53) and (54) clearly show that only if the eigenvalues coincide with each other, say if $w(\lambda) = \sqrt{\lambda^2 + 1} = 0$, the matrices W, F are not diagonalizable. Indeed, in this case there are two critical values $\lambda_c = \pm i$, and in fact, f. i. for $\lambda_c = i$, the matrix W takes the value

$$W(i) = i \begin{pmatrix} 1 & 1 \\ -1 & -1 \end{pmatrix} \quad , \tag{65}$$

which is nilpotent, namely $W(i)^2 = 0$. This property similarly holds for $F(i)$ and for $W(-i)$ and $F(-i)$. The implication is that the exponential $\exp[i(xW(\lambda_c) - tF(\lambda_c))]$ is in fact the polynomial $\mathbf{1} + i[xW(\lambda_c) - tF(\lambda_c)]$, as implied by the Taylor expansion of the exponential function. It is now a simple exercise to obtain again the Peregrine solution (60) by this method.

The extension of this technique to the VNLS equation first requires the computation of the critical values λ_c. This can be done in a systematic way so as to find *all* such critical values which eventually lead to the construction of bounded rational solutions. The starting point is the expression

$$\begin{pmatrix} u_1^{(0)}(x,t) \\ u_2^{(0)}(x,t) \end{pmatrix} = \begin{pmatrix} a_1 e^{i(qx - \nu t)} \\ a_2 e^{-i(qx + \nu t)} \end{pmatrix} \quad , \quad \nu = q^2 + 2(s_1 a_1^2 + s_2 a_2^2) \tag{66}$$

of the continuous wave solution of the VNLS equation (62) and of the corresponding matrix solution

$$\Psi^{(0)}(x,t,\lambda) = \begin{pmatrix} 1 & 0 & 0 \\ 0 & e^{i(qx - \nu t)} & 0 \\ 0 & 0 & e^{-i(qx + \nu t)} \end{pmatrix} e^{i(xW(\lambda) - tF(\lambda))} \tag{67}$$

of the Lax pair (20). The 3×3 constant matrices W, F depend only on λ and on the background solution parameters a_1, a_2, q. In this respect we note that the parameter q has no counterpart in the single wave NLS equation (18). Indeed it

represents the wave number mismatch of the two background components $u_1^{(0)}$ and $u_2^{(0)}$ as $2q$ equals the difference of these wave numbers. Its novel important feature is to have a crucial effect on the stability of the solution (66). Again the Darboux transformation method, as applied to the seed solution (66), is the convenient tool to obtain the explicit expression of new solutions of the VNLS equation (see Sect. 2). As we are interested here in obtaining rational solution, our main concern is to find the critical values of λ, namely those values for which the matrix exponential $e^{i(xW(\lambda)-tF(\lambda))}$ yields a polynomial dependence on x, t. In analogy with what we have shown above for the NLS equation, the main task is finding the eigenvalues of the matrices $W(\lambda)$ and $F(\lambda)$ together with their λ-dependence. Equivalently, and by dealing for instance with W, which is

$$W(\lambda) = \begin{pmatrix} \lambda & -is_1a_1 & -is_2a_2 \\ -ia_1 & -\lambda - q & 0 \\ -ia_2 & 0 & -\lambda + q \end{pmatrix}, \tag{68}$$

one has to investigate the λ-dependence of the three roots $w_1(\lambda)$, $w_2(\lambda)$, $w_3(\lambda)$ of the characteristic polynomial $P(w) = \det[w\mathbf{1} - W(\lambda)]$ in the entire λ-plane. This task requires numerical computations in order to find in addition the dependence of the critical values λ_c on the continuous wave parameters q, a_1, a_2. We refer the reader to [45] for the way of classifying all critical values λ_c in the parameter space and we limit ourselves to make few comments and to show few plots. Because of the complicate Cardano expression for the roots of a third degree polynomial, only the solutions with $q = 0$ can be found in simple explicit form. This particular case ($q = 0$) yields the expression of the vector analog of the NLS Peregrine solution, and, as expected, this solution exists only in the focusing case $s_1 = s_2 = -1$. In fact this solution corresponds to two critical values, $\lambda_c = \pm i\sqrt{a_1^2 + a_2^2}$. However its expression, which reads

$$\begin{pmatrix} u_1 \\ u_2 \end{pmatrix} = e^{2ip^2t}\left[\frac{(P_2 + |h|^2e^{2px})}{(M_2 + |h|^2e^{2px})}\begin{pmatrix} a_1 \\ a_2 \end{pmatrix} + \frac{hP_1e^{(px+ip^2t)}}{(M_2 + |h|^2e^{2px})}\begin{pmatrix} a_2 \\ -a_1 \end{pmatrix}\right] \tag{69}$$

has the novel feature of showing a mixture of exponential and polynomial dependence on x, t since P_2, M_2 are polynomials of degree 2, while P_1 is a polynomial of first degree. Here $p = \sqrt{a_1^2 + a_2^2}$ while h is an additional arbitrary complex parameter. Thus, if say $a_2 = 0$, this solution describes a dark soliton in the first component and a bright one in the second component which at the time of their interaction generate a Peregrine-type bump, see Fig. 4. Only if $h = 0$ this solution features a Peregrine rogue wave in both components.

If the mismatch parameter q is different from zero, rogue wave type solutions exist in all regimes but not for all values of the parameters a_1, a_2, q. To the purpose of classifying all these solutions, it is convenient to separately consider the multiplicity of the three eigenvalues of the matrix $W(\lambda)$ (68). It is plain that no critical values λ_c

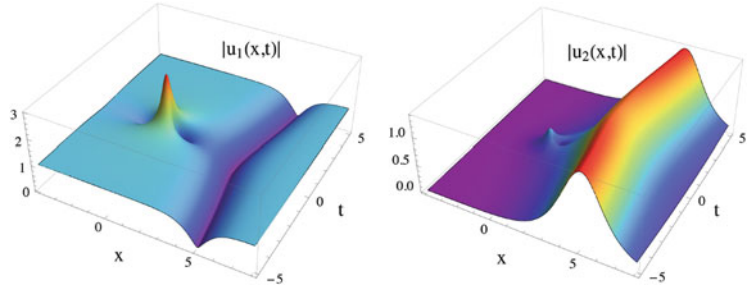

Fig. 4 $s_1 = s_2 = -1$, $q = 0$, $a_1 = 1$, $a_2 = 0$, $\lambda_c = i$, $f = 0.1$

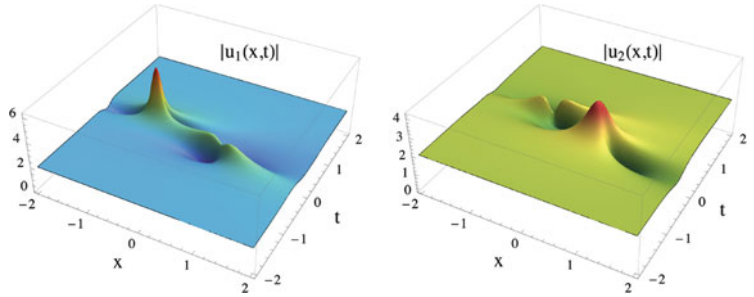

Fig. 5 $s_1 = s_2 = -1$, $q = 1$, $a_1 = a_2 = 2$, $\lambda_c = i\frac{\sqrt{27}}{2}$

exist if all the eigenvalues are simple since in this case W and F are diagonalizable and the exponential $\exp[i(xW(\lambda) - tF(\lambda))]$ cannot be a polynomial. In the case in which there is just one eigenvalue with multiplicity 3, only two critical values of λ, $\lambda_c = \pm i\frac{\sqrt{27}}{2}$, exist and only in the focusing case $s_1 = s_2 = -1$ with the restriction to the subset $a_1 = a_2 = 2q$. Figure 5 shows such a rogue wave.

If instead the matrix $W(\lambda)$ has an eigenvalue with multiplicity 2 there may exist several critical values λ_c. In this respect it is convenient to consider first the parameter subset $s_1 = s_2$, $a_1 = a_2$, $q \neq 0$ because in this particular case the critical value λ_c can be explicitly computed. It turns out that in the focusing case $s_1 = s_2 = -1$ four critical values exist for any value of q and $a_1 = a_2$, for one such solution see Fig. 6.

In the defocusing case $s_1 = s_2 = 1$ threshold phenomena appear as no critical value λ_c (alias no rogue wave) exists if $q^2 \geq 2a_1^2$ while (only) two critical values exist if $q^2 < 2a_1^2$, see Fig. 7.

In order to explore the generic case $a_1 \neq a_2$ and $q \neq 0$ one may conveniently proceed by numerically computing the critical value λ_c, see the examples of rogue wave solutions shown in Figs. 8, 9, and 10, in, respectively, focusing, defocusing and mixed cases. Still it is explicitly found that the existence of rogue waves in the defocusing regime is conditioned by the inequality $(a_1^2 + a_2^2)^3 - 12(a_1^4 - 7a_1^2a_2^2 +$

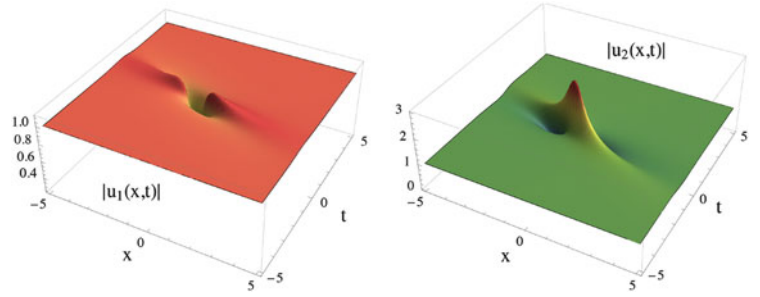

Fig. 6 $s_1 = s_2 = -1$, $q = 1$, $a_1 = a_2 = 1$, $\lambda_c = \sqrt{\frac{3}{8}}\sqrt{-3 + i\sqrt{3}}$

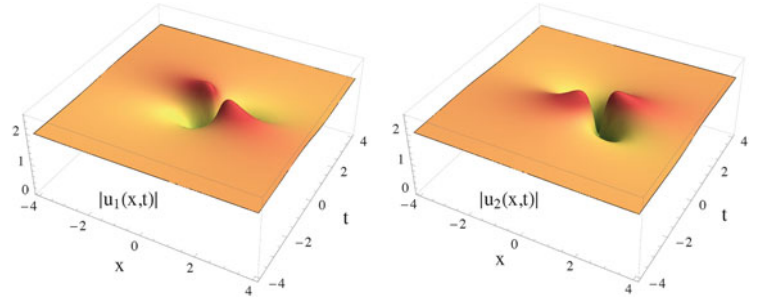

Fig. 7 $s_1 = s_2 = 1$, $q = 1$, $a_1 = a_2 = 2$, $\lambda_c = \frac{i}{2}\sqrt{-13 + 16\sqrt{2}}$

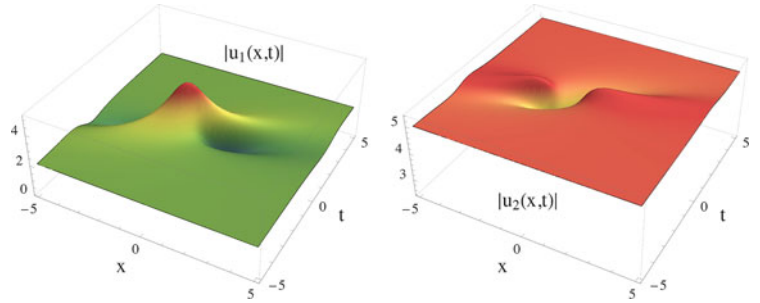

Fig. 8 $s_1 = s_2 = -1$, $q = 1$, $a_1 = 2$, $a_2 = 5$, $\lambda_c = 4.876 + 5.343i$

$a_2^4)q^2 + 48(a_1^2 + a_2^2)q^4 - 64q^6 > 0$ for the amplitudes a_1, a_2 and the mismatch parameter q.

A detailed discussion of the existence of rogue waves as related to base-band modulational instability of the continuous wave background in the defocusing regime is reported in [93, 94], (see also [92]).

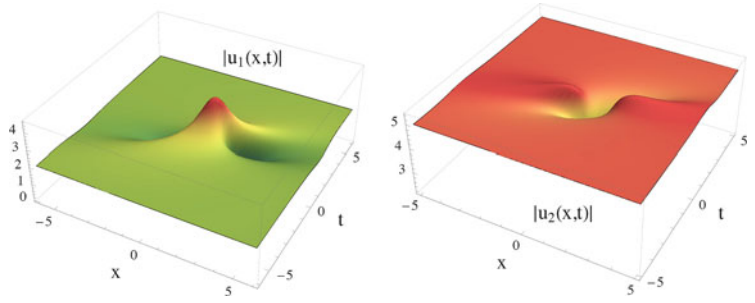

Fig. 9 $s_1 = s_2 = 1$, $q = 1$, $a_1 = 2$, $a_2 = 5$, $\lambda_c = -5.600 + 4.655i$

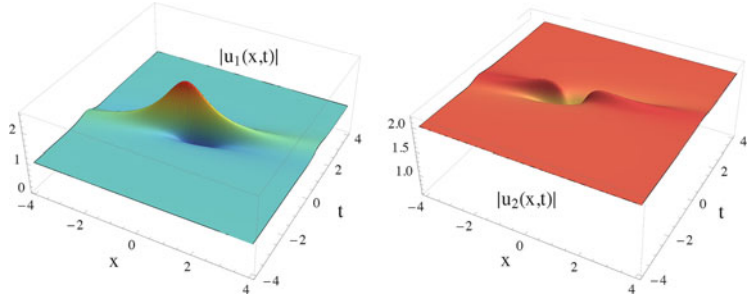

Fig. 10 $s_1 = -1$, $s_2 = 1$, $q = 1$, $a_1 = 1$, $a_2 = 2$, $\lambda_c = -1.242 + 0.636i$

5 Integrability in Action: Beyond the NLS Model

Integrable nonlinear equations modeling wave phenomena, even if approximate, as they generally are, yet play an important role in understanding and predicting experimental observations. Thanks to the mathematical property of being integrable, a number of powerful computational technique are available to investigate patterns as those due to shock waves, and even to analytically construct special interesting solutions such as multi-soliton and multi-rogue waves. To the purpose of illustrating how some of these methods work, in the previous sections we have considered the ubiquitous NLS equation as prototype integrable model, together with its extension to a system of two coupled NLS equations. All problems raised have been solved by starting from the Lax pair. Indeed, because of their dependence on the spectral variable, these two equations contain all the valuable information. Since the Lax pair plays such an essential role, it should be pointed out that finding which integrable partial differential equation is associated to a given Lax pair (as its compatibility condition) is rather easy. However the other way around is far from being a simple task, as no general method exists to prove, or disprove, the existence of a Lax pair associated with a *given* nonlinear partial differential equation. Attempts in this direction make use of a weaker definition of integrability, which can be tested by multi-scale expansion [21], or by recursively constructing symmetries [95, 96] of

the given nonlinear wave equation. Attempts to solve this problem by classifying Lax pairs also exist (see [97] and references therein).

Searching for new integrable wave equations naturally leads to change the matrices $X(\lambda)$ and $T(\lambda)$ of the Lax pair (20). This has been done in many ways, according to various purposes, during the last 45 years, and it is still common practice. In this respect we believe that the following examples may well give a good perspective of applications of integrability not only in the general context of nonlinear science but also in the more specific one of modeling wave phenomena. Let us consider first the two main features of the Lax pair of Eqs. (20), namely (1) the λ-dependence of the matrices $X(\lambda)$ and $T(\lambda)$, and (2) their dimension. In fact searching for the Lax pair associated with the KdV and the cmKdV equations, (1) and (3), requires that the matrix $T(\lambda)$ be a third degree polynomial of λ (e.g. [6]), while the matrix dimension is 2×2 as for the NLS equation. Keeping this same matrix dimension but asking that the λ-dependence be rational rather than polynomial is required to obtain the SG equation (4) [98–100] and the MTM equation (8) [101, 102]. Increasing the matrix dimension is standard strategy to extend one scalar wave equation to a system of equations to model wave-wave interactions. This is the case for instance of the VNLS (62) which requires matrices of dimension 3×3. This same dimension is required to arrive at the system (10) which models the resonant interaction of three waves [103] (see also [104] and references therein), the λ-dependence of both $X(\lambda)$ and $T(\lambda)$ being polynomial of first degree. This system can be generalized to the so-called N-wave interaction equations (e.g. [105, 106] and references therein) which again model resonant interaction of N wave fields with quadratic nonlinearity. In this case the matrix dimension has to be $n \times n$ with $N = n(n-1)/2$. Also the Lax pair matrices associated with the LWSW equation (6), which models the resonant interaction of long waves with short waves [107, 108], are 3×3 [107, 109, 110]. A further, and more substantial, way of changing the Lax pair is asking that this pair of equations be partial, rather than ordinary, differential equations by introducing more space variables. Examples of integrable equations in 2-space and 1-time dimensions are the Kadomtsev-Petviashvili [111] and Davey-Stewartson [112] equations which find their application in fluid dynamics. Other nonlinear wave equations can be added to those we have mentioned here which are integrable and also valuable in some applicative context.

As part of our discussion has been devoted to those solutions which model rogue waves, we conclude with the following collection of integrable equations which share the property of having rogue wave solutions. We observe that in fact not all integrable wave equations possess such type of solutions. In addition to the focusing NLS equation (5) with $s = -1$ [55, 113] and VNLS equation (62) [45, 68, 93], whose rogue wave solutions have been discussed above, rogue wave solutions have been identified also for the cmKdV equation (3) [114], the DNLS equation (7) [115], the MTM (8) [116], the LWSW (6) [73, 117] and the 3WRI equation (10) [45, 71, 78]. Also the following integrable equations, among others, have been recently

reported to possess rogue wave solutions

- Hirota-Maxwell-Bloch (H-MB) equation [118]:

$$\begin{aligned} & iu_t + a[u_{xx} + 2|u|^2 u] + ib[u_{xxx} + 6|u|^2 u_x] = 2p \\ & p_x = 2i\omega p + 2\eta u \\ & \eta_x = -(up^* + u^* p) \end{aligned} \tag{70}$$

  where a, b are arbitrary real constants.
- Sasa-Satsuma (SS) equation [119–121]:

$$iu_t + u_{xx} + 2|u|^2 u + i\alpha[u_{xxx} + 3(|u|^2)_x u + 6|u|^2 u_x] = 0 \tag{71}$$

  the real constant coefficient α being arbitrary.
- Kadomtsev-Petviashvili I (KP-I) equation [122, 123]:

$$(u_t - u_{xxx} - 6uu_x)_x + u_{yy} = 0 \tag{72}$$

- Davey-Stewartson II (DS-II) equation [124]:

$$iu_t + u_{xx} - u_{yy} + 2s|u|^2 u = 2\phi u \ , \ \phi_{xx} + \phi_{yy} = 2s(|u|^2)_{xx} \ , \quad s = \pm 1 \tag{73}$$

References

1. Zabusky, N., Kruskal, M.: Interaction of "solitons" in a collisionless plasma and the recurrence of initial states. Phys. Rev. Lett. **15**, 240–243 (1965)
2. Russell, J.S.: Report on waves. In: Report of the British Association for the Advancement of Science, vol. 14th Meeting (1845), pp. 311–390, plus plates 47–57. British Association for the Advancement of Science (1844)
3. Dauxois, T., Peyrard, M.: Physics of Solitons. Cambridge University Press, Cambridge (2006)
4. Scott, A.: Nonlinear Science: Emergence and Dynamics of Coherent Structures. Oxford Texts in Applied and Engineering Mathematics. Oxford University Press, Oxford (2003)
5. Remoissenet, M.: Waves Called Solitons: Concepts and Experiments. Springer, Berlin/Heidelberg (1994)
6. Ablowitz, M., Clarkson, P.: Solitons, Nonlinear Evolution Equations and Inverse Scattering. London Mathematical Society Lecture Note Series. Cambridge University Press, Cambridge (1991)
7. Toda, M.: Nonlinear Waves and Solitons. Japanese Series. Springer, Berlin (1989)
8. Drazin, P., Johnson, R.: Solitons: An Introduction. Cambridge Computer Science Texts. Cambridge University Press, Cambridge (1989)

9. Newell, A.: Solitons in Mathematics and Physics. CBMS-NSF Regional Conference Series in Applied Mathematics. SIAM, Philadelphia (1985)
10. Novikov, S., Manakov, S., Pitaevskii, L., Zakharov, V.: Theory of Solitons: The Inverse Scattering Method. Contemporary Soviet Mathematics. Plenum, New York (1984)
11. Dodd, R., Eilbeck, J., Gibbon, J., Morris, H.: Solitons and Nonlinear Wave Equations. Academic, New York (1982)
12. Calogero, F., Degasperis, A.: Spectral Transform and Solitons: Tools to Solve and Investigate Nonlinear Evolution Equations, vol. 1. North-Holland, Amsterdam (1982)
13. Ablowitz, M., Segur, H.: Solitons and the Inverse Scattering Transform. SIAM Studies in Applied Mathematics. SIAM, Philadelphia (1981)
14. Degasperis, A.: Resource letter sol-1: solitons. Am. J. Phys. **66**(6), 486–497 (1998)
15. Babelon, O., Bernard, D., Talon, M.: Introduction to Classical Integrable Systems. Cambridge Monographs on Mathematical Physics. Cambridge University Press, Cambridge (2003)
16. Mikhailov, A. (ed.): Integrability. Lecture Notes in Physics. Springer, Berlin/Heidelberg (2008)
17. Zakharov, V. (ed.) What Is Integrability? Springer Series in Nonlinear Dynamics. Springer, Berlin/Heidelberg (1991)
18. Miwa, T., Jimbo, M., Date, E.: Solitons: Differential Equations, Symmetries and Infinite Dimensional Algebras. Cambridge Tracts in Mathematics. Cambridge University Press, Cambridge (2000)
19. Faddeev, L., Takhtajan, L.: Hamiltonian Methods in the Theory of Solitons. Classics in Mathematics. Springer, Berlin/Heidelberg (1987)
20. Calogero, F.: Why are certain nonlinear PDEs both widely applicable and integrable? In: Zakharov, V.E. (ed.) What Is Integrability? Springer Series in Nonlinear Dynamics, pp. 1–62. Springer, Berlin/Heidelberg (1991)
21. Degasperis, A.: Multiscale expansion and integrability of dispersive wave equations. In: Mikhailov, A. (ed.) Integrability. Lecture Notes in Physics, vol. 767, pp. 215–244. Springer, Berlin/Heidelberg (2009)
22. Osborne, A.: Nonlinear Ocean Waves & the Inverse Scattering Transform. International Geophysics. Elsevier, Amsterdam (2010)
23. Infeld, E., Rowlands, G.: Nonlinear Waves, Solitons and Chaos. Cambridge University Press, Cambridge (2000)
24. Shen, S.: A Course on Nonlinear Waves. Nonlinear Topics in the Mathematical Sciences. Springer, Dordrecht (1993)
25. Whitham, G.: Linear and Nonlinear Waves. Wiley, New York (1974)
26. Fibich, G.: The Nonlinear Schrödinger Equation: Singular Solutions and Optical Collapse. Applied Mathematical Sciences. Springer, Cham (2015)
27. Ablowitz, M., Prinari, B., Trubatch, A.: Discrete and Continuous Nonlinear Schrödinger Systems. Cambridge University Press, Cambridge (2004)
28. Sulem, C., Sulem, P.: The Nonlinear Schrödinger Equation: Self-Focusing and Wave Collapse. Applied Mathematical Sciences. Springer, New York (1999)
29. Kelley, P.L.: Self-focusing of optical beams. Phys. Rev. Lett. **15**, 1005–1008 (1965)
30. Taniuti, T., Yajima, N.: Perturbation method for a nonlinear wave modulation. I. J. Math. Phys. **10**(8), 1369–1372 (1969)
31. Taniuti, T., Yajima, N.: Special issue devoted to the Reductive Perturbation Method for Nonlinear Wave Propagation **55** (1974)
32. Zakharov, V.E., Shabat, A.B.: Exact theory of two-dimensional self-focusing and onedimensional self-modulation of waves in nonlinear media. Sov. J. Exp. Theor. Phys. **34**, 62 (1972)
33. Zakharov, V.E., Shabat, A.B.: Interaction between solitons in a stable medium. Sov. J. Exp. Theor. Phys. **37**, 823 (1973)
34. Demontis, F., Prinari, B., van der Mee, C., Vitale, F.: The inverse scattering transform for the defocusing nonlinear Schrödinger equations with nonzero boundary conditions. Stud. Appl. Math. **131**(1), 1–40 (2013)

35. Biondini, G., Prinari, B.: On the spectrum of the Dirac operator and the existence of discrete eigenvalues for the defocusing nonlinear Schrödinger equation. Stud. Appl. Math. **132**(2), 138–159 (2014)
36. Biondini, G., Kovacic, G.: Inverse scattering transform for the focusing nonlinear Schrödinger equation with nonzero boundary conditions. J. Math. Phys. **55**(3), 031506-1–031506-22 (2014)
37. Cieslinski, J.L.: Algebraic construction of the Darboux matrix revisited. J. Phys. A Math. Theor. **42**(40), 404003 (2009)
38. Gu, C., Hu, A., Zhou, Z.: Darboux Transformations in Integrable Systems: Theory and Their Applications to Geometry. Mathematical Physics Studies. Springer, Dordrecht (2005)
39. Rogers, C., Schief, W.: Bäcklund and Darboux Transformations: Geometry and Modern Applications in Soliton Theory. Cambridge Texts in Applied Mathematics. Cambridge University Press, Cambridge (2002)
40. Matveev, V., Salle, M.: Darboux Transformations and Solitons. Springer Series in Nonlinear Dynamics. Springer, Berlin (1991)
41. Doktorov, E., Leble, S.: A Dressing Method in Mathematical Physics. Mathematical Physics Studies. Springer, Dordrecht (2007)
42. Coley, A.: Bäcklund and Darboux Transformations: The Geometry of Solitons: AARMS-CRM Workshop, June 4-9, 1999, Halifax, N.S., Canada. CRM Proceedings and Lecture Notes. American Mathematical Society, Providence (2001)
43. Degasperis, A., Lombardo, S.: Multicomponent integrable wave equations. Darboux-dressing transformation. J. Phys. A Math. Theor. **40**(5), 961–977 (2007)
44. Degasperis, A., Lombardo, S.: Multicomponent integrable wave equations. Soliton solutions. J. Phys. A Math. Theor. **42**(38), 385206 (2009)
45. Degasperis, A., Lombardo, S.: Rational solitons of wave resonant-interaction models. Phys. Rev. E Stat. Nonlinear Soft Matter Phys. **88**(5), 052914 (2013)
46. Neugebauer, G., Meinel, R.: General N-soliton solution of the AKNS class on arbitrary background. Phys. Lett. A **100**(9), 467–470 (1984)
47. Fan, E.: A unified and explicit construction of n-soliton solutions for the nonlinear Schrödinger equation. Commun. Theor. Phys. **36**(4), 401–404 (2001)
48. Steudel, H., Meinel, R., Neugebauer, G.: Vandermonde-like determinants and N-fold Darboux/Bäcklund transformations. J. Math. Phys. **38**(9), 4692–4695 (1997)
49. Benjamin, T.B., Feir, J.E.: The disintegration of wave trains on deep water, Part 1. Theory. J. Fluid Mech. **27**, 417–430 (1967)
50. Agrawal, G.: Nonlinear Fiber Optics. Academic, New York (1995)
51. Zakharov, V., Ostrovsky, L.: Modulation instability: the beginning. Phys. D Nonlinear Phenom. **238**, 540–548 (2009)
52. Kuznetsov, E.: Solitons in a parametrically unstable plasma. Sov. Phys. Dokl. (Engl. Transl.); (United States) **22**, 507–508 (1977)
53. Ma, Y.: The perturbed plane-wave solutions of the cubic Schrödinger equation. Stud. Appl. Math. **60**(1), 43–58 (1979)
54. Akhmediev, N., Eleonskii, V., Kulagin, N.: Exact first-order solutions of the nonlinear Schrödinger equation. Theor. Math. Phys. **72**(2), 809–818 (1987)
55. Peregrine, D.: Water waves, nonlinear Schrödinger equations and their solutions. J. Aust. Math. Soc. Ser. B Appl. Math. **25**, 16–43 (1983)
56. Hopkin, M.: Sea snapshots will map frequency of freak waves. Nature **430**, 492 (2004)
57. Müller, P., Garrett, C., Osborne, A.: Rogue waves – the fourteenth 'Aha Huliko'a Hawaiian winter workshop. Oceanography **18**, 66–75 (2005)
58. Perkins, P.: Dashing rogues: freak ocean waves pose threat to ships, deep-sea oil platforms. Sci. News **170**(21), 328–329 (2006)
59. Kharif, C., Pelinovsky, E., Slunyaev, A.: Rogue Waves in the Ocean. Advances in Geophysical and Environmental Mechanics and Mathematics. Springer, Berlin/Heidelberg (2009)
60. Akhmediev, N., Pelinovsky, E.: Discussion & debate: rogue waves – towards a unifying concept? Eur. Phys. J. Spec. Top. **185**, 1–4 (2010)

61. Pelinovsky, E., Kharif, C. (eds.): Extreme Ocean Waves. Springer, Cham (2008)
62. Erkintalo, M., Genty, G., Dudley, J.M.: Rogue-wave-like characteristics in femtosecond supercontinuum generation. Opt. Lett. **34**(16), 2468–2470 (2009)
63. Bonatto, C., Feyereisen, M., Barland, S., Giudici, M., Masoller, C., Leite, J., Tredicce, J.: Deterministic optical rogue waves. Phys. Rev. Lett. **107**, 053901 (2011)
64. Stenflo, L., Shukla, P.K.: Nonlinear acoustic-gravity waves. J. Plasma Phys. **75**, 841–847 (2009)
65. Bailung, H., Sharma, S.K., Nakamura, Y.: Observation of Peregrine solitons in a multicomponent plasma with negative ions. Phys. Rev. Lett. **107**, 255005 (2011)
66. Bludov, Y.V., Konotop, V.V., Akhmediev, N.: Matter rogue waves. Phys. Rev. A **80**, 033610 (2009)
67. Ankiewicz, A., Kedziora, D.J., Akhmediev, N.: Rogue wave triplets. Phys. Lett. A **375**(28–29), 2782–2785 (2011)
68. Baronio, F., Degasperis, A., Conforti, M., Wabnitz (2012) Solutions of the vector nonlinear Schrödinger equations: evidence for deterministic rogue waves. Phys. Rev. Lett. **109**, 044102 (2012)
69. Ohta, Y., Yang, J.: General high-order rogue waves and their dynamics in the nonlinear Schrödinger equation. Proc. R. Soc. Lond. A Math. Phys. Eng. Sci. **468**(2142), 1716–1740 (2012)
70. He, J., Zhang, H., Wang, L., Porsezian, K., Fokas, A.: Generating mechanism for higher-order rogue waves. Phys. Rev. E **87**, 052914 (2013)
71. Baronio, F., Conforti, M., Degasperis, A., Lombardo, S.: Rogue waves emerging from the resonant interaction of three waves. Phys. Rev. Lett. **111**, 114101 (2013)
72. Chabchoub, A., Akhmediev, N.: Observation of rogue wave triplets in water waves. Phys. Lett. A **377**(38), 2590–2593 (2013)
73. Chen, S., Grelu, P., Soto-Crespo, J.M.: Dark- and bright-rogue-wave solutions for media with long-wave-short-wave resonance. Phys. Rev. E **89**, 011201 (2014)
74. Chen, S., Soto-Crespo, J.M., Grelu, P.: Dark three-sister rogue waves in normally dispersive optical fibers with random birefringence. Opt. Express **22**(22), 27632–27642 (2014)
75. Chen, S.: Dark and composite rogue waves in the coupled Hirota equations. Phys. Lett. A **378**(38–39), 2851–2856 (2014)
76. Ling, L., Guo, B., Zhao, L.: High-order rogue waves in vector nonlinear Schrödinger equations. Phys. Rev. E **89**, 041201 (2014)
77. Chen, S., Mihalache, D.: Vector rogue waves in the Manakov system: diversity and compossibility. J. Phys. A Math. Theor. **48**(21), 215202 (2015)
78. Chen, S., Soto-Crespo, J.M., Grelu, P.: Watch-hand-like optical rogue waves in three-wave interactions. Opt. Express **23**(1), 349–359 (2015)
79. Manakov, S.V.: On the theory of two-dimensional stationary self-focusing of electromagnetic waves. Sov. J. Exp. Theor. Phys. **38**, 248 (1974)
80. Onorato, M., Proment, D., Toffoli, A.: Freak waves in crossing seas. Eur. Phys. J. Spec. Top. **185**(1), 45–55 (2010)
81. Grönlund, A., Eliasson, B., Marklund, M.: Evolution of rogue waves in interacting wave systems. EPL Lett. J. Explor. Front. Phys. **86**(2), 24001 (2009)
82. Onorato, M., Osborne, A.R., Serio, M.: Modulational instability in crossing sea states: a possible mechanism for the formation of freak waves. Phys. Rev. Lett. **96**, 014503 (2006)
83. Kivshar, Y., Agrawal, G.: Optical Solitons: From Fibers to Photonic Crystals. Elsevier, Amsterdam (2003)
84. Mumtaz, S., Essiambre, R., Agrawal, G.P.: Nonlinear propagation in multimode and multicore fibers: generalization of the Manakov equations. J. Lightwave Technol. **31**(3), 398–406 (2013)
85. Yaman, F., Li, G.: Nonlinear impairment compensation for polarization-division multiplexed WDM transmission using digital backward propagation. IEEE Photon. J. **1**(2), 144–152 (2009)
86. Winter, M., Bunge, C., Setti, D., Petermann, K.: A statistical treatment of cross-polarization modulation in DWDM systems. J. Lightwave Technol. **27**(17), 3739–3751 (2009)

87. Evangelides, J., S. G., Mollenauer, L.F., Gordon, J.P., Bergano, N.S.: Polarization multiplexing with solitons. J. Lightwave Technol. **10**(1), 28–35 (1992)
88. Kevrekidis, P., Frantzeskakis, D., Carretero-González, R.: Emergent Nonlinear Phenomena in Bose-Einstein Condensates: Theory and Experiment. Springer Series on Atomic, Optical, and Plasma Physics. Springer, Berlin/Heidelberg (2007)
89. Wang, D., Zhang, D., Yang, J.: Integrable properties of the general coupled nonlinear Schrödinger equations. J. Math. Phys. **51**(2), 023510 (2010)
90. Prinari, B., Ablowitz, M.J., Biondini, G.: Inverse scattering transform for the vector nonlinear Schrödinger equation with nonvanishing boundary conditions. J. Math. Phys. **47**, 063508 (2006). doi:http://dx.doi.org/10.1063/1.2209169
91. Forest, M.G., McLaughlin, D.W., Muraki, D.J., Wright, O.C.: Nonfocusing instabilities in coupled, integrable nonlinear Schrödinger PDEs. J. Nonlinear Sci. **10**(3), 291–331 (2000)
92. Frisquet, B., Kibler, B., Fatome, J., Morin, P., Baronio, F., Conforti, M., Millot, G., Wabnitz, S.: Polarization modulation instability in a Manakov fiber system. Phys. Rev. A **92**, 053854 (2015)
93. Baronio, F., Conforti, M., Degasperis, A., Lombardo, S., Onorato, M., Wabnitz, S.: Vector rogue waves and baseband modulation instability in the defocusing regime. Phys. Rev. Lett. **113**, 034101 (2014)
94. Baronio, F., Chen, S., Grelu, P., Wabnitz, S., Conforti, M.: Baseband modulation instability as the origin of rogue waves. Phys. Rev. A **91**, 033804 (2015)
95. Mikhailov, A., Shabat, A., Sokolov, V.: The symmetry approach to classification of integrable equations. In: Zakharov, V. (ed.) What Is Integrability? Springer Series in Nonlinear Dynamics, pp. 115–184. Springer, Berlin/Heidelberg (1991)
96. Mikhailov, A., Novikov, V.: Perturbative symmetry approach. J. Phys. A Math. Gen. **35**(22), 4775 (2002)
97. Lombardo, S., Mikhailov, A.: Reductions of integrable equations: dihedral group. J. Phys. A Math. Gen. **37**(31), 7727 (2004)
98. Ablowitz, M., Kaup, D., Newell, A., Segur, H.: Method for solving the sine-Gordon equation. Phys. Rev. Lett. **30**, 1262–1264 (1973)
99. Ablowitz, M., Kaup, D., Newell, A., Segur, H.: The inverse scattering transform- Fourier analysis for nonlinear problems. Stud. Appl. Math. **53**(4), 249–315 (1974)
100. Rajaraman, R.: Solitons and Instantons: An Introduction to Solitons and Instantons in Quantum Field Theory. North-Holland Personal Library. North-Holland, Amsterdam (1982)
101. Mikhailov, A.: Integrability of the two-dimensional Thirring model. JETP Lett. (Pis'ma Zh. Eksp. Teor. Fiz. **23**, 356–358) **23**, 320–323 (1976)
102. Kuznetsov, E., Mikhailov, A.: On the complete integrability of the two-dimensional classical Thirring model. Theor. Math. Phys. **30**(3), 193–200 (1977)
103. Kaup, D.: The three-wave interaction – a nondispersive phenomenon. Stud. Appl. Math. **55**(1), 9–44 (1976)
104. Degasperis, A., Conforti, M., Baronio, F., Wabnitz, S., Lombardo, S.: The three-wave resonant interaction equations: spectral and numerical methods. Lett. Math. Phys. **96**(1–3), 367–403 (2011)
105. Gerdjikov, V., Ivanov, R., Kyuldjiev, A.: On the N-wave equations and soliton interactions in two and three dimensions. Wave Motion **48**(8), 791–804 (2011). Nonlinear waves in action: propagation and interaction
106. Gerdjikov, V., Grahovski, G., Kostov, N.: On N-wave type systems and their gauge equivalent. Eur. Phys. J. B Condens. Matter Complex Syst. **29**(2), 243–248 (2002)
107. Newell, A.: Long waves–short waves; a solvable model. SIAM J. Appl. Math. **35**(4), 650–664 (1978)
108. Benney, D.: A general theory for interactions between short and long waves. Stud. Appl. Math. **35**(56), 81–94 (1977)
109. Zhu, J., Kuang, Y.: CUSP solitons to the long-short waves equation and the $\overline{\partial}$-dressing method. Rep. Math. Phys. **75**(2), 199–211 (2015)

110. Chowdhury, R., Chanda, P.K.: To the complete integrability of long wave–short wave interaction equations. J. Math. Phys. **27**(3), 707–709 (1986)
111. Kadomtsev, B.B., Petviashvili, V.I.: On the stability of solitary waves in weakly dispersing media. Sov. Phys. Dokl. **15**, 539 (1970)
112. Davey, A., Stewartson, K.: On three-dimensional packets of surface waves. Proc. R. Soc. Lond. Ser. A **338**, 101–110 (1974)
113. Guo, B., Ling, L., Liu, Q.P.: Nonlinear Schrödinger equation: generalized Darboux transformation and rogue wave solutions. Phys. Rev. E **85**, 026607 (2012)
114. He, J., Wang, L., Li, L., Porsezian, K., Erdélyi, R.: Few-cycle optical rogue waves: complex modified Korteweg de Vries equation. Phys. Rev. E **89**, 062917 (2014)
115. Guo, B., Ling, L., Liu, Q.P.: High-order solutions and generalized Darboux transformations of derivative nonlinear Schrödinger equations. Stud. Appl. Math. **130**(4), 317–344 (2013)
116. Degasperis, A., Wabnitz, S., Aceves, A.: Bragg grating rogue wave. Phys. Lett. A **379**(14–15), 1067–1070 (2015)
117. Chow, K., Chan, H., Kedziora, D., Grimshaw, R.: Rogue wave modes for the long wave-short wave resonance model. J. Phys. Soc. Jpn. **82**(7), 074001 (2013)
118. Li, C., He, J., Porsezian, K.: Rogue waves of the Hirota and the Maxwell-Bloch equations. Phys. Rev. E **87**, 012913 (2013)
119. Akhmediev, N., Soto-Crespo, J., Devine, N., Hoffmann, N.: Rogue wave spectra of the Sasa–Satsuma equation. Phys. D Nonlinear Phenom. **294**, 37–42 (2015)
120. Soto-Crespo, J.M., Devine, N., Hoffmann, N.P., Akhmediev, N.: Rogue waves of the Sasa-Satsuma equation in a chaotic wave field. Phys. Rev. E **90**, 032902 (2014)
121. Chen, S.: Twisted rogue-wave pairs in the Sasa-Satsuma equation. Phys. Rev. E **88**, 023202 (2013)
122. Dubard, P., Matveev, V.: Multi-rogue waves solutions: from the NLS to the KP-I equation. Nonlinearity **26**(12), R93 (2013)
123. Dubard, P., Gaillard, P., Klein, C.P., Matveev, V.: On multi-rogue wave solutions of the NLS equation and positon solutions of the KdV equation. Eur. Phys. J. Spec. Top. **185**, 247–258 (2010)
124. Ohta, Y., Yang, J.: Dynamics of rogue waves in the Davey-Stewartson II equation. J. Phys. A Math. Theor. **46**(10), 105202 (2013)

Hydrodynamic Envelope Solitons and Breathers

Amin Chabchoub, Miguel Onorato, and Nail Akhmediev

Abstract The nonlinear Schrödinger equation (NLSE) is one of the key equations in physics. It describes the evolution in time and space of wave packets and it applies to several nonlinear dispersive media, such as Bose-Einstein condensates, plasma, optics and hydrodynamics. An important feature of the NLSE is its integrability. Exact solutions and their experimental observations, ranging from solitons to breathers in various physical media, confirmed the validity of the NLSE in accurately describing the wave motion. The accuracy is surprisingly high even for the cases of severe wave focusing in a wide range of nonlinear dispersive media. In this Chapter, we will *briefly* discuss the physical relevance of exact NLSE solutions as well as review past and recent progress of experimental studies of dark and bright NLSE solutions in hydrodynamics. Validity and limitations of such weakly nonlinear models will be discussed in detail. Related promising engineering applications will be also emphasized.

1 Introduction

Localized waves on the water surface and extreme oceanic events in particular require accurate modeling for the sake of their physical understanding, prediction and prevention. The so-called rogue (or freak) waves have been frequently observed

A. Chabchoub (✉)
Department of Ocean Technology Policy and Environment, Graduate School of Frontier Sciences, The University of Tokyo, Kashiwa, Chiba 277-8563, Japan

Department of Mechanical Engineering, School of Engineering, Aalto University, FI-02150 Espoo, Finland
e-mail: amin.chabchoub@isea.k.u-tokyo.ac.jp

M. Onorato
Dipartimento di Fisica, Università degli Studi di Torino, IT-10125 Torino, Italy

Istituto Nazionale di Fisica Nucleare, INFN, Sezione di Torino, IT-10125 Torino, Italy
e-mail: miguel.onorato@unito.it

N. Akhmediev
Optical Sciences Group, Research School of Physics and Engineering, The Australian National University, Canberra, ACT 2600, Australia
e-mail: nail.akhmediev@anu.edu.au

M. Onorato et al. (eds.), *Rogue and Shock Waves in Nonlinear Dispersive Media*,
Lecture Notes in Physics 926, DOI 10.1007/978-3-319-39214-1_3

in coastal areas as well as in offshore regions [1–3]. Recently, physical mechanisms explaining the formation of rogue waves have attracted attention of several scientific communities [4–13]. Taking into account the nonlinear nature of water waves [3, 14], one of the physical mechanisms, considered to be responsible for the formation of hydrodynamic extremes, is the modulation instability (MI) [15, 16]. It has been discovered in the 1960s [17–20] and has been observed in several nonlinear media [21–23]. The MI, also referred to as the Benjamin-Feir (or Bespalov-Talanov) instability, describes the disintegration of weakly nonlinear regular wave train, initially slightly modulated in its amplitude. In the spectral domain, the MI originates from the presence of unstable side-bands on each side of the main frequency. These primary side-bands grow in amplitude generating the infinite number of additional side-bands due to the four wave mixing effect, thus, broadening the spectrum from a single frequency to a triangular comb-structure [24, 25]. The widening of the spectrum, in turn, leads to the strong periodic focusing of the wave field.

A crucial step in finding appropriate models to describe stationary and unstable hydrodynamic localized structures in finite and infinite water depth has been taken with the discovery of the nonlinear Schrödinger equation (NLSE) [20, 26] and particularly in the development of complex mathematical tools, such as the inverse scattering Transform [27], the Darboux transform method [28] and various direct routines [29–34] for solving this evolution equation. Several families of fundamental solutions have been derived and reported [35, 36]. As a result, physical understanding of nonlinear waves within the framework of integrable systems has significantly improved. Laboratory experiments and numerical studies played a major role in establishing the validity of integrable evolution equations, including the NLSE [37–41]. They also demonstrated the analogy between wave propagation in different nonlinear dispersive media, in particular, in optics and on the water surface [42, 43].

Here, we shortly review the works related to the hydrodynamic NLSE by choosing the most relevant experimental studies, related to envelope solitons and breathers in the cases of finite and infinite water depth in a sort of *crash course*. It is shown that the basic properties of the NLSE, and predictions of water surface motion based on it, agree with experiments and are reasonably accurate, even in the case of strong focusing of water waves, provided that the carrier frequency and the corresponding solution parameters are appropriately chosen. We also notice that the localized structures on the surface of shallow-water [44, 45] can be described using the NLSE solutions [46, 47] although they are not discussed here.

The chapter is organized as follows. In Sect. 2 we briefly recall the equations governing the surface gravity waves and discuss the weakly nonlinear Stokes approach. Section 3 is a review of the most relevant exact solutions of the defocusing and focusing NLSE, ranging from stationary solitons to breathers. In Sect. 4 we describe the experimental setup and the initial conditions applicable to the wave maker when generating these localized solutions in a wave flume. Sections 5 and 6 report experimental observations of hydrodynamic stationary and breather solutions. Finally, the main results are summarized in Sect. 7 and the limitations of weakly nonlinear models as well as potential applications of the NLSE approach in ocean engineering are discussed.

2 Weakly Nonlinear Water Waves Theory

In this Section we present the governing equations of an ideal fluid, consider the phenomenon of MI of Stokes waves and survey its properties within the framework of the NLSE.

2.1 Stokes Waves and Modulation Instability

A two-dimensional inviscid, incompressible and irrotational fluid of depth h with free surface is governed by the Laplace of motion and three boundary conditions [2, 48]

$$\nabla^2\phi = \phi_{xx} + \phi_{zz} = 0 \text{ for } -h \le z \le 0,\ x \in \mathbb{R} \text{ and } t \in \mathbb{R}^+, \tag{1}$$

$$\eta_t + \eta_x\phi_x - \phi_z = 0 \text{ on } z = \eta(x,t), \tag{2}$$

$$\phi_t + \frac{1}{2}(\nabla\phi)^2 + g\eta = 0 \text{ on } z = \eta(x,t), \tag{3}$$

$$\phi_z = 0 \text{ on } z = -h, \tag{4}$$

where $\phi(x,z,t)$ is the velocity potential, ∇^2 denotes the Laplace operator, $\eta(x,t)$ is the free surface elevation and g is the gravitational acceleration. The waves are propagating in one dimension along the x-axis, the coordinate z is positive upwards and the external pressure exerted on the surface of the fluid is assumed to be zero. It is easy to show that a purely sinusoidal water surface elevation is a solution of the linearized water wave problem with the corresponding linear dispersion relation

$$\omega = \sqrt{gk\tanh(kh)}. \tag{5}$$

Stokes has shown in his pioneering work [14] that periodic solutions of the weakly nonlinear problem can be obtained using the perturbation theory with the small steepness parameter ε, defined as a product of the wave amplitude a and the wavenumber k. For deep-water ($kh \to \infty$), up to second-order approximation, the surface elevation and the dispersion relation can be written in the forms

$$\eta(x,t) = a\cos(kx - \omega t) + \frac{1}{2}ka^2\cos[2(kx - \omega t)], \tag{6}$$

$$\omega = \sqrt{gk}\left(1 + \frac{a^2k^2}{2}\right). \tag{7}$$

Benjamin and Feir showed that this weakly nonlinear solution (6) is additionally unstable to perturbations with longer periods [19]. Namely, the modulation of

a regular Stokes wave train may experience an exponential growth when the modulation frequency Ω lies in the following range

$$0 < \Omega < \sqrt{2}\omega ka. \tag{8}$$

Thus, for a given steepness $\varepsilon = ak$ of the wave train, there is a modulation frequency range Ω in which second-order Stokes waves become unstable [49, 50]. We elucidate in the next subsection how this instability can be explained within the context of the NLSE.

2.2 The Nonlinear Schrödinger Equation (NLSE)

A general form of the NLSE has been derived for nonlinear dispersive media in [26, 51]. For deep-water waves, it has been first derived by Zakharov [20] and has the following form:

$$\mathrm{i}\left(\frac{\partial \Psi}{\partial t} + c_g \frac{\partial \Psi}{\partial x}\right) - \frac{\omega}{8k^2}\frac{\partial^2 \Psi}{\partial x^2} - \frac{\omega k^2}{2}|\Psi|^2 \Psi = 0. \tag{9}$$

k corresponds to the carrier wavenumber, $\omega = \sqrt{gk}$ is the angular frequency and $c_g = \omega/(2k)$ denotes the group velocity of the wave packet. Yuen and Lake derived the same Eq. (9) using Whitham's theory [37]. A more general form of evolution equation for arbitrary water depth h can be rigorously derived using the method of multiple scales [48, 52]:

$$\mathrm{i}\left(\frac{\partial \Psi}{\partial t} + c_g \frac{\partial \Psi}{\partial x}\right) - \alpha \frac{\partial^2 \Psi}{\partial x^2} - \beta |\Psi|^2 \Psi = 0, \tag{10}$$

where the coefficients α and β are

$$\alpha = -\frac{1}{2}\frac{\partial^2 \omega}{\partial k^2},$$

$$\beta = \frac{\omega k^2 \left(\cosh(4kh) + 8 - 2\tanh^2(kh)\right)}{16\sinh^4(kh)} - \frac{\omega\left(2\omega\cosh^2(kh) + kc_g\right)^2}{2\sinh^2(2kh)\left(gh - c_g^2\right)}.$$

The group velocity here is $c_g = \dfrac{\partial \omega}{\partial k}$ with ω and k related through the linear dispersion for finite water depth in Eq. (5). Depending on the signs of α and β, Eq. (10) is either a focusing or defocusing form of the NLSE. Then, it can be shown that whether the MI develops or not depends on the sign of the product $\alpha\beta$. From the above expressions for α and β we can see that $\alpha\beta > 0$ when $kh > 1.363$. In this case, the NLSE is self-focussing and the wave train modulations may experience

an exponential growth. On the other hand, when $kh < 1.363$, the NLSE is self-defocusing and all wave trains are stable.

First, we focus on the deep-water case $kh > 1.363$ when the NLSE admits the MI. The plane wave solution of Eq. (9) in infinite water depth is

$$\Psi(x,t) = a \exp\left(-\mathrm{i}\frac{a^2k^2}{2}\omega t\right). \tag{11}$$

Periodic modulations of this solution along x with modulation wavenumber K lead to the time response with the modulation frequency Ω [3, 37] which can be found from linearization of the perturbation

$$\Omega^2 = \frac{\omega^2}{8k^2}\left(\frac{K^2}{8k^2} - k^2a^2\right)K^2. \tag{12}$$

A wave train is unstable if Ω is imaginary. This happens when K lies in the range

$$0 < K < 2\sqrt{2}k^2a. \tag{13}$$

This condition is equivalent to Eq. (8) taking into account that $c_g = \dfrac{\Omega}{K} = \dfrac{\omega}{2k}$. The above linearized approach is the limiting case of the complete exact solution of the NLSE [24]. In the latter case, the modulation wavenumber K becomes a free parameter of a family of NLSE solutions. This family is presented in the next section.

3 Exact NLSE Solutions and Their Physical Interpretation

As the NLSE is an integrable equation, the initial value problem can be solved analytically for wide variety of initial conditions [27]. Another useful approach is finding initial conditions that generate known exact solutions of the NLSE. The existence of families of exact solutions of the NLSE with variable parameters [35, 53] provides certain flexibility in finding initial conditions and experimental observation of these solutions. For simplicity, below, we consider the scaled form of the NLSE

$$\mathrm{i}\,\psi_T + \psi_{XX} \pm 2|\psi|^2\psi = 0, \tag{14}$$

where dependent and independent variables are rescaled in order to simplify the coefficients in the equation. The sign of the cubic nonlinear term in (14) depends on sign of the product $\alpha\beta$ or, in other words, on the depth of the water. Specifically, the sign is negative (defocusing case) when $kh < 1.363$ and positive (focusing case) when $kh > 1.363$.

Equation (14) admits a scaling transformation [36], i.e., if $\psi(x,t)$ is a solution of (14), then so is $a\psi(aX, a^2T)$, where a is an arbitrary real parameter. This transformation allows us to add one more free parameter into the family of known solutions. In the defocusing case, the NLSE admits a family of dark soliton solutions, that can be written in the form [27]

$$\psi_D(X,T) = \left[\sin(\vartheta) + \mathrm{i}\cos(\vartheta)\tanh\{\cos(\vartheta)(X + 2\sin(\vartheta)T)\}\right]\exp(-2\,\mathrm{i}\,T).$$

Here, the real parameter ϑ controls the depth of the soliton relative to the background. Namely, the minimum soliton amplitude can be expressed in terms of ϑ: $\min|\psi_D(X,T)| = |\sin\vartheta|$ while the correction of the soliton group velocity c_g is $\sin\vartheta$. The upper panel in Fig. 1 shows an example of a gray soliton in the (X,T)-plane when $\vartheta = \pi/6$ while the lower panel shows three examples of the soliton shape in X when ϑ changes. The minimal (zero) amplitude of the soliton is reached when $\vartheta = 0$. This is the case of the black soliton [54]. It can be written in a simple form

$$\psi_B(X,T) = \tanh(X)\exp(-2\,\mathrm{i}\,T). \tag{15}$$

The localized solution of the focusing NLSE is the bright soliton with zero velocity [27]

$$\psi_S(X,T) = \mathrm{sech}(X)\exp(\mathrm{i}\,T). \tag{16}$$

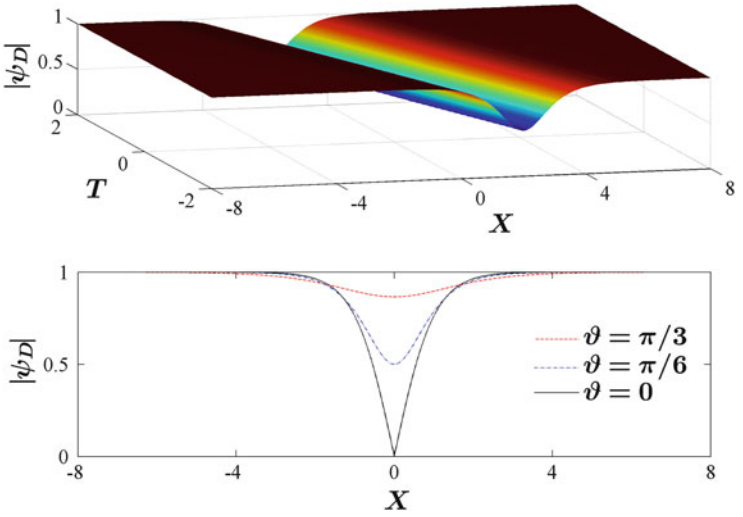

Fig. 1 *Top*: Evolution of a modulus of gray soliton in the (X,T)-plane for $a = 1$ and $\vartheta = \pi/6$. *Bottom*: Dark soliton envelopes for $\vartheta \in \{\pi/3, \pi/6, 0\}$ and a nondimensional amplitude $a = 1$ at $T = 0$

A velocity can be added to this solution using Galilean transformation [36]. Multi-soliton solutions can be constructed analytically using the Darboux transform technique [55]. Here, we restrict our attention to the case when individual solitons have zero velocities and located at the same position $X = 0$. However, their eigenvalues of inverse scattering technique differ. Namely, the eigenvalues are imaginary and they are given by $\{\mathrm{i}/2,\ 3\mathrm{i}/2,\ 5\mathrm{i}/2,\ \ldots\}$. These solutions have been first presented by Satsuma and Yajima in 1974 [56]. Examples are shown in Fig. 2. The number of fundamental solitons in these superpositions progressively increases ($N = 1, 2$ and 3, respectively). The individual solitons in these superpositions have alternating phases [55]. The advantage of this arrangement is the simple profile of the composite solution at zero T which is given by $\psi(T = 0, X) = N\,\mathrm{sech}(X)$. This specific form is the reason for calling these solutions "higher-order" solitons [57]. Instead, we name these solutions "Satsuma-Yajima solitons". Indeed, Satsuma and Yajima found these solutions investigating the initial conditions in the form $N\,\mathrm{sech}(X)$. If the soliton phases are not alternating, this feature of the solutions is lost. Instead, the amplitude of the superposition may take much higher values (up to N^2 as shown by Akhmediev and Mitskevich [55]).

Higher-order solitons are periodic breathers along the T-axis due to the difference of propagation constants of individual soliton components. For strict periodicity, all propagation constants when $N > 2$ must be commensurate. This happens for the above specific choice of the eigenvalues. The maximum compression of the higher-order solitons happens in the middle of each period. In the optimized case, the

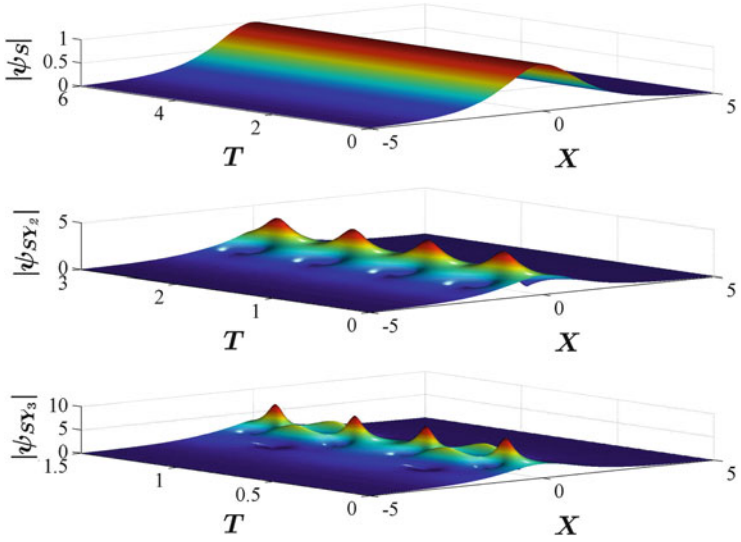

Fig. 2 *Top*: Evolution of a sech(X) envelope soliton ψ_S in normalized time and space for $a=$ 1. *Middle*: Evolution of a second-order Satsuma-Yajima solution ψ_{SY_2} with the initial condition $2\,\mathrm{sech}(X)$ in normalized time and space for $a=$ 1. *Bottom*: Evolution of a third-order Satsuma-Yajima solution ψ_{SY_3} with the initial condition $3\,\mathrm{sech}(X)$ in normalized time and space for $a=$ 1

maximum compression with the amplitude N^2 takes place at $T = 0$ [55]. The wave amplitude of up to N^2 can be considered as an extreme event. However, the periodic appearance of such events prevents us in classifying them as rogue waves. The latter suppose to be unexpected and occur only once. Then we should turn our attention to other solutions of the NLSE as prototypes of rogue waves although chaotic generation of solitons may serve as a source of rogue waves in supercontinuum generation in optical fibres [4, 58].

For the ocean, it is natural to describe rogue waves using localized solutions on a background as the ocean surface is normally covered with waves of various frequencies. As we are dealing with the envelope equation, these waves serve as the finite amplitude background. The background contains infinite amount of energy due to the vast areas of the ocean and instabilities may focus this energy into a spot. A solution in the form of a soliton on a finite background has been found in [59]. This solution is periodic due to the beating between the soliton and the background. Thus, the feature of unexpectedness in this case is missing although the amplification above the background can reach the values higher than three. More detailed investigation of these type of solutions has been provided by Ma in 1979 [60]. They are presently known as Kuznetsov-Ma (KM) solitons [61–63]. Such solution does not correspond to the MI.

In contrast, MI starts from an infinitesimal perturbation that grows exponentially at the initial stages of the process. For later times, the exponential growth is an artefact of the linear stability analysis and has to be reconsidered for larger amplitudes. Consequently, MI has been later extended to a full exact solution of the NLSE [24, 53]. These are now known as Akhmediev breathers (ABs) [64–67]. These solutions reveal the initially exponential amplitude growth of the maxima up to a highest amplitude with the subsequent decay of the field back to the background level. This growth-decay cycle of the solution occurs only once and depending on the initial conditions may have the effect of unexpectedness.

The power of complex analysis allows the solutions of the NLSE to be written as families of solutions with several parameters with particular cases assigned to a specific values of these parameters. An example is a rather general three-parameter family of NLSE solutions that includes most of the basic solutions: solitons, various single- and double-periodic solutions, rational solutions and plane waves [35]. As a particular case of this family, the KM and AB solutions can be represented as a one-parameter family of solutions where a single parameter $\mathfrak{a}$ controls the modulation period of these solutions and allows mutual transition between breathers and solitons [61, 68]. This combined family can be written in the form:

$$\psi_{A/KM}(X,T) = \left(1 + \frac{2(1-2\mathfrak{a})\cosh(2RT) + \mathrm{i}R\sinh(2RT)}{\sqrt{2\mathfrak{a}}\cos(\Omega X) - \cosh(2RT)}\right)\exp(2\mathrm{i}T), \quad (17)$$

with $R = \sqrt{8\mathfrak{a}(1-2\mathfrak{a})}$ and $\Omega = 2\sqrt{1-2\mathfrak{a}}$. When the parameter $0 < \mathfrak{a} < 0.5$, Eq. (17) describes the family of ABs. The case of maximal growth rate corresponds to $\mathfrak{a} = 0.25$. When $\mathfrak{a} > 0.5$ it represents the KM solitons. This parametrisation is not unique. A different way of representing these solutions can be found in [69].

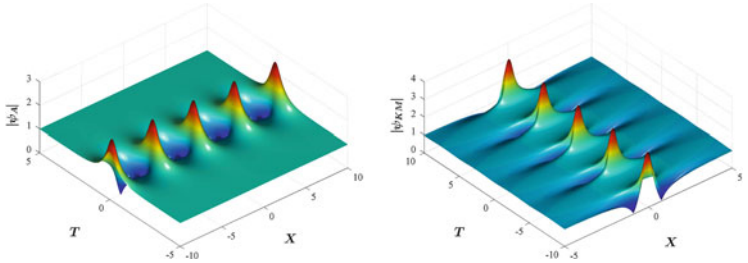

Fig. 3 *Left*: An example of a space-periodic Akhmediev breather for $\mathfrak{a} = 0.29$ and $a = 1$. *Right*: An example of a time-periodic Kuznetsov-Ma soliton for $\mathfrak{a} = 0.55$ and $a = 1$. Evolution variable in each case is T. *Source*: From [62]

One example of each of these solutions is shown in Fig. 3. Although mathematically these two solutions can be written as a single equation, they describe different physical phenomena. The AB solution is breathing only once along the T-axis while the KM soliton is evolving periodically along the evolution variable T. The beating period in the KM soliton case is related to the difference in wavenumbers of a soliton and the background wave. When the background wave is zero, the KM soliton is transformed into an ordinary constant amplitude soliton. On the other hand, the spatial period of the AB solution is explicitly given in the initial conditions.

The case of infinite period of each of these two solutions is undefined. This limit is reached when the parameter $\mathfrak{a} \to 0.5$. The solution can be found eliminating uncertainty with a L'Hopital's rule. Most of the maxima in the solution move to infinity and only one of them remains at the origin. Then, the solution is described by a rational expression which is known as the Peregrine solution

$$\psi_1(X,T) = \left(-1 + \frac{4 + 16\,\mathrm{i}\,T}{1 + 4X^2 + 16T^2}\right) \exp(2\,\mathrm{i}\,T)\,. \tag{18}$$

It was first found by Peregrine in 1983 [70]. In contrast to the ABs, the growth rate of this solution is algebraic rather than exponential. Furthermore, due to its localization both in time and in space and because its amplitude reaches three times the background this solution has been suggested to model oceanic rogue waves [71]. Indeed, such wave "appears from nowhere and disappears without a trace" [72] just like oceanic rogue waves do. The Peregrine solution is not the only one, which has these exceptional features. In fact, it is the lowest-order solution of a whole family of doubly-localized Akhmediev-Peregrine breathers (APs) [73]. Their general form is given by Akhmediev et al. [74]

$$\psi_j(X,T) = \left((-1)^j + \frac{G_j + \mathrm{i}\,H_j}{D_j}\right) \exp(2\,\mathrm{i}\,T)\,. \tag{19}$$

where the expressions for polynomials G_j, H_j and D_j are complex and are not given here. We refer to [53, 72, 74–77] for their explicit forms. Figure 4 shows profiles of

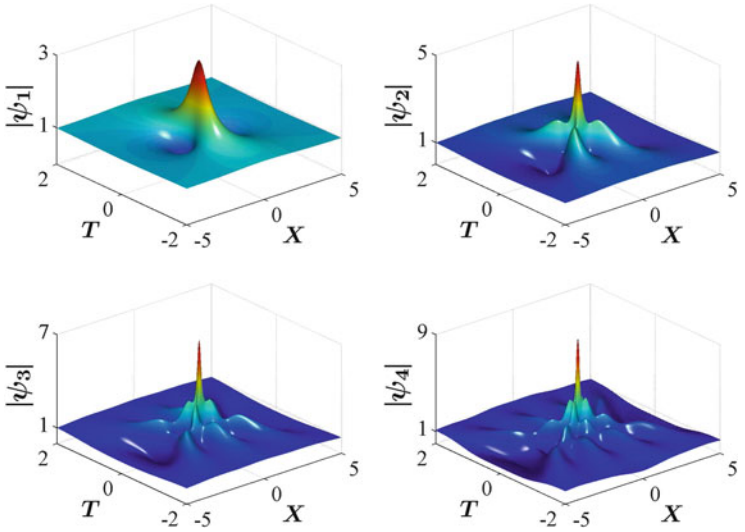

Fig. 4 Peregrine and higher-order AP solutions on (X, T)-plane for $a = 1$. *Top left*: Normalized Peregrine soliton. *Top right*: Second-order AP solution. *Bottom left*: Third-order AP solution. *Bottom right*: Fourth-order AP solution. *Source*: From [107]

four lowest-order AP solutions centered at the origin. As can be seen from Fig. 4, the increase of the order of the solution j boosts the amplitude of the rogue wave. It can be shown [74] that the amplitude amplification of the j-th order solution over the background is $2j + 1$. There are a number of recent papers reporting higher-order AP solutions with maximal amplitude compression of up to 23 times the amplitude of the background [78–80]. However, as discussed in Sect. 6, it is very hard to reproduce them experimentally in wave tanks because, unless the initial condition is very small, wave breaking occurs. Generally, higher-order solutions exist in various forms. In the limiting case, they can split into fundamental building blocks, i.e. $\frac{j(j+1)}{2}$ separate Peregrine solutions. We refer to [81–83] for particular forms of these solutions and for their general classification.

4 Experimental Setup

The methodology applied to observe wave packets and particularly exact solutions of the NLSE in a wave tank of water with depth h is straightforward. The carrier and envelope parameters and the boundary conditions, applied to the wave maker, have to be determined from the theory. The background is defined by two parameters: the amplitude a and the steepness $\varepsilon = ak$. The wavenumber of the carrier wave k is then determined directly from a and ε, while the frequency ω is derived from the linear dispersion relation. These parameters should be carefully chosen in order to keep the nonlinearity within a reasonable range to avoid wave breaking. The latter

is especially dangerous for pulsating solutions, such as multi-solitons and breathers, distorting their expected dynamics. In addition, the wavelength of the excitations should be adapted to the length and to the water depth h of the facility. The water depth defines whether the governing NLSE is defocusing ($kh < 1.363$) or focusing ($kh > 1.363$). The length of the tank should provide sufficient propagation distance for the wave packet. It should also be kept in mind that larger wavelengths and amplitudes result in stronger reflections from the beach located at the other end of the wave flume.

Once the exact dimensional form of the NLSE solution $\Psi(x,t)$ of interest is established, the boundary condition is given by the corresponding expression of the surface elevation at a spatial co-ordinate x^* that corresponds to the position of the wave generator

$$\eta_{\text{wave maker}}\left(x^*,t\right) = \text{Re}\left(\Psi\left(x^*,t\right)\exp\left[\text{i}\left(kx^* - \omega t\right)\right]\right). \tag{20}$$

At this position, the NLSE solution $\Psi(x^*,t)$ provides both a specific amplitude modulation as well as the phase of the carrier wave. These data allow accurate, to first-order, ab-initio excitation of the wave packet. Higher-order Stokes components appear rapidly in the medium due to the intrinsic nonlinear nature of water waves and their magnitude depends on the chosen carrier steepness. Therefore, the amplitude measurements at an arbitrary position must be compared to the NLSE prediction by taking into account the second-order corrections

$$\eta(x,t) = \text{Re}\left(\Psi(x,t)\exp\left[\text{i}\left(kx-\omega t\right)\right] + \frac{1}{2}k\Psi^2(x,t)\exp\left[2\text{i}\left(kx-\omega t\right)\right]\right). \tag{21}$$

The wave gauges should be calibrated accordingly before starting the experiments. The last gauge should be placed at a sufficiently large distance from the beach in order to avoid the effect of reflected waves as much as possible. The experiments for the defocusing NLSE case have been conducted in a facility with shallow-water depth and with dimensions, described in [84]. The bright soliton and breather-type solutions have been observed in a deep-water facility, described in [41].

5 Observations of Envelope Solitons on the Water Surface

In this section, we discuss laboratory experiments with dark solitons, followed by a review of observations of bright stationary envelope solitons and recent observations of multi-solitons.

5.1 Dark Solitons

Dark solitons comprise a family of solutions with variable central amplitude smaller than the background. The family is controlled by the parameter ϑ. The gray solitons have the smallest envelope amplitude depression when ϑ is close to $\pi/2$. The other limiting case when the parameter ϑ is equal to zero corresponds to the black soliton. The left panel in Fig. 5 shows the laboratory measurements of gray solitons with $\vartheta = \pi/6$ for a dimensionless depth $kh = 0.8$ and a steepness $\varepsilon = 0.06$. The right panel in Fig. 5 shows the data for $\vartheta = \pi/14$, a dimensionless depth of $kh = 0.9$ and a steepness of $\varepsilon = 0.07$. The details of these measurements as well as the position of the wave gauges can be found in [85]. The experimental parameters in Fig. 5 have been optimized for each value of the variable gray soliton velocity and the envelope depression.

Two sets of measurements corresponding to the black soliton with $\vartheta = 0$ when the envelope reaches the zero amplitude at the soliton center are shown in Fig. 6. These time-series have been also optimized by the value of group velocity c_g as described in [84]. As a result, the dimensionless depth, the carrier amplitude and the steepness parameter in the left panel were chosen to be $kh = 1.2$, $a = 0.04$ and $\varepsilon = 0.12$ respectively, while on the right panel, $kh = 1.0$, $a = 0.02$ and $\varepsilon = 0.08$.

These laboratory measurements are a clear evidence of existence of dark solitons in the case of water waves and confirm corresponding numerical hydrodynamic simulations [86]. Namely, the initial dip generated according to NLSE theory stays localized and does not change its profile when moving with the soliton group velocity. At the same time, the phase velocity is different from the group velocity. The carrier waves, having faster phase velocity, enter and exit the localized dip without causing deformations to the stationary wave envelope. It has been shown that dark solitons could cleanly propagate in the flume with the dimensionless depth

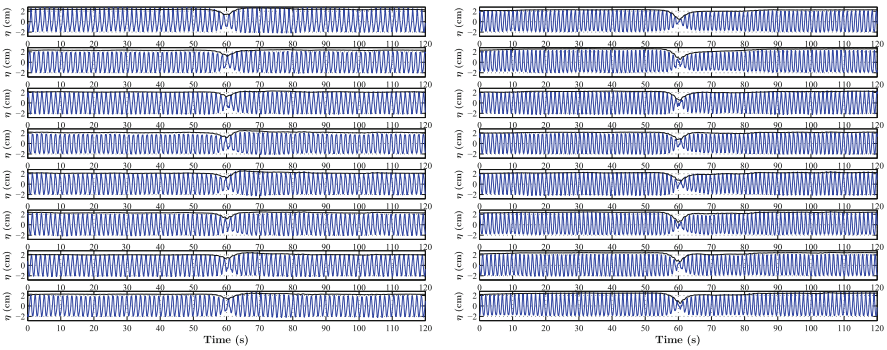

Fig. 5 Propagation of gray solitons in a wave tank with water depth $h = 0.25$ m. *Left panel*: The case of gray soliton with $\vartheta = \pi/6$ and carrier parameters $a = 0.02$ m and $\varepsilon = 0.06$. The dimensionless depth $kh = 0.8$. *Right panel*: The case of gray soliton with $\vartheta = \pi/12$ and carrier parameters $a = 0.02$ m and $\varepsilon = 0.07$ while $kh = 0.9$. *Source*: From [85]

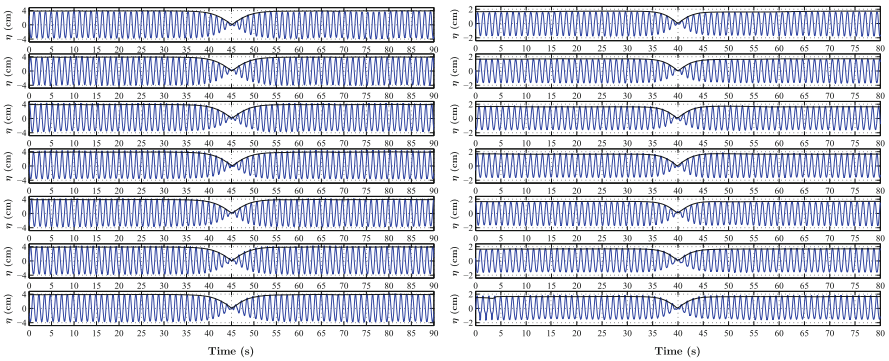

Fig. 6 Two examples of propagation of a black soliton ($\vartheta = 0$) in a water wave tank. *Left panel*: Carrier parameters $a = 0.04$ m, $\varepsilon = 0.12$ and the dimensionless depth $kh = 1.2$. *Right panel*: Carrier parameters $a = 0.02$ m, $\varepsilon = 0.08$ and the dimensionless depth $kh = 1.0$. *Source*: From [84]

of up to $kh = 0.6$. The defocusing NLSE indeed describes well the nonlinear dynamics of stationary wave packets in water wave facilities with finite water depth. These observations in water waves are an additional proof of ubiquitous applicability of defocusing NLSE in various branches of nonlinear physics. The latter include observations of dark solitons in variety of nonlinear media such as in Bose-Einstein condensates [39], in plasmas [87] and in optics [88].

5.2 *Bright Solitons*

The first envelope bright soliton observed on a water surface was reported back in the 1970s by Yuen and Lake [89]. In the same work, the authors also discussed experiments on collision of stationary envelope solitons in the wave flume, thus confirming another fundamental property of bright envelope solitons in water waves. Solitons have also been predicted [90] and observed [57] in optics opening the whole new soliton branch of modern physics [38, 91]. Meanwhile, the NLSE soliton knowledge in the water wave case was in a lethargic state (we do not discuss the KdV equation here). However, recently, the bright envelope solitons have been observed in a large wave flume for a carrier steepness of up to a remarkable value of $\varepsilon = 0.3$ [92]. The envelope solitons remained stationary over a significant propagation distance, in excellent agreement with numerical simulations, based on the higher-order spectral method (HOSM) [92]. For comparison, two parts of Fig. 7 show the measurements reported in [89] and [92], respectively.

These impressive observations confirmed the validity of the focusing NLSE in describing the nonlinear propagation of surface water waves in time and space. In the same work [89], the authors reported experiments showing that deviation from the envelope soliton solutions result in the compression of the wave envelope in

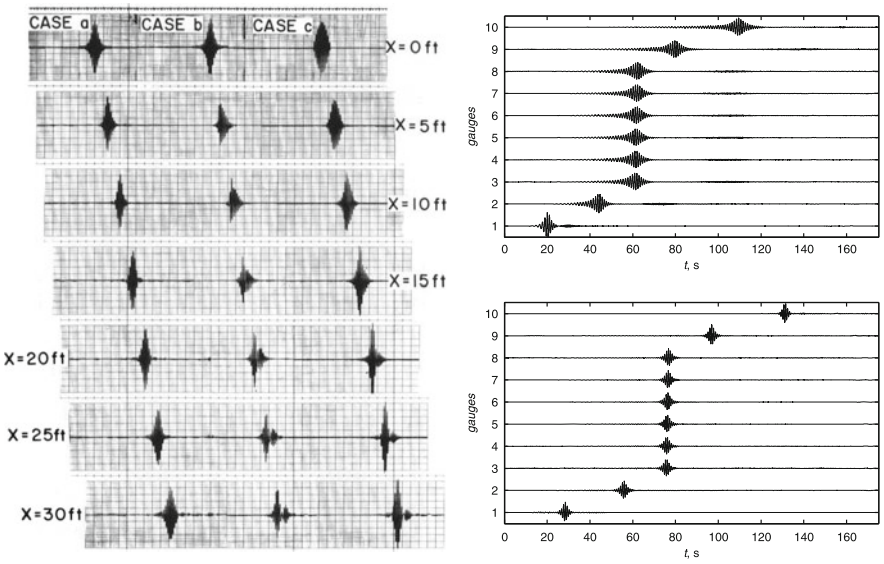

Fig. 7 *Left*: Propagation of the Sech soliton (shown as CASE a) for the initial steepness $\varepsilon = 0.14$. The Figure is taken from [89]. *Right*: Propagation of Sech soliton envelopes for significantly higher steepness values $\varepsilon = 0.3$. Both *upper* and *lower panels* on the *right* are taken from [92]

agreement with the NLSE simulations. As we will see in the next subsection, these pulsating structures can be assigned to multi-solitons which were not known at that time.

5.3 Multi-Soliton Solutions

Next, we discuss water wave experiments, which describe the evolution of multi-solitons based on exact NLSE solutions. Figure 8 shows the evolution of the second- and third-order Satsuma-Yajima solitons.

The carrier steepness has been chosen below the value when the wave breaking starts. Higher-order solitons require even smaller steepness as their maximal amplitudes and the degree of compression are higher. The third-order solution requires a smaller steepness than the second-order solution. Generally, the higher is the order of the solution, the lower should be the steepness. The convenience of Satsuma-Yajima solitons is in the possibility to start them with the Sech-shape initial condition multiplied by an integer. These initial conditions lead to a pulse compression in good agreement with the NLSE predictions. However, deviations from the theory are unavoidable. These are growing with the increase of the order of the solution and with the widening of their spectra. The most visible effect in Fig. 8 is the accumulation of the asymmetry by the pulses that start from perfectly symmetric initial conditions. The asymmetry increases with the growth of the local steepness.

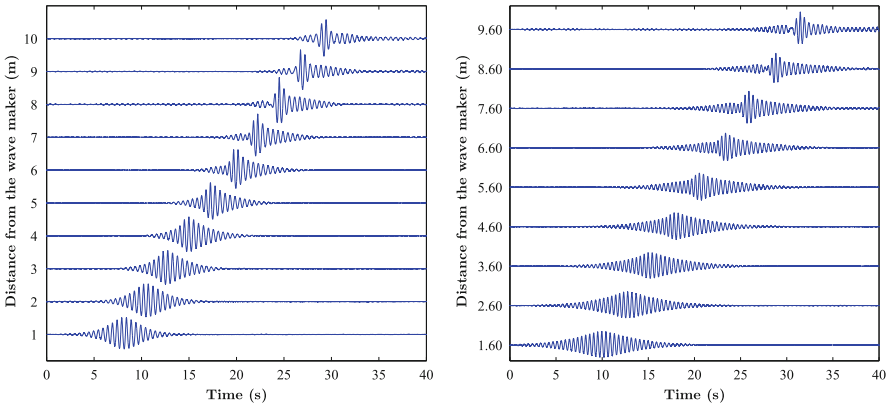

Fig. 8 *Left*: Evolution of the two-soliton solution in a water wave tank for carrier parameters $a = 0.005$ mm and $\varepsilon = 0.08$. *Right*: Evolution of the three-soliton solution in a water wave tank for carrier parameters $a = 0.002$ m and $\varepsilon = 0.04$. *Source*: From [100]

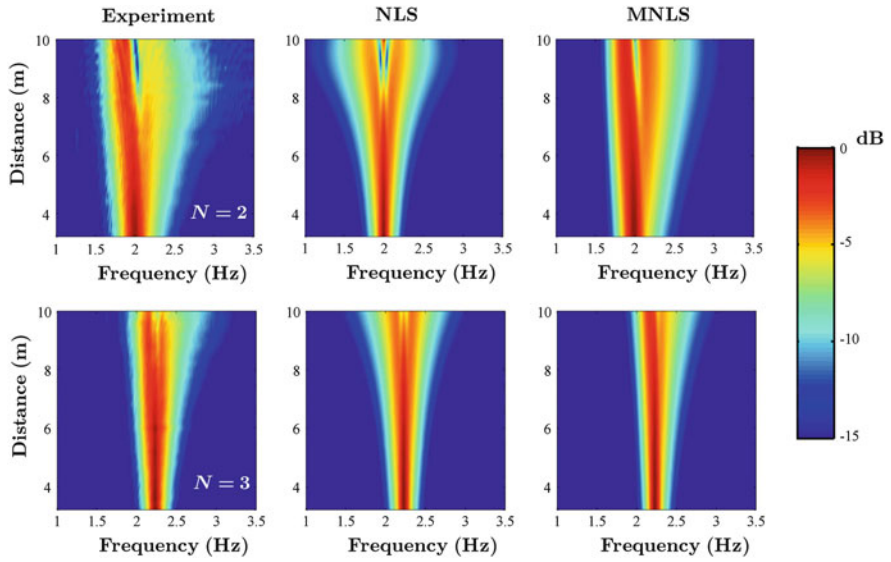

Fig. 9 Spectra of the multi-soliton Satsuma-Yajima solutions in experiment (*left column*), according to the NLSE theory (*middle column*) and when using MNLSE simulations (*right column*). *Upper row* corresponds to the two-soliton solution while the *lower row* to the three-soliton solution. Parameters are the same as in Fig. 8. *Source*: From [100]

The use of more accurate equations with the addition of higher-order dispersion to the NLSE and taking into account the mean flow provide a better approximation of the evolution dynamics [93, 94]. This can be seen from the comparison of experimental and numerical data in Fig. 9. The necessity of corrections and the

use of the modified nonlinear Schrödinger equation (MNLSE) has been stressed by Trulsen and Dysthe in [95, 96].

In analogy with the corresponding phenomenon in optics, perturbations of the NLSE and the increase of the number of solitons in the solution may cause an irreversible fission of the pulse into several fundamental solitons [97]. In the spectral domain, this corresponds to an irreversible broadening of the spectrum, a phenomenon known as supercontinuum generation [58, 97–99]. Figure 10 shows the similar hydrodynamic supercontinuum generation for initial conditions 4 sech (X) which contains four solitons [100]. Here, carrier amplitude is $a = 0.001$ m and the steepness is $\varepsilon = 0.04$. Due to the strong higher-order perturbation of the NLSE, the initial Sech-shaped envelope splits into fundamental solitons during the evolution [96]. This can be seen from the upper panels in Fig. 10. Moreover, the spectra computed from the experimental measurements in the flume at 10 m from the wave maker, shown in the lower panels in Fig. 10, reveal the generation of a supercontinuum, in complete agreement with MNLSE simulations. These experiments highlight once again the interdisciplinary and universal feature of the NLSE dynamics and similar roles of its higher-order perturbations in optics and hydrodynamics.

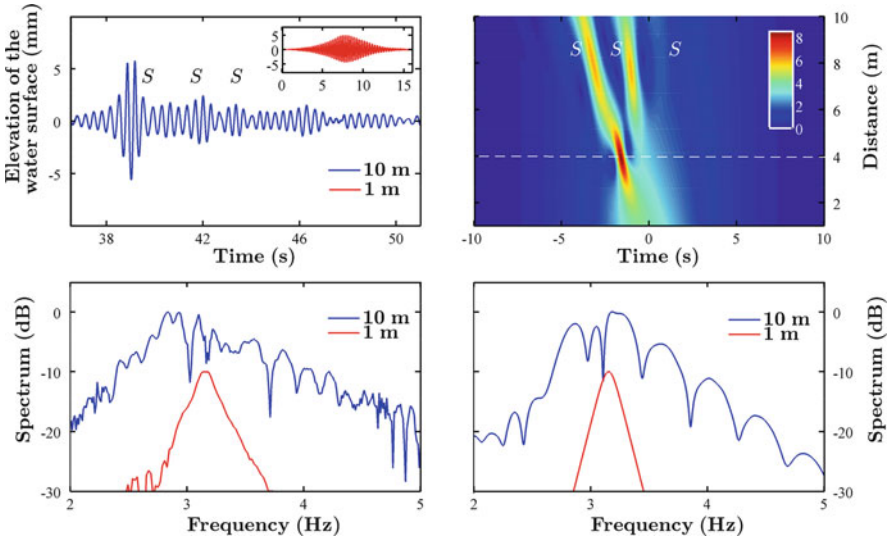

Fig. 10 *Top left*: the wave profiles of the fourth-order Satsuma-Yajima soliton measured at 1 and 10 m from the wave maker, respectively, for the carrier parameters $a = 0.001$ m and $\varepsilon = 0.04$. *Top right*: numerical MNLSE simulations, corresponding to this experiment. *Bottom left*: spectra of the measured wave profiles, shown in the *top left panel*. *Bottom right*: spectra obtained from MNLSE simulations for the same measurement positions. *Source*: from [100]

6 Observations of Breathers on a Finite Background

The behavior of hydrodynamic MI has been studied experimentally in [23, 101]. In these laboratory studies, the MI on the water surface has been triggered in a standard way by adding small side-bands to the wave carrier frequency making it unstable. At present state of knowledge, the use of exact NLSE solutions allows us to initiate the MI dynamics at any stage of its spatial or temporal evolution. In this section, we report the laboratory experiments with observation of breather solutions on a finite background. The latter are the key models in understanding the dynamics of modulationally unstable water waves. They may serve as the possible explanation for oceanic rogue waves. In the following plots, all curves showing the laboratory measurements are depicted in blue, whereas the corresponding theoretical NLSE predictions to second-order in steepness are shown in red.

6.1 Fundamental Periodic Breathers

The observation of ABs and KM solitons have been reported in [62]. Here, we present the same measurements, starting with ABs. ABs are specific NLSE solutions describing the full evolution of MI and the related exponential growth rate at its starting stage. ABs comprise a family of solutions with a free parameter $\mathfrak{a}$ or equivalently, the modulation wavenumber K. In dimensional units, for any given modulation wavenumber K, the maximal expected amplitude of an Akhmediev breather is given by Osborne [3], Onorato et al. [102]

$$|\Psi_A|_{\max} = 1 + 2\sqrt{1 - \left(\frac{K}{2\sqrt{2}k^2 a}\right)^2}. \tag{22}$$

This amplitude can be considered as the amplification factor provided that the background is 1. In the experiments, the amplitude of the carrier has been fixed to $a = 0.005\,\mathrm{m}$ for all periodic ABs and KMs. Figure 11 shows two cases of an AB evolution for $\mathfrak{a} = 0.46$ and $\mathfrak{a} = 0.49$ and for steepness values of $\varepsilon = 0.09$ and $\varepsilon = 0.08$, respectively. Increasing the parameter $\mathfrak{a}$ in the allowed range $\mathfrak{a} \in]0; 0.5[$ increases the modulation period. The amplitude amplification also increases and converges to three at the upper limit.

The comparison of experimental observations of the ABs at the maximal wave compression with the NLSE solution to the second-order correction in steepness is shown in Fig. 12. The wave dynamics which starts from the constant amplitude background with small perturbation, reaches the maximal amplitude of the breather nearly at the end of the flume. This is the curve recorded at 9 m mark in Fig. 11. It is repeated in larger scale in Fig. 12. A very good agreement between the measurements given by the blue curve and the theory predictions shown by the red

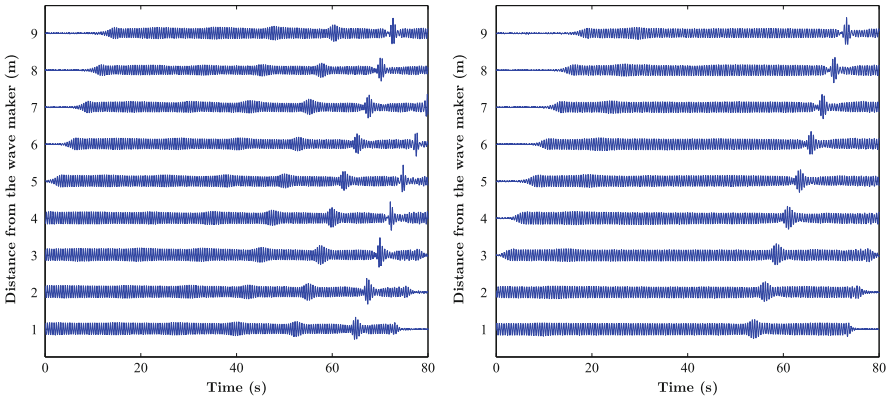

Fig. 11 *Left*: Evolution of an AB in a wave flume for $\mathfrak{a} = 0.46$ and the carrier parameters $a = 0.005$ m and $\varepsilon = 0.09$. *Right*: Evolution of an AB in a wave flume for $\mathfrak{a} = 0.49$ and the carrier parameters $a = 0.005$ m and $\varepsilon = 0.08$. *Source*: from [62]

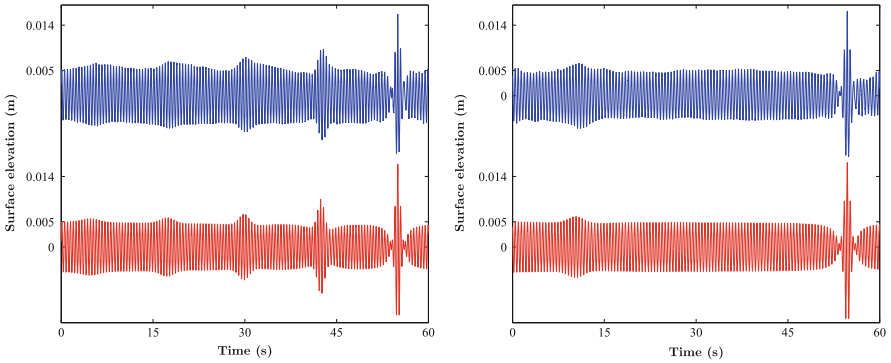

Fig. 12 *Left*: Comparison of the last wave flume measurement (*blue curve*, the same as the *upper curve* in the *left panel* of Fig. 11) with the theoretical surface elevation calculated using the NLSE solution to the second-order correction in steepness (*red curve*). *Right*: Comparison of the last wave flume measurement (*blue curve*, the same as the *upper curve* in the *right panel* of Fig. 11) with the theoretical surface elevation calculated using the NLSE solution with the second-order correction in steepness (*red curve*). *Source*: from [62]

curves can be noticed. The agreement is achieved basically on all parameters: on the value of the modulation periods, the maximal amplifications reached as well as the overall shapes of the wave profiles.

The next two cases dealing with the KM soliton propagation on the water surface are shown in Fig. 13. The soliton parameters here are $\mathfrak{a} = 1.2$ and $\mathfrak{a} = 0.9$ while the steepness values are $\varepsilon = 0.08$ and $\varepsilon = 0.09$, respectively. The maximal amplitude of the KM soliton increases with increasing the parameter $\mathfrak{a}$. The KM soliton stays as a localized formation on a background during the whole time of evolution. The amplitude is periodic with the maximal value in each case reached

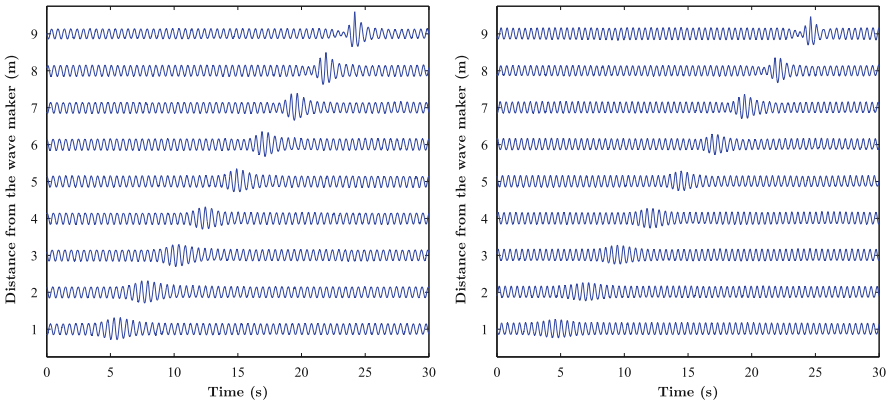

Fig. 13 *Left*: Evolution of a KM soliton in a wave flume for $\mathfrak{a} = 1.2$ and the carrier parameters $a = 0.005$ m and $\varepsilon = 0.08$. *Right*: Evolution of a KM soliton with $\mathfrak{a} = 0.9$ and carriers parameters $a = 0.005$ m and $\varepsilon = 0.09$. *Source*: From [62]

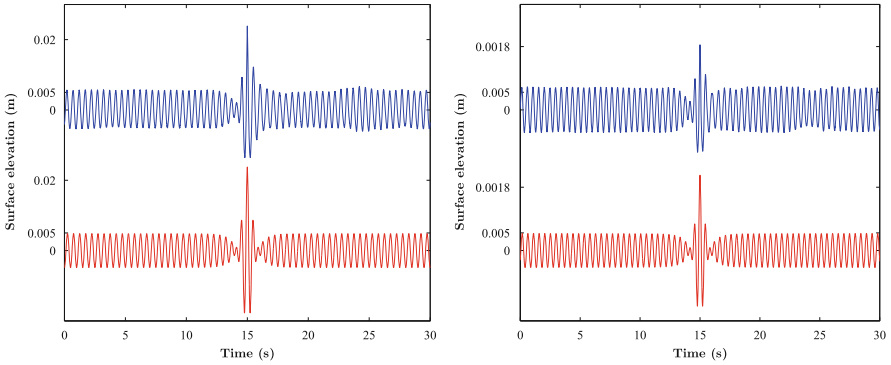

Fig. 14 *Left*: Comparison of the last wave flume measurement (*blue curve*, the same as the *upper curve* in the *left panel* of Fig. 13) with the theoretical surface elevation calculated using the NLSE solution to the second-order correction in steepness (*red curve*). *Right*: Comparison of the last wave flume measurement (*blue curve*, the same as the *upper curve* in the *right panel* of Fig. 13) with the theoretical surface elevation calculated using the NLSE solution with the second-order correction in steepness (*red curve*). *Source*: From [62]

at the 9 m mark along the flume. The comparison with the theoretical predictions is done for the curves recorded at this location. The curves are repeated in a larger scale in Fig. 14 (blue curves) for the sake of comparison with the theoretically predicted ones. In each case, the experimentally observed maximal amplitudes and the wave profiles in general are in very good agreement with the theoretically predicted ones (red curves).

6.2 *Doubly-Localized Breathers*

The Peregrine solution has been first found back in 1983 [70] but attracted attention of experimentalists only recently. It has been observed in optics [40], in hydrodynamics [41] and in plasmas [103]. Experiments in optics are designed to deal with periodic signals. Consequently, the Peregrine solution has been observed as the limiting case of AB with the modulation period increased to large values when the AB solution is transformed into the Peregrine solution [40]. On the contrary, in hydrodynamics, we can deal with isolated events preparing initial conditions for a single Peregrine solution. The first reported hydrodynamic observation of this solution [41] is shown in Fig. 15. Parameters of the background wave are chosen to be $a = 0.01$ cm and $\varepsilon = 0.11$. The evolution plots presented in Fig. 15 illustrate the reason why the Peregrine solution can be considered as prototype of oceanic rogue waves [71]. The evolution starts with the background wave which is only slightly perturbed locally. The perturbation grows by itself reaching an amplitude that is three times the amplitude of the background wave. Without the preliminary knowledge of this possibility, we could think that the high amplitude wave packet appears from nowhere.

Another interesting possibility in observation of this solution is an experiment in which the carrier phase is shifted by π. The consequence is a formation of a single deep trough rather than a high single peak. Such waves do exist in reality and have been recorded in the oceans [2]. They are as dangerous for ships as the rising upwards rogue waves. Figure 16 shows the observation of such a rogue wave hole in a laboratory for the same set of the carrier parameters as in the previous case. Other

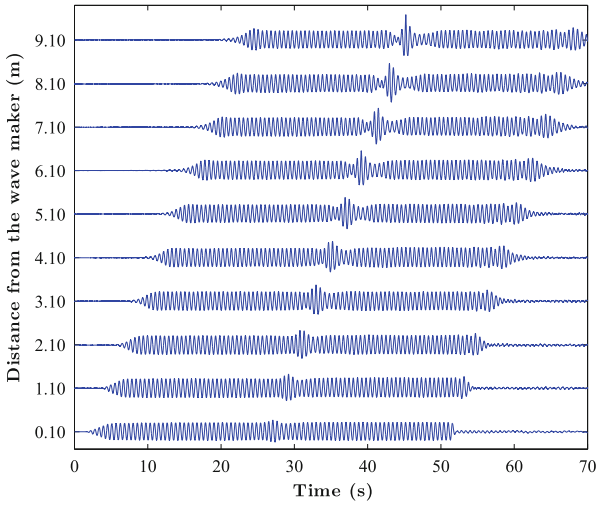

Fig. 15 Evolution of a Peregrine breather in a wave flume for carrier parameters $a = 0.01$ m and $\varepsilon = 0.11$

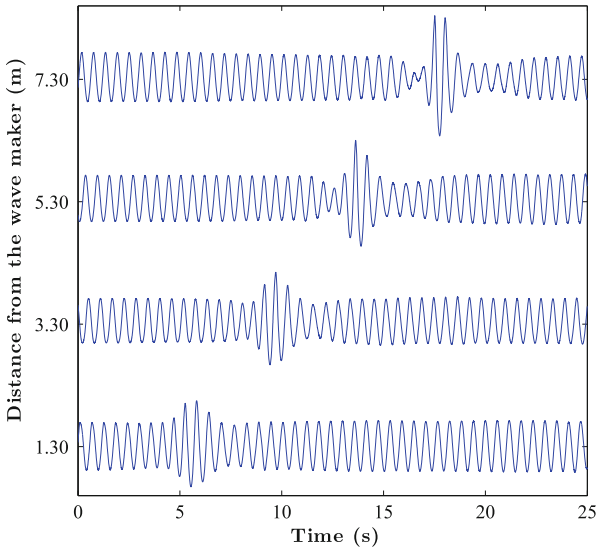

Fig. 16 Evolution of a Peregrine breather hole in a wave flume for carrier parameters $a = 0.01$ m and $\varepsilon = 0.11$. *Source*: From [104]

similar observations for various sets of the background wave parameters have been reported in [104].

The limited length of the flume in most cases does not allow us to see the full growth-decay cycle of the Peregrine breather. To overcome this difficulty, the initial conditions must be chosen to start the breather at more advanced stages of its evolution. Then, it is possible to observe the maximal breather compression point at a distance closer to the wave maker. This allows us to see not only the growth of the breather but also its decay. These observations prove that rogue waves not only "appear from nowhere" but also "disappear without a trace" [72]. In the experiments shown in Fig. 17 taken from [105], the initial conditions have been chosen to observe the maximal wave compression in the middle of the tank. Here, variations of the coordinate x^* for setting the initial conditions must be followed by decreasing the background amplitude to $a = 0.005$ m while keeping the same steepness value $\varepsilon = 0.11$ as before. The wave packet here starts from a larger localized perturbation of the background. It reaches the expected amplitude amplification of three at the mark 4.60 m. The amplitude decreases after reaching the maximum value exactly in accordance with the theoretical Peregrine solution.

Additional confirmation that we are dealing with the Peregrine solution is the comparison of the experimental and theoretical wave profiles at the point of maximal amplitude. Figure 18 shows three wave profiles for the same carrier steepness of $\varepsilon = 0.11$ but for different values of the background amplitude $a = 0.01$ m, $a = 0.02$ m and $a = 0.03$ m, respectively. The experimental and theoretical curves are close to each other in the middle of the breather and at the left hand side of it. The asymmetry

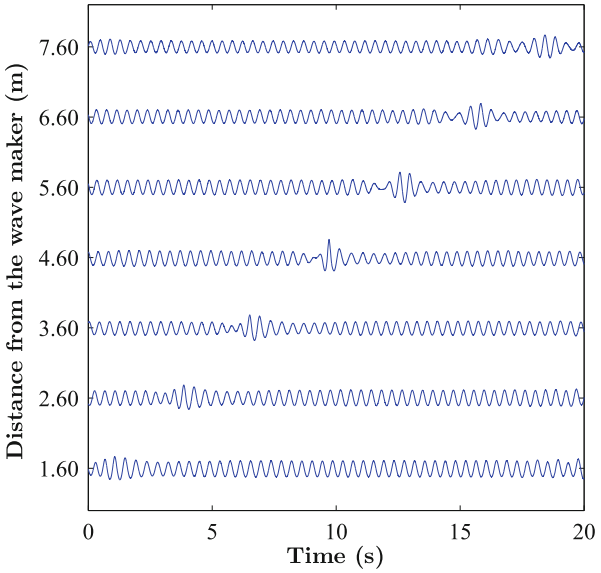

Fig. 17 Growth—decay cycle of the Peregrine breather with the maximal amplitude reached at 4.60 m from the wave maker. The background wave parameters are $a = 0.005$ m and $\varepsilon = 0.11$

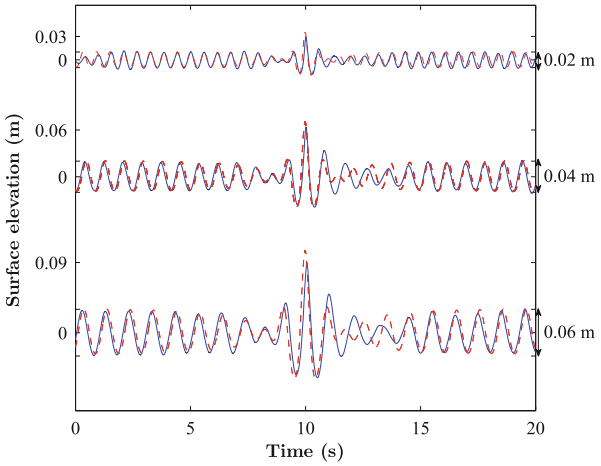

Fig. 18 Comparison of experimental observations (*blue curves*) of Peregrine solutions at the point of maximal wave amplitude with the NLSE predictions (*red curves*) for the same background steepness value $\varepsilon = 0.11$ but for three different background wave amplitudes: $a = 0.01$ m (*upper curves*), $a = 0.02$ m (*middle curves*) and $a = 0.03$ m (*bottom curves*)

and discrepancy at the right hand side are caused by the higher-order terms discussed above that are missing in the NLSE. We should also take into account the fact that the steepness of the wave is close to the wave braking limit which is $\varepsilon = 0.12$. This causes significant deviations from the predicted profiles.

The reduction of the carrier steepness in the experiments improves its agreement with the theory. Figure 19 shows three sets of experimental data for a single value of the carrier wavenumber $k = 11.63\,\mathrm{m}^{-1}$ but three values of the steepness: $\varepsilon = 0.08$, $\varepsilon = 0.05$ and $\varepsilon = 0.02$. As expected, when decreasing the steepness of the waves, the measurements are in a better agreement with the NLSE predictions. The agreement is almost perfect for the lowest value of $\varepsilon = 0.02$. Limitations of the NLSE in this case are minimal.

The high amplitude amplification of three above the background is quite remarkable and impressive although this is not the highest amplitude that could be reached. Higher-order doubly-localized AP breathers provide even larger maximal amplitudes. These solutions reach higher wave amplifications but careful choice of the carrier parameters should be done in setting the initial conditions [106, 107]. The evolution of a second-order AP breathers in the experiment and in the theory for the carrier amplitude of $a = 0.001$ m and the steepness $\varepsilon = 0.03$ are shown in Fig. 20. Here, we had to decrease the wave steepness to 0.03 in order to avoid the wave breaking. Moreover, higher-order solutions require a much longer propagation distance, compared to the basic Peregrine solution. As the tank length is shorter than required, the experiment has been split into eight stages allowing therefore the total propagation distance of 72 m, while measuring the waves 9 m from the wave maker for each run.

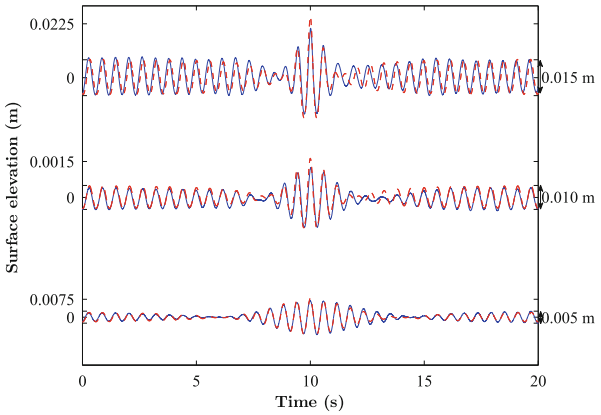

Fig. 19 Comparison of experimental observations (*blue curves*) of Peregrine solutions at the point of maximal wave amplitude with the NLSE predictions (*red curves*) for the same carrier wavenumber $k = 11.63\,\mathrm{m}^{-1}$ but for three different steepness values: $\varepsilon = 0.08$ (*upper curves*), $\varepsilon = 0.05$ (*middle curves*) and $\varepsilon = 0.02$ (*bottom curves*)

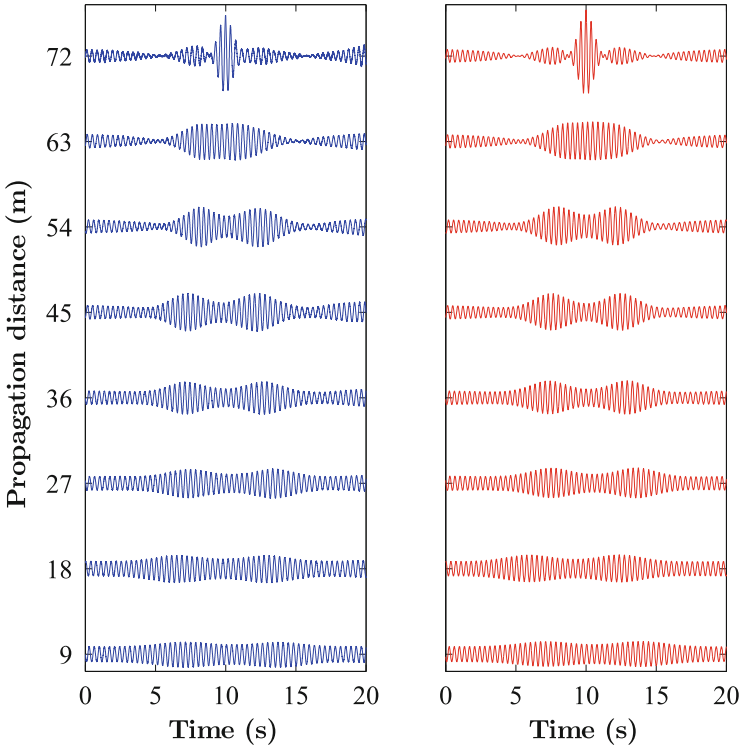

Fig. 20 Wave profile evolution of a second-order AP breather in experiment for $a = 0.001$ m and $\varepsilon = 0.03$ (*left*) and as described with the NLSE theory (*right*)

More plots and a video, demonstrating the impact of the waves on a small boat are presented in [106, 107]. Observations of the third-, the fourth- and the fifth-order AP breathers, having amplitude amplifications of seven, nine and eleven, respectively, are shown in Fig. 21. In each of these cases, we can observe a reasonably good agreement with the weakly nonlinear NLSE theory despite its expected limitations. One inconvenience we have faced in experiments in a water wave facility is that due to the amplitude increase with the order of the solution the steepness values of the carrier had to be decreased accordingly. Otherwise, the wave breaking becomes unavoidable. The most critical case in this regard is the fifth-order solution. The initial condition at the last stage of this experiment has the amplitude amplification of four which grows to eleven at the maximum point of the breather. Then the increase of the steepness to $\varepsilon = 0.02$ while keeping the same amplitude of $a = 0.001$ m indeed causes wave breaking, see [105]. Therefore, it is very difficult to observe solutions higher than the fifth-order AP breather in water waves.

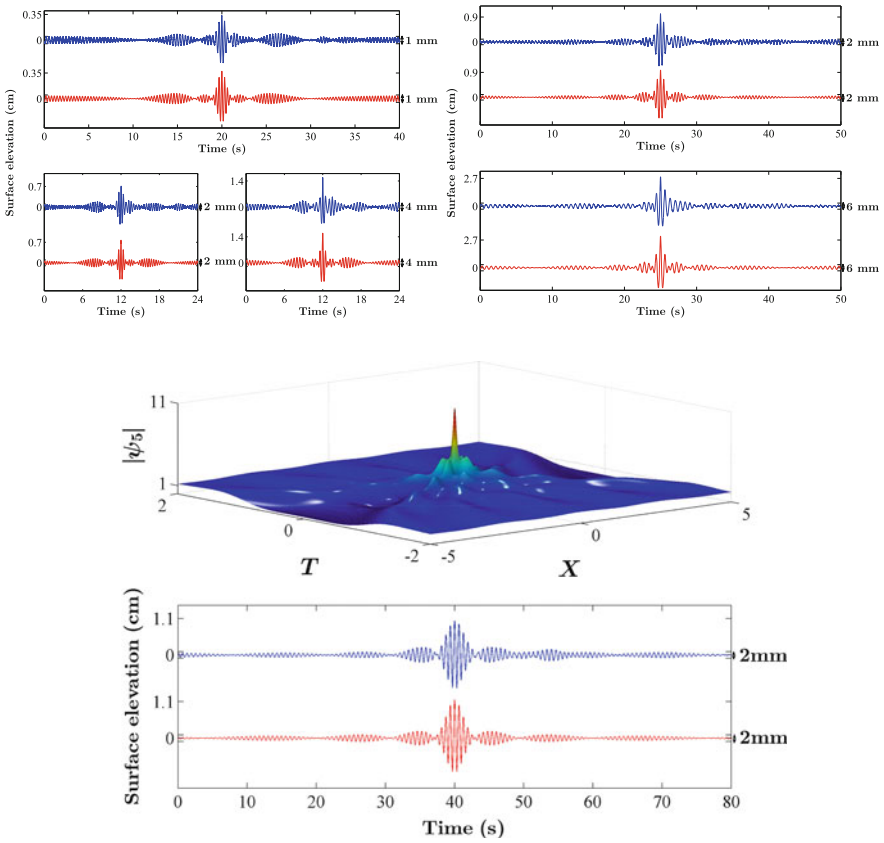

Fig. 21 *Top left set of panels*: Comparison of experimental records of the third-order doubly-localized breathers (*blue curves*) with the NLSE predictions (*red curves*) in three cases: *upper panel* is for $a = 0.0005$ m and $\varepsilon = 0.02$, *lower left panel* is for $a = 0.001$ m and $\varepsilon = 0.03$ and *lower right panel* is for $a = 0.002$ m and $\varepsilon = 0.04$. *Top right set of panels*: Comparison of experimental records of a fourth-order doubly-localized breathers (*blue curves*) with the NLSE predictions (*red curves*) in two cases: the *upper case* is for $a = 0.001$ m and $\varepsilon = 0.02$ while the *lower case* is for $a = 0.003$ m and $\varepsilon = 0.03$. *Bottom set of panels*: The *upper plot* shows the theoretical profile of the fifth-order AP breather on the dimensionless (X, T)-plane while the *lower plot* is the comparison of the corresponding wave tank measurements at $X = 0$ (*blue curve*) with the NLSE surface wave profiles calculated for $a = 0.001$ m and $\varepsilon = 0.01$ (*red curve*) at the same position. *Source*: From [107]

7 Discussions

To summarize, we have shown that the exact NLSE localized solutions can be observed in water waves. The observation of both dark and bright solitons are in good agreement with the NLSE, even in the case of comparatively large carrier steepness values. Despite the NLSE restrictions related to its weakly nonlinear

third-order approximation, we have shown that the NLSE can reasonably accurately model the dynamics of water waves. This modeling works well even for higher steepnesses which is the case for multi-solitons and breathers on a finite background. Another significant property of the NLSE such as its time-reversal invariance has been validated for the Peregrine and for the second-order AP breathers in [108]. For higher wave amplitudes, the NLSE cannot describe the slight asymmetry of the measured wave packets and their spectra. Higher-order corrections to dispersion and nonlinearity are needed in that case. These corrections together with the mean or Stokes flow lead to the MNLSE, also known as the Dysthe equation. This equation provides a better correspondence between the theory and experiments [95]. These corrections are highly efficient in modelling the multi-solitons and doubly-localized Peregrine breathers [92, 100, 109]. On the other hand, decreasing the steepness of the background waves or equivalently the nonlinearity in the dynamical system improves the correspondence of experimental data even with the NLSE predictions. Historically, the NLSE is the basic starting point of the whole new subject of rogue waves in mathematics [74, 110–113]. Extending the boundaries of understanding rogue waves naturally relies on the NLSE extensions [114–116] and other accurate equations [67, 117, 118].

Higher-order extensions to the NLSE describe such fascinating phenomena as the generation of supercontinuum [58] which is beyond the NLSE approximation. The supercontinuum was observed not only in optics but also in hydrodynamics [100]. Such expansion of ideas from optics to other disciplines makes the NLSE extensions as universal as the NLSE itself [119]. These extensions can be both integrable [114, 115, 120, 121] and non-integrable [122]. They can even contain an infinite number of terms [123, 124]. In either case, breather solutions do exist and their importance in physics cannot be overestimated [64–66]. They appear not only at macroscopic scales like in the oceans but also in quantised superfluids [125].

In absence of integrability and exact solutions, the most efficient technique to study rogue waves is numerical simulations. Numerical simulations of doubly-localized breathers analogous to the Peregrine solution using the fully nonlinear governing equations and the boundary element method have been reported in [126]. The NLSE limitations have been also discussed and analyzed using numerical simulations based on HOSM in [92, 127]. Most accurate hydrodynamic approach is based on the two-phase Navier-Stokes equations and corresponding simulations have been reported in [128, 129].

The theoretical knowledge and laboratory observations of breathers are taking us one step closer to various engineering applications [130]. For example, specific spectra such as the typical triangular spectra of the AB [131] and the Peregrine solution may be used for rogue wave predictions [132–134] or generation of ultra-wide band pulses [135]. Another approach to early detection of rogue waves is a wavelet transform [136–138]. The Peregrine breather solution hitting a scaled chemical tanker and its potential devastating effects on the ship are discussed in [130].

One more direction of research is air-water interaction that becomes important when the MI leads to wave breaking [129]. The effects of wind [139–145] and currents [146–148] on the MI are also important and deserve further studies.

We conclude with the strong belief that the world of integrable equations is an important starting platform for the studies of complex natural phenomena which are predominantly nonlinear, mostly wonderful and sometimes dangerous.

Acknowledgements Amin Chabchoub acknowledges support from the Burgundy Region, The Association of German Engineers (VDI) and the Japan Society for the Promotion of Science (JSPS). Miguel Onorato was supported by MIUR Grant PRIN 2012BFNWZ2. Nail Akhmediev acknowledges the support of the Australian Research Council (Discovery Projects DP140100265 and DP150102057) and support from the Volkswagen Stiftung.

References

1. Kharif, C., Pelinovsky, E.: Physical mechanisms of the rogue wave phenomenon. Eur. J. Mech. B. Fluids **22**(6), 603–634 (2003)
2. Kharif, C., Pelinovsky, E., Slunyaev, A.: Rogue Waves in the Ocean. Springer, Berlin (2009)
3. Osborne, A.: Nonlinear Ocean Waves & the Inverse Scattering Transform, vol. 97. Academic, New York (2010)
4. Solli, D., Ropers, C., Koonath, P., Jalali, B.: Optical rogue waves. Nature **450**(7172), 1054–1057 (2007)
5. Gramstad, O., Trulsen, K.: Can swell increase the number of freak waves in a wind sea? J. Fluid Mech. **650**, 57–79 (2010)
6. Onorato, M., Proment, D., Toffoli, A.: Triggering rogue waves in opposing currents. Phys. Rev. Lett. **107**(18), 184502 (2011)
7. Baronio, F., Degasperis, A., Conforti, M., Wabnitz, S.: Solutions of the vector nonlinear Schrödinger equations: evidence for deterministic rogue waves. Phys. Rev. Lett. **109**(4), 044102 (2012)
8. Onorato, M., Residori, S., Bortolozzo, U., Montina, A., Arecchi, F.T.: Rogue waves and their generating mechanisms in different physical contexts. Phys. Rep. **528**(2), 47–89 (2013)
9. Baronio, F., Conforti, M., Degasperis, A., Lombardo, S.: Rogue waves emerging from the resonant interaction of three waves. Phys. Rev. Lett. **111**(11), 114101 (2013)
10. Grimshaw, R., Tovbis, A.: Rogue waves: analytical predictions. Proc. R. Soc. A **469**(2157), 20130094 (2013)
11. Baronio, F., Conforti, M., Degasperis, A., Lombardo, S., Onorato, M., Wabnitz, S.: Vector rogue waves and baseband modulation instability in the defocusing regime. Phys. Rev. Lett. **113**(3), 034101 (2014)
12. Dudley, J.M., Dias, F., Erkintalo, M., Genty, G.: Instabilities, breathers and rogue waves in optics. Nat. Photonics **8**(10), 755–764 (2014)
13. Walczak, P., Randoux, S., Suret, P.: Optical rogue waves in integrable turbulence. Phys. Rev. Lett. **114**, 143903 (2015)
14. Stokes, G.G.: On the theory of oscillatory waves. Trans. Camb. Philos. Soc. **8**, 441–473 (1847)
15. Janssen, P.: The Interaction of Ocean Waves and Wind. Cambridge University Press, Cambridge (2004)
16. Babanin, A.: Breaking and Dissipation of Ocean Surface Waves. Cambridge University Press, Cambridge (2011)
17. Lighthill, M.: Contributions to the theory of waves in non-linear dispersive systems. IMA J. Appl. Math. **1**(3), 269–306 (1965)

18. Bespalov, V.I., Talanov, V.I.: Filamentary structure of light beams in nonlinear liquids. Sov. Phys. JETP Lett. **3**(2), 307 (1966)
19. Benjamin, T.B., Feir, J.: The disintegration of wave trains on deep water part 1. theory. J. Fluid Mech. **27**(3), 417–430 (1967)
20. Zakharov, V.E.: Stability of periodic waves of finite amplitude on the surface of a deep fluid. J. Appl. Mech. Tech. Phys. **9**(2), 190–194 (1968)
21. Remoissenet, M.: Waves Called Solitons: Concepts and Experiments. Springer, Berlin (2013)
22. Erkintalo, M., Hammani, K., Kibler, B., Finot, C., Akhmediev, N., Dudley, J.M., Genty, G.: Higher-order modulation instability in nonlinear fiber optics. Phys. Rev. Lett. **107**(25), 253901 (2011)
23. Hwung, H.-H., Chiang, W.-S., Hsiao, S.-C.: Observations on the evolution of wave modulation. Proc. R. Soc. Lond. A Math. Phys. Eng. Sci. **463**, 85–112 (2007)
24. Akhmediev, N., Korneev, V.I.: Modulation instability and periodic solutions of the nonlinear Schrödinger equation. Theor. Math. Phys. (USSR) **69**(2), 1089–1093 (1986)
25. Akhmediev, N., Ankiewicz, A., Soto-Crespo, J.M., Dudley, J.M.: Universal triangular spectra in parametrically-driven systems. Phys. Lett. A **375**, 775–779 (2011)
26. Benney, D.J., Newell, A.C.: The propagation of nonlinear wave envelopes. J. Math. Phys. **46**(1), 133–139 (1967)
27. Shabat, A., Zakharov, V.: Exact theory of two-dimensional self-focusing and one-dimensional self-modulation of waves in nonlinear media. Sov. Phys. JETP **34**(1), 62 (1972)
28. Matveev, V.B., Salle, M.A.: Darboux Transformations and Solitons. Springer, Berlin (1991)
29. Goldstein, P.P.: Hints on the Hirota bilinear method. Acta Phys. Pol. A **112**, 1171–1184 (2007)
30. Hientarinta, J.: Gauge symmetry and the generalization of Hirota's bilinear method. Nonlinear Math. Phys. **3**(3,4), 260–265 (1996)
31. Ablowitz, M.J., Clarkson, P.A.: Solitons, nonlinear evolution equations and inverse scattering, vol. 149. Cambridge University Press, Cambridge (1991)
32. Bullough, R.K., Caudrey, P.J.: Solitons. Springer, Berlin (1980)
33. Zakharov, V.E., Shabat, A.B.: Integration of nonlinear equations of mathematical physics by the method of inverse scattering. II. Funct. Anal. Appl. **13**(3), 166–174 (1979)
34. Ablowitz, M.J.: Nonlinear Dispersive Waves: Asymptotic Analysis and Solitons, vol. 47. Cambridge University Press, Cambridge (2011)
35. Akhmediev, N., Eleonskii, V.M., Kulagin, N.E.: Exact solutions of the first order of nonlinear Schrödinger equation. Theor. Math. Phys. (USSR) **72**(2), 809–818 (1987)
36. Akhmediev, N., Ankiewicz, A.: Solitons: Nonlinear Pulses and Beams. Chapman & Hall, London (1997)
37. Yuen, H.C., Lake, B.M.: Nonlinear dynamics of deep-water gravity waves. Adv. Appl. Mech **22**(67), 229 (1982)
38. Hasegawa, A.: Optical Solitons in Fibers. Springer, Berlin (1989)
39. Burger, S., Bongs, K., Dettmer, S., Ertmer, W., Sengstock, K., Sanpera, A., Shlyapnikov, G., Lewenstein, M.: Dark solitons in Bose-Einstein condensates. Phys. Rev. Lett. **83**(25), 5198 (1999)
40. Kibler, B., Fatome, J., Finot, C., Millot, G., Dias, F., Genty, G., Akhmediev, N., Dudley, J.M.: The Peregrine soliton in nonlinear fibre optics. Nat. Phys. **6**(10), 790–795 (2010)
41. Chabchoub, A., Hoffmann, N., Akhmediev, N.: Rogue wave observation in a water wave tank. Phys. Rev. Lett. **106**(20), 204502 (2011)
42. Chabchoub, A., Kibler, B., Finot, C., Millot, G., Onorato, M., Dudley, J.M., Babanin, A.V.: The nonlinear Schrödinger equation and the propagation of weakly nonlinear waves in optical fibers and on the water surface. Ann. Phys. **361**, 490–500 (2015)
43. Kibler, B., Chabchoub, A., Gelash, A., Akhmediev, N., Zakharov, V.E.: Superregular breathers in optics and hydrodynamics: omnipresent modulation instability beyond simple periodicity. Phys. Rev. X **5**(4), 041026 (2015)
44. Korteweg, D.J., De Vries, G.: On the change of form of long waves advancing in a rectangular canal, and on a new type of long stationary waves. Lond. Edinb. Dublin Philos. Mag. J. Sci. **39**(240), 422–443 (1895)

45. Zabusky, N.J., Kruskal, M.D.: Interaction of "solitons" in a collisionless plasma and the recurrence of initial states. Phys. Rev. Lett. **15**(6), 240 (1965)
46. Dias, F., Bridges, T.: Weakly Nonlinear Wave Packets and the Nonlinear Schrödinger Equation. Springer, Berlin (2005)
47. Grimshaw, R., Chow, K.W., Chan, H.N.: Modulational instability and rogue waves in shallow water models. In: Tobisch, E. (ed.) New Approaches to Nonlinear Waves. Lecture Notes in Physics, vol. 908. Springer, Berlin (2016)
48. Mei, C.C.: The Applied Dynamics of Ocean Surface Waves, vol. 1. World Scientific, Singapore (1983)
49. Lake, B.M., Yuen, H.C.: A note on some nonlinear water-wave experiments and the comparison of data with theory. J. Fluid Mech. **83**(1), 75–81 (1977)
50. Zakharov, V.E., Ostrovsky, L.A.: Modulation instability: the beginning. Phys. D Nonlinear Phenom. **238**(5), 540–548 (2009)
51. Chiao, R.Y., Garmire, E., Townes, C.: Self-trapping of optical beams. Phys. Rev. Lett. **13**(15), 479 (1964)
52. Hasimoto, H., Ono, H.: Nonlinear modulation of gravity waves. J. Phys. Soc. Jpn. **33**(3), 805–811 (1972)
53. Akhmediev, N., Eleonskii, V.M., Kulagin, N.E.: Generation of periodic trains of picosecond pulses in an optical fiber: exact solutions. Sov. Phys. JETP, **62**(5), 894–899 (1985)
54. Zakharov, V.E., Shabat, A.B.: On the interaction of solitons in a stable medium. Sov. Phys. JETP **37**, 823 (1973)
55. Akhmediev, N., Mitskevich, N.V.: Extremely high degree of N-soliton pulse compression in an optical fiber. IEEE J. Quantum Electron. **QE-27**(3), 849–857 (1991)
56. Satsuma, J., Yajima, N.: Initial value problems of one-dimensional self-modulation of nonlinear waves in dispersive media. Progr. Theor. Phys. Suppl. **55**, 284–306 (1974)
57. Mollenauer, L.F., Stolen, R.H., Gordon, J.P.: Experimental observation of picosecond pulse narrowing and solitons in optical fibers. Phys. Rev. Lett. **45**(13), 1095 (1980)
58. Dudley, J.M., Taylor, J.R.: Supercontinuum Generation in Optical Fibers. Cambridge University Press, Cambridge (2010)
59. Kuznetsov, E.A.: Solitons in a parametrically unstable plasma. Akademiia Nauk SSSR Doklady **236**, 575–577 (1977)
60. Ma, Y.-C.: The perturbed plane-wave solutions of the cubic Schrödinger equation. Stud. Appl. Math. **60**, 43–58 (1979)
61. Kibler, B., Fatome, J., Finot, C., Millot, G., Genty, G., Wetzel, B., Akhmediev, N., Dias, F., Dudley, J.M.: Observation of Kuznetsov-Ma soliton dynamics in optical fibre. Sci. Rep. **2**, 463 (2012)
62. Chabchoub, A., Kibler, B., Dudley, J.M., Akhmediev, N.: Hydrodynamics of periodic breathers. Philos. Trans. R. Soc. Lond. A Math. Phys. Eng. Sci. **372**(2027), 20140005 (2014)
63. Dai, C., Wang, Y., Zhang, X.: Controllable Akhmediev breather and Kuznetsov-Ma soliton trains in PT-symmetric coupled waveguides. Opt. Express **22**(24), 29862–29867 (2014)
64. Mahnke, C., Mitschke, F.: Possibility of an Akhmediev breather decaying into solitons. Phys. Rev. A **85**, 033808 (2012)
65. Frisquet, B., Kibler, B., Millot, G.: Collision of Akhmediev breathers in nonlinear fiber optics. Phys. Rev. X **3**(4), 041032 (2013)
66. Bendahmane, B., Mussot, A., Szriftgiser, P., Zerkak, O., Genty, G., Dudley, J.M., Kudlinski, A.: Experimental dynamics of Akhmediev breathers in a dispersion varying optical fiber. Opt. Lett. **39**(15), 4490 (2014)
67. Priya, N.V., Senthilvelan, M., Lakshmanan, M.: Akhmediev breathers, Ma solitons, and general breathers from rogue waves: a case study in the Manakov system. Phys. Rev. E **88**, 022918 (2013)
68. Dudley, J.M., Genty, G., Dias, F., Kibler, B., Akhmediev, N.: Modulation instability, Akhmediev Breathers and continuous wave supercontinuum generation. Opt. Express **17**(24), 21497–21508 (2009)

69. Dysthe, K.B., Trulsen, K.: Note on breather type solutions of the NLS as models for freak-waves. Phys. Scr. **T82**, 48 (1999)
70. Peregrine, D.H.: Water waves, nonlinear Schrödinger equations and their solutions. J. Aust. Math. Soc. Ser. B Appl. Math. **25**(1), 16–43 (1983)
71. Shrira, V.I., Geogjaev, V.V.: What makes the Peregrine soliton so special as a prototype of freak waves? J. Eng. Math. **67**(1–2), 11–22 (2010)
72. Akhmediev, N., Ankiewicz, A., Taki, M.: Waves that appear from nowhere and disappear without a trace. Phys. Lett. A **373**(6), 675–678 (2009)
73. Dontsop, Y.G., Essama, B.G.O., Dongo, J.M., Dedzo, M.M., Atangana, J., Yemele, D., Kofane, T.C.: Akhmediev–Peregrine rogue waves generation in a composite right/left-handed transmission line. Opt. Quant. Electron. **48**, 59 (2016)
74. Akhmediev, N., Ankiewicz, A., Soto-Crespo, J.M.: Rogue waves and rational solutions of the nonlinear Schrödinger equation. Phys. Rev. E **80**(2), 026601 (2009)
75. Ohta, Y., Yang, J.: General high-order rogue waves and their dynamics in the nonlinear Schrödinger equation. Proc. R. Soc. A **468**, 1716–1740 (2012)
76. Gaillard, P.: Wronskian representation of solutions of the NLS equation and higher Peregrine breathers. Sci. Adv. **13**(2), 71–153 (2012)
77. Gaillard, P.: Degenerate determinant representation of solutions of the nonlinear Schrödinger equation, higher order Peregrine breathers and multi-rogue waves. J. Math. Phys. **54**(1), 013504 (2013)
78. He, J., Zhang, H., Wang, L., Porsezian, K., Fokas, A.: Generating mechanism for higher-order rogue waves. Phys. Rev. E **87**(5), 052914 (2013)
79. Gaillard, P.: Tenth Peregrine breather solution to the NLS equation. Ann. Phys. **355**, 293–298 (2015)
80. Gaillard, P.: Multi-parametric deformations of the Peregrine breather of order N solutions to the NLS equation and multi-rogue waves. Adv. Res. **4**, 346–364 (2015)
81. Kedziora, D.J., Ankiewicz, A., Akhmediev, N.: Second-order nonlinear Schrödinger equation breather solutions in the degenerate and rogue wave limits. Phys. Rev. E **85**, 066601 (2012)
82. Kedziora, D.J., Ankiewicz, A., Akhmediev, N.: Triangular rogue wave cascades. Phys. Rev. E **86**(5), 056602 (2012)
83. Kedziora, D.J., Ankiewicz, A., Akhmediev, N.: Classifying the hierarchy of nonlinear-Schrödinger-equation rogue-wave solutions. Phys. Rev. E **88**(1), 013207 (2013)
84. Chabchoub, A., Kimmoun, O., Branger, H., Hoffmann, N., Proment, D., Onorato, M., Akhmediev, N.: Experimental observation of dark solitons on the surface of water. Phys. Rev. Lett. **110**(12), 124101 (2013)
85. Chabchoub, A., Kimmoun, O., Branger, H., Kharif, C., Hoffmann, N., Onorato, M., Akhmediev, N.: Gray solitons on the surface of water. Phys. Rev. E **89**(1), 011002 (2014)
86. Milewski, P.A., Vanden-Broeck, J.-M., Wang, Z.: Steady dark solitary flexural gravity waves. Proc. R. Soc. A **469**(2150), 20120485 (2013)
87. Shukla, P.K., Eliasson, B.: Formation and dynamics of dark solitons and vortices in quantum electron plasmas. Phys. Rev. Lett. **96**(24), 245001 (2006)
88. Emplit, P., Hamaide, J.-P., Reynaud, F., Froehly, C., Barthelemy, A.: Picosecond steps and dark pulses through nonlinear single mode fibers. Opt. Commun. **62**(6), 374–379 (1987)
89. Yuen, H.C., Lake, B.M.: Nonlinear deep water waves: theory and experiment. Phys. Fluids (1958–1988) **18**(8), 956–960 (1975)
90. Hasegawa, A., Tappert, F.: Transmission of stationary nonlinear optical pulses in dispersive dielectric fibers. Appl. Phys. Lett. **23** 142–144 (1973)
91. Mollenauer, L.F., Gordon, J.P.: Solitons in Optical Fibers: Fundamentals and Applications. Academic, New York (2006)
92. Slunyaev, A., Clauss, G.F., Klein, M., Onorato, M.: Simulations and experiments of short intense envelope solitons of surface water waves. Phys. Fluids (1994–present) **25**(6), 067105 (2013)

93. Dysthe, K.B.: Note on a modification to the nonlinear Schrödinger equation for application to deep water waves. Proc. R. Soc. Lond. A Math. Phys. Eng. Sci. **369**, 105–114 (1979) The Royal Society
94. Trulsen, K., Stansberg, C.T.: Spatial evolution of water surface waves: Numerical simulation and experiment of bichromatic waves. In: The Eleventh International Offshore and Polar Engineering Conference, International Society of Offshore and Polar Engineers, 2001
95. Trulsen, K., Dysthe, K.B.: A modified nonlinear Schrödinger equation for broader bandwidth gravity waves on deep water. Wave Motion **24**(3), 281–289 (1996)
96. Clamond, D., Francius, M., Grue, J., Kharif, C.: Long time interaction of envelope solitons and freak wave formations. Eur. J. Mech. B Fluids **25**(5), 536–553 (2006)
97. Husakou, A.V., Herrmann, J.: Supercontinuum generation of higher-order solitons by fission in photonic crystal fibers. Phys. Rev. Lett. **87**(20), 203901 (2001)
98. Dudley, J.M., Genty, G., Coen, S.: Supercontinuum generation in photonic crystal fiber. Rev. Mod. Phys. **78**(4), 1135 (2006)
99. Dudley, J.M., Genty, G.: Supercontinuum light. Phys. Today **66**, 29–34 (2013)
100. Chabchoub, A., Hoffmann, N., Onorato, M., Genty, G., Dudley, J.M., Akhmediev, N.: Hydrodynamic supercontinuum. Phys. Rev. Lett. **111**(5), 054104 (2013)
101. Tulin, M.P., Waseda, T.: Laboratory observations of wave group evolution, including breaking effects. J. Fluid Mech. **378**, 197–232 (1999)
102. Onorato, M., Osborne, A.R., Serio, M., Damiani, T.: Occurrence of freak waves from envelope equations in random ocean wave simulations. In: Proceedings of Rogue Waves 2000 Workshop, p. 181, 2000
103. Bailung, H., Sharma, S., Nakamura, Y.: Observation of Peregrine solitons in a multicomponent plasma with negative ions. Phys. Rev. Lett. **107**(25), 255005 (2011)
104. Chabchoub, A., Hoffmann, N., Akhmediev, N.: Observation of rogue wave holes in a water wave tank. J. Geophys. Res. Oceans (1978–2012) **117**(C11) (2012). doi:10.1029/2011JC007636
105. Chabchoub, A., Akhmediev, N., Hoffmann, N.: Experimental study of spatiotemporally localized surface gravity water waves. Phys. Rev. E **86**(1), 016311 (2012)
106. Chabchoub, A., Hoffmann, N., Onorato, M., Akhmediev, N.: Super rogue waves: observation of a higher-order breather in water waves. Phys. Rev. X **2**(1), 011015 (2012)
107. Chabchoub, A., Hoffmann, N., Onorato, M., Slunyaev, A., Sergeeva, A., Pelinovsky, E., Akhmediev, N.: Observation of a hierarchy of up to fifth-order rogue waves in a water tank. Phys. Rev. E **86**(5), 056601 (2012)
108. Chabchoub, A., Fink, M.: Time-reversal generation of rogue waves. Phys. Rev. Lett., **112**(12), 124101 (2014)
109. Shemer, L., Alperovich, L.: Peregrine breather revisited. Phys. Fluids (1994–present) **25**(5), 051701 (2013)
110. Akhmediev, N., Soto-Crespo, J.M., Ankiewicz, A.: Extreme waves that appear from nowhere: on the nature of rogue waves. Phys. Lett. A **373**, 2137–2145 (2009)
111. Akhmediev, N., Soto-Crespo, J.M., Ankiewicz, A.: How to excite a rogue wave. Phys. Rev. A **80**, 043818 (2009)
112. Dubard, P., Gaillard, P., Klein, C., Matveev, V.: On multi-rogue wave solutions of the NLS equation and positon solutions of the KdV equation. Eur. Phys. J. Spec. Topics **185**(1), 247–258 (2010)
113. Dubard, P., Matveev, V.B.: Multi-rogue waves solutions to the focusing NLS equation and the KP-I equation. Nat. Hazards Earth. Syst. Sci. **11**, 667 (2011)
114. Ankiewicz, A., Soto-Crespo, J.M., Akhmediev, N.: Rogue waves and rational solutions of the Hirota equation. Phys. Rev. E **81**, 046602 (2010)
115. Bandelow, U., Akhmediev, N.: Persistence of rogue waves in extended nonlinear Schrödinger equations: Integrable Sasa – Satsuma case. Phys. Lett. A **376**, 1558 (2012)
116. Priya, N.V., Senthilvelan, M., Lakshmanan, M.: Dark solitons, breathers, and rogue wave solutions of the coupled generalised nonlinear Schrödinger equations. Phys. Rev. E **89**, 062901 (2014)

117. Kodama, Y.: KP solitons in shallow water. J. Phys. A Math. Theor. **43**, 434004 (2010)
118. Sakaguchi, H., Kageyama, Y.: Modulational instability and breathing motion in the two-dimensional nonlinear Schrödinger equation with a one-dimensional harmonic potential. Phys. Rev. E, **88**, 053203, (2013)
119. Fu, S., Tsur, Y., Zhou, J., Shemer, L., Arie, A.: Self-similar propagation of hermite-gauss water-wave pulses. Phys. Rev. E **93**, 013127 (2016)
120. Ankiewicz, A., Wang, Y., Wabnitz, S., Akhmediev, N.: Extended nonlinear Schrödinger equation with higher-order odd and even terms and its rogue wave solutions. Phys. Rev. E **89**, 012907 (2014)
121. Guo, R., Hao, H.-Q., Gu, X.-S.: Modulation instability, breathers, and bound solitons in an erbium-doped fiber system with higher-order effects. Abstr. Appl. Anal. **2014**, 13pp. (2014). Article ID 185654
122. Ankiewicz, A., Devine, N., Akhmediev, N.: Are rogue waves robust against perturbations? Phys. Lett. A **373**, 3997–4000 (2009)
123. Kedziora, D., Ankiewicz, A., Chowdury, A., and Akhmediev, N.: Integrable equations of the infinite nonlinear Schrödinger equation hierarchy with time variable coefficients. Chaos Interdiscip. J. Nonlinear Sci. **25**(10), 103114 (2015)
124. Ankiewicz, A., Kedziora, D.J., Chowdury, A., Bandelow, U., Akhmediev, N.: Infinite hierarchy of nonlinear Schrödinger equations and their solutions. Phys. Rev. E **93**, 012206 (2016)
125. Salman, H.: Breathers on quantized superfluid vortices. Phys. Rev. Lett. **111**, 165301 (2013)
126. Ten, I., Tomita, H.: Simulation of the ocean waves and appearance of freak waves. In: Reports of RIAM Symposium, Proceedings, Kyushu University, Kasuga, Fukuoka, 17SP1-2, 2006
127. Slunyaev, A.V., Shrira, V.I.: On the highest non-breaking wave in a group: fully nonlinear water wave breathers versus weakly nonlinear theory. J. Fluid Mech. **735**, 203–248 (2013)
128. Perić, R., Hoffmann, N., Chabchoub, A.: Initial wave breaking dynamics of Peregrine-type rogue waves: a numerical and experimental study. Eur. J. Mech. B. Fluids **49**,71–76 (2015)
129. Iafrati, A., Babanin, A., Onorato, M.: Modulational instability, wave breaking, and formation of large-scale dipoles in the atmosphere. Phys. Rev. Lett. **110**(18), 184504 (2013)
130. Onorato, M., Proment, D., Clauss, G., Klein, M.: Rogue waves: From nonlinear Schrödinger breather solutions to sea-keeping test. PLOS ONE **8**(2), e54629 (2013)
131. Hammani, K., Wetzel, B., Kibler, B., Fatome, J., Finot, C., Millot, G., Akhmediev, N., Dudley, J.M.: Spectral dynamics of modulation instability described using Akhmediev breather theory. Opt. Lett. **36**(11), 2140–2142 (2011)
132. Akhmediev, N., Soto-Crespo, J.M., Ankiewicz, A., Devine, N.: Early detection of rogue waves in a chaotic wave field. Phys. Lett. A **375**(33), 2999–3001 (2011)
133. Akhmediev, N., Ankiewicz, A., Soto-Crespo, J., Dudley, J.M.: Rogue wave early warning through spectral measurements? Phys. Lett. A **375**(3), 541–544 (2011)
134. Chabchoub, A., Neumann, S., Hoffmann, N.P., Akhmediev, N.: Spectral properties of the Peregrine soliton observed in a water wave tank. J. Geophys Res Oceans (1978–2012) **117**, C11 (2012)
135. Varlot, B., Chembo, Y., Finot, C.: Akhmediev breathers as ultra-wideband pulses. Microw. Opt. Technol. Lett. **56**(3), 664 (2014)
136. Liu, P.C., Mori, N.: Characterizing freak waves with wavelet transform analysis. In: Proceedings of Rogue Waves 2000 Workshop, pp. 151–156, 2001
137. Bayindir, C.: Early detection of rogue waves by the wavelet transforms. Phys. Lett. A **380**, 156–161 (2016)
138. Cousins, W., Sapsis, T.P.: Reduced order precursors of rare events in unidirectional nonlinear water waves. J. Fluid Mech. **790**, 368–388 (2016)
139. Waseda, T., Tulin, M.P.: Experimental study of the stability of deep-water wave trains including wind effects. J. Fluid Mech. **401**, 55–84 (1999)
140. Kharif, C., Giovanangeli, J.-P., Touboul, J., Grare, L., Pelinovsky, E., Influence of wind on extreme wave events: experimental and numerical approaches. J. Fluid Mech. **594**, 209–247 (2008)

141. Onorato, M., Proment, D.: Approximate rogue wave solutions of the forced and damped nonlinear Schrödinger equation for water waves. Phys. Lett. A **376**(45), 3057–3059 (2012)
142. Montalvo, P., Kraenkel, R., Manna, M.A., Kharif, C.: Wind-wave amplification mechanisms: possible models for steep wave events in finite depth. Nat. Hazards Earth Syst. Sci. **13**, 2805–2813 (2013)
143. Chabchoub, A., Hoffmann, N., Branger, H., Kharif, C., Akhmediev, N.: Experiments on wind-perturbed rogue wave hydrodynamics using the Peregrine breather model. Phys. Fluids (1994-present) **25**(10), 101704 (2013)
144. Brunetti, M., Marchiando, N., Berti, N., Kasparian, J.: Nonlinear fast growth of water waves under wind forcing. Phys. Lett. A **378**(14), 1025–1030 (2014)
145. Brunetti, M., Kasparian, J.: Modulational instability in wind-forced waves. Phys. Lett. A **378**(48), 3626–3630 (2014)
146. Toffoli, A., Waseda, T., Houtani, H., Kinoshita, T., Collins, K., Proment, D., Onorato, M.: Excitation of rogue waves in a variable medium: An experimental study on the interaction of water waves and currents. Phys. Rev. E **87**(5), 051201 (2013)
147. Waseda, T., Kinoshita, T., Cavaleri, L., Toffoli, A.: Third-order resonant wave interactions under the influence of background current fields. J. Fluid Mech. **784**, 51–73 (2015)
148. Toffoli, A., Waseda, T., Houtani, H., Cavaleri, L., Greaves, D., Onorato, M.: Rogue waves in opposing currents: an experimental study on deterministic and stochastic wave trains. J. Fluid Mech. **769**, 277–297 (2015)

Experiments on Breathers in Nonlinear Fibre Optics

Bertrand Kibler, Julien Fatome, Christophe Finot, and Guy Millot

Abstract Since the seminal works by A. Hasegawa and co-workers in the 1980s, the modulation instability phenomenon has been widely studied and used in optical fibres, in particular for generating high-repetition-rate soliton trains and for parametric amplification of weak signals. Modulation instability is also known as a general precursor of highly localized wave structures through amplification of perturbations. We review here the recent experiments performed in nonlinear fibre optics that evidence a large class of exact pulsating solutions of the nonlinear Schrödinger equation, called breathers. Based on the coherent seeding of the modulation instability process, these results have shed new lights on extreme nonlinear dynamics and related analogies between optics and hydrodynamics.

1 Introduction

The recent development of convenient nonlinear fibre optics-based experimental setups revealed some intriguing similarities between extreme phenomena in optical systems and the rogue wave phenomena well-known in hydrodynamics [1–4]. The simplest class of almost-conservative physical systems was first investigated in detail, in particular due to the existing mathematical developments. Indeed, analogies between hydrodynamics and optics are known since the 1960–1970s thanks to two main findings: (1) the derivation of the soliton solution of the nonlinear Schrödinger equation (NLSE) in the form of secant-hyperbolic shaped (temporal or spatial) profile, and (2) the studies of the Benjamin-Feir/Bespalov-Talanov (or modulation) instability [7–13]. Wave dynamics in weakly nonlinear dispersive media, such as in optical Kerr media or on the surface of deep water, can indeed be described by the NLSE. However, it was recently shown that this correspondence applies even in the limit of extreme nonlinear wave localization described by the common mathematical model [5, 6]. Besides the well-known soliton solution, the NLSE also admits breather solutions on finite background, i.e. pulsating envelopes that well mimic the dynamic of rogue waves that may appear

B. Kibler (✉) • J. Fatome • C. Finot • G. Millot
Laboratoire Interdisciplinaire Carnot de Bourgogne, UMR6303 CNRS-UBFC, Dijon, France
e-mail: bertrand.kibler@u-bourgogne.fr

M. Onorato et al. (eds.), *Rogue and Shock Waves in Nonlinear Dispersive Media*,
Lecture Notes in Physics 926, DOI 10.1007/978-3-319-39214-1_4

from nowhere and disappear without leaving a trace. As a consequence, one can simply address the issue of rogue waves in terms of NLS breathers whose entire space-time evolution is analytically described [14]. For that reason and because of their specific dynamical properties (i.e., 'pulsating' localized waves), these unstable wave structures are originally considered as the simplest nonlinear prototypes of famous hydrodynamic rogue waves [15], in particular the doubly localized breather solutions (i.e., Peregrine soliton) [16]. Such solutions describe localized carrier perturbations with a strong amplification, they provide support to the nonlinear stage of the universal modulation instability (MI) phenomenon [17]. But surprisingly, NLS breather solutions have remained untested experimentally during almost 30 years, until the development of fibre-based experiments taking advantage of high-speed telecommunication-grade components.

It is worth mentioning that breather dynamics appear even with initial conditions that do not fulfill the mathematical ideal. Optical studies have strongly contributed to that end, thus confirming existence of breathers in nonlinear wave systems driven by noise (or with a partial degree of coherence). In such conditions, both competition and interaction between many unstable modes take place, so that rogue waves may appear intermittently or randomly in space and time with long-tailed statistics, as signatures of extreme-value phenomena [18, 19]. This represents a major step forward towards global understanding of rogue wave emergence in a turbulent environment and wave turbulence in integrable systems [20, 21]. We distinguish two MI regimes. On the one hand, the noise-driven MI that refers to the amplification of initial noise superposed to the plane wave leads to spontaneous pattern formation from stochastic fluctuations. On the other hand, the coherent seeded MI (or coherent driving of MI) refers to the preferential amplification of a specific perturbation (i.e., leading to a particular breather solution) relative to any broadband noise. In any case, the wave dynamics can be interpreted in terms of breathers and competitive interactions. Most importantly, the coherent seeded MI can be used to efficiently stabilize and manipulate the output wave, thus allowing to generate and quantitatively measure NLS breather properties in optical fibres.

In the following, we focus on the simplest breather solutions on finite background of the NLSE and we review their recent experimental evidence in nonlinear fibre optics. In Sect. 2, we provide the basic theoretical description for first- and second-order NLS breathers. In Sect. 3, we describe the distinct experimental configurations for observing breather propagation in optical fibres. We analyse the impact of different techniques to seed the MI process through numerical simulations. Section 4 presents the different experimental measurements of breathers in optical fibres that confirm predictions from the nonlinear wave theory. Finally Sect. 5 provides conclusions and an outlook on novel research directions.

2 Nonlinear Schrödinger Breathers

The phenomenon of modulation instability is usually studied in its simplistic version based on the pioneering works done in the 1960s; the effect was understood as an instability of the plane wave against the long-wave modulation and associated with the growth of spectral sidebands. A linear stability analysis is then performed to identify the instability criterion and to evaluate the initial growth rate of sidebands. This gives the basic information such as the perturbation frequency that experiences the maximum gain and defines the MI period. However, the above analysis only provides snapshots of the initial steps of MI and the whole of its dynamical evolution is not available. In particular, the dynamics of cascade of MI gain bands that generates the highly localized wave structures cannot be described. MI clearly exhibits much richer dynamics when one goes beyond the simplistic linear stability analysis [22, 23]. As an example, the long space evolution may exhibit the Fermi-Pasta-Ulam (FPU) recurrence phenomenon for the coherent seeded MI. Later, researchers also focused on approximate truncated or purely numerical approaches to address this problem in the 1990s [24–26].

However, the NLSE belongs to the remarkable class of integrable systems [7] and can be solved by using the inverse scattering transform method or other integration techniques. Surprisingly, exact breather solutions were derived during the 1970s–1980s, but remained untested. It concerns the simplest solutions that are either periodic in space and localized in time or periodic in time and localized in space; they are referred to as Kuznetsov-Ma breathers and Akhmediev breathers, respectively. Taking the period of both solutions to infinity gives rise to a first-order doubly localized breather on finite background: the Peregrine soliton. In the following we first review their properties. To this purpose we refer to the following scaled form of the self-focussing NLSE used to describe nonlinear wave propagation in an optical fibre:

$$\imath \frac{\partial \psi}{\partial \xi} + \frac{1}{2} \frac{\partial^2 \psi}{\partial \tau^2} + |\psi|^2 \psi = 0 \tag{1}$$

Here, ψ is a wave envelope of the optical field which is a function of ξ (a scaled propagation distance or longitudinal variable) and τ (a co-moving time, or transverse variable, moving with the wave-group velocity).

2.1 First-Order Breathers

A general one-parameter breather solution on finite background for the NLSE can be written compactly, as previously suggested in several works [27, 28], in particular when one aims to study the most well-known first-order solutions such

as Kuznetsov-Ma, Akhmediev and Peregrine breathers.

$$\psi(\xi,\tau) = e^{\imath\xi}\left[1 + \frac{2(1-2a)\cosh(b\xi) + \imath b\sinh(b\xi)}{\sqrt{2a}\cos(\omega\tau) - \cosh(b\xi)}\right] \tag{2}$$

Here, the governing parameter a determines the physical behaviour of the solution through the function arguments $b = [8a(1-2a)]^{1/2}$ and $\omega = 2(1-2a)^{1/2}$ directly linked to space and time evolution, respectively.

2.1.1 Kuznetsov-Ma Breathers

The first breather type solution on finite background for the NLSE was found in the 1970s by Kuznetsov, but also by Kawata and Inoue, and later by Ma [29–31]. They solved the initial value problem for the NLSE where the initial state was the plane wave solution perturbed by a large localized bump of soliton-type (such breathers approach the plane wave solution at infinite time). These solutions are periodic in space and localized in time; they are now referred to as the Kuznetsov-Ma Breather (KMB) or soliton on finite background. Such solutions can be considered as a limiting case of instability of the plane wave with respect to large perturbations. Equation (2) describes such solutions when $a > 1/2$. The parameters ω and b become imaginary such that the hyperbolic trigonometric functions become ordinary circular functions and vice-versa. As a result, the spatial period of the KMB is given by $2\pi/|b|$, and the transverse localization is determined by $2\pi/|\omega|$. Figure 1 illustrates the KMB solutions for two distinct values of the parameter a. The maximal intensity occurs at $\xi = 0$. The ratio of the maximum intensity to the background is always higher than 9. We clearly note that spatial period and temporal localization are inversely proportional to a, whereas the maximal peak intensity is proportional to a. When $a \to \infty$ the KMB solution tends to the standard soliton solution, a localized sech pulse with stable and uniform propagation.

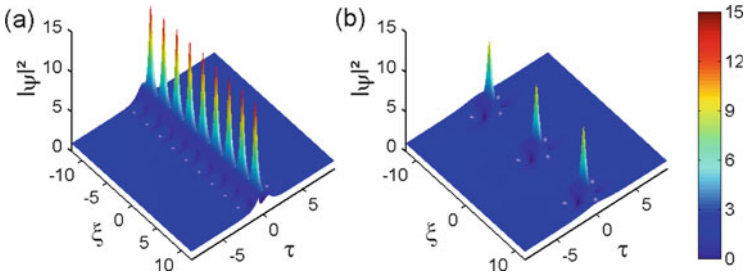

Fig. 1 Space-periodic KM breathers on a background plane wave $|\psi(\tau \to \pm\infty)| = 1$ for the following values of the governing parameter: (**a**) $a = 0.9$ and (**b**) $a = 0.55$

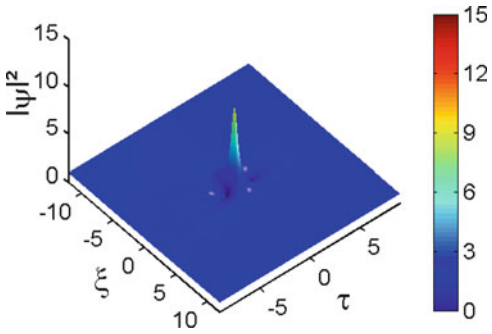

Fig. 2 Peregrine breather solution

2.1.2 Peregrine Breather

In 1983, D.H. Peregrine found a non-trivial solution in the limit of zero amplitude perturbation of KM breathers. It also corresponds to the infinite-period limiting case of previous solutions (i.e., $a = 0.5$). Apart from a simple exponential factor it is a rational function (see Eq. (3)), and it describes an isolated "intensity peak" in space-time arising out of the plane wave solution [16], as shown in Fig. 2. The Peregrine breather (PB) exhibits a ratio of the maximum intensity to the background equal to 9.

$$\psi(\xi, \tau) = e^{\imath\xi}\left[1 - \frac{4(1 + 2\imath\xi)}{1 + 4\tau^2 + 4\xi^2}\right] \tag{3}$$

2.1.3 Akhmediev Breathers

Later in the 1980s, Akhmediev et al. found a one parameter family of time-periodic solutions with the property that they approach the plane wave solution at infinite propagation; they breathe only once in space [17, 32]. They exhibit FPU-like growth-return evolution and are now widely referred to as the Akhmediev Breather (AB). These solutions are valid for initial periodic and small modulations of the plane wave (i.e. a single sideband perturbation into the MI gain band). Such solutions are given by Eq. (2) for $0 < a < 0.5$, two examples are presented in Fig. 3. Indeed AB solutions are valid over the range of modulation frequencies that experience MI gain: $0 < \omega < 2$. Note that the parameter $b > 0$ also governs the MI growth and corresponds to the MI gain calculated from the linear stability analysis. The maximum value $b = 1$ is obtained for $a = 0.25$ ($\omega = \sqrt{2}$). These time-periodic solutions provide, as a first step, a powerful framework with which to describe the full MI dynamics. The temporal period of the AB is given by $2\pi/|\omega|$, and the spatial localization is determined by $2\pi/|b|$. Contrary to the KMB, temporal period and spatial localization are here proportional to a, and the maximal peak intensity is still proportional to a, but lower than 9. When $a \to 0$ the AB solution tends to the plane

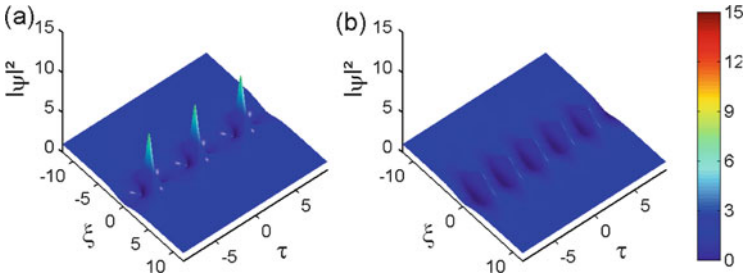

Fig. 3 Time-periodic Akhmediev breathers on a background plane wave $|\psi(\xi \to \pm\infty)| = 1$ for the following values of the governing parameter: (**a**) $a = 0.35$ and (**b**) $a = 0.05$

wave solution, while for $a \to 0.5$ (i.e., infinite-period) the AB solution tends to the Peregrine breather solution.

2.1.4 Localisation Properties

A crucial property of rogue waves is the maximum amplification of the perturbation with respect to the background wave. It clearly appears that the Peregrine breather does not exhibit the highest peak amplitude when including KM solutions. A wide range of a values gives a maximal amplification ratio beyond the factor of two. Besides this amplification factor, another key feature of rogue structures that cannot be avoided is related to their localization in space and time. The maximal spatio-temporal localisation is associated to the limiting case of PB, thus confirming extreme characteristics of PB emergence from the plane wave. The degree of localization can be determined in terms of ratios of the temporal and spatial periods ($\tau_{per} = 2\pi/|\omega|$ and $\xi_{per} = 2\pi/|b|$) relative to the individual temporal and spatial peak widths (τ_0 and ξ_0). These can be readily calculated analytically from Eq. (2) as a function of parameter a. The profile temporal width τ_0 is found with time coordinates for which the intensity is zero-valued adjacent to the peak (zeros only appear in the profile for $a > 1/8$). The spatial width ξ_0 is found with space coordinates for which the intensity is half of the peak intensity (only valid for profiles with $a < 1.1$). We then defined the spatio-temporal localization as the following product $(\xi_{per}/\xi_0)(\tau_{per}/\tau_0)$, similarly to [5].

A general description of first-order breather solutions with varying group velocity in the plane (ξ, τ) can be found in recent works [18, 33–35]. Some of them are also called quasi-Akhmediev breathers. Such breathers are neither periodic in time nor in space, they exhibit double quasi-periodicity and the line of maxima is tilted with respect to the line $\xi = 0$, so that one can define the velocity as the tangent of the angle between this line and the temporal axis [33]. However, the amplification of each peak almost remains aligned with the propagation direction. These solutions have a chance to collide (when choosing appropriate distinct velocities) and generate a giant intensity wave when synchronization of peaks is satisfied.

2.1.5 Spectral Description

In the case of Akhmediev breathers, one can easily find exact analytic expressions for the evolution of spectral components. During the initial stage of propagation, the sidebands experience exponential growth at the expense of the pump, as expected from the linear stability analysis of the modulation instability process. However the subsequent dynamics of energy exchange between multiple spectral modes are more complex. The AB solution describes growth and decay of a harmonically perturbed plane wave. In addition to the temporal description, expansion in a Fourier series and integration yield exact solutions for the pump and spectral harmonic amplitudes as a function of propagation distance [17, 36]:

$$A_0(\xi) = -1 + \frac{\imath b \sinh b\xi + \omega^2 \cosh b\xi}{\sqrt{\cosh^2 b\xi - 2a}} \tag{4}$$

$$A_n(\xi) = \frac{\imath b \sinh b\xi + \omega^2 \cosh b\xi}{\sqrt{\cosh^2 b\xi - 2a}} \times \left[\frac{\cosh b\xi - \sqrt{\cosh^2 b\xi - 2a}}{\sqrt{2a}}\right]^{|n|}$$

where A_0 and A_n are the amplitudes of the pump and the nth sideband ($n = \pm 1, \pm 2$, etc.), respectively, and ignoring factors of constant amplitude and phase. The sum $|A_0|^2 + \Sigma |A_n|^2$ is equal to 1, which is equivalent to the conservation of energy. When $\xi \to \pm\infty$, all the energy is concentrated in the pump, whereas for $\xi \to 0$ the energy of sidebands increases and the pump is progressively depleted. At the maximum spectral broadening (i.e., the maximum compression of the localized structure on finite background), the spectral amplitudes of the pump and the nth sideband are $A_0 = 1 - \omega$ and $A_n = \omega[(1 - (1 - 2a)^{1/2})/(2a)^{1/2}]^{|n|}$, respectively. Equation (4) exactly predicts the dynamics of an arbitrary number of sidebands without any assumption of an undepleted pump. Figure 4 illustrates the growth-decay cycle of sideband generation related to the spectral evolution of the AB solution for $a = 0.25$. The spectrum is associated with an exponentially decaying energy transfer from the pump frequency, it also reveals a characteristic universal triangular spectral form, when analysed logarithmically [37]. Moreover, the reciprocal energy exchange between the pump mode and an infinite number of side modes can be related to the FPU recurrence [38, 39].

As the triangular feature of the envelope spectrum on a log scale appears at an early stage of their evolution, this raises the possibility of early detection of breather emergence in chaotic optical fields [40], in particular by considering real-time measurements of optical spectra [41, 42]. The triangular spectral decay of the wings can be also easily calculated for the Peregrine breather [40].

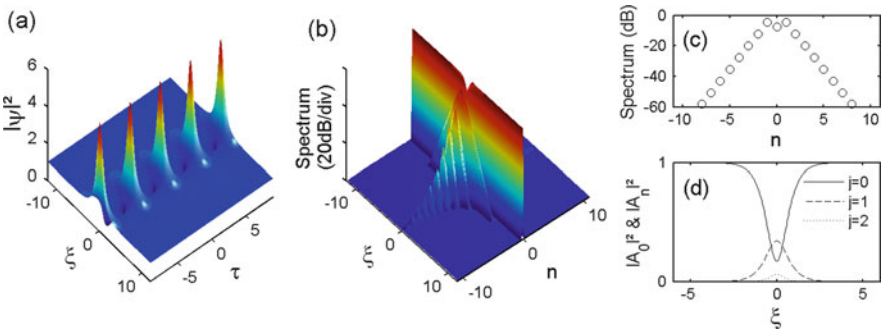

Fig. 4 Typical evolution of AB spectrum (here $a = 0.25$). (**a**, **b**) 3D illustration of both temporal and spectral intensities from Eqs. (2) and (4). (**c**) AB power spectrum at maximum sideband generation (i.e., at $\xi = 0$). (**d**) Evolution of intensities of the pump and the most significant sidebands along propagation distance

2.2 Second-Order Breathers

The NLSE also admits higher-order breather solutions. These higher-order solutions can be interpreted as a nonlinear superposition of two or more first-order breathers. Such complex waves offer the possibility of higher energy concentration in space and time, and the generation of waves with giant intensity peaks. Here we consider the nonlinear interaction of two first-order breathers, i.e. a second-order breather solution [32]. By employing the recursive Darboux method [43], one can found an explicit analytic form for the two-breather solution of the NLSE with two independent governing parameters a_j (with $j = 1, 2$) related to each breather, as reported in [44]:

$$\psi_{12}(\xi, \tau) = e^{\imath \xi} \left[1 + \frac{G + \imath H}{D} \right] \tag{5}$$

with

$$G = -(\omega_1^2 - \omega_2^2) \left[\frac{\omega_1^2 b_2}{\omega_2} \cosh(b_1 \xi_{s1}) \cos(\omega_2 \tau_{s2}) \right.$$
$$\left. - \frac{\omega_2^2 b_1}{\omega_1} \cosh(b_2 \xi_{s2}) \cos(\omega_1 \tau_{s1}) - (\omega_1^2 - \omega_2^2) \cosh(b_1 \xi_{s1}) \cosh(b_2 \xi_{s2}) \right]$$
$$H = -2(\omega_1^2 - \omega_2^2) \left[\frac{b_1 b_2}{\omega_2} \sinh(b_1 \xi_{s1}) \cos(\omega_2 \tau_{s2}) \right.$$
$$\left. - \frac{b_1 b_2}{\omega_1} \sinh(b_2 \xi_{s2}) \cos(\omega_1 \tau_{s1}) \right.$$

$$- b_1 \sinh(b_1\xi_{s1})\cosh(b_2\xi_{s2}) + b_2 \sinh(b_2\xi_{s2})\cosh(b_1\xi_{s1})\Big]$$

$$D = 2(\omega_1^2+\omega_2^2)\frac{b_1 b_2}{\omega_1\omega_2}\cos(\omega_1\tau_{s1})\cos(\omega_2\tau_{s2}) + 4b_1b_2[\sin(\omega_1\tau_{s1})\sin(\omega_2\tau_{s2}) + \sinh(b_1\xi_{s1})\sinh(b_2\xi_{s2})] - (2\omega_1^2 - \omega_1^2\omega_2^2 + 2\omega_2^2)\cosh(b_1\xi_{s1})\cosh(b_2\xi_{s2}) - 2(\omega_1^2-\omega_2^2)\left[\frac{b_1}{\omega_1}\cos(\omega_1\tau_{s1})\cosh(b_2\xi_{s2}) - \frac{b_2}{\omega_2}\cos(\omega_2\tau_{s2})\cosh(b_1\xi_{s1})\right]$$

Equation (5) describes various nonlinear combinations of Akhmediev breathers and Kuznetsov-Ma breathers with distinct governing parameters $0 < a_{1,2} < 0.5$ or $a_{1,2} > 0.5$. Each first-order breather j in the higher-order solution is described by the governing parameter a_j, the function arguments $\omega_j = 2(1-2a_j)^{1/2}$ and $b_j = [8a_j(1-2a_j)]^{1/2}$, and a shifted point from the origin (ξ_j, τ_j). The above solution describes the full wave evolution of a second-order breather during its nonlinear propagation, where $\xi_{sj} = \xi - \xi_j$ and $\tau_{sj} = \tau - \tau_j$ are shifted variables. When $\xi_1 = \xi_2 = 0$ and $\tau_1 = \tau_2 = 0$, we consider a synchronized nonlinear superposition at the origin.

Figure 5 illustrates a few examples of second-order breathers, in particular by highlighting the importance of the synchronization of the interaction between breathers. The nonlinear interaction strongly depends on the centring of the two elementary solutions in the plane (ξ, τ) [32], i.e. when their peak coincide. If the centres of the elementary solutions are separated by a large distance (time) shift along the $\xi(\tau)$ axis, the superposition tends to be linear, which prevents from the emergence of a giant intensity wave. Another degenerate solution can be found in the limit of equal governing parameters. In such a case, these degenerate solutions consist of two near-parallel lines almost periodic in structure, with only one point of intersection [44]. In the limit of infinite periods, this allows to fully establish the hierarchy of synchronized second-order breather solutions, ranging from the general case to the higher-order rational breather via degenerate breathers.

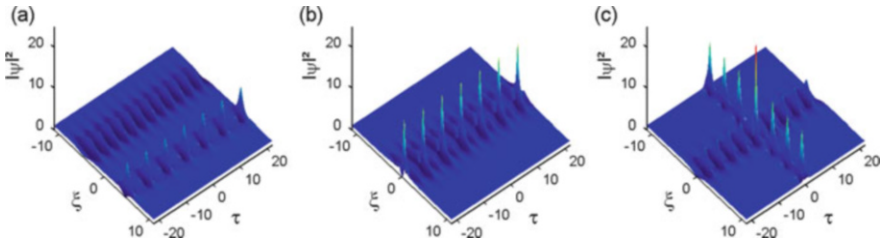

Fig. 5 Various forms of the second-order breather solution on finite background. (**a**) Nonlinear superposition of two ABs with $a_1 = 0.1$, $a_2 = 0.4$, $\tau_{1,2} = 0$, $\xi_2 = -\xi_1 = 4$. (**b**) Same parameters than in case (**a**) with synchronization at the origin $\xi_{1,2} = 0$. (**c**) Nonlinear superposition of one AB with one KMB: $a_1 = 0.25$, $a_2 = 0.8$ (synchronized collision at the origin: $\tau_{1,2} = 0$, $\xi_{1,2} = 0$)

General multi-breather solutions with more than two elementary breathers can still be studied, but their analytic expressions become very complex. For instance, a general N-breather solution of the NLSE was recently found by using the dressing method [34]. Such theoretical solutions are of considerable importance to fully describe the nonlinear stage of the modulation instability for arbitrary perturbation of the plane wave. However, for a good qualitative description of the higher-order wave structures generated, one may restrict the study to the doubly localized breathers in space and time, also called rogue-wave solutions. They exhibit a unique hierarchical structure with relatively convenient analytical forms. The lowest-order solution is known as the Peregrine breather [16], the second-order solution was first introduced in 1985 [32] and recently introduced in the context of rogue waves [45]. We then refer the reader to [46] and the references therein for a complete classification of higher-order rogue-wave solutions.

3 Experimental Configurations in Nonlinear Fiber Optics

Rogue energy localizations can be described by using theoretical breather solutions in various nonlinear dispersive systems, as reported in many theoretical or numerical works [15, 18, 47]. To confirm such an approach, as a first step, this requires their experimental evidence in real physical systems. Of course, rogue waves are not just an offshoot of such solutions, other mechanisms depending on the physical system must be taken into account, including the statistical approach when noise is present [4]. Besides its first evidence in optics, the Peregrine breather was later confirmed in other fields of physics driven by the NLSE, namely in hydrodynamics and plasma physics [6, 48]. In water wave experiments, the initial wave profiles are generated with a paddle located at one end of a tank. An electric signal, derived from the exact mathematical expression describing the water surface elevation, drives the paddle to directly modulate the surface height. Specific initial modulations such as a ratio of polynomials have been applied to the wave maker to excite rogue-wave solutions [49, 50]. But ideal perturbations in optics are nontrivial to synthesize in the temporal domain. Then, the first experimental studies in optics used non-ideal periodic perturbations based on widely accessible techniques in practice, such as the beating of two narrow-linewidth lasers to create an initial low-frequency-modulated wave or by means of usual electro-optic (intensity) modulators at gigahertz frequencies [5, 51]. Breather waves are then observed when such small- or large-amplitude perturbations on a high-power continuous wave (cw) become strongly focused due to the nonlinear wave reshaping occurring into an optical fibre. It was also observed that non-ideal initial perturbations sometimes lead to the generation of complex behaviours that may differ from the expected breather [52]. The sensitivity to initial perturbations depends on the complexity or order of the solution (i.e., the order of energy localization). There is always a tradeoff between the simplicity of the initial modulated wave (inherent to experiments) and the degree of accuracy with which we reach the mathematical ideal. Consequently, it was recently proposed to

introduce the advantages of ultrafast optics technology and programmable optical pulse shaping to study higher-order breathers, since this allows the generation of nearly arbitrarily shaped optical waveforms. The optical processing is then based on spectral line-by-line shaping of a frequency comb source (i.e., a Fourier-transform optical pulse shaping) in order to provide the ideal excitation of breather solutions in terms of phase and amplitude [53, 54].

In the following, we describe in more details the different experimental setups implemented to generate optical breathers, and we give some physical insights on the corresponding nonlinear dynamics drawn from numerical simulations of the NLSE.

3.1 Experimental Setups

Figure 6 depicts three different experimental configurations used to observe breather dynamics in nonlinear fibre optics. All the test-beds are based on commercially-available high-speed telecommunications-grade components.

These experimental configurations only differ in the linear shaping of the initial perturbation imposed to the cw. The beating of two lasers and the electro-optic modulation (see Fig. 6a, b) allow us to induce a simple sinusoidal perturbation in the temporal domain whose both amplitude and frequency can be controlled. However, in the spectral domain, the beating configuration corresponds to an

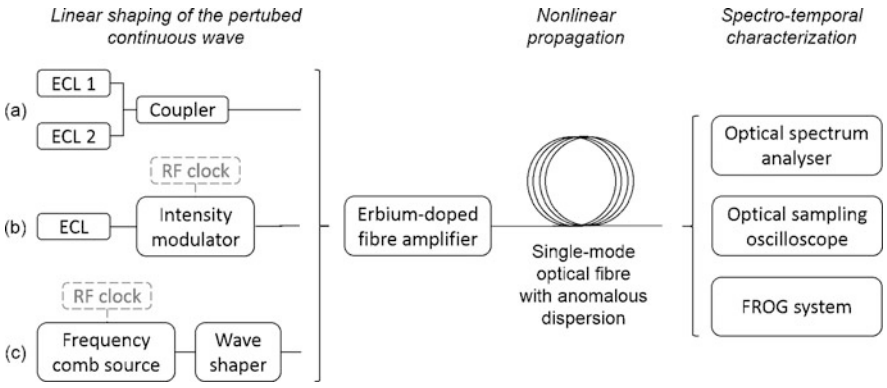

Fig. 6 Experimental configurations for observing breather dynamics in nonlinear fibre optics and based on three distinct linear shapings of the initial periodically-perturbed continuous wave: (**a**) the beating of two narrow-linewidth lasers whose perturbation frequency depends on their frequency spacing, (**b**) the electro-optic (intensity) modulation of a narrow-linewidth laser at a frequency given by a RF clock, (**c**) the linear shaping of an optical frequency comb source driven by a RF clock. ECL: external-cavity laser. FROG: frequency-resolved optical gating. Note that a phase-modulation stage to mitigate the detrimental effect of Brillouin scattering [55] is also required in the different linear-shaping configurations

asymmetric initial condition with a strong cw (i.e., ECL1 plays the role of the pump) perturbed by a weak single sideband (i.e., ECL2 plays the role of the seed) shifted by Ω from the pump. The amplitude and frequency detuning of the second laser has to be finely controlled to choose the required perturbation. While in the case of the electro-optic modulation (typically a $LiNbO_3$ intensity modulator), the initial condition is a symmetric spectrum with a strong pump perturbed by a pair of sidebands shifted by $\pm\Omega$ from the pump. Here the amplitude and frequency detuning of the perturbation is changed through an external RF signal generator. In any case, these two configurations cannot exactly generate ideal perturbation of the cw derived from previous theoretical expressions. We are limited to periodic modulations and particularly sinusoidal perturbations, and there is no control of the phase difference between the spectral components [56]. The third configuration overcomes this important issue by spectrally shaping both relative phase and intensity of each line of a frequency comb source [57, 58]. The programmable pulse shaper allows the generation of nearly arbitrarily shaped optical wave forms, in particular through a time-periodic pattern whose frequency is equal to the spectral separation of the comb lines. High resolution (about 1 GHz) systems are available to select and control individual spectral peaks [59]. The initial frequency comb can be generated by the implementation of variable-repetition-rate pulse source based on the nonlinear compression of an initial sinusoidal signal in a cavity-less optical-fibre-based device (i.e., similar to the second configuration or see [60]). The spectrum of such a pulse source can be approximated as a series of Dirac δ functions separated by the repetition rate. The width of the comb envelope depends on the nonlinear compression of the initial modulated cw and it determines the number of sidebands and their decreasing amplitude. A phase modulator is also introduced in the two first configurations or in the above frequency comb source to prevent the detrimental effect of stimulated Brillouin backscattering. Note that all the configurations restrict the experiments to study periodic perturbations of the cw, or to fit the limited time-window over which we can inscribe localized perturbation (the latter implies that no interaction occurs between neighbouring elements of the periodic pattern on the studied distance).

Whatever the linear shaping of the perturbed cw, an erbium doped-fibre amplifier (EDFA) is then used to amplify the average power of the synthesized wave before coupling into a single-mode optical fibre to undergo nonlinear propagation. The average power of the input wave is fixed so that it satisfies the value of the governing parameter a of breathers according to the fibre properties (see below for rescaling in dimensional units). At the fibre output, the optical wave profile is typically characterized using a high-dynamic-range optical spectrum analyser and an ultrafast optical sampling oscilloscope with subpicosecond resolution, or an adapted frequency-resolved optical gating (FROG) technique to retrieve the intensity and phase of periodic pulse trains on finite background fields [61].

To reconstruct the growth-decay intensity dynamics of breathers along propagation, distinct methods were already used. The direct (and destructive) method is based on cutback experiments, the low cost standard single mode fibre SMF-28 is well-suited for such measurements. More recently and inspired by hydrodynamic

experiments, an original approach of short propagation sequences for reconstructing the full wave evolution was reported. It benefits from the programmable wave shaper to shape repetitively different initial shaped conditions for a fixed and short nonlinear propagation length [54]. First, we begin with initial conditions fixed from theory at an arbitrary position from the maximal breather amplitude and we record the wave profile at the fibre output. This provides in the next step the new initial condition. Several iterations of this recording process enable to reach a long propagation distance without detrimental fibre losses.

The correspondence between theory and experiment can be retrieved by recalling that dimensional distance z (m) and time t (s) are related to the previous normalized parameters by $z = \xi L_{NL}$ and $t = \tau t_0$, where the characteristic (nonlinear) length and time scales are $L_{NL} = (\gamma P_0)^{-1}$ and $t_0 = (|\beta_2| L_{NL})^{1/2}$, respectively. The dimensional field envelope $U(z, t)$ $(W^{1/2})$ is $U = P_0^{1/2}\psi$, P_0 being the average power of the input wave. The modulation frequency ω of a single breather is related to the general governing parameter a by $2a = [1 - (\omega/\omega_c)^2]$, where the critical frequency value of the modulation instability gain is given by $\omega_c^2 = 4\gamma P_0/|\beta_2|$ [62]. $\beta_2 (< 0)$ and γ refer to the group-velocity dispersion and the nonlinear coefficient of the fibre used, respectively [55]. Consequently, the corresponding dimensional form of the NLSE is written as follows:

$$\imath \frac{\partial U}{\partial z} - \frac{\beta_2}{2} \frac{\partial^2 U}{\partial t^2} + \gamma |U|^2 U = 0 \tag{6}$$

As an example, the observation of the AB with $a = 0.45$ in the standard telecommunication single-mode fibre SMF-28 at 1550 nm ($\beta_2 = -21\ \mathrm{ps}^2\ \mathrm{km}^{-1}$ and $\gamma = 1.2\ \mathrm{W}^{-1}\ \mathrm{km}^{-1}$) requires an initially 20-GHz modulated continuous wave with average power equal to $P_0 = 0.7$ W.

3.2 Impact of Initial Conditions

Here, we discuss the impact of non-ideal initial conditions on the generation of breathers, in particular when temporal periodic perturbations are used. We performed numerical simulations based on the NLSE with three distinct input conditions for the modulated continuous wave in order to generate the AB with $a = 0.25$, namely an ideal perturbation corresponding to the theoretical AB at $\xi = -3$, and two simplified (non-ideal) perturbations with similar amplitudes induced by an intensity modulator (i.e., symmetric two-sideband perturbation) or by a weak single laser (i.e., asymmetric single-sideband perturbation). Figure 7a–c reports the evolution dynamics of the corresponding temporal intensity profiles. Even in the presence of very similar intensity modulation in the temporal domain as shown in Fig. 7d, we observe that non-ideal initial conditions used in practice yield periodic evolution as a function of propagation in contrast to the exact AB theory. However, each growth-return cycle remains well-described by the analytic AB solution. The

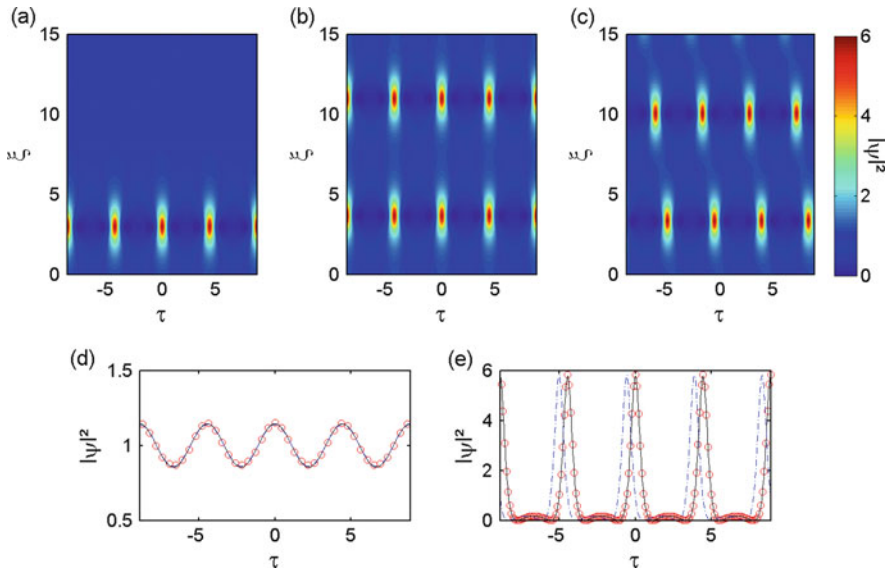

Fig. 7 Impact of initial conditions on AB dynamics during propagation (here in the case of $a = 0.25$) investigated through NLSE simulations. (**a**) Intensity evolution for exact initial condition from Eq. (2). (**b**) Intensity evolution for the symmetric two-sideband perturbation induced by an intensity modulator: $\psi = \sqrt{1 + 0.145\cos(\omega\tau)}$. (**c**) Intensity evolution for the asymmetric single-sideband perturbation: $\psi = 1 + 0.07\exp(-\imath\omega\tau)$. Note that amplitudes of perturbation were chosen to provide an initial contrast of modulation similar to the ideal case as confirmed in subplot (**d**). *Red circles* correspond to the ideal initial condition. *Solid black (dashed blue) curve* corresponds to the two-sideband (single-sideband) perturbation. (**e**) Comparison between the different intensity profiles at maximum compression of the breather

profiles of the maximally compressed breathers are in excellent agreement (see Fig. 7e). This agreement was confirmed over a range of modulation amplitudes and for various modulation frequencies across the MI gain curve [62]. Such a periodic evolution of the nonlinear stage of modulation instability as a function of propagation is reminiscent to the fundamental FPU recurrence phenomenon, it may be described by bi-periodic (elliptic) breather solutions [14].

We also notice that the breather propagates with a certain angle to the line $\tau = 0$ for the single sideband perturbation. Indeed, the inclined trajectory acts in the first steps of the initial perturbation growth whose spectrum asymmetry induces a distinct mean group velocity of AB compared to another symmetric perturbation. Similar dynamics are also observed in the final decay of the breather cycle. It is important to mention that the relative frequency position of the single perturbation to the continuous wave enables the control of the mean group velocity of the AB. The mean group velocity of the AB can be slower or faster than the group velocity of the cw. It is therefore possible to control the group velocity difference between two ABs (with distinct values of a) through a suitable choice of perturbations (with opposite sign of modulation frequency) in order to favour the collision. A simple

continuous wave that contains a bi-modulation by means of two spectral distinct sidebands may provide the required conditions for breather collision [33, 53], and the generation of a second-order breather.

The impact of initial conditions to generate the KMB with $a = 1$ is studied in Fig. 8 through NLSE simulations with two different configurations, namely the ideal perturbation at $\xi = -\pi/|b|$ (i.e., half the period), and a simplified periodic perturbation, induced by an intensity modulator, with similar amplitude and temporal width as shown in Fig. 8c. The full width at half maximum ΔT_{FWHM} of the time-varying intensity (with maximal intensity $I_{max} = (2\sqrt{2a} - 1)^2$) above background of the ideal perturbation was used to determine numerically the optimal frequency for the cosine modulation, as follows: $\Delta\tau_{sech} = 1.8\Delta T_{FWHM}$ and $f_{cos} = 1/(2.4\Delta T_{FWHM})$. Figure 8a, b reports the corresponding evolution dynamics of the intensity profiles. We observe that the cosine modulation yields periodic evolution in good agreement with the exact KMB behaviour, only slight discrepancies appear on the longitudinal period and the maximal peak power as revealed by Fig. 8d, e. The strongly modulated wave well approximates the KMB over each modulation cycle. The above analysis confirms that the periodic longitudinal dynamics observed

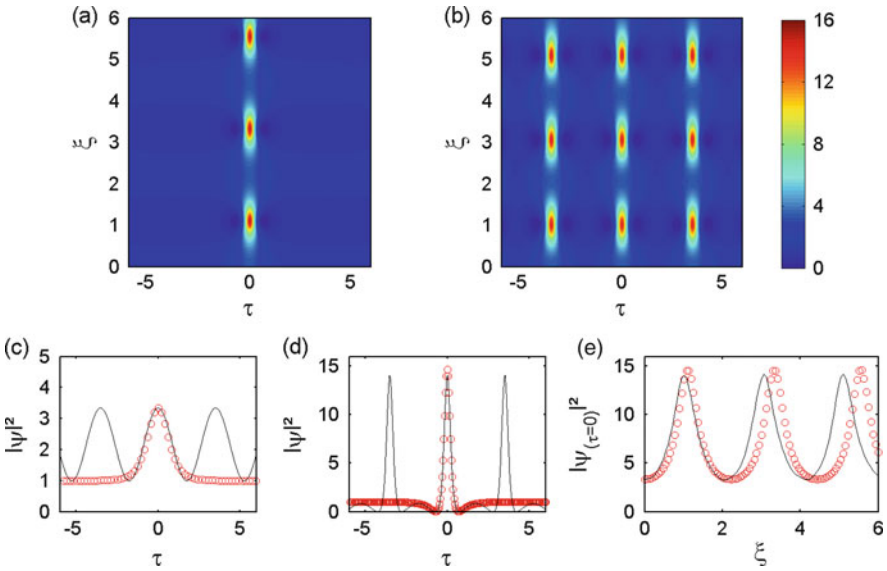

Fig. 8 Impact of initial conditions on KMB dynamics during propagation (here in the case of $a = 1$) investigated through NLSE simulations. (**a**) Intensity evolution for exact initial condition from Eq. (2). (**b**) Intensity evolution for the symmetric two-sideband perturbation induced by an intensity modulator: $\psi = \sqrt{(I_{max} + 1)/2 + (I_{max} - 1)/2\cos(2\pi f_{cos}\tau)}$. (**c**) Comparison of initial conditions. *Red circles* correspond to the ideal case. *Solid black curve* corresponds to cosine perturbation. (**d**) Comparison between the different intensity profiles at first maximum compression of the breather. (**e**) Comparison of the intensity evolution as a function of propagation distance at $\tau = 0$ to reveal the longitudinal periodicity

with a large initial modulation on a finite background can be described and interpreted in terms of Kuznetsov-Ma breathers [51]. It shows that KMB dynamics can be obtained with very different conditions in NLSE propagation. Such periodic evolution in the NLSE is also another example of FPU recurrence.

In some cases, non-ideal initial conditions lead to the observation of higher-order modulation instability [52, 63]. This higher-order instability arises from the nonlinear superposition of elementary instabilities, associated with initial single Akhmediev breather evolution followed by a regime of complex pulse splitting. The excitation of higher-order MI can be observed readily in experiments using only a single initial frequency modulation on a plane wave, provided that the modulation frequency is below a critical low frequency limit such that multiple instability harmonics fall under the elementary gain curve [64] (i.e., when $a > 0.375$ or $\omega < 1$). The harmonics actively participate in the evolutionary process since they are forced by the fundamental unstable mode, and then they grow independently at an exponential rate to dominate the global dynamics. Consequently, the evolution dynamics appear to be a complex composition of elementary breathers. Moreover, in such cases, one cannot extract a well-defined single value of recurrence distance as previously shown in Fig. 7, and a more complex recurrence is observed. Figure 9 gives some numerical examples of higher-order MI when using non-ideal excitation of a single AB delivered by an intensity modulator. For $a = 0.4$, only one harmonic of the initial excitation is located within the MI gain band (i.e., unstable mode), which leads to the emergence of two elementary breathers. For $a = 0.46$, two harmonics are now unstable, and then we observe a third-order MI evolution corresponding to the nonlinear superposition of three breathers. Note that the superposition pattern (i.e., the spatial arrangement) is also sensitive to the initial modulation amplitude. Furthermore, it is obvious that the evolution dynamics are also driven by this higher-order instability when multiple sidebands are already present in the initial perturbation, which can be interpreted in terms of higher-order breathers.

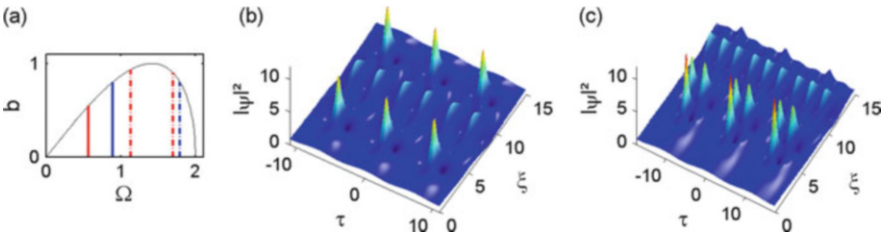

Fig. 9 Higher-order modulation instability induced by non-ideal excitation of ABs (NLSE simulations). (**a**) MI gain b curve predicted by the linear stability. *Solid lines* indicate the perturbation frequencies used in subplots (**b**, **c**) to excite ABs corresponding to $a = 0.4$ (*blue color*) and $a = 0.46$ (*red color*), respectively. *Dashed lines* indicate their corresponding harmonics that lie within the unstable region. (**b**, **c**) Intensity evolution for initial periodic modulation of the cw with a frequency calculated from $a = 0.4$ and 0.46, respectively. In both cases the initial condition is $\psi = \sqrt{1 + 0.15\cos(\omega\tau)}$

Another important issue of breather generation is the detrimental effect of linear losses occurring during propagation in optical fibres. An overview of the impact of fibre losses is given in the next section. It can be simply predicted based on the dimensional NLSE simulations taking into account a simple dissipative term in the form of $+\imath\alpha U/2$ (in the left-hand side of Eq. (6)) with $\alpha > 0$ [55]. Besides fibre losses, higher order effects linked to pulse propagation such as third-order dispersion, self-steepening, and the Raman effect can also be considered, even theoretically by extending the NLSE [65]. Rogue wave solutions were found in such equations that are integrable in special cases, such as the Sasa-Satsuma or the Hirota equations [66]. In summary, any kind of disturbance of the ideal NLSE propagation induces a deviation from the expected theoretical solutions (specific to each breather on finite background), but most of features related to their pulsating dynamics remain clearly observable. Breathers on finite background may be considered as 'robust solutions' (but unstable solutions from the mathematical point of view) [65], in the sense that they can be excited or propagated even with non-ideal conditions, and the main features of a localized high amplitude event (i.e., rogue wave) still occur.

4 Experimental Results

The first quantitative experimental evidence of breathers on finite background dates from 2010 with both temporal and spectral analyses [5]. It is worth mentioning that former works qualitatively found the MI-induced formation of pulse trains in optical fibres that are potentially described by the usual breather solutions. Indeed, the ability to generate high-repetition-rate pulse trains through coherent-driven MI in optical fibres was already studied in the 1980s [67, 68]. However, until recently, most of these experiments focused on specific initial conditions leading to soliton trains without background, the latter are more suitable for telecommunications applications (this corresponds to $0.1 < a < 0.25$, but strongly modulated initial cw was typically used, i.e. a bichromatic pumping). The design of experimental setups was based on numerical simulations or empirical laws, all this may explain why the general breather solution was not used. Note that one of the main signature of breather dynamics was reported in 2001 without comparison to theoretical solutions, it concerns the growth-decay cycle of the seeded-MI regime that can be linked to the FPU recurrence phenomenon [39]. In the following, we review the quantitative experimental demonstrations of the different classes of breather solutions. We also point out the impact of non-ideal initial excitation and fibre losses on breather dynamics. Experimental results are compared with corresponding theoretical predictions from breather solutions. Numerical simulations based on the NLSE with experimental initial conditions and/or fibre losses are not shown, since they are usually indistinguishable from experimental results.

4.1 First-Order Breathers

In 2010, we used the analytic description of NLSE breather propagation to implement experiments in optical fibre generating femtosecond pulses with strong temporal and spatial localization, and near-ideal temporal Peregrine breather (PB) characteristics. These experiments represent the first amplitude and phase measurements of a nonlinear breather structure in any continuous NLSE soliton-supporting system. The experimental setup was based on the beating of two lasers (see Fig. 6a) to induce a simple sinusoidal perturbation in the temporal domain whose both amplitude and frequency can be controlled. This technique simply allows to excite the large family of AB solutions by adapting the perturbation frequency and the input power as a function of the fibre characteristics to control the governing parameter a. The evolution towards the Peregrine breather as $a \to 1/2$ corresponds to the limit where $\omega \to 0$ is then accessible by decreasing the frequency space between lasers. They reached the divergent regime where near-PB characteristics are observed with the values of $a > 0.4$. A highly nonlinear fibre was used to reduce both fibre length and input power required to observe the Peregrine breather. Detailed temporal measurements using FROG were carried out at the distance where PB features are expected at maximum compression. The retrieved intensity and phase are shown in Fig. 10a. The FROG measurements confirm the expected temporally localized peak surrounded by a non-zero background, and the different signs of the peak and background amplitudes through the measured relative π phase difference in the vicinity of the intensity null. The measured spectral intensity was compared to the analytic spectrum for the ideal PB, the decay of

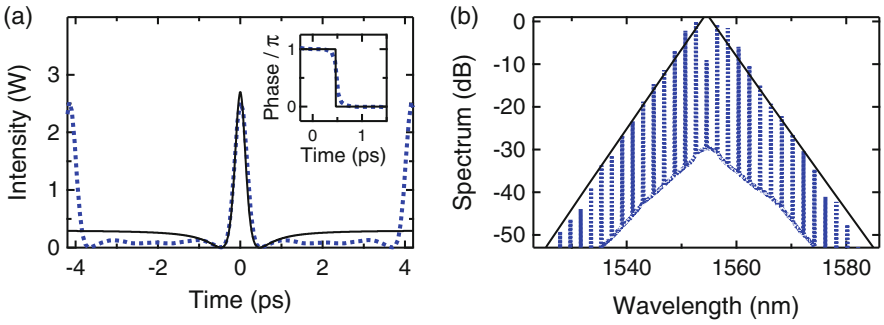

Fig. 10 Experimental results showing the measured temporal characteristics of the maximally compressed breather, and comparison with the predicted Peregrine breather solution. (**a**) Intensity and phase from experiment (*blue dots*) and for the ideal PB (*black lines*). The maximum peak power from theory is $9P_0 = 2.7\,\mathrm{W}$. (**b**) Corresponding spectral characteristics from experiment (*blue dots*) and PB theory (*black lines*). Note that the theoretical spectrum is calculated for the time-varying envelope component so that the delta-function component at the pump is not shown. (Adapted from [5])

the measured sideband intensities is well reproduced (see Fig. 10b), as follows: $\exp[-|\Omega|(|\beta_2|/\gamma P_0)^{1/2}]$.

In this work, spatial localization dynamics were studied indirectly by changing the pump-signal detuning to vary a while studying dynamical evolution by varying the input power (recall $\xi = z\gamma P_0$). Later, in 2011, we further explored the generation of the PB characteristics in the standard fibre SMF-28, using a much simplified setup [52]. This setup is based exclusively on commercially available telecommunication-ready components and standard silica SMF-28 fibre. The initially modulated cw is created through direct intensity modulation of a laser diode and the temporal characterization is easily obtained by means of an ultrafast optical sampling oscilloscope. Higher values of a were reached and with cutback measurements, the first direct observation of PB longitudinal evolution dynamics was reported. In showing that Peregrine breather characteristics appear with initial conditions that do not correspond to the mathematical ideal, such results widely impacted on studies of rogue events induced by modulation instability.

When studying the family of Akhmediev breathers with $0 < a < 0.5$, increased temporal localization is also associated with increasing spatial localization. The modulation-instability recurrence period increases asymptotically as $a \rightarrow 1/2$. Two-dimensional localization dynamics were experimentally investigated in [5] in order to find the regime where the AB approaches the Peregrine limit, even with non-ideal excitation. Based on extensive autocorrelation measurements, the degree of spatio-temporal localization was retrieved in good agreement with NLSE simulations for a large range of a values.

The exact theory describing the frequency domain evolution of ABs can be also verified. Experiments measuring pump and multiple sideband generation over a growth-return cycle of MI were performed in 2011 to quantitatively test the theory for an arbitrary value of a (i.e., for arbitrary gain) [36]. The setup is similar to the simplified configuration used to observe the PB dynamics. The excellent signal to noise ratio allowed to compare experiment and theory out to more than ten spectral sidebands and over a 30 dB dynamic range, as shown in Fig. 11. This was the most complete and highest signal of noise characterization of MI dynamics in any NLSE-governed system. We clearly observe the good agreement about the depletion dynamics of the injected modulated continuous wave pump and the near-recovery towards the initial state. This detailed analysis reveals that the temporal compression is associated with an increased spatial localization of the energy transfer to higher sideband orders. These results also confirm the validity of AB theory in describing the dynamical evolution from growth to decay over an MI cycle. Note that imperfect initial conditions of AB excitation and fibre losses here deviate the dynamics from the perfect recurrence.

Kuznetsov-Ma breathers that are periodic in space were studied experimentally in 2012 [51]. This work reported the first experimental confirmation of the pioneering theoretical studies of the KMB solution of the NLSE. The experimental configuration is similar to AB studies with the direct modulation of a single cw laser. This simple setup only generates non-ideal excitation of KMB, however, it was confirmed that seeding the modulation instability process with strong modulation amplitude

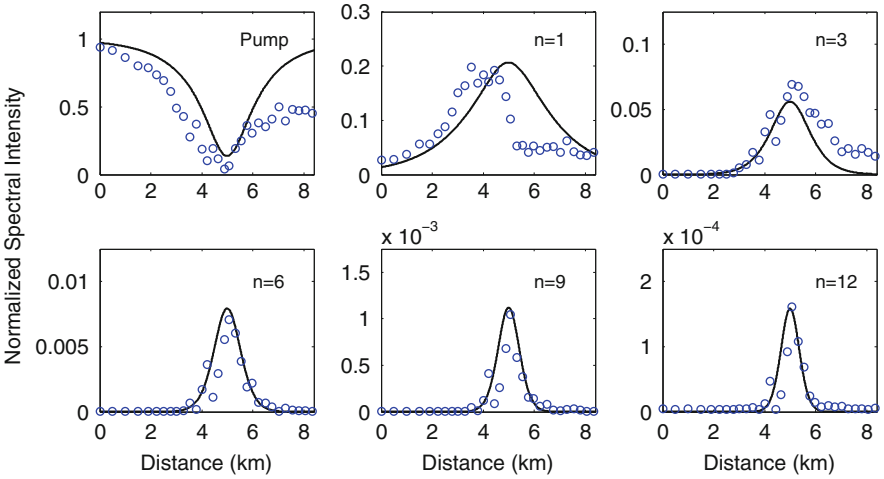

Fig. 11 Spectral dynamics as a function of propagation distance for the pump and sideband orders as shown. Experiment (*blue circles*) is compared with the exact AB theory from Eq. (4) (*black curve*). (Adapted from [36])

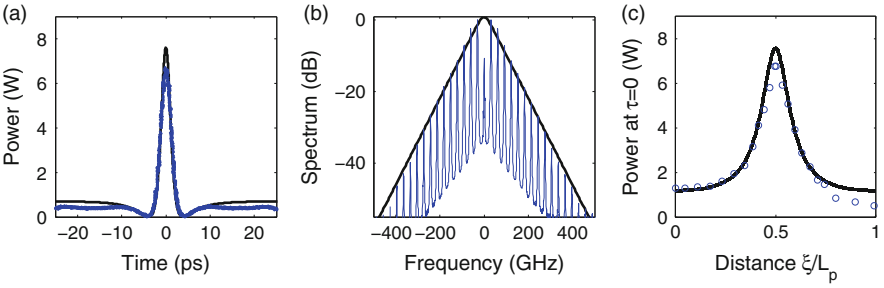

Fig. 12 (**a**, **b**) Comparison of experimental (*blue curve*) and theoretical (*black curve*) KM soliton profiles for maximum temporal compression in time and frequency domains, respectively. Note that the theoretical spectrum is calculated for the time-varying envelope component so that the delta-function component at the pump is not shown. (**c**) Evolution of the maximal power (i.e., at $\tau = 0$) as a function of normalised distance for both experiment (*blue circles*) and theory (*black line*). (Adapted from [51])

allows the observation of KM dynamics, as previously shown in Fig. 8. One cycle of the initial periodic modulation approximates the ideal KMB solution at a point of minimal intensity in its evolution. The evolving temporal profile was measured with propagation distance by means of fibre cutback experiments. Figure 12 shows the direct comparison between the generated temporal profile (at half the KMB period, $L_p/2$) and the longitudinal evolution of the power (at the centre of the modulation cycle), and the KMB theory. The agreement between experiment and theory confirms that KM solutions describes the evolution of individual modulation cycles. KMB dynamics then appear more universally than for the specific conditions

considered in the original theory. The experimental analysis of the longitudinal periodic behaviour was limited to one growth-decay cycle due to detrimental fibre losses.

Note that AB and KMB dynamics were recently studied with exact initial conditions in water waves. The experiments conducted in a water wave flume showed results that are in good agreement with theoretical predictions, thus confirming that such breather solutions can explain the generation of extreme waves in diverse nonlinear dispersive media [69].

4.2 Higher-Order Breathers

The experimental generation of higher-order breather dynamics can be classified in two categories that depend on breather excitation. The first one relies on a single-frequency non-ideal perturbation [52, 63], whereas the second category includes the simultaneous seeding of modulation instability by multiple frequencies [53, 54].

Figure 13 reports the nonlinear superposition of two or three first-order breathers, observed when a single breather (for $a > 0.375$) is excited with non-ideal perturbation. The experimental setup was based on the direct cosine modulation of a cw laser to excite an AB with parameter $a = 0.42$ or 0.464 close to the Peregrine regime. The initial evolution is only driven by the excited unstable mode, but next impacted by the second and third unstable modes with frequencies corresponding to the harmonics of initial excitation. The generated pattern in the plane (t,z) looks like a complex pulse splitting, its was explained in terms of higher-order MI since the multiple instability harmonics fall under the MI gain curve (see similar pattern in Fig. 9). The expected return to the initial state for an ideal AB is not observed. Corresponding theoretical predictions can be easily retrieved by using second or third-order breather solutions with a suitable choice of shifted variables ξ_{sj} and τ_{sj} (see Fig. 5).

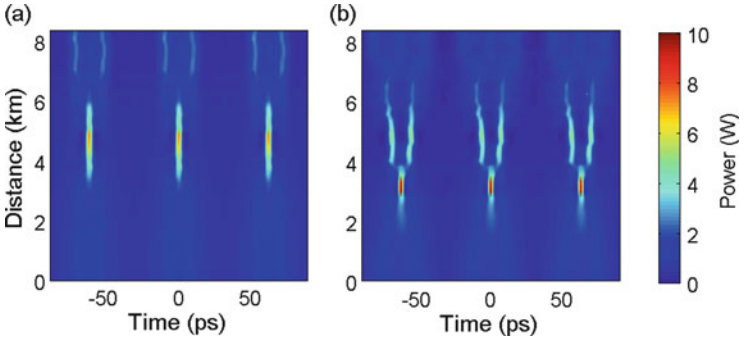

Fig. 13 Experimental measurements of spatio-temporal evolution of modulated cw undergoing higher-order MI for $a = 0.42$ (**a**) and $a = 0.464$ (**b**). (Adapted from [52, 63])

To describe giant-intensity waves, we have to consider the synchronized interaction of first-order breathers that correspond to their collision, i.e. higher-order breather solutions with shifted variables equal to zero. This requires a multiple-sideband perturbation of the continuous wave. The collision of two ABs was experimentally studied in 2013 with non-ideal excitation of the two breathers [53]. An efficient collision occurs during propagation with proper initial phase and velocity differences between breathers. The easiest way to generate two ABs was the seeding of MI process at two distinct frequencies with only two spectral sidebands. The initial cw then contains a bimodulation in the temporal domain. By controlling the initial asymmetry of the sideband amplitudes, their relative phase difference, and their relative frequency spacing from the pump (with opposite sign to favor the collision), we can find specific conditions where the two ABs collide efficiently at a specific distance. Corresponding numerical simulations (without fibre losses) are shown in Fig. 14a–c to illustrate the overall dynamics. These spatio-temporal dynamics are very well described by higher-order breather theory. In this work, such a control of spectral sidebands was created through the spectral shaping of three optical comb lines, i.e. the pump and two sidebands (see Fig. 6). The experimental observation of the giant wave profile generated at the predicted collision distance is reported in Fig. 14d. Obviously, when one of the initial sidebands was switched off,

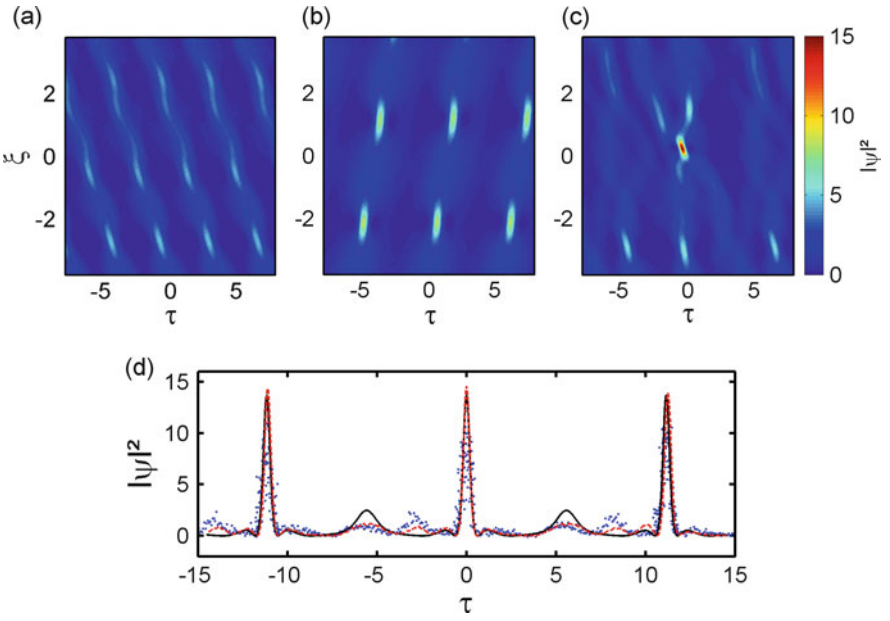

Fig. 14 NLSE simulations: single breather evolution with nonideal excitation (**a**) for $a_1 = 0.14$ and (**b**) for $a_2 = 0.34$. (**c**) Collision of the two ABs when excited simultaneously by using the superposition of previous initial conditions. (**d**) Experimental collision (*blue dots*) profile compared to ideal theory (*black curve*) and NLSE simulations with non-ideal excitation (*red dashed line*) by using normalized variables. (Adapted from [53])

the evolution of a single breather was recovered with a lower peak power. Besides the presence of secondary side lobes attributed to non-ideal excitation of ABs, the main discrepancy with the ideal second-order breather solution is the maximal peak power that can be reached. A better agreement would be conceivable if one could excite the collision on a shorter propagation distance (here 3.8 km) to minimize the impact of fibre losses.

Later, the experimental demonstration of exact higher-order breather generation was reported by combining this programmable pulse shaping technique (to shape the exact initial excitation) with short propagation sequences for reconstructing the full wave evolution (to overcome the fibre loss issue) [54]. This two-stage linear-nonlinear shaping of an optical frequency comb can be now considered as an optical rogue-wave-solution generator. As an example, the explicit analytical form of a synchronized two-breather solution of the NLSE was applied as a linear spectral filter to shape ideal modulation of a continuous wave. Relative amplitude and phase differences of 25 comb lines were managed. The additional nonlinear propagation of the tailored wave provided the first complete experimental evidence of both the growth and decay of this kind of fundamental breather solution in excellent agreement with theory, as reported in Fig. 15. A misfit parameter between the experimental shape and theory was calculated and found to be below 4 %, only due to the residual fibre losses.

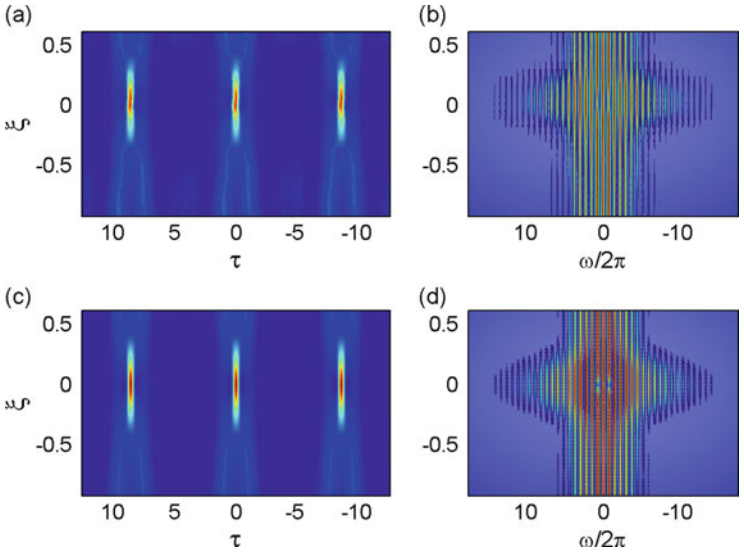

Fig. 15 Evolution of a second-order periodic breather in both temporal and spectral domains, respectively, as a function of propagation distance. (**a**, **b**) Experiments. (**c**, **d**) Analytic solution given by Eq. (5) for $a_1 = 0.2294$ and $a_2 = 0.4323$. (Adapted from [54])

5 Conclusions

This chapter presented the main features of simplest breather solutions of the NLSE. Breathers are of fundamental importance since they contribute to fully describe the growth-decay cycle of extreme localized waves emerging from modulation instability. We described the usual conditions required for their observation in optical fibres, and we reported the first complete experimental proofs of existence and control of this untested class of nonlinear waves. However, our investigations were restricted so far to an essentially reduced class of breathers and in the absence of complex dynamics. To go beyond the frontier in terms of exploring the rich dynamics of breathers, current issues mainly rely on the development of ultrafast optical arbitrary wave generation and characterization, and the design of more complex optical systems without loss (i.e., multi-variable and inhomogeneous propagation, as well as wave turbulence and perturbed NLSE-based systems). In this context, a recent work investigated the dynamics of ABs in an optical fibre with a longitudinally tailored dispersion that allows to nearly freeze the breather evolution near their point of maximal compression [70]. Furthermore, the existence of vector rogue wave solutions arising from polarization modulation instability is expected to be a crucial progress in explaining extreme waves in multicomponent systems [71–73].

Finally, the widest class of creation and annihilation dynamics of MI, also called superregular breathers, was recently and simultaneously observed in two different branches of wave physics, namely, in optics and hydrodynamics [74]. Based on the common framework of the nonlinear Schrödinger equation, this multidisciplinary approach proved the universality and reversibility of nonlinear wave formations from localized perturbations for drastically different spatial and temporal scales. In summary, the direct analogy drawn within the narrowband approximation of NLS model between ocean waves and light wave propagation in optical fibres [75], or even with other physical domains such as plasma physics, makes this research area very challenging and exciting for both fundamental and applied aspects.

Acknowledgements We gratefully acknowledge past and present collaborators in the above-described experimental works: B. Frisquet, K. Hammani, A. Chabchoub, and J. M. Dudley, as well as funding from the French National Research Agency and the Conseil Régional de Bourgogne.

References

1. Solli, D.R., Ropers, C., Koonath, P., Jalali, B.: Optical rogue waves. Nature **450**, 1054–1057 (2007)
2. Akhmediev, N., Pelinovsky, E.: Discussion & Debate: rogue waves - towards a unifying Concept? Eur. Phys. J. Spec. Top. **185**, 1–258 (2010)
3. Akhmediev, N., Dudley, J.M., Solli, D.R., Turitsyn, S.K.: Recent progress in investigating optical rogue waves. J. Opt. **15**, 060201 (2013)

4. Onorato, M., Residori, S., Bortolozzo, U., Montina, A., Arecchi, F.T.: Rogue waves and their generating mechanisms in different physical contexts. Phys. Rep. **528**, 47–89 (2013)
5. Kibler, B., Fatome, J., Finot, C., Millot, G., Dias, F., Genty, G., Akhmediev, N., Dudley, J.M.: The Peregrine soliton in nonlinear fibre optics. Nat. Phys. **6**, 790–795, 2010.
6. Chabchoub, A., Hoffmann, N.P., Akhmediev, N.: Rogue wave observation in a water wave tank. Phys. Rev. Lett. **106**, 204502 (2011)
7. Zakharov, V.E., Shabat, A.B.: Exact theory of two-dimensional self-focusing and one-dimensional self-modulation of waves in nonlinear media. Zh. Eksp. Teor. Fiz. **61**, 118 (1971) [Sov. Phys. JETP **34**, 62 (1972)]
8. Lighthill, M.J.: Contribution to the theory of waves in non-linear dispersive systems. J. Inst. Math. Appl. **1**, 269–306 (1965)
9. Whitham, G.B.: A general approach to linear and nonlinear dispersive waves using a Lagrangian. J. Fluid Mech. **22**, 273–283 (1965)
10. Bespalov, V.I., Talanov, V.J.: Filamentary structure of light beams in nonlinear liquids. JETP Lett. **3**, 307–310 (1966)
11. Benjamin, T.B., Feir, J.E.: The disintegration of wave trains on deep water. Part 1: theory. J. Fluid Mech. **27**, 417–430 (1967)
12. Benjamin, T.B.: Instability of periodic wavetrains in nonlinear dispersive systems. Proc. R. Soc. A. **299**, 59–75 (1967)
13. Zakharov, V.E.: Stability of periodic waves of finite amplitude on a surface of deep fluid. J. Appl. Mech. Tech. Phys. **9**, 190–194 (1968). (Zakharov, V.E., Ostrovsky, L.A.: Modulation instability: the beginning. Phys. D **238**, 540–548, 2009)
14. Akhmediev, N., Ankiewicz, A.: Solitons, Nonlinear Pulses and Beams. Chapman and Hall, London (1997)
15. Osborne, A.R.: Nonlinear Ocean Waves and the Inverse Scattering Transform. Academic Press, San Diego (2010)
16. Peregrine, D.H.: Water waves, nonlinear Schrödinger equations and their solutions. J. Aust. Math. Soc. Ser. B **25**, 16–43 (1983)
17. Akhmediev, N., Korneev, V.I.: Modulation instability and periodic solutions of the nonlinear Schrödinger equation. Theor. Math. Phys. **69**, 1089–1093 (1986)
18. Akhmediev, N., Soto-Crespo, J.M., Ankiewicz, A.: Extreme waves that appear from nowhere: on the nature of rogue waves. Phys. Lett. A **373**, 2137–2145 (2009)
19. Dudley, J.M., Dias, F., Erkintalo, M., Genty, G.: Instabilities, breathers and rogue waves in optics. Nat. Photon. **373**, 755–764 (2014)
20. Randoux, S., Walczak, P., Onorato, M., Suret, P.: Intermittency in integrable turbulence. Phys. Rev. Lett. **113**, 113902 (2014)
21. Walczak, P., Randoux, S., Suret, P.: Optical rogue waves in integrable turbulence. Phys. Rev. Lett. **114**, 143903 (2015)
22. Lake, B.M., Yuen, H.C., Rungaldier, H., Ferguson, W.E.: Nonlinear deep-water waves: theory and experiment. Part 2. Evolution of a continuous wave train. J. Fluid. Mech. **83**, 49–74 (1977)
23. Yuen, H.C., Lake, B.M.: Nonlinear dynamics of deep-water gravity waves. Adv. Appl. Mech. **22**, 67–229 (1982)
24. Ablowitz, M.J., Herbst, B.M.: On homoclinic structure and numerically induced chaos for the nonlinear Schrödinger equation. SIAM J. Appl. Math. **50**, 339–351 (1990)
25. Cappellini, G., Trillo, S.: Third-order three-wave mixing in single-mode fibers: exact solutions and spatial instability effects. J. Opt. Soc. Am. B **8**, 824–838 (1991)
26. Trillo, S., Wabnitz, S.: Dynamics of the nonlinear modulational instability in optical fibers. Opt. Lett. **16**, 986–988 (1991)
27. Akhmediev, N., Eleonskii, V.M., Kulagin, N.E.: Exact first-order solutions of the nonlinear Schrödinger equation. Theor. Math. Phys. **72**, 809–818 (1987)
28. Dysthe, K.B., Trulsen, K.: Note on breather-type solutions of the NLS as models for freak-waves. Phys. Scr. **82**, 48–52 (1999)
29. Kuznetsov, E.A.: Solitons in a parametrically unstable plasma. Sov. Phys. Dokl. **22**, 507–508 (1977)

30. Kawata, T., Inoue, H.: Inverse scattering method for the nonlinear evolution equations under nonvanishing conditions. J. Phys. Soc. Jpn. **44**, 1722–1729 (1978)
31. Ma, Y.C.: The perturbed plane-wave solutions of the cubic Schrödinger equation. Stud. Appl. Math. **60**, 43–58 (1979)
32. Akhmediev, N., Eleonskii, V.M., Kulagin, N.E.: Generation of periodic trains of picosecond pulses in an optical fiber: exact solutions. Sov. Phys. JETP **62**, 894–899 (1985)
33. Akhmediev, N., Soto-Crespo, J.M., Ankiewicz, A.: How to excite a rogue wave. Phys. Rev. A **80**, 043818 (2009)
34. Zakharov, V.E., Gelash, A.A.: Nonlinear stage of modulation instability. Phys. Rev. Lett. **111**, 054101 (2013)
35. Gelash, A.A., Zakharov, V.E.: Superregular solitonic solutions: a novel scenario for the nonlinear stage of modulation instability. Nonlinearity **27**, 1–39 (2014)
36. Hammani, K., Wetzel, B., Kibler, B., Fatome, J., Finot, C., Millot, G., Akhmediev, N., Dudley, J.M.: Spectral dynamics of modulation instability described using Akhmediev breather theory. Opt. Lett. **36**, 2140–2142 (2011)
37. Akhmediev, N., Ankiewicz, A., Soto-Crespo, J.M., Dudley, J.M.: Universal triangular spectra in parametrically-driven systems. Phys. Lett. A **375**, 775–779 (2011)
38. Akhmediev, N.: Nonlinear physics. Déjàă vu in optics. Nature **413**, 267–268 (2001)
39. Van Simaeys, G., Emplit, P., Haelterman, M.: Experimental demonstration of the Fermi-Pasta-Ulam recurrence in a modulationally unstable optical wave. Phys. Rev. Lett. **87**, 033902 (2001)
40. Akhmediev, N., Ankiewicz, A., Soto-Crespo, J.M., Dudley, J.M.: Rogue wave early warning through spectral measurements? Phys. Lett. A **375**, 541–544 (2011)
41. Solli, D.R., Herink, G., Jalali, B., Ropers, C.: Fluctuations and correlations in modulation instability. Nat. Photon. **6**, 463–468 (2012)
42. Wetzel, B., Stefani, A., Larger, L., Lacourt, P.A., Merolla, J.M., Sylvestre, T., Kudlinski, A., Mussot, A., Genty, G., Dias, F., Dudley, J.M.: Real-time full bandwidth measurement of spectral noise in supercontinuum generation. Sci. Rep. **2**, 882 (2012)
43. Matveev, V.B., Salle, M.: Darboux Transformations and Solitons. Springer, Berlin (1991)
44. Kedziora, D.J., Ankiewicz, A., Akhmediev, N.: Second-order nonlinear Schrödinger equation breather solutions in the degenerate and rogue wave limits. Phys. Rev. E **85**, 066601 (2012)
45. Akhmediev, N., Ankiewicz, A., Taki, M.: Waves that appear from nowhere and disappear without a trace. Phys. Lett. A **373**, 675–678 (2009)
46. Kedziora, D.J., Ankiewicz, A., Akhmediev, N.: Classifying the hierarchy of nonlinear-Schrödinger-equation rogue-wave solutions. Phys. Rev. E **88**, 013207 (2013)
47. Shrira, V.I., Geogjaev, V.V.: What makes the Peregrine soliton so special as a prototype of freak waves? J. Eng. Math. **67**, 11–22 (2010)
48. Bailung, H., Sharma, S.K., Nakamura, Y.: Observation of Peregrine solitons in a multicomponent plasma with negative ions. Phys. Rev. Lett. **107**, 255005 (2011)
49. Chabchoub, A., Hoffmann, N.P., Onorato, M., Akhmediev, N.: Super rogue waves: observation of a higher-order breather in water waves. Phys. Rev. X **2**, 011015 (2012)
50. Chabchoub, A., Hoffmann, N., Onorato, M., Slunyaev, A., Sergeeva, A., Pelinovsky, E., Akhmediev, N.: Observation of a hierarchy of up to fifth-order rogue waves in a water tank. Phys. Rev. E **86**, 056601 (2012)
51. Kibler, B., Fatome, J., Finot, C., Millot, G., Genty, G., Wetzel, B., Akhmediev, N., Dias, F., Dudley, J.M.: Observation of Kuznetsov-Ma soliton dynamics in optical fibre. Sci. Rep. **2**, 463 (2012)
52. Hammani, K., Kibler, B., Finot, C., Morin, P., Fatome, J., Dudley, J.M., Millot, G.: Peregrine soliton generation and breakup in standard telecommunications fiber. Opt. Lett. **36**, 112–114 (2011)
53. Frisquet, B., Kibler, B., Millot, G.: Collision of Akhmediev breathers in nonlinear fiber optics. Phys. Rev. X **3**, 041032 (2013)
54. Frisquet, B., Chabchoub, A., Fatome, J., Finot, C., Kibler, B., Millot, G.: Two-stage linear-nonlinear shaping of an optical frequency comb as rogue nonlinear-Schrödinger-equation-solution generator. Phys. Rev. A **89**, 023821 (2014)

55. Agrawal, G.P.: Nonlinear Fiber Optics, 5th edn. Academic Press, Oxford (2010)
56. Erkintalo, M., Genty, G., Wetzel, B., Dudley, J.M.: Akhmediev breather evolution in optical fiber for realistic initial conditions. Phys. Lett. A **375**, 2029–2034 (2011)
57. Cundiff, S.T., Weiner, A.M.: Optical arbitrary waveform generation. Nat. Photon. **4**, 760–766 (2010)
58. Weiner, A.M.: Ultrafast optical pulse shaping: a tutorial review. Opt. Commun. **284**, 3669–3692 (2011)
59. Clarke, A.M., Williams, D.G., Roelens, M.A.F., Eggleton, B.J.: Reconfigurable optical pulse generator employing a Fourier-domain programmable optical processor. J. Lightwave Technol. **28**, 97–103 (2010)
60. El Mansouri, I., Fatome, J., Finot, C., Lintz, M., Pitois, S.: All-fibered high-quality stable 20- and 40-GHz picosecond pulse generators for 160-Gb/s OTDM applications. IEEE Photon. Technol. Lett. **23**, 1487–1489 (2011)
61. Dudley, J.M., Thomson, M.D., Gutty, F., Pitois, S., Grelu, P., Millot, G.: Complete intensity and phase characterisation of optical pulse trains at terahertz repetition rates. Electron. Lett. **35**, 2042–2044 (1999)
62. Dudley, J.M., Genty, G., Dias, F., Kibler, B., Akhmediev, N.: Modulation instability, Akhmediev Breathers and continuous wave supercontinuum generation. Opt. Express **17**, 21497–21508 (2009)
63. Erkintalo, M., Hammani, K., Kibler, B., Finot, C., Akhmediev, N., Dudley, J.M., Genty, G.: Higher order modulation instability in nonlinear fiber optics. Phys. Rev. Lett. **107**, 253901 (2011)
64. Yuen, H.C., Ferguson, W.E.: Relationship between Benjamin-Feir instability and recurrence in the nonlinear Schrödinger equation. Phys. Fluids **21**, 1275 (1978)
65. Ankiewicz, A., Devine, N., Akhmediev, N.: Are rogue waves robust against perturbations? Phys. Lett. A **373**, 3997–4000 (2009)
66. Ankiewicz, A., Soto-Crespo, J.M., Chowdhury, M.A., Akhmediev, N.: Rogue waves in optical fibers in presence of third-order dispersion, self-steepening, and self-frequency shift. J. Opt. Soc. Am. B **30**, 87–94 (2013)
67. Hasegawa, A.: Generation of a train of soliton pulses by induced modulational instability in optical fibers. Opt. Lett. **9**, 288–290 (1984)
68. Tai, K., Tomita, A., Jewell, J.L., Hasegawa, A.: Generation of subpicosecond solitonlike optical pulses at 0.3 THz repetition rate by induced modulational instability. Appl. Phys. Lett. **49**, 236–238 (1986)
69. Chabchoub, A., Kibler, B., Dudley, J.M., Akhmediev, N.: Hydrodynamics of periodic breathers. Phil. Trans. R. Soc. A **372**, 20140005 (2014)
70. Bendahmane, A., Mussot, A., Szriftgiser, P., Zerkak, O., Genty, G., Dudley, J.M., Kudlinski, A.: Experimental dynamics of Akhmediev breathers in a dispersion varying optical fiber. Opt. Lett. **39**, 4490–4493 (2014)
71. Baronio, F., Degasperis, A., Conforti, M., Wabnitz, S.: Solutions of the vector nonlinear Schrödinger equations: evidence for deterministic rogue waves. Phys. Rev. Lett. **109**, 044102 (2012)
72. Baronio, F., Conforti, M., Degasperis, A., Lombardo, S., Onorato, M., Wabnitz, S.: Vector Rogue waves and baseband modulation instability in the defocusing regime. Phys. Rev. Lett. **113**, 034101 (2014)
73. Frisquet, B., Kibler, B., Fatome, J., Morin, P., Baronio, F., Conforti, M., Millot, G., Wabnitz, S.: Polarization modulation instability in a Manakov fiber system. Phys. Rev. A **92**, 053854 (2015)
74. Kibler, B., Chabchoub, A., Gelash, A., Akhmediev, N., Zakharov, V.: Superregular breathers in optics and hydrodynamics: omnipresent modulation instability beyond simple periodicity. Phys. Rev. X **5**, 041026 (2015)
75. Chabchoub, A., Kibler, B., Finot, C., Millot, G., Onorato, M., Dudley, J.M., Babanin, A.V.: The nonlinear Schrödinger equation and the propagation of weakly nonlinear waves in optical fibers and on the water surface. Ann. Phys. **361**, 490–500 (2015)

Hamiltonian Description of Ocean Waves and Freak Waves

Peter A.E.M. Janssen

Abstract Freak wave generation and decay is discussed in the context of the Hamiltonian description of ocean waves. In linear theory the probability distribution function (p.d.f.) of the surface elevation is given by the Normal distribution, while for finite amplitude waves there are, for extreme events, always deviations from the Normal, giving finite skewness and excess kurtosis. These deviations are caused by the presence of the bound waves and, in case of almost one-dimensional propagation, by non-resonant four-wave interactions.

1 Introduction

This lecture consists of two parts. In the first part we choose as starting point the *Hamiltonian* formulation of the dynamics of surface gravity waves. Using a canonical transformation there is a natural distinction between free waves and bound waves. The dynamics of the *free* waves follows from the well-known Zakharov equation, which in essence describes four-wave interactions, while the *bound* waves are a function of the free waves and are therefore regarded as 'slaves'. A number of properties of the Zakharov equation related to the stability of a uniform wave train will be discussed.

In the second part we discuss wave forecasting aspects. Wave forecasting is about forecasting the mean sea state, as reflected by the ocean wave spectrum, and therefore we need a *statistical* description of the sea state culminating in an evolution equation for the ensemble mean of the sea state, the well-known Hasselmann equation which describes the evolution of the wave spectrum owing to *resonant* four-wave interactions only.

However, for freak wave phenomena, which are sea states that are very rapidly varying in time, we also need to take into account the effects of *non-resonant interactions*. The resulting equation is a slight extension of the Hasselmann equation, and it will be shown how in the context of this statistical approach freak waves emerge and disappear. The role of the bound waves will be discussed as well.

P.A.E.M. Janssen (✉)
E.C.M.W.F., Shinfield Park, Reading, UK
e-mail: p.janssen@ecmwf.int

M. Onorato et al. (eds.), *Rogue and Shock Waves in Nonlinear Dispersive Media*,
Lecture Notes in Physics 926, DOI 10.1007/978-3-319-39214-1_5

The programme of these lectures is therefore as follows: The lectures start with a brief history of the field of surface gravity waves. This is followed by a study of the ocean wave problem in the context of its Hamiltonian formulation. In particular, a discussion is given of the assumption of weak nonlinearity, giving a natural distinction between free and bound gravity waves. The approximate evolution equation, called the Zakharov Equation, is derived, followed by a discussion of four-wave interactions and the stability of a Stokes wave train. The evolution of the wave spectrum is obtained using a method from Statistical Mechanics, and it shows the strong relation between spectral change and deviations from Gaussian statistics. This approach allows the probabilistic forecasting of extreme events. As a special case the evolution of a narrow band wave train is studied and we show the connection between the Zakharov equation and the Nonlinear Schrödinger (NLS) Equation. There is a sharp contrast between one and two-dimensional propagation. While in one dimension the NLS equation gives for large times envelope solitons, signalling the presence of extreme events, in two-dimensions envelope solitons are unstable and extreme events are much more unlikely to occur. Finally, for practical applications the concept of *maximum envelope wave height* is introduced which provides an adequate means to characterize extreme events such as freak waves.

A more detailed discussion of the Hamiltonian formulation of water waves may be found in [1, 2], while the relation between freak wave generation and non-resonant four-wave interactions is studied in much more detail in [3]

2 The Problem

Assume irrotational flow, $\nabla \times \mathbf{u} = 0$, which gives velocity field $\mathbf{u}$ in terms of a velocity potential ϕ,

$$\mathbf{u} = \nabla\phi.$$

Because of the constant water density the flow is divergence free, i.e. $\nabla \cdot \mathbf{u} = 0$, hence inside the fluid the velocity potential satisfies *Laplace's* equation,

$$\nabla^2\phi = 0.$$

The main problem for water waves is, however, with the boundary conditions at the surface, described by $z = \eta(\mathbf{x}, t)$. First of all, the surface evolves in space and time,

$$\partial\eta/\partial t + \partial\phi/\partial\mathbf{x} \cdot \partial\eta/\partial\mathbf{x} = w = \partial\phi/\partial z \text{ at } z = \eta.$$

The boundary condition at the surface then becomes the vanishing of the water pressure, where for potential flow the water pressure follows *Bernoulli's* law,

$$\partial\phi/\partial t + \frac{1}{2}(\nabla\phi)^2 + g\eta = 0, \text{ at } z = \eta.$$

Finally, in finite depth water, the normal velocity vanishes at $z = -D$.

3 Brief History

The history of ocean waves really started in the early part of the nineteenth century. In 1816 *Poisson and Cauchy* presented the solution of the linear, initial value problem. This was followed by *Stokes* [4] in 1847 who gave for a single deep-water wave train a series expansion in amplitude of the type

$$\eta = a\cos\theta + \tfrac{1}{2}a\epsilon\cos 2\theta + \cdots$$

with slope $\epsilon = ka$, $\theta = kx - \omega t$ and ω obeys the nonlinear dispersion relation $\omega = \omega_0(1 + \epsilon^2/2)$. In 1895 *Korteweg-de Vries* [5] provided for shallow water solitary wave solutions of permanent shape, explaining Scott Russell's observations. These solitary waves were obtained from the KdV equation

$$u_t + uu_x = u_{xxx}$$

and in the 1960s it was shown by means of the Inverse Scattering Transform (IST) that these solitary waves were stable entities, henceforth called *solitons*. For a while it was fairly quiet at the water wave front until *Sverdrup and Munck* [6], stimulated by the practical need for sea state information for landing operations during the second world war, developed a first ocean wave forecasting method. This was followed in the 1960s by *Whitham's* [7] work on the Variational approach, which provided a generalization of the concept of dispersion towards weakly nonlinear systems, and he introduced the deterministic version of the action balance equation. At about the same time *Phillips* [8] discovered that deep-water surface gravity waves were subject to four-wave interactions, since there were no resonant three wave interactions, while *Hasselmann* [9] established and formulated the corresponding evolution for the wave spectrum using methods from Statistical Mechanics. In 1967 *Bejamin and Feir* [10] found experimentally and theoretically that the Stokes wave train was unstable to side-band perturbations, which later was realized to be an example of a four-wave interaction process. Finally in 1968 *Zakharov* [11] discovered that irrotational water waves are a Hamiltonian system, and that in the narrow-band limit the envelope obeys the nonlinear Schrödinger (NLS) equation, an equation that was found in many other nonlinear fields of physics as well. Although the NLS equation represents a fairly simple situation, it helped to provide a unified view on the field of nonlinear waves.

4 Hamiltonian Formulation

The total energy of the fluid is given by

$$E = \frac{1}{2}\int \mathrm{d}\mathbf{x}\int_{-D_0}^{\eta}\mathrm{d}z(\nabla\phi)^2 + \frac{g}{2}\int \mathrm{d}\mathbf{x}\,\eta^2. \tag{1}$$

and this is a conserved quantity. By choosing η and $\psi = \phi(z = \eta)$ as canonical variables, Zakharov [11] realized that the kinematic boundary condition and Bernoulli's equation then follow from the Hamilton equations,

$$\frac{\partial \eta}{\partial t} = \frac{\delta E}{\delta \psi}, \quad \frac{\partial \psi}{\partial t} = -\frac{\delta E}{\delta \eta}, \tag{2}$$

where $\delta E/\delta\psi$ is the functional derivative of E with respect to $\psi = \phi(z = \eta)$, etc.

Inside the fluid the potential ϕ satisfies Laplace's equation,

$$\nabla^2 \phi = 0 \tag{3}$$

with boundary conditions

$$\phi(\mathbf{x}, z = \eta) = \psi, \tag{4}$$

and, with D_0 the water depth,

$$\frac{\partial \phi(\mathbf{x}, z)}{\partial z} = 0, \; z = -D_0. \tag{5}$$

By solving the potential problem, ϕ may be expressed in terms of the canonical variables η and ψ. Then the energy E may be evaluated in terms of the canonical variables, and the evolution in time of η and ψ follows at once from Hamilton's equations [Eq. (2)]. In particular for small steepness ϵ the potential problem (3)–(5) may be solved in an iterative fashion, as Eq. (4) is a nonlinear equation.

Introduce the Fourier transforms of η and ψ, for example

$$\eta = \int_{-\infty}^{\infty} \mathrm{d}\mathbf{k} \; \hat{\eta}(\mathbf{k}) e^{i\mathbf{k}.\mathbf{x}} \tag{6}$$

where $\hat{\eta}$ and $\hat{\psi}$ are the Fourier transforms of η and ψ. Here, $\mathbf{k}$ is the wavenumber vector, and k its absolute value. In order to proceed, introduce the linear dispersion relation for surface gravity waves

$$\omega^2 = gkT_0, \; T_0 = \tanh kD_0. \tag{7}$$

Next, anticipating the fact that we have two oscillation modes, introduce the following relation between the Fourier transform of η and ψ and the action density variable $A(\mathbf{k}, t)$

$$\hat{\eta} = \left(\frac{\omega}{2g}\right)^{1/2} \left(A(\mathbf{k}) + A^*(-\mathbf{k})\right), \hat{\psi} = -i\left(\frac{g}{2\omega}\right)^{1/2} \left(A(\mathbf{k}) - A^*(-\mathbf{k})\right). \tag{8}$$

In terms of the action variable the energy of the fluid is given by a series expansion which up to fourth order in amplitude involves *quadratic* (linear theory), *cubic* and *quartic* terms. It should now be realized that surface gravity waves do not enjoy resonant three wave interactions. For example, the resonance conditions of the type $\mathbf{k}_1+\mathbf{k}_2 = \mathbf{k}_3$ and $\omega_1+\omega_2 = \omega_3$ cannot be satisfied when the dispersion relation is given by the one for gravity waves. A simple graphical construction shows this.

Therefore, there is a canonical transformation of the type

$$A = A(a, a^*) \tag{9}$$

which removes the non-resonant third and fourth order terms as much as possible. Here, a is the amplitude of the *free waves*, while the canonical transformation generates the contributions by bound waves (i.e. second harmonics).

In terms of the action variable the energy of the fluid becomes to fourth order in amplitude

$$\begin{aligned} E = &\int \mathrm{d}\mathbf{k}_1 \omega_1 A_1 A_1^* + \int \mathrm{d}\mathbf{k}_{1,2,3} \delta_{1-2-3} V^{(-)}_{1,2,3} \left[A_1^* A_2 A_3 + c.c.\right] \\ &+ \tfrac{1}{3} \int \mathrm{d}\mathbf{k}_{1,2,3} \delta_{1+2+3} V^{(+)}_{1,2,3} \left[A_1 A_2 A_3 + c.c.\right] \\ &+ \int \mathrm{d}\mathbf{k}_{1,2,3,4} \delta_{1-2-3-4} W^{(1)}_{1,2,3,4} \left[A_1^* A_2 A_3 A_4 + c.c.\right] \\ &+ \tfrac{1}{2} \int \mathrm{d}\mathbf{k}_{1,2,3,4} \delta_{1+2-3-4} W^{(2)}_{1,2,3,4} A_1^* A_2^* A_3 A_4 \\ &+ \tfrac{1}{4} \int \mathrm{d}\mathbf{k}_{1,2,3,4} \delta_{1+2+3+4} W^{(4)}_{1,2,3,4} \left[A_1^* A_2^* A_3^* A_4^* + c.c\right] \end{aligned} \tag{10}$$

Here, $V^{()}$ and $W^{()}$ are complicated expressions of ω and $\mathbf{k}$ which are given by Krasitskii [12].

The evolution equation for A now follows from Hamilton's equation $\partial A/\partial t = -i\delta E/\delta A^*$, and evaluation of the functional derivative of the full expression for E with respect to A^* gives,

$$\begin{aligned} \frac{\partial}{\partial t} A_1 + i\omega_1 A_1 = &-i \int \mathrm{d}\mathbf{k}_{2,3} \left\{ V^{(-)}_{1,2,3} A_2 A_3 \delta_{1-2-3} + 2V^{(-)}_{3,2,1} A_2^* A_3 \delta_{1+2-3} \right. \\ &\left. + V^{(+)}_{1,2,3} A_2^* A_3^* \delta_{1+2+3} \right\} - i \int \mathrm{d}\mathbf{k}_{2,3,4} \left\{ W^{(1)}_{1,2,3,4} A_2 A_3 A_4 \delta_{1-2-3-4} \right. \\ &+ W^{(2)}_{1,2,3,4} A_2^* A_3 A_4 \delta_{1+2-3-4} + 3W^{(1)}_{4,3,2,1} A_2^* A_3^* A_4 \delta_{1+2+3-4} \\ &\left. + W^{(4)}_{1,2,3,4} A_2^* A_3^* A_4^* \delta_{1+2+3+4} \right\}. \end{aligned} \tag{11}$$

Equation (11) is the basic evolution equation of weakly nonlinear gravity waves and it includes the relevant amplitude effects up to third order. A great simplification of the expression for the energy is achieved by introducing the canonical transformation (9) that eliminates the contribution of the non-resonant second and third order terms as much as possible.

The first few terms are given by

$$\begin{aligned} A_1 = a_1 + \int \mathrm{d}\mathbf{k}_{2,3} \Big\{ & A^{(1)}_{1,2,3} a_2 a_3 \delta_{1-2-3} + A^{(2)}_{1,2,3} a_2^* a_3 \delta_{1+2-3} \\ & + A^{(3)}_{1,2,3} a_2^* a_3^* \delta_{1+2+3} \Big\} + \int \mathrm{d}\mathbf{k}_{2,3,4} \Big\{ B^{(1)}_{1,2,3,4} a_2 a_3 a_4 \delta_{1-2-3-4} \\ & + B^{(2)}_{1,2,3,4} a_2^* a_3 a_4 \delta_{1+2-3-4} + B^{(3)}_{1,2,3,4} a_2^* a_3^* a_4 \delta_{1+2+3-4} \\ & + B^{(4)}_{1,2,3,4} a_2^* a_3^* a_4^* \delta_{1+2+3+4} \Big\} \ldots . \end{aligned} \tag{12}$$

The unknowns $A^{()}$ and $B^{()}$ are obtained by systematically removing the non-resonant third- and fourth-order contributions to the wave energy, and insisting that the form of the expression for the energy remains symmetric. These expressions are quite involved and have been given in [12, 13] and [2] for example. Here, we only give the transfer coefficient for the quadratic terms explicitly.

They read

$$A^{(1)}_{1,2,3} = -\frac{V^{(-)}_{1,2,3}}{\omega_1 - \omega_2 - \omega_3}, \; A^{(2)}_{1,2,3} = -2\frac{V^{(-)}_{3,2,1}}{\omega_1 + \omega_2 - \omega_3}, \; A^{(3)}_{1,2,3} = -\frac{V^{(+)}_{1,2,3}}{\omega_1 + \omega_2 + \omega_3}$$

and they show that in the absence of resonant three wave interactions the transformation $A = A(a, a^*)$ is indeed nonsingular. Elimination of the variable A in favour of the new action variable a results in a great simplification of the wave energy E (10). It becomes

$$E = \int \mathrm{d}\mathbf{k}_1 \omega_1 a_1^* a_1 + \frac{1}{2} \int \mathrm{d}\mathbf{k}_{1,2,3,4} T_{1,2,3,4} a_1^* a_2^* a_3 a_4 \delta_{1+2-3-4}, \tag{13}$$

where the interaction coefficient $T_{1,2,3,4}$ is given by Krasitskii [12, 13]. The interaction coefficient enjoys a number of symmetry conditions, of which the most important one is $T_{1,2,3,4} = T_{3,4,1,2}$, because this condition implies that E is conserved. In terms of the new action variable a, Hamilton's equation becomes $\partial a/\partial t = -i\delta E/\delta a^*$, or,

$$\frac{\partial a_1}{\partial t} + i\omega_1 a_1 = -i \int \mathrm{d}\mathbf{k}_{2,3,4} T_{1,2,3,4} a_2^* a_3 a_4 \delta_{1+2-3-4}, \tag{14}$$

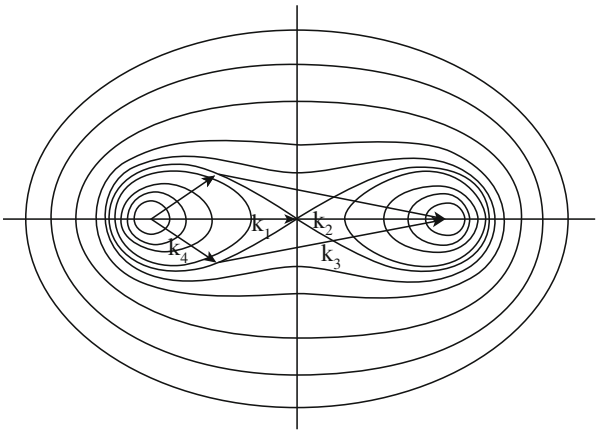

Fig. 1 Phillips' figure of eight: the graph shows how to construct a resonant quartet of surface gravity waves

which is known as the **Zakharov Equation**. Clearly, by removing the non-resonant terms, a considerable simplification of the evolution equation describing four-wave processes has been achieved.

The starting point for wave forecasting is the Zakharov equation, which gives the evolution of the free waves only. Hence, our wave forecasting system only gives the spectrum for the free waves, but this is not the complete sea state because we still have to consider the consequences of the canonical transformation. This will give rise to *bound waves*, also known as 'slave modes', and they may be obtained by means of a diagnostic relation from the knowledge of the free wave spectrum.

The Zakharov Equation is an evolution equation that describes *four-wave interactions*. Note that the *resonant* four-wave interactions: $\mathbf{k}_1+\mathbf{k}_2 = \mathbf{k}_3+\mathbf{k}_4, \omega_1+\omega_2 = \omega_3 + \omega_4$ play a special role in the evolution of surface gravity waves because these interactions give rise to an efficient resonant energy transfer. Phillips [8] has shown that for gravity waves these resonance conditions can be satisfied, while at the same time he showed that resonant *three wave interactions* are impossible. These solutions are obtained using Phillips' figure of eight, as illustrated in Fig. 1.

Many properties of the Zakharov equation have been studied in the past. Here, only results regarding the instability of the Stokes solution will be presented.

5 The Instability of Finite-Amplitude Deep-Water Waves

A finite amplitude wave has a dispersion relation which depends on the amplitude. This follows immediately from the Zakharov equation. Consider the case of a single wave, e.g.

$$a(k) = \hat{a}(t)e^{-i\omega t}\ \delta(k - k_0) \tag{15}$$

Then, substitution of (15) into (14) gives

$$\frac{\partial}{\partial t}\hat{a} = -iT_0|\hat{a}|^2\hat{a}, \tag{16}$$

where it may be verified that $T_0 = T_{0,0,0,0} = k_0^3$. Equation (16) may be solved at once by writing

$$\hat{a} = a_0 e^{-i\Omega t}$$

where Ω denotes the correction of the dispersion relation due to nonlinearity. It is given by

$$\Omega = T_0|a_0|^2 \tag{17}$$

Therefore, the dispersion relation of a weakly nonlinear gravity wave is given by

$$\omega = \omega_0(1 + \tfrac{1}{2}s^2),\ \omega_0 = \sqrt{g|k_0|}, \tag{18}$$

and s is the wave steepness, defined as wavenumber times surface elevation amplitude, hence wave steepness is related to the action density variable in the following way: $s = k_0 a_0 \sqrt{2k_0/\omega_0}$. The result (18) was obtained in [4] using a singular perturbation method.

The dependence of the dispersion relation on the wave steepness will have a profound impact on the time evolution of a weakly nonlinear wave train. This will be discussed in the next section, but let us first discuss the short time behaviour of a nonlinear wave train by means of a linear stability analysis.

To test the stability of a uniform wave train we perturb it by a pair of sidebands with wavenumber $k_\pm = k_0 \pm K$ and amplitude $A_\pm(t)$, e.g.,

$$a = \{A_0\delta(k-k_0) + A_+\delta(k-k_+) + A_-\delta(k-k_-)\}\, e^{-i\omega(k)t}.$$

Assuming that the sideband amplitudes are small compared to the amplitude A_0 of the carrier wave and neglecting the square of small quantities, the following evolution equations for $A_\pm$ are found from the Zakharov equation (15),

$$i\frac{d}{dt}A_\pm = T_{\pm,\mp}a_0^2 A_\mp^* \exp[-i(\Delta\omega + 2T_0a_0^2)t] + 2T_{\pm,\pm}a_0^2 A_\pm \tag{19}$$

where

$$\begin{aligned} T_{\pm,\pm} &= T(k_0 \pm K, k_0, k_0, k_0 \pm K) \\ T_{\pm,\mp} &= T(k_0 \pm K, k_0 \mp K, k_0, k_0) \\ T_0 &= T(k_0, k_0, k_0, k_0) \\ \Delta\omega &= 2\omega(k_0) - \omega(k_0 + K) - \omega(k_0 - K) \end{aligned}$$

and $a_0 = A_0$.

By means of the substitution

$$A_+ = \hat{A}_+ \exp[-i(\tfrac{1}{2}\Delta\omega + T_0 a_0^2)t - i\Omega t],$$
$$A_-^* = \hat{A}_-^* \exp[+i(\tfrac{1}{2}\Delta\omega + T_0 a_0^2)t - i\Omega t],$$

where Ω is still unknown, a set of differential equations is obtained that contains no explicit time dependence. A nontrivial solution is then found provided Ω satisfies the dispersion relation

$$\Omega = (T_{+,+} - T_{-,-})a_0^2 \pm \left\{-T_{+,-}T_{-,+}a_0^4 + \left[-\tfrac{1}{2}\Delta\omega + a_0^2(T_{+,+} + T_{-,-} - T_0)\right]^2\right\}^{\frac{1}{2}} \quad (20)$$

We have instability provided that the term under the square root is negative. This result, including the discussion that follows, is due to Crawford et al. [14] (see also [15, 16]).

A considerable simplification of the dispersion relation is found when close sidebands are considered. One then introduces the dimensionless perturbation wavenumber

$$\kappa = K/k_0 \quad (21)$$

and one considers $\kappa \ll 1$. The frequency mismatch is then approximately given by

$$\Delta\omega \simeq \tfrac{1}{4}\omega_0\kappa^2.$$

Expanding then the expressions for T in powers of κ and retaining only terms quadratic in the steepness s and modulation wavenumber κ, one finds

$$\Omega = \omega_0\left(-\frac{\kappa^2}{8}s^2 + \frac{\kappa^4}{64}\right)^{\frac{1}{2}}. \quad (22)$$

This is the classical result of Benjamin and Feir [10]. Instability is found for sufficiently steep waves:

$$\kappa^2 \leq 8s^2. \quad (23)$$

In Fig. 2 the normalized growth rate $\Im(\Omega)/\frac{1}{2}\omega_0 s^2$, obtained from Eq. (20), is plotted as function of the normalized sideband wave number $\Delta = \kappa/2s$. Here, we have used the wave steepness s as a label and the results of Benjamin and Feir corresponds to the limit $s \to 0$. Note that

1. small but finite amplitude gives considerable deviations from their classical result.
2. very long waves ($\Delta \to 0$) become stable again for a steepness s which is larger than 0.39. This restabilization of the very long waves is in qualitative agreement with results from Whitham's average Lagrangian approach which

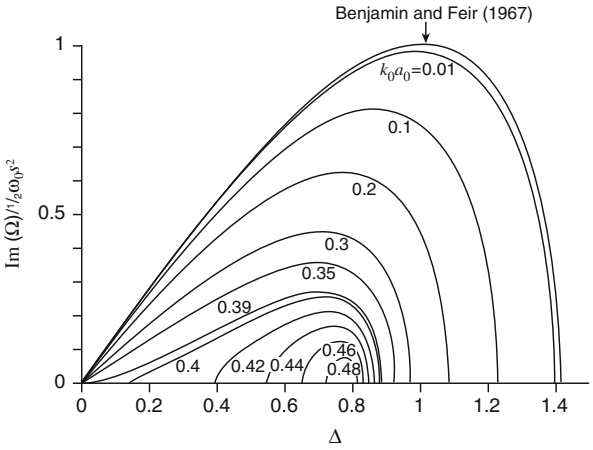

Fig. 2 Two-dimensional instability growth rates as a function of perturbation wavenumber for various values of wave steepness. The Benjamin-Feir result is recovered by taking the limit as wave steepness approaches zero

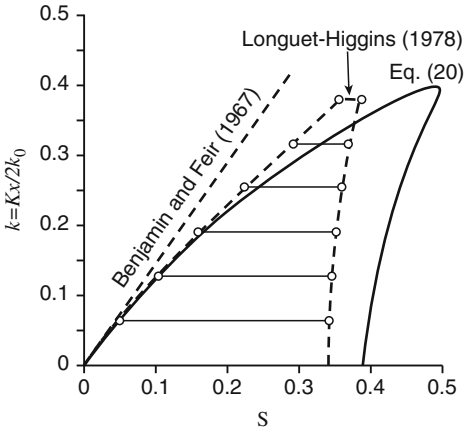

Fig. 3 Stability diagram for two-dimensional perturbations on a uniform wave train from the Zakharov equation and comparison with results from [17]

yields restabilization for $s = 0.34$. The quantitative discrepancy of only 14 % is better than expected since the present theory is formally accurate to $\mathcal{O}(s^2)$.

3. there is restabilization for all modulation wavenumbers for sufficiently large steepness ($s \simeq 0.5$). This property is in qualitative agreement with numerical results in [17]. This is shown more clearly in Fig. 3 where the marginal stability boundary is plotted in the $\kappa - s$ plane.

The agreement of the results from the Zakharov equation and experiment is also very encouraging. This is shown in Fig. 4 where normalized growth rate as function

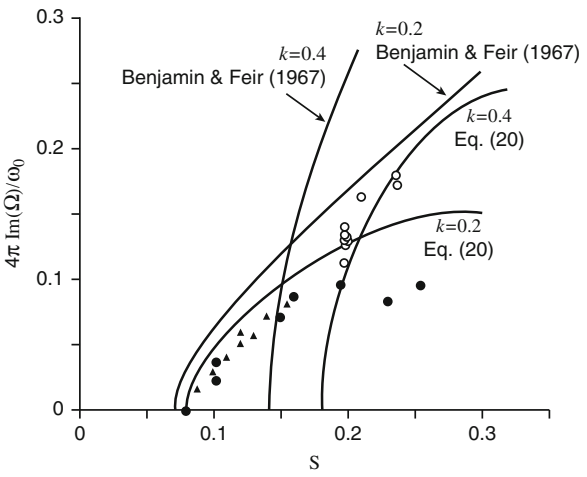

Fig. 4 Comparison of calculated instability growth rate with experimental results as a function of wave steepness for two values of perturbation wavenumber. *Symbols*: (*open circle*): $\kappa = 0.4$, (*filled circle*): $\kappa = 0.2$ [18]; (*open triangle*): data from [19]

of wave steepness is presented. The experimental results are from [18, 19]. For reference, also the theoretical result of Benjamin and Feir (22) is shown.

To summarize, we have seen that a weakly nonlinear wave train is unstable to sideband perturbations. An energy transfer occurs from the basic wave to the sidebands through a four-wave interaction process. The results from the Zakharov equation compare favourable with exact computations and experiment. This theoretical approach has a surprisingly large range of validity, considering that it is formally only valid up to $\mathcal{O}(s^2)$.

The present discussion so far was confined to the case of sidebands that propagate in the same direction as the basic wave (1-D modulations). The present theory is also applicable to two dimensional modulations. Let the basic wave propagate in the x-direction and let

$$\Delta_x = \kappa_x/2s,\ \ \Delta_y = \kappa_y/2s,$$

where $\kappa_x = K_x/k_0$ and $\kappa_y = K_y/k_0$ are the x- and y-component of the normalized sideband wavenumber vector. Returning to Eq. (20) we again expand the frequency mismatch $\Delta\omega$ for very long modulation wavelength

$$\Delta\omega = \frac{1}{4}\omega_0\kappa_x^2 - \frac{1}{2}\omega_0\kappa_y^2.$$

Also, expanding T and retaining terms to $\mathcal{O}(s^2)$ and $\mathcal{O}(|\kappa|^2)$ one finds from (20)

$$\Omega = \left(-\frac{1}{2}\Delta\omega s^2\omega_0 + \frac{1}{4}(\Delta\omega)^2\right)^{1/2}. \tag{24}$$

The stability boundary is then defined by the curves $\Delta\omega = 0$ and $\Delta\omega = 2s^2\omega_0$ and they are sketched in the Δ_x, Δ_y plane in Fig. 5.

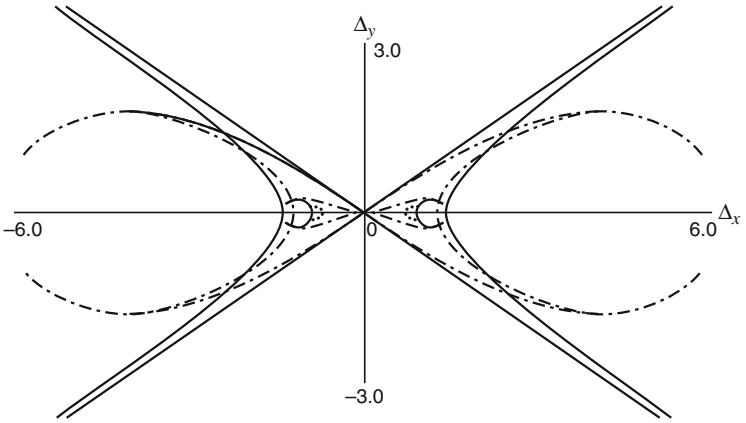

Fig. 5 Three-dimensional stability boundary from Zakharov equation in strained coordinates Δ_x and Δ_y. *Continuous line*, $k_0a_0 = 0.01$; *crossed line*, $k_0a_0 = 0.1$; *dashed dotted line*, $k_0a_0 = 0.4$; *dotted line*, $k_0a_0 = 0.48$

5.1 Narrow-Band Wave Train in 1D

In the discussion on the results of the Zakharov Equation I have introduced the idea of a narrow-band wave train. This is a very useful concept for further understanding of the Benjamin-Feir instability. Consider a narrow spectrum around a carrier wave number k_0. This simplifies the Zakharov Equation. Introducing the modulation wave number $p = k - k_0$ angular frequency is expanded around the carrier wavenumber

$$\omega(k) = \omega_0 + p\omega_0' + \frac{1}{2}p^2\omega_0'' + \ldots;\ T_{1,2,3,4} \to k_0^3$$

and this is used in the Zakharov Equation. After an inverse Fourier-transform one finds the celebrated **Nonlinear Schrödinger Equation (NLS)**

$$i\left(\frac{\partial}{\partial t} + \omega_0'\frac{\partial}{\partial x}\right)a + \frac{1}{2}\omega_0''\frac{\partial^2}{\partial x^2}a - \frac{1}{2}\omega_0 k_0^2|a|^2 a = 0,$$

which may be further simplified by going to a frame moving with the group velocity and by introduction of dimensionless units:

$$i\frac{\partial}{\partial t}a - \frac{\partial^2}{\partial x^2}a - \kappa|a|^2 a = 0. \tag{25}$$

This evolution equation for the complex amplitude (wave envelope) occurs in many branches of physics and has generated a lot of interest. There are two important cases:

1. Focusing: $\kappa > 0$, this happens for deep water waves.
2. Defocusing: $\kappa < 0$, occurs for shallow water waves ($k_0D < 1.363$).

5.2 *Properties of 1D NLS*

Here we list some interesting properties of the NLS equation, an equation that has been found in many fields of (nonlinear) physics.

1. Initial value problem in 1-D can be solved exactly by means of IST. Solution in terms of solitons and radiation modes [20].
2. Benjamin-Feir Instability, also called modulational instability or side-band instability. There is instability of the Stokes wave train when sidebands are close to the peak: $p^2 < 2\kappa a_0^2$. (only in deep water!).
3. Long term evolution of the Benjamin-Feir instability shows *Fermi-Pasta-Ulam recurrence* (See Fig. 6).

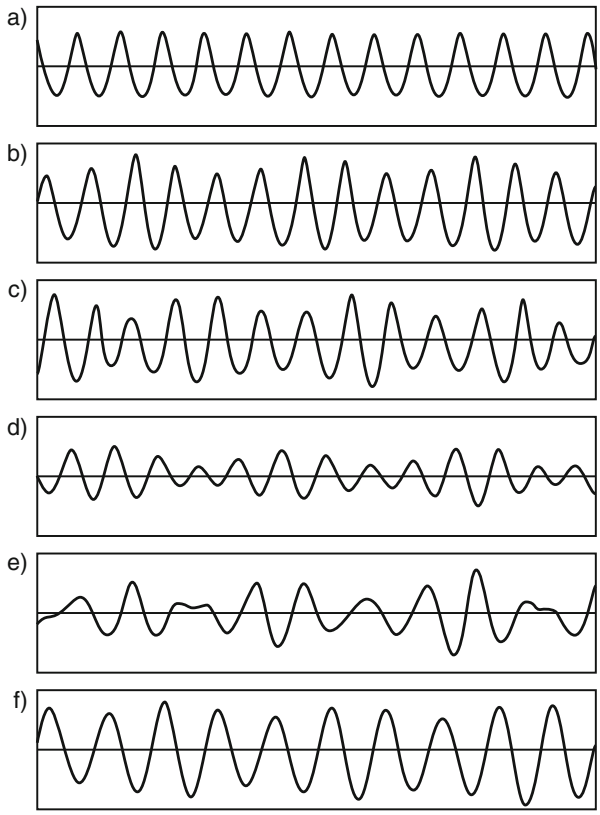

Fig. 6 The Benjamin-Feir Instability, which is the instability of a slowly varying weakly nonlinear wave train, shows Fermi-Pasta-Ulam recurrence (from [18])

5.3 NLS and Fermi-Pasta-Ulam Recurrence

Indeed, numerical solution of the NLS equation showed a perfect recurrence of the Benjamin-Feir instability. This recurrence was also found by means of an approximate solution of the NLS equation in the limit of small growth rate.

In Fig. 7 it is shown that there is a threshold for instability. Therefore, the magnitude of the growth rate may be controlled. If the distance Δ to the threshold is not too large, i.e. $\Delta \ll 1$, application of the method of multiple time scales results in the following evolution equation for the amplitude Γ of the unstable sideband [21]

$$\frac{\mathrm{d}^2}{\mathrm{d}t^2}\Gamma = \gamma^2\Gamma - \beta^2|\Gamma|^2\Gamma, \tag{26}$$

where γ is the growth rate according to linear theory and β measures the strength of nonlinearity.

Equation (26) has periodic solutions in time since the evolution equation is just equivalent to the motion of a particle in a potential well $\mathscr{V}$, displayed in the right part of Fig. 7. From (26) one finds the conservation law

$$\tfrac{1}{2}\left|\frac{\mathrm{d}\Gamma}{\mathrm{d}t}\right|^2 + \mathscr{V}(\Gamma) = \text{const}$$

where the potential is given by

$$\mathscr{V}(\Gamma) = -\tfrac{1}{2}\gamma^2|\Gamma|^2 + \tfrac{1}{4}\beta^2|\Gamma|^4.$$

It is evident from Fig. 7 and the expression for the potential $\mathscr{V}$ that for small amplitude there is instability because then the potential is convex, while for large amplitude nonlinearity is stabilizing. The evolution of the amplitude Γ in time and the corresponding effect of the instability on the amplitude of the carrier wave is displayed in Fig. 8.

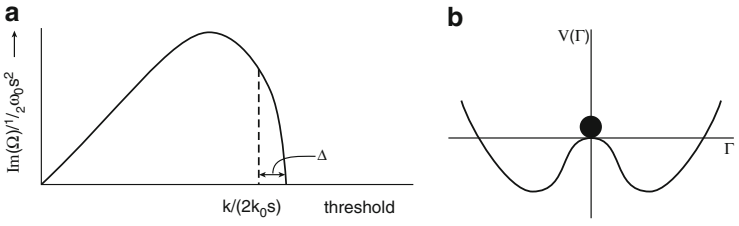

Fig. 7 *Left*: Growth rate of Benjamin-Feir instability and the definition of the distance Δ to the threshold for instability. *Right*: The potential $\mathscr{V}(\Gamma)$ as function of the amplitude $|\Gamma|$

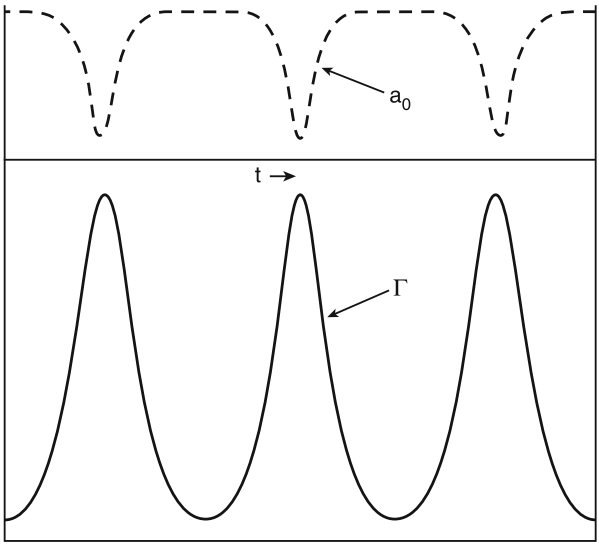

Fig. 8 Benjamin-Feir Instability and the Fermi-Pasta Ulam recurrence. Note the interplay between carrier wave (a_0) and sideband (Γ)

Clearly, the sideband is growing at the expense of the carrier wave and this is at the same time the main reason for quenching the energy transfer from the carrier wave to the sideband.

The existence of the Fermi-Pasta-Ulam recurrence illustrates the fact that nonlinear systems may have a *long memory* of the initial condition. The NLS is an integrable system and there is even Fermi-Pasta-Ulam recurrence when two or more modes are unstable [22]. However, it should be remarked that the simple picture of the Fermi-Pasta-Ulam recurrence is, probably, not universally valid, in particular, if an energy cascade is allowed by the dispersion relation of the waves.

5.4 Narrow-Band Wave Train in 2D

In the case of two-dimensional propagation the NLS equation becomes

$$i\left(\frac{\partial}{\partial t}+v_g\frac{\partial}{\partial x}\right)a+\tfrac{1}{2}\left(\frac{\partial^2\omega}{\partial k_x^2}\frac{\partial^2}{\partial x^2}+\frac{\partial^2\omega}{\partial k_y^2}\frac{\partial^2}{\partial y^2}\right)a-\tfrac{1}{2}\omega_0 k_0^2|a|^2a=0,$$

which is the evolution equation for the envelope of a wave train with carrier wave number $\mathbf{k}=(k_0,0)$ with modulations in the x-direction (p) and in the y-direction (q).

Properties of 2D NLS are:

1. There is Benjamin-Feir Instability, but it has a different character (see stability diagram in Fig. 5).
2. Envelope solitons are unstable to transverse perturbations [23].

Finally, it is emphasized that the narrow-band approximation resulting in the two-dimensional NLS equation has a restricted validity. This is clearly evident because the two-dimensional version of NLS has energy leakage to high modulation wavenumbers. As a result, after a finite time the wave energy is not confined to a small region in wavenumber space, therefore violating the original assumptions of narrow band. From the Zakharov equation we know that the instability region is finite in extent, however, even for two-dimensional perturbations.

Hence, this suggests that the two-dimensional NLS equation does not provide an appropriate description of the envelope of surface gravity waves for large times. Nevertheless, studies of the properties of the NLS equation have been vital in understanding nonlinear wave-wave interactions and in understanding the conditions under which freak waves, for example, may occur.

5.5 Nomenclature

Before we discuss the statistical approach to sea state forecasting I would first like to introduce some relevant concepts.

The sea state is represented by the wave spectrum $F = F(\mathbf{k}, \mathbf{x}, t)$. Here $\mathbf{k}$ is the wavenumber vector, such that $k = 2\pi/\lambda$ with λ the wave length. The spectrum is normalized in such a way that the integral over the spectrum gives, apart from a factor $\rho_w g$, the wave energy:

$$\int \mathrm{d}\mathbf{k} F(\mathbf{k}) = \frac{E}{\rho_w g}, \; E = \rho_w g \langle \eta^2 \rangle$$

where η denotes the surface elevation. Thus, spectrum is normalized so that its integral equals the wave variance $\langle \eta^2 \rangle$. The variance will frequently be denoted by m_0 where, in general, m_n is the nth frequency moment of the spectrum:

$$m_n = \int \mathrm{d}\mathbf{k} \; \omega^n \; F(\mathbf{k})$$

In practice we think in terms of wave heights (for a single wave this the distance between crest and trough). In a spectral context we use the concept of significant wave height. This is a statistical measure, defined as

$$H_S = 4\sqrt{m_0}$$

In a similar vein, lots of other variables may be defined using the spectrum, e.g. mean frequency, mean wave direction, wave steepness, directional width etc. An example is the 'significant' wave steepness $\epsilon = k_0 m_0^{\frac{1}{2}}$, with k_0 the peak wave number, and the relative width of the frequency spectrum $\delta_\omega = \sigma_\omega/\omega_0$. These two parameters allow to introduce a measure of coherency of the sea state, as expressed by the *Benjamin-Feir Index*

$$BFI = \epsilon\sqrt{2}/\delta_\omega.$$

In 2D, an additional parameter is of major interest in the present discussion, namely the ratio of directional width δ_θ and frequency width δ_ω,

$$R = \frac{1}{2}\frac{\delta_\theta^2}{\delta_\omega^2}.$$

6 Ocean Waves and Statistical Mechanics

Modern wave forecasting systems predict the average sea state at a certain location, hence there is no information on phases of the waves available. Using ideas from non-equilibrium statistical mechanics, deviations from Gaussian statistics can be related to the mean sea state, as expressed by the *wave spectrum*. Deviations from Gaussian statistics imply *change* of the sea state. This allows us to obtain from the deterministic Zakharov equation an evolution equation for the wave spectrum that basically gives the rate of change of the sea state due to four-wave interactions. In addition, the probability distribution function (p.d.f.) and its deviations from Normality are now known as well. Hence, for given sea state the probability of occurrence of extreme events can be obtained.

Here, the assumptions underlying our approach will be given and we are going to describe the procedure how to obtain the four-wave evolution equation and the p.d.f. of the sea surface. However, from the previous discussion we know that there is a distinction between *free* waves and *bound* waves. The 'free' wave dynamics usually gets most of the attention, but in order to obtain a complete picture of the sea state, the contribution of the bound waves to the wave spectrum and to the statistics of the waves needs to be discussed as well. We first start with the 'free' waves which is followed by a discussion of the consequence of the presence of the bound waves.

6.1 A Generation Mechanism for Freak Waves

Freak waves are examples of extreme, nonlinear ocean waves which may cause considerable damage to large vessels and oil rigs. An example of a freak wave is shown in Fig. 9. These extreme waves are generated by a combination of "luck", i.e. *constructive interference*, and *nonlinear focussing*, a process that also causes the Benjamin-Feir Instability.

Fig. 9 An example of an extreme sea state

Most of the time linear waves on the open ocean are independent and therefore the *Random Phase Approximation* applies. This means that in a good approximation ocean waves follow Gaussian statistics. However, nonlinear interactions imply correlated phases which result in deviations from Gaussian sea state. The kurtosis (which measures deviations from the Normal distribution) can be expressed in terms of the wave spectrum, and therefore for given sea state the probability of occurrence of extreme events can be obtained. Theory is validated against Monte Carlo Simulations using the Zakharov Equation.

Theoretically it is now straightforward to generate freak waves as four-wave interactions, under certain conditions (large BFI and small R!), will lead to the formation of wave groups. However, all this depends in a sensitive manner on the initial phases of the waves. The dependence on the initial phases of the waves is illustrated in Fig. 10. Starting from a sea state where all the waves have the same phase enormous waves are generated in an almost periodic fashion, in fact the envelope consists of solitons. However, the evolving sea state is less dramatic when the simulation starts from random initial phase. This emphasizes the need for a *statistical approach* as in practice the phases of the waves are not known.

6.2 Stochastic Approach: Free Waves

In wave forecasting we are interested in predicting quantities such as the second moment

$$B_{1,2} =< a_1 a_2^* >= \mathcal{O}(\epsilon^2),\ \epsilon = \text{wave steepness},$$

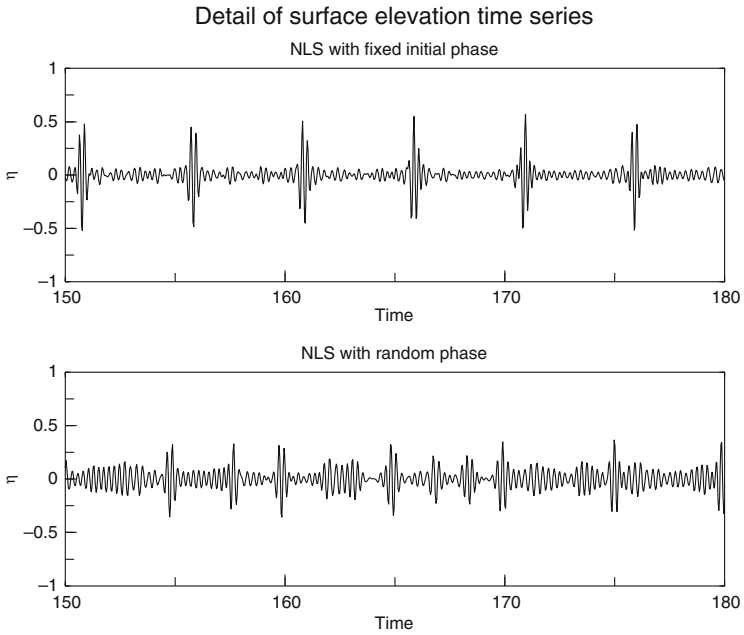

Fig. 10 Focussing of wave energy depends in a sensitive manner on the phase of the waves. Compare the case with waves having the same phase initially (*top*) with the random phase case (*bottom*). Both cases start from the same wave spectrum

where angle brackets denote an ensemble average. Following methods employed in Statistical Mechanics (Liouville → Boltzmann) one obtains from the deterministic Zakharov equation an equation for the action density N. Two assumptions are made, namely the p.d.f. of the sea state is close to a *Normal* distribution, and the sea state is *homogeneous*.

Because of nonlinearity the second moment is coupled to fourth moment, giving an infinite hierarchy of equations. Closure of the hierarchy of equations is achieved by the assumption that the sea state is close to a *Gaussian*, because nonlinearity is assumed to be weak. For example, the fourth moment is given by

$$< a_j a_k a_l^* a_m^* > = B_{j,l} B_{k,m} + B_{j,m} B_{k,l} + D_{j,k,l,m},$$

where D is the so-called fourth cumulant, which vanishes for a Gaussian sea state. For weakly nonlinear waves $D = \mathcal{O}(\epsilon^6)$ is small, but finite, and this enables one to close the hierarchy of equations.

The first two members of the BBGKY hierarchy look like:

$$\left[\frac{\partial}{\partial t} + i(\omega_i - \omega_j)\right] B_{i,j}$$

$$= -i \int \mathrm{d}\mathbf{k}_{2,3,4} [T_{i,2,3,4} < a_j^* a_2^* a_3 a_4 > \delta_{i+2-3-4} - c.c.(i \leftrightarrow j)],$$

Similarly, the equation for the fourth moment involves the sixth moment. It becomes

$$\left[\frac{\partial}{\partial t} + i(\omega_i + \omega_j - \omega_k - \omega_l)\right] < a_i a_j a_k^* a_l^* >$$
$$= -i \int \mathrm{d}\mathbf{k}_{2,3,4}[T_{i,2,3,4} < a_2^* a_k^* a_l^* a_3 a_4 a_j > \delta_{i+2-3-4} + (i \leftrightarrow j)]$$
$$+i \int \mathrm{d}\mathbf{k}_{2,3,4}[T_{k,2,3,4} < a_3^* a_4^* a_l^* a_2 a_i a_j > \delta_{k+2-3-4} + (k \leftrightarrow l)].$$

The second assumption we make is that of a *homogeneous* wave field. This assumption means that the two point correlation function $< \eta(\mathbf{x}_1)\eta(\mathbf{x}_2) >$ depends only on the distance $\mathbf{x}_1 - \mathbf{x}_2$. As a consequence of homogeneity, the second moment becomes

$$B_{i,j} = N_i \delta(\mathbf{k}_i - \mathbf{k}_j),$$

where N_i is the spectral action density.

Applying the random phase approximation to the sixth moment gives for the fourth cumulant D, subject to the initial value $D(t = 0) = 0$,

$$D_{i,j,k,l} = 2T_{i,j,k,l}\delta_{i+j-k-l} G(\Delta\omega, t)\left[N_i N_j (N_k + N_l) - (N_i + N_j) N_k N_l\right]$$

where $\Delta\omega = \omega_i + \omega_j - \omega_k - \omega_l$. The derivation of this result requires extensive use of the symmetries of T. In addition, the action density N is assumed to evolve on the slow time scale. The complex resonance function G is defined as

$$G(\Delta\omega, t) = i \int_0^t \mathrm{d}\tau e^{i\Delta\omega(\tau - t)} = R_r(\Delta\omega, t) + iR_i(\Delta\omega, t).$$

Knowledge of the fourth cumulant is essential for (a) obtaining the evolution of N caused by four-wave interactions and (b) for the determination of deviations from normality. For example, use of D in second moment equation gives

$$\frac{\partial}{\partial t} N_4 = 4 \int \mathrm{d}\mathbf{k}_{1,2,3} T_{1,2,3,4}^2 \delta_{1+2-3-4} R_i(\Delta\omega)\left[N_1 N_2 (N_3 + N_4) - N_3 N_4 (N_1 + N_2)\right] \tag{27}$$

where $\Delta\omega = \omega_1 + \omega_2 - \omega_3 - \omega_4$. Note that Eq. (27) is a slight generalization of the classical result obtained by Hasselmann [9] as this equation admits both *resonant* and *non-resonant* wave-wave interactions. This follows by observing that the imaginary part of the resonance function

$$R_i(\Delta\omega, t) = \sin(\Delta\omega t)/\Delta\omega$$

implies two timescales. For short times one has $\lim_{t\to 0} R_i(\Delta\omega, t) = t$, hence $T_{NL} = O(1/\epsilon^2\omega_0)$, the Benjamin-Feir timescale, corresponding to non-resonant interactions. On the other hand, for large times it is found that $\lim_{t\to\infty} R_i(\Delta\omega, t) = \pi\delta(\Delta\omega)$, corresponding to resonant wave-wave interactions, hence $T_{NL} = O(1/\epsilon^4\omega_0)$ [9].

Nonlinearity (both bound waves and dynamics) induce deviations from Gaussian statistics. When these deviations are small the p.d.f. of e.g. the surface elevation η will follow the well-known *Gram-Charlier expansion*, i.e. with $x = \eta/ < \eta^2 >^{1/2}$ the normalized surface elevation,

$$p(x) = \left(1 + \frac{C_3}{6}\frac{d^3}{dx^3} + \frac{C_4}{8}\frac{d^4}{dx^4} + \ldots\right) f_0, \tag{28}$$

where f_0 is given by the normal distribution

$$f_0 = \frac{1}{\sqrt{2\pi}}\, e^{-\frac{x^2}{2}}.$$

Deviations from Normality are therefore most conveniently expressed by means of skewness C_3 and kurtosis C_4. However, with four-wave interactions the free-wave contribution to skewness is vanishingly small. Therefore, for free-waves, kurtosis is of most interest. It is here defined as

$$C_4 = < \eta^4 > /3 < \eta^2 >^2 - 1.$$

Using the expression for the fourth cumulant the contribution to kurtosis by means of four-wave interactions is found to be

$$C_4^{dyn} = \frac{4}{g^2 m_0^2} \int \mathrm{d}\mathbf{k}_{1,2,3,4} T_{1,2,3,4} \delta_{1+2-3-4} \left(\omega_1\omega_2\omega_3\omega_4\right)^{\frac{1}{2}} \times R_r(\Delta\omega, t) N_1 N_2 N_3, \tag{29}$$

where $R_r(\Delta\omega, t) = (1 - \cos(\Delta\omega t))/\Delta\omega$. The form of the function R_r implies that the dynamic kurtosis is mainly determined by non-resonant interactions. The result (29) shows that deviations from Gaussianity are connected to the mean state. This expression gives the contribution of the free waves to the kurtosis, which is in general time dependent because the resonance function R_r depends on time. It is a six-dimensional integral and is in an operational context too expensive to evaluate. Some properties of the above expression for the free-wave kurtosis will be given after presenting the effect of bound waves.

6.3 Stochastic Approach: Bound Waves

We now use the canonical transformation to obtain nonlinear corrections to the free wave spectrum and to obtain contributions to skewness and kurtosis due to the bound waves. We make the two usual assumptions of a homogeneous, Gaussian sea state. The spatial correlation function is

$$\rho(\boldsymbol{\xi}) = \langle \eta(\mathbf{x}+\boldsymbol{\xi})\eta(\mathbf{x})\rangle$$

The wave number spectrum $F(\mathbf{k})$ then follows immediately by Fourier transformation in $\boldsymbol{\xi}$, i.e.

$$F(\mathbf{k}) = \frac{1}{4\pi^2}\int \mathrm{d}\boldsymbol{\xi}\ \rho(\boldsymbol{\xi})e^{i\mathbf{k}\cdot\boldsymbol{\xi}}.$$

The spatial correlation function can now be expressed in terms of the Fourier transform of the surface elevation $\hat{\eta}$, while utilizing Eq. (10) which relates $\hat{\eta}$ to the action density variable A and using the explicit expression for the canonical transformation given in (13), which is of the form

$$A = \epsilon a + \epsilon^2 b + \epsilon^3 c + ...$$

Introducing the free wave surface elevation spectrum according to

$$E(\mathbf{k}) = \frac{\omega N(\mathbf{k})}{g}$$

the wavenumber spectrum becomes:

$$F(\mathbf{k}_1) = \frac{1}{2}E_1 + \frac{1}{2}\int \mathrm{d}\mathbf{k}_{2,3}E_2E_3\left\{\mathscr{A}^2_{2,3}\delta_{1-2-3} + \mathscr{B}^2_{2,3}\delta_{1+2-3}\right\} + E_1\int \mathrm{d}\mathbf{k}_2E_2\mathscr{C}_{1,1,2,2} + \{\mathbf{k}_1 \rightarrow -\mathbf{k}_1\}, \tag{30}$$

where, with $f_1 = (\omega_1/2g)^{1/2}$,

$$\mathscr{A}_{2,3} = \frac{f_{2+3}}{f_2f_3}\left(A^{(1)}_{2+3,2,3} + A^{(3)}_{-2-3,2,3}\right),\ \mathscr{B}_{2,3} = \frac{1}{2}\frac{f_{2-3}}{f_2f_3}\left(A^{(2)}_{3-2,2,3} + A^{(2)}_{2-3,3,2}\right),$$

and

$$\mathscr{C}_{0,1,2,3} = \frac{f_0}{f_1f_2f_3}\left(B^{(2)}_{0,3,2,1} + B^{(3)}_{-0,1,2,3}\right),$$

therefore the coupling coefficients $\mathscr{A}$, $\mathscr{B}$ and $\mathscr{C}$ can all be expressed in terms of the matrix elements that determine the canonical transformation. In Fig. 11 the bound

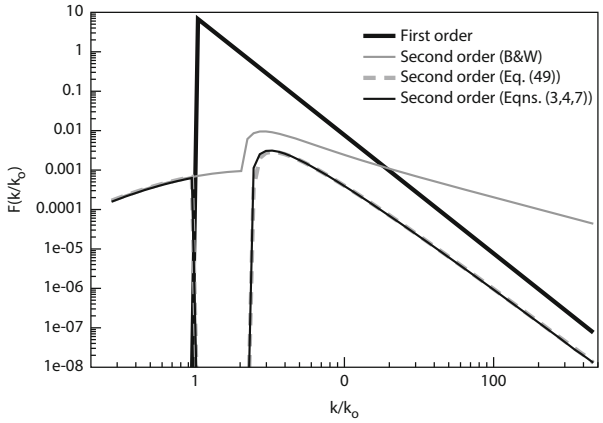

Fig. 11 Shown is the Phillips spectrum for free waves and the resulting second-order spectrum with and without (labeled B&W) the quasilinear effect. For large wavenumbers the second-order spectrum without quasi-linear effect behaves as $1/k$ resulting in a divergent expansion in powers of wave steepness

wave spectrum is shown for a one-dimensional free-wave spectrum which has the Phillips form, i.e. $E(k) = \frac{1}{2}\alpha_p k^{-3}, k/k_0 > 1$. In this case the bound-wave part of the wave spectrum can be derived analytically (cf. [2] for details). The Figure clearly shows the importance of the quasi-linear effect giving by the last term in Eq. (30). In fact, one needs to include this term in order to obtain a convergent expansion of the wave spectrum in powers of the wave steepness.

Also, in [2], an expression for the directional frequency spectrum is found as well, but in that case there is an additional contribution due to the Stokes-drift.

The properties of the frequency spectrum have been extensively studied in [2]. In order to get a feeling of how second-order effects change spectral shape I have plotted in Fig. 12 the freewave spectrum and the wave spectrum including second-order effects for two different depths $D = 3.0$ and $D = 1.7$ m. It is seen that for shallow waters second-order effects are important and in particular the low-frequency part of the spectrum depends in a sensitive manner on the actual depth value.

We can also use the canonical transformation to obtain contributions to skewness and kurtosis due to the bound waves.

By definition the skewness C_3 and excess kurtosis C_4 read

$$C_3 = \frac{\mu_3}{\mu_2^{3/2}},\ C_4 = \frac{\mu_4}{3\mu_2^2} - 1,$$

where $\mu_n = \langle \eta^n \rangle,\ n = 2, 3, 4$, are the second, third and fourth moment of the p.d.f. of the surface elevation, while the first moment $\langle \eta \rangle$ is assumed to vanish. Recall that for a Gaussian p.d.f. both C_3 and C_4 vanish. Also note that $\mu_2 = m_0$!

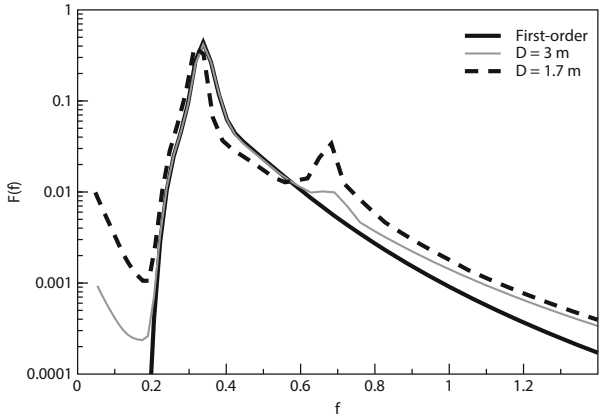

Fig. 12 Effect of second-order contributions to the wave spectrum is substantial for shallow waters, $k_0 D = \mathcal{O}(1)$

The skewness becomes

$$C_3 = \frac{3}{\mu_2^{3/2}} \int \mathrm{d}\mathbf{k}_{1,2} E_1 E_2 \left(\mathscr{A}_{1,2} + \mathscr{B}_{1,2} \right). \tag{31}$$

and the excess kurtosis has the form

$$C_4^{can} = \frac{4}{\mu_2^2} \int \mathrm{d}\mathbf{k}_{1,2,3} \mathscr{T}_{1,2,3} E_1 E_2 E_3. \tag{32}$$

The expression for the coupling matrix $\mathscr{T}$ may be found in [2]. There is one important distinction between the free-wave stats [cf. (29)] and the bound-wave stats. Equations (31) and (32) are diagnostic relations because the coupling coefficients are independent of time. Therefore, for stationary spectra the bound-wave contributions to skewness and kurtosis are constant in time while the dynamic part of the kurtosis will evolve in time. This will be studied in more detail in the next section.

6.4 Results for Skewness and Kurtosis

To summarize, skewness and kurtosis are now know in terms of multi-dimensional integrals over the wave number spectrum of the free waves. In principle, from knowledge of the evolution of the wave spectrum as obtained from a wave forecasting system, we are now able to determine these important statistical parameters. Actual values for general spectra can only be obtained by means of numerical integration. Here, in order to have some idea of the order of magnitude of these parameters, some special cases will be discussed which have an analytical solution.

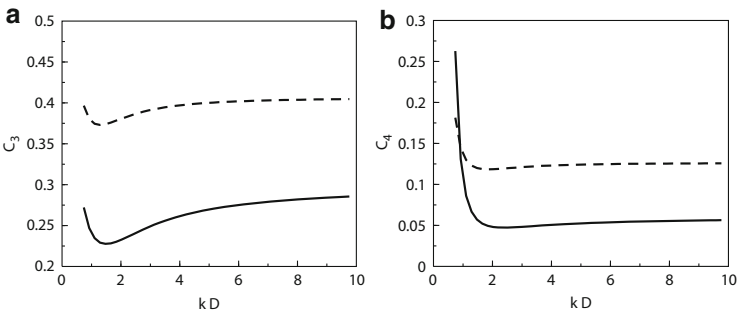

Fig. 13 Skewness C_3^{can} (*left panel*) and kurtosis C_4^{can} (*right panel*) for a steepness $\epsilon = 0.1$ as function of dimensionless depth $x = k_0 D$. *Dashed line* corresponds to the case of a Phillips' spectrum, while the *black line* corresponds to the case of a single wave train with the same variance while the carrier wavenumber equals the peak wavenumber k_0

6.4.1 Bound Waves

Simple results for skewness and kurtosis caused by the bound waves are only known for deep water. Introducing the significant steepness $\epsilon = k_0 m_0^{1/2}$ one finds for a single wave train with spectrum $E(k) = m_0 \delta(k - k_0)$

$$C_3^{can} = 3\epsilon, \; C_4^{can} = 6\epsilon^2 \tag{33}$$

More elaborate expressions are known that give the depth dependence of these statistical parameters for a single wave train (see e.g. [2]). These are shown in Fig. 13, and it is seen that in particular the kurtosis depends in a sensitive manner on depth D. For comparison, also results for the Phillips spectrum $E(k) = \frac{1}{2}\alpha_p k^{-3}, \; k \geq k_0$ are shown, suggesting that spectral shape is important in determining these parameters.

6.4.2 Free Waves

We are basically dealing here with a problem concerning the balance between dispersion of the waves and its nonlinearity (giving focusing). In 1D and in the narrow-band approximation, this balance may be expressed by the Benjamin-Feir Index, and the nonlinear focussing is connected with envelope solitons. In 2D the balance between dispersion and nonlinearity is destroyed, because solitary waves are unstable. This imbalance is measured by an additional parameter, namely the ratio R of directional width and frequency width. For simple initial spectra (characterized by variance and width only) it can be shown that large time solutions to NLS are determined in 1D by the *BFI* and in 2 D by *BFI* and R only.

Properties of the dynamic part of the kurtosis have mainly been studied for narrow-band spectra. To that end the general result (29) is applied to a spectrum that is mainly concentrated at $\omega = \omega_0$ and $\theta = \theta_0$. Introduce scaled variables

$$\nu = (\omega - \omega_0)/(\delta_\omega \omega_0), \ \phi = (\theta - \theta_0)/\delta_\theta$$

where δ_ω is the relative width of the frequency spectrum and δ_θ is the directional width. With $E = E(\nu, \phi)$ the frequency direction spectrum, the kurtosis becomes

$$C_4 = J(R, \tau) BFI^2, \tag{34}$$

where

$$J(R, \tau) = 2 \int \mathrm{d}\nu_{1,2,3} \mathrm{d}\phi_{1,2,3} E_1 E_2 E_3 G(\Delta\omega, \tau),$$

with

$$G(\Delta\omega, \tau) = \frac{1 - \cos(\Delta\omega\tau)}{\Delta\omega},$$

the real part of the resonance function. Here, $\tau = \delta_\omega^2 \omega_0 t$ is dimensionless time, and $\Delta\omega = (\nu_3 - \nu_1)(\nu_3 - \nu_2) - R(\phi_3 - \phi_1)(\phi_3 - \phi_2)$.

For a Gaussian wave spectrum $E = \frac{1}{2\pi} e^{-\frac{1}{2}(\nu^2 + \phi^2)}$ the factor $J(R, \tau)$ may be evaluated analytically, [24]. For 2D propagation the factor $J(R, \tau)$ becomes

$$J(R, \tau) = -i \int_0^\tau \frac{\mathrm{d}z}{\{(1 - 2iz + 3z^2)(1 + 2iRz + 3R^2 z^2)\}^{1/2}} + c.c. \tag{35}$$

It can be shown from (35) that for 1D propagation, i.e. $R = 0$, the dynamic part of the kurtosis has a finite value for large times,

$$\lim_{t \to \infty} J(0) = \frac{\pi}{3\sqrt{3}} \rightarrow C_4^{dyn} = \frac{\pi}{3\sqrt{3}} BFI^2,$$

in agreement with a result obtained in [25]. However, for finite R kurtosis will always decay to zero for large times.

For different values of the directional width parameter R the resulting time dependence of the dynamic part of the kurtosis is shown in Fig. 14. From the Figure it is immediately evident that 1D propagation is an exception, because for this case the kurtosis has a finite value for large times, while for finite R the kurtosis vanishes. Again, the occurrence of freak waves is connected with the generation of (Envelope) solitons. In 1D, solitons are stable entities based on the balance of dispersion and nonlinear steepening. However, the ocean surface is two-dimensional. This additional degree of freedom does not allow the formation of solitons, rather freak waves become a *transient phenomenon*.

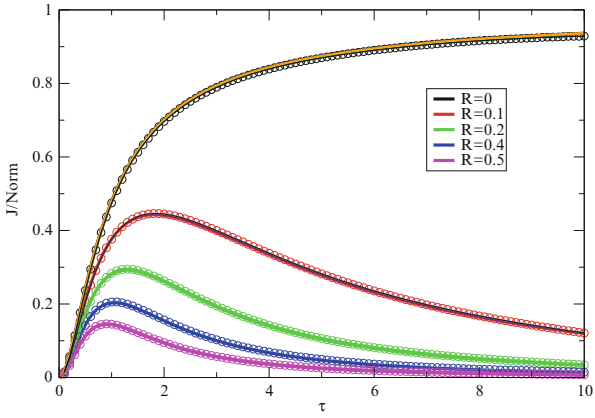

Fig. 14 NLS evolution of normalized kurtosis versus time for different values of R. Results using the expensive brute force method are shown as well

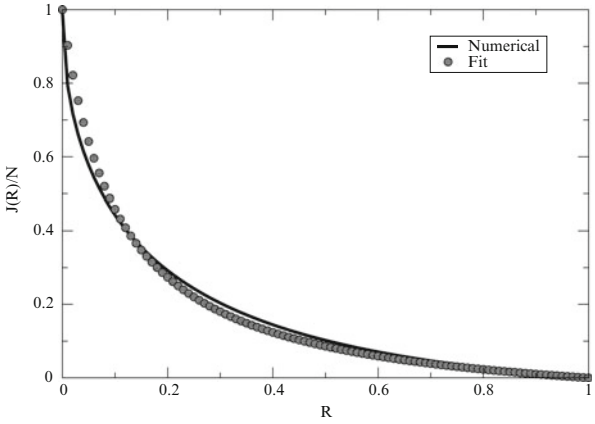

Fig. 15 Maximum value of J/N versus R. The fit (36) is shown as well

Finally, in ECMWF's freak wave warning system we cannot deal with a time dependent kurtosis. To be on the safe side it was decided to use the maximum value of J. For this reason, in Fig. 15 the dependence of the maximum value of J on R was studied. A good fit is found using

$$\frac{J}{N} = \frac{R_0(1-R)}{R+R_0},\ N = \frac{\pi}{3\sqrt{3}}, \tag{36}$$

with $R_0 = 7.44\sqrt{3}/4\pi^3$. This fit is used in ECMWF's freak wave warning system.

6.5 Comparison with Monte Carlo Simulations

It is important to determine the range of validity of the theory of resonant and non-resonant four-wave interactions. For example, this theory assumes that the wave steepness is sufficiently small and the p.d.f. of the surface elevation (28) is

close to a Gaussian. In order to address these questions we simulate the evolution of an ensemble of waves by running a deterministic model with random initial conditions. Only wave propagation in one dimension will be considered here, but in the literature there are several examples of studies that investigated the two-dimensional case (see e.g. [26]).

It should be clear that there is a strong need to investigate the occurrence of extreme wave events in the context of ensemble forecasting. The main reason is that the formation of freak waves depends in a sensitive manner on the choice of the initial phases, while in practice (at sea!) we have no knowledge of the phases of the waves. Because of this lack of knowledge of the initial phases we perform *Monte Carlo simulations* with the evolution equations for water waves: Amplitudes are drawn from the wave spectrum, while phases are randomly drawn from a uniform distribution.

The Figs. 16, 17, and 18 present some results of the ensemble mean evolution of the Zakharov equation for the 1-D case, and the numerical results are compared with the theory as developed in the present lectures. First, it is shown how for the extreme case of $BFI = 1.4$ the wave spectrum evolves in time owing to the nonlinear four-wave interactions. Note that in 1D there are no resonant interactions therefore the rate of change in time of the wave spectrum is entirely caused by non-resonant interactions. In addition, Fig. 17 shows, to what extent the nonlinear interactions cause deviations of the surface elevation p.d.f. from the Normal distribution. These deviations are quite extreme, but they are fairly well described by the p.d.f. (28). In this extreme situation the deviations from the Normal distribution are to a large extent caused by kurtosis effects. For this reason, we show in Fig. 18 the dependence of the kurtosis on the *BFI*. Overall, a fair agreement between theory and numerical simulations is noted.

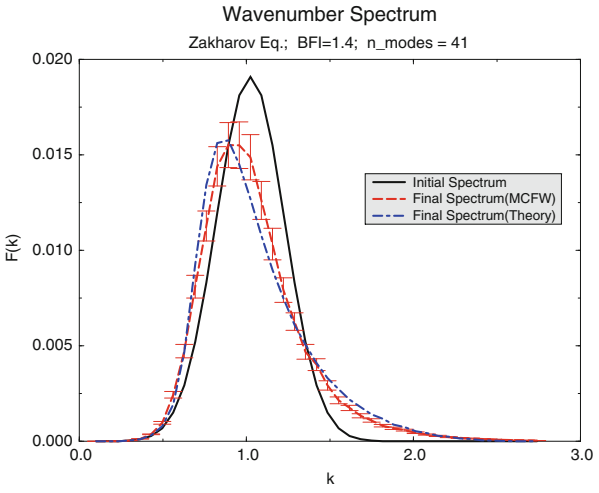

Fig. 16 Initial and final time wave number spectrum using the Zakharov equation. Error bars give 95 % confidence limits. Results from theory are shown as well

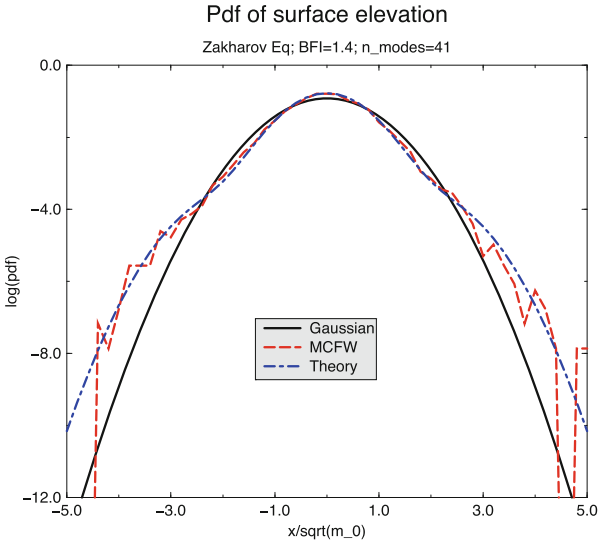

Fig. 17 Log of p.d.f. of surface elevation ($BFI = 1.4$). For reference the Gaussian distribution is shown as well. Freak waves correspond to a normalized height of 4 or larger

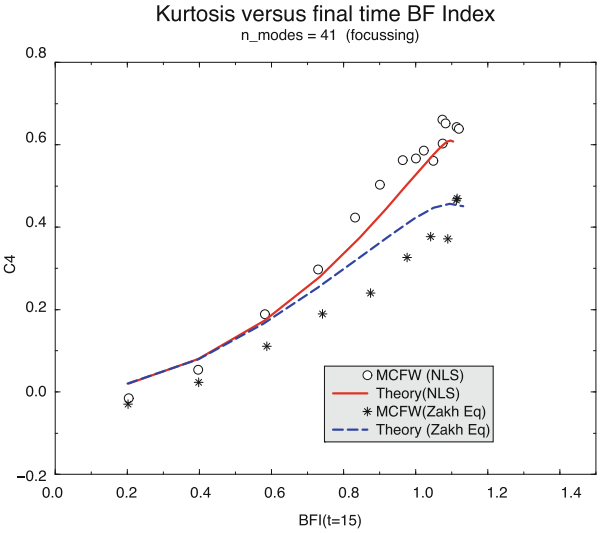

Fig. 18 Normalized Kurtosis as function of the BF Index. Shown are results for focussing from simulations with NLS and with the Zakharov equation, and corresponding theoretical results

7 Comparison with Observations from Wave Tanks

We have put forward arguments that for 1-D propagation nonlinear focussing of wave energy by means of non-resonant wave-wave interactions plays a crucial role in the formation of freak waves. On the other hand, for broader directional spectra the effect of non-resonant interactions in freak waves generation is much reduced. However, nonlinear effects connected to presence of bound waves, for example, may still give rise to finite skewness and kurtosis, resulting, therefore, in deviations from the Normal distribution, and as a consequence in an increase in the probability of extreme events. In general, we have seen that the statistical 4-wave interactions theory not only allows for a description of the average sea state, but it also gives information on the deviations of the sea state from the ensemble averaged value. Therefore, in principle, one can make statements of a probabilistic nature on the occurrence of extreme events.

Nevertheless, it should be clear that there is evidently a need of extensive experimental verification. This is not an easy task because extreme events such as freak waves formation only rarely occur in Nature. The best change we have is to try to validate our approach by performing laboratory experiments where freak wave generation may be observed under controlled circumstances. And, indeed, nowadays extensive validations in 1D and 2D wave tanks have been performed. Here, examples are given from the large wave tank in Trondheim [27, 28] and the one from the University of Tokyo [29].

Before we discuss the experimental results it is important to decide which quantity is used in the comparison between observations and theory. Traditionally, researchers have focussed on wave height as the key parameter to express the severity of the sea state. The reason for this choice is that observations of the sea state have for a long time been based on visual inspection of the surface height from a ship. Nevertheless, ocean wave prediction has always been based on a spectral description of the sea state and the key parameter to describe the sea state is the wave spectrum, which is normalized in such a way that the integral of the wave spectrum $F(\mathbf{k})$ over wavenumber space is given by the wave variance $\langle \eta^2 \rangle$, i.e. the zeroth moment of the wave spectrum becomes

$$m_0 = \int \mathrm{d}\mathbf{k} F(\mathbf{k}) = \langle \eta^2 \rangle,$$

and the connection between the spectral approach and the statistics is given by the relation

$$\mu_2 = m_0,$$

with μ_2 the already introduced second moment of the p.d.f. of the surface elevation. It is therefore more natural to characterize extreme events in terms of the 'local' energy of the sea state, which boils down to the power of a signal in nonlinear

optics and in the theory of communication [30]. Of course, there is a straightforward connection between wave energy and 'significant' wave height, but it only holds for narrow-band spectra. When energy (or, as we will see in an moment envelope wave height) is taken as the key parameter to characterize the mean sea state and its statistical aspects, then it is possible to formulate a characterization of extreme events which is not restricted to narrow-band spectra but is valid for 'arbitrary' spectral shape. A more extensive discussion of this given in [31], including a derivation of the results that follow in this Section.

Following [30], the surface elevation may, in general, be written as

$$\eta = \rho \cos \phi,$$

where the envelope ρ and the phase ϕ depend on space and time (note that the local frequency ω is just $-\partial\phi/\partial t$). The envelope ρ then may be obtained from the surface elevation η and its Hilbert transform $\zeta = H(\eta) = \rho \sin \phi$, and it is defined by

$$\rho = \sqrt{\eta^2 + \zeta^2}.$$

and the local energy equals $\rho^2/2$. In the remainder results will be presented for the scaled parameters $\eta' = \eta/\langle\eta^2\rangle^{1/2}$ and $\zeta' = \zeta/\langle\zeta^2\rangle^{1/2}$, so we scale surface elevation and its Hilbert transform by means of its variance and the primes will be dropped. The instantaneous, local wave height h is then just twice the envelope, i.e. $h = 2\rho$. Using the Gram-Charlier expansion for the surface elevation, the p.d.f. of dimensionless wave height h becomes

$$p(h) = 4h \exp(-2h^2) \left[1 + C_4 A_H(h) + C_3^2 B_H(h)\right]$$

where

$$A_H(h) = 2h^4 - 4h^2 + 1, \; B_H(h) = 4h^6 - 18h^4 + 18h^2 - 3$$

Here, C_4 and C_3 are kurtosis and skewness of the envelope wave height (time) series, and only recently general expressions for these quantities have been obtained in terms of the given free-wave spectrum (see for this [32]). For vanishing kurtosis and skewness the envelope wave height p.d.f. reduces to the Rayleigh distribution. Furthermore, in terms of the dimensionless wave energy, given by $E = 2h^2$, one may obtain the exceedance probability $P(E > E_c)$ that the wave energy exceeds a threshold value E_c by integrating the envelope wave height p.d.f.. As a result one finds

$$P(E > E_c) = \int_{E_c}^{\infty} \mathrm{d}h \, p(h) = e^{-E_c} \left[1 + C_4 A(E_c) + C_3^2 B(E_c)\right], \tag{37}$$

where

$$A(E) = \tfrac{1}{2}E(E-2), \; B(E) = \tfrac{1}{2}E(E^2 - 6E + 6) \tag{38}$$

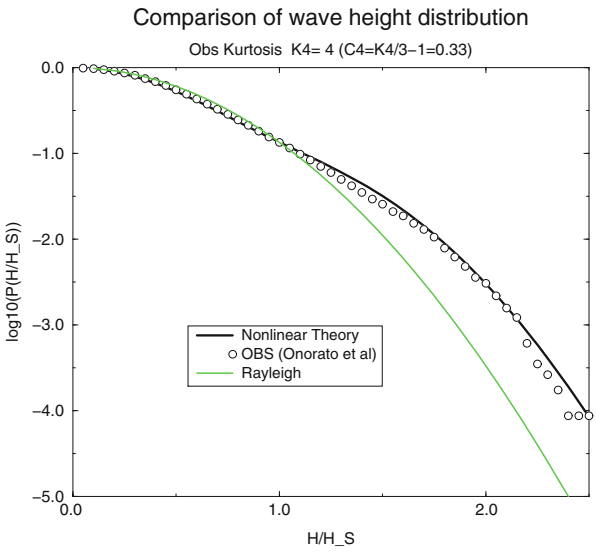

Fig. 19 Comparison of theoretical and observed [27] wave height distribution. For reference, the result from linear theory, the Rayleigh distribution, is shown as well

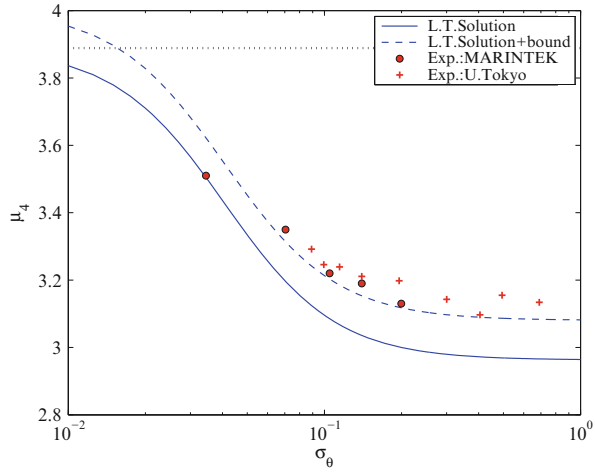

Fig. 20 Comparison of theoretical and observed [28, 29] kurtosis $\mu_4 = 3(1 + C_4)$ as function of the directional width parameter σ_θ. The *full line* shows the free-wave part of the kurtosis while the *dashed line* shows the sum of free-wave and bound-wave parts

The exceedance probability is required when one is interested in quantities such as the maximum wave height distribution.

In Fig. 19 we compare the theoretical exceedance probability with observations from the Trondheim wave tank in [27]. The experiment considered a case of one-dimensional propagation with a quite narrow frequency spectrum resulting in a *BFI* which is close to 1, and a kurtosis $C_4 = 0.33$. In such a very narrow-band case skewness effects are relatively unimportant.

Finally, we have already mentioned that when the directional width of the wave spectrum increases the impact of the non-resonant interactions on the kurtosis of the sea state is much reduced. This is illustrated in Fig. 20 where we plot the kurtosis,

defined as $\mu_4 = 3(1 + C_4)$ as a function of the directional width parameter σ_θ (in radians). Here, the theoretical value of the kurtosis C_4 consists of the sum of the free-wave part and the bound-wave part and the free-wave part shows a sensitive dependence on directional width, becoming quite small for a directional width larger than 10°, while the bound-wave part is fairly insensitive to the directional distribution. It is seen that there is a fair agreement between theory and observations.

8 Operational Implementation and Verification

We now briefly summarize the theoretical development we have followed during the lectures. From the Zakharov equation which describes the deterministic evolution of a continuum of surface gravity waves we obtained by ensemble averaging the evolution of the free-wave spectrum and the second-order spectrum. In addition, we found that the weakly nonlinear free-waves and its associated non-resonant interactions give rise to a finite contribution to the kurtosis of the surface elevation only, while the bound-waves contribute to both the skewness and the kurtosis. In principle, we can now give statements on the exceedance probability of extreme events.

The theoretical results for the skewness and kurtosis, given in Eqs. (28), (31) and (32) involve too many computations for an operational implementation such as in the ECMWF wave forecasting system. We therefore have implemented fairly crude approximations for these statistical parameters. They are essentially given by Eqs. (33) and (36). Using this, the probability distribution of surface elevation η and the envelope wave height h can be determined and from this all kinds of parameters that characterize how extreme the sea state is. We now discuss, in particular, one parameter that is of importance to characterize extreme events, namely the p.d.f. of *maximum wave height* h_{max} and its expectation value $\langle h_{max} \rangle$!

In [33] Goda obtained the maximum wave height distribution from a (time) series of N wave events. Here, the maximum (envelope) wave height distribution follows from the probability that a certain event attains the maximum value multiplied by the probability that all other events are below the maximum value while realizing there are N possibilities. Introducing the function

$$\mathscr{G}(h) = -NP(h),$$

which, apart from a minus sign, equals to the product of the number of events N and the already introduced cumulative distribution

$$P = \int_h^\infty \mathrm{d}h\, p(h),$$

one finds for large N the maximum envelope wave height distribution

$$p_{max}(h = h_{max}) = \frac{\mathrm{d}\mathscr{G}}{\mathrm{d}h} \exp(\mathscr{G}). \tag{39}$$

Close inspection of this result shows that this distribution is a double exponential function in general, but for large maximum envelope wave heights (typically of the order of 2 or larger) the p.d.f. simplifies considerable because it becomes

$$p_{max}(h) = N\, p(h).$$

Now, the remaining task is how to choose the number of events. Janssen in [34] has studied this issue extensively for time series. To that end one needs to define what an event is. It is customary to define an event with respect to a reference level h_c, therefore an event starts where the envelope has an up-crossing and finishes at the next down-crossing. The frequency of events is then determined by the up-crossing frequency, and N then equals the product of the up-crossing frequency and the length T_L of the time series. However, the frequency of events depends on the chosen reference level, and, therefore it may be more appropriate to introduce an average frequency. Janssen in [34] took as measure the average of the rate of change of h with time, $\dot{h}$, normalized with h itself. The averaging is done using the joint p.d.f. of h and $\dot{h}$ which for a Gaussian sea state can be easily obtained from the joint p.d.f. of envelope ρ and phase θ and its time derivatives (see e.g. [31]). Performing the averaging one finds for the average up-crossing frequency

$$\langle f_{up} \rangle = \langle \dot{h}/h \rangle = \nu \bar{\omega}, \tag{40}$$

where $\bar{\omega}$ is the mean angular frequency, determined by the ratio of the first and zeroth moment of the spectrum, $\bar{\omega} = m_1/m_0$, while ν is the spectral width parameter defined as $\nu = (m_0 m_2/m_1^2 - 1)^{1/2}$. When analyzing timeseries in terms of the *envelope*, the frequency scale $\nu\bar{\omega}$, which corresponds to the inverse of the timescale of the wave groups, is introduced in a natural way. The number of envelope events N is therefore, as expected, related to the number of wave groups, thus

$$N = \nu \bar{\omega}\, T_L, \tag{41}$$

and for this choice of the number of events good agreement between the maximum wave height p.d.f. and Monte Carlo simulations of a Gaussian sea state was reported. In particular, it was shown that the expected maximum envelope wave height scales with N while it does not scale with the number of waves $N_w = T_L/T_P$ (with T_P the peak period) in the time series, see [34].

From the result (39) two interesting quantities may be obtained. The first one is the expectation value of maximum wave height. It is defined by

$$\langle h_{max} \rangle = \int_0^\infty \mathrm{d}h\; h\, p_{max}(h). \tag{42}$$

Using (39) an approximate expression for the expected maximum wave height have been obtained in [31], and this expression is used in the ECMWF wave forecasting system. An example of a synoptic maximum wave height map for the tenth of February 2007 is shown in Fig. 21.

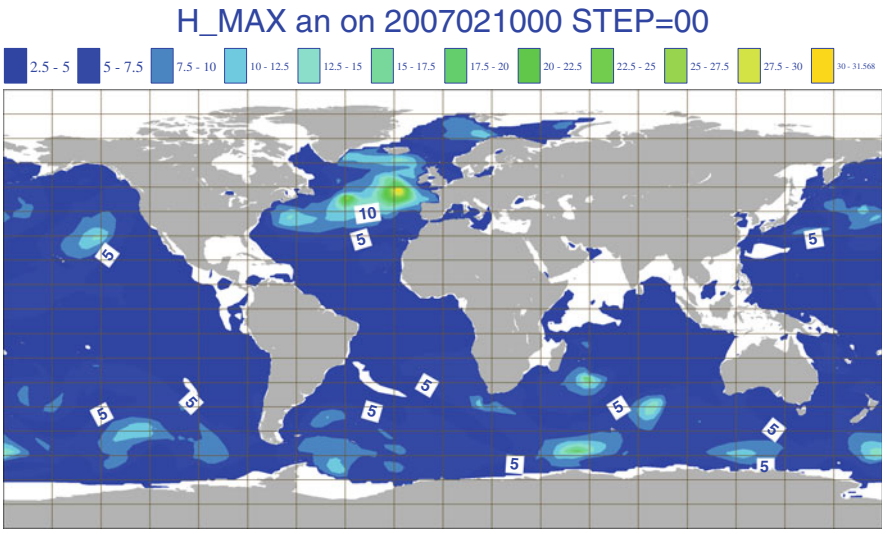

Fig. 21 Analysed maximum wave height map for 10 February 2007. Note the maximum in the North Atlantic of 31.5 m while the significant wave height was about 15 m. The duration T_L was chosen to be 3 h corresponding to a typical synoptic time scale

The second interesting quantity is an exceedance probability for maximum wave height. The probability that maximum envelope wave height equals or exceeds a given observed value, denoted by h_{max}^{obs}, is given by

$$P_{ex}(h_{max}^{obs}) = \int_{h_{max}^{obs}}^{\infty} \mathrm{d}h \; p_{max}(h) = 1 - \exp(-NP(h_{max}^{obs})) \tag{43}$$

and this quantity will be used in our discussion of a special extreme event at the end of this lecture.

8.1 Validation

For a number of reported incidents at sea I have checked that our forecasting system is indeed giving indications that there was an extreme sea state at the time of the accident. Examples are incidents with the cruiser Dawn and the cruiser Louis Majesty. But this is, of course not an objective validation!!

I regard individual events, obtained from buoy observations, just as a random draw from a large ensemble of possibilities. In order to simulate these observations a random draw is taken from the theoretical p.d.f. of H_{max} using values of mean wave height and skewness and kurtosis obtained from the wave prediction system.

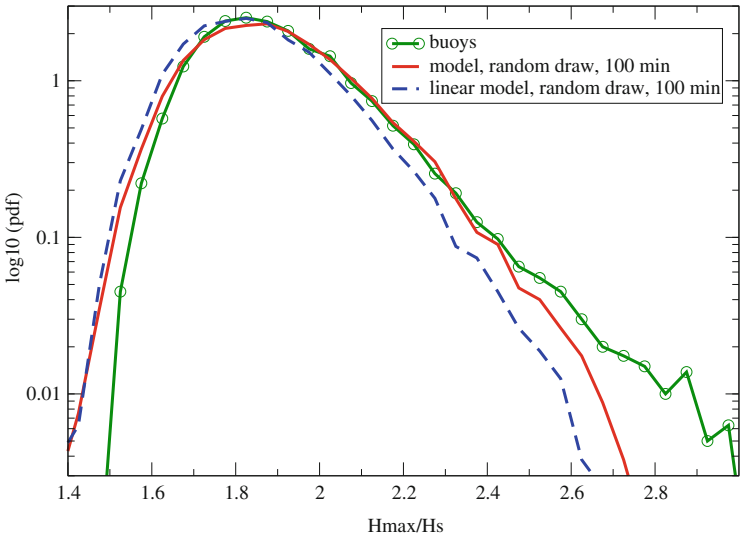

Fig. 22 Comparison of observed and modelled maximum wave height distribution based on a 30,000 collocations of Canadian buoys and operational ECMWF results (from [35])

In Fig. 22 is shown a comparison of observed and modelled probability distribution of H_{max}. The number of observations was 30,000 and they were provided by the Canadian buoy network that produces a measure for maximum wave height. These observations were collocated with modelled wave spectra produced by the operational ECMWF wave forecasting system, and from the spectra all the necessary statistical information was obtained to produce a random draw of maximum wave height. In the Figure two modelled maximum wave height p.d.f.'s are shown. The dashed blue line is obtained using linear theory so that the p.d.f. of envelope is the Rayleigh distribution. It is clear from the Figure that for large dimensionless maximum wave height h_{max} the shape of the theoretical p.d.f. really differs from the observed one. The underestimate by linear theory starts already at $h_{max} = 2$. This is fairly poor since in practice a sea state is regarded to be a potential freak wave state provided $h_{max} > 2.2$. On the other hand, when finite skewness and kurtosis produced by weakly nonlinear effects are included in the statistical model, a much better agreement between modelled and observed maximum wave height p.d.f. is found, at least in the dimensionless maximum wave height range between 2 and 2.5.

Therefore the nonlinear approach is better in dealing with extreme events, but the exception is for really extreme states with $h_{max} > 2.5$. It appears that in practice the p.d.f. of envelope wave height and maximum wave height has an *exponential tail*. This not only follows from the observed p.d.f. in Fig. 22 but also from observations in the field of nonlinear optics, [36, 37], and from numerical simulations using equations modelling four-wave interactions (see e.g. [36, 37]) and using a simple Stokes wave train [34]. As mentioned by Residori (Private Communication 2015),

for extreme waves in a nonlinear optical cavity, it has been noted that the observed probability distribution function for intensity E can be well approximated by the following simple stretched exponential form [36]

$$p(E) = Ne^{-\sqrt{c_1+c_2E}}$$

where $1/c_1$ provides a measure for deviations from Gaussian statistics which gives an exponential distribution in E, while in terms of envelope height h, with $E = 2h^2$, one obtains a Gaussian distribution function.

Janssen in [32] has successfully used the stretched exponential tail to extend the validity of the present approach to really extreme sea states. The reason that the present approach fails is probably that the Gram-Charlier expansion, given in Eq. (28), which is the basis of the present development, is not a uniformly valid expansion. Therefore, theoretically, a somewhat different approach needs to be taken for the very extreme events, but at the moment it is not clear how to proceed. What is clear, however, is that there is ample evidence for an exponential tail for large deviations, and it would be of great interest to try to understand whether this exponential behaviour is in some sense universal.

8.2 A Special Case: The Draupner Freak Wave

The Draupner wave event occurred on New Years day 1995 at 3 pm in the afternoon and was one of the first recorded freak wave events. The first 10 min of the time series, obtained from [38], is shown in Fig. 23. In addition, the time series for the envelope ρ is shown as well. This event is quite extreme since the dimensionless maximum envelope wave height $h_{max}^{obs} = 3.1$ while the local dimensionless energy E is close to 20. Draupner is the name of an oil rig that is located in the North Sea between the Norwegian and Scottish coast and has a depth of about 70 m. At the time of the freak wave event the wave spectrum was mainly windsea with a rather broad directional distribution. Winds were quite strong and generated such long waves that the sea state consisted of intermediate shallow water waves, with $k_0D = 1.45$, where k_0 is the peak wavenumber. The storm that generated the windsea was a combination of a large scale low located over the southern part of Sweden and a small scale polar low that propagated rapidly during the day from the Norwegian Sea to the Wadden Sea, while at the time of the freak wave event it was close to the Draupner platform. Simulation of such a complicated meteorological situation is not a straightforward task but it was Cavaleri *et al.* [39] who managed to simulate this event for the first time using a high-resolution version of the ECMWF coupled atmosphere, ocean-wave forecasting system. The simulation produced the model spectra which were required for the evaluation of the relevant statistical parameters such as skewness and kurtosis.

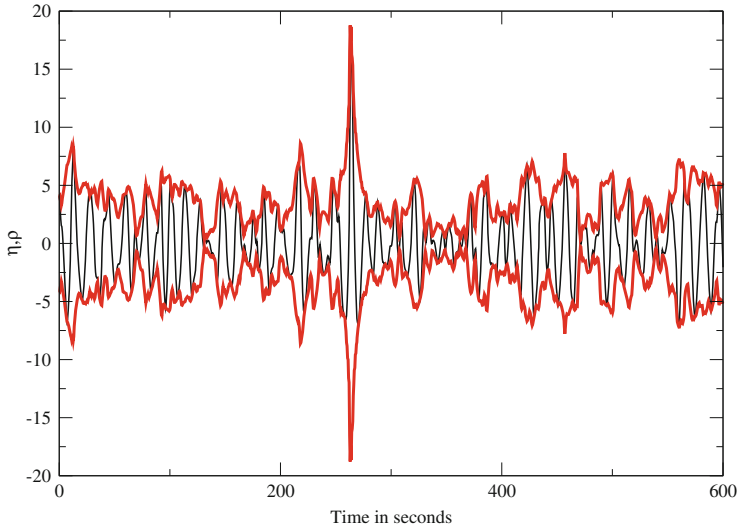

Fig. 23 Time series of the Draupner freak wave (in *black*). The envelope time series ρ is shown in *red* and this clearly illustrates how extreme this event is. The corresponding local wave energy at the maximum is about 20 times the average wave energy

I will argue now that in the context of the present statistical approach it is only possible to try to answer the question how likely the Draupner freak wave event is. Recall (see Sect. 6.1) that such extreme events are caused by constructive interference which are additionally amplified by finite amplitude effects such as the presence of bound waves and focussing by four-wave interactions. This means that an extreme event is similar to the luck of the draw from the lottery since we have no detailed knowledge of the phases of the individual waves. For this reason I have followed a statistical approach, but it should be clear that this approach cannot be validated against an exceptional singular event such as Draupner is. At best one can determine how likely such an event is in the context of our model of 'reality'. Traditionally, for time series it then seems reasonable to apply Eq. (43) which gives the probability that the maximum envelope wave height exceeds the observed maximum wave height. However, if one is interested in the likelihood of an event then considering only the time domain seems to be too restrictive. I decided therefore to determine for a domain of the size of a model grid box the probability that maximum wave height exceeds the observed value at the Draupner location. Evaluation of this exceedance probability relies, of course on an accurate modelling of the skewness and kurtosis parameter, on an accurate modelling of the tail of the envelope wave height distribution and on an accurate estimation of the number of envelope events N in the spatial domain. A discussion of these important details is given in [32].

Combining everything together I show in Fig. 24 the time series of the exceedance probability given in Eq. (43), where I have chosen for observed

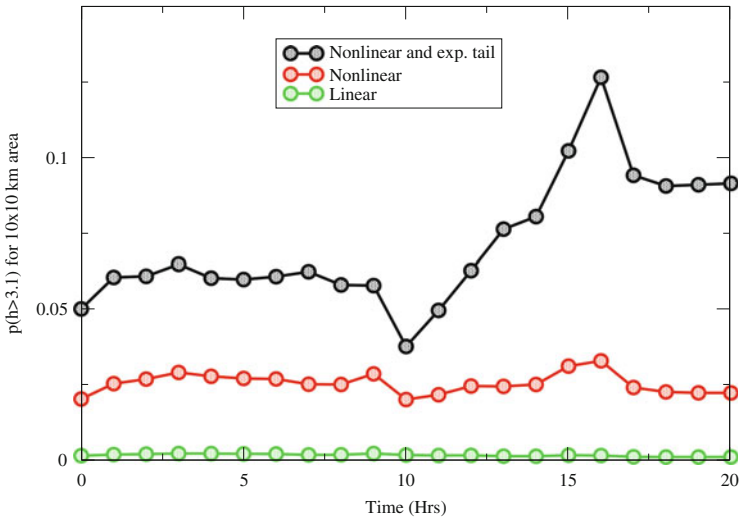

Fig. 24 Evolution in time of simulated exceedance probability $P_{ex}(h^{obs}_{max})$ for $h^{obs}_{max} = 3.1$. Location is the Draupner platform on the 1st of January 1995

dimensionless maximum wave height $h^{obs}_{max} = 3.1$. The size of the spatial domain is $10 \times 10\,\mathrm{km}^2$. Three cases are shown, namely, probabilities according to linear theory (a Gaussian sea state), nonlinear theory and nonlinear theory with an exponential tail. It is seen that according to nonlinear theory with exponential tail added it is fairly likely that the freak wave event could have happened in the Draupner area, but, on the other hand, according to linear theory this does not seem to be very likely. Furthermore with some optimism in mind, it could be argued that there is evidence that the freak wave event should have most likely occurred around 15:00–16:00 h in the afternoon simply because the exceedance probability is maximum at that time. The reason for the maximum is that the waves are so long that shallow water effects play a role. As shown in Fig. 13, in particular the bound-wave part of the kurtosis is a sensitive function of the dimensionless depth and increases quite sharply when the waves become more shallow. Note that for the Draupner wave event the directional wave spectrum was very broad so that the free waves contribution to the kurtosis is not dominant.

9 Conclusions

It is clear that even after 200 years ocean waves is still a very lively field. The last 50 years we have seen tremendous improvements in our ability to forecast waves and by using the methods of Statistical Mechanics we have made great progress in understanding the subject. It has been made plausible how the probability of

the occurrence of extreme events can be related to the mean sea state. A first attempt to develop an operational freak wave system seems to give realistic results. Nevertheless, further developments are required. For example, the determination of the kurtosis of the wave field is based on the narrow-band approximation, which does not give a truthful description of what happens when two or more nonlinear wave trains are present. Further validation of this approach in the field is evidently needed. Global satellite data, such as from the Altimeter and the SAR, would be an ideal source for information on extreme events. However, still a lot of work is needed to extract extreme sea state information from these data.

References

1. Janssen, P.: The Interaction of Ocean Waves and Wind. Cambridge University Press, Cambridge (2004)
2. Janssen, P.A.E.M.: On some consequences of the canonical transformation in the hamiltonian theory of water waves. J. Fluid Mech. **637**, 1–44 (2009)
3. Janssen, P.A.E.M.: Nonlinear four-wave interactions and freak waves. J. Phys. Oceanogr. **33**(4), 863–884 (2003)
4. Stokes, G.G.: On the theory of oscillatory waves. Trans. Camb. Philos. Soc. **8**, 441–473 (1847)
5. Korteweg, D.J., De Vries, G.: Xli. on the change of form of long waves advancing in a rectangular canal, and on a new type of long stationary waves. Lond. Edinb. Dublin Philos. Mag. J. Sci. **39**(240), 422–443 (1895)
6. Sverdrup, H.U., Munk, W.H.: Wind Sea and Swell: Theory of Relations for Forecasting, 44 pp. H.O. Pub. 601, US Navy Hydrographic Office, Washington, DC (1947)
7. Whitham, G.: Linear and Nonlinear Waves. Wiley, New York (1974)
8. Phillips, O.: On the dynamics of unsteady gravity waves of finite amplitude part 1. The elementary interactions. J. Fluid Mech. **9**(02), 193–217 (1960)
9. Hasselmann, K.: On the non-linear energy transfer in a gravity-wave spectrum part 1. General theory. J. Fluid Mech. **12**(04), 481–500 (1962)
10. Benjamin, T.B., Feir, J.: The disintegration of wave trains on deep water part 1. Theory. J. Fluid Mech. **27**(03), 417–430 (1967)
11. Zakharov, V.E.: Stability of periodic waves of finite amplitude on the surface of a deep fluid. J. Appl. Mech. Tech. Phys. **9**(2), 190–194 (1968)
12. Krasitskii, V.P.: On reduced equations in the hamiltonian theory of weakly nonlinear surface waves. J. Fluid Mech. **272**, 1–20 (1994)
13. Krasitskii, V.: On the canonical transformation of the theory of weakly nonlinear waves with nondecay dispersion law. Sov. Phys. JETP **98**, 1644–1655 (1990)
14. Crawford, D.R., Lake, B.M., Saffman, P.G., Yuen, H.C.: Stability of weakly nonlinear deep-water waves in two and three dimensions. J. Fluid Mech. **105**, 177–191 (1981)
15. Yuen, H.C., Lake, B.M.: Nonlinear dynamics of deep-water gravity waves. Adv. Appl. Mech **22**(67), 229 (1982)
16. Krasitskiy, V., Kalmykov, V.: Four-wave reduced equations for surface gravity waves. Izvestiia-Russian Academy of Sciences Atmospheric and Oceanic Physics C/C of Izvestiia-Rossiiskaia Akademiia Nauk Fizika Atmosfery i Okeana **29**, 222–222 (1993)
17. Longuet-Higgins, M.S.: The instabilities of gravity waves of finite amplitude in deep water II. Subharmonics. Proc. R. Soc. Lond. A Math. Phys. Eng. Sci. **360**(1703), 489–505 (1978)
18. Lake, B.M., Yuen, H.C., Rungaldier, H., Ferguson, W.E.: Nonlinear deep-water waves: theory and experiment. Part 2. Evolution of a continuous wave train. J. Fluid Mech. **83**(01), 49–74 (1977)

19. Benjamin, T.B.: Instability of periodic wavetrains in nonlinear dispersive systems. Proc. R. Soc. Lond. A Math. Phys. Eng. Sci. **299**(1456), 59–76 (1967)
20. Shabat, A., Zakharov, V.: Exact theory of two-dimensional self-focusing and one-dimensional self-modulation of waves in nonlinear media. Sov. Phys. JETP **34**(1), 62 (1972)
21. Janssen, P.A.E.M.: Modulational instability and the fermi-pasta-ulam recurrence. Phys. Fluids (1958–1988) **24**(1), 23–26 (1981)
22. Osborne, A.R., Onorato, M., Serio, M.: The nonlinear dynamics of rogue waves and holes in deep-water gravity wave trains. Phys. Lett. A **275**(5), 386–393 (2000)
23. Zakharov, V., Rubenchik, A.: Instability of waveguides and solitons in nonlinear media. Sov. J. Exp. Theor. Phys. **38**, 494 (1974)
24. Fedele, F.: On the kurtosis of deep-water gravity waves. J. Fluid Mech. **782**, 25–36 (2015)
25. Mori, N., Janssen, P.A.E.M.: On kurtosis and occurrence probability of freak waves. J. Phys. Oceanogr. **36**(7), 1471–1483 (2006)
26. Mori, N., Onorato, M., Janssen, P.A.E.M.: On the estimation of the kurtosis in directional sea states for freak wave forecasting. J. Phys. Oceanogr. **41**(8), 1484–1497 (2011)
27. Onorato, M., Osborne, A., Serio, M., Cavaleri, L., Brandini, C., Stansberg, C.: Observation of strongly non-gaussian statistics for random sea surface gravity waves in wave flume experiments. Phys. Rev. E **70**(6), 067302 (2004)
28. Onorato, M., Waseda, T., Toffoli, A., Cavaleri, L., Gramstad, O., Janssen, P., Kinoshita, T., Monbaliu, J., Mori, N., Osborne, A., et al.: Statistical properties of directional ocean waves: the role of the modulational instability in the formation of extreme events. Phys. Rev. Lett. **102**(11), 114502 (2009)
29. Waseda, T.: Impact of directionality on the extreme wave occurrence in a discrete random wave system. In: Proceedings of 9th International Workshop on Wave Hindcasting and Forecasting, Victoria, Canada (2006)
30. Gabor, D.: Theory of communication. Part 1: The analysis of information. J. Inst. Electr. Eng. III Radio Commun. Eng. **93**(26), 429–441 (1946)
31. Janssen, P.A.E.M.: On a random time series analysis valid for arbitrary spectral shape. J. Fluid Mech. **759**, 236–256 (2014)
32. Janssen, P.A.E.M.: How rare is the draupner wave event? ECMWF Technical Memorandum, vol. 775 (2015)
33. Gōda, Y.: Random Seas and Design of Maritime Structures. World scientific, Singapore (2010)
34. Janssen, P.A.E.M.: Notes on the maximum wave height distribution. ECMWF Technical Memorandum, vol. 755 (2015)
35. Janssen, P.A.E.M., Bidlot, J.-R.: On the extension of the freak wave warning system and its verification. ECMWF Technical Memorandum, vol. 588 (2009)
36. Montina, A., Bortolozzo, U., Residori, S., Arecchi, F.: Non-gaussian statistics and extreme waves in a nonlinear optical cavity. Phys. Rev. Lett. **103**(17), 173901 (2009)
37. Walczak, P., Randoux, S., Suret, P.: Optical rogue waves in integrable turbulence. Physical Rev. Lett. **114**(14), 143903 (2015)
38. Haver, S.: A possible freak wave event measured at the draupner jacket January 1, 1995. In: Proceedings of Rogue Waves 2004, pp. 1–8 (2004)
39. Cavaleri, L., Barbariol, F., Benetazzo, A., Bertotti, L., Bidlot, J., Janssen, P.A.E.M., Wedi, N.: The draupner wave: a fresh look and the emerging view, submitted (2015)

Modelling Transient Sea States with the Generalised Kinetic Equation

Sergei Y. Annenkov and Victor I. Shrira

Abstract For historical and technical reasons evolution of random weakly nonlinear wave fields so far has been studied primarily in a quasi-stationary environment, where the main modelling tool is the kinetic equation. In the context of oceanic waves sharp changes of wind do occur quite often and can generate transient sea states with characteristic timescales of up to hundreds of wave periods. It is of great fundamental and practical interest to understand wave field behaviour during short-lived and transient events. At present nothing is known about such ephemeral sea states. One, but not the only, reason was that there were no adequate modelling tools. The generalised kinetic equation (gKE) derived without assumptions of quasi-stationarity seems to fill this gap. Here we study transient events with the gKE aiming to understand what is going during such events and capabilities of the gKE in capturing them. We find how wave spectra evolve being subjected to sharp changes of wind, while tracing in parallel the concomitant evolution of higher moments characterizing the field departure from gaussianity. We demonstrated the capability of the gKE to capture short-lived events, in particular, we found sharp brief increase of kurtosis during squalls, which suggests significant increase of the likelihood of freak waves during such events. Although the study was focussed upon wind wave context the approach is generic and is transferrable to random weakly nonlinear wave fields of other nature.

1 Introduction

Winds over the sea are known to be variable on all timescales, including rapid changes over tens of minutes [5]. Although sharp changes of wind do occur quite often and can generate transient sea states with characteristic timescales of up to hundreds of wave periods, at present very little is known about such sea states. An experimental study of short lived transient phenomena is extremely difficult, if not impossible apart from laboratory wind wave tanks; so far, no systematic laboratory study have been undertaken. In wind wave modelling the fast variability was not

S.Y. Annenkov (✉) • V.I. Shrira
School of Computing and Mathematics, Keele University, Keele ST5 5BG, UK
e-mail: s.annenkov@keele.ac.uk; v.i.shrira@keele.ac.uk

M. Onorato et al. (eds.), *Rogue and Shock Waves in Nonlinear Dispersive Media*,
Lecture Notes in Physics 926, DOI 10.1007/978-3-319-39214-1_6

taken into account for two main reasons. First, the wind forecasting did not resolve such scales (although the situation has radically improved very recently) and, hence, there was no need in such modelling for operational forecasting. Now the time resolution of wind forecasting has dramatically improved, which makes modelling of transient states highly desirable. Second, on the theoretical side, there have been no adequate mathematical tool able to describe evolution of random wave fields on such short scales. This second difficulty was not specific for wind waves, but is common for all random nonlinear wave fields. What in the wave field behaviour during short-lived and transient events is of fundamental interest in and beyond the context of wind waves? It is a priori plausible that during these events freak waves are more likely. It would be of obvious interest to check this assumption and describe quantitatively the evolution of the wave field statistical characteristics. Since there is now a surge of interest in freak waves in other physical contexts, such a clarification is relevant beyond the water wave context. Here we report the progress in clarifying these questions achieved by employing a new mathematical tool—the generalised kinetic equation (gKE). In what follows we consider only the water wave context.

Most of the existing approaches to the modelling of random weakly nonlinear waves are based on the kinetic equation (KE) which in the water wave context is also often referred to as the Hasselmann equation [15, 22]. For water waves it was first derived by Hasselmann [9] in the form

$$\frac{dn(\mathbf{k},t)}{dt} = S_{inp} + S_{diss} + S_{nl},$$

were $n(\mathbf{k},t)$ is the two-dimensional wave action spectrum as a function of wavevector $\mathbf{k}$ and time t, the terms S_{inp} and S_{diss} describes wind forcing and dissipation respectively. The interaction term S_{nl}, dominant for energy carrying waves, is derived from first principles employing an asymptotic procedure based upon smallness of nonlinearity parameter ε and a number of additional assumptions:

$$S_{nl} = 4\pi \int T^2_{0123} f_{0123} \delta_{0+1-2-3} \delta(\omega_0 + \omega_1 - \omega_2 - \omega_3)\, \mathrm{d}\mathbf{k}_{123}, \tag{1}$$

where $f_{0123} = n_2 n_3 (n_0 + n_1) - n_0 n_1 (n_2 + n_3)$, $n_i \equiv n(\mathbf{k}_i)$ are spectral densities at wavevectors $\mathbf{k}_i$, $\delta_{0+1-2-3} \equiv \delta(\mathbf{k}_0 + \mathbf{k}_1 - \mathbf{k}_2 - \mathbf{k}_3)$ and T_{0123} is given by an explicit (but long) expression.

Crucially, the expression for S_{nl} is derived under the assumption of quasi-stationarity of the random wave field, and the resulting equation has the built-in $O(\varepsilon^{-4})$ timescale of evolution. Therefore, strictly speaking, the Hasselmann equation is not applicable to situations with rapid changes of environment, such as wind gusts. Due to the lack of alternatives, this fact is usually ignored. The Hasselmann theory was used to model the response to an instant and sharp increase or decrease of wind (e.g. [21]). It is not clear to what extent these results can be trusted, since the conditions of validity of the Hasselmann equation are clearly violated. There is experimental evidence that after a sharp change of wind random wind waves appear

to evolve faster than the $O(\varepsilon^{-4})$ timescale predicted by the KE [3, 4, 19, 20]. An example of a natural phenomenon that cannot be legitimately described on the basis of the Hasselmann equation is a squall, understood as a sharp increase of wind for a short time. Squalls are an important natural hazard, and their implications for wind waves are poorly understood.

In [1], extending the seminal work by Janssen [12] a generalised kinetic equation (gKE) was derived, without employing the $O(\varepsilon^{-4})$ scaling assumption. The nonlinear term of the gKE differs from the classical S_{nl} in two important aspects. First, it is nonlocal in time: the evolution of a spectrum depends not just on the spectrum itself at the chosen instant, but on the previous history of evolution. Therefore, the gKE requires an initial condition for a fourth-order correlator specified below which contains some residual information about the "previous" history. If this correlator is taken as zero at the initial moment, which corresponds to prescribing completely uncorrelated phases at the start of the evolution (we will refer to such a situation as "cold start"), the correlator ceases to be zero at later times. Second, while the Hasselmann S_{nl} includes only exactly resonant wave interactions, the gKE explicitly includes all interactions, although, as one might expect, the evolution primarily depends on those interaction that are close to resonance. First attempts at the numerical simulation of the gKE were made by Gramstad and Stiassnie [7, 8], who examined the initial stage of evolution of model spectra. One of the prime purposes of this study is to present and discuss in detail a new efficient parallel algorithm for the numerical simulation of the gKE and to perform computations of spectral evolution under constant and changing wind. In this context we systematically examine and demonstrate the capabilities of the gKE. To this end we compare the gKE simulations with the simulations of the Hasselmann equation, the latter is integrated using the well-established WRT algorithm, the code for which was kindly provided by G. van Vledder. Under constant wind, there is very little difference between the predictions of the KE and gKE: according to both equations spectra approach the same asymptotic regime for large time. For sharp changes of wind only the gKE is expected to be valid, and we demonstrate with the gKE how the wave spectra respond to such changes, for example, how a sharp increase of wind leads to a new quasi-equilibrium of spectrum with the increased forcing. However, in itself the spectral evolution provides only statistically averaged characteristics of the field (e.g. significant wave height, steepness, position of the spectral peak, etc), and does not reveal changes in the probability of anomalously large, freak waves. To address this question one also needs to find the probability density function of the height elevations, or, as an intermediate step, dynamics of higher moments of surface elevation such as skewness and kurtosis. An important feature of the gKE is that along with the spectral evolution, it also provides the dynamical component of kurtosis, which is linked to the real part of the same fourth order cumulant whose imaginary part determines the spectral evolution. The second constituent of kurtosis—the bound harmonic kurtosis can also be found in terms of the spectrum $n(\mathbf{k}, t)$ [13]. The skewness can be also expressed in terms of $n(\mathbf{k}, t)$ [13]. Thus, expressing the higher moments as functions of the spectrum, we can

obtain the probability density function (p.d.f) of the surface elevation, which is the key characteristics of the field evolution from the freak wave perspective. A disproportionally large share of studies of freak waves is concerned with narrow band spectra [14, 16], which is relevant for nonlinear optics but is questionable for oceanic water waves. Here we consider only broadband wave fields with the spectral width sufficient for the kinetic description to work, typical of oceanic conditions.

The paper is organised as follows. In Sect. 2, we present a brief review of the assumptions employed in the derivation of the two kinetic equations: KE and gKE. In Sect. 3, the numerical algorithm for the gKE is discussed in detail. In Sect. 4, we show the results of the simulations of the spectral evolution under constant wind, and perform the comparison with the classical KE. Section 5 discusses examples of wave field evolution forced by rapidly changing wind. Section 6 considers the effect of periodic remixing of phases in the numerical simulations of the gKE. Section 7 provides the conclusions and discussion.

2 Theoretical Background

Consider a random field of potential waves at the surface of ideal incompressible fluid of infinite depth. The non-potential effects, which are always present due to wind, are assumed to be in the higher orders. The classic Hasselmann equation

$$\frac{\partial n_0}{\partial t} = 4\pi \int T^2_{0123} f_{0123} \delta_{0+1-2-3} \delta(\omega_0 + \omega_1 - \omega_2 - \omega_3)\, \mathrm{d}\mathbf{k}_{123} + S_f, \tag{2}$$

is valid as long as the interest is confined to slow $O(\varepsilon^{-4})$ evolution. Here $n_i \equiv n(\mathbf{k}_i)$ is the spectral density of wave action at wavenumber $\mathbf{k}_i$ (second-order correlator), $f_{0123} = n_2 n_3 (n_0 + n_1) - n_0 n_1 (n_2 + n_3)$ and S_f is a forcing/dissipation term.

Virtually all studies of long-term evolution of realistic broadband wind wave spectra are based on (2). There are several approximations involved in its derivation. Here, we present only a brief review; a detailed discussion can be found e.g. in [15, 18]. First, it is assumed that a wave field is statistically homogeneous in space, which implies

$$\langle b(\mathbf{k}, t) b^*(\mathbf{k}_1, t) \rangle = n(\mathbf{k}) \delta(\mathbf{k} - \mathbf{k}_1) \equiv n_{\mathbf{k}} \delta_{01}. \tag{3}$$

where $b(\mathbf{k}, t)$ is the (deterministic) complex amplitude at wavevector $\mathbf{k}$ and angular brackets denote ensemble averaging.

The second crucial assumption is quasi-Gaussianity of the wave field. In the zeroth approximation in ε a free wave field has Gaussian statistics, for which all odd-order correlators vanish, and the fourth-order correlator decomposes into products of pair correlators,

$$J^{(0)}_{0123} \delta_{0+1-2-3} = \langle b_0^* b_1^* b_2 b_3 \rangle = n_0 n_1 \left(\delta_{0-2} \delta_{1-3} + \delta_{0-3} \delta_{1-2} \right). \tag{4}$$

In the next approximation in ε correlations due to resonant nonlinear interactions result in deviations from Gaussianity and manifest themselves in a non-zero fourth-order cumulant $J^{(1)}_{0123}$. The essential hypothesis is that the wave field is presumed to remain quasi-Gaussian over the timescale of evolution, that is, for all times the cumulant $J^{(1)}_{0123}$ should remain small compared to $J^{(0)}_{0123}$. By virtue of the same approximation, cumulants of orders higher than four are neglected. Then the differential equation for the cumulant $J^{(1)}_{0123}$ is obtained in the form

$$\left(\mathrm{i}\frac{\partial}{\partial t} + \Delta\omega\right) J^{(1)}_{0123} = -2T_{0123} f_{0123}, \tag{5}$$

where $\Delta\omega = \omega_0 + \omega_1 - \omega_2 - \omega_3$, and $f_{0123} = n_2 n_3 (n_0 + n_1) - n_0 n_1 (n_2 + n_3)$. If the evolution of a wave field is assumed to depend only on slow time μt, so that $\mu/\Delta\omega \ll 1$, then an approximate solution to (5) for large time is obtained in terms of generalised functions

$$J^{(1)}_{0123}(t) = -2T_{0123}\left[\frac{P}{\Delta\omega} + \mathrm{i}\pi\delta(\Delta\omega)\right] f_{0123}(t), \tag{6}$$

where P stands for "principal value". Together with the equation for the evolution of n_0

$$\frac{\partial n_0}{\partial t} = 2\mathrm{Im}\int T_{0123} J^{(1)}_{0123}\delta_{0+1-2-3}\,\mathrm{d}\mathbf{k}_{123}. \tag{7}$$

this leads to the Hasselmann equation (2). Here we've omitted the forcing/dissipation term S_f.

Therefore, the third crucial assumption is quasi-stationarity: a wave field evolves slowly (it is commonly assumed that $\mu \sim \varepsilon^4$ while $\Delta\omega$ for four-wave interactions is $O(\varepsilon^2)$), and a large-time limit is taken. The latter implies that the approach is only applicable to wave fields evolving for a long time under slowly-varying conditions (no faster than the slow $O(\varepsilon^{-4})$ implied for the wave field itself).

The assumption of quasi-stationarity is in fact very restrictive. A wave field can be driven out of equilibrium by a number of factors, and there is no reason to assume a priori that it will evolve on the $O(\varepsilon^{-4})$ timescale. Besides that, wind forcing in natural conditions is known to be variable on all timescales.

If we drop the assumption of quasi-stationarity, that is, include faster variability of statistical moments of a wave field, we should use, instead of (6), the exact solution to (5) in the form

$$J^{(1)}_{0123}(t) = 2\mathrm{i}T_{0123}\int_0^t \mathrm{e}^{-\mathrm{i}\Delta\omega(\tau-t)} f_{0123}\,\mathrm{d}\tau + J^{(1)}_{0123}(0)\mathrm{e}^{\mathrm{i}\Delta\omega t}, \tag{8}$$

where $J^{(1)}_{0123}(0)$ is the initial value of the cumulant. This leads to the *generalized kinetic equation* (gKE) derived in [1]

$$\frac{\partial n_0}{\partial t} = 4\mathrm{Re}\int\left\{T^2_{0123}\left[\int_0^t \mathrm{e}^{-\mathrm{i}\Delta\omega(\tau-t)} f_{0123}\,\mathrm{d}\tau\right] - \frac{\mathrm{i}}{2}T_{0123}J^{(1)}_{0123}(0)\mathrm{e}^{\mathrm{i}\Delta\omega t}\right\}\delta_{0+1-2-3}\,\mathrm{d}\mathbf{k}_{123} + S_f\,. \tag{9}$$

Various properties of this equation were thoroughly discussed in the review [18]. In the next section, we consider the numerical algorithm which we employ to simulate wave field evolution with the gKE.

3 Numerical Algorithm

Development of a numerical algorithm for the Hasselmann equation has a long history that spans over about 50 years. Despite considerable effort and substantial progress in computational resources, the numerical simulation of the equation is still considered to be difficult and time-consuming, and therefore impractical for implementation in operational wave models. The main difficulty lies in the fact that the integrand in the Hasselmann equation is specified at the resonant surface, which has a very complex functional form.

From the point of view of numerics, gKE (Eq. (9)) at first glance looks much more complicated than the KE (Eq. (2)). First, it is not restricted to resonant surface, but formally includes all resonant and non-resonant interactions (although it is reasonable to assume that only the interactions that are not too far from the resonance surface contribute to the spectral evolution). Although this fact dramatically increases the number of interactions that need to be considered, they can be treated in parallel, efficiently utilizing the advantages of modern supercomputers. (We note that at this time, we are not aware of a parallel algorithm for computation of the nonlinear interaction term of the Hasselmann equation).

Second, the gKE is nonlocal in time, so that the evolution of the spectrum depends on the time integration over the previous history of evolution, starting from the initial moment when the value of cumulant $J^{(1)}_{0123}(0)$ is prescribed as the initial condition. However, the gKE can be solved iteratively. On each time step, the value of $J^{(1)}_{0123}$ is computed according to (8) and taken as the new initial condition, so that the time integration is performed over one timestep only.

Therefore, we adopt the following strategy. First, we specify a computational grid $\omega_{min} \le \omega \le \omega_{max}$ and $\theta_{min} \le \theta \le \theta_{max}$, where ω is frequency (it is convenient to have frequency spaced logarithmically) and θ is angle. For each three grid points with wavevectors $\mathbf{k}_1, \mathbf{k}_2, \mathbf{k}_3$, a fourth wave is found as $\mathbf{k}_4 = \mathbf{k}_1 + \mathbf{k}_2 - \mathbf{k}_3$. Since $\mathbf{k}_4$ generally does not coincide with one of the grid points, bilinear interpolation is used

to find the corresponding amplitude. All interaction coefficients are pre-calculated, stored and distributed evenly across the parallel processors. The initial condition for $J^{(1)}_{0123}(0)$ is taken as zero; this choice is referred to as "cold start". Then, the right-hand side of gKE (9) and the value of $J^{(1)}_{0123}$ on each timestep according to (8) are computed, and $J^{(1)}_{0123}$ is used as the new initial condition on the next timestep. We employ the standard Runge-Kutta-Fehlberg time-stepping algorithm with automatic step choice. Since almost all computations are performed in parallel, the algorithm has a nearly perfect scalability (that is, the computational time for each timestep is nearly inversely proportional to the number of parallel processors used).

4 Simulations with Constant Wind

In order to test and validate the new numerical algorithm for the gKE we carry out simulations in parallel with the classic WRT algorithm for the KE. First we present a few simulations of a wave field evolution under a constant wind, i.e. when the gKE and the KE are both applicable and are expected to give essentially the same evolution. In both cases, the employed computational grid has 101 logarithmically spaced points in the range $0.5 \le \omega \le 3$ and 31 uniformly spaced angles $-7\pi/9 \le \theta \le 7\pi/9$. For the gKE simulations, all interactions satisfying $\Delta\omega/\omega_{min} \le 0.25$, where ω_{min} is the minimum frequency of waves within the interacting quartet, were taken into account. Thus, the algorithm accounts for all resonant and approximately resonant interactions allowing a large mismatch. The total number of interactions exceeds $3 \cdot 10^9$. Time stepping is performed by Runge-Kutta-Fehlberg algorithm with absolute tolerance 10^{-10} and timestep limited from above by approximately $1/3$ characteristic wave period. Initial conditions were specified as the spectra parameterised by Donelan et al. [6] for $2 \le U_{10}/c_p \le 6$, where c_p is the phase speed of the initial spectral peak, in the form

$$E(\omega) = 4\pi^2 \frac{\alpha g^2}{\omega^5} (\omega/\omega_p) \exp\left[-\left(\omega/\omega_p\right)^{-4}\right] \gamma^{\exp\left[-\left(\omega/\omega_p - 1\right)^2/\left(2\sigma^2\right)\right]} D_\omega(\theta), \qquad (10)$$

where ω_p is the frequency of the spectral peak, and the spectral parameters α, γ and σ are linked to the inverse wave age parameter U_{10}/c_p, with U_{10} being the wind speed in the mean direction of wave propagation at the 10 m height. The parameters have the following values [6]

$$\alpha = 0.006(U_{10}/c_p)^{0.55}$$

$$\sigma = 0.08\left[1 + 4/(U_{10}/c_p)^3\right]$$

$$\gamma = \begin{cases} 1.7 & \text{for } 0.83 < U_{10}/c_p < 1, \\ 1.7 + 6.0 \lg(U_{10}/c_p) & \text{for } U_{10}/c_p \ge 1 \end{cases}$$

The directional spread has the form

$$D_\omega(\theta) = \frac{1}{2}\beta \mathrm{sech}^2(\beta\theta), \tag{11}$$

where the mean wave direction corresponds to $\theta = 0$, and

$$\beta = \begin{cases} 2.61(\omega/\omega_p)^{1.3} & \text{for } 0.56 < \omega/\omega_p < 0.95, \\ 2.28(\omega/\omega_p)^{-1.3} & \text{for } 0.95 < \omega/\omega_p < 1.6, \\ 1.24 & \text{otherwise.} \end{cases}$$

Wind forcing is according to [10]:

$$S_{inp} = \gamma(\mathbf{k})n(\mathbf{k}),$$
$$\gamma(\mathbf{k}) = 0.12\frac{\rho_a}{\rho_w}\omega(\zeta - 1)^2 \quad \text{for} \quad 1 < \zeta < 7.4$$

and zero otherwise, where

$$\zeta = 0.85\frac{U_{10}}{c_{ph}}\cos\theta,$$

ρ_a/ρ_w is the ratio of air and water densities, and c_{ph} is the wave phase speed.

One example of the results for $U_{10}/c_p = 5$ is shown in Fig. 1 (we will omit the subscript at U_{10} in the remainder of the paper). There is very little difference in

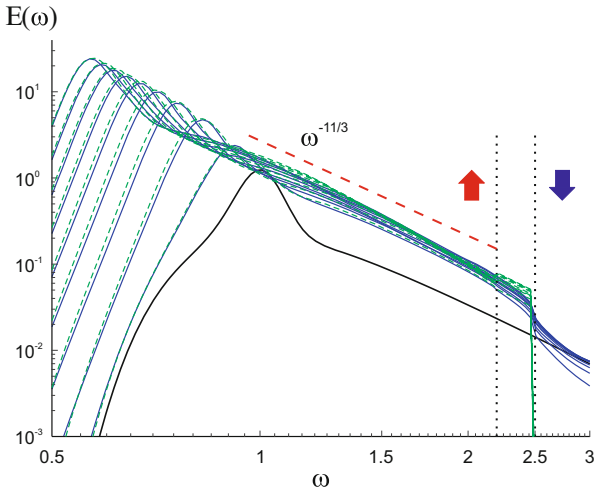

Fig. 1 Evolution of the energy spectrum $E(\omega)$ with time, under constant wind forcing with initial $U/c_p = 5$. Spectra are plotted every 100 characteristic periods, gKE (*blue curves*) vs KE (*dashed green curves*)

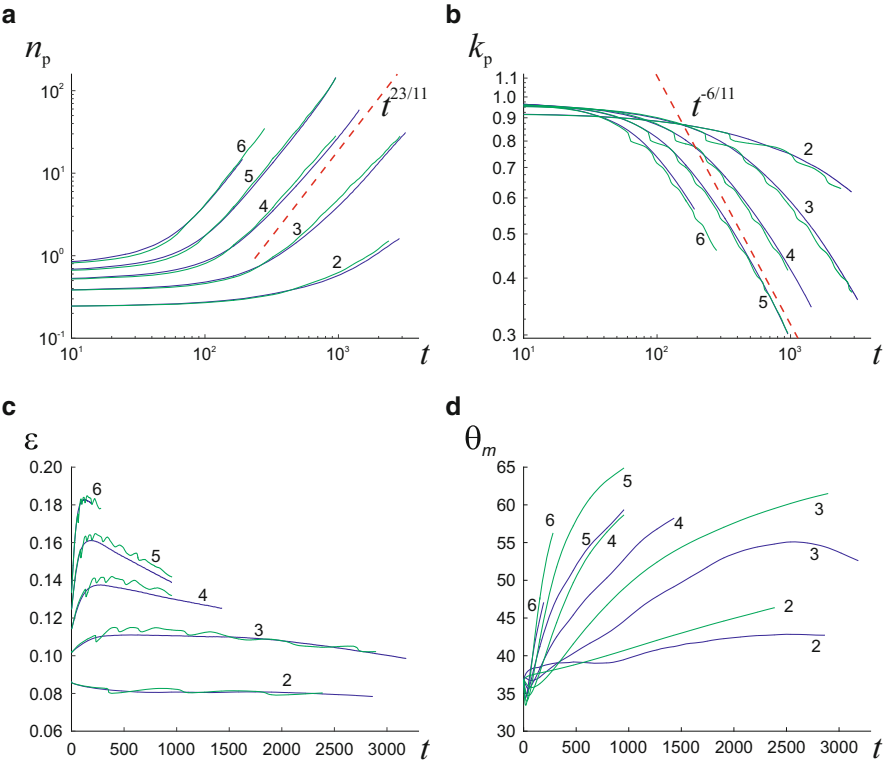

Fig. 2 Evolution of various spectral characteristics for simulations with constant wind, with wind speed in the range $2 \le U/c_p \le 6$, where c_p is the initial phase speed of the spectral peak. *Blue curves*: gKE, *green curves*: KE. Numbers indicate the wind speed U/c_p. (**a**) amplitude of the peak (**b**) peak wavenumber (**c**) wave steepness (**d**) directional spread θ_m (second moment of directional distribution

the spectral evolution obtained with both equations. The energy spectrum follows the familiar route of self-similar evolution under a constant wind, with the spectral slope close to the theoretically predicted angle $\omega^{-11/3}$ [22]. In Fig. 2, we show the evolution of a number of spectral characteristics for different wind speeds, both for the gKE and the KE: amplitude and wavenumber of the spectral peak, wave steepness and the directional spread (the average of the second-order moment of directional distribution), defined as

$$\theta_m = \overline{\theta_2(k)}, \qquad \theta_2(k) = \left(\int_0^{\pi/2} \theta^2 D(k,\theta)\, \mathrm{d}\theta \right)^{1/2} \left(\int_0^{\pi/2} D(k,\theta)\, \mathrm{d}\theta \right)^{-1/2},$$

where $D(k,\theta)$ is the angular distribution of the spectrum [11]. All characteristics demonstrate very close behaviour and tend to the same known asymptotics. The

only considerable difference is seen in the evolution of the directional spread, which is noticeably slower in the case of the gKE, for all wind speeds.

One of the important features of the gKE is that it also allows one to obtain the evolution of higher moments of the surface elevation along with the evolution of the spectrum. The fourth moment of the surface elevation η

$$m_4 = \langle \eta^4 \rangle = \frac{3}{2} \mathrm{Re} \int (\omega_0 \omega_1 \omega_2 \omega_3)^{1/2} J^{(1)}_{0123} \, \mathrm{d}\mathbf{k}_{0123}$$

when the departure from gaussianity is small can be presented as a sum of two components: the first, $m_4^{(d)}$, is due to wave resonant interactions and the second—due to wave field bound harmonics. In the context of freak wave predictions the kurtosis, an appropriately normalized and centred fourth moment, is a more telling characteristics of the field departure from gaussianity. Its component due to wave interactions called "dynamical kurtosis"

$$C_4^{(d)} = m_4^{(d)} / m_2^2 - 3, \qquad \text{where } m_2 = \int \omega_0 n_0 \, \mathrm{d}\mathbf{k}_0$$

represents a weighted integral of $\mathrm{Re} J^{(1)}_{0123}$. When we simulate field evolution using gKE we find the correlator $J^{(1)}_{0123}$ at each time step. Thus, the dynamical kurtosis is conveniently obtained along with the spectral evolution (which, according to (9), is linked to $\mathrm{Im} J^{(1)}_{0123}$). Note that while the spectral evolution depends only on the interactions close to resonance, all resonant and non-resonant interactions contribute to kurtosis. Therefore, in reality it may be necessary to add a certain correction. This is illustrated in Fig. 3, where the evolution of $C_4^{(d)}$ obtained along with the spectrum is shown together with the corrected $C_4^{(d)}$, obtained using all the interactions. In what follows only the corrected $C_4^{(d)}$ is used.

In Fig. 4, we show the evolution of $C_4^{(d)}$ for a wide range of wind speeds. We choose "cold start" as initial condition, hence the value of the kurtosis is initially zero, then there is a rather sharp spike, depending on wind speed, although even for the high winds the value of $C_4^{(d)}$ does not exceed 0.05. Then the dynamical kurtosis appears to approach a universal curve, remarkably, irrespective of the wind. The initial sharp spike is due to the chosen initial condition: although Donelan's parametrization is close to quasi-equilibrium, it does not quite coincide with it.

The other component of non-gaussianity is due to bound harmonics, and can be calculated from the spectrum, if the dynamic non-gaussianity is small, i.e., if the dynamical kurtosis $C_4^{(d)} \ll 1$. Second moment has the form

$$\begin{aligned} \mu_2 = \langle \eta^2 \rangle &= \int \omega_0 n_0 \, \mathrm{d}\mathbf{k}_0 + \int \left(\mathscr{A}^2_{0,1} + \mathscr{B}^2_{0,1} + 2\mathscr{C}_{0,0,1,1} \right) \omega_0 \omega_1 n_0 n_1 \, \mathrm{d}\mathbf{k}_{01} \\ &= \int \omega_0 n_0 \, \mathrm{d}\mathbf{k}_0 \end{aligned}$$

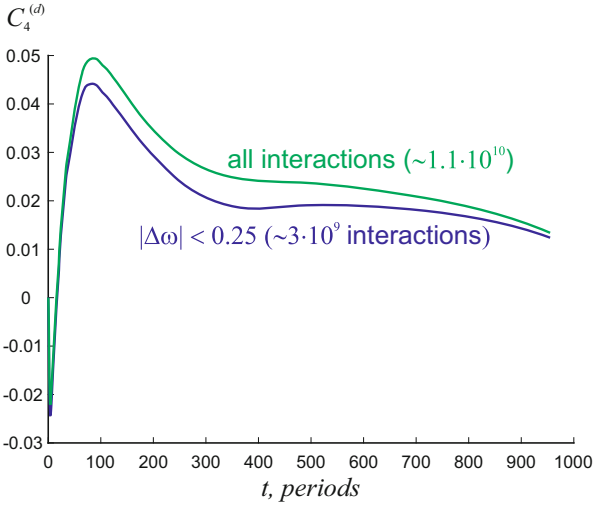

Fig. 3 Evolution of dynamical kurtosis for $U/c_p = 5$: value obtained along with simulations (*blue*) and using all resonant and non-resonant interactions (*green*)

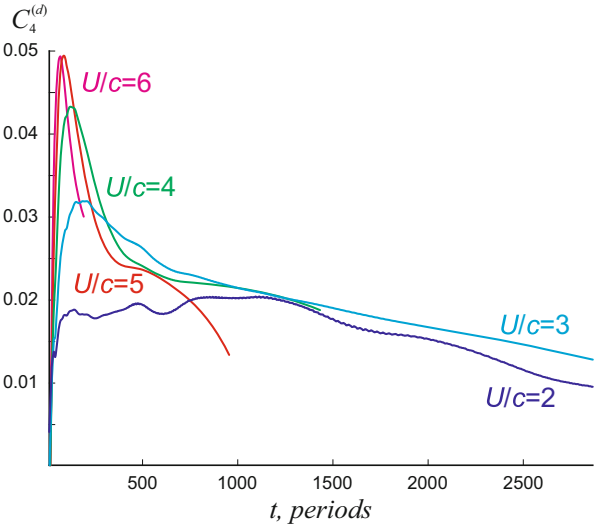

Fig. 4 Evolution of the dynamical kurtosis $C_4^{(d)}$ for various wind speeds U/c_p

The second integral in the right-hand side cancels due to symmetry [2]. Third moment and fourth moments have the form (see [2] for details)

$$\mu_3 = \langle \eta^3 \rangle = 3 \int (\mathscr{A}_{0,1} + \mathscr{B}_{0,1}) \omega_0 \omega_1 n_0 n_1 \, \mathrm{d}\mathbf{k}_{01}$$

$$\mu_4 = 3 \int \omega_0 \omega_1 n_0 n_1 \, \mathrm{d}\mathbf{k}_{01} + 12 \int \mathscr{J}^{(4)}_{012} \omega_0 \omega_1 \omega_2 n_0 n_1 n_2 \, \mathrm{d}\mathbf{k}_{012}$$

Then, the bound harmonic components of skewness and kurtosis are

$$C_3^{(b)} = \frac{\mu_3}{\mu_2^{3/2}}, \qquad C_4^{(b)} = \frac{\mu_4}{\mu_2^2} - 3.$$

Coefficients were derived by Janssen [13].

In Fig. 5, we show the evolution of bound harmonics kurtosis $C_4^{(b)}$ for different wind speeds. Bound harmonics kurtosis is an integral characteristic of the spectrum, so it depends on wind, with approximately quadratic dependence on wave steepness. Evolution of the skewness is shown in Fig. 6 and is similar (but the dependence on the steepness is approximately linear in this case).

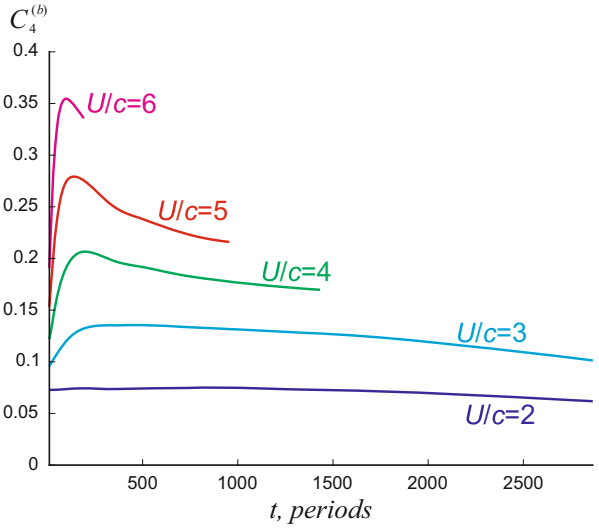

Fig. 5 Evolution of the bound harmonics kurtosis $C_4^{(b)}$ for various wind speeds U/c_p

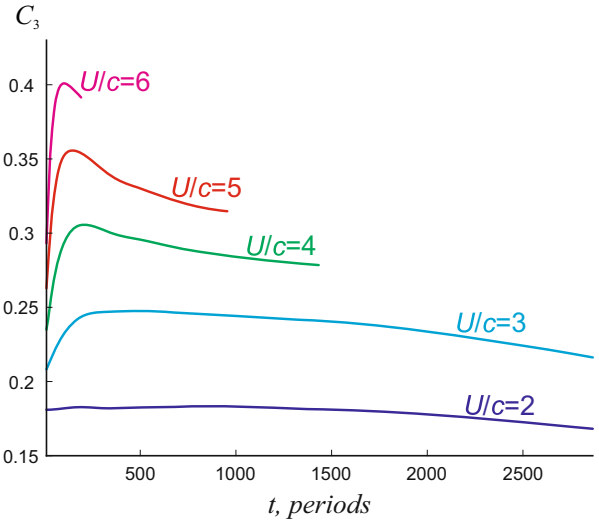

Fig. 6 Evolution of the skewness $C_3^{(b)}$ for various wind speeds U/c_p

5 Sharp Changes of Wind Speed

In this section, we perform simulations with the gKE for the case of wind which is, at a certain moment of time, instantly increasing to a larger value (from U/c_p equal to 2,3,4 to 5 or 7.5). Spectral evolution for the example with $U/c_p = 3$ initially and then, after approximately 800 periods of evolution, instantly increasing to $U/c_p = 7.5$, is shown in Fig. 7. Before the increase, the spectrum is in the quasi-stationary state, evolving according to the asymptotics shown in Fig. 2. After the increase, the spectrum undergoes a rapid transition towards a new quasi-stationary state, corresponding to the increased forcing. Figure 8 shows the evolution of the dynamical kurtosis for all cases of instant wind increase. A sharp increase of forcing leads to a very rapid increase of $C_4^{(d)}$ (for a few dozens of characteristic periods), which then returns to the value close to the original one. Bound harmonics kurtosis (Fig. 9) again follows the evolution of the total energy of the spectrum. The bound harmonics kurtosis attains an order of magnitude larger values and thus to leading order determines the departure from gaussianity. The relaxation of its peak values to quasi-stationary curve happens on a much longer scale than the relaxation of the dynamical kurtosis.

Figure 10 shows the evolution of the dynamical kurtosis for the case of squall (wind instantly increasing to $U/c_p = 5$ or 7 and then instantly decreasing to the original value after 300 and 100 characteristic periods respectively). The dynamical kurtosis starts decreasing, after a sharp maximum, before the end of the squall, but the end of squall accelerates the decrease. Bound harmonics kurtosis (Fig. 11) after the squall decreases to a new value close to its value before the squall and then

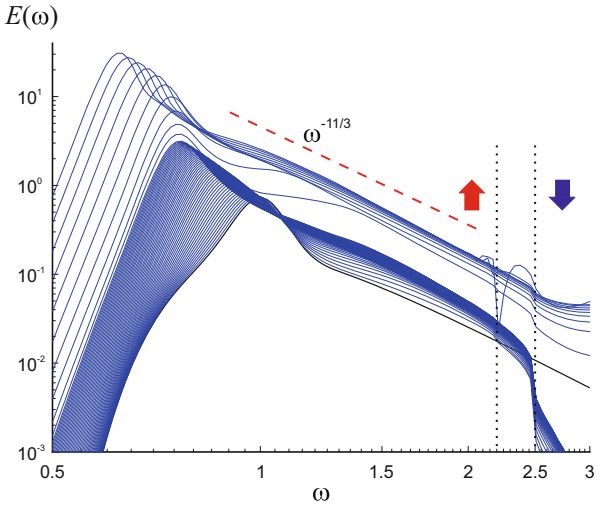

Fig. 7 Evolution of the energy spectrum $E(\omega)$ with time, under constant wind forcing with initial $U/c_p = 3$, after about 800 periods instantly increasing by a factor of 2.5. Spectra are plotted every 22 characteristic periods

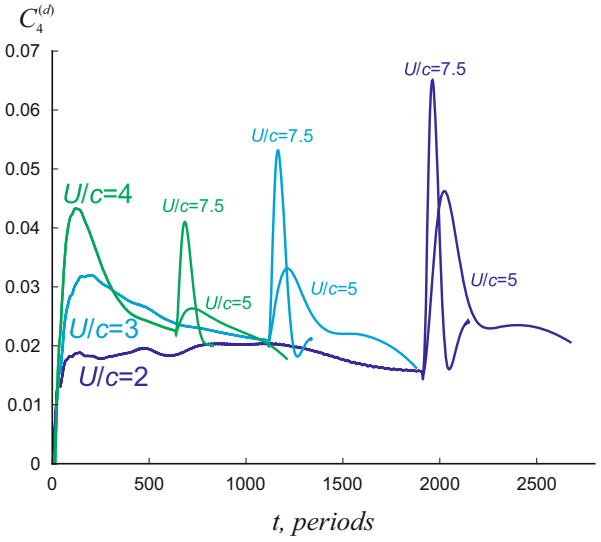

Fig. 8 Evolution of the dynamical kurtosis $C_4^{(d)}$, initially under constant wind forcing with initial $U/c_p = 2, 3, 4$, then instantly increasing to 5 or 7.5

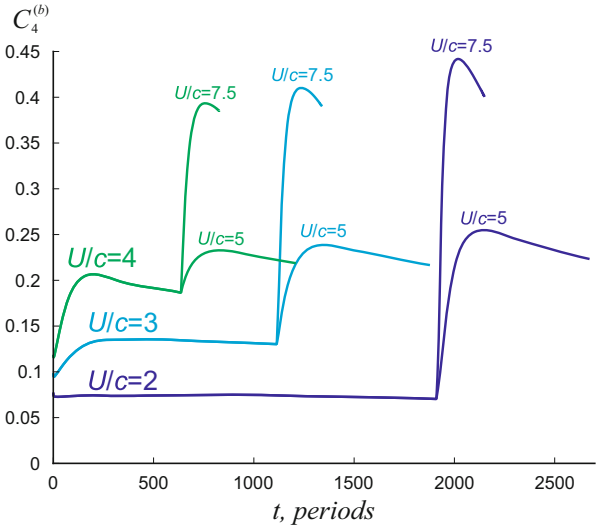

Fig. 9 Evolution of the bound harmonics kurtosis $C_4^{(b)}$, initially under constant wind forcing with initial $U/c_p = 2, 3, 4$, then instantly increasing to 5 or 7.5

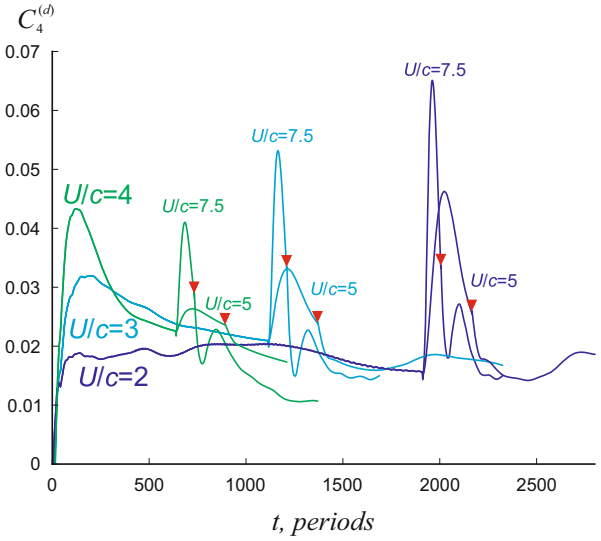

Fig. 10 Evolution of the dynamical kurtosis $C_4^{(d)}$, initially under constant wind forcing with initial $U/c_p = 2, 3, 4$, then instantly increasing to 5 or 7.5 and decreasing back to the initial value. *Red triangles* mark end of squall

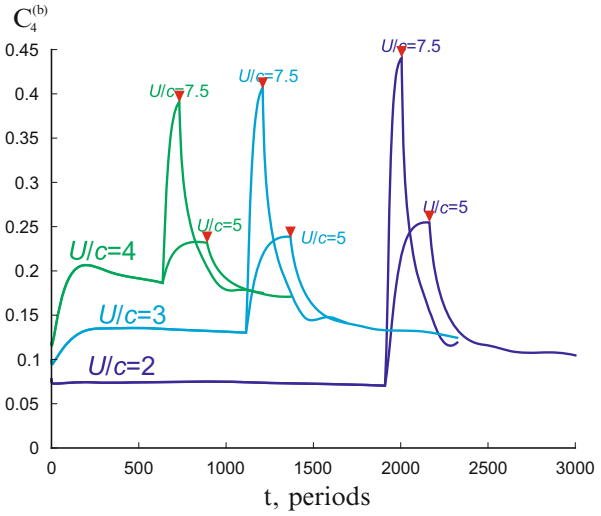

Fig. 11 Evolution of the bound harmonics kurtosis $C_4^{(b)}$, initially under constant wind forcing with initial $U/c_p = 2, 3, 4$, then instantly increasing to 5 or 7.5 and decreasing back to the initial value. *Red triangles* mark end of squall

continues the slow decrease along a certain curve, irrespective of the value of wind speed.

6 Wave Field Decorrelation

In contrast to simulations with in the KE, for numerical simulations of the gKE it is necessary to specify an initial condition for the cumulant $J^{(1)}_{0123}$, which summarizes the "previous" evolution of the spectrum. At the start of a simulation, this condition is usually set at zero and is referred to as "cold start". This means that the phases are initially completely uncorrelated, and then small correlations arise during the evolution. In water wave context the "cold start" is in fact an artificial unphysical event, except for the case of wave tank modelling of the spectrum initially set up by a wavemaker. However it is a natural initial condition in nonlinear optics for waves propagating in a fibre [17]. It is assumed that the memory of the cold start is lost after a few hundred periods of the evolution. The authors of [8] studied the effect of setting $J^{(1)}_{0123}$ to zero periodically during the evolution, and found that it has a considerable effect in the purely one-dimensional case where the spectral evolution otherwise stops, but the evolution of the two-dimensional spectra is not much affected. They suggested that periodical setting $J^{(1)}_{0123}$ to zero might be a way to improve efficiency of simulation with the gKE. In order to better understand how the setting $J^{(1)}_{0123}$ to zero affects the evolution of the spectrum and of the

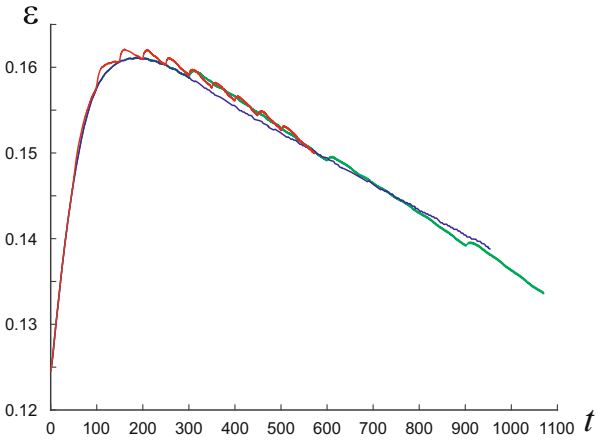

Fig. 12 Evolution of wave steepness for U/c_p initially equal to 5: with the decorrelation of phases every 50 periods (*red curve*), every 300 periods (*green curve*), and without decorrelation (*blue curve*)

dynamical kurtosis, we repeat the numerical experiment shown in Fig. 1 with setting the cumulant $J^{(1)}_{0123}$ to zero every 50 and every 300 characteristic periods. This is equivalent to the periodic decorrelation of the phases of the interacting waves. The effect is mostly noticeable in the evolution of the wave steepness, which is shown in Fig. 12. The remixing of the phases leads to an instant stop of the energy flux to high wavenumbers, which puts the spectral evolution to a stop and results in a fast, within a dozen periods, small but noticeable increase of the wave steepness, which then returns to its original evolution. The effect of the phases decorrelation is more pronounced in the evolution of the dynamical kurtosis, shown in Fig. 13. The kurtosis is set to zero by the remixing of the phases, but then, approximately over a hundred wave periods, returns to the original evolution. Therefore remixing could be justified only for the situations when the external conditions are steady and one is interested in average value of kurtosis over timescales of thousands of wave periods. The effect of mixing on evolution of spectra is hardly visible and therefore is not shown. The overall conclusion is that for the simulations of spectra periodic phase decorrelation is harmless (unless we are interested in the high-frequency part of the spectrum). However, we note that this conclusion was made on the basis of our gKE simulations of wave field evolution with a simplified wind forcing. An increase in the tail of the spectrum means increase of surface roughness and, hence, increase of wind forcing. Therefore a caution is advised in using periodic phase decorrelation even when the only aim of modelling is to simulate the spectral evolution. The same conclusion holds if the aims of the simulations include also modelling the evolution of the dynamical kurtosis.

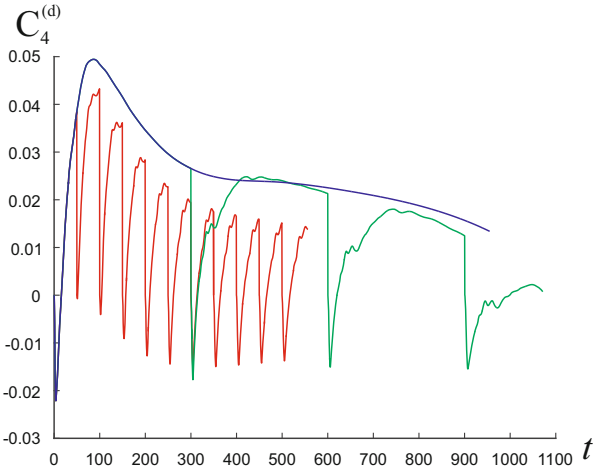

Fig. 13 Evolution of the dynamical kurtosis for U/c_p initially equal to 5: with the decorrelation of phases every 50 periods (*red curve*), every 300 periods (*green curve*), and without decorrelation (*blue curve*)

7 Concluding Remarks

In this paper, we outlined new opportunities arising in modelling of transient sea states with the use of the gKE employing a new efficient parallel algorithm. We showed samples of numerical simulation of wind waves with the gKE, and performed a number of simulations for the case of constant and instantly changing wind. Simulations for the constant wind were compared with the corresponding simulations of the classic Hasselmann equation, using the well-established WRT algorithm. For the case of constant wind forcing, for which the KE and the gKE are both applicable, we have validated the new gKE algorithm by the direct comparison with the simulations performed with the KE. We have performed simulations with the gKE for instantly increasing wind forcing, and for the case of squall, where wind forcing increases and then decreases to the initial value. We demonstrated joint evolution of spectra and skewness and of both components of kurtosis. For the steady wind conditions the important new and unexpected result is that the dynamical kurtosis (which for a given shape of the spectrum is proportional to the square of steepness) tends to evolve along a universal curve which is practically independent of wind, while, as demonstrated in Fig. 2c, the integral wave steepness strongly depends on wind.

There are numerous implications for modelling short-lived transient sea states. First, since at present there are no tools for such modelling, it is crucial that we have demonstrated that it is indeed feasible to simulate transient wave field evolution using the gKE. The simulations results proved to be robust. The algorithm is highly parallel and scalable, and the unrelenting advance of computing capabilities makes

it a plausible candidate to replace with time the KE as the main tool of wave modelling.

We stress that the gKE is not just a better version of the KE. It is an essentially different equation with its own properties discussed in [18] and peculiarities showing up in the simulations. The first key difference is that in contrast to the KE, two initial conditions are required: $n(\mathbf{k}, 0)$ and $J^{(1)}_{0123}(0)$. Although having $n(\mathbf{k}, 0)$ it is possible to find $J^{(1)}_{0123}(0)$ approximately, we for simplicity used the cold start initial condition. What we have demonstrated here for the first time, is that approximately a hundred periods after the cold start its effect in all wave field characteristics, including the kurtosis, is forgotten. This conclusion is closely linked to the issue of the legitimacy of periodic randomization of phases employed by Gramstad and Stiassnie [8], which promises certain gains for the gKE simulations. We have found that for simulations of spectral evolution a periodic phase randomization is indeed justified, albeit with a few caveats mentioned in Sect. 6. Remarkably, the dynamical kurtosis evolution returns to the same curve after about a hundred periods after each randomization (see Fig. 13). We stress that the curve appears to be independent of wind. Since the bound harmonic kurtosis and skewness are functions of the spectrum $n(\mathbf{k}, t)$, the conclusion equally applies to these characteristics and, hence, to the pdf of wave heights which is a function of kurtosis and skewness. Note that the anomalous bounce of kurtosis after the cold start shown in Fig. 4 is not an artifact caused by randomization, but is caused by the fact that the initial spectra are not in equilibrium with wind forcing and, hence, rather far from the quasi-equilibrium state. A comparison between Figs. 4 and 13 clearly demonstrates this point.

The simulations of squall presented here serve dual purpose. They demonstrate the capability of the gKE to capture short-lived events and give us for the first time an idea how the spectra and the higher moments evolve under such circumstances. We also advance in addressing the question of quantifying the changes in the likelihood of freak waves. The simulations demonstrate a possibility of quite significant short-lived jumps of kurtosis. Translating these results into quantifying the corresponding changes of pdf and increase of likelihood of freak waves is straightforward but goes beyond the scopes of the present work and will be considered in a dedicated work.

Acknowledgements The work was made possible thanks to the UK NERC grant NE/M016269/1. It was also supported by EU FP7 612610. The access to the ECMWF supercomputing facility (special project SPGBVSSA) is gratefully acknowledged. We are grateful to G. van Vledder for providing his code for the Hasselmann equation.

References

1. Annenkov, S.Y., Shrira, V.I.: Role of non-resonant interactions in the evolution of nonlinear random water wave fields. J. Fluid Mech. **561**, 181–207 (2006)
2. Annenkov, S.Y., Shrira, V.I.: Large-time evolution of statistical moments of wind–wave fields. J. Fluid Mech. **726**, 517–546 (2013)

3. Autard, L.: Etude de la liaison entre la tension du vent à la surface et les propriétés des champs de vagues de capillarité-gravité developpés. Ph.D. thesis, Université Aix-Marseille I and II (1995)
4. Caulliez, G.: Response of dominant wind wave fields to abrupt wind increase. In: EGU General Assembly Conference Abstracts, vol. 15, p. 11313 (2013)
5. Cavaleri, L.: Wind variability. In: Komen, G. (ed.) Dynamics and Modelling of Ocean Waves, pp. 320–331. Cambridge University Press, Cambridge (1994)
6. Donelan, M.A., Hamilton, J., Hui, W.: Directional spectra of wind-generated waves. Philos. Trans. R. Soc. Lond. A **315**(1534), 509–562 (1985)
7. Gramstad, O., Babanin, A.: Implementing new nonlinear term in third generation wave models. In: ASME 2014 33rd International Conference on Ocean, Offshore and Arctic Engineering, p. V04BT02A057 (2014)
8. Gramstad, O., Stiassnie, M.: Phase-averaged equation for water waves. J. Fluid Mech. **718**, 280–303 (2013)
9. Hasselmann, K.: On the non-linear energy transfer in a gravity-wave spectrum. Part 1: general theory. J. Fluid Mech. **12**, 481–500 (1962)
10. Hsiao, S.V., Shemdin, O.H.: Measurements of wind velocity and pressure with a wave follower during MARSEN. J. Geophys. Res. **88**, 9841–9849 (1983)
11. Hwang, P.A., Wang, D.W., Walsh, E.J., Krabill, W.B., Swift, R.N.: Airborne measurements of the wavenumber spectra of ocean surface waves. Part II: directional distribution. J. Phys. Oceanogr. **30**, 2768–2787 (2000)
12. Janssen, P.A.E.M.: Nonlinear four-wave interactions and freak waves. J. Phys. Oceanogr. **33**, 863–884 (2003)
13. Janssen, P.A.E.M.: On some consequences of the canonical transformation in the hamiltonian theory of water waves. J. Fluid Mech. **637**, 1–44 (2009)
14. Janssen, P.A.E.M.: Hamiltonian description of ocean waves and freak waves. In: Onorato, M. (ed.) Rogue and Shock Waves in Nonlinear Dispersive Media. Springer, Berlin (2016)
15. Nazarenko, S.V.: Wave Turbulence. Lecture Notes in Physics, vol. 825. Springer, Berlin (2011)
16. Onorato, M., Residori, S., Bortolozzo, U., Montina, A., Arecchi, F.: Rogue waves and their generating mechanisms in different physical contexts. Phys. Rep. **528**, 47–89 (2013)
17. Picozzi, A., Garnier, J., Hansson, T., Suret, P., Randoux, S., Millot, G., Christodoulides, D.: Optical wave turbulence: towards a unified nonequilibrium thermodynamic formulation of statistical nonlinear optics. Phys. Rep. **542**, 1–132 (2014)
18. Shrira, V.I., Annenkov, S.Y.: Towards a new picture of wave turbulence. In: Shrira, V., Nazarenko, S. (eds.) Advances in Wave Turbulence. World Scientific Series on Nonlinear Science, vol. 83, pp. 239–281 (World Scientific, Singapore, 2013)
19. van Vledder, G.P., Holthuijsen, L.H.: The directional response of ocean waves to turning winds. J. Phys. Oceanogr. **23**, 177–192 (1993)
20. Waseda, T., Toba, Y., Tulin, M.P.: Adjustment of wind waves to sudden changes of wind speed. J. Oceanogr. **57**, 519–533 (2001)
21. Young, I.R., van Agthoven, A.: The response of waves to a sudden change in wind speed. In: Perrie, W. (ed.) Nonlinear Ocean Waves. Advances in Fluid Mechanics Series, pp. 133–162. WIT Press, Southampton (2013)
22. Zakharov, V.E., L'vov, V.S., Falkovich, G.: Kolmogorov Spectra of Turbulence I: Wave Turbulence. Springer, Berlin (1992)

Rogue Waves in Random Sea States: An Experimental Perspective

Alessandro Toffoli

Abstract Despite being rare events, rogue waves have been recorded in the ocean. Here the current knowledge on wave statistics and the probability of occurrence of rogue waves is revisited from an experimental perspective. Starting from the instability of uniform wave packets to side band perturbations, the most accredited generating mechanism, the appearance of rogue waves in random wave fields is discussed. As an initial condition, unidirectional wave propagation is considered. Under these circumstances, wave instability results in a substantial deviation from Gaussian statistics. Directional spreading of wave energy, which characterizes realistic oceanic waves, attenuates the effect of wave instability weakening non-Gaussian properties. It is demonstrated, however, that the interaction between waves and an opposing current can sometimes act as a catalyst for modulational instability. This triggers the formation of rogues waves even in directional sea states, where rogue waves are the least expected.

1 Introduction

Large oscillations of the water surface with exceptional height and abnormal shape are normally known as rogue (or freak) waves. Although a consensus on a definition has never been reached, a rogue wave is normally identified by a crest-to-trough height exceeding 2–2.2 times the significant wave height *Hs* (the average of the highest 1/3 of the waves in a record), or a crest height *C* exceeding 1.2–1.3 times *Hs*, or a combination of both [1–3]. Possible generating mechanisms include simple linear focussing, bottom topography, wave-current interaction and high-order nonlinear wave-wave interactions [1, 2]. Despite being an infrequent phenomenon (rogue waves have been believed to be a sailor's myth until not long ago!), such extreme events have been recorded in the ocean for the past decades [4–7] and blamed for causing a number of ship accidents worldwide [5, 8].

A. Toffoli (✉)
Department of Infrastructure Engineering , Melbourne School of Engineering,
The University of Melbourne, Parkville, VIC 3010, Australia
e-mail: toffoli.alessandro@gmail.com

M. Onorato et al. (eds.), *Rogue and Shock Waves in Nonlinear Dispersive Media*,
Lecture Notes in Physics 926, DOI 10.1007/978-3-319-39214-1_7

Knowledge of the physics and statistics (in the form of the probability density function, $p.d.f.$) of surface gravity waves is essential in ocean engineering. Features of the most extreme wave expected within the life cycle of the structure is indeed needed for establishing structural responses and ensuring structural integrity. For offshore platforms, moreover, extreme wave probability is vital to define the air gap between the highest elevation of the water surface and the lowest deck.

Ships and offshore platforms are designed to withstand sea states for a specified return period, i.e. a time period during which a hazard appears on average only once. The sea state is expressed in the form of a directional spectral density function $E(\omega_i, \vartheta_l)$ [9], where ω_i is the angular frequency and ϑ_l is the direction of propagation. Ships refer normally to a 25-year sea state, while offshore structures are generally designed for a 100-year return period. Furthermore, Norwegian offshore standards [10] impose even stricter requirements for air gaps to withstand a 10,000-year sea state. The design spectrum, however, only provides an average description of the sea state, but it does not contain any information on the instantaneous position of the water surface. Therefore, short-term statistics for individual wave characteristics (heights, crests and troughs) has to be further derived with theoretical or semi-empirical probability density functions with the design spectrum as input [11].

Provided the waves are of small amplitude (i.e. gently sloping), a rough approximation of the water surface elevation can be calculated as a linear solution of the Euler equations for random, directional, surface gravity waves [12]:

$$\eta^{(1)}(\mathbf{x}, t) = \sum_{i=1}^{N_\omega} \sum_{l=1}^{M_\vartheta} a_{il} \cos[k_i(x \cos \vartheta_l + y \sin \vartheta_l) - \omega_i t + \varepsilon_{il}], \tag{1}$$

where t is time, $\mathbf{x}=(x, y)$ is the position vector and ε_{il} uniformly distributed random phases. The wavenumber k_i is related to frequency through the linear dispersion relation $\omega_i = \sqrt{g k_i \tanh(k_i h)}$. N_ω is the total number of frequencies and M_ϑ is the total number of directions considered in the model. The spectral amplitudes a_{il} are calculated as follows:

$$a_{il} = a(\omega_i, \vartheta_l) = \sqrt{2E(\omega_i, \vartheta_l)\Delta\omega\Delta\vartheta}. \tag{2}$$

Note that Hasselmann [13] also considered random variations of the amplitudes to define a proper statistical framework. However, if a directional sea is simulated, the addition of different directional components, each with a random phase at the same frequency, automatically restores the statistical variability of the amplitudes [14].

For linear waves (1), the statistical properties of the water surface elevation can be approximated by the Normal (Gaussian) distribution. Statistics of wave heights, crests and troughs can be conveniently estimated by the Rayliegh density function [11]. For realistic oceanic conditions, however, the wave steepness $k_p\, Hs/2$ (where

k_p is the wavenumber associated to the spectral peak period) is not small enough to ensure the hypothesis of small amplitude. As a result, waves exhibit sharper and higher crests and flatter and shallower troughs than the linear model (1) would predict. This asymmetry is the most obvious manifestation of nonlinearity in the ocean [15]. It can be modelled by adding a second-order, phase-locked, correction to the linear solution (1). Following the work by Sharma and Dean [16], a second-order correction for a generic random, directional sea state can be written as

$$\eta^{(2)}(\mathbf{x},t) = \frac{1}{4}\sum_{i,j=1}^{N_\omega}\sum_{l,m=1}^{M_\vartheta} a_{il}a_{jm}\left[K^{-}_{ijlm}\cos(\varphi_{il}-\varphi_{jm}) + K^{+}_{ijlm}\cos(\varphi_{il}+\varphi_{jm})\right], \tag{3}$$

where $\varphi_{il} = k_i(x\cos\theta_l + y\sin\theta_l) - \omega_i t + \varepsilon_{il}$, and K^{+}_{ijlm} and K^{-}_{ijlm} are the coefficients of the sum and difference contributions [14, 16–18]. For completeness, the analytical expressions of the interaction kernels $K^{\pm}$ are reported in Appendix. Note that K^{+} generates high frequency components with local maxima for every crests and troughs in the linear signal and it is responsible for the sharpening of crests and flattening of troughs. K^{-}, on the other hand, generates a long frequency component that results in a set down of the mean water level under the most energetic groups (see, for example, Fig. 1 in [14]). Note, however, that the contribution of K^{-} is reversed, if the directional spreading of the wave spectrum is very broad [18].

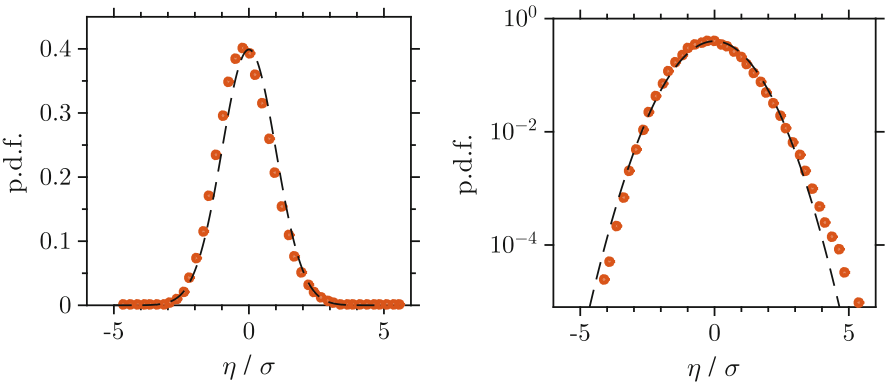

Fig. 1 Example of the probability density function $p.d.f.(x = x_0)$ of water surface elevation in a sea state with $Hs = 6.5$ m and $Tp = 10$ s ($k_pHs/2 = 0.13$); Gaussian density function (*solid line*); second-order surface elevation (*dots*). *Left panel* shows probability levels on a linear scale to highlights the skewness; the *right panel* presents probability levels in a logarithmic scale to highlights deviation at the tails of the distribution. The surface elevation η is normalised by means of the standard deviation σ

For an arbitrary input spectrum, the $p.d.f.$ of the second-order surface elevation $\eta = \eta^{(1)} + \eta^{(2)}$ can be inferred from Monte Carlo simulations of Eqs. (1) and (3) (see details in [14, 18]). An example $p.d.f.$ is presented in Fig. 1, for a sea state with significant wave height $Hs = 6.5$ m and peak period $Tp = 10$ s. This automatically defines a wave steepness $k_p\, Hs/2 = 0.13$. Second-order nonlinearity induces a weak, and yet notable, deviation from Gaussian statistics. The vertical asymmetry of the water profile, i.e. sharp crests and flat troughs, positively skews the $p.d.f.$ (see left panel in Fig. 1). Furthermore, the increase of crest heights and reduction of trough depths modify the tails of the $p.d.f.$, which start deviating from the Gaussian distribution at probability levels as low as 10^{-2} (see right panel in Fig. 1). It is important to mention that, on average, the increase of crest heights compensates the shallowing of wave troughs. Therefore, there is no significant effect on wave height statistics, which satisfy the Rayleigh distribution also at second-order.

Under a unidirectional, narrow banded approximation (i.e. the wave energy is confined along one specific direction of propagation and concentrated around a small frequency band nearby the spectral peak), second-order-based distributions for wave crests and troughs can be derived theoretically (see, for example, [19–21]). Density functions for more general unidirectional and directional spectra were obtained by fitting simulated distributions with a two-parameter Weibull density function and then parameterising the coefficients of the fitted distributions. These semi-empirical functions are generally known as the Forristall distributions [14] and are applied in standard design practice. An example of the probability of exceedance for the wave crests, $S(C > C_0)$, for a unidirectional sea state (as derived in [14]) is presented in Fig. 2. As a reference, the Rayleigh distribution is also reported. It is evident that second-order has a substantial effect on the tail of the wave crest distribution. Compared with linear waves (Raleigh distribution), the exceedance probability for extreme and rogue wave crests ($C > 1.2\, Hs$) increases by one order of magnitude. It is important to mention that the strength of second-order nonlinearity is directly proportional to the wave steepness. But it is slightly weakened by the wave directional spreading in infinite water depths and slightly strengthened by directionality in finite water depths [14, 18].

Second-order theory matches field data reasonably well [14, 18]. Nevertheless, recent hurricanes in the Gulf of Mexico have remarked a persisted vulnerability of marine structures to extreme waves [22]. During severe storms, in fact, the wave steepness may not be sufficiently small to neglect nonlinearity beyond second-order. If higher-order nonlinearity develops, uniform wave trains may destabilize under the effect of side band perturbations, provided the wave train is sufficiently steep and the side bands are sufficiently narrow banded [23–25]. This may force an individual wave to grow up to a maximum of three times its initial amplitude at the expense of the surrounding waves. The mechanism, generally known as Benjamin-Feir or modulational instability [26], is the most accredited for the generation of rogue waves in the ocean [1, 2]. An example of modulational instability of a regular

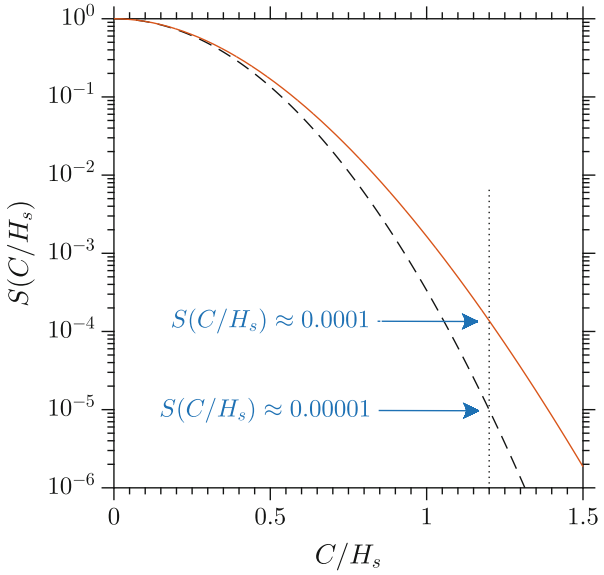

Fig. 2 Example of wave crest distribution in the form of the probability of exceedance $S(C/Hs)$ in a sea state with $Hs = 6.5\,\mathrm{m}$ and $Tp = 10\,\mathrm{s}$ ($kpHs/2 = 0.13$): Rayleigh distribution (*dashed line*); Forristall (second-order) distribution [14] (*solid line*)

wave packet in a water wave tank is reported in Fig. 3. The initial configuration is defined by a carrier wave of amplitude a_0 and two side bands of amplitudes $b^{\pm}$. The overall steepness of the packet is $k_0 \times (a_0 + b^{\pm}) = 0.1$, where $k_0 = 6.28\,\mathrm{m}^{-1}$ is the wavenumber of the carrier wave. The side bands are located to a wavenumber $k_0 \pm \Delta k$ such that 11 individual waves fall within the perturbation. This specific configuration ensures that Benjamin-Feir Index [23, 24], a ratio of nonlinearity (wave steepness) and dispersion (bandwidth), is $O(1)$, and hence that the wave packet is indeed unstable. As waves propagate, energy is exchanged (reversibly) from the carrier to the side bands in an asymmetric way (cf. [27]). The wave amplitude quickly grows and doubles its initial value after a distance of 20–25 wavelengths from the generation.

Modulational instability remains active in random wave fields [28] and may lead to strong deviations from Gaussian and second-order wave statistics even for steepness $k_p\, Hs/2$ as low as 0.1 [29–35]. This, however, only occurs if the wave spectrum is sufficiently narrow banded both in the frequency and directional domain. For broad directional sea states (typical for wind-generated waves), the effect of modulational instability ceases and rogue wave probability remains within second-order predictions.

Interestingly enough, nevertheless, the presence of a background current can trigger the formation of extreme waves, sustaining deviations from benchmark

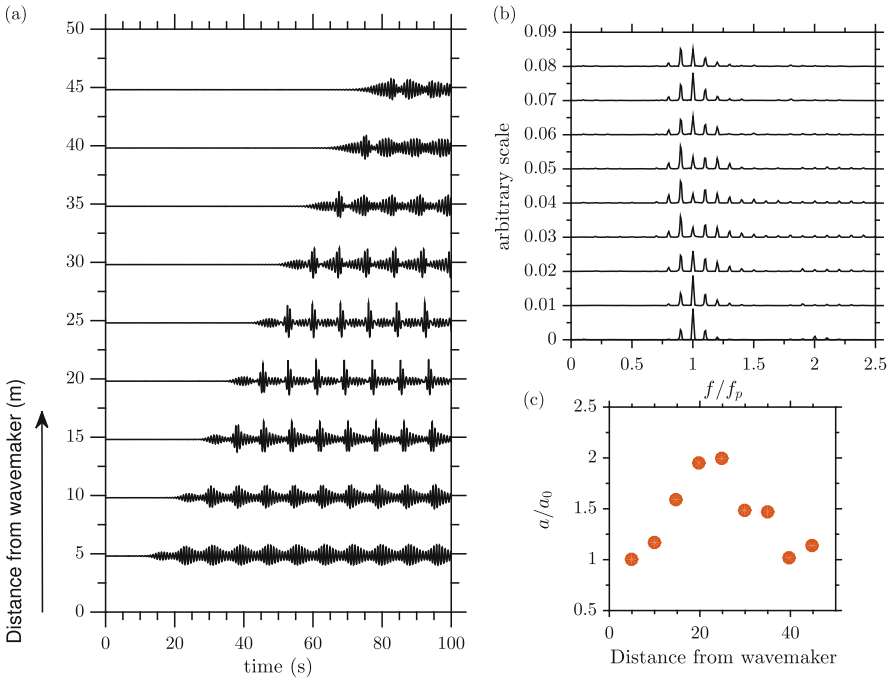

Fig. 3 Evolution of a regular wave packet composed by a carrier wave of amplitude a_0 and two side band perturbations of amplitudes $b^{\pm}$; the overall steepness $k_0 \times (a_0 + b^{\pm}) = 0.1$, where k_0 is the wavenumber of the carrier wave; number of waves under the perturbation $N = 5$. Evolution of surface elevation (**a**); evolution of wave spectrum (**b**); and wave amplification (**c**)

statistics also in directional wave fields (e.g. [36, 37]). It is known that wave energy can be refracted and focused in space, leading to the formation of large amplitude waves in regions of strong currents such as the Gulf Stream, the Kuroshio Current and the Agulhas Current [8, 38, 39]. When propagating over a current with adverse gradients in the horizontal velocity (i.e. an accelerating opposing current or a decelerating following current), waves also undergo a transformation that shortens the wavelength and increases the wave height [40, 41]. As a result, waves become steeper, amplifying nonlinear processes [42–45]. Therefore, an initial wave whose perturbation is stable (or weakly unstable) in terms of the modulational instability may become strongly unstable, generating rogue waves also when they are the least expected, because of a shift of the modulational instability band [37, 46–49]. An example of current-induced instability of an otherwise stable wave packets is shown in Fig. 4.

In the present chapter, the statistical properties of water waves are revisited from an experimental point of view. Modulational instability and its impact on wave statistics are discussed for directional sea states in the absence and in the presence of a background current. Experimental data used herein were collected in the ocean

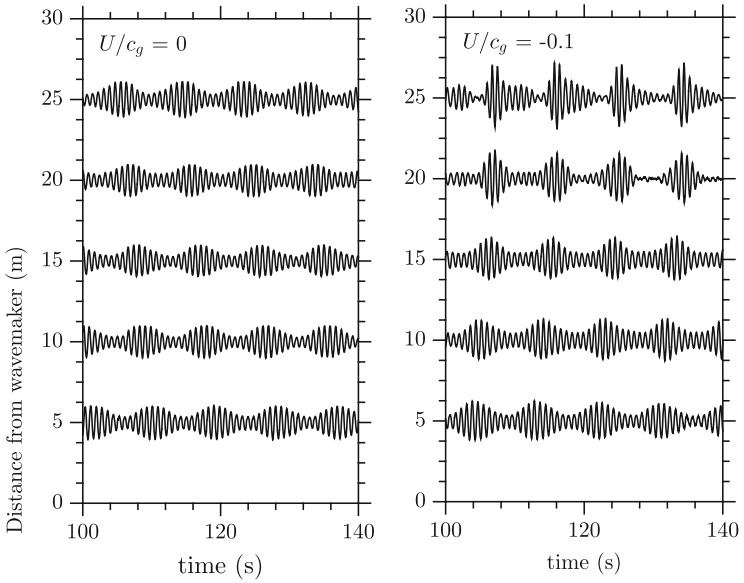

Fig. 4 Evolution of a regular wave packet composed by a carrier wave of amplitude a_0 and two side band perturbations of amplitudes $b^{\pm}$; the overall steepness $k_0 \times \sqrt{a_0^2 + b^{+2} + b^{-2}} = 0.064$, where k_0 is the wavenumber of the carrier wave; number of waves under the perturbation $N = 11$. Evolution in the absence of current ($U/c_g = 0$, where c_g is the group velocity, in the *left panel*); evolution in the presence of an opposing current ($U/c_g = -0.1$, where c_g is the group velocity, in the *right panel*)

wave basin at Marintek (Norway) and in the directional wave basin at Plymouth University (UK). In Sect. 2, an experimental model for nonlinear wave evolution in the absence of background currents is discussed. Statistical properties are presented and assessed against second-order predictions. Without loss of generality, the analysis is limited to the wave crest distribution. In Sect. 3, the interaction between waves and current and its effect on the wave crests distribution is shown. Concluding remarks are presented in the last Section.

2 Wave Crest Distribution in the Absence of a Background Current

2.1 Experimental Model

An experimental model of the nonlinear evolution of an initial, Gaussian, random wave field was set up in the ocean wave basin at MARINTEK (Norway) [29, 30]. The facility is 70 m wide and 50 m long. The water depth is adjustable and it can

reach a maximum depth of 10 m. For the purpose of the present experiment, the water depth was fixed to 3 m. The basin is equipped with a directional wavemaker composed by 144 individually controlled flaps along the 70 m side. Each flap is 0.434 m wide and hinged at a depth of 1.02 m below the water surface. The wavemaker can generate directional seas within a wide range of directional distributions of the energy (from purely unidirectional to broad directional conditions). A second wavemaker is installed on the 50 m (lefthand). It was not operated and hence it acted as a vertical wall. Beaches are deployed opposite to the wavemakers to absorb wave energy. A schematic of the basin and the experimental set up is shown in Fig. 5.

The experiment model consisted in tracing the surface elevation as waves propagate along the basin; no circulation of the body of water was imposed, i.e. no current. Measurements of the water surface elevation were taken at different distances from the wavemaker (and along the central axis) with resistance wave gauges (see Fig. 5). Probes were held across the water surface by light tripods laying on the bottom and deployed at 5 m intervals. A sampling frequency of 80 Hz was applied. Three three-probe arrays were deployed to allow the reconstruction of directional properties along the tank. An additional eight-probe array, arranged as a regular heptagon plus a central probe, was also installed in the middle of the basin to gather more detailed directional spectra.

Random waves were FFT–generated from an initial directional wave spectrum $E(\omega, \vartheta) = S(\omega)D(\vartheta)$ with 16,384 frequencies distributed between 0.0–10.0 Hz. Complex Fourier amplitudes were calculated with their modules randomly chosen from a Rayleigh distribution around the "target" spectrum. The phases were randomly chosen from a uniform distribution between 0 and 2π.

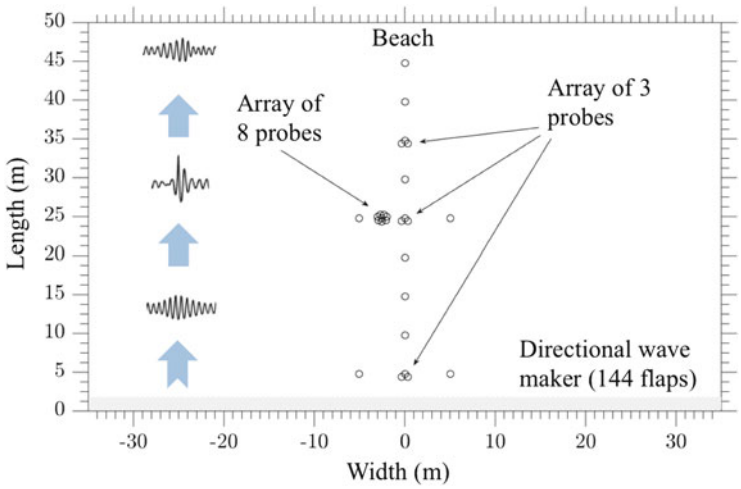

Fig. 5 Experimental set up in the ocean wave basin at Marintek (Norway): waves only (not in scale)

The frequency spectrum $S(\omega)$ was defined by the JONSWAP formulation [50]. The peak period was imposed to be $Tp = 1$ s, which corresponds to a dominant wavelength of 1.56 m. Considering the depth of 3 m, deep water waves were thus generated ($k_p\ h \approx 12$, where h is the water depth). The Phillips parameter α was set equal to 0.014. Two different values of the peak enhancement factor, γ, were selected. This choice is twofold: it defines different degrees of nonlinearity as measured by the wave steepness $k_p\,Hs/2$ and dispersion as measured by the spectral bandwidth δ_ω. For both cases, the Benjamin–Feir Index $BFI = k_pHs\sqrt{2}/2\delta_\omega$ (see [51] for details on the calculation of the BFI) is approximately 1, meaning rogue-wave-prone sea states. The values of the peak enhancement factor γ as well as the one of the wave steepness and Benjamin–Feir Index are summarized in Table 1.

The directional distribution $D(\vartheta)$ was defined by a $cos^N(\vartheta - \vartheta_m)$ function [9]. In order to consider different degrees of directional spreading, different values of the spreading coefficient N were used, raging from almost unidirectional (very large N) to directional (small N) conditions. The following values have been selected: $N = \infty$ (unidirectional), 840, 200, 90, 50, 24. To put this into perspective, note that $N = 24$ corresponds to a relatively narrow swell [52]. Directional distributions are shown in Fig. 6; a $sech^2$ function is also added as reference for the directional distribution of typical wind-generated wave fields (wind sea). Because

Table 1 Parameters of input frequency spectra $S(\omega)$

Exp. ID	Tp (s)	Hs (m)	γ	k_pHs	BFI
A	1.0	0.06	3.0	0.13	0.70
B	1.0	0.08	6.0	0.16	1.10

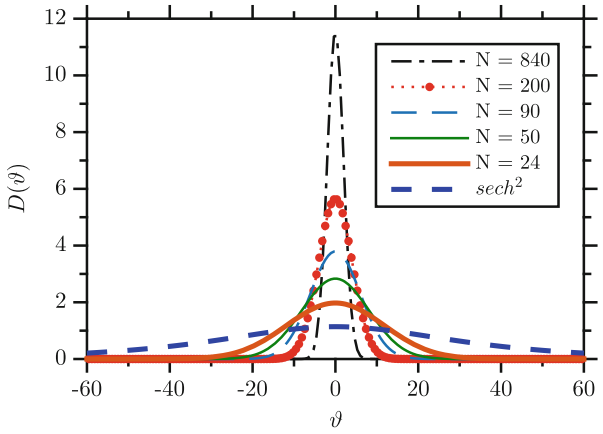

Fig. 6 Analytical form of the directional distribution as a function of angle ϑ for different values of the spreading coefficient N; the $sech^2$ distribution is included are reference for wind generated wave fields

the directional spreading has a stabilising effect on the wave field, the *BFI* in Table 1 lessens with the broadening of the wave spectrum ($BFI_{Dir} = \sqrt{BFI^2(1-R)}$, where $R = 0.5\delta_\vartheta/\delta_\omega$ with δ_ϑ being the directional width [53]). As an example, $BFI = 1.10$ in Table 1 drops to $BFI_{Dir} = 1.01$ for a directional spreading coefficient $N = 840$ and to $BFI_{Dir} = 0.26$ for $N = 24$.

For each input spectrum, four realisations (10 min each) of the random sea surface were performed by using different sets of random amplitudes and phases. The statistics of irregular wave fields generated in this way follow fairly well the law of "natural" statistics of randomly chosen finite time series realizations of irregular wave models with continuous spectra.

2.2 *Evolution of the Wave Spectrum*

The initial (input) spectral condition does not remain steady, but it varies slightly as the wave field propagates along the basin. Records of significant wave height along the basin show that a fraction of energy is loss (see Fig. 7). On average, *Hs* drops by about 5 % and 9 % for the configuration in experiment A and B, respectively. Although the present experiments were not specifically designed to study breaking

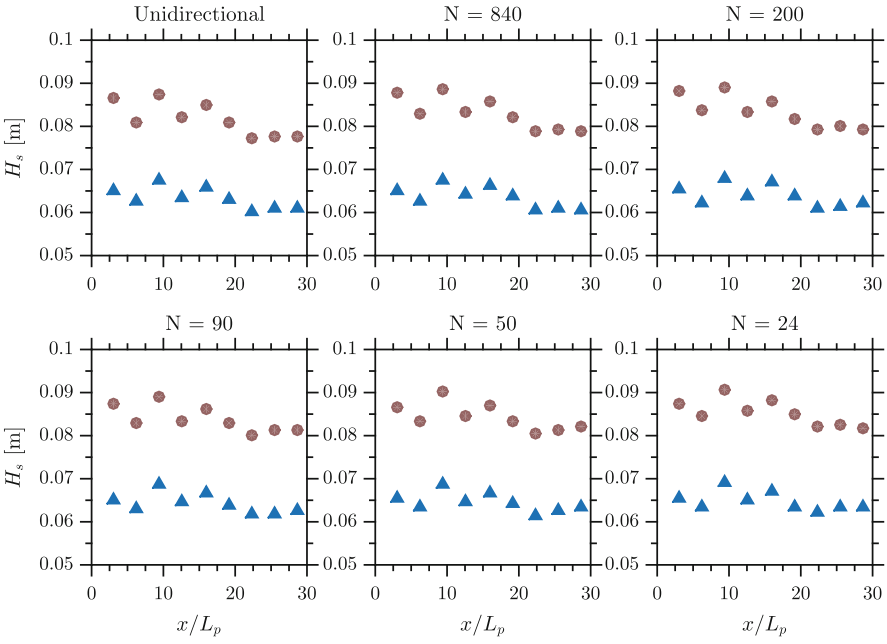

Fig. 7 Significant wave height as a function of the non-dimensional distance from the wavemaker: experiment A (*open triangle*), experiment B (*open circle*)

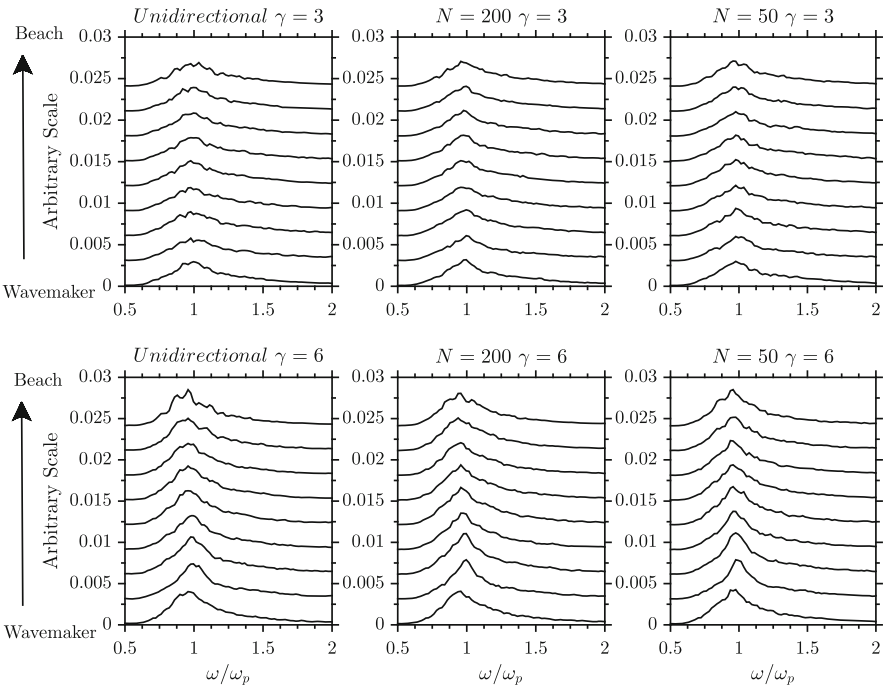

Fig. 8 Frequency wave spectra for experiment A (*upper panels*) and experiment B (*lower panels*) at different distances from the wave maker ($x/L_p = 3.1$, $x/L_p = 15.9$ and $x/L_p = 28.7$)

dissipation, wave breaking occurred regularly, especially during the more energetic and nonlinear tests in experiment *B*, justifying this energy loss (see [29, 54] for more details).

The remaining wave energy is then redistributed from high to low frequencies, producing the downshift of the spectral peak (i.e. the dominant wave becomes longer). The evolution of the wave spectrum for different sea states is shown in Fig. 8. This is already notable after an evolution of about 16 dominant wavelengths (peak frequency drops by about 2 %) and becomes even more substantial further down the basin (4 % and 6 % for experiment A and B, respectively). Note that the downshift is consistent with numerical simulations in [55, 56], where a change of the spectrum is already observed on the scale of the Benjamin–Feir instability [57] as a result of quasi-resonant interactions.

2.3 Evolution of the Wave Crest Distribution

In the following, the evolution of the wave crest distribution is discussed as a function of the normalized distance from the wavemaker (x/L_p, with L_p the peak

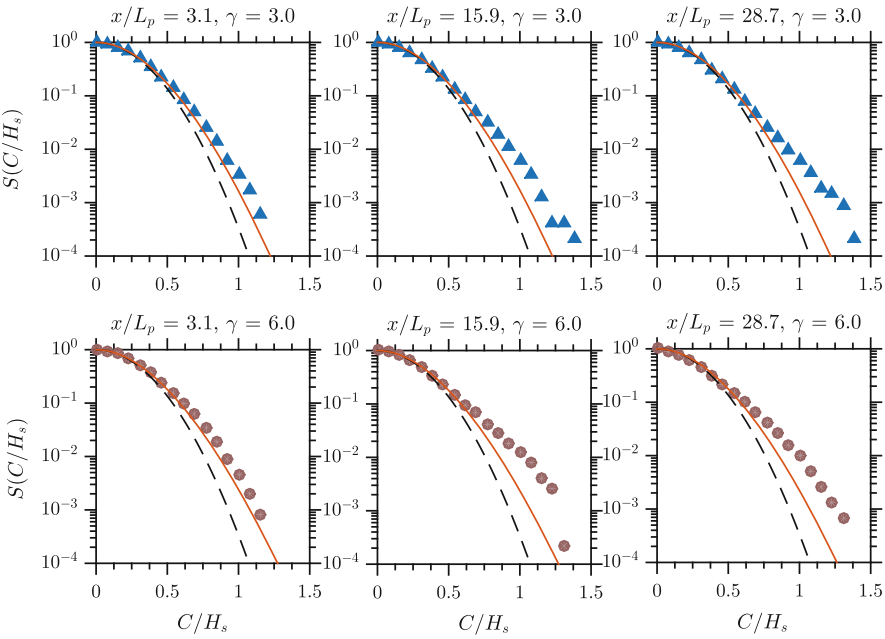

Fig. 9 Evolution of the wave crest distribution for sea states with directional spreading coefficient $N = \infty$: experiment A (*upper panels*); experiment B (*lower panels*). Experimental data (*markers*), Rayleigh distribution (*dashed line*) and Forristall distribution [14] (*solid line*) are shown

wavelength of the input wave spectrum). Wave crests C are extracted from recorded time series at each gauge with a standard zero-crossing analysis. The significant wave height at each probe is used as normalizing factor. Figures 9, 10 and 11 present the probability of exceedance $S(C/Hs)$ at $x/L_p = 3.1$, 15.9 and 28.7, i.e. nearby the wavemaker, middle basin and nearby the beach, respectively. As an example, only sea states with directional spreading coefficient $N = \infty$, 200 and 50 are shown. The Rayleigh and the Forristall [14] distributions are included for benchmarking linear and second-order wave statistics. Note that, for a more conservative estimate, the two-dimensional Forristall distribution for unidirectional sea states is applied throughout this discussion.

As soon as waves start propagating at the wavemaker, second-order harmonics are generated. Regardless the initial spectral shape, the wave crest distribution at $x/L_p = 3.1$ departs from the Rayleigh function and fits the second-order Forristall distribution [14] as one would expect. For unidirectional sea states ($N = \infty$), wave conditions are the most favorable for the development of modulational instability. As a result, the percentage of extreme and rogue waves in the records increases quickly as the wave field propagates. As a result, the wave crest distribution deviates substantially from the Forristall distribution [14]. Strongly non-Gaussian

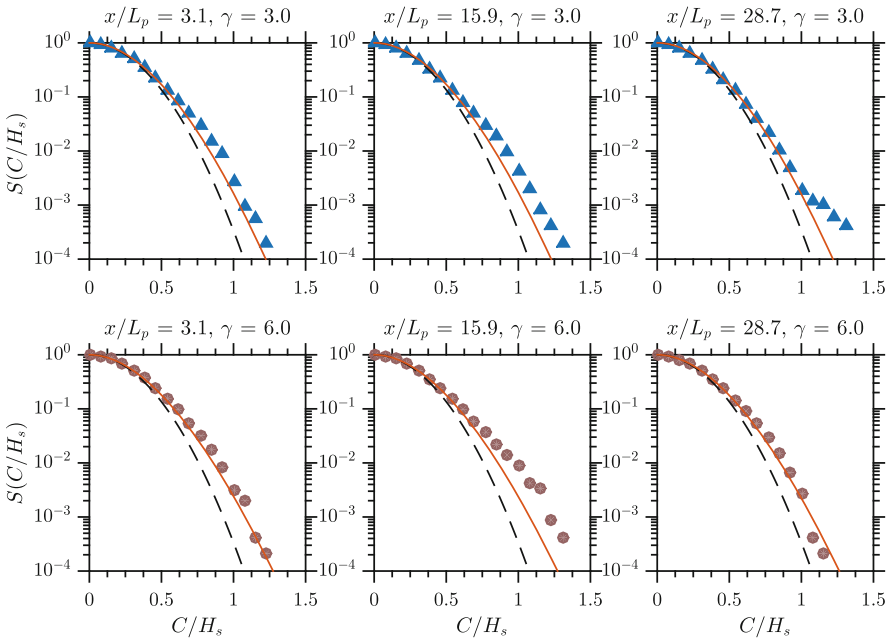

Fig. 10 Evolution of the wave crest distribution for sea states with directional spreading coefficient $N = 200$: experiment A (*upper panels*); experiment B (*lower panels*). Experimental data (*markers*), Rayleigh distribution (*dashed line*) and Forristall distribution [14] (*solid line*) are shown

characteristics are reached towards the end of the basin ($x/L_p = 28.7$) for the less nonlinear cases in experiment A and approximately at the centre of the basin ($x/L_p = 15.9$) for more nonlinear conditions in experiment B (Fig. 9). Overall, the occurrence probability of rogue wave crests ($C > 1.2H_s$) is 0.003, which is one order of magnitude greater than the Forristall distribution [14].

The broadening of the wave spectrum (i.e. energy is distributed over a range of direction) somewhat weakens the effect of modulational instability on wave statistics. The deviation from second-order wave statistics still remains significant for sea state with $N = 200$ in experiment B, where $S(C/Hs) \approx 0.001$ (Fig. 10), but is less substantial in experiment A ($S(C/Hs) \approx 0.0005$). For sufficiently broad sea states, eventually, deviations from the Forristall distribution [14] cease (Fig. 10), regardless the level of nonlinearity that is applied. In our experiment, this is already clear for directional sea states as broad as $N = 50$, where the empirical distribution fits the second-order crest distribution. In the absence of any forcing factors such as a background current, these results substantiate a transition from strongly to weakly non-Gaussian characteristics with the increase of the wave directional spreading. For completeness, a summary of wave crest distribution for all directional sea states considered herein is presented in Fig. 12.

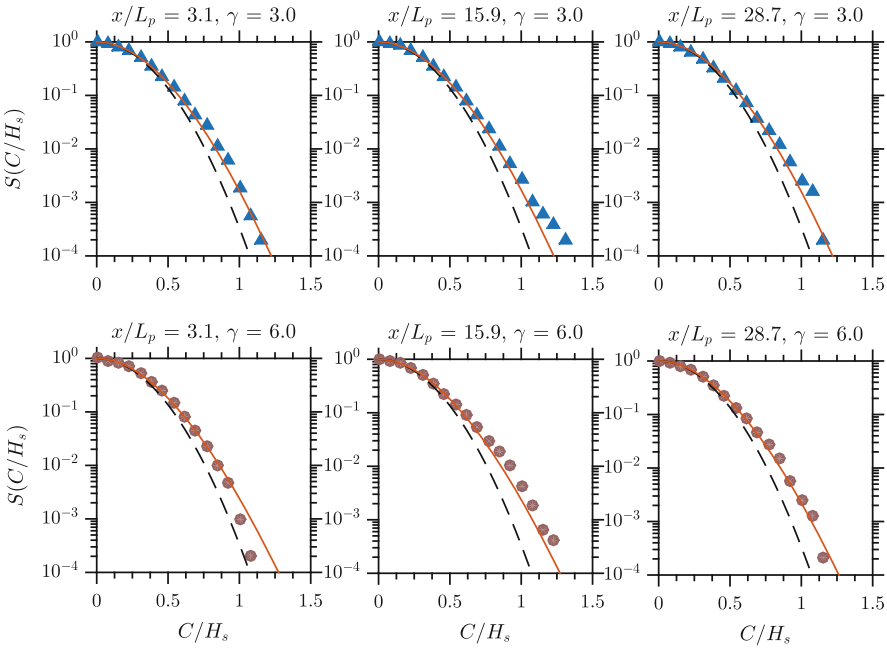

Fig. 11 Evolution of the wave crest distribution for sea states with directional spreading coefficient $N = 50$: experiment A (*upper panels*); experiment B (*lower panels*). Experimental data (*markers*), Rayleigh distribution (*dashed line*) and Forristall distribution [14] (*solid line*) are shown

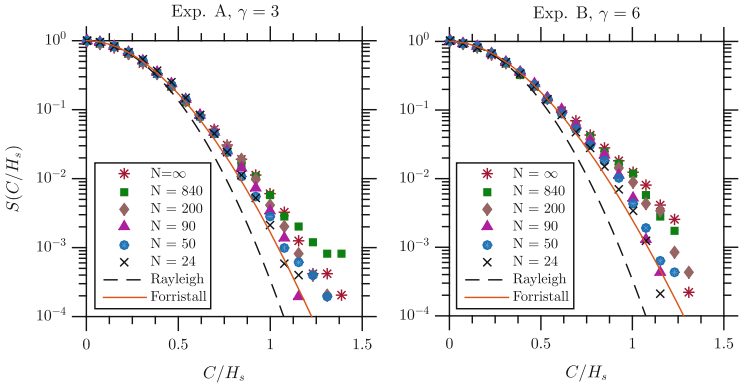

Fig. 12 Wave crest distribution at $x/L_p = 15.9$ for all directional wave spectra

3 Wave Crest Distribution in the Presence of a Background Current

3.1 Experimental Model

The experimental model consisted in monitoring the evolution of waves, when entering into a region of opposing current. Tests were carried out in the directional wave basin of the COAST Laboratory at Plymouth University (see schematic in Fig. 13). The facility is 35 m long and 15.5 m wide. The floor is movable and it was set to a depth of 3 m. Similarly to the basin at Marintek (see Sect. 2), this facility allows propagation in two horizontal dimensions and it is equipped with 24 individually controlled wave paddles for the generation of directional wave fields. At the other end of the wavemaker, a convex beach is installed for wave energy absorption. A background current is forced by a multi-pump recirculating hydraulic system, which is capable of producing a water flow with speed (U) ranging from 0.03 to 0.4 m/s (both following and opposing the waves). Inlet/outlet are located on the floor just in front of the wave pistons and the beach. For an opposing current (i.e. propagating against the waves), the particular location of the outlet ensures a gradual deceleration of surface velocity, while approaching the wavemaker. This, in turn, ensures that waves are subjected to an adverse current gradient immediately after being generated.

The evolution of the surface elevation was traced by 10 capacitance wave gauges deployed at interval of 2.5 m, starting from the wavemaker and approximately 2.5 m from the (left) side wall. Probes were operated at a sampling frequency of 128 Hz. A propeller current-meter was used to monitor the average current velocity (over a 1-min window). Longitudinal, transverse and vertical profiles of the horizontal velocity are presented in Fig. 14. Records indicate a sharp gradient from 0 m/s to

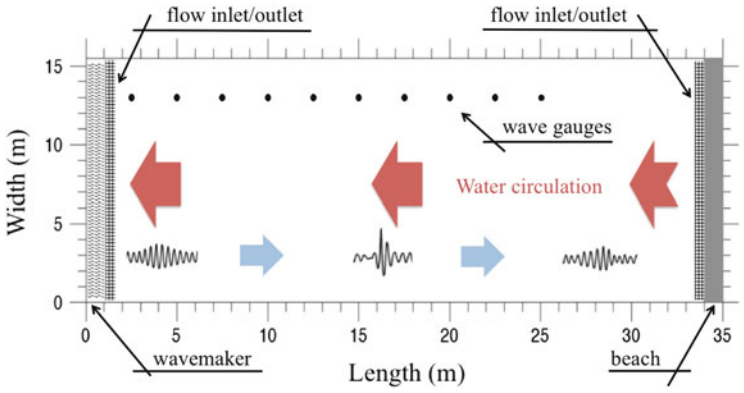

Fig. 13 Experimental set up in the ocean wave basin at the University of Plymouth (UK): waves and current (not in scale)

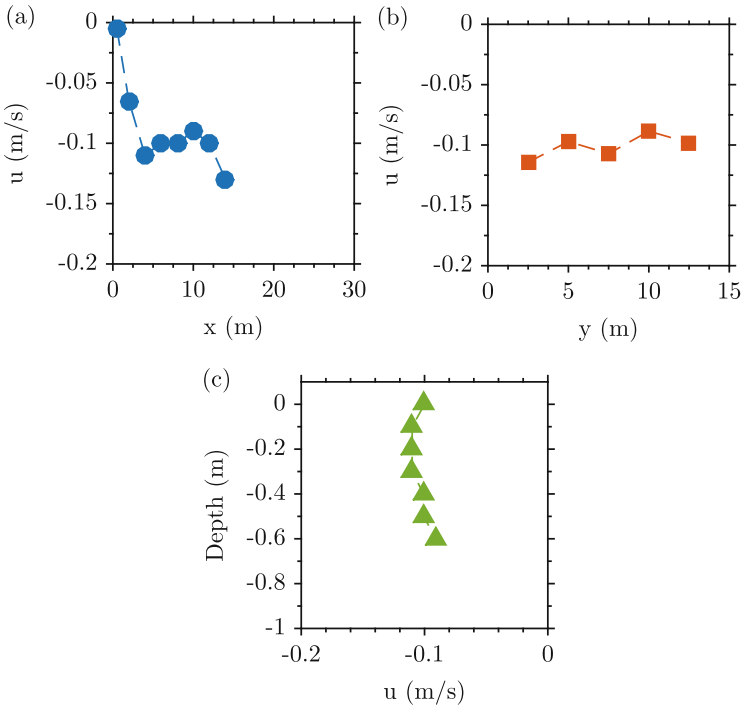

Fig. 14 Average velocity in the wave basin at the University of Plymouth: longitudinal profile (panel a); transverse profile (panel b); and vertical profile (panel c)

the regime speed within the first 2 m from the wavemaker. Towards the centre of the basin, there is a slight deceleration (between 2 and 10 m from the wavemaker), while the current sharply accelerates in the proximity of the centre (see Fig. 14a). Transversely, the current remains stable. Additional 10-min time series of velocity were gathered to monitor temporal oscillations with an ADV properly seeded. Over time, the standard deviation was about 15 % due to long period oscillations of about 80 s.

Two different initial conditions were tested. In the first instance, a unidirectional sea state with a low wave steepness was applied. To this end, a JONSWAP spectrum with $Tp = 0.7$ s (hence wavelength $L_p = 0.765$ m, group velocity $c_g = 0.55$ m/s and relative water depth $k_p h = 24.6$), $Hs = 0.015$ m and $\gamma = 3$ was imposed at the wavemaker. The resulting sea state is characterised by a wave steepness $k_p Hs/2 = 0.062$. Therefore, waves are expected to remain weakly non-Gaussian in the absence of any current. To set a reference, the evolution of the input wave field was first traced with no current. Experiments were then repeated with opposing currents at the following nominal velocities: $U = -0.02, -0.08, -0.13$, and -0.19 m/s.

A second test was carried out with a directional sea state. Again, a JONSWAP spectrum was used to model the frequency domain and a $cos^N(\vartheta)$ function was applied for the directional domain. The spectrum was defined with $Tp = 0.7$ s,

$Hs = 0.03$ m and $\gamma = 3$. The resulting wave field is characterised by steepness $k_p Hs/2 = 0.12$. The directional spreading coefficient N was set equal to 50. This condition is similar (but not identical) to the one in experiment A (see Sect. 2). In the absence of a background current, the selected directional spreading ensures weak non-Gaussian properties. Tests were conducted without current and then repeated with opposing currents at nominal velocities of $U = -0.02$, -0.08, -0.13 and -0.19 m/s.

3.2 *Evolution of the Wave Spectrum*

The evolution of significant wave height, as a function of x/L_p, and of the wave spectrum is presented in Figs. 15 and 16, respectively. In the absence of a current ($U/c_g = 0$), H_s remains fairly stable along the tank. Quasi-resonant nonlinear interactions (modulational instability) have a marginal effect, resulting in only a weak spectral downshift (see examples of spectral evolution in Fig. 16) [58–60]. Note that the downshift is slightly more accentuated in the directional sea state (right panel in Fig. 16) than the one observed in the unidirectional sea state, due to the higher initial wave steepness. Wave breaking was not detected.

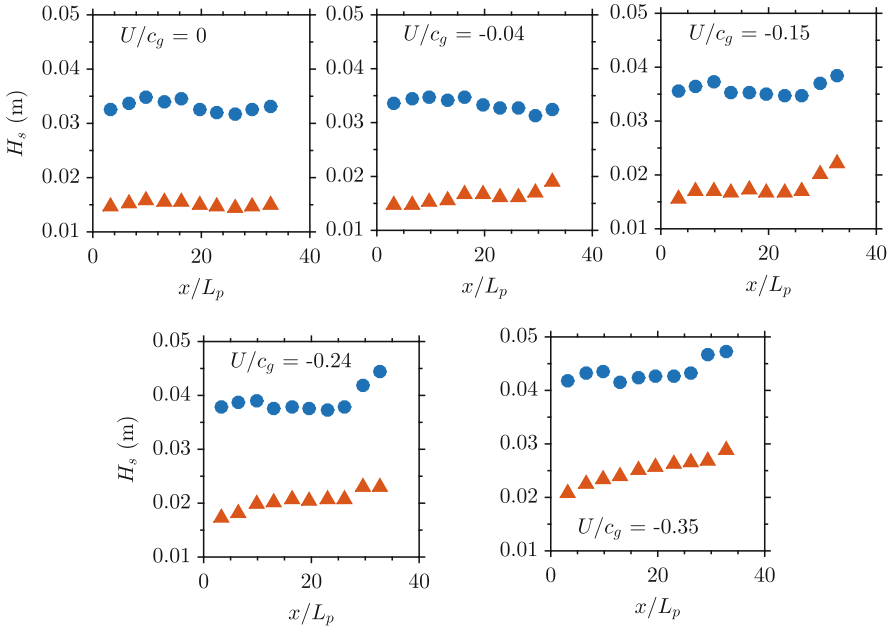

Fig. 15 Significant wave height as a function of the non-dimensional distance from the wave-maker: unidirectional wave field (*open triangle*); directional wave field (*open circle*)

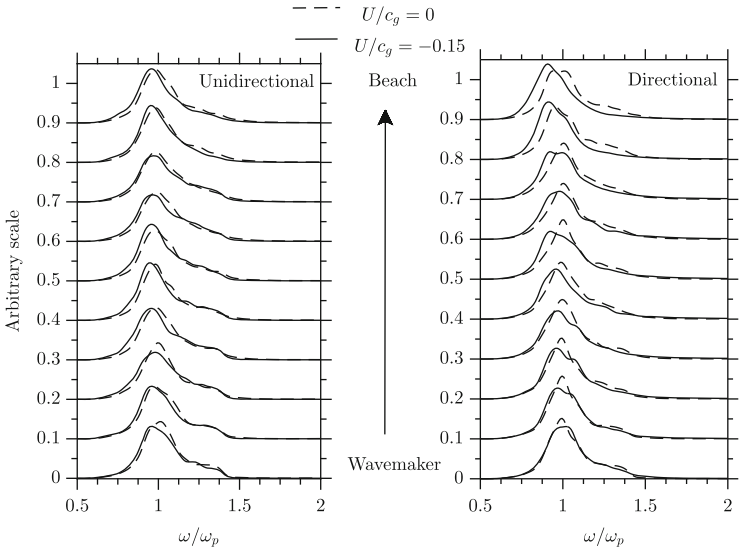

Fig. 16 Frequency wave spectra for experiment A: $x/L_p = 3.1$ (*dashed-dotted line*); $x/L_p = 15.9$ (*dashed line*); $x/L_p = 28.7$ (*solid line*)

When waves enter into a region of adverse current gradient, an immediate increase of significant wave height takes place (Fig. 15). Further growth of *Hs* was detected further down the basin due to the variability of the current field. However, no breaking dissipation is observed. This does not exclude that some individual waves may sporadically break, though. The opposing current also forces the wavelength to compress, increasing the dominant wavenumber. The transformation that waves undergo implies an increase of the steepness and hence nonlinearity: as an example, $k_pHs/2$ grows up to about 0.1 for $U/c_g \approx -0.15$, while $k_pHs/2 \approx 0.16$ for $U/c_g \approx -0.35$ in unidirectional sea states. As a consequence, a more substantial (and quicker) downshift of the spectral is observed as waves propagate along the basin (see Fig. 16). For the less nonlinear unidirectional sea state, peak frequency drops by about 6 %, while it drops by about 10 % in the directional sea state.

3.3 Evolution of the Wave Crest Distribution

As an example, the evolution of the wave crests distribution along the basin with and without water circulation is presented in Fig. 17 for the unidirectional case only. The Rayleigh and the Forristall distribution [14] are presented for reference too. The initial conditions of the input sea state were chosen to suppress nonlinearity of order higher than second in the absence of current. Therefore, as the wave field

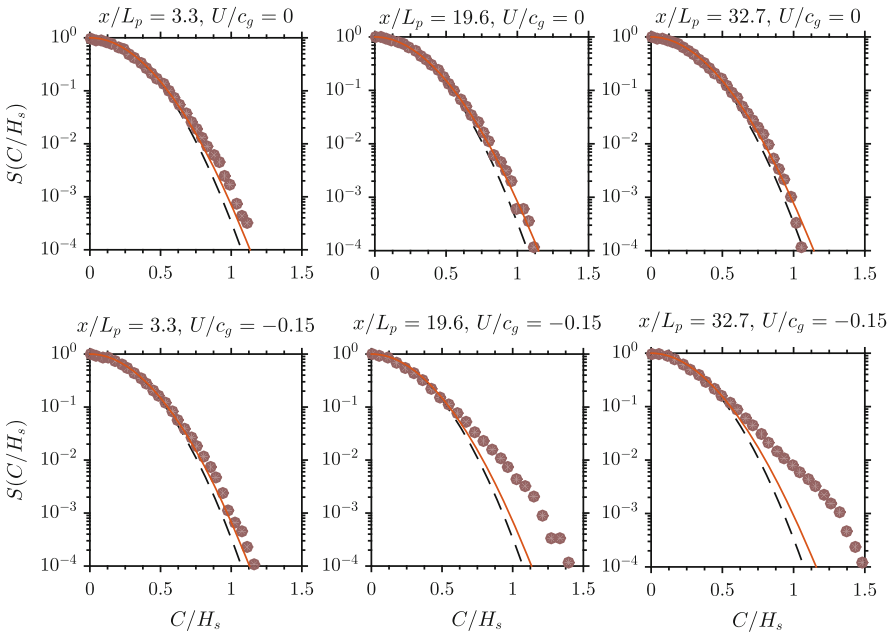

Fig. 17 Evolution of the wave crest distribution for unidirectional sea states without (*upper panels*) and with current (*lower panels*): experimental data (*open circle*), Rayleigh distribution (*dashed line*) and Forristall distribution [14] (*solid line*)

propagates, the wave crest distribution does not depart (at least not significantly) from the second-order Forristall distribution [14] (see upper panels in Fig. 17).

The interaction with current generates an increase of wave steepness. As an immediate result, this changes the intensity of second-order nonlinearity. The Forristall distribution [14], therefore, shows a more notable deviation from the Rayleigh function as wave steepness changes along the basin (see lower panels in Fig. 17).

The increase of wave steepness is strong enough to also trigger higher-order nonlinear mechanisms (modulational instability). In this respect, the wave crest distribution shows a clear dynamical behaviour, deviating strongly from the Forristall distribution [14]. After $x/L_p = 32.7$, the empirical distribution shows that rogue wave crests would occur with a probability of 0.005. This is more than one order of magnitude greater than what observed in the absence of the current (and predicted by the second-order theory).

As a summary, Fig. 18 reports the wave crest distribution at the gauge where maximum deviation from second-order wave statistics was observed for different current velocities. This result substantiates the key role of the current in destabilizing the wave field and enhancing the rogue wave probability. It is interesting to note

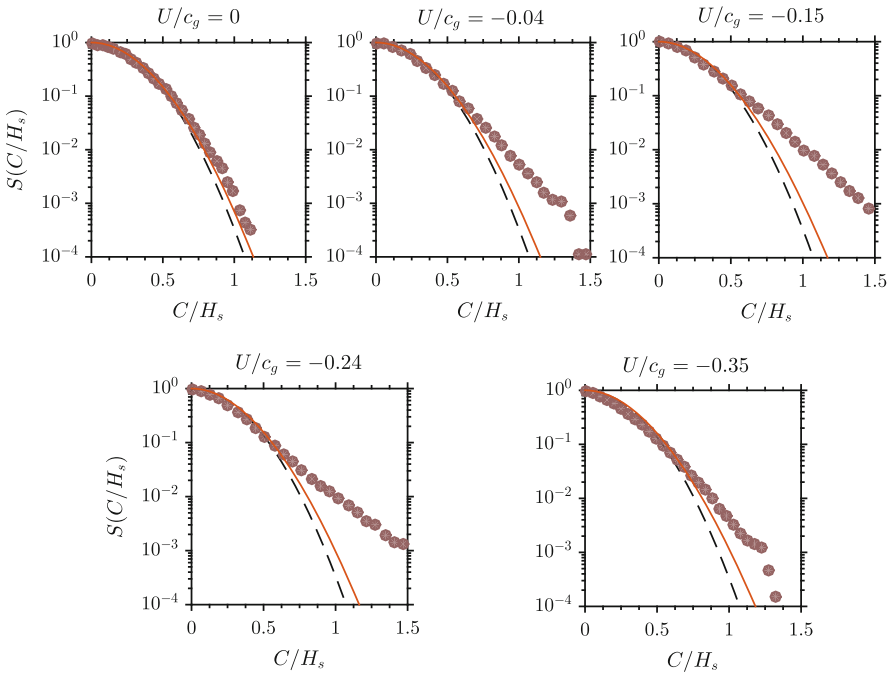

Fig. 18 Wave crest distribution for unidirectional sea states at different current speed and at probes of maximum deviation from benchmark distributions: experimental data (*open circle*), Rayleigh distribution (*dashed line*) and Forristall distribution [14] (*solid line*)

that strong departures from the Forristall distribution [14] already occurs for current speed as low as $U/c_g = -0.04$ and maximizes for $U/c_g = -0.24$. For a stronger current ($U/c_g = -0.35$), the deviation is somewhat reduced. Although breaking dissipation did not played a significant role in any of the tests, sporadic breaking with a concurrent limitation of crest height cannot be completed ruled out, especially for such a strong current.

It is now instructive to verify whether the effect of the current activates instability also in directional sea states. Figure 19 shows the empirical wave crest distribution at the gauges of maximum deviation from the second-order distribution and for different current velocities. As also observed in Fig. 11 (lower panels), the selected sea states (directional spreading coefficient $N = 50$) does not lead to any significant deviation from the Forristall distribution [14] in the absence of the current, despite the relatively large steepness. In the presence of the current, however, the empirical wave crest distribution deviates notably from second-order wave statistics for any current. Although the effect is less intense than in the unidirectional test, the rogue wave crest probability is about one order of magnitude higher than second-order theory would predict.

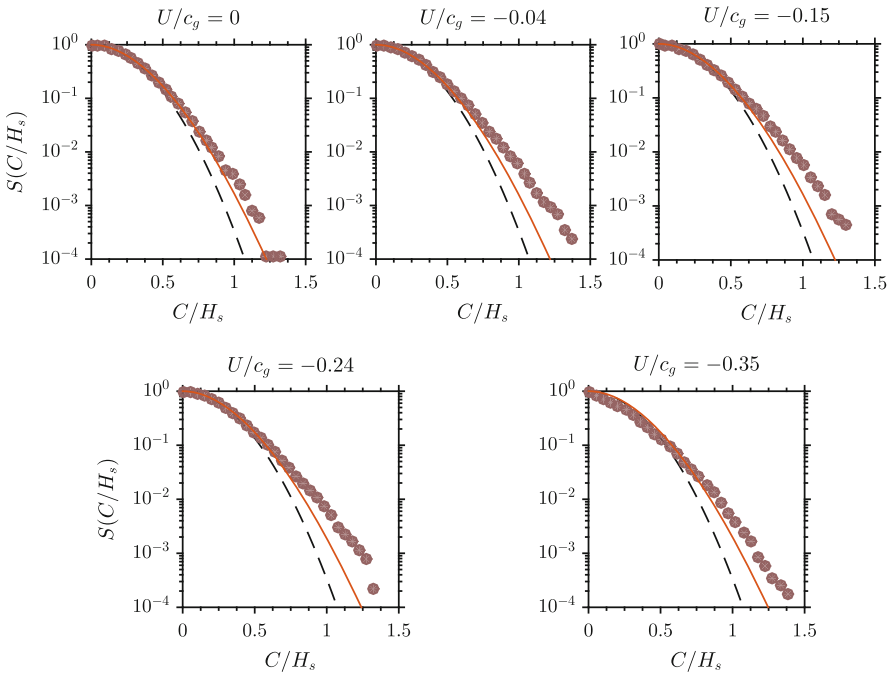

Fig. 19 Wave crest distribution for directional sea states at different current speed and at probes of maximum deviation from benchmark distributions: experimental data (*open circle*), Rayleigh distribution (*dashed line*) and Forristall distribution [14] (*solid line*)

4 Conclusions

The statistical properties of unidirectional and directional wave fields, in the form of the wave crest distribution, were discussed with the aid of laboratory experiments that were carried out in large wave basins. The effect of nonlinearity higher than second-order was assessed. Conditions without and with water circulation (i.e. a background current) were considered. Specifically, the former was employed to explore the effect of the wave directional spreading, while the latter was used to investigate the effect of wave-current interaction.

It is nowadays well established that a steep, unidirectional wave field characterized by an energy spectrum sufficiently narrow banded in the frequency domain can develop nonlinear processes such as modulational instability. Allowing enough space for nonlinearity to fully evolve, wave instability results in strong non-Gaussian statistics. The wave crest distribution, in this regard, is observed to substantially deviate from standard second-order distributions such as the Forristall distribution [14]. Directional spreading of wave energy, nevertheless, attenuates the effect of modulational instability. While deviations still remain notable for narrow directional distributions, wave crests fit second-order predictions for broad directional spectra (Fig. 12), typical of wind-generated waves.

The presence of a background current, however, can strengthen modulational instability, sustaining strong non-Gaussian statistics. When interacting with an opposing current, waves are subjected to a transformation, which shrinks the wavelength and increases the wave height. As a consequence, the steepness, an indication of the degree of nonlinearity of the wave field, increases. Experimental data, in this regard, substantiate that an otherwise stable unidirectional wave field can exhibit strong deviations from second-order wave statistics, when interacting with an opposing current (Fig. 18). Interestingly enough, wave-current interaction also plays a substantial role in directional sea states, acting as a catalyst on modulational wave instability. Despite intrinsic weakly non-Gaussian properties of directional sea states, the interaction with an opposing current can in fact reinforce nonlinearity and lead to significant deviations from second-order wave statistics, making rogues possible even when they are the least expected.

Acknowledgements The experimental work was supported by the European Community's Sixth Framework Programme through the grant to the budget of the Integrated Infrastructure Initiative HYDROLAB III, Contract no. 022441 (RII3), and the School of Marine Science and Engineering at Plymouth University. The author also acknowledges support from the Grants-in-Aid for Scientific Research of the Japan Society for the Promotion of Science (JSPS), the International Science Linkages (ISL) Program of the Australian Academy of Science.

Appendix

The analytical form of the coupling coefficients K^{+}_{ijlm} and K^{-}_{ijlm} of the second order theory are as follows:

$$K^{+}_{ijlm} = [D^{+}_{ijlm} - (k_i k_j \cos(\theta_l - \theta_m) - R_i R_j)](R_i R_j)^{-1/2} + (R_i + R_j) \tag{4}$$

$$K^{-}_{ijlm} = [D^{-}_{ijlm} - ((k_i k_j \cos(\theta_l - \theta_m) + R_i R_j)](R_i R_j)^{-1/2} + (R_i + R_j) \tag{5}$$

where

$$D^{+}_{ijlm} = \frac{(\sqrt{R_i} + \sqrt{R_j})\{\sqrt{R_i}(k_j^2 - R_j^2) + \sqrt{R_j}(k_i^2 - R_i^2)\}}{(\sqrt{R_i} + \sqrt{R_j})^2 - k^{+}_{ijlm}\tanh(k^{+}_{ijlm}h)} + \frac{2(\sqrt{R_i} + \sqrt{R_j})^2(k_i k_j \cos(\theta_l - \theta_m) - R_i R_j)}{(\sqrt{R_i} + \sqrt{R_j})^2 - k^{+}_{ijlm}\tanh(k^{+}_{ijlm}h)} \tag{6}$$

$$D^{-}_{ijlm} = \frac{(\sqrt{R_i} - \sqrt{R_j})\{\sqrt{R_j}(k_i^2 - R_i^2) - \sqrt{R_i}(k_j^2 - R_j^2)\}}{(\sqrt{R_i} - \sqrt{R_j})^2 - k^{-}_{ijlm}\tanh(k^{-}_{ijlm}h)} + \frac{2(\sqrt{R_i} - \sqrt{R_j})^2(k_i k_j \cos(\theta_l - \theta_m) + R_i R_j)}{(\sqrt{R_i} - \sqrt{R_j})^2 - k^{-}_{ijlm}\tanh(k^{-}_{ijlm}h)} \tag{7}$$

$$k^{-}_{ijlm} = \sqrt{k_i^2 + k_j^2 - 2k_i k_j \cos(\theta_l - \theta_m)} \tag{8}$$

$$k^{+}_{ijlm} = \sqrt{k_i^2 + k_j^2 + 2k_i k_j \cos(\theta_l - \theta_m)} \tag{9}$$

$$R_i = \omega_i^2 / g \tag{10}$$

References

1. Dysthe, K., Krogstad, H.E., Müller, P.: Oceanic rogue waves. Annu. Rev. Fluid Mech. **40**, 287–310 (2008)
2. Onorato, M., Residori, S., Bortolozzo, U., Montina, A., Arecchi, F.T.: Rogue waves and their generating mechanisms in different physical contexts. Phys. Rep. **528**(2), 47–89 (2013)
3. Guedes, C., Soares, Cherneva, Z., Antão, E.M.: Abnormal waves during Hurricane Camille. J. Geophys. Res. (Oceans) **109**(C8) (2004)
4. Haver, S., Andersen, J.: Freak waves: rare realizations of a typical population or typical realizations of a rare population? In: Proceedings of 10th International Offshore and Polar Engineering (ISOPE) Conference, Seattle (2000)
5. Kharif, C., Pelinovsky, E.: Physical mechanisms of the rogue wave phenomenon. Eur. J. Mech. B/Fluid **21**(5), 561–577 (2002)
6. de Pinho, U.F., Liu, P.C., Ribeiro, C.E.P.: Freak waves at Campos basin, Brazil. Geofizika **21**, 53–67 (2004)
7. Magnusson, A.K., Donelan, M.A.: The Andrea wave characteristics of a measured North Sea rogue wave. J. Offshore Mech. Arct. Eng **135**(3), 031108 (2013)
8. Lavrenov, I.: The wave energy concentration at the Agulhas Current of South Africa. Nat. Hazard **17**, 117–127 (1998)
9. Hauser, D., Kahma, K.K., Krogstad, H.E., Lehner, S., Monbaliu, J., Wyatt, W.L. (eds.): Measuring and Analysing the Directional Spectrum of Ocean Waves. Cost Office, Brussels (2005)
10. NORSOK. Standard N-003: Action and action effects. Norwegian Technology Standardization, Oslo (2007)
11. Ochi, M.K.: Ocean Waves: The Stochastic Approach. Cambridge University Press, Cambridge (1998)
12. Whitham, G.: Linear and Nonlinear Waves. Wiley Interscience, New York (1974)
13. Hasselmann, K.: On the non–linear energy transfer in a gravity–wave spectrum. Part 1: General theory. J. Fluid Mech. **12**, 481–500 (1962)
14. Forristall, G.: Wave crests distributions: observations and second-order theory. J. Phys. Ocean. **30**, 1931–1943 (2000)
15. Longuet-Higgins, M.: The effect of non-linearities on statistical distribution in the theory of sea waves. J. Fluid Mech. **17**, 459–480 (1963)
16. Sharma, N., Dean, R.: Second-order directional seas and associated wave forces. Soc. Petrol. Eng. J. **4**, 129–140 (1981)
17. Dalzell, J.: A note on finite depth second–order wave–wave interactions. Appl. Ocean Res. **21**, 105–111 (1999)
18. Toffoli, A., Onorato, M., Babanin, A.V., Bitner-Gregersen, E., Osborne, A.R., Monbaliu, J.: Second–order theory and set–up in surface gravity waves: a comparison with experimental data. J. Phys. Ocean. **37**, 2726–2739 (2007)
19. Arhan, M., Plaisted, R.O.: Non–linear deformation of sea–wave profiles in intermediate and shallow water. Oceanol. Acta **4**(2), 107–115 (1981)
20. Tayfun, M.A.: Narrow–band nonlinear sea waves. J. Geophys. Res. **85**(C3), 1548–1552 (1980)

21. Toffoli, A., Bitner-Gregersen, E., Onorato, M., Babanin, A.V.: Wave crest and trough distributions in a broad–banded directional wave field. Ocean Eng. **35**, 1784–1792 (2008)
22. Bitner-Gregersen, E.M., Bhattacharya, S.K., Chatjigeorgiou, I.K., Eames, I., Ellermann, K., Ewans, K., Hermanski, G., Johnson, M.C., Ma, N., Maisondieu, C., Nilva, A., Rychlik, I., Waseda, T.: Recent developments of ocean environmental description with focus on uncertainties. Ocean Eng. **86**, 26–46 (2014)
23. Janssen, P.A.E.M.: Nonlinear four–wave interaction and freak waves. J. Phys. Ocean. **33**(4), 863–884 (2003)
24. Onorato, M., Osborne, A., Serio, M., Bertone, S.: Freak wave in random oceanic sea states. Phys. Rev. Lett. **86**(25), 5831–5834 (2001)
25. Fedele, F.: On the kurtosis of deep-water gravity waves. J. Fluid Mech. **782**, 25–36 (2015)
26. Zakharov, V., Ostrovsky, L.: Modulation instability: the beginning. Physica D **238**(5), 540–548 (2009)
27. Tulin, M.P., Waseda, T.: Laboratory observation of wave group evolution, including breaking effects. J. Fluid Mech. **378**, 197–232 (1999)
28. Alber, I.E.: The effects of randomness on the stability of two-dimensional surface wavetrains. Proc. R. Soc. Lond. A **363**(1715), 525–546 (1978)
29. Onorato, M., Cavaleri, L., Fouques, S., Gramstad, O., Janssen, P.A.E.M., Monbaliu, J., Osborne, A.R., Pakozdi, C., Serio, M., Stansberg, C., Toffoli, A., Trulsen, K.: Statistical properties of mechanically generated surface gravity waves: a laboratory experiment in a 3d wave basin. J. Fluid Mech. **627**, 235–257 (2009)
30. Onorato, M., Waseda, T., Toffoli, A., Cavaleri, L., Gramstad, O., Janssen, P.A.E.M., Kinoshita, T., Monbaliu, J., Mori, N., Osborne, A.R., Serio, M., Stansberg, C., Tamura, H., Trulsen, K.: Statistical properties of directional ocean waves: the role of the modulational instability in the formation of extreme events. Phys. Rev. Lett. **102**, 114502 (2009)
31. Waseda, T., Kinoshita, T., Tamura, H.: Evolution of a random directional wave and freak wave occurrence. J. Phys. Oceanogr. **39**, 621–639 (2009)
32. Cherneva, Z., Tayfun, M.A., Soares, C.G.: Statistics of nonlinear waves generated in an offshore wave basin. J. Geophys. Res. **114**(C8) (2009)
33. Shemer, L., Sergeeva, A.: An experimental study of spatial evolution of statistical parameters in a unidirectional narrow-banded random wavefield. J. Geophys. Res. **114**(C1) (2009)
34. Katsardi, V., De Lutio, L., Swan, C.: An experimental study of large waves in intermediate and shallow water depths. Part I: wave height and crest height statistics. Coast. Eng. **73**, 43–57 (2013)
35. Latheef, M., Swan, C.: A laboratory study of wave crest statistics and the role of directional spreading. Proc. R. Soc. A **469** (2013)
36. Heller, E.J., Kaplan, L., Dahlen, A.: Refraction of a gaussian seaway. J. Geophys. Res. **113**(C9) (2008)
37. Toffoli, A., Waseda, T., Houtani, H., Cavaleri, L., Greaves, D., Onorato, M.: Rogue waves in opposing currents: an experimental study on deterministic and stochastic wave trains. J. Fluid Mech. **769**, 277–297 (2015)
38. Lavrenov, I., Porubov, A.V.: Three reasons for freak wave generation in the non-uniform current. Eur. J. Mech. B/Fluids **25**, 574–585 (2006)
39. White, B.S., Fornberg, B.: On the chance of freak waves at the sea. J. Fluid Mech. **255**, 113–138 (1998)
40. Longuet-Higgins, M.S., Stewart, R.W.: The changes in amplitude of short gravity waves on steady non-uniform currents. J. Fluid Mech. **10**(4), 529–549 (1961)
41. Peregrine, D.H.: Interaction of water waves and current. In: Chia-Shun Yih (ed.) Advances in Applied Mechanics, pp. 9–117. Elsevier (1976)
42. Chawla, A.: An experimental study on the dynamics of wave blocking and breaking on opposing currents. Ph.D. thesis, University of Delaware (2000)
43. Gerber, M.: The Benjamin–Feir instability of a deep water stokes wavepacket in the presence of a non-uniform medium. J. Fluid Mech. **176**, 311–332 (1987)

44. Lai, R.J., Long, S.R., Huang, N.: Laboratory studies of wave-current interaction: kinematics of the strong interaction. J. Geophysic. Res. **94**(C11), 16201–16214 (1989)
45. Smith, R., Giant waves. J. Fluid Mech. **77**(3), 417–431 (1976)
46. Hjelmervik, K.B., Trulsen, K.: Freak wave statistics on collinear currents. J. Fluid Mech. **637**, 267–284 (2009)
47. Onorato, M., Proment, D., Toffoli, A.: Triggering rogue waves in opposing currents. Phys. Rev. Lett. **107**, 184502 (2011)
48. Toffoli, A., Cavaleri, L., Babanin, A.V., Benoit, M., Bitner-Gregersen, E.M., Monbaliu, J., Onorato, M., Osborne, A.R., Stansberg, C.T.: Occurrence of extreme waves in three-dimensional mechanically generated wave fields propagating over an oblique current. Nat. Hazards Earth Syst. Sci. **11**, 1–9 (2011)
49. Toffoli, A., Waseda, T., Houtani, H., Kinoshita, T., Collins, K., Proment, D., Onorato, M.: Excitation of rogue waves in a variable medium: an experimental study on the interaction of water waves and currents. Phys. Rev. E **87**, 051201 (2013)
50. Komen, G., Cavaleri, L., Donelan, M., Hasselmann, K., Hasselmann, H., Janssen, P.: Dynamics and Modeling of Ocean Waves. Cambridge University Press, Cambridge (1994)
51. Onorato, M., Osborne, A., Serio, M., Cavaleri, L., Brandini, C., Stansberg, C.: Extreme waves, modulational instability and second order theory: wave flume experiments on irregular waves. Eur. J. Mech. B/Fluids **25**, 586–601 (2006)
52. Goda, Y.: Random seas and design on marine structures. Advanced Series on Ocean Engineering, vol. 15. World Scientific, Singapore (2000)
53. Janssen, P., Bidlot, J.-R.: On the extension of the freak wave warning system and its verification. ECMWF Technical Memorandum No. 588 (2009)
54. Toffoli, A., Babanin, A.V., Onorato, M., Waseda, T.: Maximum steepness of oceanic waves: field and laboratory experiments. Geophys. Res. Lett. **37**, L05603 (2010)
55. Dysthe, K.B., Trulsen, K., Krogstad, H., Socquet-Juglard, H.: Evolution of a narrow–band spectrum of random surface gravity waves. J. Fluid Mech. **478**, 1–10 (2003)
56. Socquet-Juglard, H., Dysthe, K., Trulsen, K., Krogstad, H., Liu, J.: Probability distributions of surface gravity waves during spectral changes. J. Fluid Mech. **542**, 195–216 (2005)
57. Onorato, M., Osborne, A.R., Serio, M., Resio, D., Puskarev, A., Zakharov, V.E., Brandini, C.: Freely decaying weak turbulence for sea surface gravity waves. Phys. Rev. Lett. **89**(4), 144501 (2002)
58. Yuen, H.C., Lake, B.M.: Nonlinear dynamics of deep-water gravity waves. Adv. Appl. Mech. **22**, 20–228 (1982)
59. Dysthe, K.B., Trulsen, K., Krogstad, H.E., Socquet-Juglard, H.: Evolution of a narrow-band spectrum of random surface gravity waves. J. Fluid Mech. **478**, 1–10 (2003)
60. Dias, F., Kharif, C.: Nonlinear gravity and capillary-gravity waves. Annu. Rev. Fluid Mech. **31**(1), 301–346 (1999)

Introduction to Wave Turbulence Formalisms for Incoherent Optical Waves

Antonio Picozzi, Josselin Garnier, Gang Xu, and Sergio Rica

Abstract We provide an introduction to different wave turbulence formalisms describing the propagation of partially incoherent optical waves in nonlinear media. We consider the nonlinear Schrödinger equation as a representative model accounting for a nonlocal or a noninstantaneous nonlinearity, as well as higher-order dispersion effects. We discuss the wave turbulence kinetic equation describing, e.g., wave condensation or wave thermalization through supercontinuum generation; the Vlasov formalism describing incoherent modulational instabilities and the formation of large scale incoherent localized structures in analogy with long-range gravitational systems; and the weak Langmuir turbulence formalism describing spectral incoherent solitons, as well as spectral shock or collapse singularities. Finally, recent developments and some open questions are discussed, in particular in relation with a wave turbulence formulation of laser systems and different mechanisms of breakdown of thermalization.

A. Picozzi (✉)
Laboratoire Interdisciplinaire Carnot de Bourgogne, Université de Bourgogne Franche-Comté, 9 Av. A. Savary, 21078 Dijon, France
e-mail: Antonio.Picozzi@u-bourgogne.fr

J. Garnier
Laboratoire de Probabilités et Modèles Aléatoires, University Paris Diderot, 75205 Paris Cedex 13, France
e-mail: garnier@math.univ-paris-diderot.fr

G. Xu
PhLAM/IRCICA, CNRS-Université Lille 1, UMR 8523/USR 3380, F-59655 Villeneuve d'Ascq, France
e-mail: gang.xu@ircica.univ-lille1.fr

S. Rica
Facultad de Ingeniería y Ciencias, Universidad Adolfo Ibáñez, Avda. Diagonal las Torres 2640, Peñalolén, Santiago, Chile
e-mail: sergio.rica@uai.cl

M. Onorato et al. (eds.), *Rogue and Shock Waves in Nonlinear Dispersive Media*,
Lecture Notes in Physics 926, DOI 10.1007/978-3-319-39214-1_8

1 Introduction

1.1 From Incoherent Solitons to Wave Turbulence

The coherence properties of partially incoherent optical waves propagating in nonlinear media have been studied since the advent of nonlinear optics in the 1960s, because of the natural poor degree of coherence of laser sources available at that time. However, it is only recently that the dynamics of incoherent nonlinear optical waves received a renewed interest. The main motive for this renewal of interest is essentially due to the first experimental demonstration of incoherent solitons in photorefractive crystals [1, 2]. The formation of an incoherent soliton results from the *spatial self-trapping* of incoherent light that propagates in a highly noninstantaneous response nonlinear medium [3, 4]. This effect is possible because of the noninstantaneous photorefractive nonlinearity that averages the field fluctuations provided that its response time, τ_R, is much longer than the correlation time t_c that characterizes the incoherent beam fluctuations, i.e., $t_c \ll \tau_R$. The remarkable simplicity of experiments realized in photorefractive crystals has led to a fruitful investigation of the dynamics of incoherent nonlinear waves. Several theoretical approaches have been developed to describe such experiments [5–8], which have been subsequently shown to be formally equivalent one to each other [9, 10].

The field of incoherent optical solitons has become a blooming area of research, as illustrated by several important achievements, e.g., the existence of incoherent dark solitons [11, 12], the modulational instability of incoherent waves [13–15], incoherent solitons in resonant interactions [16, 17], in liquid crystals [18], in nonlocal nonlinear media [19, 20], in spin waves [21], or spectral incoherent solitons in optical fibers [22, 23]. Nowadays, statistical nonlinear optics constitutes a growing field of research covering various topics of modern optics, e.g., supercontinuum generation [24], filamentation [25], random lasers [26], or extreme rogue wave events emerging from optical turbulence [27–29].

From a broader perspective, statistical nonlinear optics is fundamentally related to fully developed turbulence [30, 31], a subject which still constitutes one of the most challenging problems of theoretical physics [32, 33]. In its broad sense, the kinetic wave theory provides a nonequilibrium thermodynamic description of developed turbulence. We schematically report in Fig. 1a qualitative and intuitive physical insight into the analogy which underlies the kinetic wave approach and the kinetic theory relevant for a gas system. The wave turbulence theory occupies a rather special place on the road-map of modern science, at the interface between applied mathematics, fluid dynamics, statistical physics and engineering. It has potential applications and implications in a diverse range of subjects including oceanography, plasma physics and condensed matter physics. This chapter is aimed at introducing the wave turbulence theory as an appropriate theoretical framework to describe the propagation of incoherent optical waves.

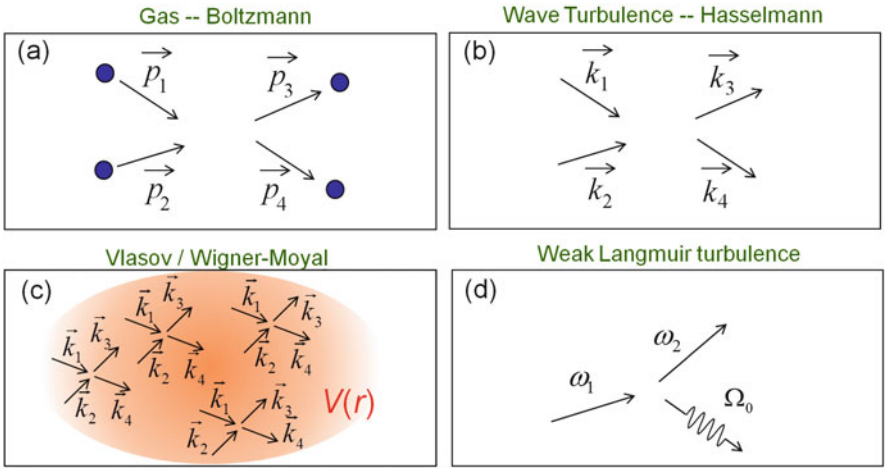

Fig. 1 Analogy between a system of classical particles and the propagation of an incoherent optical wave in a cubic nonlinear medium. (**a**) As described by the kinetic gas theory (Boltzmann kinetic equation), collisions between particles are responsible for an irreversible evolution of the gas towards thermodynamic equilibrium. (**b**) In complete analogy, the (Hasselmann) WT kinetic equation and the underlying four-wave mixing describe an irreversible evolution of the incoherent optical wave toward the thermodynamic Rayleigh-Jeans equilibrium state. (**c**) When the incoherent optical wave exhibits an inhomogeneous statistics, the four-wave interaction no longer takes place locally, i.e., the quasi-particles feel the presence of an effective self-consistent potential, $V(r)$, which prevents them from relaxing to thermal equilibrium. The dynamics of the incoherent optical wave turns out to be described by a Vlasov-like kinetic equation. (**d**) In the presence of a noninstantaneous nonlinear interaction, the causality condition inherent to the response function changes the physical picture: the nonlinear interaction involves a material excitation (e.g., molecular vibration in the example of Raman scattering). The dynamics of the incoherent optical wave turns out to be described by a kinetic equation analogous to the weak Langmuir turbulence equation. Note however that a highly noninstantaneous nonlinear response is no longer described by the weak Langmuir turbulence equation, but instead by the 'long-range' Vlasov-like equation (see Fig. 3)

In the following we provide a panoramic overview of the subjects covered by this chapter. Note that these topics have been usually discussed separately in the literature within different contexts.

1.1.1 Wave Turbulence Formulation: Thermalization and Condensation

Consider the nonlinear propagation of a partially coherent optical wave characterized by fluctuations that are statistically homogeneous in space (note that caution should be exercised when separating the description of statistically homogeneous and inhomogeneous random waves, since a homogeneous statistical wave can become inhomogeneous as a result of the incoherent MI (see Sect. 4), or the instability of the Zakharov-Kolmogorov spectrum [34]). In complete analogy with a system

of classical particles, the incoherent optical field evolves, owing to nonlinearity, towards a thermodynamic equilibrium state, as schematically illustrated in Fig. 1a,b. A detailed theoretical description of the process of dynamical thermalization constitutes a difficult problem. However, a considerable simplification occurs when wave propagation is essentially dominated by linear dispersive effects, so that a weakly nonlinear description of the field becomes possible [30, 32, 33]. The weak-(or wave-)turbulence (WT) theory has been the subject of lot of investigations in the context of plasma physics [35], in which it is often referred to the so-called "random phase-approximation" approach [30, 35–39]. This approach may be considered as a convenient way of interpreting the results of the more rigorous technique based on a multi-scale expansion of the cumulants of the nonlinear field, as originally formulated in [40–42]. This theory has been reviewed in [43], and studied in more details through the analysis of the probability distribution function of the random field in [33]. In a loose sense, the so-called 'random phase approximation' may be considered as justified when phase information becomes irrelevant to the wave interaction due to the strong tendency of the waves to decohere. The random phases can thus be averaged out to obtain a weak turbulence description of the incoherent wave interaction, which is formally based on irreversible kinetic equations [30]. It results that, in spite of the formal reversibility of the equation governing wave propagation, the kinetic equation describes an irreversible evolution of the field to thermodynamic equilibrium. This equilibrium state refers to the fundamental Rayleigh-Jeans spectrum, whose tails are characterized by an equipartition of energy among the Fourier modes. The mathematical statement of such irreversible process relies on the H-theorem of entropy growth, whose origin is analogous to the Boltzmann's H-theorem relevant for gas kinetics. Note that the terminology 'wave turbulence' is often employed in the literature to denote the study of wave systems governed by this type of irreversible kinetic equations, whose structure is analogous to the Boltzmann kinetic formulation (see, e.g., [30, 33, 39]). However, in many cases in this review the terminology 'wave turbulence' will be employed in a broader sense, which also includes different forms of nonequilibrium kinetic formalisms, such as the Vlasov or the weak Langmuir turbulence descriptions of a wave system (see Fig. 1). We remark that besides this *nonequilibrium* kinetic approach, the equilibrium properties of a random nonlinear wave may be studied on the basis of *equilibrium* statistical mechanics by computing appropriate partition functions [44–49].

In this chapter we will discuss different processes of optical wave thermalization on the basis of the WT theory, as well as some mechanisms responsible for its inhibition. In particular, the phenomenon of supercontinuum generation can be interpreted, under certain conditions, as a consequence of the natural thermalization of the optical field toward the thermodynamic equilibrium state [50–52]. Furthermore, wave thermalization can be characterized by a self-organization process, in the sense that it is thermodynamically advantageous for the system to generate a large-scale coherent structure in order to reach the most disordered equilibrium state. A remarkable example of this counterintuitive phenomenon is provided by wave condensation [53–57], whose thermodynamic equilibrium properties are analogous

to those of quantum Bose-Einstein condensation. Classical wave condensation can be interpreted as a redistribution of energy among different modes, in which the (kinetic) energy is transferred to small scales fluctuations, while an inverse process increases the power (i.e., number of 'particles') into the lowest allowed mode, thus leading to the emergence of a large scale coherent structure.

We note in this respect that the phenomenon of condensation has been recently extended to optical cavities in different circumstances [58–65], which raises important questions, such as e.g., the relation between laser operation and the phenomenon of Bose-Einstein condensation (see Sect. 5 below) [66]. From a different perspective, when a wave system is driven away from equilibrium by an external source, it no longer relaxes towards the Rayleigh-Jeans equilibrium distribution. A typical physical example of forced system can be the excitation of hydrodynamic surface waves by the wind. This corresponds to the generic problem of developed turbulence. In general, it refers to a system in which the frequency-scales of forcing and damping differ significantly. The nonlinear interaction leads to an energy redistribution among the frequencies (modes). A fundamental problem is to find the stationary spectrum of the system, i.e., the law of energy distribution over the different scales. The WT theory provides an answer to this vast issue under the assumption that the nonlinear interaction is weak—the so-called Kolmogorov-Zakharov spectra of turbulence [30]. An experiment aimed at observing these nonequilibrium stationary turbulent states in the context of optics has been reported in [67] (see [68] for a complete review). Beyond optics, we refer the interested reader to different comprehensive reviews concerning this vast area of research [30, 32, 33, 39, 43].

1.1.2 Vlasov and Wigner-Moyal Formulations: Incoherent Solitons

When the nonlinear material is characterized by a nonlocal or a highly-noninstantaneous response, the dynamics of the incoherent wave turns out to be essentially governed by an effective nonlinear potential $V(r)$. This potential is *self-consistent* in the sense that it depends itself on the averaged intensity distribution of the random field, as schematically illustrated in Fig. 1c. Actually, the mechanism underlying the formation of an incoherent soliton state finds its origin in the existence of such self-consistent potential, which is responsible for a spatial self-trapping of the incoherent optical beam. From this point of view, the very nature of incoherent optical solitons is analogous to the random phase solitons predicted in plasma physics a long time ago in the framework of the Vlasov equation [69–71]. This analogy with nonlinear plasma waves has been also exploited in optics in different circumstances [72–74], in particular in the framework of the Wigner-Moyal formalism [8, 75], or to interpret the existence of a threshold in the incoherent modulational instability as a consequence of the phenomenon of Landau damping [8].

Incoherent spatial solitons can be also supported by a nonlocal spatial nonlinearity, instead of the traditional noninstantaneous nonlinearity inherent to the

photorefractive experiments. A nonlocal wave interaction means that the response of the nonlinearity at a particular point is not determined solely by the wave intensity at that point, but also depends on the wave intensity in the neighborhood of this point. Nonlocality thus constitutes a generic property of a large number of nonlinear wave systems [76–83], and the dynamics of nonlocal nonlinear waves has been widely investigated in this last decade [84–88]. In particular, in the highly nonlocal limit, i.e., in the limit where the range of the nonlocal response is much larger than the size of the beam, the propagation equation reduces to a linear and local equation with an effective guiding potential given by the nonlocal response function. The optical beam can thus be guided by the nonlocal response of the material, a process originally termed 'accessible soliton' [78, 79, 88, 89]. In this highly nonlocal limit, it has been shown both theoretically and experimentally that a speckled beam can be guided and trapped by the effective waveguide induced by the nonlocal response [19, 90].

More recently, the long-term evolution of a modulationally unstable homogeneous wave has been studied in the presence of a nonlocal response [20]. Contrarily to the expected soliton turbulence process where a coherent soliton is eventually generated in the midst of thermalized small-scale fluctuations [46, 91–93], a highly nonlocal response is responsible for an *incoherent soliton turbulence* process [20]. It is characterized by the spontaneous formation of an incoherent soliton structure starting from an initially homogeneous plane-wave. A WT approach of the problem revealed that this type of incoherent solitons can be described in detail in the framework of a long-range Vlasov equation, which is shown to provide an accurate statistical description of the nonlocal random wave even in the *highly nonlinear regime* of interaction. We note that this Vlasov equation differs from the traditional Vlasov equation considered for the study of incoherent modulational instability and incoherent solitons in plasmas [70, 71, 94], hydrodynamics [95] and optics [8, 73, 74, 96]. The structure of this Vlasov equation is in fact analogous to that recently used to describe systems of particles with long-range interactions [97]. For this reason we will term this equation 'long-range Vlasov' equation. It is important to underline that the long-range nature of a highly nonlocal nonlinear response prevents the wave system from reaching thermal equilibrium [20]. This fact can be interpreted intuitively in analogy with gravitational long-range systems and the Vlasov-like description of the dynamics of formation and interaction of galaxies in the Universe [97].

1.1.3 Weak Langmuir Turbulence Formulation: Spectral Incoherent Solitons and Incoherent Shocks

When the incoherent wave propagates in a nonlinear medium whose non-instantaneous response time cannot be neglected (e.g., Raman effect in optical fibers), the dynamics turns out to be strongly affected by the causality property inherent to the nonlinear response function (see Fig. 1). The kinetic wave theory reveals in this case that the appropriate description is provided by a formalism

analogous to that used to describe weak Langmuir turbulence in plasmas [22, 98]. A major prediction of the theory is the existence of spectral incoherent solitons [22, 23, 99]. This incoherent soliton is of a fundamental different nature than the incoherent solitons discussed here above. In particular, it does not exhibit a confinement in the spatiotemporal domain, but exclusively in the frequency domain. For this reason this incoherent structure has been termed 'spectral incoherent soliton'. Indeed, because the optical field exhibits a stationary statistics, the soliton behavior only manifests in the spectral domain. Then contrarily to the expected thermalization process, the incoherent wave self-organizes into these incoherent soliton structures, which can thus be regarded as nonequilibrium and nonstationary stable states of the incoherent field.

As discussed here above, the existence of a highly nonlocal response changes the dynamics of spatially incoherent nonlinear waves in a profound way. A natural question is to see how a highly noninstantaneous nonlinear response can change the dynamics of temporally incoherent waves. In this temporal long-range regime, the spectral dynamics of the field can exhibit incoherent shock waves [100]. They manifest themselves as an unstable singular behavior of the spectrum of incoherent waves, i.e., 'spectral wave-breaking'. Note that shock waves play an important role in many different branches of physics [101]. However, it should be underlined that, at variance with conventional coherent shock waves, which require the strong nonlinear regime, incoherent shocks develop into the highly incoherent regime of propagation, in which linear dispersive effects dominate nonlinear effects. The weakly nonlinear kinetic approach then reveals that these incoherent shocks are described, as a rule, by singular integro-differential kinetic equations, which involve the Hilbert transform as singular operator. In this way, the theory reveals unexpected links with the 3D vorticity equation in incompressible fluids [102], or the integrable Benjamin-Ono equation [103, 104], which was originally derived in hydrodynamics to model internal waves in stratified fluids [105, 106].

1.1.4 Breakdown of Thermalization and the FPU Problem

The relationship between formal reversibility and actual dynamics can be rather complex for infinite dimensional Hamiltonian systems like classical optical waves. In integrable systems, one may expect that the dynamics is essentially periodic in time, reflecting the underlying regular phase-space structure of nested tori. This recurrent behavior is broken in nonintegrable systems, where the dynamics is in general governed by an irreversible process of diffusion in phase space. The essential properties of this irreversible evolution to equilibrium can be described by the wave turbulence theory.

It is instructive to discuss the phenomenology of nonlinear wave thermalization from a broader perspective. We recall in this respect the fundamental assumption of statistical mechanics that a closed system with many degrees of freedom ergodically samples all equal energy points in phase space. In order to analyze the limits of this assumption, Fermi, Pasta and Ulam (FPU) considered in the 1950s a

one-dimensional chains of particles with anharmonic forces between them [107]. They argued that, owing to the nonlinear coupling, an initial state in which the energy is in the first few lowest modes would eventually relax to a state of thermal equilibrium where the energy is equidistributed among all modes on the average. However they observed that, instead of leading to the thermalization of the system, the energy transfer process involves only a few modes and exhibits a reversible behavior, in the sense that after a sufficiently (long) time the system nearly goes back to its initial state. This recurrent behavior could not be interpreted in terms of Poincaré recurrences, a feature which motivated an intense research activity. Fundamental mathematical and physical discoveries, like the Kolmogorov-Arnold-Moser theorem and the formulation of the soliton concept, have led to a better understanding of the Fermi-Pasta-Ulam problem, although it is by no means completely understood [107, 108].

We should note that, in spite of the large number of theoretical studies, experimental demonstrations of FPU recurrences have been reported in very few systems. In particular, the FPU recurrences associated to modulational instability of the NLS equation have been experimentally studied in deep water waves [109], and, more recently, in optical wave systems [110, 111]. In relation with the FPU problem, we will comment some mechanisms which inhibit the irreversible process of optical wave thermalization toward the Rayleigh-Jeans distribution, as described in detail by the WT kinetic equation. In particular, the WT theory reveals the existence of local invariants in frequency space, which lead to a novel family of equilibrium states of a different nature than the expected thermodynamic (Rayleigh-Jeans) equilibrium states [112, 113].

1.2 Organization of the Chapter

The chapter is structured in three different parts aimed at introducing the three different formalisms discussed above. We will start with the Vlasov formalism in Sect. 2, which describes in particular incoherent MI and incoherent solitons. Next we will consider the weak Langmuir turbulence formalism in Sect. 3, which describes spectral incoherent solitons, as well as spectral shocks and collapse singularities. In Sect. 4 we will consider the wave turbulence kinetic equation, which will be discussed in the framework of optical wave thermalization and condensation. Finally some generalizations concerning the wave turbulence formulation of laser systems and the breakdown of thermalization, as well as some open problems will be discussed in the last Sect. 5.

2 Vlasov Formalism

In this Section we study the transverse spatial evolution of a partially coherent wave that propagates in a nonlocal nonlinear medium. We consider the case where the random wave exhibits fluctuations that are statistically inhomogeneous in space. As illustrated schematically in Fig. 2, the dynamics of the incoherent wave is described by different forms of the Vlasov equation, whose self-consistent potential depends on the degree of nonlocality.

2.1 Nonlocal Nonlinear Response

2.1.1 NLS Model

A nonlocal nonlinear response of the medium is found in several wave systems such as, e.g., dipolar Bose-Einstein condensates [76], atomic vapors [77], nematic liquid crystals [78, 79, 114], photorefractive media [82], thermal susceptibilities [80, 81, 115], and plasmas physics [83]. For this reason the impact of nonlocality on the dynamics of nonlocal nonlinear waves has been widely investigated [88], in

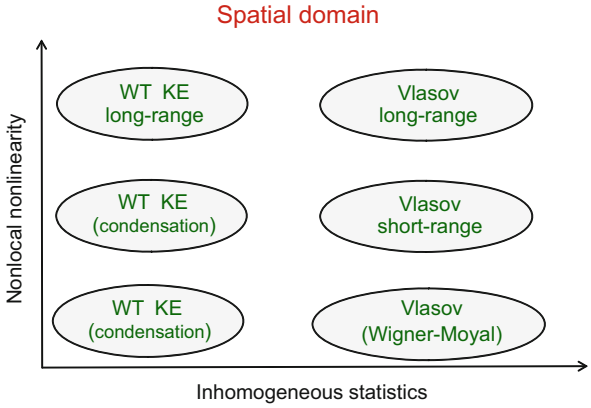

Fig. 2 Schematic illustration of the validity of the fundamental kinetic equations in the framework of a spatially nonlocal nonlinear response—the *vertical arrow* denotes the amount of nonlocality of the nonlinear interaction, while the *horizontal arrow* represents the amount of inhomogeneous statistics of the incoherent wave. When the incoherent wave is characterized by fluctuations that are statistically homogeneous in space, the relevant kinetic description is provided by the wave turbulence kinetic equation ('WT KE'), which describes in particular the processes of optical wave thermalization or condensation (see Sect. 4). When the incoherent wave exhibits an inhomogeneous statistics, the relevant kinetic description is provided by different variants of the Vlasov equation, whose self-consistent potential depends on the amount of nonlocality in the system (see Sect. 2). The Vlasov equation describes in particular the phenomena of incoherent modulational instability and the formation of incoherent soliton states

particular through the analysis of MI [84], of dark solitons [87], or the inhibition of collapse in multi-dimensional systems [85, 86].

We consider here the standard form of the nonlocal NLS model equation describing wave propagation in nonlinear media that exhibit a nonlocal response

$$i\partial_z\psi + \alpha\nabla^2\psi + \gamma\psi \int U(\boldsymbol{x}-\boldsymbol{x}')\,|\psi|^2(\boldsymbol{x}',z)\,d\boldsymbol{x}' = 0, \tag{1}$$

where $\boldsymbol{x}$ denotes the position in the transverse plane of dimension d and ∇^2 denotes the corresponding transverse Laplacian ($\nabla^2 = \partial_x^2$ for $d = 1$, $\nabla^2 = \partial_x^2 + \partial_y^2$ for $d = 2$). The nonlocal response function $U(\boldsymbol{x})$ is a real and even function normalized in such a way that $\int U(\boldsymbol{x})\,d\boldsymbol{x} = 1$, so that in the limit of a local response [$U(\boldsymbol{x}) = \delta(\boldsymbol{x})$, $\delta(\boldsymbol{x})$ being the Dirac function], Eq. (1) recovers the standard local NLS equation. The parameters $\alpha = 1/(2k_L)$ and γ refer to the linear and nonlinear coefficients, respectively, where $k_L = n2\pi/\lambda_L$, n being the linear refractive index of the material and λ_L the wavelength of the laser source. A positive (negative) value of γ corresponds to a focusing (defocusing) nonlinear interaction. Besides the momentum, Eq. (1) conserves the power (or number of particles) $\mathscr{N} = \int |\psi(\boldsymbol{x})|^2 d\boldsymbol{x}$, and the Hamiltonian $\mathscr{H} = \mathscr{E} + \mathscr{U}$, where

$$\mathscr{E}(z) = \alpha \int |\nabla\psi(\boldsymbol{x},z)|^2\,d\boldsymbol{x} \tag{2}$$

denotes the linear (kinetic) contribution, and

$$\mathscr{U}(z) = -\frac{\gamma}{2}\iint |\psi(\boldsymbol{x},z)|^2\,U(\boldsymbol{x}-\boldsymbol{x}')\,|\psi(\boldsymbol{x}',z)|^2\,d\boldsymbol{x}\,d\boldsymbol{x}' \tag{3}$$

the nonlinear contribution to the total energy $\mathscr{H}$. We denote by σ the spatial extension of $U(\boldsymbol{x})$, which characterizes the amount of nonlocality in the system. This length scale has to be compared with the healing length $\Lambda = \sqrt{\alpha/(|\gamma|\rho)}$, where $\rho = \mathscr{N}/L^d$ is the density of power (intensity), L being the size of the periodic box in the numerical simulations. We recall that Λ denotes the typical wavelength excited by the modulational instability of a homogeneous background in the limit of a local nonlinearity, $\sigma \to 0$. An other important length scale is the typical length Δ that characterizes the homogeneity of the statistics. It reflects the typical length scale over which the fluctuations of the incoherent wave can be considered as homogeneous in space.

2.1.2 Homogeneous vs Inhomogeneous Statistics

The kinetic equation consists of an equation describing the evolution of the spectrum of the field during its propagation in the nonlinear medium. Note that, in the particular case in which diffraction effects can be neglected ($\alpha = 0$), an expression

for the evolution of the second order correlation function can be obtained in explicit form, see [116, 117].

As schematically described through Figs. 2, 3, the structure of a kinetic equation depends on the nature of the statistics of the random wave. The statistics is said to be homogeneous (or stationary in the temporal domain), if the correlation function $B(\boldsymbol{x_1}, \boldsymbol{x_2}, z) = \langle \psi(\boldsymbol{x_1}, z)\psi^*(\boldsymbol{x_2}, z)\rangle$ only depends on the distance $|\,\boldsymbol{x_1} - \boldsymbol{x_2}\,|$. In the following, the brackets $\langle . \rangle$ denote an average over the realizations of the initial noise of the random wave $\psi(\boldsymbol{x}, z = 0)$.

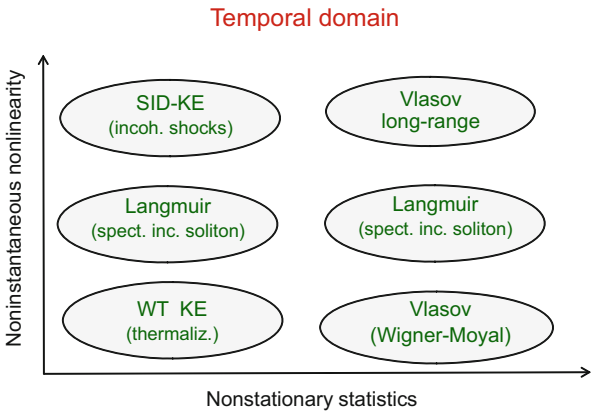

Fig. 3 Schematic illustration of the validity of the fundamental kinetic equations in the framework of a temporally noninstantaneous nonlinear response—the *vertical arrow* denotes the amount of noninstantaneous response of the nonlinearity, while the *horizontal arrow* represents the amount of non-stationary statistics of the incoherent wave. The diagram for the temporal domain reported here is similar to that reported in the spatial domain in Fig. 2. The essential difference between the spatial and the temporal domain relies on the fact that in the temporal domain the response function is constrained by the causality condition. It turns out that when the finite response time of the nonlinearity cannot be neglected, the relevant kinetic description is provided by an equation analogous to the weak Langmuir turbulence equation (see Sect. 3), which describes for instance non-localized spectral incoherent solitons. In the presence of a highly noninstantaneous nonlinear response and a stationary statistics of the incoherent wave, the weak Langmuir turbulence reduces to singular integro-differential kinetic equations ('SID-KE'), e.g., Benjamin-Ono equation, which describe spectral singularities such as dispersive shock waves and collapse behaviors. Conversely, when the wave exhibits a non-stationary statistics still in the presence of a highly noninstantaneous response, the dynamics is ruled by a 'temporal long-range' Vlasov equation, whose self-consistent potential is constrained by the causality condition of the noninstantaneous response function, which breaks the Hamiltonian structure of the Vlasov equation (see Sect. 2.4). The WT kinetic equation ('WT KE') turns out to be relevant for an instantaneous nonlinear response and a statistically stationary incoherent wave, as will be discussed in the framework of supercontinuum generation in Sect. 5.2

2.2 Short-Range Vlasov Equation

We follow the standard procedure to derive an equation for the evolution of the autocorrelation function of the field, $B(\boldsymbol{x},\boldsymbol{\xi},z) = \langle\psi(\boldsymbol{x}+\boldsymbol{\xi}/2,z)\psi^*(\boldsymbol{x}-\boldsymbol{\xi}/2,z)\rangle$, with

$$\boldsymbol{x} = (\boldsymbol{x}_1+\boldsymbol{x}_2)/2,\ \boldsymbol{\xi} = \boldsymbol{x}_1-\boldsymbol{x}_2. \tag{4}$$

Because of the nonlinear character of the NLS equation, the evolution of the second-order moment of the wave depends on the fourth-order moment. In the same way, the equation for the fourth-order moment depends on the sixth-order moment, and so on. One obtains in this way an infinite hierarchy of moment equations, in which the nth order moment depends on the $(n+2)$th order moment of the field. This makes the equations impossible to solve unless some way can be found to truncate the hierarchy. This refers to the fundamental problem of achieving a closure of the infinite hierarchy of the moment equations [30, 32, 33, 43]. A simple way to achieve a closure of the hierarchy is to assume that the field has Gaussian statistics. This approximation is justified in the weakly nonlinear regime, $L_d/L_{nl} \ll 1$ (or $|\mathscr{U}/\mathscr{E}| \ll 1$), where $L_d = \lambda_c^2/\alpha$ is the diffraction length, λ_c being the coherence length, and $L_{nl} = 1/(|\gamma|\rho)$ is the characteristic length of nonlinear interaction.

Exploiting the property of factorizability of moments of Gaussian fields, one obtains the following closed equation for the evolution of the autocorrelation function

$$i\partial_z B(\boldsymbol{x},\boldsymbol{\xi},z) = -2\alpha\nabla_{\boldsymbol{x}}.\nabla_{\boldsymbol{\xi}}B(\boldsymbol{x},\boldsymbol{\xi},z) - \gamma P(\boldsymbol{x},\boldsymbol{\xi},z) - \gamma Q(\boldsymbol{x},\boldsymbol{\xi},z), \tag{5}$$

where

$$P(\boldsymbol{x},\boldsymbol{\xi}) = B(\boldsymbol{x},\boldsymbol{\xi})\int U(\boldsymbol{y})\big[N(\boldsymbol{x}-\boldsymbol{y}+\boldsymbol{\xi}/2) - N(\boldsymbol{x}-\boldsymbol{y}-\boldsymbol{\xi}/2)\big]d\boldsymbol{y} \tag{6}$$

$$\begin{aligned} Q(\boldsymbol{x},\boldsymbol{\xi}) = \int U(\boldsymbol{y})\big[&B(\boldsymbol{x}-\boldsymbol{y}/2+\boldsymbol{\xi}/2,\boldsymbol{y})B(\boldsymbol{x}-\boldsymbol{y}/2,\boldsymbol{\xi}-\boldsymbol{y}) + \\ &- B(\boldsymbol{x}-\boldsymbol{y}/2,\boldsymbol{\xi}+\boldsymbol{y})B(\boldsymbol{x}-\boldsymbol{y}/2-\boldsymbol{\xi}/2,-\boldsymbol{y})\big]d\boldsymbol{y}, \end{aligned} \tag{7}$$

and

$$N(\boldsymbol{x},z) \equiv B(\boldsymbol{x},\boldsymbol{\xi}=0,z) = \left\langle|\psi|^2\right\rangle(\boldsymbol{x},z) \tag{8}$$

denotes the averaged power of the field, which depends on the spatial variable $\boldsymbol{x}$ because the statistics of the field is *a priori* inhomogeneous. Note that we have omitted the z-label in Eqs. (6), (7).

Equations (5)–(7) is quite involved. To provide an insight into its physics we assume that the incoherent wave exhibits a quasi-homogeneous statistics, that is to say λ_c (i.e. the length scale of the random fluctuations) is much smaller than the

length scale of homogeneous statistics Δ (i.e. typically the size of the incoherent beam), $\varepsilon = \lambda_c/\Delta \ll 1$. We assume that the range of the response function is of the same order as the healing length, $\sigma \sim \Lambda$. Defining the local spectrum of the wave as the Wigner-like transform of the autocorrelation function,

$$n_{\boldsymbol{k}}(\boldsymbol{x}, z) = \int B(\boldsymbol{x}, \boldsymbol{\xi}, z)\, \exp(-i\boldsymbol{k}.\boldsymbol{\xi})\, d\boldsymbol{\xi}, \tag{9}$$

and performing a multiscale expansion of the solution

$$B(\boldsymbol{x}, \boldsymbol{\xi}, z) = B^{(0)}\big(\varepsilon\boldsymbol{x}, \boldsymbol{\xi}, \varepsilon z\big) + O(\varepsilon), \tag{10}$$

we obtain in the first-order in ε the following Vlasov-like kinetic equation [118]

$$\partial_z n_{\boldsymbol{k}}(\boldsymbol{x}, z) + \partial_{\boldsymbol{k}}\tilde{\omega}_{\boldsymbol{k}}(\boldsymbol{x}, z).\partial_{\boldsymbol{x}} n_{\boldsymbol{k}}(\boldsymbol{x}, z) - \partial_{\boldsymbol{x}}\tilde{\omega}_{\boldsymbol{k}}(\boldsymbol{x}, z).\partial_{\boldsymbol{k}} n_{\boldsymbol{k}}(\boldsymbol{x}, z) = 0. \tag{11}$$

The generalized dispersion relation reads

$$\tilde{\omega}_{\boldsymbol{k}}(\boldsymbol{x}, z) = \omega(\boldsymbol{k}) + V_{\boldsymbol{k}}(\boldsymbol{x}, z), \tag{12}$$

where $\omega(\boldsymbol{k}) = \alpha k^2$ is the linear dispersion relation of the NLS equation (1), and the self-consistent potential reads

$$V_{\boldsymbol{k}}(\boldsymbol{x}, z) = -\frac{\gamma}{(2\pi)^d} \int (1 + \tilde{U}_{\boldsymbol{k}-\boldsymbol{k}'})\, n_{\boldsymbol{k}'}(\boldsymbol{x}, z)\, d\boldsymbol{k}', \tag{13}$$

where $\tilde{U}(\boldsymbol{k}) = \int U(\boldsymbol{x}) \exp(-i\boldsymbol{k}.\boldsymbol{x})\, d\boldsymbol{x}$ is the Fourier transform of $U(\boldsymbol{x})$ [$\tilde{U}(\boldsymbol{k})$ being real and even] and

$$N(\boldsymbol{x}, z) = \frac{1}{(2\pi)^d} \int n_{\boldsymbol{k}}(\boldsymbol{x}, z)\, d\boldsymbol{k} \tag{14}$$

is the averaged spatial intensity profile of the wave [see Eq. (8)].

2.2.1 Properties of the Vlasov Equation

Several important properties of the Vlasov equation (11) result from its Poisson bracket structure. More specifically, the Vlasov equation can be recast in Hamiltonian form by means of the following Liouville's equation

$$d_z n_{\boldsymbol{k}}(z, \boldsymbol{x}) \equiv \partial_z n + \dot{\boldsymbol{x}}.\partial_{\boldsymbol{x}} n + \dot{\boldsymbol{k}}.\partial_{\boldsymbol{k}} n = 0, \tag{15}$$

where the variables $\boldsymbol{k}$ and $\boldsymbol{x}$ appear as canonical conjugate variables,

$$\dot{\boldsymbol{k}} = \partial_z \boldsymbol{k} = -\partial_{\boldsymbol{x}} \tilde{\omega}, \tag{16}$$

$$\dot{\boldsymbol{x}} = \partial_z \boldsymbol{x} = \partial_{\boldsymbol{k}} \tilde{\omega}, \tag{17}$$

where the generalized dispersion relation (12) plays the role of an effective Hamiltonian.

The Vlasov equation is a formally reversible equation, i.e., it is invariant under the transformation $(z, \boldsymbol{k}) \rightarrow (-z, -\boldsymbol{k})$. Moreover, it conserves the number of particles, $\mathscr{N} = (2\pi)^{-d} \iint n_{\boldsymbol{k}}(\boldsymbol{x}, z)\, d\boldsymbol{x} d\boldsymbol{k}$, the momentum $\mathscr{P} = (2\pi)^{-d} \iint \boldsymbol{k}\, n_{\boldsymbol{k}}(\boldsymbol{x}, z)\, d\boldsymbol{x} d\boldsymbol{k}$, and the Hamiltonian

$$\mathscr{H} = \frac{1}{(2\pi)^d} \iint \omega(\boldsymbol{k})\, n_{\boldsymbol{k}}(\boldsymbol{x})\, d\boldsymbol{x} d\boldsymbol{k} - \frac{\gamma}{2(2\pi)^{2d}} \iiint n_{\boldsymbol{k}_1}(\boldsymbol{x})\, \tilde{U}_{\boldsymbol{k}_1 - \boldsymbol{k}_2}\, n_{\boldsymbol{k}_2}(\boldsymbol{x}) d\boldsymbol{x} d\boldsymbol{k}_1 d\boldsymbol{k}_2. \tag{18}$$

In addition, the Vlasov equations (11)–(13) also conserves the so-called Casimirs, $\mathscr{M} = \iint f[n]\, d\boldsymbol{x} d\boldsymbol{k}$, where $f[n]$ is an arbitrary functional of the distribution $n_{\boldsymbol{k}}(\boldsymbol{x}, z)$.

2.3 Long-Range Vlasov Equation

2.3.1 Long-Range Response

Let us now consider a long-range nonlocal nonlinear response, $\sigma/\Lambda \gg 1$. Note that in this case the random field exhibits fluctuations whose spatial inhomogeneities are of the same order as the range of the nonlocal potential, $\sigma \sim \Delta$. The derivation of the long-range Vlasov equation is obtained by following a procedure similar to that for the short-range case ($\sigma \sim \Lambda$), except that we have to introduce the following scaling for the nonlocal potential

$$U(\boldsymbol{x}) = \varepsilon^d U^{(0)}(\varepsilon \boldsymbol{x}). \tag{19}$$

Note that the pre-factor ε^d is required by the normalization condition, $\int U(\boldsymbol{x}) d\boldsymbol{x} = \int U^{(0)}(\varepsilon \boldsymbol{x})\, d(\varepsilon^d \boldsymbol{x}) = 1$. Following the multiscale expansion technique [118], one can derive the Vlasov-like kinetic Eq. (11), with the effective dispersion relation

$$\tilde{\omega}_{\boldsymbol{k}}(\boldsymbol{x}, z) = \omega(\boldsymbol{k}) + V(\boldsymbol{x}, z), \tag{20}$$

and the long-range self-consistent potential

$$V(\boldsymbol{x}, z) = -\gamma \int U(\boldsymbol{x} - \boldsymbol{x}')\, N(\boldsymbol{x}', z)\, d\boldsymbol{x}'. \tag{21}$$

This effective potential then appears as a convolution of the nonlocal response with the intensity profile of the incoherent wave. Contrarily to the short-range potential, it does not depend on the spatial frequency $\boldsymbol{k}$. The long-range Vlasov equation conserves the number of particles, $\mathscr{N} = (2\pi)^{-d} \iint n_{\boldsymbol{k}}(\boldsymbol{x}, z)\, d\boldsymbol{x}d\boldsymbol{k}$, the momentum $\mathscr{P} = (2\pi)^{-d} \iint \boldsymbol{k}\, n_{\boldsymbol{k}}(\boldsymbol{x}, z)\, d\boldsymbol{x}\, d\boldsymbol{k}$, the Hamiltonian

$$\mathscr{H} = \frac{1}{(2\pi)^d} \iint \omega(\boldsymbol{k})\, n_{\boldsymbol{k}}(\boldsymbol{x}, z)\, d\boldsymbol{x}d\boldsymbol{k} + \frac{1}{2} \int V(\boldsymbol{x}, z) N(\boldsymbol{x}, z)\, d\boldsymbol{x}, \tag{22}$$

as well as the Casimirs, $\mathscr{M} = \iint f[n]\, d\boldsymbol{x}d\boldsymbol{k}$, where $f[n]$ is an arbitrary functional of the distribution $n_{\boldsymbol{k}}(\boldsymbol{x}, z)$.

2.3.2 Validity of the Long-Range Vlasov Equation

It is important to underline that, thanks to the long-range nonlocal response, the system exhibits a self-averaging property of the nonlinear response,

$$\int U(\boldsymbol{x} - \boldsymbol{x'})|\psi(\boldsymbol{x}', z)|^2 d\boldsymbol{x}' \simeq \int U(\boldsymbol{x} - \boldsymbol{x}') N(\boldsymbol{x}', z) d\boldsymbol{x}'.$$

Substitution of this property into the nonlocal NLS equation (1) thus leads to a closure of the hierarchy of the moment equations. More specifically, using statistical arguments similar as those in [96], one can show that, owing to the highly nonlocal response, the statistics of the incoherent wave turns out to be Gaussian. Then contrarily to a conventional Vlasov equation, whose validity is constrained by the assumptions of (1) weakly nonlinear interaction and (2) quasi-homogeneous statistics, the long-range Vlasov equation provides an *exact* statistical description of the random wave $\psi(\boldsymbol{x}, z)$ in the highly nonlocal regime, $\varepsilon \ll 1$. This property is corroborated by the fact that the Vlasov equation considered here is formally analogous to the Vlasov equation considered to study long-range interacting systems [97, 119]. In this context, it has been rigorously proven that, in the limit of an infinite number of particles, the dynamics of *mean-field Hamiltonian systems* is governed by the long-range Vlasov equation [97]. Note however that the term 'long-range' used in [97] refers to a response function whose integral diverges, $\int U(\boldsymbol{x})\, d\boldsymbol{x} = +\infty$, while the response functions considered here refer to exponential or Gaussian shaped functions typically encountered in optical materials (see e.g., [88]). We finally note that the validity of the long-range Vlasov equation in the strongly nonlinear regime has been recently confirmed by direct numerical simulations in a recent work in which collective large scale incoherent shocks have been reported [120].

2.3.3 Incoherent Modulational Instability

Modulational (or Benjamin-Feir) Instability (MI) refers to the phenomenon in which an initially plane- (or continuous-) wave tends to break up spontaneously into periodic modulations while it propagates through a nonlinear medium. In the frequency domain, this phenomenon can be interpreted as a phase-matched partially degenerate four-wave mixing process in which an intense pump wave yields energy to a pair of weak sideband waves. In the following we shall see that an incoherent field that exhibits a homogeneous statistics may become modulationally unstable with respect to the growth of weakly statistical inhomogeneities, i.e., the incoherent field thus becomes statistically inhomogeneous [13–15, 94].

The phenomenon of incoherent MI has been the subject of a detailed investigation in the optical context with an inertial nonlinear response [8, 13, 118]. We present here the phenomenon of incoherent MI in the framework of the long-range Vlasov formalism. For the sake of simplicity, we limit the incoherent MI analysis to the one-dimensional case. We assume that the incident field exhibits a homogeneous statistics, except for small perturbations that depend on x and z. Note that any homogeneous stationary distribution, n_k^0, is a solution of the Vlasov equation, that is, $\partial_z n_k^0 = 0$. We perturb this stationary solution according to $n_k(x,z) = n_k^0 + \delta n_k(x,z)$, with $|\delta n_k(x,z)| \ll n_k^0$, and linearize the Vlasov equation

$$\partial_z \delta n_k(x,z) + 2\alpha k \partial_x \delta n_k(x,z) + \frac{\gamma}{2\pi} \partial_k n_k^0 \int dx' \partial_x U(x-x') \int dk \delta n_k(x',z) = 0 \qquad (23)$$

This equation can be solved by a Fourier-Laplace transform,

$$\tilde{\delta n}_k(K,\lambda) = \int_0^\infty dz \int_{-\infty}^{+\infty} dx \, \exp(-\lambda z - iKx) \, \delta n_k(x,z),$$

which gives the dispersion relation

$$-1 = \frac{\gamma}{\pi} \alpha K^2 \tilde{U}(K) \int_{-\infty}^{+\infty} \frac{n_k^0}{(i\lambda - 2\alpha K k)^2} \, dk, \qquad (24)$$

where $\tilde{U}(K) = \int U(x) \exp(-iKx) \, dx$. Assuming that the initial spectrum is Lorentzian-shaped, $n_k^0 = 2N_0 \Delta k / (k^2 + (\Delta k)^2)$ [i.e., $(2\pi)^{-1} \int n_k^0 dk = N_0$], Eq. (24) gives

$$\lambda(K) = -2\alpha \Delta k |K| + |K| \sqrt{2\alpha\gamma N_0 \tilde{U}(K)}, \qquad (25)$$

where the incoherent MI gain reads $g_{\mathrm{MI}}(K) = 2\Re[\lambda(K)]$.

First of all, we can note that incoherent MI requires a focusing nonlinearity, $\gamma > 0$, as for the usual coherent MI. However, contrary to coherent MI, a focusing nonlinearity is not a sufficient condition for the occurrence of incoherent MI. Indeed,

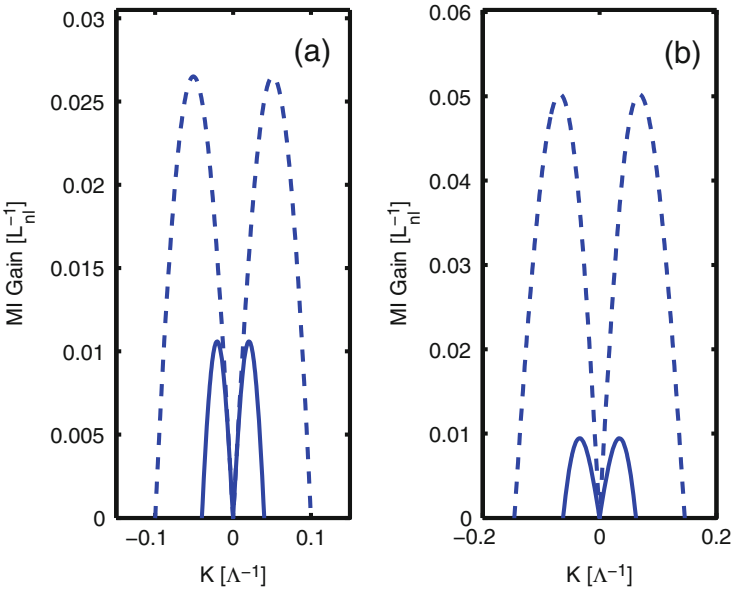

Fig. 4 Spatial incoherent MI: Plots of the MI gain given by Eq. (25), $g_{\mathrm{MI}}(K) = 2\Re[\lambda(K)]$, for an exponential response function, $U(x) = \exp(-|x|/\sigma)/(2\sigma)$: (**a**) $\sigma = 10\Lambda$ (*dashed*), $\sigma = 25\Lambda$ (*continuous*), for $\Delta k = 0.5\Lambda^{-1}$. (**b**) $\Delta k = 0.4\Lambda^{-1}$ (*dashed*), $\Delta k = 0.6\Lambda^{-1}$ (*continuous*), for $\sigma = 10\Lambda$

we remark in the MI gain expression (25) the existence of a damping term, which introduces a threshold for incoherent MI [8, 13, 74]. Note that, the existence of a threshold for incoherent MI was shown to be formally related to an effective Landau damping [8]. In this way, the stabilizing effect of the partial coherence does not refer to a genuine dissipative damping, but rather a self-action effect analogous to Landau damping of electron plasma waves that causes a redistribution of the spectrum $n_k(x, z)$. This effective damping significantly reduces the MI gain and the optimal MI frequency, K_{MI}, as illustrated in Fig. 4.

It is interesting to note that in the limit of a local response ($\tilde{U}(K) = 1$), Eq. (25) reduces to a straight line. This leads to an unphysical result: the MI gain increases with the modulation frequency K. This pathology stems from the fact that the derivation of the Vlasov equation with a local nonlinearity is constrained by the assumption of *quasi-homogeneous statistics*. However, as discussed above in Sect. 2.3.1, the assumption of quasi-homogeneous statistics is automatically satisfied in the presence of a long-range nonlocality. Accordingly, the incoherent MI gain curve (25) is bell-shaped, with a maximum growth-rate at some optimal frequency, K_{MI}.

2.3.4 Incoherent Solitons

The Vlasov equation describes the evolution of the averaged spectrum of a random wave. Hence, a spatially localized and stationary solution of the Vlasov equation describes an incoherent soliton state. The mechanism underlying the formation of an incoherent soliton is schematically explained in Fig. 5. We consider here the case of bright solitons with a focusing nonlinearity ($\gamma > 0$), and again we limit the study to the pure one-dimensional situation. Let us consider the stationary Vlasov equation

$$2\alpha k\, \partial_x n_k^{st}(x) - \partial_x V(x)\, \partial_k n_k^{st}(x) = 0. \tag{26}$$

where the self-consistent potential is given by $V(x) = -\gamma \int U(x-x')\, N(x')\, dx'$ [see Eq. (21)]. Let us now recall an important observation originally pointed out in the seminal paper [69], namely the fact that the solution to Eq. (26) can be expressed as an arbitrary function of the effective Hamiltonian, $h = \alpha k^2 + V(x)$. To find an explicit analytical solution to Eq. (26), we make use of this observation by following the procedure outlined in [70]. In this work, Hasegawa obtained an analytical soliton solution of the Vlasov equation in the limit of a *local nonlinear interaction*, $U(x) = \delta(x)$. This solution has been recently generalized to a nonlocal interaction in [20]. The idea of the method is to argue that the 'particles' that constitute the soliton are trapped by the self-consistent potential $V(x)$ provided that their energy is negative, $h \leq 0$. This determines a specific interval of momenta for the trapped particles, $-k_c \leq k \leq k_c$, where $k_c = \sqrt{-V/\alpha}$ (note that $V < 0$ in the focusing regime, see Fig. 5). According to Eq. (14), the intensity profile of the soliton solution thus reads $N(x) = (2\pi)^{-1} \int_{-k_c}^{+k_c} n_k^{st}(x)\, dk$. By means of a simple change of variables, this

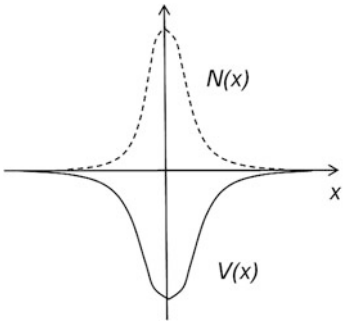

Fig. 5 Schematic representation of the self-trapping mechanism underlying the formation of an incoherent soliton solution of the Vlasov equation. A soliton forms when the optical beam induces an attractive potential $V(x) < 0$ (waveguide) owing to a focusing nonlinearity ($\gamma > 0$). In turn, the optical beam is guided in its own induced potential $V(x)$

integral can thus be expressed in the form of a Fredholm equation

$$N = \frac{1}{2\pi} \int_V^0 \frac{n^{st}(h)}{\sqrt{h - V}} dh. \tag{27}$$

A solution to this equation can be obtained under the assumption that $U(x)$ and $N(x)$ are Gaussian-shaped [20]. Assuming $U(x) = (2\pi\sigma^2)^{-1/2} \exp[-x^2/(2\sigma^2)]$ and $N(x) = \mathcal{N}(2\pi\sigma_N^2)^{-1/2} \exp[-x^2/(2\sigma_N^2)]$, and making use of the Laplace convolution theorem, we have

$$n_k^{st}(x) = Q_\eta \left[c_\eta N^\eta(x) - \beta k^2\right]^{\frac{1}{\eta} - \frac{1}{2}}, \tag{28}$$

where

$$Q_\eta = \frac{2\pi\beta^{\frac{1}{2}} \Gamma(\eta^{-1} + 1)}{\Gamma(\eta^{-1} + 1/2)\Gamma(1/2)c_\eta^{1/\eta}}, \tag{29}$$

$\Gamma(x)$ being the Gamma function, and

$$c_\eta = \frac{(2\pi)^{\frac{\eta}{2} - \frac{1}{2}} \gamma \sigma_N^\eta}{\mathcal{N}^{\eta - 1} \sqrt{\sigma^2 + \sigma_N^2}}, \tag{30}$$

with

$$\eta = \frac{1}{1 + (\sigma/\sigma_N)^2}. \tag{31}$$

This analytical solution is self-consistent, in the sense that it verifies the condition (27), and it is straightforward to check by direct substitution that it is indeed a solution of (27).

The fact that the above solution generalizes the solution obtained by Hasegawa [70] becomes apparent by remarking that Eq. (28) can be expressed as

$$n^{st}(h) \sim (-h)^{\frac{1}{\eta} - \frac{1}{2}}. \tag{32}$$

In the limit of a local potential, $U(x) = \delta(x)$, the parameter $\eta \to 1$, and (32) recovers the solution $n^{st}(h) \sim \sqrt{-h}$ [70]. Note however that for a local nonlinearity [70], the analytical solution is valid for *any* form of the intensity distribution, $N(x)$, a property that was subsequently interpreted in the framework of a ray-optics approach [121]. Conversely, for a nonlocal nonlinearity, the analytical solution (28)–(31) refers to a Gaussian-shaped intensity profile.

2.3.5 Vlasov Simulations: Incoherent Soliton Turbulence

The phenomena of incoherent MI and subsequent incoherent soliton formation can be visualized by means of a direct numerical integration of the long-range Vlasov equations (11), (21). This is illustrated in Fig. 6, which reports the evolution of the spectrum of the incoherent wave during its propagation. The simulation starts from a homogeneous spectrum, $n_k(x, z = 0) \simeq n_k^0$, which is periodically perturbed to seed the incoherent MI. Because of the nonlinear Hamiltonian flow, particles following different orbits travel at different angular speeds, a process known as 'phase-mixing'. Each MI-modulation thus starts spiralling in the phase-space (x, k), which leads to the formation of four localized incoherent structures, which are

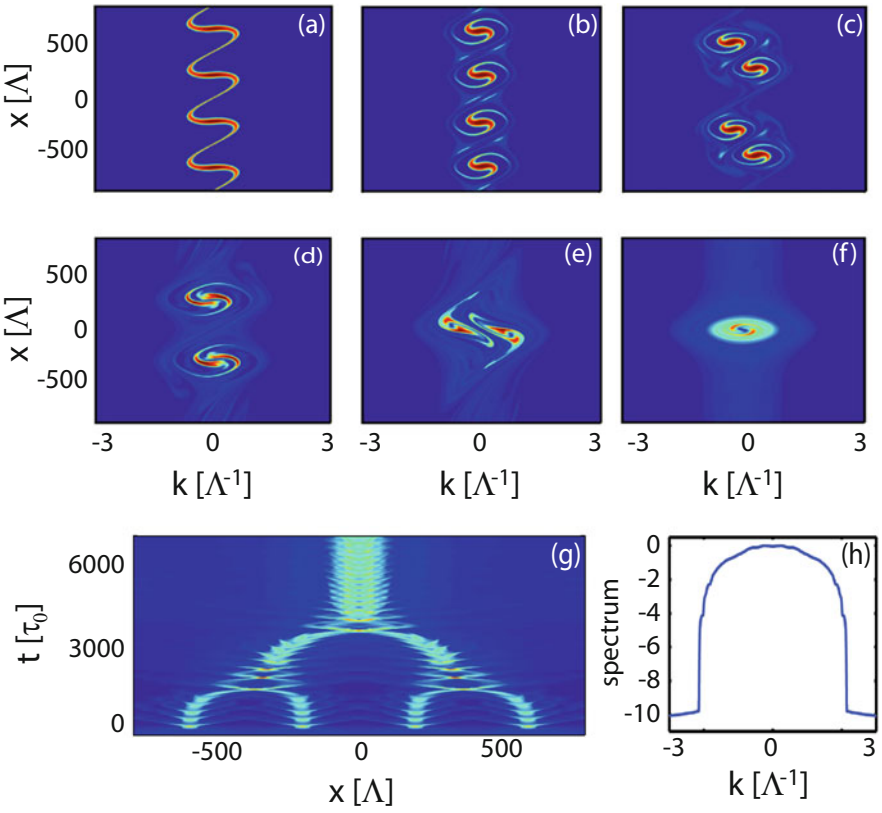

Fig. 6 Incoherent soliton turbulence: Numerical simulation of the long-range Vlasov equations (11), (21), showing the evolution of the local spectrum, $n_k(x)$, during the propagation. The initial homogeneous spectrum exhibits incoherent MI: the four modulations excited by the initial condition lead to the generation of four incoherent structures, which slowly coalesce into two, and then into one incoherent soliton state. (**a**) $z = 300$, (**b**) $z = 1000$, (**c**) $z = 1500$, (**d**) $z = 3000$, (**e**) $z = 4000$, (**f**) $z = 10^4$ (in units of L_{nl}), $\sigma = 10^2 \Lambda$. (**g**) Corresponding evolution of the spatial intensity profile, $N(x, z)$. (**h**) Corresponding spectrum $S(k, z_0)$ at $z_0 = 700 L_{nl}$. *Source*: from [20]

mutually attracted and coalesce into two, and eventually into a single incoherent structure. Note that this process is analogous to the soliton turbulence scenario that occurs for *coherent* solitons [91]. The phase-mixing then leads to a smoothing and homogenization of the perturbations on the incoherent structure, which thus slowly tend to relax toward a stationary incoherent soliton state. Note that the asymptotic evolution of inhomogeneous Vlasov states is a long standing mathematical problem [122].

2.4 Temporal Version: Non Hamiltonian Long-Range Vlasov Equation

We remark that, as discussed above through Fig. 3, the long-range Vlasov formalism also plays a role in the temporal domain in the presence of a highly noninstantaneous nonlinear response (temporal nonlocality). Because of the causality condition inherent to the response function in the temporal domain, the Vlasov equation no longer exhibit a Hamiltonian structure [118]. The corresponding Vlasov formalism predicts different interesting behaviors, such as the existence of incoherent solitons in the normal dispersion regime, in contrast to conventional solitons which are known to require anomalous dispersion. For a review on the long-range Vlasov formalism in the temporal domain, see [118].

3 Weak Langmuir Turbulence Formalism

In this Section we study the temporal evolution of a partially coherent wave that propagates in a nonlinear medium characterized by a noninstantaneous response. As discussed in Sect. 1 through Fig. 3, a delayed nonlinearity leads to a kinetic description which is formally analogous to the weak Langmuir turbulence kinetic equation, irrespective of the nature of the fluctuations that may be either stationary or non-stationary. In the presence of a temporal long-range response and a stationary statistics of the incoherent wave, the weak Langmuir turbulence formalism reduces to a family of singular integro-differential kinetic equations (e.g., Benjamin-Ono equation) that describe incoherent dispersive shock waves and incoherent collapse singularities in the spectral evolution of the random wave.

3.1 Noninstantaneous Nonlinear Response

A typical example of noninstantaneous nonlinear response in one dimensional systems is provided by the Raman effect in optical fibers [123]. We consider the

standard 1D NLS equation accounting for a noninstantaneous nonlinear response function

$$i\partial_z\psi + \beta\partial_{tt}\psi + \gamma\psi \int_{-\infty}^{+\infty} R(t-t')\,|\psi|^2(t',z)\,dt' = 0, \tag{33}$$

where the response function $R(t)$ is constrained by the causality condition. In the following we use the convention that $t > 0$ corresponds to the leading edge of the pulse, so that the causal response will be on the trailing edge of a pulse, i.e., $R(t) = 0$ for $t > 0$. We will write the response function in the form $R(t) = H(-t)\bar{R}(-t)$, where $\bar{R}(t)$ is a smooth function from $[0,\infty)$ to $(-\infty,\infty)$, while the Heaviside function $H(-t)$ guarantees the causality property. As we will see, this convention will allow us to easily compare the dynamics of temporal and spatial incoherent solitons. Because of the causality property, the real and imaginary parts of the Fourier transform of the response function

$$\tilde{R}(\omega) = \tilde{U}(\omega) + i\,g(\omega), \tag{34}$$

are related by the Kramers-Krönig relations. We recall that $\tilde{U}(\omega)$ is even, while the gain spectrum $g(\omega)$ is odd. The causality condition breaks the Hamiltonian structure of the NLS equation, so that Eq. (33) only conserves the total power ('number of particles') of the wave $\mathcal{N} = \int |\psi|^2(t,z)\,dt$. The typical temporal range of the response function $R(t)$ denotes the response time, τ_R. Note that $\beta = -\frac{1}{2}\partial^2_\omega k(\omega)$ in Eq. (33), so that $\beta > 0$ ($\beta < 0$) denotes the regime of anomalous (normal) dispersion.

3.2 Short-Range Interaction: Spectral Incoherent Solitons

The dynamics is ruled by the comparison of the response time, τ_R, with the 'healing time', $\tau_0 = \sqrt{|\beta|L_{nl}}$. We remind that the weakly nonlinear regime of interaction refers to the regime in which linear dispersive effects dominate nonlinear effects, i.e., $L_d/L_{nl} \ll 1$ where $L_d = t_c^2/|\beta|$ and $L_{nl} = 1/(|\gamma|\rho)$ refer to the dispersive and nonlinear characteristic lengths respectively, t_c being the correlation time of the partially coherent wave. We consider here the case of a noninstantaneous nonlinearity characterized by a short-range response time, i.e., $\tau_R \sim \tau_0$. In this regime, it can be shown that the kinetic equation governing the evolution of the incoherent wave takes a form analogous to the WT Langmuir kinetic equation [22, 118]:

$$\partial_z n_\omega(z) = \frac{\gamma}{\pi}\, n_\omega(z) \int_{-\infty}^{+\infty} g(\omega-\omega')\, n_{\omega'}(z)\, d\omega', \tag{35}$$

where we have implicitly assumed that the incoherent wave exhibits fluctuation that are statistically stationary (homogeneous) in time—a generalized WT Langmuir equation can be obtained for a non-stationary statistics [118]. We first note that this equation does not account for dispersion effects (it does not involve the parameter β), although the role of dispersion in its derivation is essential in order to verify the criterion of weakly nonlinear interaction, $L_d/L_{nl} \ll 1$. The fact that the dynamics ruled by the WT Langmuir equation does not depend on the sign of the dispersion coefficient has been verified by direct numerical simulations of the NLS Eq. (33) [99]. The kinetic Eq. (35) conserves the power of the field $N = \frac{1}{2\pi}\int n_\omega(z)\, d\omega$. Moreover, as discussed above for the Vlasov equation, the WT Langmuir equation (35) is a formally reversible equation [it is invariant under the transformation $(z, \omega) \to (-z, -\omega)$], a feature which is consistent with the fact that it also conserves the non-equilibrium entropy $S = \frac{1}{2\pi}\int \log[n_\omega(z)]\, d\omega$.

The WT Langmuir equation admits solitary wave solutions [22, 74, 98, 99]. This may be anticipated by remarking that, as a result of the convolution product in (35), the odd spectral gain curve $g(\omega)$ amplifies the low-frequency components of the wave at the expense of the high-frequency components, thus leading to a global red-shift of the spectrum. We remind that these incoherent solitons are termed 'spectral' because they can only be identified in the spectral domain, since in the temporal domain the field exhibits stochastic fluctuations at any time, t.

3.2.1 Numerical Simulations

Typical spectral incoherent soliton behaviors are reported in Fig. 7. The initial condition is an incoherent wave characterized by a Gaussian spectrum with δ-correlated random spectral phases, so that the initial wave exhibits stationary fluctuations. The Gaussian spectrum is superposed on a background of small noise of averaged intensity $n_0 = 10^{-5}$. This is important in order to sustain a steady soliton propagation, otherwise the soliton undergoes a slow adiabatic reshaping so as to adapt its shape to the local value of the noise background. The relative intensity of the background noise with respect to the average power of the wave plays an important role in the dynamics of discrete spectral incoherent solitons. Indeed, the *continuous* spectral incoherent soliton is known to become narrower (i.e., of higher amplitude) as the intensity of the background noise decreases. Accordingly, a transition from a continuous to a discrete spectral incoherent soliton behavior occurs as the relative intensity of the background noise is decreased: as the spectral soliton becomes narrower than ω_R, the leading edge of the tail of the spectrum will be preferentially amplified, thus leading to the formation of a discrete spectral incoherent soliton. In order to test the validity of the WT Langmuir theory, we reported in Fig. 7 a direct comparison with NLS simulations. We underline that an excellent agreement has been obtained between the simulations of the NLS equation and the WT Langmuir equation, without using any adjustable parameter [99].

Note that if the background noise level increases in a significant way and becomes of the same order as the amplitude of the spectral soliton, the incoherent

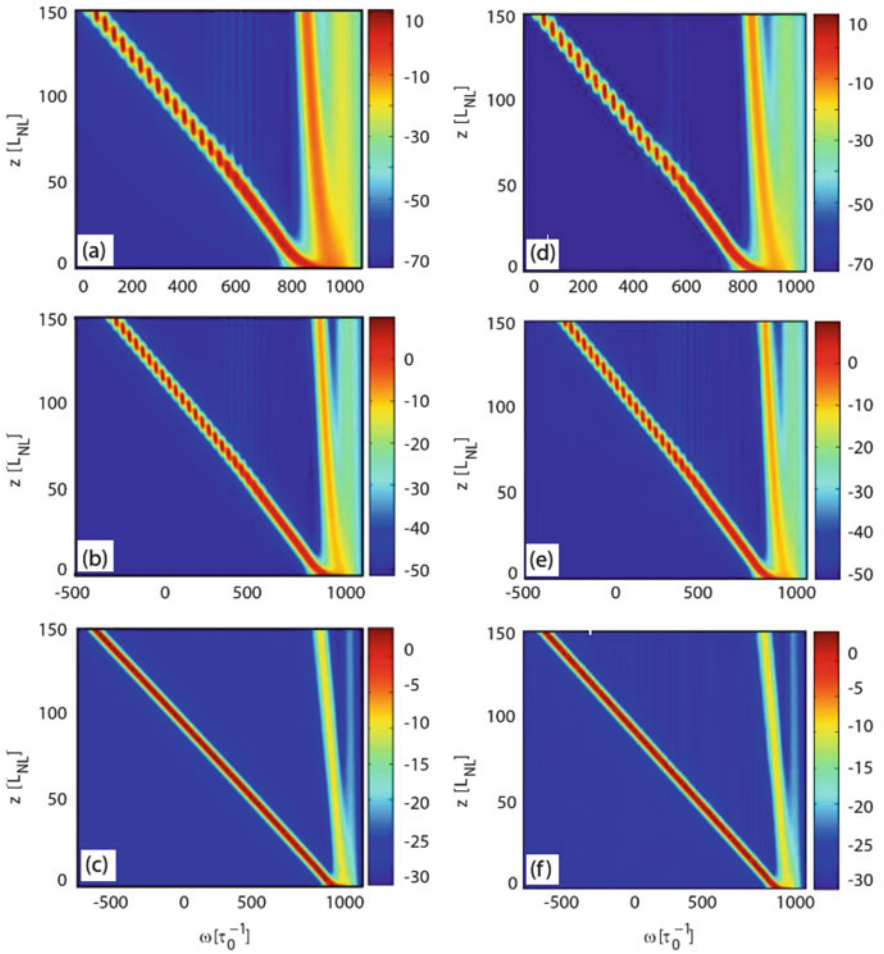

Fig. 7 Spectral incoherent solitons: Transition from discrete to continuous solitons. *Left column* (**a**)–(**c**): Evolution of the non-averaged spectrum of the optical field, $|\tilde{\psi}|^2(z,\omega)$ (in dB-scale), obtained by integrating numerically the NLS equation (33) for three different values of the noise background, $n_0 = 10^{-7}$ (**a**), $n_0 = 10^{-5}$ (**b**), $n_0 = 10^{-3}$ (**c**). *Right column* (**d**)–(**f**): Corresponding evolution of the averaged spectrum, $n(z,\omega)$ (in dB-scale), obtained by solving the Langmuir WT equation (35): The comparison reveals a quantitative agreement, without using adjustable parameters. We considered the typical Raman-like gain spectrum, $g(\omega)$ ($\beta\gamma < 0$). *Source*: from [99]

wave enters a novel regime [124]. This regime is characterized by an oscillatory dynamics of the incoherent spectrum which develops within a spectral cone during the propagation. Such spectral dynamics exhibits a significant spectral blue shift, which is in contrast with the expected Raman-like spectral red shift.

3.2.2 Analytical Soliton Solution

The WT Langmuir kinetic equation (35) admits analytical soliton solutions [74, 118, 125]. More precisely, it is possible to compute the width and velocity of the soliton given its peak amplitude n_m in the regime $n_m \gg n_0$, where n_0 denotes the spectral amplitude of the background noise. We introduce the antiderivative of the spectral gain $G(\omega) = -\int_{\omega}^{\infty} g(\omega')d\omega'$. The gain spectrum $g(\omega)$ is characterized by its typical gain amplitude g_i and its typical spectral width ω_i. Regardless of the details of the gain curve $g(\omega)$, g_i and ω_i can be assessed by two characteristic quantities, namely the gain slope at the origin $\partial_\omega g(0)$ and the total amount of gain $G(0) = -\int_0^{\infty} g(\omega)d\omega$. A dimensional analysis allows to express g_i and ω_i in terms of these two quantities, $g_\mathrm{i} = \frac{1}{\sqrt{2}}(-\partial_\omega g(0))^{1/2}\big[-\int_0^{\infty} g(\omega)d\omega\big]^{1/2}$, $\omega_\mathrm{i} = \sqrt{2}\big[-\int_0^{\infty} g(\omega)d\omega\big]^{1/2}/\big[-\partial_\omega g(0)\big]^{1/2}$. With these definitions, the function $G(\omega)$ can be written in the following normalized form $G(\omega) = g_\mathrm{i}\omega_\mathrm{i}h(\omega/\omega_\mathrm{i})$, where the dimensionless function $h(x)$ verifies $h(0) = 1$, $h'(0) = 0$, and $h''(0) = -2$. Proceeding as in [125], the profile of the soliton in the regime $n_m \gg n_0$ is of the form [74], $\log\left(\frac{n_\omega(z)}{n_0}\right) = \log\left(\frac{n_m}{n_0}\right)h\left(\frac{\omega - Vz}{\omega_\mathrm{i}}\right)$, or equivalently:

$$n_\omega(z) - n_0 = \big(n_m - n_0\big)\exp\Big[-\log\Big(\frac{n_m}{n_0}\Big)\frac{(\omega - Vz)^2}{\omega_\mathrm{i}^2}\Big], \tag{36}$$

where the velocity of the soliton is

$$V = -\frac{n_m - n_0}{\log^{3/2}\left(\frac{n_m}{n_0}\right)}\frac{\gamma g_\mathrm{i}\omega_\mathrm{i}^2}{\sqrt{\pi}}, \tag{37}$$

and its full width at half maximum is $\omega_\mathrm{sol} = 2\omega_\mathrm{i}\log^{1/2}(2)/\log^{1/2}(n_m/n_0)$.

Spectral incoherent solitons have been recently generalized in the framework of the generalized NLS equation accounting for the self-steepening term and a frequency dependence of the nonlinear Kerr coefficient [126]. Such nonlinear dispersive effects are shown to strongly affect the dynamics of the incoherent wave. A generalized WT Langmuir kinetic equation is derived and its predictions have been found in quantitative agreement with the numerical simulations of the NLS equation, without adjustable parameters [126].

The structure of discrete spectral incoherent solitons can also be interpreted with an analytical soliton solution of the *discretized* WT Langmuir equation derived in [127]. In this way, discrete frequency bands of the soliton are modelled as coupled Dirac δ-functions in frequency space (δ-peak model). However, the simulations show that, when injected as initial condition into the WT Langmuir equation with a Raman-like gain spectrum, the analytical soliton solution rapidly relaxes during the propagation toward a discrete spectral incoherent solution [99]. This property reveals the incoherent nature of discrete spectral incoherent solitons.

We finally note that the emergence of continuous and discrete spectral incoherent solitons has been identified experimentally owing to the Raman effect in photonic crystal fibers in the context of supercontinuum generation, a feature discussed in detail in [23].

3.3 Long-Range Interaction: Spectral Singularities

In this section we present the procedure which allows one to derive appropriate reduced kinetic equations from the WT Langmuir equation in the long-range limit, i.e., the limit of a highly noninstantaneous nonlinear response, $\tau_R \gg \tau_0$. As discussed here above, the causality condition leads to a gain spectrum $g(\omega)$ that decays algebraically at infinity, a property which introduces singularities into the convolution operator of the WT Langmuir equation (35). The mathematical procedure consists in accurately addressing these singularities, see [100]. It reveals that, as a general rule, a singular integro-differential operator arises systematically in the derivation of the reduced kinetic equation [100, 128]. The resulting singular integro-differential kinetic equation then originates in the causality property of the nonlinear response function.

These singular integro-differential kinetic equations find a direct application in the description of dispersive shock waves, i.e., shock waves whose singularity is regularized by dispersion effects instead of dissipative (viscous) effects [101]. Dispersive shock waves have been constructed mathematically [129] and observed in ion acoustic waves [130] long ago, though it is only recently that they emerged as a general signature of singular fluid-type behavior, in particular in Bose-Einstein condensates [131, 132] and nonlinear optics [80, 81, 133, 134].

These previous studies on dispersive shock waves have been discussed for coherent, i.e., deterministic, amplitudes of the waves. Through the analysis of the WT Langmuir equation, we will see that incoherent waves can exhibit dispersive shock waves of a different nature that their coherent counterpart. They manifest themselves as a wave breaking process ("gradient catastrophe") in the spectral dynamics of the incoherent field [100]. Contrary to conventional shocks which are known to require a strong nonlinear regime, these incoherent shocks develop into the weakly nonlinear regime. This WT kinetic approach also reveals unexpected links with the 3D vorticity equation in incompressible fluids [102], or the integrable Benjamin-Ono equation [103], which was originally derived in hydrodynamics.

3.3.1 Damped Harmonic Oscillator Response: Spectral Dispersive Shock Waves

The derivation of singular integro-differential kinetic equations has been developed for a general form of the response function (see the Supplemental of [100]). Here we illustrate the theory by considering two physically relevant examples of response

functions, which, respectively, induce and inhibit the formation of incoherent shock waves.

Let us first consider the example of the damped harmonic oscillator response, $\bar{R}(t) = \frac{1+\eta^2}{\eta\tau_R}\sin(\eta t/\tau_R)\exp(-t/\tau_R)$. Figure 8 reports a typical evolution of the spectrum of the incoherent wave obtained by numerical simulations of the NLS equation (33). Here we considered the highly incoherent limit, $\Delta\omega \gg \Delta\omega_g$ ($t_c \ll \tau_R$). We see that the low frequency part of the spectrum exhibits a self-steepening process, whose wave-breaking is ultimately regularized by the development of large amplitude and rapid spectral oscillations typical of a dispersive shock wave. This behavior has been described by deriving a singular integro-differential kinetic equation from the WT Langmuir equation in the long-range regime ($\tau_R \gg \tau_0$):

$$\tau_R^2 \partial_z n_\omega = \gamma(1+\eta^2)\Big(n_\omega \partial_\omega n_\omega - \frac{1}{\tau_R} n_\omega \mathscr{H} \partial_\omega^2 n_\omega\Big), \tag{38}$$

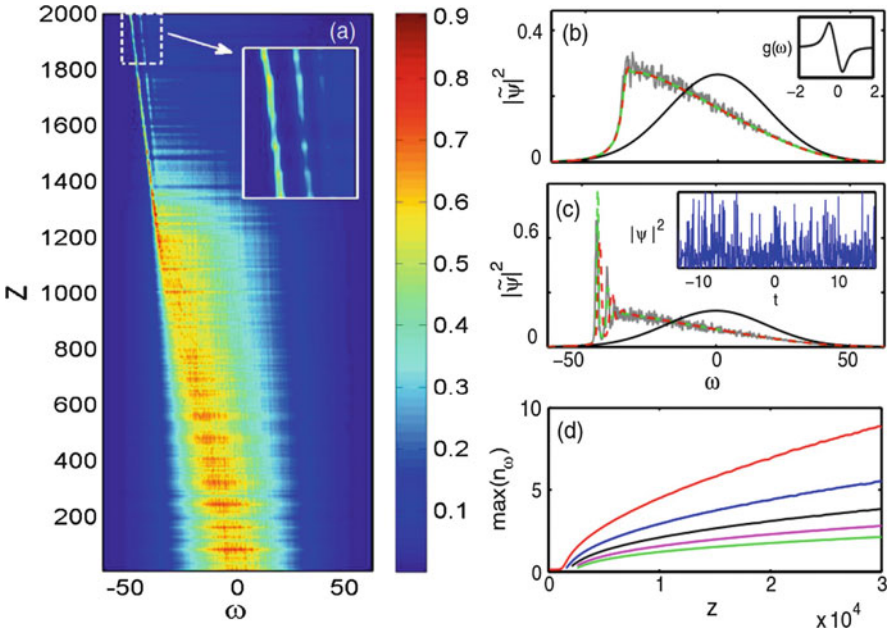

Fig. 8 Incoherent dispersive shock waves with a Raman-like response function: (**a**) Numerical simulation of the NLS equation (33): The stochastic spectrum $|\tilde{\psi}|^2(\omega, z)$ develops an incoherent shock at $z \simeq 1200 L_{nl}$ ($\tau_R = 3\tau_0, \eta = 1$). Snapshots at $z = 1040 L_{nl}$ (**b**), $z = 1400 L_{nl}$ (**c**): NLS (33) (*gray*) is compared with WT Langmuir equation (35) (*green*), singular kinetic equation [Eq. (38)] (*dashed–red*), and initial condition (*solid black*). (**d**) First five maxima of n_ω vs z in the long-term post-shock dynamics: the spectral peaks keep evolving, revealing the non-solitonic nature of the incoherent dispersive shock wave. Insets: (**b**) gain spectrum $g(\omega)$, note that $\Delta\omega_g$ is much smaller than the initial spectral bandwidth of the wave [*black line* in (**b**)]. (**c**) corresponding temporal profile $|\psi(t)|^2$ showing the incoherent wave with stationary statistics. *Source*: from [100]

where the singular operator $\mathscr{H}$ refers to the Hilbert transform,

$$\mathscr{H}f(\omega) = \frac{1}{\pi}\mathscr{P}\int_{-\infty}^{+\infty}\frac{f(\omega-u)}{u}du,$$

where we recall that $\mathscr{P}$ denotes the Cauchy principal value. This kinetic equation describes the essence of incoherent dispersive shock waves: The leading-order Burgers term describes the formation of the shock, which is subsequently regularized by the nonlinear dispersive term involving the Hilbert operator. We remark in Fig. 8 that a quantitative agreement is obtained between the simulations of Eq. (38) and those of the NLS and WT Langmuir equations, without adjustable parameters. Also note that in the presence of a strong spectral background noise, the derived singular equation coincides with the Benjamin-Ono equation, which is a completely integrable equation [100].

3.3.2 Exponential Response: Spectral Collapse Singularity

As described by the general theory reported in [100], the previous scenario of incoherent dispersive shock waves changes in a dramatic way when the response function is not continuous at the origin, as it occurs for a purely exponential response function, $\bar{R}(t) = \exp(-t/\tau_R)/\tau_R$. In this case, considering the limit $\tau_R/\tau_0 \gg 1$, the singular kinetic equation takes the form:

$$\tau_R\partial_z n_\omega = -\gamma n_\omega \mathscr{H} n_\omega - \frac{\gamma}{\tau_R} n_\omega \partial_\omega n_\omega + \frac{\gamma}{2\tau_R^2} n_\omega \mathscr{H}\partial_\omega^2 n_\omega. \tag{39}$$

Interestingly, the first term of (39) was considered as a one-dimensional model of the vorticity formulation of the 3D Euler equation of incompressible fluid flows [102]. In this work, the authors found an explicit analytical solution to the equation $\tau_R\partial_z n_\omega = -\gamma n_\omega \mathscr{H} n_\omega$. For a given initial condition $n_\omega(z=0) = n_\omega^0$ the solution has the form

$$n_\omega(z) = \frac{4n_\omega^0}{\left(2 + (\gamma z/\tau_R)\mathscr{H} n_\omega^0\right)^2 + (\gamma z/\tau_R)^2 (n_\omega^0)^2}. \tag{40}$$

There is blow up if and only if there exists ω such that $n_\omega^0 = 0$ and $\mathscr{H} n_\omega^0 < 0$. Then the blow up distance z_c is given by $z_c = -2\tau_R/[\gamma \mathscr{H} n^0_{\omega=\omega_0}]$, where ω_0 is such that $n^0_{\omega_0} = 0$. It can be shown [100] that, if the initial condition decays faster than a Lorentzian, the spectrum exhibits a collapse-like dynamics, which is ultimately arrested by a small background noise. In this process, the spectrum moves at velocity $\tilde{c}$, while its peak amplitude increases according to $\sim 4\tau_R^2/[\gamma^2 z^2 n^0(\omega = \tilde{c}z)]$. This property is confirmed by the simulations of the NLS equation, as illustrated in Fig. 9.

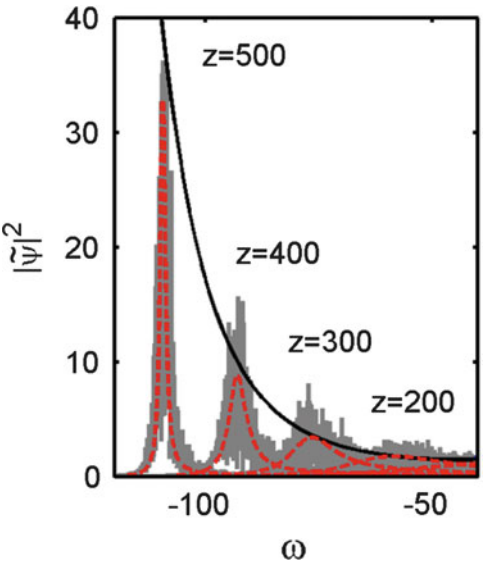

Fig. 9 Inhibition of incoherent shocks with an exponential response function. Without background spectral noise the spectrum exhibits a collapse-like behavior: NLS (33), *gray*; singular kinetic equation (39), *dashed–red* ($\tau_R = 5\tau_0$). The *dark continuous line* denotes the theoretical behavior $\sim 1/[z^2 n^0(\omega = \tilde{c}z)]$, with $\tilde{c} = -\gamma N/\tau_R$, predicted from the first term of equation (39) and the corresponding analytical solution (40). *Source*: from [100]

4 Wave Turbulence Kinetic Equation

In the previous Sects. 2, 3 we considered the Vlasov and WT Langmuir equations which are quadratic nonlinear equations whose derivations refer to a first-order closure of the hierarchy of moments equations. These kinetic equations are formally reversible and describe, in particular, the spontaneous formation of incoherent soliton structures. Let us now consider the following two limits. (1) In the spatial domain the limit of homogeneous statistics of a broadband incoherent wave, so that the Vlasov equation becomes irrelevant, as commented through Fig. 2 in Sect. 1. (2) In the temporal domain the limit of stationary statistics and instantaneous response of the nonlinearity, so that the WT Langmuir equation becomes irrelevant, as commented through Fig. 3. In both limits, we thus need to close the hierarchy of the moments equations to the second-order. The analysis reveals that in this case the appropriate formalism for the description of the random wave is provided by the (Hasselmann) WT kinetic equation, which is a cubic nonlinear equation.

4.1 Kinetic Equation in a Waveguide

4.1.1 Properties of the Kinetic Equation

The WT description of a random wave has been essentially developed in the ideal situation in which the random wave is supposed ‘infinitely extended in space’, an assumption that may be considered as justified when its correlation length is

much smaller than the size of the whole beam. However, the propagation of an incoherent localized beam is eventually affected by incoherent diffraction, which inevitably affects the processes of thermalization and condensation. In the following we derive the WT kinetic equation by considering the propagation of the incoherent beam in an optical waveguide. In the guided configuration, incoherent diffraction is compensated by a confining potential, thus allowing to study the thermalization and the condensation of the optical field over large propagation distances. Accordingly, we consider the NLS equation with a confining potential $V(\boldsymbol{x})$ and we formulate a WT description of the random wave into the basis of the eigenmodes of the waveguide (i.e., potential's eigenmodes), instead of the usual plane-wave Fourier basis relevant to statistically homogeneous random waves [$V(\boldsymbol{x}) = 0$] [135].

The NLS equation with a confining potential $V(\boldsymbol{x})$ reads

$$i\partial_z\psi = -\alpha\nabla^2\psi + V(\boldsymbol{x})\psi - \gamma|\psi|^2\psi. \tag{41}$$

Note that in this section we deal essentially with a defocusing nonlinearity, $\gamma < 0$ (so as to ensure the stability of the homogeneous plane-wave solution, i.e., condensate). We recall that this NLS equation conserves the power of the optical field, $N = \int |\psi|^2\, d\boldsymbol{x}$. The NLS equation also conserves the total energy (Hamiltonian) $H = E + U$, which has a linear contribution,

$$E = \int \alpha|\nabla\psi|^2\, d\boldsymbol{x} + \int V(\boldsymbol{x})|\psi|^2\, d\boldsymbol{x}, \tag{42}$$

and a nonlinear contribution,

$$U = -\frac{\gamma}{2}\int |\psi|^4\, d\boldsymbol{x}. \tag{43}$$

The potential $V(\boldsymbol{x})$ models the waveguide in which the optical beam propagates. If one considers a multimode optical fiber, the waveguide potential exhibits a revolution symmetry with respect to the axis of propagation of the beam. Then a direct correspondence exists between $V(|\boldsymbol{x}|)$ and the transverse refraction index profile of the waveguide. For a graded-index multimode fiber, we have $V(|\boldsymbol{x}|) = qx^2$ if $|\boldsymbol{x}| \leq a$ and $V(|\boldsymbol{x}|) = V_0$, if $|\boldsymbol{x}| \geq a$, where $q = V_0/a^2$ [135]. This potential is schematically illustrated in Fig. 10. In this way the finite depth of the potential $V_0 < \infty$ introduces an effective frequency cut-off for the classical wave. This is due to the fact that the nonlinear coupling among bounded and unbounded modes is negligible, because of the poor spatial overlap of the corresponding modes.[1]

[1]The efficiency of the generation of unbounded modes ($\omega \leq V_0$) is several orders of magnitude smaller than the conversion efficiency between bounded modes ($\omega \leq V_0$), so that their excitations can be neglected [for details see Appendix 4 in [135]].

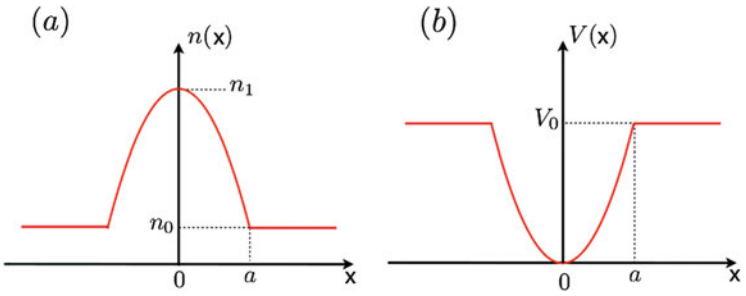

Fig. 10 Refractive index profile $n(x)$ of an optical waveguide (*graded-index fiber*) (**a**), and corresponding confining potential $V(x)$ in the NLS equation (41) (**b**). The finite depth of the potential introduces an effective frequency cut-off for the classical wave problem. The existence of an inhomogeneous (e.g., parabolic) potential reestablishes wave condensation in the thermodynamic limit in 2D, in analogy with quantum Bose-Einstein condensation

4.1.2 Basic Considerations

We assume that the initial random field $\psi(\boldsymbol{x}, z = 0)$ can be expanded into the orthonormal basis of the eigenmodes of the linearized NLS equation [Eq. (41) with $\gamma = 0$],

$$\psi(\boldsymbol{x}, z = 0) = \sum_m c_m(z = 0)\, u_m(\boldsymbol{x}), \tag{44}$$

where the index $\{m\}$ labels the two numbers (m_x, m_y) needed to specify the mode that $u_m(\boldsymbol{x})$ refers to. The modal coefficients are random variables uncorrelated with one another, $\left\langle c_m(z = 0) c_n^*(z = 0) \right\rangle = n_m(z = 0)\, \delta^K_{n,m}$, $\delta^K_{n,m}$ being the Kronecker's symbol. We remark that this formalism is also known as the Karhunen-Loeve expansion [118]. The eigenmodes $u_m(\boldsymbol{x})$ are orthonormal, $\int u_m(\boldsymbol{x})\, u_n^*(\boldsymbol{x})\, d\boldsymbol{x} = \delta^K_{n,m}$, and satisfy the 'stationary' (i.e., z-independent) Schrödinger equation

$$\beta_m u_m(\boldsymbol{x}) = -\alpha \nabla^2 u_m(\boldsymbol{x}) + V(\boldsymbol{x}) u_m(\boldsymbol{x}), \tag{45}$$

with the corresponding eigenvalues β_m.

As it propagates through the waveguide the incoherent field $\psi(\boldsymbol{x}, z)$ can be represented as a superposition of modal waves with random coefficients $c_m(z)$, which denotes the respective modal occupancy:

$$\psi(\boldsymbol{x}, z) = \sum_m c_m(z)\, u_m(\boldsymbol{x})\, \exp(-i\beta_m z). \tag{46}$$

In the linear regime of propagation $\gamma = 0$, we have $c_m(z) = c_m(z = 0)$. In the nonlinear regime, we will follow in the next section the procedure of the random phase approximation underlying the WT theory [30, 39]. In particular, the

modal occupancies $c_m(z)$ are still random variables uncorrelated with one another, $\langle c_m(z) c_n^*(z) \rangle = n_m(z)\, \delta^K_{n,m}$. The modal occupancies $n_m(z)$ satisfy a coupled system of nonlinear equations that we shall describe below.

The average local power of the field is $\langle |\psi(\boldsymbol{x}, z)|^2 \rangle = \sum_m n_m(z)\, |u_m(\boldsymbol{x})|^2$, and a spatial integration over $\boldsymbol{x}$ gives the total average power of the beam

$$N = \sum_m n_m(z), \tag{47}$$

which is a conserved quantity. The parameter $n_m(z)$ thus denotes the amount of power in the mode $\{m\}$. It can be obtained by projecting the field $\psi(\boldsymbol{x}, z)$ on the corresponding eigenmode $u_m(\boldsymbol{x})$,

$$n_m(z) = \Big\langle \Big| \int \psi(\boldsymbol{x}, z)\, u_m^*(\boldsymbol{x})\, d\boldsymbol{x} \Big|^2 \Big\rangle = \big\langle |c_m(z)|^2 \big\rangle . \tag{48}$$

Wave condensation takes place when the fundamental mode becomes macroscopically populated, i.e., when $n_0 \gg n_m$ for $m \neq 0$ [136, 137].

In the same way, by substituting the modal expansion of the incoherent field $\psi(\boldsymbol{x}, z)$ into the expression of the linear energy (42), one obtains

$$E(z) = \sum_m E_m(z) = \sum_m n_m(z)\, \beta_m. \tag{49}$$

The total linear energy is the sum of the modal energies weighted by the corresponding modal occupancy $n_m(z)$.

4.1.3 Wave Turbulence Kinetic Equation in a Waveguide

We now study the influence of a weak nonlinear coupling among the modes, so that the modal occupancies defined by (48) depend on z, $n_m(z)$. This weakly nonlinear regime precisely corresponds to the regime investigated numerically in Sect. 4.3.7. Substituting the modal expansion (46) into the NLS equation (41), one obtains

$$i\partial_z a_m = \beta_m a_m - \gamma \sum_{p,q,s} W_{mpqs} a_p a_q^* a_s \tag{50}$$

where $a_m(z) = c_m(z) \exp(-i\beta_m z)$, and the fourth-order tensor is defined by the overlap integral

$$W_{mpqs} = \int u_m^*(\boldsymbol{x}) u_p(\boldsymbol{x}) u_q^*(\boldsymbol{x}) u_s(\boldsymbol{x})\, d\boldsymbol{x}. \tag{51}$$

Equation (50) conserves the total power $N = \sum_m |a_m|^2$ and the Hamiltonian

$$H = \sum_m \beta_m |a_m|^2 - \frac{\gamma}{4} \sum_{m,p,q,s} \left(W_{mpqs} a_m^* a_p a_q^* a_s + W_{mpqs}^* a_m a_p^* a_q a_s^* \right). \tag{52}$$

Starting from Eq. (50) and following the procedure of the random phase approximation [30, 39], we derived in [135] the irreversible kinetic equation governing the nonlinear evolution of the modal occupancies. For this purpose, we take the continuum limit of the discrete sum over the modes $\{m\}$, which is justified when one deals with a large number of modes, i.e., $V_0/\beta_0 \gg 1$. The substitution of the discrete sums by continuous integrals also refers to the so-called 'semiclassical description of the excited states' [137]. Its validity implies that the relevant excitation energies contributing to the discrete sum are much larger than the level spacing β_0, i.e., the spreading of the modal occupancies is much larger than β_0. In [135], the following kinetic equation governing the irreversible evolution of the modal occupancies has been derived:

$$\begin{aligned} \partial_z \tilde{n}_{\boldsymbol{\kappa}}(z) = & \frac{4\pi\gamma^2}{\beta_0^6} \iiint d\boldsymbol{\kappa}_1 d\boldsymbol{\kappa}_2 d\boldsymbol{\kappa}_3 \delta(\tilde{\beta}_{\boldsymbol{\kappa}_1} + \tilde{\beta}_{\boldsymbol{\kappa}_3} - \tilde{\beta}_{\boldsymbol{\kappa}_2} - \tilde{\beta}_{\boldsymbol{\kappa}}) |\tilde{W}_{\boldsymbol{\kappa}\boldsymbol{\kappa}_1\boldsymbol{\kappa}_2\boldsymbol{\kappa}_3}|^2 \\ & \times \tilde{n}_{\boldsymbol{\kappa}} \tilde{n}_{\boldsymbol{\kappa}_1} \tilde{n}_{\boldsymbol{\kappa}_2} \tilde{n}_{\boldsymbol{\kappa}_3} \left(\tilde{n}_{\boldsymbol{\kappa}}^{-1} + \tilde{n}_{\boldsymbol{\kappa}_2}^{-1} - \tilde{n}_{\boldsymbol{\kappa}_1}^{-1} - \tilde{n}_{\boldsymbol{\kappa}_3}^{-1} \right) \\ & + \frac{8\pi\gamma^2}{\beta_0^2} \int d\boldsymbol{\kappa}_1 \delta(\tilde{\beta}_{\boldsymbol{\kappa}_1} - \tilde{\beta}_{\boldsymbol{\kappa}}) |\tilde{U}_{\boldsymbol{\kappa}\boldsymbol{\kappa}_1}(\tilde{\mathbf{n}})|^2 (\tilde{n}_{\boldsymbol{\kappa}_1} - \tilde{n}_{\boldsymbol{\kappa}}), \end{aligned} \tag{53}$$

where

$$\tilde{U}_{\boldsymbol{\kappa}\boldsymbol{\kappa}_1}(\tilde{\mathbf{n}}) = \frac{1}{\beta_0^2} \int d\boldsymbol{\kappa}' \, \tilde{W}_{\boldsymbol{\kappa}\boldsymbol{\kappa}_1\boldsymbol{\kappa}'\boldsymbol{\kappa}'} \, \tilde{n}_{\boldsymbol{\kappa}'}. \tag{54}$$

The functions with a tilde refer to the natural continuum extension of the corresponding discrete functions, i.e., $\tilde{n}_{\boldsymbol{\kappa}}(z) = n_{[\boldsymbol{\kappa}/\beta_0]}(z)$, $\tilde{\beta}_{\boldsymbol{\kappa}} = \beta_{[\boldsymbol{\kappa}/\beta_0]}$, $\tilde{W}_{\boldsymbol{\kappa}\boldsymbol{\kappa}_1\boldsymbol{\kappa}_2\boldsymbol{\kappa}_3} = W_{[\boldsymbol{\kappa}/\beta_0][\boldsymbol{\kappa}_1/\beta_0][\boldsymbol{\kappa}_2/\beta_0][\boldsymbol{\kappa}_3/\beta_0]}$ and so on, where $[x]$ denotes the integer part of x.

The kinetic equations (53), (54) differs from the conventional WT kinetic equation in several respects. First, we remark the presence of the new second term in Eq. (53). Note that this term vanishes when the occupation of a mode depends only on its energy $\tilde{\beta}$. Actually, this term enforces an isotropization of the mode occupancies amongst the modes with the same modal energy. Another important property of the kinetic equation (53) is the presence of the function $\tilde{W}_{\boldsymbol{\kappa}\boldsymbol{\kappa}_1\boldsymbol{\kappa}_2\boldsymbol{\kappa}_3}$ in the collision term. We will discuss this term through the analysis of some particular examples of waveguide configurations.

4.1.4 Application to Specific Examples

The kinetic equations (53), (54) is general and, in principle, relevant to different types of waveguide configurations. We briefly comment this aspect by considering different concrete examples.

We first comment the parabolic potential relevant to graded-index multimode fibers. It is also known to play an important role in experiments involving weakly interacting Bose gases [137]. In the ideal parabolic limit ($V_0 \to \infty$), $u_m(\boldsymbol{x})$ refer to the normalized Hermite-Gaussian functions with corresponding eigenvalues $\beta_m = \beta_{m_x,m_y} = \beta_0(m_x + m_y + 1)$,

$$u_{m_x,m_y}(x,y) = \kappa(\pi m_x!\, m_y!\, 2^{m_x+m_y})^{-1/2} H_{m_x}(\kappa x)\, H_{m_y}(\kappa y)\, \exp[-\kappa^2(x^2+y^2)/2], \tag{55}$$

where $\kappa = (q/\alpha)^{1/4}$. In the continuum limit, we have $\tilde{\beta}_{\boldsymbol{\kappa}} = \kappa_x + \kappa_y + \beta_0$. This expression plays the role of a generalized *anisotropic* dispersion relation, whose wave vector reads $\boldsymbol{\kappa} = \beta_0(m_x, m_y)$. The parabolic potential will be discussed in more detail below, in relation with wave condensation in a waveguide in Sect. 4.3.7.

An other example that can easily be illustrated is the circular waveguide of radius R, whose index of refraction is supposed to be constant for $|\boldsymbol{x}| < R$ ('step-index' waveguide). We assume the waveguide to be of infinite depth for simplicity. The field can be expanded into the orthonormal basis of the Bessel functions, $\psi(\boldsymbol{x}, z) = \sum_{l,s} c_{l,s}(z) u_{l,s}(\boldsymbol{x}) \exp(-i\beta_{l,s} z)$, with

$$u_{l,s}(\boldsymbol{x}) = \frac{1}{\sqrt{\pi R^2 J_{l+1}^2(x_{l,s})}} J_l(x_{l,s}|\boldsymbol{x}|/R) \exp(il\theta), \tag{56}$$

where $J_l(x)$ is the Bessel function of the first kind, $x_{l,s}$ is the sth zero of $J_l(x)$, and $(|\boldsymbol{x}|, \theta)$ are the polar coordinates. With these notations, the eigenvalues read $\beta_{l,s} = \alpha x_{l,s}^2/R^2$. In a similar way as above, the passage to the continuum limit can be done by defining the wave vector $\boldsymbol{\kappa} = \beta_{0,1}(l, s)$, which thus leads to the kinetic equation for the evolution of $\tilde{n}_{\boldsymbol{\kappa}}(z)$. Note that with this parametrization of the wave vectors $\boldsymbol{\kappa}$ the density of states $\rho(\beta)$ is uniform.

We finally show that Eq. (53) recovers the traditional WT equation when the field is expanded into the usual plane-wave basis with periodic boundary conditions

$$u_{m_x,m_y}(\boldsymbol{x}) = \frac{1}{L} \exp[2i\pi(m_x x + m_y y)/L], \tag{57}$$

where L stands for the box size and $\boldsymbol{k} = \frac{2\pi}{L}(m_x, m_y)$ the usual wave-vector. This expansion is relevant to the homogeneous problem, i.e., in the absence of the confining potential [$V(x) = 0$]. It models the evolution of the random wave in the presence of a box-shaped confining potential, $V(\boldsymbol{x})$, whose frequency cutoff, $k_c = \pi/dx$ mimics the finite depth of the waveguide, $V_0 \sim \alpha k_c^2$. With this plane-

wave modal expansion, one obtains $|\tilde{W}_{\boldsymbol{\kappa}\boldsymbol{\kappa}_1\boldsymbol{\kappa}_2\boldsymbol{\kappa}_3}|^2 = \frac{(2\pi)^2}{L^6}\delta(\boldsymbol{k}_1+\boldsymbol{k}_3-\boldsymbol{k}_2-\boldsymbol{k})$. Because of the Dirac δ-function, the second term in the kinetic equation (53) vanishes, which thus leads to the standard form of the WT kinetic equation

$$\partial_z \tilde{n}_{\boldsymbol{k}}(z) = \mathrm{Coll}[\tilde{n}_{\boldsymbol{k}}], \tag{58}$$

with the collision term

$$\mathrm{Coll}[\tilde{n}_{\boldsymbol{k}}] = \kappa_0\gamma^2 \iiint d\boldsymbol{k}_1 d\boldsymbol{k}_2 d\boldsymbol{k}_3 \delta\left(\omega_{k_1}+\omega_{k_3}-\omega_{k_2}-\omega_k\right)\delta(\boldsymbol{k}_1+\boldsymbol{k}_3-\boldsymbol{k}_2-\boldsymbol{k})\mathscr{Q}(\tilde{\mathbf{n}}), \tag{59}$$

where $\kappa_0 = 4\pi/(2\pi)^2$, the dispersion relation is $\omega(k) = \alpha k^2$, and

$$\mathscr{Q}(\tilde{\mathbf{n}}) = \tilde{n}_{\boldsymbol{k}}\tilde{n}_{\boldsymbol{k}_1}\tilde{n}_{\boldsymbol{k}_2}\tilde{n}_{\boldsymbol{k}_3}\left(\tilde{n}_{\boldsymbol{k}}^{-1}+\tilde{n}_{\boldsymbol{k}_2}^{-1}-\tilde{n}_{\boldsymbol{k}_1}^{-1}-\tilde{n}_{\boldsymbol{k}_3}^{-1}\right). \tag{60}$$

As discussed in the Introduction, this kinetic equation can be derived by making use of a rigorous mathematical technique based on a multi-scale expansion of the cumulants of the nonlinear wave, as originally formulated in [40–42], and recently studied in more details through the analysis of the probability distribution function of the random field [33].

It is interesting to note that in the 1D case, the degenerate phase-matching conditions lead to a vanishing collision term in Eq. (59). This aspect has been discussed in [138], in relation with integrable turbulence, a subject of growing interest [29, 139]. Notice that the presence of a nonlocal nonlinearity also leads to a vanishing collision term in 1D—though contrary to the integrable NLS case, the hierarchy of the moments equations can be closed to the next order in the presence of nonlocality. Instead of the usual four-wave resonant interaction [Eq. (58)], one obtains in this case a six-wave resonant interaction process. We refer the reader to [68] for a detailed discussion of this interesting six-wave nonlinear dynamics.

4.2 Thermalization and Nonequilibrium Kolmogorov-Zakharov Stationary States

We will describe the essential properties of the WT kinetic equation by considering the standard version of the homogeneous WT kinetic equation, i.e., Eqs. (58)–(60) [with $V(\boldsymbol{x}) = 0$], while the influence of the potential trap will be discussed in Sect. 4.3.7. Note that, to avoid cumbersome notations, in the following we drop the tilde notation adopted here above [in particular we substitute the notation $\tilde{n}_{\boldsymbol{k}}(z)$ with the standard notation $n_{\boldsymbol{k}}(z)$]. We will also generalize the presentation of the results to a spatial dimension $d = 2$ or $d = 3$ in the framework of the dimensionless NLS equation

$$i\partial_z\psi = -\nabla^2\psi + a|\psi|^2\psi. \tag{61}$$

For $d = 2$, the spatial variable has been normalized with respect to the healing length $\Lambda = (\alpha L_{nl})^{1/2}$ (see Sect. 2). In the same way, for $d = 3$ the additional temporal variable has been normalized with respect to the healing time $\tau_0 = (|\beta| L_{nl})^{1/2}$ (see Sect. 3). The variables can be recovered in real units through the transformation: $z \to z L_{nl}, t \to t\tau_0, \boldsymbol{x} \to \boldsymbol{x}\Lambda, \psi \to \psi\sqrt{\rho}$, where we recall that $\rho = N/L^d$ denotes the wave intensity (see Sect. 2). Note that in this section we deal essentially with a defocusing nonlinearity, so as to ensure the stability of the homogeneous plane-wave solution ('condensate'). The parameter $a = -\text{sign}(\gamma)$ then denotes the sign of the nonlinearity, $a > 0$ ($a < 0$) for a defocusing (focusing) nonlinearity. We keep in mind that for $d = 3$ the Laplacian operator in Eq. (61) accounts for both diffraction and dispersion effects, $\nabla^2 = \partial_{xx} + \partial_{yy} + \partial_{tt}$, where we implicitly assumed that the wave propagates in the anomalous dispersion regime, so that chromatic dispersion acts in the same way as diffraction effects, and thus ensures the stability of the monochromatic plane-wave solution in the defocusing regime [140].

4.2.1 Thermodynamic Rayleigh-Jeans Spectrum

The WT kinetic equation has a structure analogous to the celebrated Boltzmann's equation, which is known to describe the evolution of a dilute classical gas far from the equilibrium state [141]. For this reason the kinetic equation (58) exhibits properties similar to those of the Boltzmann's equation. It conserves the total power (or quasi-particle number) of the field

$$N = L^d \int n_{\boldsymbol{k}}(z) d\boldsymbol{k}, \tag{62}$$

the momentum

$$\boldsymbol{P} = L^d \int \boldsymbol{k} n_{\boldsymbol{k}}(z) d\boldsymbol{k}, \tag{63}$$

and the kinetic (linear) energy

$$E = L^d \int \omega(\boldsymbol{k})\, n_{\boldsymbol{k}}(z) d\boldsymbol{k}. \tag{64}$$

Let us remark that Eq. (58) does not conserve the total energy H, but only its linear contribution E. This results from the fact that the nonlinear energy has a negligible contribution in the perturbation expansion procedure of the kinetic theory ($|U/E| \ll 1$).

In analogy with the Boltzmann's equation, the kinetic wave equation is not reversible with respect to the propagation distance z. The irreversible character of Eq. (58) is expressed by the H-theorem of entropy growth, $dS/dz \geq 0$, where the

nonequilibrium entropy reads

$$S(z) = L^d \int \log[n_{\boldsymbol{k}}(z)] d\boldsymbol{k}. \tag{65}$$

As in standard statistical mechanics, the thermodynamic equilibrium state is determined from the extremum of entropy, subject to the constraint of conservation of kinetic energy (64), momentum (63) and power (62). The method of the Lagrange multipliers thus gives the thermodynamic Rayleigh-Jeans equilibrium distribution

$$n_{\boldsymbol{k}}^{eq} = \frac{T}{\omega(k) - \boldsymbol{k}.\boldsymbol{v} - \mu}. \tag{66}$$

The parameters T, μ and $\boldsymbol{v}$ are in principle arbitrary and refer to the temperature, chemical potential and mean velocity, by analogy with thermodynamics. We underline that there exist a one-to-one correspondence between $(T, \mu, \boldsymbol{v})$ and the conserved quantities $(E, N, \boldsymbol{P})$. This means that the evolution of the wave is described in the framework of the microcanonical statistical ensemble, in contrast with the conventional canonical treatment using a thermal bath [137]. Note that the equilibrium distribution (66) yields an exactly vanishing collision term (58), $\text{Coll}[n^{eq}] = 0$. This means that once the spectrum has reached the equilibrium distribution (66), it no longer evolves during the propagation, $\partial_z n_{\boldsymbol{k}} = 0$.

In many cases the equilibrium distribution is spherically symmetric and the Rayleigh-Jeans distribution takes the following simplified form

$$n_k^{eq} = \frac{T}{\omega(k) - \mu}. \tag{67}$$

This equilibrium spectrum is Lorentzian-shaped and the chemical potential characterizes the correlation length of the field at equilibrium, $\lambda_c^{eq} \sim 1/\sqrt{-\mu}$. However, we will see that the Langrange multiplier associated to momentum conservation plays an essential role for the study of multiple interacting wave-packets [142], or in the presence of higher-order dispersion effects that lead to an asymmetric supercontinuum equilibrium spectrum, see Sect. 5.2.

4.2.2 Nonequilibrium Kolmogorov-Zakharov Stationary Spectra

As discussed in the introduction, the process of thermalization is physically relevant when one considers a Hamiltonian wave system, which can be considered as an 'isolated' system. Conversely, when one considers a dissipative system which is driven far from equilibrium by an external source, then it no longer relaxes toward the Rayleigh-Jeans equilibrium distribution (66). A typical physical example of forced system could be the excitation of hydrodynamic surface waves by the wind. In general, the frequency-scales of forcing and damping differ significantly. The

nonlinear interaction leads to an energy redistribution among the frequencies and an important problem is to find the stationary spectra of the system.

V.E. Zakharov was the first to realize that the kinetic equation of weak-turbulence theory also admits nonequilibrium stationary solutions [30, 143]. Contrary to the Rayleigh-Jeans equilibrium distribution, these stationary solutions carry a non-vanishing flux of conserved quantities, i.e., the energy and the particle fluxes. Such nonequilibrium stationary distributions are the analogue of the Kolmogorov spectra of hydrodynamic turbulence proposed by Kolmogorov in his theory in 1941. Zakharov used a clever set of 'conformal transformations' to show that the kinetic equation admits finite flux spectra as exact stationary solutions.

The formation of these nonequilibrium stationary solutions requires the existence of a permanent forcing or damping in the system, a feature that has been widely studied theoretically [30, 32, 33] (also see [144, 145]), and experimentally in different circumstances (e.g., surface waves, spin waves, surface tension waves, capillary waves, elastic waves). In optics, an experiment aimed at observing these nonequilibrium stationary spectra has been reported in [67] and reviewed in [68]. In this case, the optical system is forced at the entry of the nonlinear medium ($z = 0$), and the formation of the nonstationary spectrum was observed in the transient propagation of the optical wave. Actually, in optics the propagation length z plays the role of time, so that the observation of a permanent nonequilibrium stationary state would require a forcing and a damping at any z. This situation is rather artificial in optics, so that, so far, Kolmogorov-Zakharov spectra did not play a major role in nonlinear optics experiments. For this reason, we will not discuss such nonequilibrium stationary states and refer the reader to [30, 33, 43] for details. For concreteness, we just give here the expressions of the nonequilibrium stationary solutions

$$n_{\boldsymbol{k}}^{Q} = C_Q \frac{Q^{1/3}}{k^{\alpha_Q}} \tag{68}$$

$$n_{\boldsymbol{k}}^{P} = C_P \frac{P^{1/3}}{k^{\alpha_P}} \tag{69}$$

where Q and P are the particle and energy fluxes in frequency space and C_P, C_Q are prefactors. These solutions are exact stationary solutions of the WT kinetic equation (58). The exponents α_Q and α_P depend on the scaling of the dispersion relation and on the explicit nonlinearities. Considering the particular example of the NLS equation (61), one obtains $\alpha_Q = d - 2/3$ and $\alpha_P = d$, where d denotes the spatial dimension.

It is interesting to note that the process of relaxation to a stationary spectrum can be described by means of self-similar solutions of the WT kinetic equation. In substance, the non-stationary solution describes a self-similar front that propagates in frequency-space and which leaves a quasi-stationary state in its wake. This self-similar relaxation solution can be obtained for both equilibrium and nonequilibrium Kolmogorov-Zakharov stationary solutions of the kinetic equation. We refer the

reader to [38, 146–148] for more details concerning the properties of these self-similar solutions. So far, these non-stationary solutions have not been exploited in the context of optical waves.

4.3 Wave Condensation

The phenomenon of wave thermalization can be characterized by a self-organization process, in the sense that it is thermodynamically advantageous for the system to generate a large-scale coherent structure in order to reach the most disordered equilibrium state. A remarkable example of this counterintuitive phenomenon is provided by wave condensation [33, 53, 55, 57, 135, 149], whose thermodynamic equilibrium properties are analogous to those of quantum Bose-Einstein condensation [55]. Classical wave condensation can be interpreted as a redistribution of energy among different modes, in which the (kinetic) energy is transferred to small scales fluctuations, while an inverse process increases the power (i.e., number of 'particles') into the lowest allowed mode, thus leading to the emergence of a large scale coherent structure [55, 57, 149, 150]. It is important to note that the phenomenon of wave condensation has been extended in this last decade to optical cavity systems [58–61, 64, 65, 151], which raises interesting questions on the relation between laser operation and the Bose-Einstein condensation of photons [66, 152–154]. These aspects will be discussed in more details in Sect. 5.

4.3.1 Wave Condensation in the Cubic NLS Equation

4.3.2 3D: Condensation in the Thermodynamic Limit

To describe the thermodynamic equilibrium properties of the condensation process in three dimensions it is important to point out some preliminary observations. We remark that the distribution (67) realizes the maximum of the entropy $S[n_k]$ and vanishes exactly the collision term, $\mathrm{Coll}[n_k^{eq}] = 0$. However, note that Eq. (67) is only a *formal* solution, because it does not lead to converging expressions for the energy E and the power N in the limits $k \to \infty$, a feature which is usually termed 'ultraviolet catastrophe'. The usual way to regularize such unphysical divergence is to introduce an ultraviolet cut-off k_c. Note that a frequency cut-off appears naturally in the numerical simulation through the spatial discretization (dx) of the NLS equation (61), $k_c = \pi/dx$. As will be discussed in detail in Sect. 4.3.7, an effective physical frequency cut-off arises naturally in the guided wave configuration of the optical field.

Following the procedure of [55], one can combine Eqs. (62)–(64) and (67), which gives the expression for the power of the field at equilibrium

$$\frac{N}{L^3} = 4\pi\, Tk_c \left[1 - \frac{\sqrt{-\mu}}{k_c} \arctan\left(\frac{k_c}{\sqrt{-\mu}}\right)\right], \tag{70}$$

$$\frac{E}{L^3} = \frac{4\pi\, Tk_c^3}{3} \left[1 + 3\frac{\mu}{k_c^2} + 3\left(\frac{-\mu}{k_c^2}\right)^{\frac{3}{2}} \arctan\left(\frac{k_c}{\sqrt{-\mu}}\right)\right]. \tag{71}$$

An inspection of Eq. (70) reveals that μ tends to 0^- for a non-vanishing temperature T, keeping a constant power density N/L^3. This means that the correlation length λ_c diverge to infinity [see Eq. (67)]. By analogy with the Bose-Einstein transition in quantum systems, such a divergence of the equilibrium distribution at $\boldsymbol{k} = 0$ reveals the existence of a condensation process.

As in standard Bose-Einstein condensation, the fraction of condensed power N_0/N vs the temperature T (or the energy E), may be calculated by setting $\mu = 0$ in the equilibrium distribution (67). Note that the assumption $\mu = 0$ for $T \leq T_c$ can be justified rigorously in the thermodynamic limit (i.e., $L \to \infty$, $N \to \infty$, keeping N/L^3 constant). One readily obtains $(N - N_0)/L^3 = 4\pi Tk_c$ and $E/L^3 = 4\pi Tk_c^3/3$, which gives

$$N_0/N = 1 - E/E_c, \tag{72}$$

where the critical energy reads $E_c = Nk_c^2/3$. Alternatively, the fraction of condensed power may be expressed as a function of the temperature,

$$N_0/N = 1 - T/T_c, \tag{73}$$

where $T_c = 3E_c/(4\pi L^3 k_c^3)$. As in standard Bose-Einstein condensation, N_0 vanishes at the critical temperature T_c, and N_0 becomes the total number of particles as T tends to 0.

4.3.3 Weakly Nonlinear Regime: Weak Condensate Amplitude

The linear behavior of n_0 vs E in Eq. (72) is consistent with the results of numerical simulations. However note that Eq. (72) is derived for a spherically symmetric continuous distribution of $n_{\boldsymbol{k}}$, while in the numerics the integration is discretized. A discretization of Eq. (72) leads to a better agreement between the theory and the numerical simulations of Eq. (61) [55]. More precisely, making use of wave turbulence theory, one may express the averaged total energy of the field $\langle H \rangle$ in terms of the condensed particles n_0, which gives [57]

$$\frac{\langle H \rangle}{L^3} = (n - n_0)\frac{\sum'_{\boldsymbol{k}} 1}{\sum'_{\boldsymbol{k}} \frac{1}{k^2}} + a\left(n^2 - \frac{1}{2}n_0^2\right), \tag{74}$$

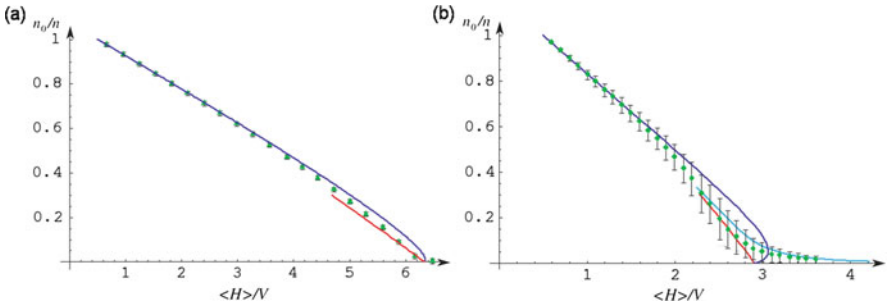

Fig. 11 Condensate fraction n_0/n vs total energy density $\langle H \rangle / L^d$. Points (*diamond*) refer to numerical simulations of the normalized NLS Eq. (61) for $d = 3, N_* = 32^3$ modes (**a**), and $d = 2, N_* = 32^2$ modes (**b**) [$N/L^d = 1, dx = 1$ ($k_c = \pi$)]. Each numerical point corresponds to a time average over 3000 time units once the equilibrium state is reached. The *red line* corresponds to the condensation curve in the presence of a small condensate amplitude [WT regime, Eq. (74)], while the *blue line* in the presence of a high-condensate amplitude [Bogoliubov regime, Eq. (75)]. The *green line* in (**b**) refers to the condensation curve for a non-vanishing chemical potential, [Eq. (76), (77)]. The bars denote the amplitude of the fluctuations of n_0/n at equilibrium. *Source*: from [57]

where $\sum'_{\boldsymbol{k}}$ denotes the sum over the whole frequency space which excludes the mode $\boldsymbol{k} = 0$ ($n_0 \equiv N_0/L^d$, $n \equiv N/L^d$). This expression is plotted in Fig. 11 (red line), and it is in good agreement with the numerical simulations in the regime of weak condensation (typically $n_0 < 0.3$).

4.3.4 Bogoliubov Regime: Strong Condensate Amplitude

To describe the regime of strong condensation, one has to take into account the "interactions between the quasi-particles". To include the nonlinear (interaction) contribution, the Bogoliubov's expansion procedure of a weakly interacting Bose gas has been adapted to the classical wave problem. The interested reader may find the details of the analysis in [55, 57]. One obtains the following closed relation between the total energy and the fraction of condensed power

$$\frac{\langle H \rangle}{L^3} = (n - n_0) \frac{\sum'_{\boldsymbol{k}} 1}{\sum'_{\boldsymbol{k}} \frac{k^2 + a n_0}{k^4 + 2 a n_0 k^2}} + \frac{a}{2} \left[n^2 + (n - n_0)^2 \right]. \tag{75}$$

In the presence of high-condensate amplitudes, this expression is in quantitative agreement with the numerical simulations of the NLS equation (61), without any adjustable parameter (see Fig. 11).

4.3.5 2D: Condensation Beyond the Thermodynamic Limit

Let us now consider the condensation process in two dimensions. The analysis exposed above in 3D may readily be applied to 2D, which gives $N/L^2 = \pi T \log(1 - k_c^2/\mu)$. It becomes apparent from this expression that, for a fixed power density N/L^2, μ reaches zero for a vanishing temperature T. In complete analogy with the Bose-Einstein condensation, this indicates that condensation no longer takes place in 2D. In other terms, the critical temperature T_c tends to zero because of the infrared divergence of the equilibrium distribution $n_{\boldsymbol{k}}^{eq}$. Actually, this result is rigorously correct in the thermodynamic limit (i.e., $L \to \infty$, $N \to \infty$, keeping $n \equiv N/L^2$ constant). Nevertheless, for situations of physical interest in which N and L are finite, wave condensation is re-established in two dimensions, a property confirmed by the numerical simulations [57]. Indeed, one can calculate the critical temperature for condensation in two dimensions, $T_c = nL^2/\sum_{\boldsymbol{k}}' 1/k^2$ [150]. This expression reveals that the discrete sum in frequency space provides a non-vanishing value of T_c, while T_c tends to zero in the thermodynamic limit, because of the (infrared) logarithmic divergence of the continuous integral $\int d\boldsymbol{k}/k^2$.

In complete analogy with quantum Bose-Einstein condensation, for a finite surface of the optical beam, wave condensation occurs for a non-vanishing value of the chemical potential, $\mu \neq 0$. The condensation curve may thus be derived without the implicit assumption $\mu = 0$. The interested reader may find the details in [57]. One obtains

$$\frac{\langle H \rangle(\mu)}{L^2} = (n - n_0) \frac{\sum_{\boldsymbol{k}}' \frac{k^2}{k^2 - \mu}}{\sum_{\boldsymbol{k}}' \frac{1}{k^2 - \mu}} + a \left(n^2 - \frac{1}{2} n_0^2 \right), \tag{76}$$

$$\frac{n_0(\mu)}{n} = \frac{1}{-\mu} \frac{1}{\sum_{\boldsymbol{k}} \frac{1}{k^2 - \mu}}. \tag{77}$$

We plotted in Fig. 11b the condensate fraction n_0/n [Eq. (77)] vs the energy density $\langle H \rangle/L^2$ [Eq. (76)], as a parametric function of μ. It reveals that a non-vanishing chemical potential makes the transition to condensation "smoother", with the appearance of a characteristic "tail" in the condensation curve. Such a "tail" progressively disappears as the surface L^2 increases, so that the condensation curve n_0/n vs $\langle H \rangle/L^2$ tends to the expression derived in the thermodynamic limit, i.e., Eq. (76) with $\mu = 0$ recovers Eq. (74). Let us remark that the theory is in quantitative agreement with the numerical simulations of the NLS equation (61), as illustrated in Fig. 11.

It results that the critical behaviour of the two-dimensional condensation curve looks similar to that of a genuine "phase transition". Note however that, strictly speaking, "phase transitions" only occur in the thermodynamic limit, so that such terminology is not appropriate for the two dimensional problem considered here. Nevertheless, if one considers the macroscopic occupation of the fundamental mode $\boldsymbol{k} = 0$ as the essential characteristic of condensation, one may say that wave

condensation do occur in 2D. It is important to note that for $d = 2$, nearby the transition to condensation some clear evidence of a Berezinskii-Kosterlitz-Thouless transition has been provided, with an algebraic decay of the correlation function of the field [155].

4.3.6 Condensation Beyond the Cubic NLS Equation: Nonlocal and Saturable Nonlinearities

The phenomenon of classical wave condensation has been essentially studied in the framework of the NLS equation in the presence of a pure cubic Kerr nonlinearity. In many cases, however, realistic optical experiments are not modelled by a cubic Kerr nonlinearity. In a recent work [149], it has been shown that wave condensation can take place with more complex nonlinearities. The examples of the nonlocal nonlinearity and of the saturable nonlinearity were considered in [149], which refer to natural extensions of the cubic nonlinearity [140]. It was shown that the generalized NLS equation accounting either for a nonlocal or a saturable nonlinearity describes a process of wave condensation completely analogous to that described in the framework of the cubic Kerr nonlinearity. Following the procedure of the previous Sect. 4.3.1, analytical expressions of the condensate fraction are derived in both the weakly and the strongly nonlinear regimes of propagation, and a quantitative agreement is obtained with the simulations [149].

4.3.7 Condensation in a Waveguide

In the previous Sect. 4.3.1 we have considered wave condensation in the ideal limit in which the incoherent wave is expanded in the plane-wave Fourier basis with periodic boundary conditions. As discussed above, this approach of wave condensation requires the introduction of a frequency cut-off in the theory [55, 57], so as to regularize the ultraviolet catastrophe inherent to classical nonlinear waves. From the physical point of view, such a frequency cut-off is not properly justified for classical waves. We will see that an effective frequency cut-off arises naturally in the guided-wave configuration of the optical beam. This frequency cut-off plays a key role in wave condensation (see Sect. 4.3.1), since it prevents the divergence of the critical energy for condensation [135] [see Eq. (72)]. Moreover, we have also seen that in 2D, wave condensation does not occur in the thermodynamic limit [55, 57]. We will see that a parabolic waveguide configuration reestablishes wave condensation in two dimensions, in analogy with quantum Bose-Einstein condensation [137]. Accordingly, wave condensation and thermalization can be studied accurately through the analysis of the two-dimensional spatial evolution of a guided optical beam.

4.3.8 Rayleigh-Jeans Distribution in a Waveguide

The starting point is the WT kinetic derived in Sect. 4.1 into the basis of the eigenfunctions of the potential $V(\boldsymbol{x})$. Here we follow [135] to describe wave condensation in an optical waveguide. The kinetic equations (53), (54) conserves the power $N = \beta_0^{-2} \int d\boldsymbol{\kappa} n_{\boldsymbol{\kappa}}$ and the energy $E = \beta_0^{-2} \int d\boldsymbol{\kappa} \beta_{\boldsymbol{\kappa}} n_{\boldsymbol{\kappa}}$, where we recall that $\beta_{\boldsymbol{\kappa}} = \kappa_x + \kappa_y + \beta_0$. Contrarily to the homogeneous WT kinetic equation (58), the kinetic equation (53), (54) does not conserve the momentum, a feature which is consistent with the fact that the potential $V(\boldsymbol{x})$ prevents momentum conservation in the NLS equation (41). The kinetic equations (53), (54) exhibits a H-theorem of entropy growth, $d\mathscr{S}/dz \geq 0$, where the nonequilibrium entropy reads $\mathscr{S}(z) = \beta_0^{-2} \int d\boldsymbol{\kappa} \ln(n_{\boldsymbol{\kappa}})$. The Rayleigh-Jeans equilibrium state $n_{\boldsymbol{\kappa}}^{eq}$ realizing the maximum of entropy, subject to the constraints of conservation of E and N, is obtained by introducing the corresponding Lagrange's multipliers,

$$n_{\boldsymbol{\kappa}}^{eq} = \frac{T}{\beta_{\boldsymbol{\kappa}} - \mu}. \tag{78}$$

Note that, in a way akin to the usual Rayleigh-Jeans distribution (67), the temperature denotes the amount of energy $\mathscr{E}_{\boldsymbol{\kappa}}$ that is equipartitioned among the modes of the waveguide. Indeed, in the tails of the equilibrium distribution (78), i.e., $\beta_{\boldsymbol{\kappa}} \gg |\mu|$, we have $\mathscr{E}_{\boldsymbol{\kappa}} = \beta_{\boldsymbol{\kappa}} n_{\boldsymbol{\kappa}}^{eq} \sim T$ [see Eq. (49)]. Also note that the equilibrium state (78) cancels both collisions terms of the kinetic Eqs. (53), (54).

This equilibrium property of energy equipartition has been confirmed by the numerical simulations of the NLS equation (41) with a truncated parabolic potential, as illustrated in Fig. 12. To be concrete, in the numerical simulations we considered a realistic graded-index multimode optical fiber, with a radium of $15\,\mu$m and an index difference of $n_1 - n_0 = 10^{-3}$ (see Fig. 10), and a refractive index of reference $n_0 = 1.45$. With these parameters the number of modes is $N_* = 66$. It is important to note that silica fibers exhibit a focusing nonlinearity, $\gamma < 0$ in Eq. (41). The incoherent beam may thus exhibit filamentation effects (i.e., speckle beam fragmentation) during its propagation in the fiber. However, as revealed by the numerical simulations, the beam does not exhibit filamentation effects because we consider the weakly nonlinear regime of propagation, in which the linear energy dominates the nonlinear energy, $U/E \ll 1$. The weakly nonlinear condition can easily be satisfied in the framework of the considered optical fiber system, since the nonlinearity of silica fibers is known to be relatively small as compared to other types of commonly used nonlinear optical media. In the numerical simulations, the following standard value of the nonlinear silica coefficient was considered $n_2 = -2 \times 10^{-8}\,\mu\text{m}^2/\text{W}$, together with a power of the beam of 94 kW.

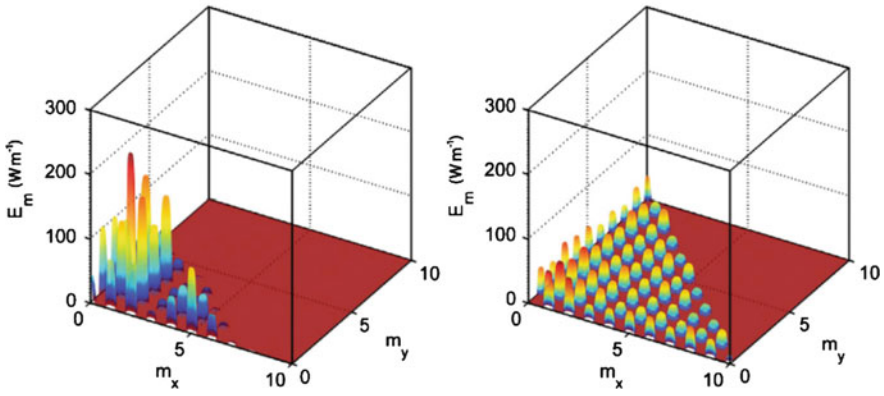

Fig. 12 Condensation and thermalization in a trap: Numerical simulation of the NLS equation (41) with a parabolic potential $V(\boldsymbol{x})$, showing the establishment of energy equipartition among the modes of the waveguide: Energy per mode, $\mathscr{E}_m = \beta_m n_m$ [see Eq. (49)] vs the mode $m = (m_x, m_y)$, in the initial condition (**a**), and averaged over the propagation once the equilibrium state is reached, i.e., $\partial_z \mathscr{S} \simeq 0$ (**b**). The amount of power n_m in the mode $m = (m_x, m_y)$ is calculated by projecting the field amplitude into the corresponding eigenmode [see Eq. (48)]. Energy almost reaches an equipartition among all modes, except the fundamental condensed mode $m_x = m_y = 0$ which is macroscopically populated [not shown in (**a**), (**b**)]. In particular, we considered a truncated parabolic potential (Fig. 10), so that $\beta_{m_x,m_y} \simeq \beta_0(m_x + m_y + 1)$ and only modes whose eigenvalue verifies $\beta_{m_x,m_y} \leq V_0$ are guided. *Source*: from [135]

4.3.9 Frequency Cut-Off, Density of States and Thermodynamic Limit

The number of modes involved in the dynamics with a trap $V(\boldsymbol{x})$ is finite because of the truncation of the potential (see Fig. 10, $V_0 < \infty$). In this way the truncated potential introduces an effective frequency cut-off for the classical nonlinear wave, because modes whose eigenvalues exceed the potential depth, $\beta_{\boldsymbol{\kappa}} > V_0$, are not guided during the propagation. A more rigorous justification of this aspect is given in the Appendix of [135]. Note that this is in contrast with the homogeneous problem [$V(\boldsymbol{x}) = 0$ in Eq. (41)], as discussed in Sect. 4.3.1. In this case, the frequency cut-off k_c is introduced by the spatial discretization (dx) of the NLS equation, i.e., $k_c = \pi/dx$, so that in the continuous limit $k_c \to \infty$ (see, e.g., [55]).

Let us discuss the importance of the truncation of the potential ($V_0 < \infty$) through the example of a parabolic potential considered in the numerical simulations (see Figs. 12, 13). Considering the constraint, $\beta_0 \leq \beta(\boldsymbol{\kappa}) \leq V_0$, as well as the assumption $\beta_0 \ll V_0$ (i.e., large number of modes $N_* \gg 1$), the power of the field at equilibrium reads $N = (T/\beta_0^2) \int_0^{V_0} d\kappa_x \int_0^{V_0-\kappa_x} (\kappa_x + \kappa_y + \beta_0 - \mu)^{-1} d\kappa_y$, which gives

$$N = \frac{T}{\beta_0^2} \left[V_0 - \tilde{\mu} \ln \left(\frac{-\tilde{\mu}}{V_0 - \tilde{\mu}} \right) \right], \tag{79}$$

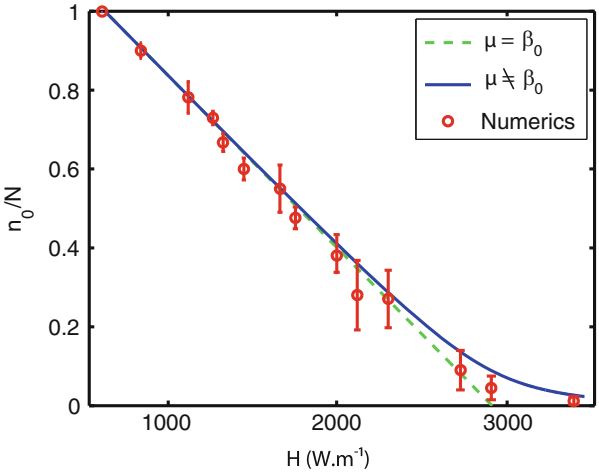

Fig. 13 Wave condensation in a trap: Fraction of power condensed in the fundamental mode at equilibrium, n_0/N, vs the energy of the field, H, for a truncated parabolic potential (parameters are given in Sect. 4.3.7). The *red points* refer to the results of the numerical simulations of the NLS equation (41) with a parabolic potential $V(\boldsymbol{x})$. They have been obtained by averaging n_0/N over the propagation distance once the equilibrium state is reached, i.e., $\partial_z \mathscr{S} \simeq 0$. The '*error-bars*' denote the amount of fluctuations (standard deviation) of n_0/N once equilibrium is reached. The *continuous blue line* refers to the theoretical condensation curve given in Eqs. (82)–(83), while the *dashed green line* refers to the corresponding thermodynamic limit [$\tilde{\mu} \to 0$ in Eqs. (82)–(83)]. In these plots the eigenvalues β_m and eigenmodes $u_m(\boldsymbol{x})$ in Eqs. (82)–(83) account for the truncation of the potential ($V_0 < \infty$). *Source*: from [135]

where we defined $\tilde{\mu} = \mu - \beta_0$. In order to comment expression (79), we recall that in the homogeneous problem [$V(\boldsymbol{x}) = 0$ in Eq. (41)] wave condensation was shown to only occur in 3D, while in 2D the chemical potential was shown to reach zero for a vanishing temperature [55, 57, 150]. In analogy with Bose-Einstein condensation in quantum gases, this means that wave condensation does not occur in the thermodynamic limit in 2D. Conversely, Eq. (79) reveals that $\tilde{\mu} \to 0$ for a non-vanishing critical temperature, $T_c = 4\alpha Nq/V_0$, which indicates that the presence of a parabolic potential $V(\boldsymbol{x})$ reestablishes wave condensation in the thermodynamic limit in 2D. Indeed, the thermodynamic limit for a parabolic potential corresponds to taking $N \to \infty$ and $q \to 0$, keeping constant the product Nq [137]. This result is in complete analogy with the well-known fact that a parabolic potential reestablishes Bose-Einstein condensation in 2D [137]. There is however a difference with quantum condensation. Bose-Einstein condensation is known to be reestablished in a parabolic potential of infinite depth, $V_0 \to \infty$, while here T_c tends to zero in the limit $V_0 \to \infty$. Contrary to the quantum case, one also needs to introduce a finite depth of the potential, $V_0 < \infty$, to get wave condensation in 2D. This condition is satisfied for any optical waveguide configuration.

4.3.10 Condensate Fraction in the Waveguide

We now look for a relation between the fraction of condensed power n_0/N and the temperature T or the energy E, in a way completely analogous to what has been done for the homogeneous problem ($V(\boldsymbol{x}) = 0$) in Sect. 4.3.1. As in the usual interpretation of Bose-Einstein condensation in a trap, we set $\mu = \beta_0$ in the equilibrium distribution (78). Note that the assumption $\tilde{\mu} = \mu - \beta_0 = 0$ for $T \leq T_c$ can be justified rigorously in the 2D thermodynamic limit. Isolating the fundamental mode, one has $N - n_0 = (T/\beta_0^2) \iint_{\mathscr{D}} 1/(\kappa_x + \kappa_y)\, d^2\boldsymbol{\kappa}$, where $n_0 = T/[\beta_0^2(\beta_0 - \mu)]$. We thus readily obtain $N - n_0 = TV_0/\beta_0^2$. Proceeding in a similar way for the energy, one obtains $E - n_0\beta_0 = \frac{TV_0^2}{2\beta_0^2}(1 + 2\beta_0/V_0)$. Eliminating the temperature from the expressions for E and N gives the following expression of the condensate fraction

$$\frac{n_0}{N} = 1 - \frac{E - E_0}{NV_0/2}, \tag{80}$$

where $E_0 = N\beta_0$ refers to the minimum energy, i.e. the energy of the field when all the power is condensed, $n_0/N = 1$. The condensate amplitude n_0/N increases as the energy E decreases, and condensation arises below the critical energy

$$E_c = E_0 + NV_0/2 = \frac{NV_0}{2}\left(1 + \frac{2\beta_0}{V_0}\right). \tag{81}$$

This expression deserves to be commented in two respects. First, because of the truncation of the waveguide potential ($V_0 < \infty$), the value of E_c does not diverge to infinity. This is in contrast with the homogeneous problem [$V(\boldsymbol{x}) = 0$ in Eq. (41)], as discussed above in 2D in Sect. 4.3.1. In this case the critical value of the energy behaves as $E_c \sim Nk_c^2/\ln(k_c)$, where $k_c = \pi/dx$ is the arbitrary frequency cut-off. In the continuous limit in which the spatial discretization of the NLS equation tends to zero, $dx \to 0$, the critical value of the energy E_c diverges to infinity (see, e.g., [55, 57]). A second point that could be remarked in Eq. (81) is that wave condensation is reestablished in the thermodynamic limit in 2D. Indeed, writing Eq. (81) in the following form, $E_c/S = Nq(1 + 2\beta_0/V_0)/(2\pi)$, where $S = \pi a^2$ is the waveguide surface, it becomes apparent that the energy density E_c/S does not tend to zero in the thermodynamic limit ($N \to \infty, q \to 0$, keeping Nq constant). As discussed in the previous Sect. 4.3.9, this is again in contrast with the homogeneous problem and the plane-wave expansion of the field, in which E_c/S tends to zero logarithmically in the thermodynamic limit [57, 150].

The simple analysis of Eqs. (80), (81) outlined above provides physical insight into the process of wave condensation. However, a direct quantitative comparison with the numerical simulations requires the derivation of the condensation curve relating the condensate fraction to the Hamiltonian, as discussed above in Sect. 4.3.1 for the homogeneous problem, $V(\boldsymbol{x}) = 0$. For this purpose, we note that Eq. (80) can be improved along three lines. (1) The continuous integrals by a discrete sum

over the modes of the waveguide. One obtains $n_0/N = 1 - (E - E_0)\sum'(m_x + m_y)^{-1}/(E_0(N_* - 1))$, where we recall that N_* is the number of modes of the waveguide, and $\sum'$ denotes the sum over all modes $\{m = (m_x, m_y)\}$ excluding the fundamental mode $m = 0$. In the continuous limit we have $\sum' \frac{1}{m_x+m_y} \to \beta_0^{-1} \iint_{\mathscr{D}} \frac{d^2\boldsymbol{\kappa}}{\kappa_x+\kappa_y} = V_0/\beta_0$ and the number of modes $N_* = \beta_0^{-2} \iint_{\mathscr{D}} d^2\boldsymbol{\kappa} = V_0^2/(2\beta_0^2)$, so that the above equation recovers Eq. (80). (2) A generalization of the expression of the condensate fraction, n_0/N vs E, can be done beyond the thermodynamic limit [57, 150], i.e., without the implicit assumption $\tilde{\mu} = 0$ for $T \leq T_c$. From the physical point of view, this means that we take into account the finite size of the optical waveguide. (3) We include the contribution of the nonlinear energy U into the expression of the condensation curve. We split the contribution of the fundamental mode into the modal expansion of the field, $\psi(\boldsymbol{x}, z) = \psi_0(\boldsymbol{x}, z) + \varepsilon(\boldsymbol{x}, z)$, where $\psi_0(\boldsymbol{x}, z) = c_0(z)u_0(\boldsymbol{x})\exp(-i\beta_0 z)$ is the coherent condensate contribution and $\varepsilon(\boldsymbol{x}, z) = \sum_{m\neq 0} c_m(z)u_m(\boldsymbol{x})\exp(-i\beta_m z)$ is the incoherent contribution. This expansion can be substituted into the expression of U in Eq. (43), and then computed in explicit form by making use of the random phase approximation [135]. The generalizations (1)–(3) finally lead to the following expression of the condensation curve beyond the thermodynamic limit, including the nonlinear contribution of the energy

$$\frac{n_0}{N}(\tilde{\mu}) = \frac{1}{-\tilde{\mu}\sum_m \frac{1}{\beta_m-\beta_0-\tilde{\mu}}} \tag{82}$$

$$\langle H\rangle(\tilde{\mu}) = N\frac{\sum_m \frac{\beta_m}{\beta_m-\beta_0-\tilde{\mu}}}{\sum_m \frac{1}{\beta_m-\beta_0-\tilde{\mu}}} + \langle U\rangle(\tilde{\mu}), \tag{83}$$

where $\langle U\rangle(\tilde{\mu})$ is a cumbersome expression given in [135]. The fraction of condensed power n_0/N is thus coupled to the total energy $\langle H\rangle$ through the non-vanishing chemical potential, $\tilde{\mu} = \mu - \beta_0 \neq 0$. The parametric plot of (82), (83) with respect to $\tilde{\mu}$ is reported in Fig. 13 (continuous line). As for the homogeneous problem [$V(\boldsymbol{x}) = 0$], the long tail in the condensation curve at high energies H is due to the non-vanishing chemical potential, $\tilde{\mu} \neq 0$. In the thermodynamic limit $\tilde{\mu} \to 0$, the condensation curve (82), (83) recovers the straight line discussed above through Eqs. (80), (81) (see the dashed line in Fig. 13). Let us remark the good agreement between the theoretical condensation curve and the simulations, without using adjustable parameters. We finally note that Eqs. (82), (83) are valid for various different types of waveguide index profiles, provided one makes use of the appropriate eigenvalues β_m and eigenmodes $u_m(\boldsymbol{x})$ (see [135]).

5 Generalizations and Perspectives

5.1 Turbulence in Optical Cavities

The phenomenon of condensation discussed above in Sect. 4.3 has been recently interpreted within a broader perspective in different active and passive optical cavity configurations [58–65]. This raises important questions, such as e.g., the relation between laser operation and the phenomenon of Bose-Einstein condensation. As a matter of fact, these questions are still the subject of vivid debate—we refer the reader to [66, 152, 154, 156] for some recent discussions on this important problem.

An important analogy with condensation has been also discussed in the dynamics of active mode-locked laser systems in the presence of additive noise source [60, 154, 157]. On the basis of their previous works [158, 159], the authors showed that the formation of coherent pulses in actively mode-locked lasers exhibits in certain conditions a transition of the laser mode system to a light pulse state that is similar to Bose-Einstein condensation, in the sense that it is characterized by a macroscopic occupation of the fundamental mode as the laser power is increased. The analysis is based on statistical light-mode dynamics with a mapping between the distribution of the laser eigenmodes to the equilibrium statistical physics of noninteracting bosons in an external potential.

5.1.1 Wave Turbulence in Raman Fiber Lasers

The dynamics of Raman fiber lasers has been also shown to exhibit some interesting analogies with condensation-like phenomena [59, 64, 65]. Here we discuss in more detail these systems in light of the WT theory that has been developed to describe their turbulent dynamics. For more details, we refer the interested reader to [63] for an overview on the WT description of Raman fiber lasers (also see the more recent work [160]).

In [161], the Raman fiber laser is modelled as a turbulent system whose optical power spectrum results from a weakly nonlinear interaction among the multiple modes of the cavity. Performing a mean field approach in which the Raman Stokes field does not evolve significantly over one cavity round trip, the authors of [161] first establish a differential equation for the evolution of the complex amplitude E_n of the nth longitudinal mode

$$\tau_{rt}\frac{dE_n}{dt} - \frac{1}{2}(g-\delta_n)E_n(t) = -\frac{i}{2}\gamma L \sum_{l\neq 0} E_{n-l}(t) \times \sum_{m\neq 0} E_{n-m}(t)E^*_{n-m-l}(t)\exp(2i\beta\, ml\Delta^2\, c\, t). \quad (84)$$

In their approach, the time evolution of E_n is determined by the Raman gain g, the dispersion of the fiber, the losses δ_n of the fiber and of the cavity mirrors, and the four-wave mixing process. γ is the Kerr coupling coefficient and β represents the second-order dispersion coefficient of the cavity fiber. $\Delta = 1/\tau_{rt} = c/2L$ is the free spectral range of the Fabry-Perot cavity that has a length L. Gain, losses and dispersive effects occurring inside the whole laser cavity are supposed to influence the formation of the optical power spectrum through their dependence in frequency-space. In particular fiber Bragg grating mirrors are considered as spectral filters introducing parabolic losses in frequency space ($\delta_n = \delta_0 + \delta_2(n\Delta)^2$). Dispersive effects occurring inside the laser cavity are supposed to be dominantly governed by the second-order dispersion β of the cavity fiber. It must be emphasized that Eq. (84) refers to the discretized version of the one-dimensional NLS equation, in which gain and losses terms have been added [162]. In other words, the approach developed by the authors of [161] amounts to apply a WT treatment to a one-dimensional NLS equation, whose integrability is broken by the presence of gain and loss terms.

Assuming an exponential decay for the correlation function among the modes, $\langle E_n(t)E_n^*(t')\rangle = I_n \exp(-|t-t'|/\tau)$, the following WT kinetic equation that governs the temporal evolution of the intracavity spectrum was derived [161]

$$\tau_{rt}\frac{dI(\Omega)}{dt} = (g - \delta(\Omega))I(\Omega) + S_{\mathrm{FWM}}(\Omega), \tag{85}$$

where $I(\Omega) = \langle E_n E_n^*\rangle/\Delta$. The mathematical expression of the collision term $S_{\mathrm{FWM}}(\Omega)$ can be separated into two parts

$$S_{\mathrm{FWM}}(\Omega) = -\delta_{\mathrm{NL}}I(\Omega) + (\gamma L)^2 \int \frac{\mathscr{F}[I]\, d\Omega_1\, d\Omega_2}{(3\tau_{rt}/\tau)[1 + (4\tau L\beta/3\tau_{rt})^2\Omega_1^2\Omega_2^2]}, \tag{86}$$

where the functional reads $\mathscr{F}[I] = I(\Omega - \Omega_1)I(\Omega - \Omega_2)I(\Omega - \Omega_1 - \Omega_2)$, while the nonlinear term responsible for four-wave-mixing-induced losses δ_{NL} reads

$$\delta_{\mathrm{NL}} = (\gamma L)^2 \int \frac{\mathscr{G}[I]\, d\Omega_1\, d\Omega_2}{(3\tau_{rt}/\tau)[1 + (4\tau L\beta/3\tau_{rt})^2\Omega_1^2\Omega_2^2]}, \tag{87}$$

where $\mathscr{G}[I] = [I(\Omega - \Omega_1) + I(\Omega - \Omega_2)]I(\Omega - \Omega_1 - \Omega_2) - I(\Omega - \Omega_1)I(\Omega - \Omega_1)$. A stationary solution of the WT kinetic equation (85) has been obtained by Babin et al. in [161], which exhibits the following hyperbolic-secant structure, $I(\Omega) = 2I/\big(\pi\Gamma\cosh(2\Omega/\Gamma)\big)$, where Γ is the width of the intracavity laser power spectrum. This analytical solution is in very good agreement with spectra recorded in experiments in which the fiber laser operates well above threshold, in various different configurations, even in regimes in which the mean field approximation should no longer hold [163]. Although the WT approach developed in [161] has undoubtedly provided a new insight into the physics of Raman fiber lasers, some other numerical and experimental works have raised some interesting questions concerning the applicability of the WT approach to the description of the spectral

broadening phenomenon. In particular, numerical simulations of the mean field equations introduced in [161] revealed that the shape of the laser optical power spectrum strongly depends on the sign of the second-order dispersion coefficient [59]. This cannot be captured by the WT theory, which is inherently insensitive to the sign of the second-order dispersion parameter. As pointed out in [162, 164], the formation of the Stokes spectrum is also deeply influenced both by dispersive effects and by the spectral shape of the fiber Bragg grating mirrors used to close the laser cavity.

5.1.2 Laminar-Turbulent Transition in Raman Fiber Lasers

Fast recording techniques have been recently exploited for the experimental characterization of a laminar-turbulent transition in Raman fiber lasers [65]. The fiber laser used in the these experiments has been specifically designed. It is made with dispersion-free ultra-wideband super-Gaussian fiber grating mirrors. Slightly changing the pump power, an abrupt transition with a sharp increase in the width of laser spectrum has been observed, together with an abrupt change of the statistical properties of the Stokes radiation. The laminar state observed before the transition is associated to a multimode Stokes emission with a relatively narrow linewidth and relatively weak fluctuations of the Stokes power. On the other hand, the turbulent state corresponds to a high multimode operation with a wider spectrum and stronger fluctuations of the Stokes power. The laminar-turbulent transition has been also studied by means of intensive numerical simulations (see Fig. 14) [59, 64, 65]. The simulations reveal that, by increasing the pump power, the mechanism underlying the laminar-turbulent transition relies on the generation of an increasing number of

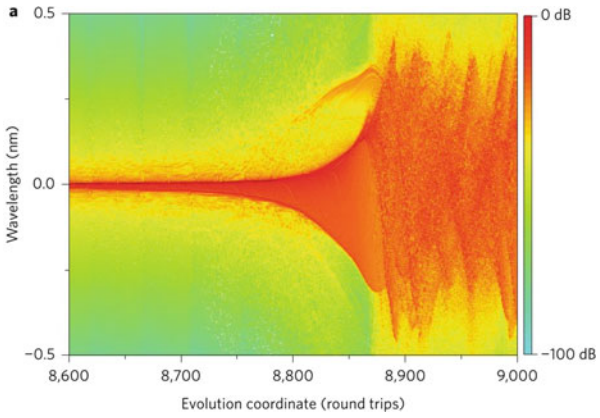

Fig. 14 Numerical simulations evidencing the laminar-turbulent transition in a Raman fiber laser. The evolution of the laser optical power spectrum is plotted as a function of number of round trips inside the laser cavity. *Source*: from [65]

dark (or grey) solitons. This experimental work opens new fields of investigations, in particular as regard the impact of phase-defects on the turbulent dynamics of purely 1D wave systems.

5.1.3 Wave Kinetics of Random Fiber Lasers

Random lasers are a rapidly growing field of research, with implications in soft-matter physics, light localization, and photonic devices [26, 165, 166]. Considering a different perspective, the authors of [160] described the cyclic wave dynamics inherent to laser systems by considering weakly dissipative modifications of the integrable NLS equation. In this way, a 'local kinetic equation' describing the turbulent dynamics of a random fiber laser system is derived [160]. The key property of this kinetic equation is that the δ-function reflecting energy conservation at each elementary four-wave interaction is substituted by an effective Lorentzian function that involves a frequency dependent gain. As a remarkable result, the collision term of the local kinetic equation does not vanish in spite of the trivial resonant conditions inherent to the 1D four-wave interaction with a purely quadratic dispersion relation [138]. From this point of view, the local kinetic equation exhibits properties reminiscent of those considered in [38, 167], although the equations are different, e.g., as regard the renormalization of the dispersion relation by the nonlinearity and the additional nonlinear damping. Then at variance with the purely conservative (Hamiltonian) system, in active cyclic laser systems, the interactions are mediated by a non-homogenous gain, which leads to an effective interaction over the finite interval of the evolution coordinate. We also note that the local kinetic equation is derived under a double separation of scales, i.e., the turbulent regime is dominated by dispersive effects as compared to gain effects, and the gain itself if much larger than gain variation over the typical spectral width of the radiation. Furthermore, the authors confirm their theoretical work by means of direct experimental measurements in random fibre lasers: In the high-power regime, the equilibrium spectrum of the random laser measured experimentally is found in good agreement with the nonequilibrium stationary solution of the local kinetic equation, see Fig. 15. Finally, the theory is also completed by means of a generalization of the linear kinetic Schawlow-Townes theory. For more details on these aspects we refer the reader to [160].

5.1.4 Turbulent Dynamics in Passive Optical Cavities

As commented above, a classical wave can exhibit a genuine process of wave condensation as it propagates in a 2D conservative Kerr material, [33, 55, 135]. Actually, a phenomenon completely analogous to such conservative condensation process can occur in an incoherently pumped passive optical cavity, despite the fact that the system is inherently dissipative [62]. For this purpose, let consider a *passive optical cavity* pumped by an incoherent optical wave, whose time correlation, t_c,

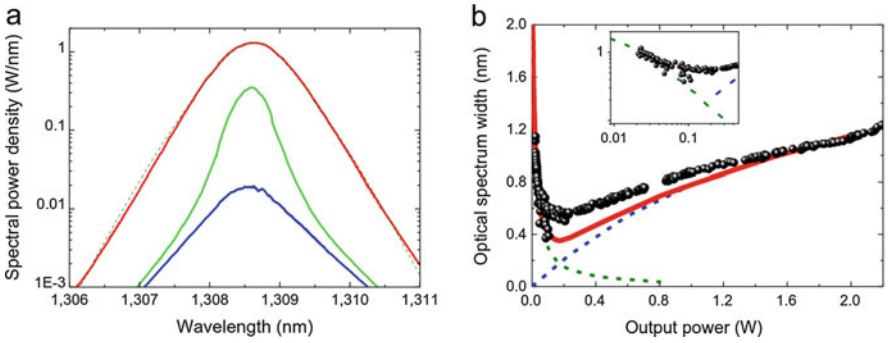

Fig. 15 Nonlinear kinetic description of the random fiber laser optical spectrum. (**a**) Optical spectrum measured experimentally: near the generation threshold (*blue curve*, laser power = 0.025 W), slightly above the generation threshold (*green curve*, 0.2W) and well above the generation threshold (red curve, 1.5 W). The optical spectrum predicted by the local wave kinetic equation, for laser power 1.5 W is shown by *dashed red line*. (**b**) Spectrum width as a function of the laser's output power in theory and experiment. Experimental data are shown by *black circles*. The prediction for the spectrum broadening from the nonlinear kinetic theory based on the local wave kinetic equation (*blue dashed line*). The prediction for the spectral narrowing from the modified linear kinetic Schawlow-Townes theory (*dashed green line*). The *red line* denotes the sum of nonlinear and linear contributions. The inset shows the spectral narrowing near the threshold in log-scale. For more details see [160]. *Source*: from [160]

is much smaller than the round trip time, $t_c \ll \tau_{rt}$. In this way, the optical field from different cycles are mutually incoherent with one another, which makes the optical cavity *non-resonant*. Because of this property, the cavity does not exhibit the widely studied dynamics of pattern formation [168, 169]. Instead, the dynamics of the cavity exhibits a turbulent behavior that can be characterized by an irreversible process of thermalization toward energy equipartition. A mean-field WT equation was derived in [62], which accounts for the incoherent pumping, the nonlinear interaction and both the cavity losses and propagation losses. In spite of the dissipative nature of the cavity dynamics, the intracavity field undergoes a condensation process below a critical value of the incoherence (kinetic energy) of the pump. This phenomenon is illustrated in Fig. 16a, which shows the temporal evolution of the condensate fraction in the intracavity field: After a transient, the fraction of power condensed in the fundamental transverse mode of the cavity saturates to a constant value, which is found in agreement with the theory. Figure 16b reports the condensation curve, i.e., the fraction of condensed power at equilibrium vs the kinetic energy of the injected pump wave. This latter quantity reflects the degree of coherence of the pump wave and plays the role of the control parameter of the transition to wave condensation in the cavity configuration. We remark in Fig. 16b that the condensate fraction in this dissipative optical cavity is found in agreement with the theory inherited from the conservative Hamiltonian NLS equation, without using adjustable parameters. For more details on the simulations and the theory, we refer the reader to [62].

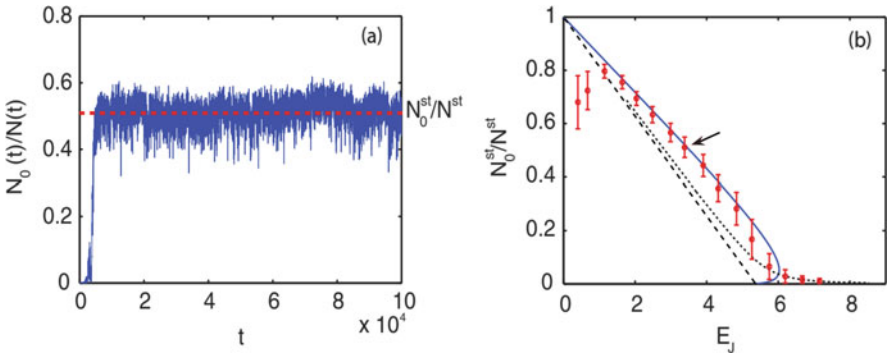

Fig. 16 Wave condensation in an incoherently pumped passive optical cavity. (**a**) Evolution of the fraction of condensed power $N_0(t)/N(t)$ vs time t: The condensate growth saturates to a constant value N_0^{st}/N^{st}, which is in agreement with the theory [62]. (**b**) *Condensation curve*: fraction of condensed power in the stationary equilibrium state N_0^{st}/N^{st} vs the kinetic energy of the pump E_J. The *condensation curve* is computed for a fixed value of the pump intensity J_0, while E_J is varied by modifying the degree of coherence of the pump (i.e., its spectral width). The *blue solid line* refers to the (Bogoliubov) strong condensation regime. The *black dotted line* refers to the weak condensation regime beyond the thermodynamic limit ($\mu \neq 0$), while the *dashed black line* refers to the thermodynamic limit ($\mu \to 0$). The *red points* correspond to the NLS numerical simulations with the cavity boundary conditions. For more details, see [62]. *Source*: from [62]

Let us note an important difference that distinguishes the thermalization and condensation processes discussed here with those reported in the quantum photon context in [61, 170]. In these works the thermalization process is achieved thanks to the presence of dye molecules, which thus play the role of an external thermostat. Conversely, in the passive cavity configuration considered here, the process of thermalization solely results from the four-wave interaction mediated by the intracavity Kerr medium, while the 'temperature' is controlled by varying the kinetic energy (degree of coherence) of the injected pump.

In a recent experimental work [171], the incoherently pumped passive cavity has been implemented in a fully integrated optical fiber system, nearby the zero-dispersion wavelength of the fiber. The dynamics of the cavity exhibits a quasi-soliton turbulent behavior which is reminiscent of the turbulent dynamics of the purely Hamiltonian wave system considered in [172, 173]. The analysis reveals that, as the coherence of the injected pump wave is degraded, the cavity undergoes a transition from the coherent quasi-soliton regime toward the highly incoherent (weakly nonlinear) turbulent regime characterized by short-lived and extreme rogue wave events. This transition can then be interpreted in analogy with a phenomenon of quasi-soliton condensation. The experiments realized in the incoherently pumped passive optical cavity have been characterized by means of complementary spectral and temporal PDF measurements [171].

An unexpected result of [171] is that quasi-soliton condensation can take place efficiently, even in the presence of a low cavity finesse, in contrast with wave-condensation in 2D defocusing media discussed here above, which requires a high

finesse [62]. This can be interpreted as a consequence of the fact that the process of thermalization of an optical wave constitutes a prerequisite for the phenomenon of wave-condensation in a defocusing medium, while wave thermalization is known to require a high cavity finesse. There is another important difference which distinguishes wave-condensation and (quasi-)soliton condensation. Wave-condensation is known to exhibit a property of long-range order and coherence, in the sense that the correlation function of the field amplitude does not decay at infinity, $\lim_{|\mathbf{r}-\mathbf{r}'|\to\infty} \langle A(\mathbf{r})\, A^*(\mathbf{r}')\rangle \neq 0$, a property consistent with the idea that the coherence length of a plane-wave diverges to infinity [55]. This is in contrast with the spatial localized character of a (quasi-)soliton, which naturally limits the range of coherence to the characteristic spatial width of the (quasi-)soliton structure. Wave-condensation then appears to be more sensitive to the "boundary conditions" of the system, and thus results less robust than (quasi-)soliton condensation when considered in an optical cavity system.

5.2 *Optical Wave Thermalization Through Supercontinuum Generation*

The phenomenon of SC generation is characterized by a dramatic spectral broadening of the optical field during its propagation [24, 174]. As a rather general rule, the process of spectral broadening is interpreted through the analysis of the following main nonlinear effects: the four-wave mixing effect, the soliton fission, the Raman self-frequency shift and the generation of dispersive waves [174]. Due to such a multitude of nonlinear effects involved in the process, a complete and satisfactory theoretical description of SC generation is still lacking. However, there is a growing interest in developing new theoretical tools aimed at describing SC generation in more details, see e.g., [175].

The general physical picture of SC generation in PCFs can be summarized as follows. When the PCF is pumped with long pulses in the anomalous dispersion regime, MI is known to lead to the generation of a train of soliton-like pulses, which in turn lead to the emission of Cherenkov radiation in the form of spectrally shifted dispersive waves. These optical solitons are known to exhibit a self-frequency shift towards longer wavelengths as a result of the Raman effect. One encounters the same picture if the PCF is characterized by two zero dispersion wavelengths. In this case the Raman frequency shift of the solitons is eventually arrested in the vicinity of the second zero dispersion wavelengths. The SC spectrum then results to be essentially bounded by the corresponding dispersive waves [24, 176]. The important aspect to underline here is that in all these regimes *the existence of coherent soliton structures plays a fundamental role into the process of SC generation*.

This physical picture of SC generation changes in a significant way when one considers the regime in which long and intense pump pulses are injected into the PCF. Indeed, in this highly nonlinear regime, the spectral broadening process is

essentially dominated by the combined effects of the Kerr nonlinearity and higher-order dispersion, i.e., by four-wave mixing processes [177]. In this regime the optical field exhibits rapid and random temporal fluctuations, which prevent the formation of robust and persistent coherent soliton structures. It turns out that the optical field exhibits an incoherent turbulent dynamics, in which coherent soliton structures do not play any significant role. In the following we shall term this regime the 'incoherent regime of SC generation' [178].

In these last years a nonequilibrium thermodynamic interpretation of this incoherent regime of SC generation has been formulated [23, 50, 51, 99, 178] on the basis of the WT theory. In the following we remind the main aspect of optical wave thermalization through SC generation. For more details we refer the interested reader to the short review article [179]. The generalized NLS equation is known to describe the main properties of SC generation in a PCF [123, 174]. In its simplest form that neglects the Raman effect, the shock term, the generalized NLS equation takes the form:

$$i\frac{\partial\psi}{\partial z} + \sum_{j\geq 2}^{m} \frac{i^j \beta_j}{j!}\frac{\partial^j \psi}{\partial t^j} + \gamma|\psi|^2\psi = 0, \tag{88}$$

with the corresponding dispersion relation:

$$k(\omega) = \sum_{j\geq 2}^{m} \frac{\beta_j \omega^j}{j!}. \tag{89}$$

In the following we consider dispersion curves of PCFs characterized by two zero dispersion wavelengths, whose accurate description requires a high-order Taylor expansion of the dispersion relation ($m > 4$ and even). Starting from the high-order dispersion NLS equation (88), one can derive the irreversible WT kinetic equation governing the evolution of the averaged spectrum of the field $n(z,\omega)$ $[\langle\tilde{\psi}(z,\omega_1)\tilde{\psi}^*(z,\omega_2)\rangle = n(z,\omega_1)\,\delta(\omega_1-\omega_2)]$:

$$\partial_z n(z,\omega_1) = Coll[n], \tag{90}$$

with the collision term

$$\begin{aligned} Coll[n] = &\iiint d\omega_2\, d\omega_3\, d\omega_4\; n(\omega_1)n(\omega_2)n(\omega_3)n(\omega_4) \\ &\times W\left[n^{-1}(\omega_1) + n^{-1}(\omega_2) - n^{-1}(\omega_3) - n^{-1}(\omega_4)\right] \end{aligned} \tag{91}$$

where '$n(\omega)$' stands for '$n(z,\omega)$' in Eq. (91). As usual in the WT kinetic equation, the phase-matching conditions of energy and momentum conservation are expressed by the presence of Dirac δ-functions in $W = \frac{\gamma^2}{\pi}\,\delta(\omega_1+\omega_2-\omega_3-\omega_4)\,\delta[k(\omega_1) + k(\omega_2) - k(\omega_3) - k(\omega_4)]$, where $k(\omega)$ refers to the linear dispersion relation.

Equation (90) conserves the power density $N/T_0 = \int n(z,\omega)\, d\omega$, the density of kinetic energy $E/T_0 = \int k(\omega)\, n(z,\omega)\, d\omega$ and the density of momentum $P/T_0 = \int \omega\, n(z,\omega)\, d\omega$, where T_0 refers to the considered numerical time window. It also exhibits a H-theorem of entropy growth, $\partial_z \mathscr{S} \geq 0$, where the nonequilibrium entropy reads $\mathscr{S}(z) = \int \log[n(z,\omega)]\, d\omega$. The Rayleigh-Jeans equilibrium distribution is obtained by maximising the entropy under the constraints imposed by the conservation of the energy, momentum and power, which gives

$$n^{eq}(\omega) = \frac{T}{k(\omega) + \lambda\omega - \mu}, \tag{92}$$

where T and μ are by analogy with thermodynamics the temperature and the chemical potential of the incoherent wave at equilibrium.

The meaning of the parameter λ becomes apparent through the analysis of the group-velocity v_g of the optical field $[k'(\omega) \equiv \partial k/\partial\omega = 1/v_g(\omega)]$. Indeed, recalling the definition of an average, $\langle \mathscr{A} \rangle_{eq} = \int \mathscr{A}\, n^{eq}(\omega)\, d\omega / \int n^{eq}(\omega)\, d\omega$ and making use of the equilibrium spectrum (92), one readily obtains

$$\left\langle k'(\omega) \right\rangle_{eq} = -\lambda\,. \tag{93}$$

The parameter λ then denotes the average of the inverse of the group-velocity of the optical field at equilibrium. We report in Fig. 17c the comparison of the theoretical prediction (92) with the results of the numerical simulations of the high-order NLS equation (88). A quantitative agreement is obtained between the simulations and the theory (92), without using adjustable parameters [51]. The Rayleigh-Jeans spectrum is characterized by a double-peaked structure, which results from the presence of two zero dispersion wavelengths in the dispersion curve of the PCF. The relaxation toward thermal equilibrium is also corroborated by the saturation of the process of entropy production illustrated in Fig. 17b. Note however that a notable discrepancy is visible in the tails of the spectrum in Fig. 17c, as if the thermalization process were not achieved in a complete fashion. Actually, the simulations reveal that the tails of the spectrum exhibits a very slow process of spectral broadening, which apparently tends to evolve toward the expected Rayleigh-Jeans tails—though the required propagation length is extremely large. This aspect will be discussed in more detail in Sect. 5.3. Note that the good agreement between the theory and the simulations has been obtained in a variety of configurations, e.g., under cw or incoherent pumping, as discussed in detail in [50, 51].

5.2.1 Thermodynamic Phase-Matching

The thermodynamic equilibrium spectrum given in Eq. (92) is characterized by a double peak structure, which originates from the two zero dispersion wavelengths that characterize the PCF dispersion curve. It is important to underline, however, that the frequencies (ω_1, ω_2) of the two peaks of $n^{eq}(\omega)$ do not simply correspond to the

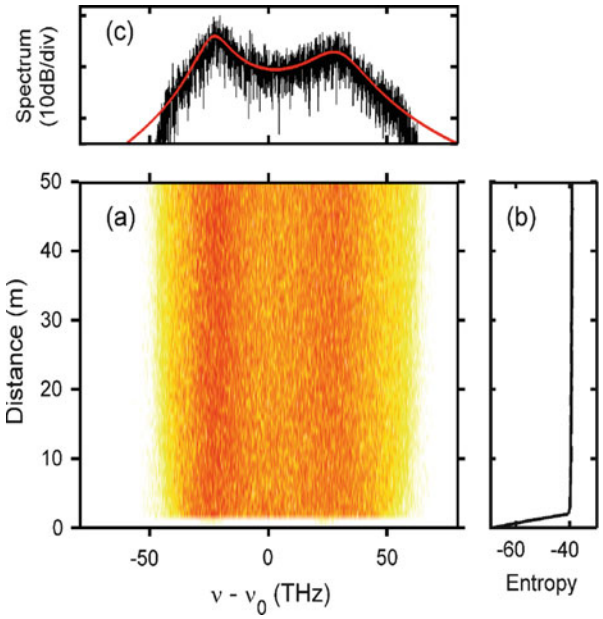

Fig. 17 Optical wave thermalization through SC generation. (**a**) Simulation of the instantaneous NLS equation (88) with a dispersion curve featured by two zero-dispersion wavelengths (for more details see [179]). (**b**) Optical wave thermalization is characterized by a process of entropy production, which saturates to a constant level once the equilibrium state is reached, as described by the H-theorem of entropy growth. (**c**) Comparison of the thermodynamic Rayleigh-Jeans equilibrium spectrum $n^{eq}(\omega)$ [Eq. (92)] (*red line*), and the numerical spectrum corresponding to an averaging over the last 20 m of propagation. A good agreement is obtained without adjustable parameters—note however a discrepancy in the tails of the spectrum (see the text for discussion)

minima of the dispersion relation, i.e. $k'(\omega_{1,2}) \neq 0$. To further analyze this aspect, let us write the thermodynamic equilibrium spectrum in the form $n^{eq}(\omega) = T/\mathscr{F}(\omega)$, with $\mathscr{F}(\omega) = k(\omega) + \lambda\omega - \mu$. The two frequencies (ω_1, ω_2) which maximize the equilibrium spectrum (92) satisfy $\mathscr{F}'(\omega_1) = \mathscr{F}'(\omega_2) = 0$, i.e., $k'(\omega_1) = k'(\omega_2) = -\lambda$. This observation reveals that *the two frequencies* (ω_1, ω_2) *of the double peaked equilibrium spectrum (92) are selected in such a way that the corresponding group-velocities coincide with the average group-velocity of the optical wave*,

$$v_g(\omega_1) = v_g(\omega_2) = 1/\left\langle k'(\omega)\right\rangle_{eq} = -1/\lambda. \tag{94}$$

It can be shown that there exists, in principle, a unique pair of frequencies (ω_1, ω_2) satisfying the conditions given by Eqs. (94). In other terms, for a given thermodynamic equilibrium spectrum (92), there exists a *unique* pair of frequencies (ω_1, ω_2) that leads to a matched group-velocity of the double peaked spectrum [51]. In this sense, Eq. (94) can be regarded as a thermodynamic phase-matching condition.

The thermodynamic phase-matching given by Eq. (94) then imposes a matching of the group-velocities of the two spectral peaks of the SC spectrum. The fact that different wave-packets naturally tend to propagate with the same group-velocity was discussed in [142]. This can be interpreted in analogy with basic equilibrium thermodynamic properties, namely that an isolated system can only exhibit a uniform motion of translation (and rotation) as a whole, while any macroscopic internal motion is not possible at thermodynamic equilibrium [180]. In this way, it was shown that a velocity locking is required, in the sense that it prevents "a macroscopic internal motion in the wave system." We refer the interested reader to [51, 118] for more details on this aspect.

5.3 Breakdown of Thermalization

As discussed in the introduction section in relation with the Fermi-Pasta-Ulam problem, thermalization does not necessarily in nonlinear systems. By considering the one-dimensional NLS equation, we present in this section two different mechanisms that inhibit the process of optical wave thermalization toward the Rayleigh-Jeans distribution. Depending on whether the dispersion relation is truncated up to the third, or fourth-order, the wave system exhibits different types of relaxation processes. Provided that the interaction occurs in the weakly nonlinear regime, the WT theory provides an accurate description of such mechanisms of breakdown of thermalization.

5.3.1 Truncated Thermalization

We consider here the 1D NLS equation in which the dispersion relation is truncated to the fourth-order. In this case, the WT theory reveals the existence of an irreversible evolution toward a Rayleigh-Jeans equilibrium state characterized by a compactly supported spectral shape [52]. This phenomenon of truncated thermalization may explain the physical origin of the abrupt SC spectral edges discussed above in Sect. 5.2. Besides its relevance in the context of SC generation, this phenomenon is also important from a fundamental point of view. Indeed, *it unveils the existence of a genuine frequency cut-off that arises in a system of classical waves described by the generalized NLS equation*, a feature of importance considering the well-known ultraviolet catastrophe of ensemble of classical waves [118].

The starting point is the NLS equation (88) accounting for third- and fourth-orders dispersion effects, as well as the corresponding WT kinetic equation (90). The kinetic theory reported in [52] reveals that the process of thermalization to the Rayleigh-Jeans spectrum (92) is not achieved in a complete way, but turns out to be

truncated within a specific frequency interval defined by the bounds, $\omega \in [\omega_-, \omega_+]$, with

$$\omega_\pm = -\frac{\tilde{\alpha}}{4\tilde{\beta}\tau_0} \pm \frac{\sqrt{21}}{12\tilde{\beta}\tau_0}\sqrt{3\tilde{\alpha}^2 + 8\tilde{\beta}}, \tag{95}$$

where $\tilde{\alpha}$ and $\tilde{\beta}$ refer to the normalized third- and fourth-orders dispersion parameters, namely $\tilde{\alpha} = L_{nl}\beta_3/\left(6\tau_0^3\right)$, and $\tilde{\beta} = L_{nl}\beta_4/\left(24\tau_0^4\right)$, where $\tau_0 = \sqrt{\beta_2 L_{nl}/2}$ is the corresponding healing time, i.e., the characteristic time for which linear and nonlinear effects are of the same order of magnitude [118].

The confirmation of this process of truncated thermalization by the numerical simulations has not been a trivial task. This is due to the fact that in the usual configurations of SC generation discussed above, the cascade of MI side-bands generated by the cw pump in the early stage of propagation spreads beyond the frequency interval predicted by the theory. As already discussed, the MI process is inherently a coherent nonlinear phase-matching effect which is not described by the WT kinetic equation [Eqs. (90), (91)]. This explains why the numerical simulations reported above (or in [50, 51]) did not evidence a precise signature of this phenomenon of truncated thermalization.

In order to analyze the theoretical predictions in more detail, one needs to decrease the injected pump power so as to maintain the (cascaded) MI side-bands within the frequency interval (95). Intensive numerical simulations of the NLS equation in this regime of reduced pump power have been performed in [52]. This study reveals that the nonlinear dynamics slows down in a dramatic way, so that the expected process of thermalization requires huge nonlinear propagation lengths. This results from the fact that the normalized parameters $\tilde{\alpha}$ and $\tilde{\beta}$ decrease as the pump power decreases, so that the NLSE approaches the integrable limit, which does not exhibit thermalization [138]. We report in Fig. 18 the wave spectra at different propagation lengths obtained by solving the NLS equation with $\tilde{\alpha} = 0.1$ and $\tilde{\beta} = 0.02$. In the early stage of propagation, $z \sim 200$, the spectrum remains confined within the frequency interval $[\omega_-, \omega_+]$ predicted by the theory [Eq. (95)], although the spectrum exhibits a completely different spectral profile than the expected Rayleigh-Jeans distribution. As a matter of fact, the process of thermalization requires enormous propagation lengths, as illustrated in Fig. 18d, which shows that the wave spectrum eventually relaxes toward a truncated Rayleigh-Jeans distribution. For more details on these numerical simulations, we refer the reader to [118].

5.3.2 Anomalous Thermalization

Here we discuss another mechanism that inhibits the natural process of thermalization. We consider the 1D NLS equation by truncating the dispersion relation up to the third order. We will see that the incoherent wave exhibits an irreversible

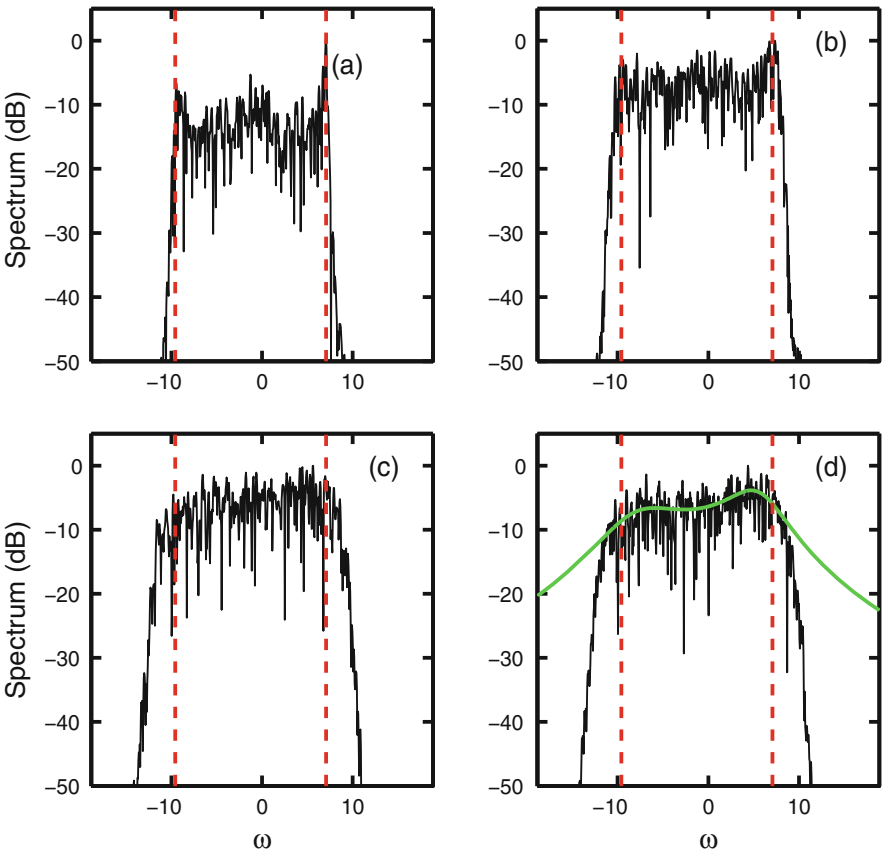

Fig. 18 Truncated thermalization of incoherent waves: Spectra $|\tilde{\psi}|^2(\omega, z)$ obtained by solving the NLS equation (88) with solely third and fourth-order dispersion effects ($\tilde{\alpha} = 0.1$, $\tilde{\beta} = 0.02$): (**a**) $z = 200$, (**b**) $z = 10^4$, (**c**) $z = 5 \times 10^5$, (**d**) $z = 10^6$. After a long transient, the wave relaxes toward a truncated Rayleigh-Jeans distribution [Eq. (92), *green line*] (**d**). The *dashed red lines* denote the frequencies $\omega_{\pm}$ in Eq. (95)—ω is here in units of τ_0^{-1}. *Source*: from [52]

evolution toward an equilibrium state of a different nature than the conventional Rayleigh-Jeans equilibrium state. The WT kinetic equation reveals that this effect of anomalous thermalization is due to the existence of a local invariant in frequency space J_ω, which originates in degenerate resonances of the system [112, 113]. In contrast to conventional integral invariants that lead to a generalized Rayleigh-Jeans distribution, here, it is the local nature of the invariant J_ω that makes the new equilibrium states different than the usual Rayleigh-Jeans equilibrium states. We remark that local invariants and the associated process of anomalous thermalization have been also identified in the 1D vector NLS equation, a configuration in which optical fiber experiments have been also performed, see [112].

The starting point is the NLS equation (88) accounting for third-order dispersion effects, as well as the corresponding WT kinetic equation (90). A refined analysis of the WT kinetic equation reveals a remarkable property, namely the existence of a local invariant in frequency space:

$$J(\omega) = n(\omega, z) - n(q - \omega, z), \tag{96}$$

where $q = 2s\omega_*$, ω_* being the zero-dispersion angular frequency, and $s = \text{sign}(\beta_2)$ [112, 113]. This invariant is 'local' in the sense that it is verified for each frequency ω individually, $\partial_z J(\omega) = 0$. It means that the subtraction of the spectrum by the reverse of itself translated by q, remains invariant during the whole evolution of the wave. The invariant (96) finds its origin in the following degenerate resonance of the phase-matching conditions: a pair of frequencies $(\omega, q - \omega)$ may resonate with any pair of frequencies $(\omega', q - \omega')$, because $k(\omega) + k(q - \omega) = sq^2/3$ does not depend on ω. Because of the existence of this local invariant, the incoherent wave relaxes toward an equilibrium state of fundamental different nature than the expected thermodynamic Rayleigh-Jeans spectrum:

$$n^{loc}(\omega) = \frac{J_\omega}{2} + \frac{1}{\lambda}\left(1 + \sqrt{1 + \left(\frac{\lambda J_\omega}{2}\right)^2}\right). \tag{97}$$

Here, the parameter λ is determined from the initial condition through the conservation of the power. We remark that the equilibrium distribution (97) vanishes exactly the collision term of the kinetic equation, i.e., it is a stationary solution. The equilibrium distribution is characterized by a remarkable property: it exhibits a constant spectral pedestal, $n^{loc}(\omega) \to 2/\lambda$ for $|\omega| \gg |\omega_*|$. We remark in this respect that in the tails of the spectrum ($|\omega| \gg |\omega_*|$), the invariant J_ω vanishes, so that a constant spectrum ($n_\omega = const$) turns out to be a stationary solution of the WT kinetic equation. The existence of the process of anomalous thermalization has been confirmed by the numerical simulations of both the NLS equation and the WT kinetic equation, as illustrated in Fig. 19. For more details on theoretical and numerical simulations of anomalous thermalization, we refer the reader to [113, 118, 181].

5.3.3 Local vs Integral Invariants

The equilibrium distribution (97) is of a fundamental different nature than the conventional Rayleigh-Jeans distribution. In particular, as discussed just above, $n^{loc}(\omega)$ is characterized by a constant spectral pedestal in the tails of the spectrum. The kinetic theory reveals that the difference between $n^{loc}(\omega)$ and $n^{eq}(\omega)$ is due to the existence of the local invariant J_ω. Let us briefly discuss the 'local' nature of the invariant J_ω in regard to the *integral* invariants investigated in [182–185] in line with the problem of integrability. First of all, one may note that the possible existence of

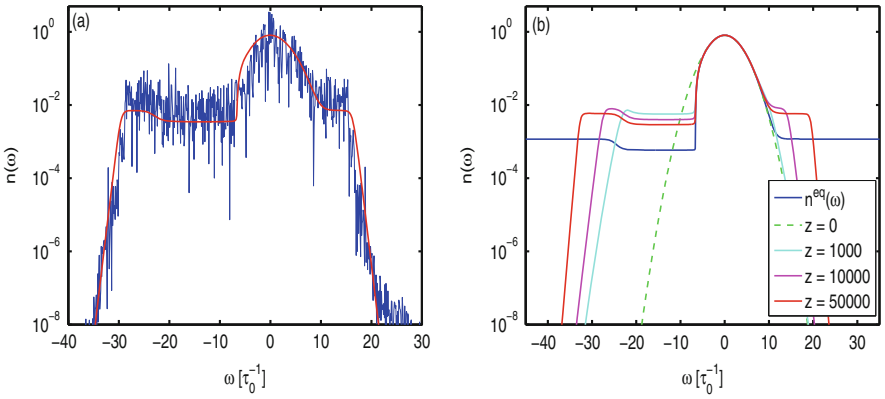

Fig. 19 Anomalous thermalization of incoherent waves: (**a**) Spectral evolution obtained by integrating numerically the NLSE with third-order dispersion (*blue*) and the corresponding WT kinetic equation (*red*) at $z = 20,000$ for $\tilde{\alpha} = 0.05$ (**a**). (**b**) Numerical simulations of the WT kinetic equation showing the spectral profile $n(z,\omega)$ at different propagation lengths z: a constant spectral pedestal emerges in the tails of the spectrum ($\tilde{\alpha} = 0.05$). The spectrum slowly relaxes toward the equilibrium state $n^{loc}(\omega)$ given by Eq. (97) (*blue*). *Source*: from [181]

a set of additional *integral* invariants, $Q_j = \int \phi_j(\omega)\, n_\omega(z)\, d\omega$, would still lead to a (generalized) Rayleigh-Jeans distribution,

$$n^{eq}(\omega) = \frac{T}{k(\omega) + \sum_j \lambda_j \phi_j(\omega) - \mu}, \tag{98}$$

where λ_j refer to the Lagrangian multipliers associated to the conservation of Q_j [185]. The *local* invariant J_ω thus leads to an equilibrium spectrum $n^{loc}(\omega)$ of a different nature than the generalized Rayleigh-Jeans spectrum (98).

One may wonder whether the local invariant J_ω may generate the existence of integral invariants of the kinetic equation (i.e., Eqs. (90), (91) with $m = 3$). We can easily verify that $Q = \int \phi_\omega\, n_\omega(z)\, d\omega$ is a conserved quantity of the kinetic equation whenever ϕ_ω satisfies the following relation

$$\phi_{\omega_1} + \phi_{q-\omega_1} = \phi_{\omega_2} + \phi_{q-\omega_2}, \tag{99}$$

for any couple of frequencies (ω_1, ω_2). In other terms, it is sufficient that $\phi_\omega + \phi_{q-\omega}$ does not depend on ω for Q to be a conserved quantity of the kinetic equation. A simple way to satisfy this condition is to construct ϕ_ω as follows, $\phi_\omega = \varphi_\omega - \varphi_{q-\omega}$. In this way, regardless of the particular choice of the function φ_ω,

$$Q = \int \left(\varphi_\omega - \varphi_{q-\omega}\right)\, n_\omega(z)\, d\omega, \tag{100}$$

is a conserved quantity of the kinetic equation. This shows that the existence of a local invariant (J_ω) can generate an infinite set of integral invariants Q.

5.4 Emergence of Rogue Waves from Optical Turbulence

In this section we briefly comment some open interesting issues related to optical wave turbulence in fibers. An interesting problem concerns a proper description of the emergence of extreme rogue waves (RW) from a turbulent environment. A rather commonly accepted opinion is that RWs can be conveniently interpreted in the light of exact analytical solutions of integrable nonlinear wave equations, the so-called Akhmediev breathers, or more specifically their limiting cases of infinite spatial and temporal periods, the rational soliton solutions, such as Peregrine and higher-order solutions of the integrable 1D NLSE—see the recent reviews [27, 28]. Rational soliton solutions can be regarded as a coherent and deterministic approach to the understanding of RW phenomena. On the other hand, RWs are known to spontaneously emerge from an incoherent turbulent state [29, 139, 186–190]. This raises a difficult problem, since the description of the turbulent system requires a statistical WT approach, whereas rational soliton solutions are inherently coherent deterministic structures. This problem was addressed in the optical fiber context in [172, 173] by considering a specific NLSE model that exhibits a quasi-soliton turbulence scenario, a feature that can be interpreted in analogy with wave condensation, see Sect. 5.1.4. It was shown that the deterministic description of rogue wave events in terms of rational soliton solutions is not inconsistent with the corresponding statistical WT description of the turbulent system [173]. It is important to stress that the emergence of RW events was shown to solely occur near by the transition to (quasi-)soliton condensation. From a different perspective, the fluctuations of the condensate fraction in 2D wave condensation have been recently computed theoretically, revealing that large fluctuations solely occur near by the transition to condensation, while they are significantly quenched in the strongly condensed Bogoliubov regime (small 'temperature'), and almost completely suppressed in the weakly nonlinear turbulent regime (high 'temperature'). This result is consistent with the general idea that nearby second-order phase-transitions, physical systems are inherently sensitive to perturbations and thus exhibit large fluctuations. One can then address a possible alternative point of view on the question of the spontaneous emergence of rogue waves from a conservative turbulent environment: Is it possible to interpret the sporadic emergence of RW events as the natural large fluctuations inherent to the phase transition to soliton condensation? This issue may pave the way for a statistical mechanics approach based on the idea of scaling and universal theory of critical phenomena to the description of RWs.

Acknowledgements The authors are grateful to many collaborators for fruitful discussions: P. Aschieri, S.A. Babin, J. Barré, B. Barviau, P. Béjot, F. Biancalana, D. Christodoulides, S. Coen, C. Conti, D. Faccio, C. Finot, M. Guasoni, R. Kaiser, B. Kibler, M. Haelterman, K. Hammani, T.

Hansson, H.R. Jauslin, M. Lisak, C. Michel, G. Millot, C. Montes, S. Nazarenko, M. Onorato, S. Pitois, E.V. Podivilov, S. Residori, M. Segev, S. Trillo, S. Wabnitz, V.E. Zakharov. The authors also acknowledge P. Suret, S. Randoux, D. Churkin and S. Turitsyn for their deep insights and valuable contributions in the understanding of optical turbulence, in particular in dissipative laser systems or near by the limit of integrability. A.P. is especially grateful to T. Dauxois and S. Ruffo for their introduction into the physics of long-range interactions. It is also a pleasure for A.P. to thank M. Onorato, S. Residori and F. Baronio for their fantastic work in organizing the conference "Rogue and Shock Waves in Nonlinear Dispersive Media," held in Cargese (France, July 2015), where I had a chance to participate. A.P. acknowledges support from the French National Research Agency (ANR-12-BS04-0011 OPTIROC), as well as from the Labex ACTION (ANR-11-LABX-01-01) program. A.P. also acknowledges support from the European Research Council under the European Community's Seventh Framework Programme (FP7/20072013 Grant Agreement No. 306633, PETAL project).

References

1. Mitchell, M., Chen, Z., Shih, M., Segev, M.: Self-trapping of partially spatially incoherent light. Phys. Rev. Lett. **77**, 490 (1996)
2. Mitchell, M., Segev, M.: Self-trapping of incoherent white light. Nature (London) **387**, 880 (1997)
3. Segev, M., Christodoulides, D.: Incoherent solitons. In: Trillo, S., Torruellas, W. (eds.) Spatial Solitons. Springer, Berlin (2001)
4. Kivshar, Y., Agrawal, G.: Optical Solitons: From Fibers to Photonic Crystals. Academic, New York (2003)
5. Pasmanik, G.A.: Self-interaction of incoherent light beams. Sov. Phys. JETP **39**, 234 (1974)
6. Mitchell, M., Segev, M., Coskun, M.T., Christodoulides, D.: Theory of self-trapped spatially incoherent light beams. Phys. Rev. Lett. **79**, 4990 (1997)
7. Christodoulides, D., Coskun, T., Mitchell, M., Segev, M.: Theory of incoherent self-focusing in biased photorefractive media. Phys. Rev. Lett. **78**, 646 (1997)
8. Hall, B., Lisak, M., Anderson, D., Fedele, R., Semenov, V.E.: Statistical theory for incoherent light propagation in nonlinear media. Phys. Rev. E **65**, 035602 (2002)
9. Christodoulides, D.N., Eugenieva, E.D., Coskun, T.H., Segev, M., Mitchell, M.: Equivalence of three approaches describing partially incoherent wave propagation in inertial nonlinear media. Phys. Rev. E **63**, 035601 (2001)
10. Lisak, M., Helczynski, L., Anderson, D.: Relation between different formalisms describing partially incoherent wave propagation in nonlinear optical media. Opt. Commun. **220**, 321 (2003)
11. Christodoulides, D.N., Coskun, T.H., Mitchell, M., Chen, Z., Segev, M.: Theory of incoherent dark solitons. Phys. Rev. Lett. **80**, 5113 (1998)
12. Chen, Z., Mitchell, M., Segev, M., Coskun, T.H., Christodoulides, D.N.: Self-trapping of dark incoherent light beams. Science **280**, 889 (1998)
13. Soljacic, M., Segev, M., Coskun, T., Christodoulides, D., Vishwanath, A.: Modulation instability of incoherent beams in noninstantaneous nonlinear media. Phys. Rev. Lett. **84**, 467 (2000)
14. Kip, D., Soljacic, M., Segev, M., Eugenieva, E., Christodoulides, D.: Modulation instability and pattern formation in spatially incoherent light beams. Science **290**, 495–498 (2000)
15. Kibler, B., Michel, C., Garnier, J., Picozzi, A.: Temporal dynamics of incoherent waves in noninstantaneous response nonlinear Kerr media. Opt. Lett. **37**, 2472 (2012)
16. Picozzi, A., Haelterman, M.: Parametric three-wave soliton generated from incoherent light. Phys. Rev. Lett. **86**, 2010–2013 (2001)

17. Picozzi, A., Haelterman, M., Pitois, S., Millot, G.: Incoherent solitons in instantaneous response nonlinear media. Phys. Rev. Lett. **92**, 143906 (2004)
18. Peccianti, M., Assanto, G.: Incoherent spatial solitary waves in nematic liquid crystals. Opt. Lett. **26**(22), 1791–1793 (2001)
19. Rotschild, C., Schwartz, T., Cohen, O., Segev, M.: Incoherent spatial solitons in effectively-instantaneous nonlocal nonlinear media. Nat. Photonics **2**, 371 (2008)
20. Picozzi, A., Garnier, J.: Incoherent soliton turbulence in nonlocal nonlinear media. Phys. Rev. Lett. **107**(23), 233901 (2011)
21. Wu, M., Krivosik, P., Kalinikos, B., Patton, C.: Random generation of coherent solitary waves from incoherent waves. Phys. Rev. Lett. **96**, 227202 (2006)
22. Picozzi, A., Pitois, S., Millot, G.: Spectral incoherent solitons: a localized soliton behavior in frequency space. Phys. Rev. Lett. **101**, 093901 (2008)
23. Kibler, B., Michel, C., Kudlinski, A., Barviau, B., Millot, G., Picozzi, A.: Emergence of spectral incoherent solitons through supercontinuum generation in a photonic crystal fiber. Phys. Rev. E **84**, 066605 (2011)
24. Dudley, J.M., Taylor, J.R.: Supercontinuum Generation in Optical Fibers. Cambridge University Press, Cambridge (2010)
25. Couairon, A., Mysyrowicz, A.: Femtosecond filamentation in transparent media. Phys. Rep. **441**(2), 47–189 (2007)
26. Wiersma, D.S.: The physics and applications of random lasers. Nat. Phys. **4**(5), 359–367 (2008)
27. Onorato, M., Residori, S., Bortolozzo, U., Montina, A., Arecchi, F.: Rogue waves and their generating mechanisms in different physical contexts. Phys. Rep. (2013)
28. Dudley, J.M., Dias, F., Erkintalo, M., Genty, G.: Instabilities, breathers and rogue waves in optics. Nat. Photonics **8**(10), 755–764 (2014)
29. Walczak, P., Randoux, S., Suret, P.: Optical rogue waves in integrable turbulence. Phys. Rev. Lett. **114**, 143903 (2015)
30. Zakharov, V.E., L'vov, V.S., Falkovich, G.: Kolmogorov Spectra of Turbulence I. Springer, Berlin (1992)
31. Frisch, U.: Turbulence. The Legacy of A. N. Kolmogorov. Cambridge University Press, Cambridge (1995)
32. Newell, A.C., Rumpf, R.: Wave turbulence. Annu. Rev. Fluid Mech. **43**, 59–78 (2011)
33. Nazarenko, S.: Wave Turbulence. Lecture Notes in Physics, vol. 825. Springer, Berlin (2011)
34. Newell, A.C., Rumpf, B., Zakharov, V.E.: Spontaneous breaking of the spatial homogeneity symmetry in wave turbulence. Phys. Rev. Lett. **108**, 194502 (2012)
35. Tsytovich, V.N.: Nonlinear Effects in Plasma. Plenum, New York (1970)
36. Hasselmann, K.: On the non-linear energy transfer in a gravity-wave spectrum. Part 1. General theory. J. Fluid Mech. **12**, 481–500 (1962)
37. Hasselmann, K.: On the non-linear energy transfer in a gravity-wave spectrum. Part 2. Conservation theorems, wave-particle analogy, irreversibility. J. Fluid Mech. **15**, 273–281 (1963)
38. Dyachenko, S., Newell, A.C., Pushkarev, A., Zakharov, V.E.: Optical turbulence: weak turbulence, condensates and collapsing filaments in the nonlinear Schrödinger equation. Phys. D **57**, 96 (1992)
39. Zakharov, V., Dias, F., Pushkarev, A.: One-dimensional wave turbulence, Phys. Rep. **398**, 1 (2004)
40. Benney, D.J., Saffman, P.G.: Nonlinear interactions of random waves in dispersive medium. Proc. R. Soc. London Ser. A **289**, 301 (1966)
41. Newell, A.: The closure problem in a system of random gravity waves. Rev. Geophys. **6**, 1 (1968)
42. Benney, D.J., Newell, A.: Random wave closure. Stud. Appl. Math. **48**, 29 (1969)
43. Newell, A.C., Nazarenko, S., Biven, L.: Wave turbulence and intermittency. Phys. D **152-153**, 520–550 (2001)

44. Rasmussen, K., Cretegny, T., Kevrekidis, P.G., Gronbech-Jensen, N.: Statistical mechanics of a discrete nonlinear system. Phys. Rev. Lett. **84**, 3740 (2000)
45. Jordan, R., Turkington, B., Zirbel, C.L.: A mean-field statistical theory for the nonlinear Schrödinger equation. Phys. D **137**, 353 (2000)
46. Rumpf, R., Newell, A.C.: Coherent structures and entropy in constrained, modulationally unstable, nonintegrable systems. Phys. Rev. Lett. **87**, 054102 (2001)
47. Rumpf, B.: Simple statistical explanation for the localization of energy in nonlinear lattices with two conserved quantities. Phys. Rev. E **69**, 016618 (2004)
48. Derevyanko, S.A.: Thermalized polarization dynamics of a discrete optical-waveguide system with four-wave mixing. Phys. Rev. A **88**, 033851 (2013)
49. Antenucci, F., Ibáñez Berganza, M., Leuzzi, L.: Statistical physics of nonlinear wave interaction. Phys. Rev. B **92**, 014204 (2015)
50. Barviau, B., Kibler, B., Kudlinski, A., Mussot, A., Millot, G., Picozzi, A.: Experimental signature of optical wave thermalization through supercontinuum generation in photonic crystal fiber. Opt. Express **17**, 7392 (2009)
51. Barviau, B., Kibler, B., Picozzi, A.: Wave turbulence description of supercontinuum generation: influence of self-steepening and higher-order dispersion. Phys. Rev. A **79**, 063840 (2009)
52. Barviau, B., Garnier, J., Xu, G., Kibler, B., Millot, G., Picozzi, A.: Truncated thermalization of incoherent optical waves through supercontinuum generation in photonic crystal fibers. Phys. Rev. A **87**(3), 035803 (2013)
53. Davis, M., Morgan, S., Burnett, K.: Simulations of Bose fields at finite temperature. Phys. Rev. Lett. **87**, 160402 (2001)
54. Davis, M., Morgan, S., Burnett, K.: Simulations of thermal Bose fields in the classical limit. Phys. Rev. A **66**, 053618 (2002)
55. Connaughton, C., Josserand, C., Picozzi, A., Pomeau, Y., Rica, S.: Condensation of classical nonlinear waves. Phys. Rev. Lett. **95**, 263901 (2005)
56. Zakharov, V., Nazarenko, S.: Dynamics of the Bose-Einstein condensation. Phys. D **201**, 203 (2005)
57. During, G., Picozzi, A., Rica, S.: Breakdown of weak-turbulence and nonlinear wave condensation. Phys. D **238**, 1524 (2009)
58. Conti, C., Leonetti, M., Fratalocchi, A., Angelani, L., Ruocco, G.: Condensation in disordered lasers: theory, 3d+1 simulations, and experiments. Phys. Rev. Lett. **101**, 143901 (2008)
59. Turitsyna, E., Falkovich, G., Mezentsev, V., Turitsyn, S.: Optical turbulence and spectral condensate in long-fiber lasers. Phys. Rev. A **80**, 031804 (2009)
60. Weill, R., Fischer, B., Gat, O.: Light-mode condensation in actively-mode-locked lasers. Phys. Rev. Lett. **104**(17), 173901 (2010)
61. Klaers, J., Schmitt, J., Vewinger, F., Weitz, M.: Bose-Einstein condensation of photons in an optical microcavity. Nature **468**, 545 (2010)
62. Michel, C., Haelterman, M., Suret, P., Randoux, S., Kaiser, R., Picozzi, A.: Thermalization and condensation in an incoherently pumped passive optical cavity. Phys. Rev. A **84**, 033848 (2011)
63. Turitsyn, S.K., Babin, S.A., Turitsyna, E.G., Falkovich, G.E., Podivilov, E., Churkin, D.: Optical wave turbulence. In: Shira, V., Nazarenko, S. (eds.) Wave Turbulence. World Scientific Series on Nonlinear Science Series A, vol. 83. World Scientific, Singapore (2013)
64. Turitsyna, E., Falkovich, G., El-Taher, A., Shu, X., Harper, P., Turitsyn, S.: Optical turbulence and spectral condensate in long fibre lasers. Proc. R. Soc. A **468**, 2145 (2012)
65. Turitsyna, E., Smirnov, S., Sugavanam, S., Tarasov, N., Shu, X., Babin, S., Podivilov, E., Churkin, D., Falkovich, G., Turitsyn, S.: The laminar-turbulent transition in a fibre laser. Nat. Photonics **7**(10), 783–786 (2013)
66. Carusotto, I., Ciuti, C.: Quantum fluids of light. Rev. Mod. Phys. **85**, 299–366 (2013)
67. Bortolozzo, U., Laurie, J., Nazarenko, S., Residori, S.: Optical wave turbulence and the condensation of light. J. Opt. Soc. Am. B **26**, 2280 (2009)

68. Laurie, J., Bortolozzo, U., Nazarenko, S., Residori, S.: One-dimensional optical wave turbulence: experiment and theory. Phys. Rep. **514**, 121 (2012)
69. Bernstein, I., Green, J., Kruskal, M.: Exact nonlinear plasma oscillations. Phys. Rev. **108**, 546 (1957)
70. Hasegawa, A.: Dynamics of an ensemble of plane waves in nonlinear dispersive media. Phys. Fluids **18**, 77 (1975)
71. Hasegawa, A.: Envelope soliton of random phase waves. Phys. Fluids **20**, 2155 (1977)
72. Marklund, M., Shukla, P.K.: Nonlinear collective effects in photon-photon and photon-plasma interactions. Rev. Mod. Phys. **78**, 591–640 (2006)
73. Dylov, D., Fleischer, J.: Observation of all-optical bump-on-tail instability. Phys. Rev. Lett. **100**, 103903 (2008)
74. Garnier, J., Picozzi, A.: Unified kinetic formulation of incoherent waves propagating in nonlinear media with noninstantaneous response. Phys. Rev. A **81**, 033831 (2010)
75. Mendonça, J.T., Tsintsadze, N.L.: Analog of the Wigner-Moyal equation for the electromagnetic field. Phys. Rev. E **62**, 4276–4282 (2000)
76. Lahaye, T., Menotti, C., Santos, L., Lewenstein, M., Pfau, T.: The physics of dipolar bosonic quantum gases. Rep. Prog. Phys. **72**, 126401 (2009)
77. Skupin, S., Saffman, M., Krolikowski, K.: Nonlocal stabilization of nonlinear beams in a self-focusing atomic vapor. Phys. Rev. Lett. **98**, 263902 (2007)
78. Conti, C., Peccianti, M., Assanto, G.: Route to nonlocality and observation of accessible solitons. Phys. Rev. Lett. **91**, 073901 (2003)
79. Conti, C., Peccianti, M., Assanto, G.: Observation of optical spatial solitons in a highly nonlocal medium. Phys. Rev. Lett. **92**, 113902 (2004)
80. Ghofraniha, N., Conti, C., Ruocco, G., Trillo, S.: Shocks in nonlocal media. Phys. Rev. Lett. **99**, 043903 (2007)
81. Conti, C., Fratalocchi, A., Peccianti, M., Ruocco, G., Trillo, S.: Observation of a gradient catastrophe generating solitons. Phys. Rev. Lett. **102**, 083902 (2009)
82. Segev, M., Crosignani, B., Yariv, A., Fischer, B.: Spatial solitons in photorefractive media. Phys. Rev. Lett. **68**, 923–926 (1992)
83. Litvak, A., Sergeev, A.: One dimensional collapse of plasma waves. JETP Lett. **27**, 517 (1978)
84. Wyller, J., Krolikowski, W., Bang, O., Rasmussen, J.J.: Generic features of modulational instability in nonlocal Kerr media. Phys. Rev. E **66**, 066615 (2002)
85. Turitsyn, S.: Spatial dispersion of nonlinearity and stability of multidimensional solitons. Theor. Math. Phys. **64**, 226 (1985)
86. Bang, O., Krolikowski, W., Wyller, J., Rasmussen, J.J.: Collapse arrest and soliton stabilization in nonlocal nonlinear media. Phys. Rev. E **66**, 046619 (2002)
87. Dreischuh, A., Neshev, D.N., Petersen, D.E., Bang, O., Krolikowski, W.: Observation of attraction between dark solitons. Phys. Rev. Lett. **96**, 043901 (2006)
88. Krolikowski, W., Bang, O., Nikolov, N., Neshev, D., Wyller, J., Rasmussen, J., Edmundson, D.: Modulational instability, solitons and beam propagation in spatially nonlocal nonlinear media. J. Opt. B: Quantum Semiclassical Opt. **6**, S288 (2004)
89. Snyder, A., Mitchell, D.: Accessible solitons. Science **276**, 1538 (1997)
90. Cohen, O., Buljan, H., Schwartz, T., Fleischer, J., Segev, M.: Incoherent solitons in instantaneous nonlocal nonlinear media. Phys. Rev. E **73**, 015601 (2006)
91. Zakharov, V., Pushkarev, A., Shvets, V., Yan'kov, V.: Soliton turbulence. JETP Lett. **48**, 83 (1988)
92. Jordan, R., Josserand, C.: Self-organization in nonlinear wave turbulence. Phys. Rev. E **61**, 1527 (2000)
93. Rumpf, R., Newell, A.C.: Localization and coherence in nonintegrable systems. Phys. D **184**, 162 (2003)
94. Zakharov, V.E., Musher, S.L., Rubenchik, A.M.: Hamiltonian approach to the description of non-linear plasma phenomena. Phys. Rep. **129**, 285 (1985)
95. Onorato, M., Osborne, A., Fedele, R., Serio, M.: Landau damping and coherent structures in narrow-banded $1 + 1$ deep water gravity waves. Phys. Rev. E **67**, 046305 (2003)

96. Garnier, J., Ayanides, J.-P., Morice, O.: Propagation of partially coherent light with the maxwell-debye equation. J. Opt. Soc. Am. B **20**, 1409 (2003)
97. Campa, A., Dauxois, T., Ruffo, S.: Statistical mechanics and dynamics of solvable models with long-range interactions. Phys. Rep. **480**, 57–159 (2009)
98. Musher, S., Rubenchik, A., Zakharov, V.: Weak Langmuir turbulence. Phys. Rep. **252**, 177 (1995)
99. Michel, C., Kibler, B., Picozzi, A.: Discrete spectral incoherent solitons in nonlinear media with noninstantaneous response. Phys. Rev. A **83**, 023806 (2011)
100. Garnier, J., Xu, G., Trillo, S., Picozzi, A.: Incoherent dispersive shocks in the spectral evolution of random waves. Phys. Rev. Lett. **111**(11), 113902 (2013)
101. Whitham, G.: Linear and Nonlinear Waves. Wiley, New York (1974)
102. Constantin, P., Lax, P., Majda, A.: A simple one-dimensional model for the three-dimensional vorticity equation. Commun. Pure Appl. Math. **38**, 715–724 (1985)
103. Fokas, A., Ablowitz, M.: The inverse scattering transform for the benjamin-ono equation – a pivot to multidimensional problems. Stud. Appl. Math. **68**, 1 (1983)
104. Coifman, R., Wickerhauser, V.: The scattering transform for the benjamin-ono equation. Stud. Appl. Math. **6**, 825 (1990)
105. Benjamin, T.: Internal waves of permanent form in fluids of great depth. J. Fluid Mech. **29**, 559 (1967)
106. Ono, H.: Algebraic solitary waves in stratified fluids. J. Phys. Soc. Japan **39**, 1082 (1975)
107. Gallavotti, G.E.: The Fermi-Pasta-Ulam Problem: A Status Report. Lecture Notes in Physics. Springer, Berlin (2007)
108. Onorato, M., Vozella, L., Proment, D., Lvov, Y.V.: Route to thermalization in the α-fermi–pasta–ulam system. Proc. Natl. Acad. Sci. **112**(14), 4208–4213 (2015)
109. Lake, B., Yuen, H., Rundgaldier, H., Ferguson, W.: Nonlinear deep-water waves: theory and experiment. part 2. evolution of a continuous wave train. J. Fluid Mech. **83**, 49 (1977)
110. Simaeys, G., Emplit, P., Haelterman, M.: Experimental demonstration of the Fermi-Pasta-Ulam recurrence in a modulationally unstable optical wave. Phys. Rev. Lett. **87**, 033902 (2001)
111. Mussot, A., Kudlinski, A., Droques, M., Szriftgiser, P., Akhmediev, N.: Fermi-pasta-ulam recurrence in nonlinear fiber optics: the role of reversible and irreversible losses. Phys. Rev. X **4**, 011054 (2014)
112. Suret, P., Randoux, S., Jauslin, H., Picozzi, A.: Anomalous thermalization of nonlinear wave systems. Phys. Rev. Lett. **104**, 054101 (2010)
113. Michel, C., Suret, P., Randoux, S., Jauslin, H., Picozzi, A.: Influence of third-order dispersion on the propagation of incoherent light in optical fibers. Opt. Lett. **35**, 2367 (2010)
114. Peccianti, M., Assanto, G.: Nematicons. Phys. Rep. **516**(4), 147–208 (2012)
115. Rotschild, C., Cohen, O., Manela, O., Segev, M., Carmon, T.: Solitons in nonlinear media with an infinite range of nonlocality: first observation of coherent elliptic solitons and of vortex-ring solitons. Phys. Rev. Lett. **95**(21), 213904 (2005)
116. Babenko, V., Zel'dovich, B.Y., Malyshev, V., Sychev, A.A.: Spectrum of a giant laser pulse under frequency self-modulation conditions. Quantum Electron. **3**(2), 97–99 (1973)
117. Manassah, J.T.: Self-phase modulation of incoherent light revisited. Opt. Lett. **16**, 1638 (1991)
118. Picozzi, A., Garnier, J., Hansson, T., Suret, P., Randoux, S., Millot, G., Christodoulides, D.: Optical wave turbulence: towards a unified nonequilibrium thermodynamic formulation of statistical nonlinear optics. Phys. Rep. **542**(1), 1–132 (2014)
119. Levin, Y., Pakter, R., Rizzato, F.B., Teles, T.N., Benetti, F.P.: Nonequilibrium statistical mechanics of systems with long-range interactions. Phys. Rep. **535**(1), 1–60 (2014)
120. Xu, G., Vocke, D., Faccio, D., Garnier, J., Roger, T., Trillo, S., Picozzi, A.: From coherent shocklets to giant collective incoherent shock waves in nonlocal turbulent flows. Nat. Commun. **6**, 8131 (2015)
121. Snyder, A., Mitchell, D.: Big incoherent solitons. Phys. Rev. Lett. **80**, 1422 (1998)
122. Mouhot, C., Villani, C.: On Landau damping. Acta Math. **207**, 29 (2011)
123. Agrawal, G.: Nonlinear Fiber Optics, 5th edn. Academic, New York (2012)

124. Xu, G., Garnier, J., Trillo, S., Picozzi, A.: Spectral dynamics of incoherent waves with a noninstantaneous nonlinear response. Opt. Lett. **38**, 2972–2975 (2013)
125. Montes, C.: Photon soliton and fine structure due to nonlinear compton scattering. Phys. Rev. A **20**, 1081 (1979)
126. Xu, G., Garnier, J., Conforti, M., Picozzi, A.: Generalized description of spectral incoherent solitons. Opt. Lett. **39**, 4192–4195 (2014)
127. Musher, S., Rubenchik, A., Zakharov, V.: Weak Langmuir turbulence of an isothermal plasma. JETP **42**, 80 (1976)
128. Xu, G., Garnier, J., Trillo, S., Picozzi, A.: Impact of self-steepening on incoherent dispersive spectral shocks and collapselike spectral singularities. Phys. Rev. A **90**, 013828 (2014)
129. Gurevich, A., Pitaevskii, L.: Nonstationary structure of a collisionless shock wave. Sov. Phys. JETP **38**, 291 (1974)
130. Taylor, R., Baker, D., Ikezi, H.: Observation of collisionless electrostatic shocks. Phys. Rev. Lett. **24**, 206 (1970)
131. Hoefer, M.A., Ablowitz, M.J., Coddington, I., Cornell, E.A., Engels, P., Schweikhard, V.: Dispersive and classical shock waves in Bose-Einstein condensates and gas dynamics. Phys. Rev. A **74**, 023623 (2006)
132. Chang, J.J., Engels, P., Hoefer, M.A.: Formation of dispersive shock waves by merging and splitting Bose-Einstein condensates. Phys. Rev. Lett. **101**, 170404 (2008)
133. Ghofraniha, N., Gentilini, S., Folli, V., DelRe, E., Conti, C.: Shock waves in disordered media. Phys. Rev. Lett. **109**, 243902 (2012)
134. Ghofraniha, N., Amato, L.S., Folli, V., Trillo, S., DelRe, E., Conti, C.: Measurement of scaling laws for shock waves in thermal nonlocal media. Opt. Lett. **37**, 2325–2327 (2012)
135. Aschieri, P., Garnier, J., Michel, C., Doya, V., Picozzi, A.: Condensation and thermalization of classsical optical waves in a waveguide. Phys. Rev. A **83**, 033838 (2011)
136. Leggett, A.: Quantum Liquids. Oxford University Press, Oxford (2006)
137. Pitaevskii, S., Stringari, L.: Bose-Einstein Condensation. Oxford Science Publications, Oxford (2003)
138. Suret, P., Picozzi, A., Randoux, S.: Wave turbulence in integrable systems: nonlinear propagation of incoherent optical waves in single-mode fibers. Opt. Express **19**, 17852 (2011)
139. Randoux, S., Walczak, P., Onorato, M., Suret, P.: Intermittency in integrable turbulence. Phys. Rev. Lett. **113**, 113902 (2014)
140. Boyd, R.: Nonlinear Optics, 3rd edn. Academic, New York (2008)
141. Huang, K.: Statistical Mechanics. Wiley, New York (1963)
142. Pitois, S., Lagrange, S., Jauslin, H.R., Picozzi, A.: Velocity locking of incoherent nonlinear wave packets. Phys. Rev. Lett. **97**, 033902 (2006)
143. Zakharov, V.: Weak turbulence spectrum in a plasma without a magnetic field. Sov. Phts. JETP **24**, 455 (1967)
144. Annenkov, S.Y., Shrira, V.I.: Evolution of wave turbulence under gusty forcing. Phys. Rev. Lett. **107**, 114502 (2011)
145. Annenkov, S.Y., Shrira, V.I.: Fast nonlinear evolution in wave turbulence. Phys. Rev. Lett. **102**, 024502 (2009)
146. Connaughton, C., Newell, A.C., Pomeau, Y.: Non–stationary spectra of local wave turbulence. Phys. D **184**(1–4), 64–85 (2003). Complexity and Nonlinearity in Physical Systems – A Special Issue to Honor Alan Newell
147. Lacaze, R., Lallemand, P., Pomeau, Y., Rica, S.: Dynamical formation of a Bose-Einstein condensate. Phys. D **152**, 779 (2001)
148. Escobedo, M., Valle, M.A.: Instability of the rayleigh-jeans spectrum in weak wave turbulence theory. Phys. Rev. E **79**, 061122 (2009)
149. Picozzi, A., Rica, S.: Condensation of classical optical waves beyond the cubic nonlinear Schrödinger equation. Opt. Commun. **285**, 5440 (2012)
150. Picozzi, A.: Towards a nonequilibrium thermodynamic description of incoherent nonlinear optics. Opt. Express **15**, 9063 (2007)

151. Assémat, E., Picozzi, A., Jauslin, H.R., Sugny, D.: Instabilities of optical solitons and Hamiltonian singular solutions in a medium of finite extension. Phys. Rev. A **84**, 013809 (2011)
152. Kirton, P., Keeling, J.: Nonequilibrium model of photon condensation. Phys. Rev. Lett. **111**, 100404 (2013)
153. Sob'yanin, D.N.: Bose-Einstein condensation of light: general theory. Phys. Rev. E **88**, 022132 (2013)
154. Fischer, B., Weill, R.: When does single-mode lasing become a condensation phenomenon? Opt. Express **20**, 26704–26713 (2012)
155. Nazarenko, S., Onorato, M., Proment, D.: Bose-einstein condensation and berezinskii-kosterlitz-thouless transition in the two-dimensional nonlinear schrödinger model. Phys. Rev. A **90**, 013624 (2014)
156. Kirton, P., Keeling, J.: Thermalization and breakdown of thermalization in photon condensates. Phys. Rev. A **91**, 033826 (2015)
157. Weill, R., Levit, B., Bekker, A., Gat, O., Fischer, B.: Laser light condensate: experimental demonstration of light-mode condensation in actively mode locked laser. Opt. Express **18**(16), 16520–16525 (2010)
158. Gordon, A., Fischer, B.: Phase transition theory of many-mode ordering and pulse formation in lasers. Phys. Rev. Lett. **89**, 103901 (2002)
159. Weill, R., Rosen, A., Gordon, A., Gat, O., Fischer, B.: Critical behavior of light in mode-locked lasers. Phys. Rev. Lett. **95**, 013903 (2005)
160. Churkin, D.V., Kolokolov, I.V., Podivilov, E.V., Vatnik, I.D., Nikulin, M.A., Vergeles, S.S., Terekhov, I.S., Lebedev, V.V., Falkovich, G., Babin, S.A., et al.: Wave kinetics of random fibre lasers. Nat. Commun. **2**, 6214 (2015)
161. Babin, S.A., Churkin, D.V., Ismagulov, A.E., Kablukov, S.I., Podivilov, E.V.: Four-wave-mixing-induced turbulent spectral broadening in a long Raman fiber laser. J. Opt. Soc. Am. B **24**, 1729 (2007)
162. Dalloz, N., Randoux, S., Suret, P.: Influence of dispersion of fiber bragg grating mirrors on formation of optical power spectrum in Raman fiber lasers. Opt. Lett. **35**, 2505–2507 (2010)
163. Randoux, S., Dalloz, N., Suret, P.: Intracavity changes in the field statistics of Raman fiber lasers. Opt. Lett. **36**(6), 790–792 (2011)
164. Turitsyna, E.G., Turitsyn, S.K., Mezentsev, V.K.: Numerical investigation of the impact of reflectors on spectral performance of Raman fibre laser. Opt. Express **18**, 4469 (2010)
165. Turitsyn, S.K., Babin, S.A., El-Taher, A.E., Harper, P., Churkin, D.V., Kablukov, S.I., Ania-Castanon, J.D., Karalekas, V., Podivilov, E.V.: Random distributed feedback fibre laser. Nat. Photonics **4**, 231 (2010)
166. Turitsyn, S.K., Babin, S.A., Churkin, D.V., Vatnik, I.D., Nikulin, M., Podivilov, E.V.: Random distributed feedback fibre lasers. Phys. Rep. **542**(2), 133–193 (2014). Random Distributed Feedback Fibre Lasers
167. L'vov, V.S., L'vov, Y., Newell, A.C., Zakharov, V.: Statistical description of acoustic turbulence. Phys. Rev. E **56**, 390–405 (1997)
168. Leo, F., Coen, S., Kockaert, P., Gorza, S.-P., Emplit, P., Haelterman, M.: Temporal cavity solitons in one-dimensional Kerr media as bits in an all-optical buffer. Nat. Photonics **4**, 471 (2010)
169. Arecchi, T., Boccalettic, S., Ramazza, P.: Pattern formation and competition in nonlinear optics. Phys. Rep. **318**, 1 (1999)
170. Klaers, J., Vewinger, F., Weitz, M.: Thermalization of a two-dimensional photonic gas in a white wall photon box. Nat. Phys. **6**(7), 512–515 (2010)
171. Conforti, M., Mussot, A., Fatome, J., Picozzi, A., Pitois, S., Finot, C., Haelterman, M., Kibler, B., Michel, C., Millot, G.: Turbulent dynamics of an incoherently pumped passive optical fiber cavity: quasisolitons, dispersive waves, and extreme events. Phys. Rev. A **91**, 023823 (2015)
172. Hammani, K., Kibler, B., Finot, C., Picozzi, A.: Emergence of rogue waves from optical turbulence. Phys. Lett. A **374**, 3585 (2010)

173. Kibler, B., Hammani, K., Finot, C., Picozzi, A.: Rogue waves, rational solitons and wave turbulence theory. Phys. Lett. A **375**, 3149 (2011)
174. Dudley, J.M., Genty, G., Coen, S.: Supercontinuum generation in photonic crystal fiber. Rev. Mod. Phys. **78**, 1135 (2006)
175. Korhonen, M., Friberg, A.T., Turunen, J., Genty, G.: Elementary field representation of supercontinuum. J. Opt. Soc. Am. B **30**, 21–26 (2013)
176. Mussot, A., Beaugeois, M., Bouazaoui, M., Sylvestre, T.: Tailoring cw supercontinuum generation in microstructured fibers with two-zero dispersion wavelengths. Opt. Express **15**, 11553–11563 (2007)
177. Wadsworth, W., Joly, N., Knight, J., Birks, T., Biancalana, F., Russell, P.: Supercontinuum and four-wave mixing with q-switched pulses in endlessly single-mode photonic crystal fibres. Opt. Express **12**, 299–309 (2004)
178. Barviau, B., Kibler, B., Coen, S., Picozzi, A.: Towards a thermodynamic description of supercontinuum generation. Opt. Lett. **33**, 2833 (2008)
179. Kibler, B., Michel, C., Barviau, B., Millot, G., Picozzi, A.: Thermodynamic approach of supercontinuum generation. Opt. Fiber Technol. **18**, 257 (2012)
180. Landau, L., Lifchitz, E.: Statistical Physics, Part 1. Pergamon Press, New York (1980)
181. Michel, C., Garnier, J., Suret, P., Randoux, S., Picozzi, A.: Kinetic description of random optical waves and anomalous thermalization of a nearly integrable wave system. Lett. Math. Phys. **96**(1), 415–447 (2011)
182. Zakharov, V., Schulman, E.: Degenerative dispersion laws, motion invariants and kinetic equations. Physica **4D**, 192 (1980)
183. Zakharov, V., Schulman, E.: To the integrability of the system of two coupled nonlinear Schrödinger equations. Physica **4D**, 270 (1982)
184. Zakharov, V., Schulman, E.: On additional motion invariants of classical Hamiltonian wave systems. Physica **29D**, 283 (1988)
185. Balk, A., Ferapontov, E.: In: Zakharov, V. (ed.) Nonlinear Waves and Weak Turbulence. American Mathematical Society Translations. American Mathematical Society, Providence, RI (1998)
186. Onorato, M., Osborne, A., Serio, M., Cavaleri, L., Brandini, C., Stansberg, C.: Extreme waves, modulational instability and second order theory: wave flume experiments on irregular waves. European Journal of Mechanics-B/Fluids **25**(5), 586–601 (2006)
187. Akhmediev, N., Soto-Crespo, J., Ankiewicz, A.: Extreme waves that appear from nowhere: on the nature of rogue waves. Phys. Lett. A **373**(25), 2137–2145 (2009)
188. Janssen, P.A.E.M.: The Interaction of Ocean Waves and Wind. Cambridge University Press, Cambridge (2004)
189. Ankiewicz, A., Soto-Crespo, J., Akhmediev, N.: Rogue waves and rational solutions of the Hirota equation. Phys. Rev. E **81**(4), 046602 (2010)
190. Viotti, C., Dutykh, D., Dudley, J.M., Dias, F.: Emergence of coherent wave groups in deep-water random sea. Phys. Rev. E **87**, 063001 (2013)

Integrable Turbulence with Nonlinear Random Optical Waves

Stéphane Randoux and Pierre Suret

Abstract The field of integrable turbulence deals with the general question of statistical changes that are experienced by ensembles of nonlinear random waves propagating in systems ruled by integrable equations. In this chapter, we specifically focus on the one-dimensional nonlinear Schrödinger equation that describes quantitatively very well experiments performed with single mode fibers and optical waves randomly fluctuating in time. As a result of nonlinear propagation, the power spectrum of the random wave broadens and takes exponential wings both in focusing and in defocusing propagation regimes. Heavy-tailed deviations from gaussian statistics are observed in focusing regime while low-tailed deviations from gaussian statistics are observed in defocusing regime. After some transient evolution, the wave system is found to exhibit a statistically stationary state in which neither the probability density function of the wave field nor the spectrum change with the evolution variable. Separating fluctuations of small scale from fluctuations of large scale both in focusing and defocusing regime, we evidence the phenomenon of intermittency; i.e., small scales are characterized by large heavy-tailed deviations from Gaussian statistics, while the large ones are almost Gaussian.

1 Introduction

Interaction among waves in nonlinear media have been studied for decades in many fields of physics, such as nonlinear acoustics, plasma physics, hydrodynamics or nonlinear optics. Wave turbulence (WT) is the common designation for the fields of dispersive waves which are engaged in stochastic nonlinear interaction over a wide range of scales [1, 2]. Numerous examples of WT can be found in ocean, plasmas or Bose-Einstein condensates [1]. Despite the extremely large literature on turbulence, there is still no complete and satisfying theory about statistics of nonlinear incoherent waves.

S. Randoux (✉) • P. Suret
Laboratoire de Physique des Lasers, Atomes et Molecules, UMR-CNRS 8523,
Université de Lille, Lille, France
e-mail: stephane.randoux@univ-lille1.fr; pierre.suret@univ-lille1.fr

M. Onorato et al. (eds.), *Rogue and Shock Waves in Nonlinear Dispersive Media*,
Lecture Notes in Physics 926, DOI 10.1007/978-3-319-39214-1_9

In the restricted case of weakly nonlinear interaction and nearly gaussian statistics, the WT theory provides a framework for the statistical description of turbulence in non-integrable wave systems dominated by resonant interactions [1–3]. WT theory is based on a perturbation expansion procedure in which linear dispersive effects are supposed to dominate nonlinear effects. In this way a large separation of the linear and nonlinear length scales takes place, so that the statistics of the field can be assumed to be approximately Gaussian. This allows one to achieve the closure of the infinite hierarchy of moment's equations, thus leading to a WT kinetic description of the evolution of the power spectrum of the field (i.e. the second-order moment of the gaussian field) [4, 5]. It is now well established that WT theory provides a detailed description of the process of thermalization and condensation of optical waves that occur in nonintegrable wave systems ruled by 2D or 3D nonlinear Schrödinger equations (NLSEs) [6, 7]. WT theory has been also considered in purely 1D wave systems in various circumstances [8–10]. One of the most important developments in WT theory is the discovery made by V.E. Zakharov in 1965 of a new type of solutions of kinetic equations corresponding to a constant energy flux through scales. These solutions are called Kolmogorov-Zakharov spectra.[1]

It is only relatively recently that optics has emerged as a field of research that is able to provide a better understanding of the origins of the onset of turbulence [11–16]. In particular, a laminar-turbulent transition has been recently observed in a fiber laser, a dissipative wave system described by a generalized and non-integrable one dimensional NLSE (1D-NLSE) [17].

Optics is also a field of research that is very favorable for the investigation of the spatio-temporal properties of wave systems exhibiting an integrable or a nearly-integrable dynamics. In this respect, the pure and integrable 1D-NLSE plays a very specific role. For instance, breathers on finite background that constitute particular solutions of the focusing 1D-NLSE have been experimentally observed in optics and in hydrodynamics and they are now considered as prototypes for rogue waves [18–26]. Ubiquitous phenomena such as wave breaking or intermittency [1, 27–30] typifying many hydrodynamical experiments have also been observed very recently in integrable optical wave systems ruled by the 1D-NLSE [31, 32].

The theoretical framework combining a statistical approach of random waves together with the property of integrability of the 1D-NLSE is known as *integrable turbulence*. This emerging field of research recently introduced by V. Zakharov relies on the analysis of complex phenomena found in nonlinear random waves systems described by an integrable equation [15, 32–37]. For these integrable systems, given an initial condition, the spectrum generally relaxes to a statistically stationary state that in general is different from the standard thermal equilibrium

[1] Kolmogorov-Zakharov cascade may appear when the spectrum (i.e. scales) of nonlinear random waves can be divided into three parts: a pumping spectral range (with an external source of energy, often at large scales), a spectral range with dissipation (often at small scales) and an intermediate inertial range with no dissipation [1, 2]. On the other hand, thermalization emerges in some systems without dissipation and pumping.

characterized by the equipartition of energy.[2] The prediction of the spectra of such final state and of its statistical properties is the objective of the works undertaken in the field of integrable turbulence.

Non-integrability of the model equation is usually considered as a prerequisite for the applicability of WT theory, because it implies a process of irreversible diffusion in phase space that is consistent with the formal irreversibility of the kinetic equation. On the other hand, the dynamics of integrable systems having a low number of degrees of freedom is essentially periodic in time, reflecting the underlying regular phase-space of nested-tori. Applying the usual WT theory to the integrable 1D scalar NLSE, all collision terms in the kinetic equation vanish identically at any order [15, 33, 38]. Accordingly, the WT theory predicts that the spectrum of an incoherent light wave propagating in a single-mode optical fiber does not evolve during the propagation.

This conclusion has been found to be in contradiction with experiments and numerical simulations reported in 2006 [39], in which a significant evolution of the power spectrum of the optical field has been found to occur during propagation in a single-mode optical fiber [39]. In hydrodynamical numerical simulations performed with envelope equations and experiments made in water tanks, non gaussian statistics of the wave height has also been found to emerge from random initial conditions [40–42].

So far, these behaviors have been only described from a modified treatment of the traditional WT theory that has been initially proposed by Janssen [43] and that has been recently applied to optics [12, 15, 38]. The usual WT theory is commonly used to treat wave systems that are ruled by *non* integrable equations and in which the long-time evolution is dominated by resonant interactions among waves (i.e. Fourier components). However it has been shown that the short term evolution of WT can be influenced by non-resonant terms [44]. In the revisited treatment of WT theory, "quasi-kinetic" equations that describe the evolution of the wave spectrum are derived by keeping the contribution of non resonant terms.[3] This WT treatment describes adequately the transient evolutions and the stationary state of the power spectrum and of the PDF of field fluctuations that are observed in the weakly nonlinear regime[15, 38, 43].

There are now many open questions regarding integrable turbulence in the strongly nonlinear regime that is extensively discussed below. The inverse scattering theory (IST) provides a natural framework for the investigation of statistical

[2] In the process of wave thermalization, the "equipartition of energy" corresponds to the equipartition of linear kinetic energy (linear part of the Hamiltonian).

[3] The resonances in wave mixing are determined by double equalities involving frequencies and wave vectors of Fourier components. In the case of one dimensional four-wave mixing, these equalities are $k_1 + k_2 = k_3 + k_4$ and $\omega_1(k_1) + \omega_2(k_2) = \omega_3(k_3) + \omega_4(k_4)$. $\omega(k)$ is the linear dispersion relation. For Eq. (1) where $\omega(k) = k^2$, it is straightforward to show that the two resonant conditions imply $k_1 = k_3$ or $k_1 = k_4$ which is a trivial interaction (no energy is exchanged among different Fourier components). In the case of the integrable 1D-NLSE, the changes of the spectrum and of the statistical properties are thus only induced by non resonant terms.

properties of nonlinear wave systems ruled by integrable equations. In particular, IST has been used in [45] to describe some experiments examining nonlinear diffraction of localized incoherent light beams [46]. The theoretical description of these experiments can be made by using standard tools of the IST because it is fully compatible with the central assumption of IST that the wave field decays at infinity. IST has thus been used both in the focusing and in the defocusing regimes to determine some mathematical expressions for the PDF of the wave field [45].

Note that the IST has also been introduced as a tool for nonlinear Fourier analysis of random wave trains [47–49]. This tool has been successfully implemented in several circumstances to determine the content of random wave trains in terms of nonlinear oscillating modes. In particular, the IST analysis has been used to analyze the soliton content in freak (rogue) wave time series [50] and more recently, to evidence the presence of soliton turbulence in shallow water ocean surface waves [51]. Recently, we have also shown that numerical IST analysis can be implemented to get a highly accurate spectral signature of noise-generated structures that are found in the 1D-NLSE problem with some random initial conditions [52].

In this Chapter, we review a number of results recently obtained by the authors from optical fiber experiments and numerical simulations [32, 37, 53] in the anomalous and normal dispersion regime. The dynamics of the waves in the considered fibers is described with high accuracy by the focusing and defocusing 1D-NLSE. In the focusing regime, the idea is to implement optical fiber experiments conceptually analogous to the water tank experiment described in [41] where waves with a finite spectral bandwidth and random phases are generated at one end of the tank and the evolution of the statistical properties of the wave field is followed along the flume. Using an original setup to overcome bandwidth limitations of usual detectors, we evidence strong distortions of the statistics of nonlinear random light characterizing the occurrence of optical rogue waves in integrable turbulence.

In the defocusing regime, modulational instability is not possible and the evolution of incoherent waves does not lead to the formation of rogue waves. The statistics of wave intensity, initially following the central limit theorem, changes along the fiber resulting in a decrease of the tails of the PDF. This implies that the probability of finding a rogue wave is lower than the one described by linear theory. Implementing an optical filtering technique, we also report on the statistics of intensity of light fluctuations on different scales and we observe that the PDF of the wave intensity show tails that strongly depend on the scales. This reveals the phenomenon of intermittency, previously mentioned, that is similar to the one reported in several other wave systems, though fundamentally far from being described by an integrable wave equation.

The chapter is organized as follows: numerical simulations of focusing and defocusing 1D-NLSE are first considered and described in Sect. 2. Optical fiber experiments designed to investigate changes in the statistics of random light fields and showing results in agreement with simulations are presented in Sect. 3. In Sect. 4, we show that the integrable wave system under consideration exhibits a phenomenon of intermittency both in focusing and defocusing regime. In Sect. 5, we summarize our work and we discuss open questions about integrable turbulence.

2 Spatio-Temporal, Spectral and Statistical Features Arising from Nonlinear Propagation of Random Waves in Systems Ruled by the Integrable 1D-NLSE

2.1 General Framework and Description of the Random Initial Condition

Our study enters within the general framework of the integrable 1D-NLSE[4]:

$$i\psi_t + \psi_{xx} + 2\,\sigma\,|\psi|^2\,\psi = 0 \tag{1}$$

where $\psi(x,t)$ is the complex wave envelope. The parameter σ determines the focusing ($\sigma = +1$) or defocusing ($\sigma = -1$) nature of the propagation regime. In nonlinear fiber optics, it is relatively easy to explore each of the two propagation regimes just by changing either the fiber or the wavelength of light [54]. Equation (1) conserves the energy (or Hamiltonian) $H = H_L + H_{NL}$ that has a nonlinear contribution $H_{NL} = -\sigma \int |\psi(x,t)|^4 dx$ and a linear (kinetic) contribution $H_L = \int k^2 |\widehat{\psi}(k,t)|^2 dk$, the Fourier transform being defined as $\widehat{\psi}(k,t) = 1/\sqrt{2\pi} \int \psi_0(x,t) e^{-ikx} dx$. Equation (1) also conserves the number of particules (or power) $N = \int |\psi(x,t)|^2 dx$ and the momentum $P = \int k |\psi(k,t)|^2 dk$.

In the study presented here, the initial conditions that are used are *non-decaying* random complex fields. Thus we examine a situation that is very different from the problem of nonlinear diffraction of *spatially* incoherent waves already considered in [45, 46, 55, 56]. In these papers, the nonlinear propagation of a speckle pattern of *limited and finite* spatial extension is studied in focusing and defocusing media. On the other hand we consider here continuous random waves of infinite spatial extension. This corresponds for instance to an experimental situation in which a partially coherent and continuous (i.e. not pulsed) light source of high power is launched inside a single-mode optical fiber [32, 37]. In numerical simulations, the random waves are confined in a box of size L and periodic boundary conditions ($\psi(x=0,t) = \psi(x=L,t)$) are used to describe their time evolution [1].

The random complex field $\psi(x, t=0) = \psi_0(x)$ used as initial condition here is made from a discrete sum of Fourier components :

$$\psi(x, t=0) = \psi_0(x) = \sum_n \widehat{\psi_{0n}} e^{ink_0 x}. \tag{2}$$

[4]We use in this chapter the usual and natural variables (t, x). Note that in single optical fiber experiments, the time t has to be replaced by the evolution variable z that represents the propagation distance along the fiber. The variable of x "becomes" the physical time t. Time and space are thus exchanged and in this case the 1D-NLSE takes the form of Eq. (5).

with $\widehat{\psi_{0n}} = 1/L \int_0^L \psi_0(x) e^{-ink_0 x} dx$ and $k_0 = 2\pi/L$. The Fourier modes $\widehat{\psi_{0n}} = |\widehat{\psi_{0n}}| e^{i\phi_{0n}}$ are complex variables. In the random phase and amplitude (RPA) model, generation of a random initial complex field is achieved by taking $|\widehat{\psi}_{0n}|$ and ϕ_{0n} as randomly-distributed variables [1]. Here, we will mainly use the so-called random phase (RP) model in which only the phases ϕ_{0n} of the Fourier modes are considered as being random [1]. In this model, the phase of each Fourier mode is randomly and uniformly distributed between $-\pi$ and π. Moreover, the phases of separate Fourier modes are not correlated so that $< e^{i\phi_{0n}} e^{i\phi_{0m}} >= \delta_{nm}$. In the previous expression, the brackets represent an average operation made over an ensemble of many realizations of the random process. δ_{nm} is the Kronecker symbol defined by $\delta_{nm} = 1$ if $n = m$ and $\delta_{nm} = 0$ if $n \neq m$.

With the assumptions of the RP model above described, the statistics of the initial field is homogeneous, which means that all statistical moments of the initial complex field $\psi_0(x)$ do not depend on x [11, 12]. The power spectrum $n_0(k_n)$ of the random field $\psi_0(x)$ then reads as :

$$< \widehat{\psi_{0n}} \widehat{\psi_{0m}} >= n_{0n} \delta_{nm} = n_0(k_n). \tag{3}$$

with $k_n = n k_0$. In the limit where $L \to \infty$, the frequency separation between two neighboring frequency components k_n and k_{n+1} tends to zero and the discrete spectrum $n_0(k_n)$ becomes a continuous spectrum $n_0(k)$.

The RP model is often used in the contexts of hydrodynamics where the power spectrum $n_0(k)$ is given by the so-called JONSWAP spectrum [57, 58]. It has also been used in optics where simple gaussian or sech profiles are often used for the function $n_0(k)$ [15, 32, 37].

In this section, we consider a random complex initial field having a gaussian optical power spectrum that reads

$$n_0(k) = n_0 \exp\left[-\left(\frac{k^2}{\Delta k^2}\right)\right] \tag{4}$$

where Δk is the half width at $1/e$ of the power spectrum. Figure 1 shows a typical example of a partially coherent complex field generated using the RP model and a power spectrum given by Eq. (4). Figure 1b shows that the values of the spectral phases $\phi_0(k)$ are randomly distributed between $-\pi$ and π. Figure 1c shows the random evolution of the real part $R_0(x) = \Re(\psi_0(x))$ of the initial field that is computed from the spectra shown in Fig. 1a, b. We do not present here the evolution of the imaginary part $I_0(x) = \Im(\psi_0(x))$ of the initial field because it is qualitatively very comparable to what is shown in Fig. 1c. However it is important to notice that the RP model produces a random field having real and imaginary parts that are statistically independent, i.e. $< R_0(x) I_0(x) >= 0 \ \forall x$. The spatial evolution of the power $P_0(x) = |\psi_0(x)|^2 = R_0^2(x) + I_0^2(x)$ of the random initial field is shown in Fig. 1d. Note that the numerical values of the parameters n_0 and Δk have been

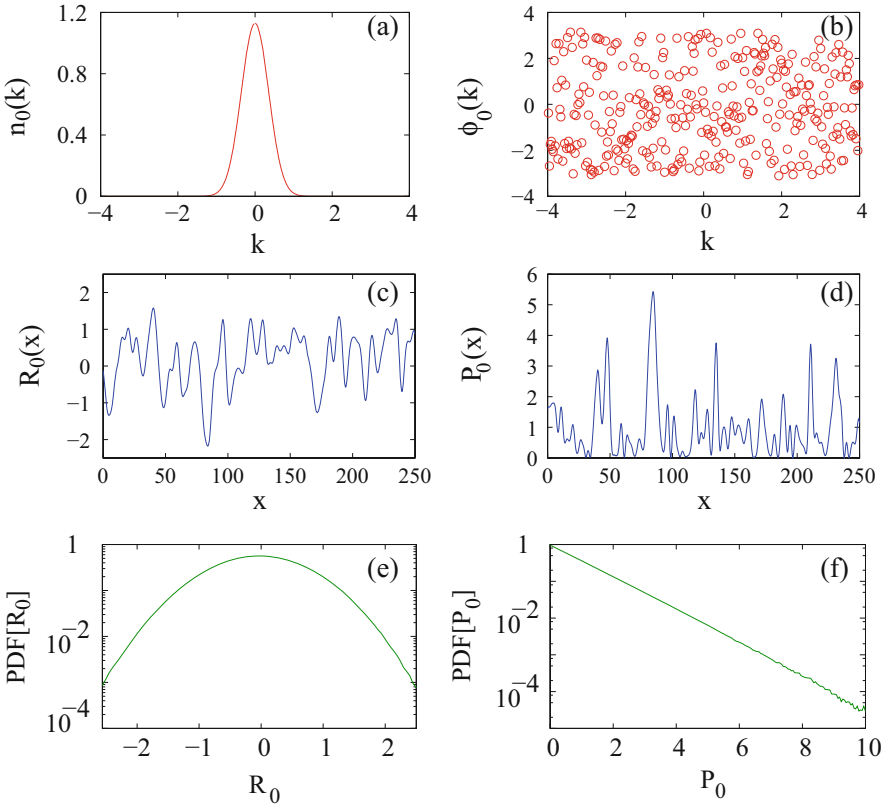

Fig. 1 Reproduced from [53] (**a**) Gaussian power spectrum $n_0(k)$ of the initial condition such as defined by Eq. (4) ($\Delta k = 0.5$, $n_0 = 1.129$). (**b**) Spectral distribution of the phases $\phi_0(k)$ of the Fourier modes used to compute the random initial field $\psi_0(x)$. (**c**) Real part $R_0(x) = \Re(\psi_0(x))$ and (**d**) power $P_0(x) = |\psi_0(x)|^2$ of the random field computed from spectra shown in (**a**), (**b**). (**e**) PDF of $R_0(x)$ and (**f**) PDF of $P_0(x)$ showing that the initial condition has a gaussian statistics

chosen in such a way that the number of particules $N = 1/L \int_0^L |\psi(x,t)|^2 dx$ is equal to unity.

As previously described, the random complex field $\psi_0(x)$ used as initial condition is produced from the linear superposition of a large number of independent Fourier modes having randomly distributed phases. As stated by the central limit theorem, the statistics of the random process produced from such a superposition follows the normal law. The RP model thus produces a complex field having quadratures that are statistically independent and that have the same gaussian statistics. It is straightforward to prove that the statistics of power fluctuations P_0 follows the exponential distribution [36, 59]. Note that the PDF for the fluctuations of the amplitude $A_0(x) = |\psi_0(x)|$ is given by the Rayleigh distribution defined by $PDF[A_0/ < A_0 >] = A_0/ < A_0 > . exp(-A_0/ < A_0 >)$ [36, 59].

In order to illustrate these statistical features from numerical simulations, we have performed the analysis of the statistical properties of the complex field generated from the RP model by producing an ensemble of 10^4 realizations of the random initial field. From this ensemble, it is in particular possible to compute the PDF for the fluctuations of $R_0(x) = \Re(\psi_0(x))$ and of $P_0(x) = |\psi_0(x)|^2$. Figure 1e shows that the PDF of $R_0(x)/ < R_0(x) >$ is gaussian. The PDF of the normalized imaginary part $I_0(x)/ < I_0(x) >$ of the complex field is not shown here but it is rigorously identical to the PDF of $R_0(x)/ < R_0(x) >$. As it is illustrated in Fig. 1f, the PDF of the power is given by the exponential distribution, i.e. $PDF[P_0/ < P_0 >] = exp(-P_0/ < P_0 >)$.

2.2 Focusing Regime

In this Section, we consider the focusing regime ($\sigma = +1$) and we use numerical simulations of Eq. (1) to investigate the propagation of a partially coherent wave generated at $t = 0$ by the random complex field described in Sect. 2.1. We will consider the spatio-temporal dynamics of the partially coherent wave and we will also discuss spectral and statistical changes occurring in time.

Our numerical simulations have been performed by using a pseudo-spectral method working with a step-adaptative algorithm permitting to reach a specified level of numerical accuracy. The numerical simulations are performed by using a box of size $L = 257.36$ that has been discretized by using 4096 points. Statistical properties of the random wave are computed from an ensemble of 10^4 realizations of the random initial condition.

Figure 2a shows the spatio-temporal evolution of the partially-coherent wave seeded by a random initial field having properties that are described in Sect. 2.1 and that are synthesized in Fig. 1. At the initial stage of the nonlinear evolution ($t \sim 0$), the power $|\psi(x,t)|^2$ of the wave is slowly and randomly modulated. The spatial scale of the fluctuations of $|\psi(x,t)|^2$ at $t \sim 0$ is determined by Δk and it is typically around 10 in the simulations shown in Fig. 2 (see also Fig. 1d). Numerical simulations show that series of peaks emerge from the random initial condition. The density of these peaks is higher is those regions of space where the complex field exhibits high peak power fluctuations at the initial time $t = 0$, see e. g. the region where $x \in [-50, -40]$ in Fig. 2 and in Fig. 3a, c, e. While the localized peaks shown in Fig. 2a drift with small velocities in the (x,t) plane, their peak power increases with time. This increase of the peak power of the localized structures goes simultaneously with a reduction of their spatial width. The typical spatial scale of the power fluctuations evolves from a value of ~ 10 at initial stage ($t = 0$) to the healing length of ~ 1 at long evolution time ($t > 10$) (see Fig. 3a, c, e).

A clear signature of the change in the fluctuation scale can be observed in the Fourier space. As shown in Fig. 3b, d, f, the power spectrum $|\widehat{\psi}(k,t)|^2$ of the random wave is indeed found to significantly broaden with time. Let us emphasize that the

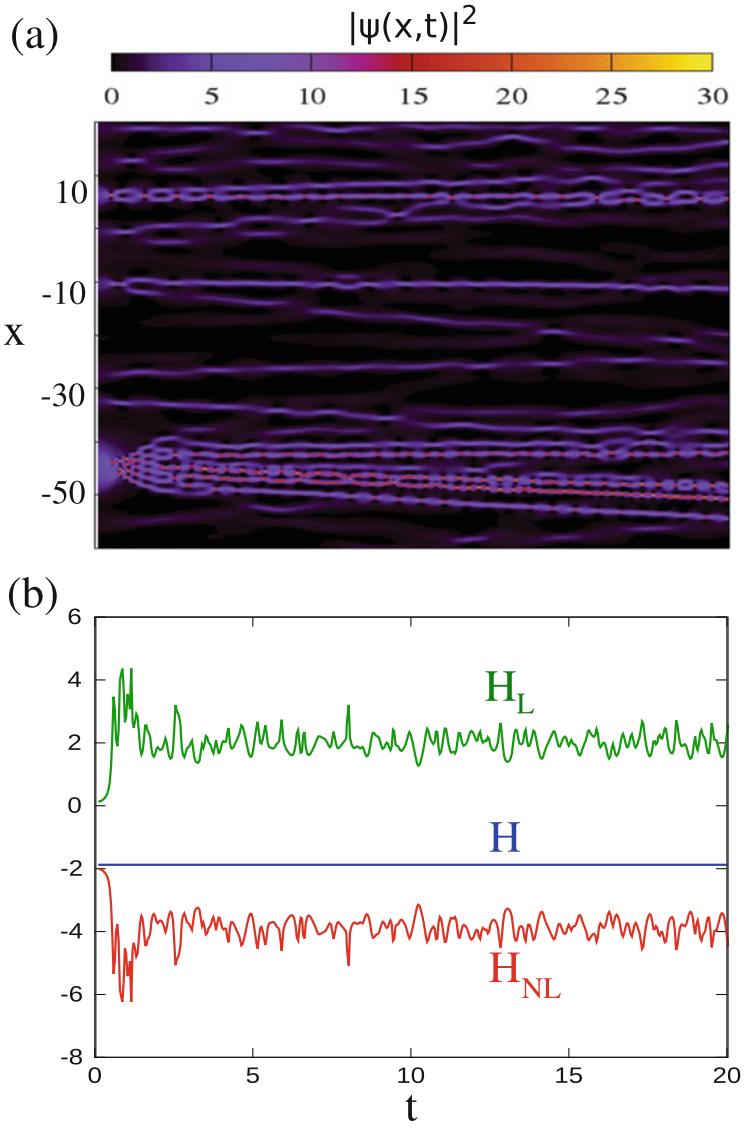

Fig. 2 Reproduced from [53]. Numerical simulations of Eq. (1) in focusing regime ($\sigma = +1$). (**a**) Spatio-temporal evolution of the power $|\psi(x,t)|^2$ of the wave while starting from the random complex field having a gaussian power spectrum and a gaussian statistics, see Fig. 1. (**b**) Corresponding time evolution of linear (kinetic) energy H_L and of nonlinear energy H_{NL}

power spectrum of the wave broadens while always keeping exponentially decaying wings.

The evolution of the typical space scales and peak powers of the random fluctuations that is described above goes together with a process of energy balance

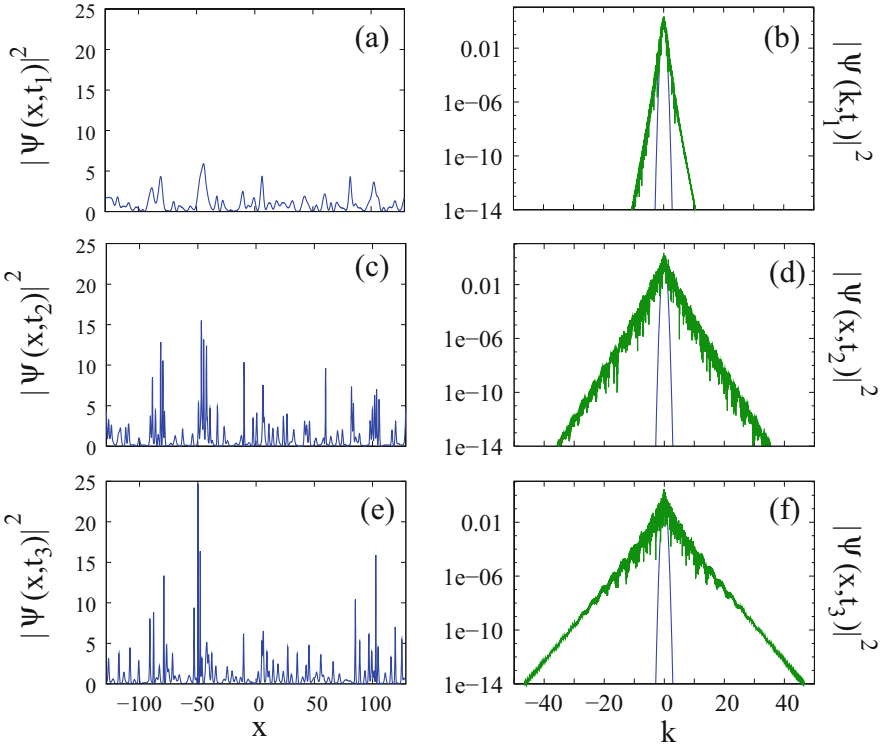

Fig. 3 Reproduced from [53]. Numerical simulations of Eq. (1) in focusing regime ($\sigma = +1$). Spatial evolution of the power $|\psi(x,t)|^2$ of the random wave at times (**a**) $t_1 = 0.24$, (**c**) $t_1 = 2.44$, (**e**) $t_1 = 16.04$. Power spectra (*green lines*) $|\psi(k,t)|^2$ of the random wave at times (**b**) $t_1 = 0.24$, (**d**) $t_1 = 2.44$, (**f**) $t_1 = 16.04$. The spectra plotted in *blue lines* represent the gaussian power spectrum of the random initial complex field defined by Eqs. (3) and (4)

between linear and nonlinear effects. Figure 2b shows the evolutions in time of the linear (kinetic) energy H_L and of the nonlinear energy H_{NL} that are associated with the spatio-temporal evolution plotted in Fig. 2a. The wave system is initially placed in a highly nonlinear regime in which the nonlinear energy is one order of magnitude greater than the linear energy ($|H_{NL}| \simeq 10|H_L|$). As a result of nonlinear propagation, linear and nonlinear effects come into balance and after a short transient evolution, the wave system reaches a state in which linear and nonlinear energies have the same order of magnitude ($|H_{NL}| \simeq 2|H_L|$, see Fig. 2b).

It is interesting to compare the spatio-temporal evolution shown in Fig. 2a with the one shown in Fig. 2a of [26]. In [26], the authors study the nonlinear evolution in space and time of a condensate perturbated by a small noise, i. e. $\psi_0(x) = 1 + \eta(x)$ where $|\eta(x)| << 1$ is a small noise with broad spectrum. As shown in Fig. 2a of [26], the fact that there is only a weak random modulation of the initial condition gives rise to a spatiotemporal diagram in which localized structures are distributed

in space and time in a way that is more regular than the random pattern shown in Fig. 2a of this chapter. Starting from our initial condition with a broad gaussian spectrum, there are some wide regions of space in which no localized structures are observable while there are some other regions of space including many localized structures. As shown in [37], the localized structures emerging from a complex field having initially a gaussian statistics can be locally fitted by some analytical functions corresponding to solitons on finite background, such as e. g. the Peregrine soliton. Fitting procedures implemented in the numerical work presented in [26] have shown that many solitons on finite background can be also found while seeding the wave system from a condensate perturbated by a small noise.

Despite localized structures looking like solitons on finite background can be observed while starting from those two different random initial conditions, significantly different statistical features are observed at long evolution time. It has been shown in [36] that gaussian statistics emerges from the nonlinear evolution of the noisy condensate. As shown in Fig. 4, heavy-tailed deviations from Gaussianity are contrarily found to emerge from a random complex field having initially a gaussian statistics [37]. It is an open question to understand how the interplay among localized structures does not produce the same statistics at long evolution time while starting from different noisy initial conditions.

Figure 4 shows the time evolution of the PDF of $|\psi(x,t)|^2$. The nonlinear random field has a statistical evolution in which the PDF of power fluctuations continuously moves from the exponential distribution (plotted in red line in Fig. 4) to the heavy-tailed distribution plotted in blue line in Fig. 4. For $t > 10$, the wave system reaches a statistical stationary state in which the PDF no longer changes with time [37]. This statistical stationary state is determined by the interaction of coherent nonlinear structures such as for instance solitons (with zero background) [60], solitons on finite background (Akhmediev breathers, Peregrine solitons...) [61] and also linear dispersive radiation [35, 62, 63]. It is now an open question to determine the mechanisms in integrable turbulence that lead to the establishment of a stationary state in which statistical properties of the wave system do not change in time. Tools

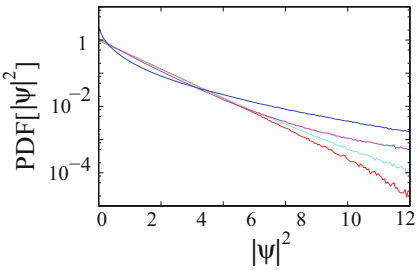

Fig. 4 Reproduced from [53]. Numerical simulations of Eq. (1) in focusing regime ($\sigma = +1$). PDF of the power $|\psi(x,t)|^2$ at time $t = 0$ (*red line*), $t = 0.2$ (*cyan line*), $t = 0.4$ (*magenta line*), $t = 10$ and $t^* = 20$ (*blue line*). The PDF is stationary from $t \sim 10$, i.e. the PDF plotted in *blue line* does not change with time for $t > 10$

from the inverse scattering theory could be used to investigate this question of fundamental importance [45, 52, 55, 56, 63–65].

2.3 Defocusing Regime

In this Section, we consider the defocusing regime ($\sigma = -1$) and we use numerical simulations of Eq. (1) to investigate the propagation of a partially coherent wave generated at $t = 0$ by a random complex field identical to the one used in Sect. 2.2.

Figure 5a shows the spatio-temporal evolution of the partially-coherent wave seeded by a random initial field identical to the one used in Fig. 2a. Spatiotemporal features emerging from the nonlinear propagation in defocusing regime drastically contrast with those found in the focusing regime. Instead of bright localized structures, we now observe the emergence of dark localized structures propagating at various speeds in the (x, t) plane. Figure 6a, b show that the initial stage of nonlinear evolution is now characterized by a fast decay of the peaks of highest intensities, see e. g. the region where $x \in [-50, -40]$. During the initial evolution of the random wave, the leading and trailing edges of peaks of highest intensities strongly sharpen. This leads to some gradient catastrophes which are regularized by the generation of dispersive shock waves (DSWs) [66–69]. As in the focusing case, the typical spatial scale of the random fluctuations decreases from ~ 10 at the initial stage ($t = 0$) to the healing length of ~ 1 at long evolution time ($t > 10$). The stochastic evolution shown in Fig. 6c is determined by the interaction of nonlinear coherent structures such as dark solitons or DSWs and of linear radiation.

Figure 6b, d, f show that nonlinear propagation in defocusing regime induces a spectral broadening of the random wave. This spectral broadening phenomenon is quantitatively less pronounced than the one observed in the focusing regime, see Fig. 3b, d, f. However the power spectrum of the wave broadens while always keeping exponentially decaying wings, as in the focusing regime.

The spatiotemporal evolution shown in Fig. 5a and in Fig. 6a, c, e goes together with a process of energy balance between linear and nonlinear effects. Figure 5b shows the time evolutions of the linear (kinetic) energy H_L and of the nonlinear energy H_{NL} that are associated with the spatio-temporal evolution plotted in Fig. 5a. The wave system is initially placed in a highly nonlinear regime in which the nonlinear energy is one order of magnitude greater than the linear energy ($H_{NL} \sim 10H_L$). As in the focusing regime, linear and nonlinear effects come into balance and after a short transient evolution, the wave system reaches a state in which H_{NL} and H_L have the same order of magnitude, see Fig. 5b.

In the defocusing regime, the nonlinear random field has a statistical evolution in which the PDF of power fluctuations continuously moves from the exponential distribution (plotted in red line in Fig. 7) to the low-tailed distribution plotted in blue line in Fig. 7. As in the focusing regime, the wave system exhibits a statistical stationary state and the PDF computed at $t = 10$ (magenta line in Fig. 7) does not change anymore with time [32]. This statistical stationary state is determined by

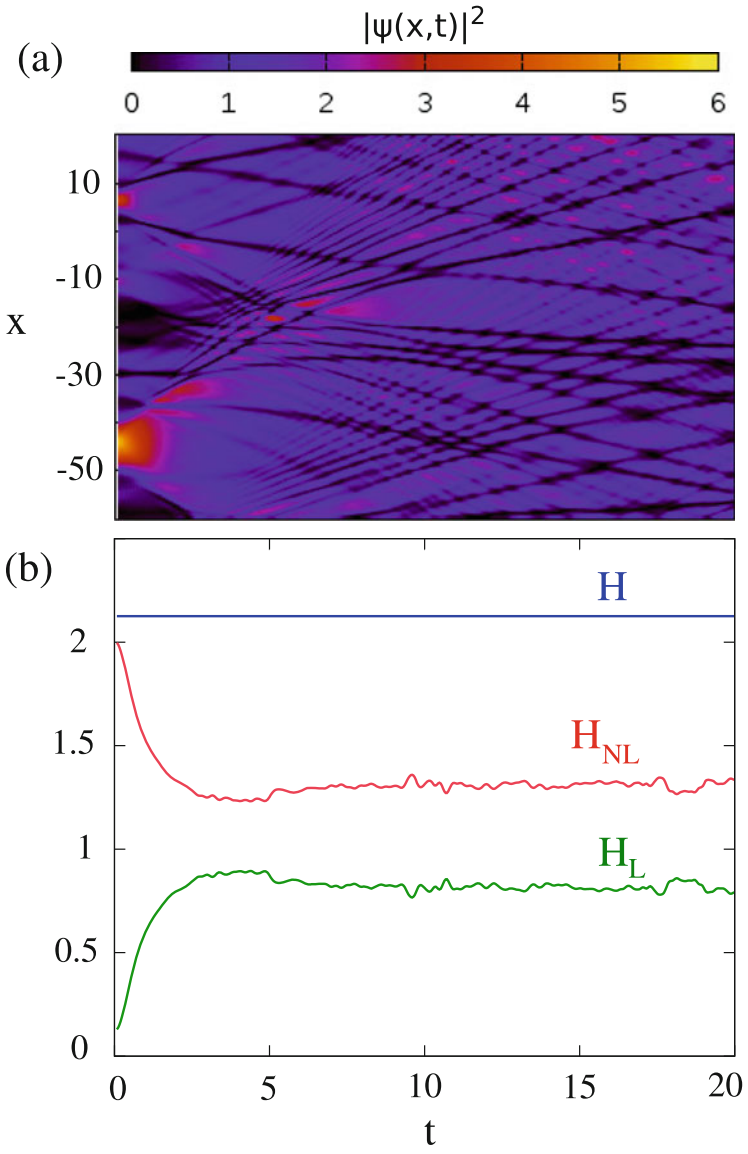

Fig. 5 Reproduced from [53]. Numerical simulations of Eq. (1) in defocusing regime ($\sigma = -1$). (**a**) Spatio-temporal evolution of the power $|\psi(x,t)|^2$ of the wave while starting from the random complex field having a gaussian power spectrum and a gaussian statistics, see Fig. 1. (**b**) Corresponding time evolution of linear (kinetic) energy H_L and of nonlinear energy H_{NL}

the interaction of coherent nonlinear structures such as for instance dark solitons, dispersive shock waves and also linear radiation. As for the focusing regime, it is an open question to determine the mechanisms in integrable turbulence that lead to the establishment of a stationary state in which statistical properties of the wave system

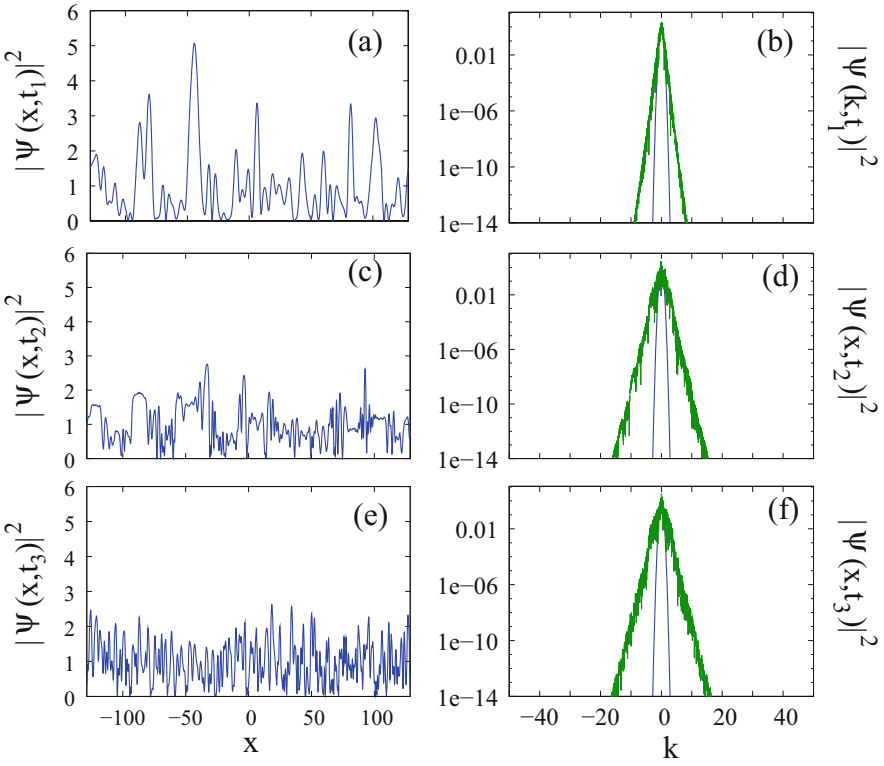

Fig. 6 Reproduced from [53]. Numerical simulations of Eq. (1) in defocusing regime ($\sigma = -1$). Spatial evolution of the power $|\psi(x,t)|^2$ of the random wave at times (**a**) $t_1 = 0.24$, (**c**) $t_1 = 2.44$, (**e**) $t_1 = 16.04$. Power spectra (*green lines*) $|\psi(k,t)|^2$ of the random wave at times (**b**) $t_1 = 0.24$, (**d**) $t_1 = 2.44$, (**f**) $t_1 = 16.04$. The spectra plotted in *blue lines* represent the gaussian power spectrum of the random initial complex field defined by Eqs. (3) and (4)

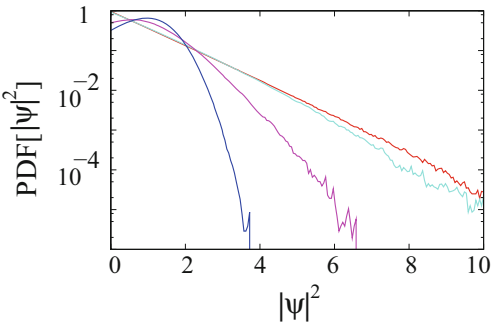

Fig. 7 Reproduced from [53]. Numerical simulations of Eq. (1) in defocusing regime ($\sigma = -1$). PDF of the power $|\psi(x,t)|^2$ at time $t = 0$ (*red line*), $t = 0.2$ (*cyan line*), $t = 1$ (*magenta line*), $t = 10$ and $t^* = 20$ (*blue line*). The PDF is stationary from $t \sim 10$, i.e. the PDF plotted in *blue line* does not change with time for $t > 10$

do not change in time. Tools of the inverse scattering transform could be of interest for the investigation of this question [70].

3 Optical Fiber Experiments in Focusing and in Defocusing Propagation Regimes

Optical fiber experiments provide versatile and powerful tabletop laboratory to investigate the complex dynamics of 1D-NLSE, hydrodynamic-like phenomena and the statistical properties of nonlinear random waves [12, 17, 19, 25, 31, 71–74].

One of the most critical constraint of these experiments is the finite spectral bandwidth of usual detectors. The typical response time of the fastest detector and oscilloscope is several tens of picoseconds. On the other hand, with the usual parameters of standard experiments using optical fibers, the typical "healing time" scale characterizing the equilibrium between the nonlinearity and the dispersion is around one picosecond [37]. For this reason, the picosecond is also the order of magnitude of the time scale associated to the power fluctuations of partially coherent fiber lasers [71, 72, 75].

As a consequence spectral filters are therefore often used to reveal extreme events in time-domain experiments [32, 74, 76, 77]. In the case of pulsed experiments, it is possible to evidence shot-to-shot spectrum fluctuations with a dispersive Fourier transform measurement [74, 78–80]. To the best of our knowledge, up to our recent works [37, 75], the *accurate and well-calibrated* measurement of the PDF characterizing temporal fluctuations of the power of *random light* with time scale of the order of picosecond had never been performed.

We have developed an original setup based on asynchronous optical sampling (OS) which allows the precise measurement of statistics of random light rapidly fluctuating with time (see Fig. 8).

The "random light" under investigation is a partially coherent wave and it is called the "signal". The signal is optically sampled with 140 fs-pulses and the PDF is computed from the samples. The optical sampling is obtained from the second order nonlinearity $\chi^{(2)}$ in a BBO crystal. The sum-frequency generation (SFG) between the signal at $\lambda_S = 1064\,\text{nm}$ and short "pump" pulses having a central wavelength $\lambda_P = 800\,\text{nm}$ provide samples of the signal at a wavelength $\lambda = 457\,\text{nm}$. The full dynamics of the signal cannot be recovered with this asynchronous optical sampling technique. However this setup enables an accurate measurement of the PDF of random fluctuations having time scale of the order of 250 fs [37]. Note that very recently, optical rogue waves emerging in integrable turbulence and having sub-picosecond time scales have been directly observed with a time microscope device [81].

The statistical quantity measured in asynchronous optical sampling experiments is the PDF of the optical power i.e. not the PDF of the maxima or of the wave height but the PDF of occurrence of each value of optical power. In the experiments

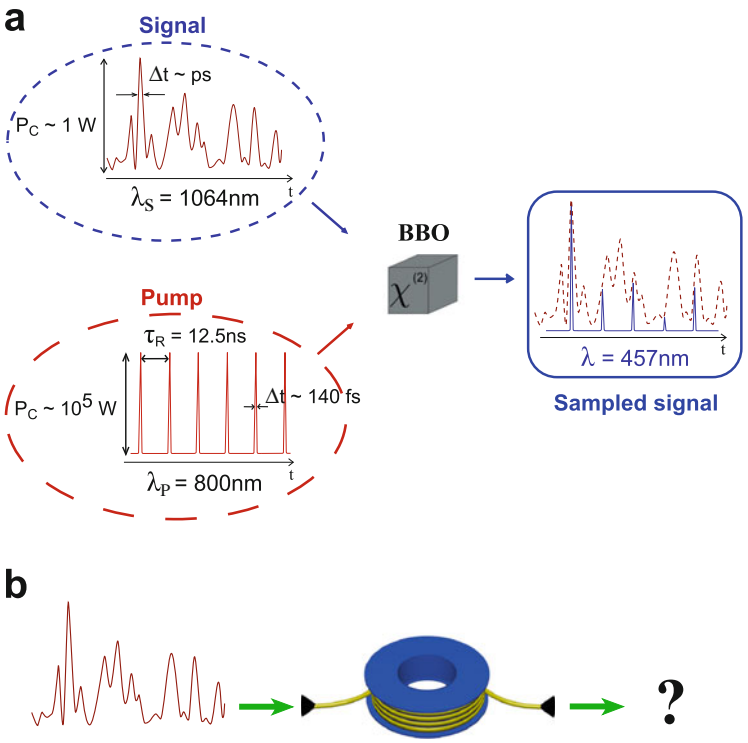

Fig. 8 Reproduced from [53]. Experimental measurement of the statistics of random light (**a**) Principle. Optical sampling of the partially-coherent wave fluctuating with time (the signal) is achieved from sum frequency generation in a second order ($\chi^{(2)}$) crystal. *Blue pulses* are generated at $\lambda = 457$ nm from the interaction of the signal with periodic femtosecond pump pulses inside a $\chi^{(2)}$ crystal. PDF is computed from the peak powers of the *blue pulses*. (**b**) Nonlinear propagation in optical fiber. The initial partially coherent light is launched inside a single mode optical fiber either in the focusing (fiber 1) or defocusing (fiber 2) regime of dispersion. The statistics and the spectrum are measured before and after the propagation in the fiber

reported in [37], the linearly polarized partially coherent wave is emitted by a "continuous" wave (cw) Ytterbium fiber laser at $\lambda_S = 1064$ nm. This cw laser emits numerous (typically 10^4) uncorrelated longitudinal modes. The reader can refer to [37] for the details of the experimental setup and of the statistics measurement procedure.

We present results obtained with two different fibers (fiber 1 and 2) having opposite sign of the group velocity dispersion at the wavelength of the signal $\lambda_S = 1064$ nm. The fiber 1 is a 15 m-long highly nonlinear photonic crystal fiber (provided by Draka France company) with a nonlinear third order coefficient $\gamma \simeq 50\,\mathrm{W}^{-1}\,\mathrm{km}^{-1}$ and a group velocity dispersion coefficient $\beta_2 \simeq -20\,\mathrm{ps}^2/\mathrm{km}$. The fiber 2 is a 100 m-long polarization maintaining fiber with a nonlinear third order coefficient $\gamma \simeq 6\,\mathrm{W}^{-1}\,\mathrm{km}^{-1}$ and a group velocity dispersion coefficient

$\beta_2 \simeq +20\,\mathrm{ps}^2/\mathrm{km}$. We launch a mean power $< P >= 0.6\mathrm{W}$ in the experiments performed with the fiber 1 (focusing case) and a mean power $< P >= 4.\mathrm{W}$ in the experiments performed with the fiber 2 (defocusing case). Note that the results obtained with the fiber 1 have been presented in detail in [37] whereas the results obtained with the fiber 2 are new.

We first measure the PDF at the output of the laser. In all experiments presented in this letter, the mean output power of the Ytterbium laser is fixed at $\langle P \rangle = 10\,\mathrm{W}$. At this operating point, the statistics of the partially coherent wave follows the normal law. Indeed, as plotted in red in Fig. 9c, d, the PDF of the normalized power $P/\langle P \rangle$ is very close to the exponential function. Assuming that the real part and the imaginary parts are statistically independent, this exponential distribution of power corresponds to a gaussian statistics of the field. It is important to note that the dashed black lines in Fig. 9c, d are not a fitted exponential function but represent the exact

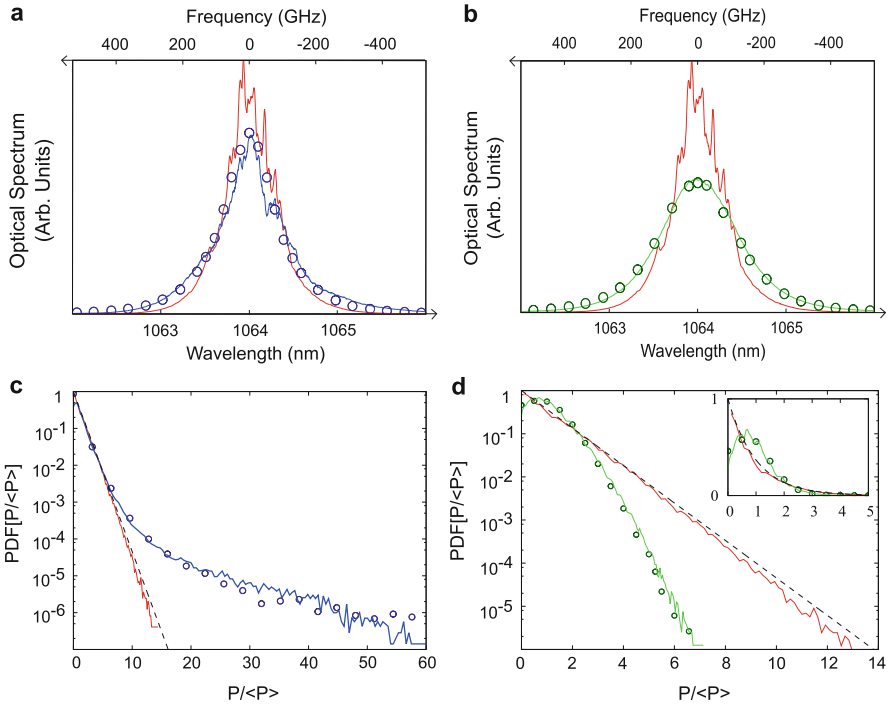

Fig. 9 Reproduced from [53]. Experiments. (**a**), (**b**): Optical spectra. Input spectrum (*red line*). Spectrum at the output of fiber 1 (*blue line*) and fiber 2 (*green line*). The circles represents optical spectra computed from numerical simulation of 1D-NLSE. (**c**), (**d**): PDF of normalized optical power $P/\langle P \rangle$ plotted in logarithmic scale. Normalized exponential distribution $PDF[P/ < P >] = \exp(-P/ < P >)$ (*black dashed line*). PDF of the input random light (*red line*). PDF of the light at the output of the fiber 1 (*blue solid line*) and at the output of the fiber 2 (*green solid line*). The *dashed lines* represent the PDF computed from numerical simulation of 1D-NLSE with the parameters of the experiments. The *inset* represents the same PDF in vertical linear scale

normalized $PDF[P/\langle P\rangle] = \exp(-P/\langle P\rangle)$. To the best of our knowledge, PDF of so rapidly fluctuating optical signals has never been *quantitatively* compared to the normalized exponential distribution.

We use the output of the laser as a random source and we launch the partially coherent signal into optical fibers 1 and 2. Experiments have been carefully designed to be very well described by the 1D-NLSE. In particular, the signal wavelength $\lambda_s = 1064\,\text{nm}$ is far from the zero-dispersion wavelength ($\lambda_0 \simeq 970\,\text{nm}$ for the fiber 1 and $\lambda_0 > 1300\,\text{nm}$ for the fiber 2). Moreover the optical spectral widths (see Fig. 9a, b) remain sufficiently narrow to neglect stimulated Raman scattering (SRS) and high-order dispersion effects. The linear losses experienced by optical fields in single pass in the fibers are negligible. These total losses are around 0.3 % in the fiber 1 and around around 2.5 % in the fiber 2.

Despite the broadening of the optical spectrum is of nearly the same importance in focusing and in defocusing regimes (see Fig. 9a, b) our experiments reveal that the distortions of the statistics of the random waves strongly depend on the sign of the group velocity dispersion coefficient.

The experiments performed in the *focusing* regime (fiber 1) reveal the occurrence of numerous extreme events (RW) (see blue curve in Fig. 9c). The comparison between the initial PDF (see red line in Fig. 9c) and the output PDF (see blue curve 9c) shows an impressive change in the statistical distribution of optical power. The initial field follows the normal law and its PDF is an exponential function whereas the output PDF of optical power exhibits a strong heavy-tail.

On the other hand, the PDF experimentally measured at the output of fiber 2 in the defocusing regime exhibits a very low tail (see Fig. 9d). Light fluctuations of a high power are found with a probability that has been strongly reduced as compared to the normal law. Moreover, contrary to the initial exponential distribution, the most probable value for the power is not the zero value (see inset of Fig. 9d).

Numerical simulations show that experiments presented above are very well described by the integrable 1D-NLSE. The initial conditions are computed from the random phase assumption as in Sect. 2.1. We have performed Monte Carlo simulations with ensemble average over thousands of realizations. We integrate the 1D-NLSE with experimental parameters:

$$i\frac{\partial \psi}{\partial z} = \frac{\beta_2}{2}\frac{\partial^2 \psi}{\partial t^2} - \gamma|\psi|^2\psi \tag{5}$$

where β_2 is the group velocity dispersion coefficient and γ is the effective Kerr coefficient. Optical spectra and PDFs computed from the numerical integration of the 1D-NLSE are in quantitative agreement with experiments both in the focusing and in the defocusing cases (see dashed blue and green lines in Fig. 9).

Moreover, the numerical simulations show that integrable turbulence is characterized by a statistical stationary state both in focusing and defocusing regime (see Fig. 10). In particular, the average of the nonlinear and linear parts of the Hamiltonian ($\langle H_{NL}\rangle$ and $\langle H_L\rangle$) evolves to constant values (see Fig. 10a, b). Note that

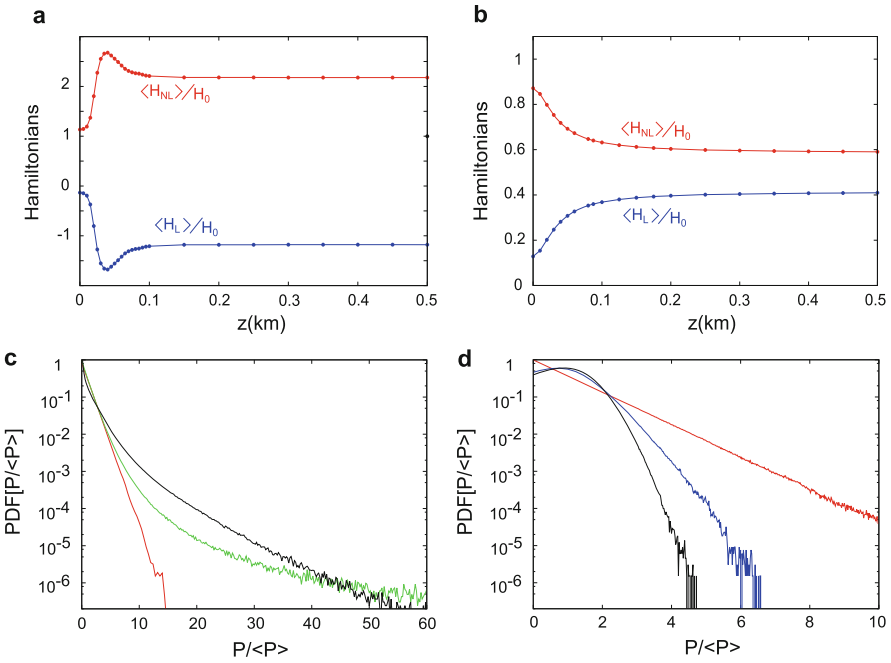

Fig. 10 Reproduced from [53]. Numerical Simulations. (**a**) and (**b**): evolution of the average of the nonlinear H_{NL} and linear H_L Hamiltonians in the focusing (**a**) and defocusing (**b**) cases. H_{NL} and H_L are normalized to the value of the Hamiltonian (constant of motion) $H = H_{NL} + H_L$ before the averaging over hundreds of realizations. (**c**) PDFs computed at different z in the focusing case. $z = 0$ m (*red line*), $z = 15$ m (*green line*, identical to dashed green line in Fig. 9c) and $z = 100$ m (stationary PDF). (**d**) PDFs computed at different z in the defocusing case. $z = 0$ m (*red line*), $z = 100$ m (*blue line*, identical to *dashed blue line* in Fig. 9d) and $z = 500$ m (stationary PDF)

we represent here the average of H_{NL} and H_L over hundreds of realizations whereas the values of H_{NL} and H_L computed on only *one* realization are plotted in Sect. 2.

Figure 10c represents PDFs computed from numerical simulations for different lengths of propagation in the focusing regime of dispersion. The red line is the PDF at $z = 0$ m, the blue line is the PDF at $z = 15$ m corresponding to the experiments (see Fig. 9c) and the black line corresponds at the stationary PDF (computed at $z = 500$ m). Figure 10d represents PDFs computed from numerical simulations for different lengths of propagation in the defocusing regime of dispersion. The red line is the PDF at $z = 0$ m, the blue line is the PDF at $z = 100$ m corresponding to the experiments (see Fig. 9d) and the black line corresponds to the stationary PDF (computed at $z = 500$ m).

Note that comparable deviations from gaussian statistics have been reported in 1D "spatial experiments" in which the transverse intensity profile of optical beams randomly fluctuates in space [46]. In these spatial experiments performed in focusing and defocusing regime, the speckle fields are localized and random waves decay to zero at infinity [45, 46]. IST with usual zero-boundary conditions has been

used in [45] to describe these experiments. In the long-term evolution of the wave system with zero boundary conditions, solitons separate from dispersive waves in the focusing regime. In the defocusing regime, only dispersive waves persist at long evolution time.

On the contrary, our experiments and numerical simulations are made with non-zero boundary conditions and with non-localized random waves. This widens the perspectives of experimental integrable turbulence studies. With random waves having an infinite spatial extension, solitons and dispersive waves never separate from each other and they always interact. Moreover breathers and solitons on finite background can emerge from nonlinear interaction in the focusing regime. In the defocusing case, the fact that the random field does not decay at infinity means that dark solitons can be sustained and interact all-together with dispersive waves at any time (any value of z in our fiber experiments).

As a conclusion of Sect. 3, we have experimentally studied the evolution of the statistics of random waves whose propagation is very well described by 1D-NLSE both in focusing and defocusing case.

In the defocusing case, we have experimentally and numerically demonstrated that the probability of occurrence of large waves decreases as a result of nonlinear propagation.

In the focusing case, we have evidenced the statistical emergence of RW from nonlinear propagation of random light. In [37], we have also shown that solitons on finite background such as Akhmediev breathers, Peregrine solitons or Kuznetsov-Ma solitons having a short duration and a high power seem to emerge on the top of the highest fluctuations.

This result may seem surprising because Akhmediev breathers correspond to the nonlinear stage of modulational instability when a small sinusoidal perturbation is added to an *infinite* plane wave. However, observation of structures very similar to solitons on finite background in the case of partially coherent waves with 100 % of modulation may be related to the theoretical results in [82] which prove the Peregrine soliton emerges on the top of a single hump (*with zero boundary conditions*) in the weak dispersion limit.

This strengthens the idea that the emergence of deterministic solutions of 1D-NLSE such as breathers on finite background in nonlinear random fields is a major mechanism for the formation of rogue waves [24, 25, 61, 83, 84]. Note that the emergence of such coherent structures in incoherent fields has been already theoretically studied in *non integrable* wave turbulence [85, 86] and in integrable turbulence emerging from a modulationaly unstable condensate [34, 36, 61]. As a conclusion, the identification of the structures and the mechanism of their formation is a wide and open question.

Note finally that in one dimensional deep water experiments, relatively small deviations from Gaussianity have been observed and interpreted in the framework of wave turbulence theory [43, 87, 88]. On the contrary, our optical fiber setup provides an accurate laboratory for the exploration of strongly nonlinear random wave systems ruled by the 1D-NLSE.

4 Separation of Scales and Intermittency Phenomenon

Statistical features presented in Sect. 2 and in Sect. 3 are relevant to global random fields in the sense that all the fluctuations scales of the random waves are taken into account and contribute to the statistics. However, separating large scales from small scales is known to provide rich statistical information about nonlinear systems of random waves. In this respect, the phenomenon of intermittency is defined in the general context of turbulence as a departure from the Gaussian statistics that grows increasingly from large scales to small scales [27].

Following the definition given by Frisch in [27], a random function $R(x)$ of space x is defined as being intermittent when it displays some activity over a fraction of space that decreases with the scale under consideration. Considering stationary random processes, the intermittency phenomenon can be evidenced and quantified by using spectral filtering methods. The existence of deviations from Gaussianity is usually made through the measurement of the kurtosis of the fluctuations that are found at the output of some frequency filter. Considering the high-pass filtered signal $R_\xi^>(x)$ defined in the spatial domain as

$$R(x) = \int dk e^{ikx} \tilde{R}(k), \tag{6}$$

$$R_\xi^>(x) = \int_{|k|>\xi} dk e^{ikx} \tilde{R}(k), \tag{7}$$

the random function $R(x)$ is intermittent at small scales if the kurtosis:

$$\kappa(\xi) = \frac{\langle (R_\xi^>(x))^4 \rangle}{\langle (R_\xi^>(x))^2 \rangle^2} \tag{8}$$

grows without bound with the filter frequency ξ [27].

Although we are going to use here the definition of intermittency given by Frisch [Eqs. (6)–(8)], it should be emphasized that the exact nature of the spectral filtering process is not of a fundamental importance and that the intermittency phenomenon can also be evidenced from the use of various frequency filters. Spectral fluctuations can be examined at the output of an ideal one-mode spectral filter passing only a single Fourier component [1, 30]. Time fluctuations at the output of bandpass frequency filters can also be considered [27, 32, 89]. PDFs of second-order differences of the wave height have also been measured in wave turbulence [28]. Using this kind of filtering techniques, the phenomenon of intermittency has been initially reported in fully developed turbulence [27] but it is also known to occur in wave turbulence [28–30], solar wind [90] or in the Faraday experiment [91]. So far, the intermittency phenomenon has been ascribed to physical systems that are described by non-integrable equations. We are going to use numerical simulations

of Eq. (1) to show that intermittency is a statistical phenomenon that also occurs in the field of integrable turbulence [32].

Taking the wave system extensively described in Sect. 2, we now consider the spatial fluctuations of the real part $\Re(\psi(x,t^*))$ of the complex field $\psi(x,t^*)$ that has reached the stationary statistical state at $t^* = 20$. In other words, the filtering process and the statistical treatment defined by Eqs. (6)–(8) are now applied to the random variable $R(x) = \Re(\psi(x,t^*))$. Spatial and statistical features found at the output of the highpass frequency filter are shown in Fig. 11 for the focusing regime.

When $\xi = 0$, the random process $R(x)$ is not filtered and Fig. 11a shows the spatial evolution of the random variable $R(x)/ < R(x) >= \Re(\psi(x,t^*))/ < \Re(\psi(x,t^*)) >$ in this situation. Figure 11d represents the corresponding PDF of $R(x)/ < R(x) >$. Without any filtering process, the heavy-tailed deviations from Gaussianity shown in Fig. 11d are identical to those already shown in Fig. 4

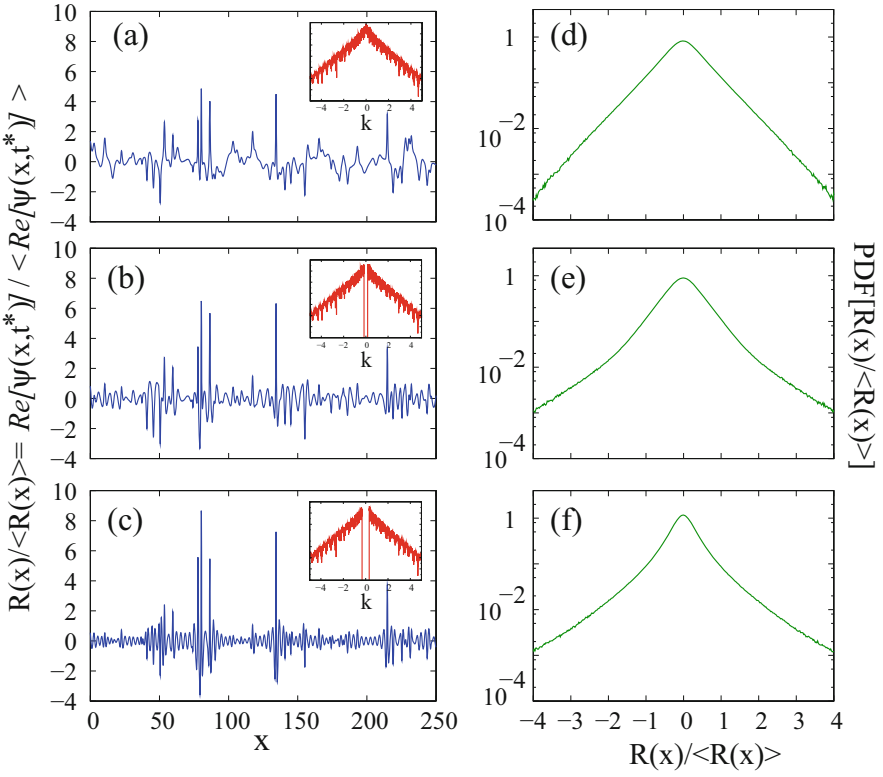

Fig. 11 Reproduced from [53]. Numerical simulations of Eq. (1) in the focusing regime ($\sigma = +1$) for $t^* = 20$. (**a**) Spatial fluctuations of $R(x)/ < R(x) >= \Re(\psi(x,t^*))/ < \Re(\psi(x,t^*)) >$ that are found at the output of an ideal highpass frequency filter having a cutoff frequency $\xi = 0$ [Eq. (6)] and (**d**) corresponding PDF of $R(x)/ < R(x) >$. (**b**) and (**e**), same as (**a**) and (**d**) for $\xi = 1$. (**c**) and (**f**), same as (**a**) and (**d**) for $\xi = 2$. The insets in (**a**), (**b**), (**c**) represents the Fourier power spectra of the random fields plotted in (**a**), (**b**), (**c**)

but for $|\psi(x,t^*)|^2$. Increasing the cutoff frequency ξ of the ideal highpass filter [Eq. (6)], fluctuations of smaller and smaller scales are observed at the output of the highpass filter together with peaks of higher and higher amplitudes, see Fig. 11b, c. Figure 11e, f show that deviations from Gaussianity become heavier when the cutoff frequency ξ of the highpass filter is increased. These statistical features represent qualitative signatures of the intermittency phenomenon. Computing the kurtosis $\kappa(\xi)$ of $R(x) = \Re(\psi(x,t^*))$ for increasing values of the cutoff frequency ξ, we find a monotonic increase that complies with the definition of the intermittency phenomenon given by Frisch, see Fig. 13a [27].

As shown in Fig. 12, features qualitatively similar to those described for the focusing regime are found in the defocusing regime. Figure 12a (resp. Fig. 12d) shows the spatial evolution (resp. the PDF) of $R(x)/ < R(x) >= \Re(\psi(x,t^*))/ < \Re(\psi(x,t^*)) >$ for $\xi = 0$, when the random process is not filtered. The low-tailed

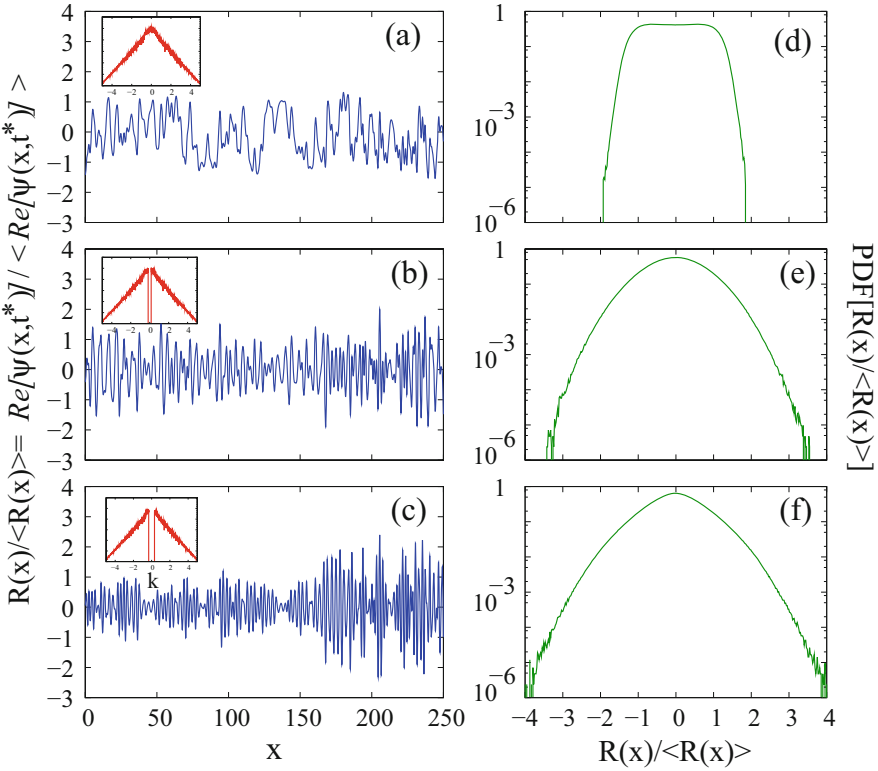

Fig. 12 Reproduced from [53]. Numerical simulations of Eq. (1) in the defocusing regime ($\sigma = -1$) for $t^* = 20$. (**a**) Spatial fluctuations of $R(x)/ < R(x) >= \Re(\psi(x,t^*))/ < \Re(\psi(x,t^*)) >$ that are found at the output of an ideal highpass frequency filter having a cutoff frequency $\xi = 0$ [Eq. (6)] and (**d**) corresponding PDF of $R(x)/ < R(x) >$. (**b**) and (**e**), same as (**a**) and (**d**) for $\xi = 1$. (**c**) and (**f**), same as (**a**) and (**d**) for $\xi = 2$. The insets in (**a**), (**b**), (**c**) represents the Fourier power spectra of the random fields plotted in (**a**), (**b**), (**c**)

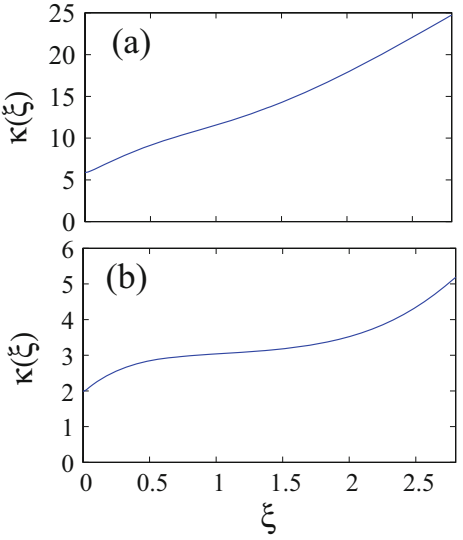

Fig. 13 Reproduced from [53]. Numerical simulations of Eq. (1) for $t^* = 20$. Evolution of the kurtosis κ as a function of the cutoff frequency ξ of the highpass filter defined by Eq. (6). (**a**) Focusing regime ($\sigma = +1$). (**b**) Defocusing regime ($\sigma = -1$)

deviations from Gaussianity shown in Fig. 12d are identical to those already shown in Fig. 7 but for $|\psi(x, t^*)|^2$. They characterize the stationary statistical state found in the defocusing regime. Increasing the cutoff frequency ξ of the ideal highpass filter [Eq.(6)], fluctuations of smaller and smaller scales are observed at the output of the highpass filter together with peaks of higher and higher amplitudes, see Fig. 12b, c. Figure 12e, f show that deviations from PDF computed for $\xi = 0$ become heavier when the cutoff frequency ξ of the highpass filter is increased. As shown in Fig. 13b, the kurtosis $\kappa(\xi)$ monotonically increases with ξ, as for the focusing regime. Let us recall that a kurtosis κ equal to 3 corresponds to a random field having a gaussian statistics. The fact that the initial value of the kurtosis $\kappa(\xi = 0)$ is lower (resp. greater) than 3 in defocusing (resp. focusing) regime complies with the fact that the unfiltered field exhibit low-tailed (resp. heavy-tailed) deviations from Gaussianity at $t^* = 20$. Note that the growth of the kurtosis $\kappa(\xi)$ is greater in focusing regime than in defocusing regime, see Fig. 13.

5 Conclusion

The work presented in this chapter deals with the general question of statistical changes experienced by ensembles of nonlinear random waves propagating in systems ruled by integrable equations. It enters within the framework of "integrable turbulence" which is a new field of research introduced by Zakharov to address specifically this question that "composes a new chapter of the theory of turbulence" [33]. In our work, we have specifically focused on optical fiber systems accurately described by the integrable one-dimensional nonlinear Schrödinger equation. We

have considered random complex fields having a gaussian statistics and an infinite extension at initial stage. Numerical simulations with periodic boundary conditions and optical fiber experiments have been used to investigate spectral and statistical changes experienced by nonlinear waves both in focusing and in defocusing propagation regimes.

As a result of propagation in the strongly nonlinear regime, the power spectrum of the random waves is found to broaden while taking exponential wings both in focusing and in defocusing regimes, see Sects. 2.2 and 2.3. In the nonlinear regime, this spectral broadening phenomenon is a signature of a process in which the typical spatial scale of the random fluctuations decreases to reach the healing length of the wave system at long evolution time. Numerical simulations have revealed that heavy-tailed deviations from gaussian statistics occur in the focusing regime while low-tailed deviations from gaussian statistics are found in the defocusing regime. These statistical behaviors have been observed in optical fiber experiments relying on the implementation of an original and fast detection scheme, see Sect. 3. Numerical simulations made at long evolution times have also shown that the wave system exhibits a statistically stationary state in which neither the PDF of the wave field nor the spectrum change with the evolution variable. Separating fluctuations of small scale from fluctuations of large scale, we have finally revealed the phenomenon of intermittency; i.e., small scales are characterized by large heavy-tailed deviations from Gaussian statistics, while the large ones are almost Gaussian. This intermittency phenomenon has been observed both in focusing and in defocusing propagation regimes, see Sect. 4.

As underlined in Sect. 1, the determination of the PDF of a random wave field represents an issue of importance in the field of integrable turbulence. Given a nonlinear partial differential integrable equation together with some given initial and boundary conditions, there is no systematic theory that allows one to determine the PDF of the wave field at asymptotic stage (i.e. long evolution time).

The wave turbulence (WT) theory describes out-of-equilibrium statistical mechanics of random nonlinear waves in the *weakly* nonlinear regime[1, 12]. Taking into account non resonant terms, WT treatment has been shown to properly describe the evolution of the kurtosis of the wave field together with spectral changes that occur in the weakly nonlinear regime [15, 38, 43]. The general theory of integrable turbulence (in particular in the strongly nonlinear regime) is however still an open fundamental question.

Our experiments and numerical simulations made with non-decaying and non-localized random waves open new questions about statistical properties of incoherent waves in integrable turbulence. First, the statistical properties characterizing the asymptotic stage of integrable turbulence are of fundamentally different natures for waves fluctuating around a constant background and for decaying waves. With continuous random waves having an infinite spatial extension, the nonlinear evolution of the random wave can no longer produce individualized solitons at long time. On the other hand, solitons never separate from each other and they always interact. Moreover solitons on finite background can emerge from nonlinear interaction in the focusing regime. In the defocusing case, the fact that the random

field does not decay at infinity means that dark solitons can be sustained and interact at any time (any value of z in our fiber experiments).

In our work, the relevant boundary conditions are periodic boundary conditions in a box of size L. Random waves of infinite spatial extension such as the ones considered in experiments reported in Sect. 3 can be described by taking the limit of a box of infinite spatial extension ($L \to \infty$). Rigorously speaking, the theoretical framework for dealing with integrable wave systems and periodic boundary conditions is finite gap theory [92]. So far, no theoretical work has been made in this framework to determine statistical properties of ensembles of nonlinear random waves. However some recent results point out the possibility to use the inverse scattering transform for the focusing nonlinear Schrödinger equation with nonzero boundary conditions [52, 65, 93].

The gaussian statistics of the initial condition is a key point of our experimental work. In the focusing regime of the 1D-NLSE, the statistics of the field measured in the statistically stationary state strongly depends on the nature of the initial condition. In our experiments and numerical simulations made with a complex field having initially a gaussian statistics, heavy-tailed deviations from Gaussianity have been observed in the statistically stationary state (i.e. at long time), as discussed in Sect. 2.2 and in Sect. 3. If the initial condition is now made from a plane wave (or a condensate) with an additional noise, the nonlinear stage of modulational instability is characterized by a stationary statistics following the normal law [36]. The fact that there exists such a strong qualitative difference between statistics measured in the stationary state while starting from different noisy initial condition is an intriguing issue.

Several fundamental questions are now opened in the field of integrable turbulence. First of all, the different scenarios leading to the emergence of coherent structures from the propagation of random waves in systems described by 1D-NLSE are not clearly identified and classified. Even the precise identification of the coherent structures themselves is a complex outstanding.

Roughly speaking, the problem of the evolution of a plane wave with small perturbation is often associated with the modulational instability and the emergence of the solitons on finite background (Akhmediev breathers, Peregrine solitons…) [20]. On the other hand, a large initial pulse with zero boundary conditions is known to evolve with complex dynamical features such as dispersive shock waves in the defocusing regime [66, 69, 94] or N-solitons structures in the focusing regime [54, 60]. In integrable turbulence, the stochasticity of the initial conditions together with the non-zero boundary conditions leads to an extremely nontrivial new class of problems.

In the focusing regime, the breather solutions with non-zero background of the 1D-NLSE such as Akhmediev breathers or the Peregrine solitons are often considered as prototypes of rogue waves [24, 61]. These coherent structures have been generated in optical fiber experiments [20, 21] and in hydrodynamical experiments [18]. The interaction of solitons [95] and the collision of breathers have been studied theoretically and experimentally [22]. These nice and important studies need now to be extended in the context of random nonlinear waves. In particular, one

of the open questions is the understanding of the emergence of coherent structures from the two different types of initial conditions, the plane wave with small noise on one hand and the random wave computed from the RP model on the other hand.

A very recent work [65] investigates the influence of the strength of the noise added to an initial plane wave. Many open questions arise from this fundamental problem. In particular, the emergence of solitons or breathers on finite background in both cases (initial conditions made of a condensate or initial conditions made of partially coherent waves with Gaussian statistics) is a complex and wide question.

In the strongly nonlinear regime (i.e. when $H_{NL} >> H_L$ in the initial stage), high-amplitude structures first emerge on the top of the initial fluctuations. If one fluctuation is isolated, the complex "breather-like" dynamics might resemble the one of the N-solitons solutions of 1D-NLSE with zero boundary conditions [54, 60]. A striking result of [82] is that the evolution of a single hump in the semi-classical (small-dispersion) regime generically leads to the emergence of a Peregrine breather. Our numerical simulations [37] and recent experimental [81] results seem to confirm this universal behavior in the context of random waves. The mathematical theory of the dispersive regularization of gradient catastrophes is probably of crucial importance for the understanding of the mechanisms leading to the emergence of coherent structures in the weak dispersion limit (when $H_{NL} >> H_L$ in the initial stage) [82, 96, 97]. Numerical computations of IST spectra will probably be helpful in the classification of the structures emerging in integrable turbulence [52].

Up to now, there is no complete theory that describes the statistical properties of integrable turbulence [32, 34, 36, 37, 65, 81]. To conclude, a major open question in integrable turbulence is to understand the link between the local dynamics (the coherent structures) and the statistical properties of the nonlinear random waves.

Acknowledgements This work has been partially supported by Ministry of Higher Education and Research, Nord-Pas de Calais Regional Council and European Regional Development Fund (ERDF) through the Contrat de Projets Etat-Région (CPER) 2007–2013, as well as by the Agence Nationale de la Recherche through the LABEX CEMPI project (ANR-11-LABX-0007) and the OPTIROC project (ANR-12-BS04-0011 OPTIROC). The authors acknowledge to T. Grava (Trieste, Italy), G. El (Loughborough University) and M. Onorato (University of Torino) for fruitful discussions. The authors acknowledge P. Walczak for his major contribution to the work presented in this chapter.

References

1. Nazarenko, S.: Wave Turbulence. Lecture Notes in Physics. Springer, Berlin, Heidelberg (2011). 10.1007/978-3-642-15942-8
2. Zakharov, V., L'vov, V., Falkovich, G.: Kolmogorov Spectra of Turbulence I. Springer, Berlin (1992)
3. Newell, A.C., Rumpf, B.: Wave turbulence. Annu. Rev. Fluid Mech. **43**, 59–78 (2011)
4. Newell, A.C., Nazarenko, S., Biven, L.: Wave turbulence and intermittency. Physica D **152–153**, 520–550 (2001). Advances in Nonlinear Mathematics and Science: A Special Issue to Honor Vladimir Zakharov

5. Dyachenko, S., Newell, A., Pushkarev, A., Zakharov, V.: Optical turbulence: weak turbulence, condensates and collapsing filaments in the nonlinear schrödinger equation. Physica D **57**(1–2), 96–160 (1992)
6. Connaughton, C., Josserand, C., Picozzi, A., Pomeau, Y., Rica, S.: Condensation of classical nonlinear waves. Phys. Rev. Lett. **95**, 263901 (2005)
7. Aschieri, P., Garnier, J., Michel, C., Doya, V., Picozzi, A.: Condensation and thermalization of classical optical waves in a waveguide. Phys. Rev. A **83**, 033838 (2011)
8. Zakharov, V., Dias, F., Pushkarev, A.: One-dimensional wave turbulence. Phys. Rep. **398**(1), 1–65 (2004)
9. Bortolozzo, U., Laurie, J., Nazarenko, S., Residori, S.: Optical wave turbulence and the condensation of light. J. Opt. Soc. Am. B **26**, 2280–2284 (2009)
10. Barviau, B., Kibler, B., Picozzi, A.: Wave-turbulence approach of supercontinuum generation: influence of self-steepening and higher-order dispersion. Phys. Rev. A **79**, 063840 (2009)
11. Picozzi, A.: Towards a nonequilibrium thermodynamic description of incoherent nonlinear optics. Opt. Express **15**, 9063 (2007)
12. Picozzi, A., Garnier, J., Hansson, T., Suret, P., Randoux, S., Millot, G., Christodoulides, D.: Optical wave turbulence: towards a unified nonequilibrium thermodynamic formulation of statistical nonlinear optics. Phys. Rep. **542**(1), 1–132 (2014)
13. Michel, C., Haelterman, M., Suret, P., Randoux, S., Kaiser, R., Picozzi, A.: Thermalization and condensation in an incoherently pumped passive optical cavity. Phys. Rev. A **84**(3), 033848 (2011)
14. Conforti, M., Mussot, A., Fatome, J., Picozzi, A., Pitois, S., Finot, C., Haelterman, M., Kibler, B., Michel, C., Millot, G.: Turbulent dynamics of an incoherently pumped passive optical fiber cavity: quasisolitons, dispersive waves, and extreme events. Phys. Rev. A **91**, 023823 (2015)
15. Suret, P., Picozzi, A., Randoux, S.: Wave turbulence in integrable systems: nonlinear propagation of incoherent optical waves in single-mode fibers. Opt. Express **19**, 17852–17863 (2011)
16. Turitsyn, S.K., Bednyakova, A.E., Fedoruk, M.P., Papernyi, S.B., Clements, W.R.L.: Inverse four-wave mixing and self-parametric amplification in optical fibre. Nat. Photonics **9**, 608 (2015)
17. Turitsyna, E.G., Smirnov, S.V., Sugavanam, S., Tarasov, N., Shu, X., Podivilov, S.B.E., Churkin, D., Falkovich, G., Turitsyn, S.: The laminar-turbulent transition in a fibre laser. Nat. Photonics **7**, 783–786 (2013)
18. Chabchoub, A., Hoffmann, N.P., Akhmediev, N.: Rogue wave observation in a water wave tank. Phys. Rev. Lett. **106**, 204502 (2011)
19. Chabchoub, A., Hoffmann, N., Onorato, M., Genty, G., Dudley, J.M., Akhmediev, N.: Hydrodynamic supercontinuum. Phys. Rev. Lett. **111**, 054104 (2013)
20. Kibler, B., Fatome, J., Finot, C., Millot, G., Dias, F., Genty, G., Akhmediev, N., Dudley, J.M.: The peregrine soliton in nonlinear fibre optics. Nature Physics **6**(10), 790–795 (2010)
21. Kibler, B., Fatome, J., Finot, C., Millot, G., Genty, G., Wetzel, B., Akhmediev, N., Dias, F., Dudley, J.M.: Observation of kuznetsov-ma soliton dynamics in optical fibre. Sci. Rep. **2** (2012)
22. Frisquet, B., Kibler, B., Millot, G.: Collision of akhmediev breathers in nonlinear fiber optics. Phys. Rev. X **3**(4), 041032 (2013)
23. Kibler, B., Chabchoub, A., Gelash, A., Akhmediev, N., Zakharov, V.E.: Superregular breathers in optics and hydrodynamics: omnipresent modulation instability beyond simple periodicity. Phys. Rev. X **5**, 041026 (2015).
24. Akhmediev, N., Ankiewicz, A., Taki, M.: Waves that appear from nowhere and disappear without a trace. Phys. Lett. A **373**(6), 675–678 (2009)
25. Dudley, J.M., Dias, F., Erkintalo, M., Genty, G.: Instabilities, breathers and rogue waves in optics. Nat. Photonics **8**, 755 (2014)
26. Toenger, S., Godin, T., Billet, C., Dias, F., Erkintalo, M., Genty, G., Dudley, J.M.: Emergent rogue wave structures and statistics in spontaneous modulation instability. Sci. Rep. **5**, Paper No. 10380 (2015)

27. Frisch, U.: Turbulence, the Legacy of A.N. Kolmogorov. Cambridge University Press, Cambridge (1995)
28. Falcon, E., Fauve, S., Laroche, C.: Observation of intermittency in wave turbulence. Phys. Rev. Lett. **98**, 154501 (2007)
29. Falcon, E., Roux, S.G., Laroche, C.: On the origin of intermittency in wave turbulence. Europhys. Lett. **90**(3), 34005 (2010)
30. Nazarenko, S., Lukaschuk, S., McLelland, S., Denissenko, P.: Statistics of surface gravity wave turbulence in the space and time domains. J. Fluid Mech. **642**, 395–420 (2010)
31. Fatome, J., Finot, C., Millot, G., Armaroli, A., Trillo, S.: Observation of optical undular bores in multiple four-wave mixing. Phys. Rev. X **4**, 021022 (2014)
32. Randoux, S., Walczak, P., Onorato, M., Suret, P.: Intermittency in integrable turbulence. Phys. Rev. Lett. **113**, 113902 (2014)
33. Zakharov, V.E.: Turbulence in integrable systems. Stud. Appl. Math. **122**(3), 219–234 (2009)
34. Zakharov, V.E., Gelash, A.A.: Nonlinear stage of modulation instability. Phys. Rev. Lett. **111**, 054101 (2013)
35. Pelinovsky, E., Shurgalina, E., Sergeeva, A., Talipova, T., El, G., Grimshaw, R.: Two-soliton interaction as an elementary act of soliton turbulence in integrable systems. Phys. Lett. A **377**(3–4), 272–275 (2013)
36. Agafontsev, D., Zakharov, V.E.: Integrable turbulence and formation of rogue waves. Nonlinearity **28**(8), 2791 (2015)
37. Walczak, P., Randoux, S., Suret, P.: Optical rogue waves in integrable turbulence. Phys. Rev. Lett. **114**, 143903 (2015)
38. Soh, D.B.S., Koplow, J.P., Moore, S.W., Schroder, K.L., Hsu, W.L.: The effect of dispersion on spectral broadening of incoherent continuous-wave light in optical fibers. Opt. Express **18**, 22393–22405 (2010)
39. Barviau, B., Randoux, S., Suret, P.: Spectral broadening of a multimode continuous-wave optical field propagating in the normal dispersion regime of a fiber. Opt. Lett. **31**, 1696 (2006)
40. Onorato, M., Osborne, A.R., Serio, M., Damiani, T.: Occurrence of freak waves from envelope equations in random ocean wave simulations. Rogue Wave **2000**, 181 (2000)
41. Onorato, M., Osborne, A.R., Serio, M., Cavaleri, L., Brandini, C., Stansberg, C.T.: Observation of strongly non-gaussian statistics for random sea surface gravity waves in wave flume experiments. Phys. Rev. E **70**, 067302 (2004)
42. Onorato, M., Osborne, A., Serio, M., Cavaleri, L.: Modulational instability and non-gaussian statistics in experimental random water-wave trains. Phys. Fluids (1994-present) **17**(7), 078101 (2005)
43. Janssen, P.A.E.M.: Nonlinear four-wave interactions and freak waves. J. Phys. Oceanogr. **33**, 863 (2003)
44. Annenkov, S.Y., Shrira, V.I.: Fast nonlinear evolution in wave turbulence. Phys. Rev. Lett. **102**, 024502 (2009)
45. Derevyanko, S., Small, E.: Nonlinear propagation of an optical speckle field. Phys. Rev. A **85**(5), 053816 (2012)
46. Bromberg, Y., Lahini, U., Small, E., Silberberg, Y.: Hanbury Brown and Twiss interferometry with interacting photons. Nat. Photonics **4**, 721–726 (2010)
47. Osborne, A.R., Segre, E., Boffetta, G., Cavaleri, L.: Soliton basis states in shallow-water ocean surface waves. Phys. Rev. Lett. **67**, 592–595 (1991)
48. Osborne, A.R.: Behavior of solitons in random-function solutions of the periodic korteweg–de vries equation. Phys. Rev. Lett. **71**, 3115–3118 (1993)
49. Osborne, A.R., Petti, M.: Laboratory generated, shallow water surface waves: Analysis using the periodic, inverse scattering transform. Phys. Fluids **6**(5), 1727–1744 (1994)
50. Slunyaev, A.: Nonlinear analysis and simulations of measured freak wave time series. Eur. J. Mech. B. Fluids **25**(5), 621–635 (2006). Rogue waves European Geosciences Union Assembly
51. Costa, A., Osborne, A.R., Resio, D.T., Alessio, S., Chrivì, E., Saggese, E., Bellomo, K., Long, C.E.: Soliton turbulence in shallow water ocean surface waves. Phys. Rev. Lett. **113**, 108501 (2014)

52. Randoux, S., Suret, P., El, G.: Identification of rogue waves from scattering transform analysis of periodized waveforms (2015). arXiv:1512.04707
53. Randoux, S., Walczak, P., Onorato, M., Suret, P.: Nonlinear random optical waves: integrable turbulence, rogue waves and intermittency. Physica D (2016). http://dx.doi.org/10.1016/j.physd.2016.04.001
54. Agrawal, G.P.: Nonlinear Fiber optics, 3rd edn. Optics and Photonics. Academic, New York (2001)
55. Bass, F., Kivshar, Y., Konotop, V.: Diffraction of nonlinear spatially incoherent wave. Sov. Phys. JETP **65**, 245 (1987)
56. Derevyanko, S.A., Prilepsky, J.E.: Random input problem for the nonlinear Schrödinger equation. Phys. Rev. E **78**, 046610 (2008)
57. Islas, A.L., Schober, C.M.: Predicting rogue waves in random oceanic sea states. Phys. Fluids **17**(3), Paper No. 031701 (2005)
58. Onorato, M., Osborne, A.R., Serio, M., Bertone, S.: Freak waves in random oceanic sea states. Phys. Rev. Lett. **86**, 5831–5834 (2001)
59. Mandel, L., Wolf, E.: Optical Coherence and Quantum Optics. Cambridge University Press, Cambridge (1995). Cambridge Books Online
60. Yang, J.: Nonlinear Waves in Integrable and Nonintegrable Systems, vol. 16. SIAM, Philadelphia (2010)
61. Akhmediev, N., Soto-Crespo, J., Ankiewicz, A.: Extreme waves that appear from nowhere: on the nature of rogue waves. Phys. Lett. A **373**(25), 2137–2145 (2009)
62. Efimov, A., Yulin, A.V., Skryabin, D.V., Knight, J.C., Joly, N., Omenetto, F.G., Taylor, A.J., Russell, P.: Interaction of an optical soliton with a dispersive wave. Phys. Rev. Lett. **95**, 213902 (2005)
63. Böhm, M., Mitschke, F.: Soliton-radiation beat analysis. Phys. Rev. E **73**, 066615 (2006)
64. El, G. A., Kamchatnov, A.M.: Kinetic equation for a dense soliton gas. Phys. Rev. Lett. **95**, 204101 (2005)
65. Soto-Crespo, J.M., Devine, N., Akhmediev, N.: Integrable turbulence and rogue waves: breathers or solitons? Phys. Rev. Lett. **116**, 103901 (2016)
66. El, G., Hoefer, M.: Dispersive shock waves and modulation theory (2016). arXiv preprint arXiv:1602.06163
67. Conforti, M., Trillo, S.: Dispersive wave emission from wave breaking. Opt. Lett. **38**, 3815–3818 (2013)
68. El, G.A., Grimshaw, R.H.J., Kamchatnov, A.M.: Wave breaking and the generation of undular bores in an integrable shallow water system. Stud. Appl. Math. **114**(4), 395–411 (2005)
69. Kamchatnov, A., Kraenkel, R.A., Umarov, B.: Asymptotic soliton train solutions of the defocusing nonlinear Schrödinger equation. Phys. Rev. E **66**(3), 036609 (2002)
70. Fratalocchi, A., Conti, C., Ruocco, G., Trillo, S.: Free-energy transition in a gas of noninteracting nonlinear wave particles. Phys. Rev. Lett. **101**, 044101 (2008)
71. Babin, S.A., Churkin, D.V., Ismagulov, A.E., Kablukov, S.I., Podivilov, E.V.: Four-wave-mixing-induced turbulent spectral broadening in a long raman fiber laser. J. Opt. Soc. Am. B **24**, 1729 (2007)
72. Turitsyn, S.K., Babin, S.A., El-Taher, A.E., Harper, P., Churkin, D.V., Kablukov, S.I., Ania-Castañón, J.D., Karalekas, V., Podivilov, E.V.: Random distributed feedback fibre laser. Nat. Photonics **4**, 231 (2010)
73. Gorbunov, O.A., Sugavanam, S., Churkin, D.: Revealing statistical properties of quasi-cw fibre lasers in bandwidth-limited measurements. Opt. Express **22**(23), 28071–28076 (2014)
74. Solli, D.R., Ropers, C., Koonath, P., Jalali, B.: Optical rogue waves. Nature **450**, 1054–1057 (2007)
75. Walczak, P., Randoux, S., Suret, P.: Statistics of a turbulent raman fiber laser. Opt. Lett. **40**(13), 3101 (2015)
76. Erkintalo, M., Genty, G., Dudley, J.M.: Rogue-wave-like characteristics in femtosecond supercontinuum generation. Opt. Lett. **34**, 2468–2470 (2009)

77. Randoux, S., Suret, P.: Experimental evidence of extreme value statistics in raman fiber lasers. Opt. Lett. **37**, 500–502 (2012)
78. Jalali, B., Solli, D., Goda, K., Tsia, K., Ropers, C.: Real-time measurements, rare events and photon economics. Eur. Phys. J. Special Topics **185**(1), 145–157 (2010)
79. Wetzel, B., Stefani, A., Larger, L., Lacourt, P.-A., Merolla, J.-M., Sylvestre, T.: Kudlinski, A., Mussot, A., Genty, G., Dias, F., Dudley, J.: Real-time full bandwidth measurement of spectral noise in supercontinuum generation. Sci. Rep. **2**, Paper No. 882 (2012)
80. Goda, K., Jalali, B.: Dispersive fourier transformation for fast continuous single-shot measurements. Nat. Photonics **7**(2), 102–112 (2013)
81. Suret, P., Koussaifi, R.E., Tikan, A., Evain, C., Randoux, S., Szwaj, C., Bielawski, S.: Direct observation of rogue waves in optical turbulence using time microscopy (2016). arXiv preprint arXiv:1603.01477
82. Bertola, M., Tovbis, A.: Universality for the focusing nonlinear schrödinger equation at the gradient catastrophe point: rational breathers and poles of the tritronquée solution to painlevé i. Commun. Pure Appl. Math. **66**(5), 678–752 (2013)
83. Dudley, J.M., Genty, G., Dias, F., Kibler, B., Akhmediev, N.: Modulation instability, akhmediev breathers and continuous wave supercontinuum generation. Opt. Express **17**, 21497–21508 (2009)
84. Akhmediev, A., Dudley, J.M., Solli, D.R., Turitsyn, S.K.: Recent progress in investigating optical rogue waves. J. Opt. **15**(6), 060201 (2013)
85. Hammani, K., Kibler, B., Finot, C., Picozzi, A.: Emergence of rogue waves from optical turbulence. Phys. Lett. A **374**(34), 3585–3589 (2010)
86. Kibler, B., Hammani, K., Michel, C., Finot, C., Picozzi, A.: Rogue waves, rational solitons and wave turbulence theory. Phys. Lett. A **375**(35), 3149–3155 (2011)
87. Mori, M.O., Nobuhito, M., Janssen, P.A.E.M.: On the estimation of the kurtosis in directional sea states for freak wave forecasting. J. Phys. Oceanogr. **41**, 1484 (2011)
88. Onorato, M., Residori, S., Bortolozzo, U., Montina, A., Arecchi, F.: Rogue waves and their generating mechanisms in different physical contexts. Phys. Rep. **528**(2), 47–89 (2013)
89. Sreenivasan, K.R.: On the fine-scale intermittency of turbulence. J. Fluid Mech. **151**, 81–103 (1985)
90. Alexandrova, O., Carbone, V., Veltri, P., Sorriso-Valvo, L.: Solar wind cluster observations: turbulent spectrum and role of hall effect. Planet. Space Sci. **55**(15), 2224–2227 (2007). Dynamical Processes in Space Plasmas Dynamical Processes in Space Plasmas
91. Bosch, E., van de Water, W.: Spatiotemporal intermittency in the faraday experiment. Phys. Rev. Lett. **70**, 3420–3423 (1993)
92. Osborne, A.: Nonlinear Ocean Waves. Academic, New York (2010)
93. Biondini, G., Kovačič, G.: Inverse scattering transform for the focusing nonlinear schrödinger equation with nonzero boundary conditions. J. Math. Phys. **55**(3), Paper No. 031506 (2014)
94. Kamchatnov, A., Gammal, A., Kraenkel, R.A.: Dissipationless shock waves in Bose-Einstein condensates with repulsive interaction between atoms. Phys. Rev. A **69**(6), 063605 (2004)
95. Pelinovsky, E., Kharif, C., et al.: Extreme Ocean Waves. Springer, Berlin (2008)
96. Kamvissis, S., McLaughlin, K.D.-R., Miller, P.D.: Semiclassical Soliton Ensembles for the Focusing Nonlinear Schrodinger Equation (AM-154). vol. 154 (Princeton University Press, Princeton, NJ, 2003)
97. El, G.A., Khamis, E.G., Tovbis, A.: Dam break problem for the focusing nonlinear schrödinger equation and the generation of rogue waves (2015). Arxiv Preprint arXiv:1505.01785

Whitham Modulation Equations and Application to Small Dispersion Asymptotics and Long Time Asymptotics of Nonlinear Dispersive Equations

Tamara Grava

Abstract In this chapter we review the theory of modulation equations or Whitham equations for the travelling wave solution of KdV. We then apply the Whitham modulation equations to describe the long-time asymptotics and small dispersion asymptotics of the KdV solution.

1 Introduction

The theory of modulation refers to the idea of slowly changing the constant parameters in a solution to a given PDE. Let us consider for example the linear PDE in one spatial dimension

$$u_t + \epsilon^2 u_{xxx} = 0, \tag{1}$$

where ϵ is a small positive parameter. Such equation admits the exact travelling wave solution

$$u(x,t) = a\cos\left(k\frac{x}{\epsilon} + \omega\frac{t}{\epsilon}\right), \quad \omega = k^3$$

where a and k are constants. Here $\frac{x}{\epsilon}$ and $\frac{t}{\epsilon}$ are considered as fast variables since $0 < \epsilon \ll 1$. The general solution of Eq. (1) restricted for simplicity to even initial

T. Grava (✉)
School of Mathematics, University of Bristol, Bristol BS8 1TW, UK

Mathematic Area, SISSA, Via Bonomea 265, 34100 Trieste, Italy
e-mail: grava@sissa.it; tamara.grava@bristol.ac.uk

M. Onorato et al. (eds.), *Rogue and Shock Waves in Nonlinear Dispersive Media*,
Lecture Notes in Physics 926, DOI 10.1007/978-3-319-39214-1_10

data $f(x)$ is given by

$$u(x,t;\epsilon) = \int_0^\infty F(k;\epsilon)\cos\left(k\frac{x}{\epsilon} + \omega\frac{t}{\epsilon}\right)dk$$

where the function $F(k;\epsilon)$ depends on the initial conditions by the inverse Fourier transform $F(k;\epsilon) = \frac{1}{\pi\epsilon}\int_{-\infty}^{\infty} f(x)e^{-ik\frac{x}{\epsilon}}dx$.

For fixed ϵ, the large time asymptotics of $u(x,t;\epsilon)$ can be obtained using the method of stationary phase

$$u(x,t;\epsilon) \simeq F(k;\epsilon)\sqrt{\frac{2\pi}{t|\omega''(k)|}}\cos\left(k\frac{x}{\epsilon} + \omega\frac{t}{\epsilon} - \frac{\pi}{4}\operatorname{sign}\omega''(k)\right), \tag{2}$$

where now $k = k(x,t)$ solves

$$x + \omega'(k)t = 0. \tag{3}$$

We will now obtain a formula compatible with (2) using the modulation theory. Let us assume that the amplitude a and the wave number k are slowly varying functions of space and time:

$$a = a(x,t), \quad k = k(x,t).$$

Plugging the expression

$$u(x,t;\epsilon) = a(x,t)\cos\left(k(x,t)\frac{x}{\epsilon} + \omega(x,t)\frac{t}{\epsilon}\right),$$

into Eq. (1) one obtains from the terms of order one the equations

$$k_t = \omega'(k)k_x, \quad a_t = \omega'(k)a_x + \frac{1}{2}a\omega''(k)k_x, \tag{4}$$

which describe the modulation of the wave parameters a and k. The curve $\frac{dx}{dt} = -\omega'(k)$ is a characteristic for both the above equations. On such curve

$$\frac{dk}{dt} = 0, \quad \frac{da}{dt} = \frac{1}{2}a\omega''(k)k_x.$$

We look for a self-similar solution of the above equation in the form $k = k(z)$ with $z = x/t$. The first equation in (4) gives

$$(z + \omega'(k))k_z = 0$$

which has the solutions $k_z = 0$ or $z + \omega'(k) = 0$. This second solution is equivalent to (3). Plugging this solution into the equation for the amplitude a one gets

$$\frac{da}{dt} = -\frac{a}{2t}, \quad \text{or } a(x,t) = \frac{a_0(k)}{\sqrt{t}},$$

for an arbitrary function $a_0(k)$. Such expression gives an amplitude $a(x,t)$ compatible with the stationary phase asymptotic (2).

2 Modulation of Nonlinear Equation

Now let us consider a similar problem for a nonlinear equation, by adding a nonlinear term $6uu_x$ to Eq. (1)

$$u_t + 6uu_x + \epsilon^2 u_{xxx} = 0. \tag{5}$$

Such equation is called Korteweg de Vries (KdV) equation, and it describes the behaviour of long waves in shallow water. The coefficient 6 is front of the nonlinear term, is just put for convenience. The KdV equation admits the travelling wave solution

$$u(x,t;\epsilon) = \eta(\phi), \quad \phi = \frac{1}{\epsilon}(kx - \omega t + \phi_0),$$

where we assumed that η is a 2π-periodic function of its argument and ϕ_0 is an arbitrary constant. Plugging the above ansatz into the KdV equation one obtains after a double integration

$$\frac{k^2}{2}\eta_\phi^2 = -\eta^3 + V\eta^2 + B\eta + A, \quad V = \frac{\omega}{2k}, \tag{6}$$

where A and B are integration constants and V is the wave velocity. In order to get a periodic solution, we assume that the polynomial $-\eta^3 + V\eta^2 + B\eta + A = -(\eta - e_1)(\eta - e_2)(\eta - e_3)$ with $e_1 > e_2 > e_3$. Then the periodic motion takes place for $e_2 \le \eta \le e_1$ and one has the relation

$$k\frac{d\eta}{\sqrt{2(e_1 - \eta)(\eta - e_2)(\eta - e_3)}} = d\phi, \tag{7}$$

so that integrating over a period, one obtains

$$2k\int_{e_2}^{e_1} \frac{d\eta}{\sqrt{2(e_1 - \eta)(\eta - e_2)(\eta - e_3)}} = \oint d\phi = 2\pi.$$

It follows that the wavenumber $k = \dfrac{2\pi}{L}$ is expressed by a complete integral of the first kind:

$$k = \pi \frac{\sqrt{(e_1 - e_3)}}{\sqrt{2}K(m)}, \quad m = \frac{e_1 - e_2}{e_1 - e_3}, \quad K(m) := \int_0^{\frac{\pi}{2}} \frac{d\psi}{\sqrt{1 - m^2 \sin^2 \psi}}, \tag{8}$$

and the frequency

$$\omega = 2k(e_1 + e_2 + e_3)\,, \tag{9}$$

is obtained by comparison with the polynomial in the r.h.s. of (6). Performing an integral between e_1 and η in Eq. (7) one arrives to the equation

$$\int_0^{\psi} \frac{d\psi'}{\sqrt{1 - s^2 \sin^2 \psi'}} = -\phi \frac{\sqrt{e_1 - e_3}}{\sqrt{2}k} + K(m), \quad \cos\psi = \frac{\sqrt{\eta - e_1}}{\sqrt{e_2 - e_1}}.$$

Introducing the Jacobi elliptic function $\mathrm{cn}\left(-\phi \dfrac{\sqrt{e_1 - e_3}}{\sqrt{2}k} + K(m); m\right) = \cos\psi$ and using the above equations we obtain

$$u(x,t;\epsilon) = \eta(\phi) = e_2 + (e_1 - e_2)\mathrm{cn}^2\left(\frac{\sqrt{e_1 - e_3}}{\sqrt{2}\epsilon}\left(x - \frac{\omega}{k}t + \frac{\phi_0}{k}\right) - K(m); m\right), \tag{10}$$

where we use also the evenness of the function $\mathrm{cn}(z;m)$.

The function $\mathrm{cn}^2(z;m)$ is periodic with period $2K(m)$ and has its maximum at $z = 0$ where $\mathrm{cn}(0;m) = 1$ and its minimum at $z = K(m)$ where $\mathrm{cn}(K(m);m) = 0$. Therefore from (10), the maximum value of the function $u(x,t;\epsilon)$ is $u_{max} = e_1$ and the minimum value is $u_{\min} = e_2$.

2.1 Whitham Modulation Equations

Now, as we did it in the linear case, let us suppose that the integration constants A, B and V depend weekly on time and space

$$A = A(x,t), \quad B = B(x,t), \quad V = V(x,t).$$

It follows that the wave number and the frequency depends weakly on time and space too. We are going to derive the equations of $A = A(x,t)$, $B = B(x,t)$ and $V = V(x,t)$ in such a way that (10) is an approximate solution of the KdV equation (5) up to sub-leading corrections. We are going to apply the nonlinear analogue of

the WKB theory introduced in [17]. For the purpose let us assume that

$$u = u(\phi(x,t), x, t), \quad \phi = \frac{\theta}{\epsilon} \tag{11}$$

Pluggin the ansatz (11) into the KdV equation one has

$$u_\phi \frac{\theta_t}{\epsilon} + u_t + 6u(u_\phi \frac{\theta_x}{\epsilon} + u_x) + \frac{\theta_x^3}{\epsilon} u_{\phi\phi\phi} + 3\theta_x^2 u_{\phi\phi x} + 3\theta_x \epsilon u_{\phi xx} + 3\theta_{xx}\epsilon u_{\theta x}$$
$$+3\theta_{xx}\theta_x u_{\phi\phi} + \theta_{xxx}\epsilon u_\phi + \epsilon^2 u_{xxx} = 0. \tag{12}$$

Next assuming that u has an expansion in power of ϵ, namely $u = u_0 + \epsilon u_1 + \epsilon^2 u_2 + \ldots$ one obtain from (12) at order $1/\epsilon$

$$\theta_t u_{0,\phi} + 6\theta_x u_0 u_{0,\phi} + \theta_x^3 u_{0,\phi\phi\phi} = 0.$$

The above equation gives the cnoidal wave solution (10) if $u_0(\phi) = \eta(\phi)$ and

$$\theta_t = -\omega, \quad \theta_x = k, \tag{13}$$

where k and ω are the frequency and wave number of the cnoidal wave as defined in (8) and (9) respectively. Compatibility of Eq. (13) gives

$$k_t + \omega_x = 0, \tag{14}$$

which is the first equation we are looking for. To obtain the other equations let us introduce the linear operator

$$\mathscr{L} := \omega \frac{\partial}{\partial\phi} - 6k \frac{\partial}{\partial\phi} u_0 - k^3 \frac{\partial^3}{\partial\phi^3},$$

with formal adjoint $\mathscr{L}^\dagger = \omega \frac{\partial}{\partial\phi} - 6ku_0 \frac{\partial}{\partial\phi} - k^3 \frac{\partial^3}{\partial\phi^3}$. Then at order ϵ^0 Eq. (12) gives

$$\mathscr{L} u_1 = R(u_0), \quad R(u_0) := u_{0,t} + 6u_0 u_{0,x} + 3\theta_x^2 u_{0,\phi\phi x} + 3\theta_{xx}\theta_x u_{0,\phi\phi}.$$

In a similar way it is possible to get the equations for the higher order correction terms. A condition of solvability of the above equation can be obtained by observing that the integral over a period of the l.h.s of the above equation against the constant function and the function u_0 is equal to zero because 1 and u_0 are in the kernel of

$\mathscr{L}^{\dagger}$. Therefore it follows that

$$0 = \int_0^{2\pi} R(u_0)d\phi = \partial_t \int_0^{2\pi} u_0 d\phi + 3\partial_x \int_0^{2\pi} u_0^2 d\phi$$

and

$$0 = \int_0^{2\pi} u_0 R(u_0)d\phi = \partial_t \int_0^{2\pi} \frac{1}{2}u_0^2 d\phi + 2\partial_x \int_0^{2\pi} u_0^3 d\phi$$
$$+3\int_0^{2\pi} u_0(\theta_x^2 u_{0,\phi\phi x} + \theta_{xx}\theta_x u_{0,\phi\phi})d\phi.$$

By denoting with the bracket $\langle\,.\,\rangle$ the average over a period, we rewrite the above two equations, after elementary algebra and an integration by parts, in the form

$$\partial_t\langle u_0\rangle + 3\partial_x\langle u_0^2\rangle = 0 \tag{15}$$
$$\partial_t\langle u_0^2\rangle + 4\partial_x\langle u_0^3\rangle - 3\partial_x\langle\theta_x^2 u_{0,\phi}^2\rangle = 0. \tag{16}$$

Using the identities

$$\langle u_0 u_{0,\phi\phi} + u_{0,\phi}^2\rangle = 0, \quad \langle u_{0,\phi\phi}\rangle = 0,$$

and (6), we obtained the identities for the elliptic integrals

$$\int_{e_1}^{e_2} \frac{5\eta^3 - 4V\eta^2 - 3B\eta - 2A}{\sqrt{-\eta^3 + V\eta^2 + B\eta + A}}d\eta = 0, \quad \int_{e_1}^{e_2} \frac{-3\eta^2 + 2V\eta + B}{\sqrt{-\eta^3 + V\eta^2 + B\eta + A}}d\eta = 0.$$

Introducing the integral $W := \frac{\sqrt{2}}{\pi}\int_{e_1}^{e_2}\sqrt{-\eta^3 + V\eta^2 + B\eta + A}d\eta$ and using the above two identities and the relations $k = W_A$, $\langle u_0\rangle = 2\pi k W_B$ and $\langle u_0^2\rangle = 2\pi k W_V$ where W_A, W_B and W_V are the partial derivatives of W with respect to A, B and V respectively, we can reduce (14), (15) and (16) to the form

$$\frac{\partial}{\partial t}W_A + 2V\frac{\partial}{\partial x}W_A - 2W_A\frac{\partial}{\partial x}V = 0 \tag{17}$$
$$\frac{\partial}{\partial t}W_B + 2V\frac{\partial}{\partial x}W_B + W_A\frac{\partial}{\partial x}B = 0 \tag{18}$$
$$\frac{\partial}{\partial t}W_V + 2V\frac{\partial}{\partial x}W_V - 2W_A\frac{\partial}{\partial x}A = 0. \tag{19}$$

Equations (17), (18) and (19) are the Whitham modulation equations for the parameters A, B and V. The same equations can also be derived according to

Whitham's original ideas of averaging method applied to conservation laws, to Lagrangian or to Hamiltonians [57]. Using e_1, e_2 and e_3 as independent variables, instead of their symmetric function A, B and V, Whitham reduced the above three equations to the form

$$\frac{\partial}{\partial t}e_j + \sum_{k=1}^{3} \sigma_j^k \frac{\partial}{\partial x} e_k = 0, \quad j = 1, 2, 3, \tag{20}$$

for the matrix σ_j^k given by

$$\sigma = 2V - W_A \begin{pmatrix} \partial_{e_1} W_A & \partial_{e_2} W_A & \partial_{e_3} W_A \\ \partial_{e_1} W_B & \partial_{e_2} W_B & \partial_{e_3} W_B \\ \partial_{e_1} W_V & \partial_{e_2} W_B & \partial_{e_3} W_V \end{pmatrix}^{-1} \begin{pmatrix} 2 & 2 & 2 \\ e_2 + e_3 & e_1 + e_3 & e_1 + e_2 \\ 2e_2e_3 & 2e_1e_3 & 2e_1e_2 \end{pmatrix},$$

where $\partial_{e_i} W_A$ is the partial derivative with respect to e_i and the same notation holds for the other quantities. Equations (20) is a system of quasi-linear equations for $e_j = e_j(x, t), j = 1, 2, 3$. Generically, a quasi-linear 3×3 system cannot be reduced to a diagonal form. However Whitham, analyzing the form of the matrix σ, was able to get the Riemann invariants that reduce the system to diagonal form. Indeed making the change of coordinates

$$\beta_1 = \frac{e_2 + e_1}{2}, \quad \beta_2 = \frac{e_1 + e_3}{2}, \quad \beta_3 = \frac{e_2 + e_3}{2}, \tag{21}$$

with

$$\beta_3 < \beta_2 < \beta_1,$$

the Whitham modulation equations (20) are diagonal and take the form

$$\frac{\partial}{\partial t}\beta_i + \lambda_i \frac{\partial}{\partial x}\beta_i = 0, \quad i = 1, 2, 3, \tag{22}$$

where the characteristics speeds $\lambda_i = \lambda_i(\beta_1, \beta_2, \beta_3)$ are

$$\lambda_i = 2(\beta_1 + \beta_2 + \beta_3) + 4\frac{\prod_{i \neq k}(\beta_i - \beta_k)}{\beta_i + \alpha}, \tag{23}$$

$$\alpha = -\beta_1 + (\beta_1 - \beta_3)\frac{E(m)}{K(m)}, \quad m = \frac{\beta_2 - \beta_3}{\beta_1 - \beta_3}, \tag{24}$$

where $E(m) = \int_0^{\pi/2} \sqrt{1 - m \sin \psi^2} d\psi$ is the complete elliptic integral of the second kind. Another compact form of the Whitham modulations equations (22) is

$$\frac{\partial k}{\partial \beta_i} \frac{\partial \beta_i}{\partial t} + \frac{\partial \omega}{\partial \beta_i} \frac{\partial \beta_i}{\partial x} = 0, \quad i = 1, 2, 3, \tag{25}$$

where the above equations do not contain the sum over repeated indices. Observe that the above expression can be derived from the conservation of waves (14) by assuming that the Riemann invariants $\beta_1 > \beta_2 > \beta_3$ vary independently. Such form (25) is quite general and easily adapts to other modulation equations (see for example the book [34]). The equations (25) gives another expression for the speed $\lambda_i = 2(\beta_1 + \beta_2 + \beta_3) + 2\frac{k}{\partial_{\beta_i} k}$ which was obtained in [30].

The Whitham equations are a systems of 3×3 quasi-linear hyperbolic equations namely for $\beta_1 > \beta_2 > \beta_3$ one has [42]

$$\lambda_1 > \lambda_2 > \lambda_3.$$

Using the expansion of the elliptic integrals as $m \to 0$ (see e.g. [40])

$$K(m) = \frac{\pi}{2}\left(1 + \frac{m}{4} + \frac{9}{64}m^2 + O(m^3)\right), \quad E(m) = \frac{\pi}{2}\left(1 - \frac{m}{4} - \frac{3}{64}m^2 + O(m^3)\right), \tag{26}$$

and $m \to 1$

$$E(m) \simeq 1 + \frac{1}{2}(1 - \sqrt{m})\left[\log \frac{16}{1-m} - 1\right], \quad K(m) \simeq \frac{1}{2} \log \frac{16}{1-m}, \tag{27}$$

one can verify that the speeds λ_i have the following limiting behaviour respectively

- at $\beta_2 = \beta_1$

$$\begin{aligned} &\lambda_1(\beta_1, \beta_1, \beta_3) = \lambda_2(\beta_1, \beta_1, \beta_3) = 4\beta_1 + 2\beta_3 \\ &\lambda_3(\beta_1, \beta_1, \beta_3) = 6\beta_3; \end{aligned} \tag{28}$$

- at $\beta_2 = \beta_3$ one has

$$\begin{aligned} &\lambda_1(\beta_1, \beta_3, \beta_3) = 6\beta_1 \\ &\lambda_2(\beta_1, \beta_3, \beta_3) = \lambda_3(\beta_1, \beta_3, \beta_3) = 12\beta_3 - 6\beta_1. \end{aligned} \tag{29}$$

Namely, when $\beta_1 = \beta_2$, the equation for β_3 reduces to the Hopf equation $\frac{\partial}{\partial t}\beta_3 + 6\beta_3\frac{\partial}{\partial x}\beta_3 = 0$. In the same way when $\beta_2 = \beta_3$ the equation for β_1 reduces to the Hopf equation.

In the coordinates β_i, $i = 1, 2, 3$ the travelling wave solution (10) takes the form

$$u(x,t;\epsilon) = \beta_1 + \beta_3 - \beta_2 + 2(\beta_2 - \beta_3)\mathrm{cn}^2\left(K(m)\frac{\Omega}{\pi\epsilon} + K(m); m\right), \tag{30}$$

where

$$\Omega := kx - \omega t + \phi_0 = \pi\frac{\sqrt{\beta_1 - \beta_3}}{K(m)}(x - 2t(\beta_1 + \beta_2 + \beta_3)) + \phi_0, \quad m = \frac{\beta_2 - \beta_3}{\beta_1 - \beta_3}. \tag{31}$$

We recall that

$$k = \pi\frac{\sqrt{\beta_1 - \beta_3}}{K(m)}, \quad \omega = 2k(\beta_1 + \beta_2 + \beta_3), \tag{32}$$

are the wave-number and frequency of the oscillations respectively.

In the formal limit $\beta_1 \to \beta_2$, the above cnoidal wave reduce to the soliton solution since $\mathrm{cn}(z, m) \overset{m\to 1}{\to} \mathrm{sech}(z)$, while the limit $\beta_2 \to \beta_3$ is the small amplitude limit where the oscillations become linear and $\mathrm{cn}(z, m) \overset{m\to 0}{\to} \cos(z)$. Using identities among elliptic functions [40] we can rewrite the travelling wave solution (30) using theta-functions

$$u(x,t,\epsilon) = \beta_1 + \beta_2 + \beta_3 + 2\alpha + 2\epsilon^2\frac{\partial^2}{\partial x^2}\log\vartheta\left(\frac{\Omega(x,t)}{2\pi\epsilon}; \tau\right), \tag{33}$$

with α as in (24) and where for any $z \in \mathbb{C}$ the function $\vartheta(z;\tau)$ is defined by the Fourier series

$$\vartheta(z;\tau) = \sum_{n\in\mathbb{Z}} e^{\pi i n^2\tau + 2\pi i n z}, \quad \tau = i\frac{K'(m)}{K(m)}. \tag{34}$$

Formula (33) comes out when dealing with the theory of finite-gap integration of the KdV equation and it is a particular case of the Its-Matveev formula [33] that describes the quasi-periodic solutions of the KdV equation through higher order θ-functions.

Remark 2.1 We remark that for fixed β_1, β_2 and β_3, formulas (30) or (33) give an exact solution of the KdV equation (5), while when $\beta_j = \beta_j(x,t)$ evolves according to the Whitham equations, such formulas give an approximate solution of the KdV equation (5). We also remark that in the derivation of the Whitham equations, we did not get any information for an eventual modulation of the arbitrary phase ϕ_0. The modulation of the phase requires a higher order analysis, that won't be explained here. However we will give below a formula for the phase.

Remark 2.2 The Riemann invariants β_1, β_2 and β_3 have an important spectral meaning. Let us consider the spectrum of the Schrödinger equation

$$\epsilon^2 \frac{d^2}{dx^2}\Psi + u\Psi = -\lambda\Psi,$$

where $u(x,t;\epsilon)$ is a solution of the KdV equation. The main discovery of Gardener, Green Kruskal and Miura [23] is that the spectrum of the Schrödinger operator is constant in time if $u(x,t;\epsilon)$ evolve according to the KdV equation. This important observation is the starting point of inverse scattering and the modern theory of integrable systems in infinite dimensions.

If $u(x,t;\epsilon)$ is the travelling wave solution (33), where $\beta_1 > \beta_2 > \beta_3$ are constants, then the Schrödinger equation coincides with the Lamé equation and its spectrum coincides with the Riemann invariants $\beta_1 > \beta_2 > \beta_3$. The stability zones of the spectrum are the bands $(-\infty, \beta_3] \cup [\beta_2, \beta_1]$. The corresponding solution $\Psi(x,t;\lambda)$ of the Schrödinger equation is quasi-periodic in x and t with monodromy

$$\Psi(x+\epsilon L, t;\lambda) = e^{ip(\lambda)L}\Psi(x,t;\lambda)$$

and

$$\Psi(x,t+\epsilon T;\lambda) = e^{iq(\lambda)T}\Psi(x,t;\lambda),$$

where ϵL and ϵT are the wave-length and the period of the oscillations. The functions $p(\lambda)$ and $q(\lambda)$ are called quasi-momentum and quasi-energy and for the cnoidal wave solution they take the simple form

$$p(\lambda) = \int_{\beta_2}^{\lambda} dp(\lambda'), \quad q(\lambda) = \int_{\beta_2}^{\lambda} dq(\lambda'),$$

where dp and dq are given by the expression

$$dp(\lambda) = \frac{(\lambda+\alpha)d\lambda}{2\sqrt{(\gamma_1-\lambda)(\lambda-\gamma_2)(\lambda-\gamma_3)}}, \quad dq(\lambda) = 12\frac{(\lambda^2 - \frac{1}{2}(\gamma_1+\gamma_2+\gamma_3)\lambda + \gamma)d\lambda}{2\sqrt{(\gamma_1-\lambda)(\lambda-\gamma_2)(\lambda-\gamma_3)}}$$

with the constant α defined in (24) and $\gamma = \frac{\alpha}{6}(\gamma_1+\gamma_2+\gamma_3)+\frac{1}{3}(\gamma_1\gamma_2+\gamma_1\gamma_3+\gamma_2\gamma_3)$ Note that the constants α and γ are chosen so that

$$\int_{\beta_3}^{\beta_2} dp = 0, \quad \int_{\beta_3}^{\beta_2} dq = 0.$$

The square root $\sqrt{(\beta_1-\lambda)(\lambda-\beta_2)(\lambda-\beta_3)}$ is analytic in the complex place $\mathbb{C}\backslash\{(-\infty,\beta_3]\cup[\beta_2,\beta_1]\}$ and real for large negative λ so that $p(\lambda)$ and $q(\lambda)$ are real in the stability zones. The Whitham modulation equations (22) are equivalent to

$$\frac{\partial}{\partial t}dp(\lambda) + \frac{\partial}{\partial x}dq(\lambda) = 0, \tag{35}$$

for any λ. Indeed by multiplying the above equation by $(\lambda-\beta_i)^{\frac{3}{2}}$ and taking the limit $\lambda \to \beta_i$, one gets (22). Furthermore

$$k = \int_{\beta_2}^{\beta_1} dp, \quad \omega = \int_{\beta_2}^{\beta_1} dq,$$

with k and ω the wave-number and frequency as in (32), so that integrating (35) between β_1 and β_2 and observing that the integral does not depend on the path of integration one recovers the equation of wave conservation (14).

3 Application of Whitham Modulation Equations

As in the linear case, the modulation equations have important applications in the description of the solution of the Cauchy problem of the KdV equation in asymptotic limits. Let us consider the initial value problem

$$\begin{cases} u_t + 6uu_x + \epsilon^2 u_{xxx} = 0 \\ u(x,0;\epsilon) = f(x), \end{cases} \tag{36}$$

where $f(x)$ is an initial data independent from ϵ. When we study the solution of such initial value problem $u(x,t;\epsilon)$ one can consider two limits:

- the long time behaviour, namely

$$u(x,t;\epsilon) \overset{t\to\infty}{\to} ?, \quad \epsilon \text{ fixed};$$

- the small dispersion limit, namely

$$u(x,t;\epsilon) \overset{\epsilon\to 0}{\to} ?, \quad x \text{ and } t \text{ in compact sets.}$$

These two limits have been widely studied in the literature. The physicists Gurevich and Pitaevski [28] were among the first to address these limits and gave an heuristic solution imitating the linear case. Let us first consider one of the case studied by Gurevich and Pitaevski, namely a decreasing step initial data

$$f(x) = \begin{cases} c & \text{for} \quad x < 0, \quad c > 0, \\ 0 & \text{for} \quad x > 0. \end{cases} \tag{37}$$

Using the Galileian invariance of KdV equation, namely $x \to x + 6Ct$, $t \to t$ and $u \to u + C$, every initial data with a single step can be reduced to the above form. The above step initial data is invariant under the rescaling $x/\epsilon \to x$ and $t/\epsilon \to$, therefore, in this particular case it is completely equivalent to study the small ϵ asymptotic, or the long time asymptotics of the solution.

Such initial data is called compressive step, and the solution of the Hopf equation $v_t + 6vv_x = 0$ ($\epsilon = 0$ in (36)) develop a shock for $t > 0$. The shock front $s(t)$ moves with velocity $3ct$ while the multi-valued piece-wise continuos solution of the Hopf equation $v_t + 6vv_x = 0$ for the same initial data is given by

$$v(x,t) = \begin{cases} c & \text{for } x < 6tc, \\ \dfrac{x}{6t} & \text{for } 0 \le x \le 6tc, \\ 0 & \text{for } x \ge 0. \end{cases}$$

For $t > 0$ the solution $u(x,t;\epsilon)$ of the KdV equation develops a train of oscillations near the discontinuity. These oscillations are approximately described by the travelling wave solution (33) of the KdV equation where $\beta_i = \beta_i(x,t)$, $i = 1,2,3$, evolve according to the Whitham equations. However one needs to fix the solution of the Whitham equations. Given the self-similar structure of the solution of the Hopf equation, it is natural to look for a self-similar solution of the Whitham equation in the form $\beta_i = \beta_i(z)$ with $z = \dfrac{x}{t}$. Applying this change of variables to the Whitham equations one obtains

$$(\lambda_i - z)\frac{\partial \beta_i}{\partial z} = 0, \quad i = 1,2,3, \tag{38}$$

whose solution is $\lambda_i = z$ or $\partial_z \beta_i = 0$. A natural request that follows from the relations (28) and (29) is that at the right boundary of the oscillatory zone z_+, when $\beta_1(z_+) = \beta_2(z_+)$, the function β_3 has to match the Hopf solution that is constant and equal to zero, namely $\beta_3(z_+) = 0$. Similarly, at the left boundary z_- when $\beta_2(z_-) = \beta_3(z_-)$, the function $\beta_1(z_-) = c$ so that it matches the Hopf solution. From these observations it follows that the solution of (38) for $z_- \le z \le z_+$ is

given by

$$\beta_1(z) = c, \quad \beta_3(z) = 0, \quad z = \lambda_2(c, \beta_2, 0). \tag{39}$$

In order to determine the values $z_\pm$ it is sufficient to let $\beta_2 \to c$ and $\beta_2 \to 0$ respectively in the last equation in (39). Using the relations (28) and (29) one has $\lambda_2(c, c, 0) = 4c$ and $\lambda_2(c, 0, 0) = -6c$ so that

$$z_- = -6c, \quad \text{or } x_-(t) = -6ct \quad \text{and} \quad z_+ = 4c, \quad \text{or } x_+(t) = 4ct.$$

According to Gurevich and Pitaevski for $-6ct < x < 4t$ and $t \gg 1$, the asymptotic solution of the Korteweg de Vries equation with step initial data (37) is given by the modulated travelling wave solution (30), namely

$$u(x, t; \epsilon) \simeq c - \beta_2 + 2\beta_2 \,\mathrm{cn}^2\left(\frac{\sqrt{c}}{\epsilon}(x - 2t(c + \beta_2)) + \frac{K(m)}{\pi\epsilon}\phi_0 + K(m); m\right), \tag{40}$$

with

$$m = \frac{\beta_2(x, t)}{c},$$

where $\beta_2(x, t)$ is given by (39). The phase ϕ_0 in (40) has not been described by Gurevich and Pitaevski. Finally in the remaining regions of the $(x, t > 0)$ one has

$$u(x, t, \epsilon) \simeq \begin{cases} c \text{ for } x < -6ct, \\ 0 \text{ for } x > 4ct. \end{cases}$$

This heuristic description has been later proved in a rigorous mathematical way (see the next section). We remark that at the right boundary $x_+(t)$ of the oscillatory zone, when $\beta_2 \to c$, $\beta_1 \to c$ and $\beta_3 \to 0$, the cnoidal wave (40) tends to a soliton, $cn(z; m) \to \mathrm{sech} z$ as $m \to 1$.

After some computations, the limit of the elliptic solution (40) gives

$$u(x, t, \epsilon) \simeq 2c \,\mathrm{sech}^2\left[\frac{x - x_+(t)}{\epsilon}\sqrt{c} + \frac{1}{2}\log\left(\frac{16c}{c - \beta_2}\right) + \frac{\tilde{\phi}_0}{\epsilon}\right], \tag{41}$$

where the logarithmic term is due to the expansion of the complete elliptic integral $K(m)$ as in (27) and $c - \beta_2 = O(\epsilon)$. The determination of the limiting value of the phase $\tilde{\phi}_0$ requires a deeper analysis [9]. The important feature of the above formula is that if the argument of the sech term is approximately zero near the point $x_+(t)$, then the height of the rightmost oscillation is twice the initial step c. This occurs for a single step initial data (see Fig. 1) while for step-like initial data as in Fig. 2 this less evident.

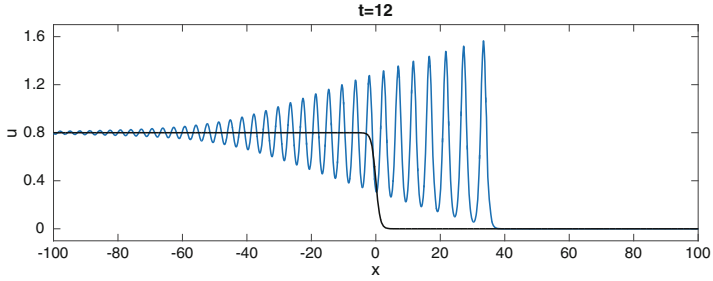

Fig. 1 In *black* the initial data (a smooth step) and in *blue* KdV solution at time $t = 12$ and $\epsilon = 1$. One can clearly see the height of the rightmost oscillation (approximately a soliton) is about two times the height of the initial step

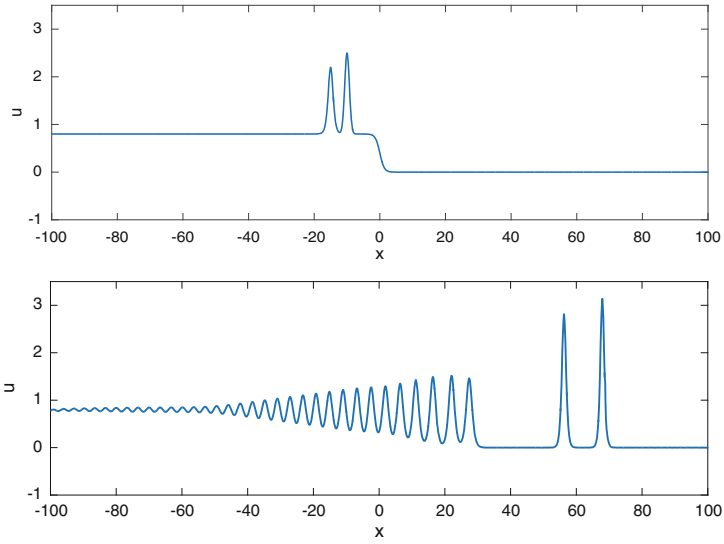

Fig. 2 On *top* the step-like initial data and on *bottom* the solution at time $t = 12$. One can clearly see the soliton region containing two solitons and the collision-less shock region where modulated oscillations are formed

The Gurevich Pitaevsky problem has been studied also for perturbations of the KdV equation with forcing, dissipative or conservative non integrable terms [21, 34, 35] and applied to the evolution of solitary waves and undular bores in shallow-water flows over a gradual slope with bottom friction [22].

3.1 Long Time Asymptotics

The study of the long time asymptotic of the KdV solution was initiated around 1973 with the work of Gurevich and Pitaevski [28] for step-initial data and Ablowitz and Newell [2] for rapidly decreasing initial data. By that time it was clear that for rapidly decreasing initial data the solution of the KdV equation splits into a number of solitons moving to the right and a decaying radiation moving to the left. The first numerical evidence of such behaviour was found by Zabusky and Kruskal [39]. The first mathematical results were given by Ablowitz and Newell [2] and Tanaka [48] for rapidly decreasing initial data. Precise asymptotics on the radiation part were first obtained by Zakharov and Manakov [58], Ablowitz and Segur [3] and Buslaev and Sukhanov [7], Venakides [54]. Rigorous mathematical results were also obtained by Deift and Zhou [12], inspired by earlier work by Its [32]; see also the review [14] and the book [46] for the history of the problem. In [3, 29] the region with modulated oscillations of order O(1) emerging in the long time asymptotics was called *collisionless shock region*. In the physics and applied mathematics literature such oscillations are also called dispersive shock waves, dissipationless shock wave or undular bore. The phase of the oscillations was obtained in [15]. Soon after the Gurevich and Pitaevski's paper, Khruslov [37] studied the long time asymptotic of KdV via inverse scattering for step-like initial data. In more recent works, using the techniques introduced in [12], the long time asymptotic of KdV solution has been obtained for step like initial data improving some error estimates obtained earlier and with the determination of the phase ϕ_0 of the oscillations [20], see also [1]. Long time asymptotic of KdV with different boundary conditions at infinity has been considered in [5]. The long time asymptotic of the expansive step has been considered in [43].

Here we report from [20] about the long time asymptotics of KdV with step like initial data $f(x)$, namely initial data converging rapidly to the limits

$$\begin{cases} f(x) \to 0 & \text{for } x \to +\infty \\ f(x) \to c > 0 & \text{for } x \to -\infty, \end{cases} \tag{42}$$

but in the finite region of the x plane any kind of regular behaviour is allowed. The initial data has to satisfy the extra technical assumption of being sufficiently smooth. Then the asymptotic behaviour of $u(x, t; \epsilon)$ for fixed ϵ and $t \to \infty$ has been obtained applying the Deift-Zhou method in [12] see Fig. 2:

- in the region $x/t > 4c + \delta$, for some $\delta > 0$, the solution is asymptotically given by the sum of solitons if the initial data contains solitons otherwise the solution is approximated by zero at leading order;
- in the region $-6c + \delta_1 < x/t < 4c - \delta_2$, for some $\delta_1, \delta_2 > 0$, (*collision-less shock region*) the solution $u(x, t; \epsilon)$ is given by the modulated travelling wave (40), or

using ϑ-function by (33), namely

$$u(x,t;\epsilon) = \beta_2(x,t) - c + 2c\frac{E(m)}{K(m)} + \frac{2k^2}{(2\pi)^2}\left(\log\vartheta\left(\frac{kx-\omega t+\phi_0}{2\pi\epsilon};\tau\right)\right)'' + o(1) \tag{43}$$

where

$$k = \pi\frac{\sqrt{c}}{K(m)}, \quad \omega = 2k(c+\beta_2), \quad m = \frac{\beta_2(x,t)}{c}$$

with $\beta_2 = \beta_2(x,t)$ determined by (39). In the above formula the prime in the $\log\vartheta$ means derivative with respect to the argument, namely $(\log\vartheta(z_0;\tau))'' = \frac{d^2}{dz^2}\log\vartheta(z+z_0;\tau))|_{z=0}$. The phase ϕ_0 is

$$\phi_0 = \frac{k}{\pi}\int_{\beta_2}^{c}\frac{\log|\bar{T}(i\sqrt{z})T_1(i\sqrt{z})|dz}{\sqrt{z(c-z)(z-\beta_2)}}, \tag{44}$$

where T and T_1 are the transmission coefficients of the Schrödinger equation $\epsilon^2\frac{d^2}{dx^2}\Psi + f(x)\Psi = -\lambda\Psi$ from the right and left respectively.

The remarkable feature of formula (43) is that the description of the collisionless shock region for step-like initial data coincides with the formula obtained by Gurevich and Pitaevsky for the single step initial data (37) up to a phase factor. Indeed the initial data is entering explicitly through the transmission coefficients only in the phase ϕ_0 of the oscillations.

- In the region $x/t < -6t - \delta_3$, for some constant $\delta_3 > 0$, the solution is asymptotically close to the background c up to a decaying linear oscillatory term.

We remark that the higher order correction terms of the KdV solution in the large time asymptotics can be found in [3, 7, 20, 58]. For example in the region $x < -6tc$ the solution is asymptotically close to the background c up to a decaying linear oscillatory term. We also remark that the boundaries of the above three regions of the (x,t) plane have escape our description. In such regions the asymptotic description of the KdV solution is given by elementary functions or Painlevé trascendents see [47] or the more recent work [6].

The technique introduced by Deift-Zhou [12] to study asymptotics for integrable equations has proved to be very powerful and effective to study asymptotic behaviour of many other integrable equations like for example the semiclassical limit of the focusing nonlinear Schrödinger equation [36], the long time asymptotics of the Camassa-Holm equation [6] or the long time asymptotic of the perturbed defocusing nonlinear Schrödinger equation [13].

3.2 Small ϵ Asymptotic

The idea of the formation of an oscillatory structure in the limit of small dispersion of a dispersive equation belongs to Sagdeev [45]. Gurevish and Pitaevskii in 1973 called the oscillations, arising in the small dispersion limit of KdV, *dispersive shock waves* in analogy with the shock waves appearing in the zero dissipation limit of the Burgers equation. A very recent experiment in a water tank has been set up where the dispersive shock waves have been reproduced [52].

The main steps for the description of the dispersive shock waves are the following:

- as long as the solution of the Cauchy problem for Hopf equation $v_t + 6vv_x = 0$ with the initial data $v(x,0) = f(x)$ exists, then the solution of the KdV equation $u(x,t;\epsilon) = v(x,t) + O(\epsilon^2)$. Generically the solution of the Hopf equation obtained by the method of characteristics

$$v(x,t) = f(\zeta), \quad x = f(\zeta)t + \zeta, \tag{45}$$

  develops a singularity when the function $\zeta = \zeta(x,t)$ given implicitly by the map $x = f(\zeta)t + \zeta$ is not uniquely defined. This happens at the first time when $f'(\zeta)t + 1 = 0$ and $f''(\zeta) = 0$ (see Fig. 3). These two equations and (45) fix uniquely the point (x_c, t_c) and $u_c = v(x_c, t_c)$. At this point, the gradient blow up: $v_x(x,t)|_{x_c,t_c} \to \infty$.
- The solution of the KdV equations remains smooth for all positive times. Around the time when the solution of the Hopf equation develops its first singularity at time t_c, the KdV solution, in order to compensate the formation of the strong gradient, starts to oscillate, see Fig. 3. For $t > t_c$ the solution of the KdV equation $u(x,t;\epsilon)$ is described as $\epsilon \to 0$ as follows:
  - there is a cusp shape region of the (x,t) plane defined by $x_-(t) < x < x_+(t)$ with $x_-(t_c) = x_+(t_c) = x_c$. Strictly inside the cusp, the solution $u(x,t;\epsilon)$ has

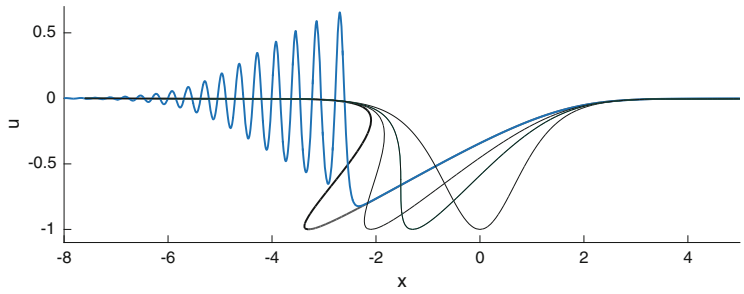

Fig. 3 In *blue* the solution of the KdV equation for the initial data $f(x) = -\text{sech}^2(x)$ at the time $t = 0.55$ for $\epsilon = 10^{-1}$. In *black* the (multivalued) solution of the Hopf equation for the same initial data and for several times: $t = 0$, $t = t_c = 0.128$, $t = 0.35$ and $t = 0.55$

an oscillatory behaviour which is asymptotically described by the travelling wave solution (33) where the parameters $\beta_j = \beta_j(x,t)$, $j = 1,2,3$, evolve according to the Whitham modulation equations.
– Strictly outside the cusp-shape region the KdV solution is still approximated by the solution of the Hopf equation, namely $u(x,t;\epsilon) = v(x,t) + O(\epsilon^2)$.

Later the mathematicians Lax-Levermore [41] and Venakides [55, 56] gave a rigorous mathematical derivation of the small dispersion limit of the KdV equation by solving the corresponding Cauchy problem via inverse scattering and doing the small ϵ asymptotic. Then Deift, Venakides and Zhou [16] obtained an explicit derivation of the phase ϕ_0. The error term $O(\epsilon^2)$ of the expansion outside the oscillatory zone was calculated in [11]. For analytic initial data, the small ϵ asymptotic of the solution $u(x,t;\epsilon)$ of the KdV equation is given for some times $t > t_c$ and within a cusp $x_-(t) < x < x_+(t)$ in the (x,t) plane by the formula (33) where $\beta_j = \beta_j(x,t)$ solve the Whitham modulations equations (22). The phase ϕ_0 in the argument of the theta-function will be described below. In the next section we will explain how to construct the solution of the Whitham equations.

3.2.1 Solution of the Whitham Equations

The solution $\beta_1(x,t) > \beta_2(x,t) > \beta_3(x,t)$ of the Whitham equations can be considered as branches of a multivalued function and it is fixed by the following conditions.

- Let (x_c,t_c) be the critical point where the solution of the Hopf equation develops its first singularity and let $u_c = v(x_c,t_c)$. Then at $t = t_c$

$$\beta_1(x_c,t_c) = \beta_2(x_c,t_c) = \beta_3(x_c,t_c) = u_c;$$

- for $t > t_c$ the solution of the Whitham equations is fixed by the boundary value problem
  - when $\beta_2(x,t) = \beta_3(x,t)$, then $\beta_1(x,t) = v(x,t)$;
  - when $\beta_1(x,t) = \beta_2(x,t)$, then $\beta_3(x,t) = v(x,t)$,

  where $v(x,t)$ solve the Hopf equation, see Fig. 4.

From the integrability of the KdV equation, one has the integrability of the Whitham equations [18]. This is a non trivial fact. However we give it for granted and assume that the Whitham equations have an infinite family of commuting flows:

$$\frac{\partial}{\partial s}\beta_i + w_i \frac{\partial}{\partial x}\beta_i = 0, \quad i = 1,2,3.$$

The compatibility condition of the above flows with the Whitham equations (22), implies that $\frac{\partial}{\partial t}\frac{\partial}{\partial s}\beta_i = \frac{\partial}{\partial s}\frac{\partial}{\partial t}\beta_i$. From these compatibility conditions it follows that

$$\frac{1}{w_i - w_j}\frac{\partial}{\partial \beta_j} w_i = \frac{1}{\lambda_i - \lambda_j}\frac{\partial}{\partial \beta_j}\lambda_i, \quad i \neq j \tag{46}$$

where the speeds λ_i's are defined in (22).

Tsarev [53] showed that if the $w_i = w_i(\beta_1, \beta_2, \beta_3)$ satisfy the above linear overdetermined system, then the formula

$$x = \lambda_i t + w_i, \quad i = 1, 2, 3, \tag{47}$$

that is a generalisation of the method of characteristics, gives a local solution of the Whitham equations (22). Indeed by subtracting two equations in (47) with different indices we obtain

$$(\lambda_i - \lambda_j)t + w_i - w_j = 0, \quad \text{or} \quad t = -\frac{w_i - w_j}{\lambda_i - \lambda_j}. \tag{48}$$

Taking the derivative with respect to x of the hodograph equation (47) gives

$$\sum_{j=1}^{3}\left(\frac{\partial \lambda_i}{\partial \beta_j}t + \frac{\partial w_i}{\partial \beta_j}\right)\frac{\partial \beta_j}{\partial x} = 1.$$

Substituting in the above formula the time as in (48) and using (46), one get that only the term with $j = i$ surveys, namely

$$\left(\frac{\partial \lambda_i}{\partial \beta_i}t + \frac{\partial w_i}{\partial \beta_i}\right)\frac{\partial \beta_i}{\partial x} = 1.$$

In the same way, making the derivative with respect to time of (47) one obtains

$$\left(\frac{\partial \lambda_i}{\partial \beta_i}t + \frac{\partial w_i}{\partial \beta_i}\right)\frac{\partial \beta_i}{\partial t} + \lambda_i = 0.$$

The above two equations are equivalent to the Whitham system (22). The transformation (47) is called also hodograph transform. To complete the integration one needs to specify the quantities w_i that satisfy the linear overdetermined system (46). As a formal ansatz we look for a conservation law of the form

$$\partial_s k + \partial_x(kq) = 0,$$

with k the wave number and the function $q = q(\beta_1, \beta_2, \beta_3)$ to be determined (recall that $q = 2(\beta_1 + \beta_2 + \beta_3)$ for the Whitham equations (22)). Assuming that the β_i

evolves independently, such ansatz gives w_i of the form

$$w_i = \frac{1}{2}\left(v_i - 2\sum_{k=1}^{3}\beta_k\right)\frac{\partial q}{\partial \beta_i} + q, \quad i = 1,2,3. \tag{49}$$

Plugging the expression (49) into (46), one obtains equations for the function $q = q(\beta_1, \beta_2, \beta_3)$

$$\frac{\partial q}{\partial \beta_i} - \frac{\partial q}{\partial \beta_j} = 2(\beta_i - \beta_j)\frac{\partial^2 q}{\partial \beta_i \partial \beta_j}, i \neq j,\ i,j = 1,2,3. \tag{50}$$

Such system of equations is a linear over-determined system of Euler-Poisson Darboux type and it was obtained in [30] and [50]. The boundary conditions on the β_i specified at the beginning of the section fix uniquely the solution. The integration of (50) was performed for particular initial data in several different works (see e.g. [34], or [30, 44]) and for general smooth initial data in [50, 51]. The boundary conditions require that when $\beta_1 = \beta_2 = \beta_3 = \beta$, then $q(\beta, \beta, \beta) = h_L(\beta)$ where h_L is the inverse of the decreasing part of the initial data $f(x)$. The resulting function $q(\beta_1, \beta_2, \beta_3)$ is [50]

$$q(\beta_1, \beta_2, \beta_3) = \frac{1}{2\sqrt{2}\pi}\int_{-1}^{1}\int_{-1}^{1} d\mu d\nu \frac{h_L(\frac{1+\mu}{2}(\frac{1+\nu}{2}\beta_1 + \frac{1-\nu}{2}\beta_2) + \frac{1-\mu}{2}\beta_3)}{\sqrt{1-\mu}\sqrt{1-\nu^2}}. \tag{51}$$

For initial data with a single negative hump, such formula is valid as long as $\beta_3 > f_{min}$ which is the minimum value of the initial data. When β_3 goes beyond the hump one needs to take into account also the increasing part h_R of the inverse the initial data f, namely [51] (Fig. 4)

$$q(\beta_1, \beta_2, \beta_3) = \frac{1}{2\pi}\int_{\beta_2}^{\beta_1} \frac{d\lambda\left(\int_{\beta_3}^{-1}\frac{d\xi h_R(\xi)}{\sqrt{\lambda-\xi}} + \int_{-1}^{\lambda}\frac{d\xi h_L(\xi)}{\sqrt{\lambda-\xi}}\right)}{\sqrt{(\beta_1-\lambda)(\lambda-\beta_2)(\lambda-\beta_3)}}. \tag{52}$$

Equations (47) define $\beta_j, j = 1,2,3$, in an implicit way as a function of x and t. The actual solvability of (47) for $\beta_j = \beta_j(x,t)$ was obtained in a series of papers by Fei-Ran Tian [49, 51]. The Whitham equations are a systems of hyperbolic equations, and generically their solution can suffer blow up of the gradients in finite time. When this happen the small ϵ asymptotic of the solution of the KdV equation is described by higher order θ-functions and the so called multi-phase Whitham equations [24]. So generically speaking the solvability of system (47) is not an obvious fact. The main results of [49, 50] concerning this issue are the following:

- if the decreasing part of the initial data, h_L is such that $h_L'''(u_c) < 0$ (generic condition) then the solution of the Whitham equation exists for short times $t > t_c$.

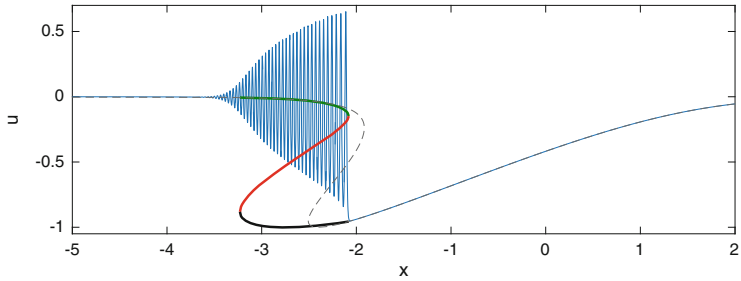

Fig. 4 The *thick line* (*green*, *red* and *black*) shows the solution of the Whitham equations $\beta_1(x,t) \geq \beta_2(x,t) \geq \beta_3(x,t)$ at $t = 0.4$ as branches of a multivalued function for the initial data $f(x) = -\text{sech}^2(x)$. At this time, β_3 goes beyond the negative hump of the initial data and formula (52) has been used. The solution of the Hopf equation including the multivalued region is plotted with a *dashed grey line*, while the solution of the KdV equation for $\epsilon = 10^{-2}$ is plotted with a *blue line*. We observe that the multivalued region for the Hopf solution is sensible smaller then the region where the oscillations develops, while the Whitham zone is slightly smaller

- If furthermore, the initial data $f(x)$ is step-like and non increasing, then under some mild extra assumptions, the solution of the Whitham equations exists for short times $t > t_c$ and for all times $t > T$ where T is a sufficiently large time.

These results show that the Gurevich Pitaevski description of the dispersive shock waves is generically valid for short times $t > t_c$ and, for non increasing initial data, for all times $t > T$ where T is sufficiently large. At the intermediate times, the asymptotic description of the KdV solution is generically given by the modulated multiphase solution of KdV (quasi-periodic in x and t) where the wave parameters evolve according to the multi-phase Whitham equations [24]. The study of these intermediate times has been considered in [1, 4, 27].

To complete the description of the dispersive shock wave we need to specify the phase of the oscillations in (54). Such phase was derived in [16] and takes the form

$$\phi_0 = -kq, \tag{53}$$

where $k = \dfrac{\pi\sqrt{\beta_1 - \beta_3}}{K(m)}$ is the wave number and the function $q = q(\beta_1, \beta_2, \beta_3)$ has been defined in (51) or (52). The simple form (53) of the phase was obtained in [25]. Finally the solution of the KdV equation $u(x,t;\epsilon)$ as $\epsilon \to 0$ is described as follows

- in the region strictly inside the cusp $x_-(t) < x < x_+(t)$ it is given by the asymptotic formula

$$u(x,t,\epsilon) = \beta_1 + \beta_2 + \beta_3 + 2\alpha + 2\epsilon^2 \frac{\partial^2}{\partial x^2} \log \vartheta \left(\frac{kx - \omega t - kq)}{2\pi\epsilon}; \tau \right) + O(\epsilon) \tag{54}$$

where $\beta_j = \beta_j(x,t)$ is the solution of the Whitham equation constructed in this section, see Fig. 5. The wave number k, the frequency ω and the quantities τ and α are defined in (31), (34) and (24) respectively and q is defined in (51) and (52). When performing the x-derivative in (54) observe that

$$\partial_x(kx - \omega t - kq) = k,$$

because of (47) and (49).

- For $x > x_+(t) + \delta$ and $x < x_-(t) - \delta$ for some positive $\delta > 0$, the KdV solution is approximated by

$$u(x,t,\epsilon) = v(x,t) + O(\epsilon^2)$$

where $v(x,t)$ is the solution of the Hopf equation.

Let us stress the meaning of the formula (54): such formula shows that the leading order behaviour of the KdV solution $u(x,t;\epsilon)$ in the limit $\epsilon \to 0$ and for generic initial data is given in a cusp-shape region of the (x,t) plane by the periodic travelling wave of KdV. However to complete the description one still needs to solve an initial value problem, for three hyperbolic equations, namely the Whitham equations, but the gain is that these equations are independent from ϵ.

A first approximation of the boundary $x_\pm(t)$ of the oscillatory zone for $t - t_c$ small, has been obtained in [25] by taking the limit of (47) when $\beta_1 = \beta_2$ and $\beta_2 = \beta_3$. This gives

$$x_+(t) \simeq x_c + 6u_c(t - t_c) + \frac{4\sqrt{10}}{3\sqrt{-h_L'''(u_c)}}(t - t_c)^{\frac{3}{2}},$$

$$x_-(t) \simeq x_c + 6u_c(t - t_c) - \frac{36\sqrt{2}}{\sqrt{-h_L'''(u_c)}}(t - t_c)^{\frac{3}{2}},$$

where h_L is the decreasing part of the initial data. Such formulas coincide with the one obtained in [28] for cubic initial data.

We conclude pointing out that in [25] a numerical comparison of the asymptotic formula (54) with the actual KdV solution $u(x,t;\epsilon)$ has been considered for the initial data $f(x) = -\text{sech}^2 x$. Such numerical comparison has shown the existence of transition zones between the oscillatory and non oscillatory regions that are described by Painlevé trascendant and elementary functions [8–10]. Looking for example to Fig. 5 it is clear that the KdV oscillatory region is slightly larger then the region described by the elliptic asymptotic (54) where the oscillations are confined to $x_-(t) \le x \le x_+(t)$.

Of particular interest is the solution of the KdV equation near the region where the oscillations are almost linear, namely near the point $x_-(t)$. It is known [27, 49] that taking the limit of the hodograph transform (47) when $\beta_2 = \beta_3 = \xi$ and

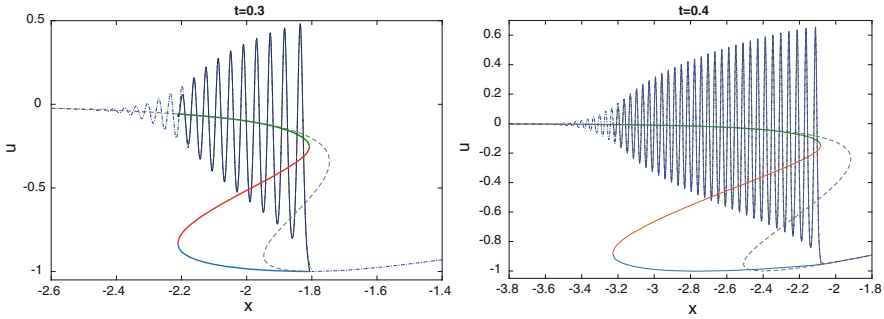

Fig. 5 The solution of the KdV equation and its approximations for the initial data $f(x) = -\text{sech}^2(x)$ and $\epsilon = 10^{-2}$ at two different times $t = 0.3$ and $t = 0.4$. The *blue dash-dot line* is the KdV solution, the *black line* is the elliptic asymptotic formula (54) which is on top of the KdV solution, the *black dash line* is the solution of the Hopf equation while the *green*, *red* and aviation *blue lines* are the solution of the Whitham equations $\beta_1 \geq \beta_2 \geq \beta_3$

$\beta_1 = v$, one obtains the system of equations

$$\begin{cases} x_-(t) = 6tv(t) + h_L(v(t)), \\ 6t + \phi(\xi(t); v(t)) = 0, \\ \partial_\xi \phi(\xi(t); v(t)) = 0, \end{cases} \tag{55}$$

that determines uniquely $x_-(t)$ and $v(t) > \xi(t)$. In the above equation the function

$$\phi(\xi; v) = \frac{1}{2\sqrt{v-\xi}} \int_\xi^v \frac{h_L'(y)dy}{\sqrt{y-\xi}}, \tag{56}$$

and h_L is the decreasing part of the initial data. The behaviour of the KdV solution is described near the edge $x_-(t)$ by linear oscillations, where the envelope of the oscillations is given by the Hasting Mcleod solution to the Painlevé II equation:

$$q''(s) = sq + 2q^3(s). \tag{57}$$

The special solution in which we are interested, is the Hastings-McLeod solution [31] which is uniquely determined by the boundary conditions

$$q(s) = \sqrt{-s/2}(1 + o(1)), \quad \text{as } s \to -\infty, \tag{58}$$

$$q(s) = \text{Ai}(s)(1 + o(1)), \quad \text{as } s \to +\infty, \tag{59}$$

where $\text{Ai}(s)$ is the Airy function. Although any Painlevé II solution has an infinite number of poles in the complex plane, the Hastings-McLeod solution $q(s)$ is smooth for all real values of s [31] .

The KdV solution near $x_-(t)$ and in the limit $\epsilon \to 0$ in such a way that

$$\lim_{\substack{\epsilon\to 0\\ x\to x_-(t)}} \frac{x-x^-(t)}{\epsilon^{2/3}},$$

remains finite, is given by [10]

$$u(x,t,\epsilon) = v(t) - \frac{4\epsilon^{1/3}}{c^{1/3}} q\left(s(x,t,\epsilon)\right) \cos\left(\frac{\Theta(x,t)}{\epsilon}\right) + O(\epsilon^{\frac{2}{3}}). \tag{60}$$

where

$$\Theta(x,t) = 2\sqrt{v-\xi}(x-x^-) + 2\int_\xi^v (h_L'(y)+6t)\sqrt{y-\xi}dy$$

and

$$c = -\sqrt{v-\xi}\frac{\partial^2}{\partial\xi^2}\phi(\xi;v) > 0, \qquad s(x,t,\epsilon) = -\frac{x-x_-(t)}{c^{1/3}\sqrt{v-\xi}\,\epsilon^{2/3}}.$$

Note that the leading order term in the expansion (60) of $u(x,t,\epsilon)$ is given by $v(t)$ that solves the Hopf equation while the oscillatory term is of order $\epsilon^{1/3}$ with oscillations of wavelength proportional to ϵ and amplitude proportional to the Hastings-McLeod solution q of the Painlevé II equation. From the practical point of view it is easier to use formula (60), then (54) since one needs to solve only an ODE (the Painlevé II equation) and three algebraic equations, namely (55). One can see from Fig. 6 that the asymptotic formula (60) gives a good approximation (up to

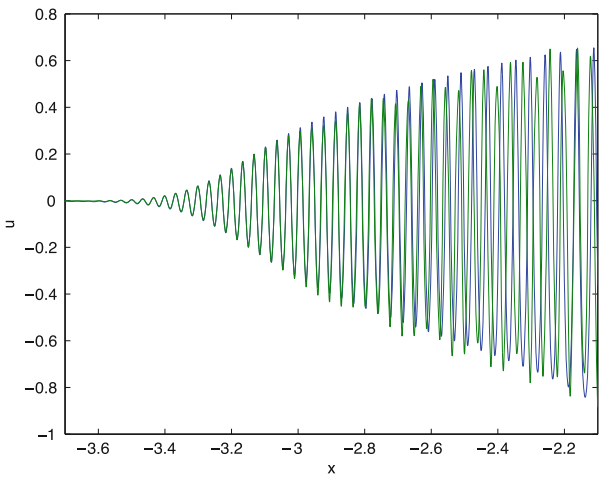

Fig. 6 The solution of the KdV equation in *blue* and its approximation (60) in *green* for the initial data $f(x) = -\text{sech}^2(x)$ and $\epsilon = 10^{-2}$ at $t = 0.4$. One can see that the *green and blue lines* are completely overlapped when the oscillations are small

an error $O(\epsilon^{\frac{2}{3}})$) of the KdV solution near the leading edge where the oscillations are linear, while inside the Whitham zone, it gives a qualitative description of the oscillations [26].

We conclude by stressing that the asymptotic descriptions reviewed in this chapter for the KdV equation can be developed for other integrable equations like the nonlinear Schrödinger equation, [36] the Camass-Holm equation [6] or the modified KdV equation [38], see also [19] for a more general class of equations.

Acknowledgements Tamara Grava acknowledges the support by the Leverhulme Trust Research Fellowship RF-2015-442 from UK and PRIN Grant "Geometric and analytic theory of Hamiltonian systems in finite and infinite dimensions" of Italian Ministry of Universities and Researches.

References

1. Ablowitz, M.J., Baldwin, D.E.: Interactions and asymptotics of dispersive shock waves—Korteweg-de Vries equation. Phys. Lett. A **377**(7), 555–559 (2013)
2. Ablowitz, M.J., Newell, A.C.: The decay of the continuous spectrum for solutions of the Korteweg-de Vries equation. J. Math. Phys. **14** , 1277–1284 (1973)
3. Ablowitz, M.J., Segur, H.: Asymptotic solutions of the Korteweg-de Vries equation. Stud. Appl. Math. **57**, 13–44 (1977)
4. Ablowitz, M.J., Baldwin, D.E., Hoefer, M.A.: Soliton generation and multiple phases in dispersive shock and rarefaction wave interaction. Phys. Rev. E (3) 80(1), 016603, 5 pp. (2009)
5. Bikbaev, R.F., Sharipov, R.A.: The asymptotic behavior, as $t \to \infty$ of the solution of the Cauchy problem for the Korteweg de Vries equation in a class of potentials with finite-gap behavior as $\to \pm\infty$. Theoret. Math. Phys. **78** (3), 244–252 (1989)
6. Boutet de Monvel, A., Its, A., Shepelsky, D.: Painlevé-type asymptotics for the Camassa-Holm equation. SIAM J. Math. Anal. **42**(4), 1854–1873 (2010)
7. Buslaev, V.S., Sukhanov, V.V.: Asymptotic behavior of solutions of the Korteweg de Vries equation. J. Sov. Math. **34**, 1905–1920 (1986) (in English)
8. Claeys, T., Grava, T.: Solitonic asymptotics for the Korteweg-de Vries equation in the small dispersion limit. SIAM J. Math. Anal. **42** (5), 2132–2154 (2010)
9. Claeys, T., Grava, T.: Universality of the break-up profile for the KdV equation in the small dispersion limit using the Riemann-Hilbert approach. Commun. Math. Phys. **286**(3), 979–1009 (2009)
10. Claeys, T., Grava, T.: Painlevé II asymptotics near the leading edge of the oscillatory zone for the Korteweg-de Vries equation in the small-dispersion limit. Commun. Pure Appl. Math. **63**(2), 203–232, (2010)
11. Claeys, T., Grava, T.: The KdV hierarchy: universality and a Painlevé transcendent. Int. Math. Res. Not. IMRN **22**, 5063–5099 (2012)
12. Deift, P., Zhou, X.: A steepest descent method for oscillatory Riemann-Hilbert problems. Asymptotics for the MKdV equation. Ann. Math. **137**(2), 295–368 (1993)
13. Deift, P., Zhou, X.: Perturbation theory for infinite-dimensional integrable systems on the line. A case study. Acta Math. **188**(2), 163–262 (2002)
14. Deift, P.A., Its, A.R., Zhou, X.: Long-time asymptotics for integrable nonlinear wave equations. In: Important Developments in Soliton Theory. Springer Series in Nonlinear Dynamics, pp. 181–204. Springer, Berlin (1993)
15. Deift, P., Venakides, S., Zhou, X.: The collisionless shock region for the long-time behavior of solutions of the KdV equation. Commun. Pure Appl. Math. **47**(2), 199–206 (1994)

16. Deift, P., Venakides S., Zhou, X.: New result in small dispersion KdV by an extension of the steepest descent method for Riemann-Hilbert problems. IMRN **6**, 285–299 (1997)
17. Dobrohotov, M., Ju, S., Maslov, V.P.: Finite-zone almost periodic solutions in WKB-approximations. In: Current Problems in Mathematics, vol. 15, pp. 3–94, 228. Akad. Nauk SSSR, Moscow (1980)
18. Dubrovin, B., Novikov, S.P.: Hydrodynamic of weakly deformed soliton lattices. Differential geometry and Hamiltonian theory. Russ. Math. Surv. **44**(6) (1989), 35–124
19. Dubrovin, B., Grava, T., Klein, C., Moro, A.: On critical behaviour in systems of Hamiltonian partial differential equations. J. Nonlinear Sci. **25**(3), 631–707 (2015)
20. Egorova, I., Gladka, Z., Kotlyarov, V., Teschl, G.: Long-time asymptotics for the Korteweg–de Vries equation with step-like initial data. Nonlinearity **26**(7) (2013), 1839–1864
21. El, G.A.: Resolution of a shock in hyperbolic systems modified by weak dispersion. Chaos **15**(3), 037103, 21 pp. (2005)
22. El, G.A., Grimshaw, R.H.J., Kamchatnov, A.M.: Analytic model for a weakly dissipative shallow-water undular bore. Chaos **15**(3) 037102, 13 pp. (2005)
23. Gardner, C.S., Green J.M., Kruskal, M.D., Miura, R.M.: Phys. Rev. Lett. **19**, 1095 (1967)
24. Flaschka, H., Forest, M., McLaughlin, D.H.: Multiphase averaging and the inverse spectral solution of the Korteweg-de Vries equations. Commun. Pure App. Math. **33**, 739–784 (1980)
25. Grava, T., Klein, C.: Numerical solution of the small dispersion limit of Korteweg-de Vries and Whitham equations. Commun. Pure Appl. Math. **60**(11), 1623–1664 (2007)
26. Grava, T., Klein, C.: A numerical study of the small dispersion limit of the Korteweg-de Vries equation and asymptotic solutions. Phys. D **241**(23–24), 2246–2264 (2012)
27. Grava, T., Tian, F.-R.: The generation, propagation, and extinction of multiphases in the KdV zero-dispersion limit. Commun. Pure Appl. Math. **55**(12), 1569–1639 (2002)
28. Gurevich, A.V., Pitaevskii, L.P.: Decay of initial discontinuity in the Korteweg de Vries equation. JETP Lett. **17**, 193–195 (1973)
29. Gurevich, A.V., Pitaevskii, L.P.: Nonstationary structure of a collisionless shock wave. Sov. Phys. JETP **38**, 291–297 (1974)
30. Gurevich, A.V., Krylov, A.L., El, G.A.: Evolution of a Riemann wave in dispersive hydrodynamics. Soviet Phys. JETP **74**(6), 957–962 (1992)
31. Hastings, S.P., McLeod, J.B.: A boundary value problem associated with the second Painlevé transcendent and the Korteweg-de Vries equation. Arch. Ration. Mech. Anal. **73**, 31–51 (1980)
32. Its, A.R.: Asymptotics of solutions of the nonlinear Schrödinger equation and isomonodromic deformations of systems of linear differential. Sov. Math. Dokl. **24**, 452–456 (1981)
33. Its, A.R., Matveev, V.B.: Hill operators with a finite number of lacunae. Funct. Anal. Appl. **9**(1), 65–66 (1975)
34. Kamchatnov, A.M.: Nonlinear Periodic Waves and Their Modulations. An Introductory Course, xiv+383 pp. World Scientific Publishing, River Edge, NJ (2000). ISBN:981-02-4407-X
35. Kamchatnov, A.M.: On Whitham theory for perturbed integrable equations. Physica D **188**, 247–261 (2004)
36. Kamvissis, S., McLaughlin, K.D.T.-R., Miller, P.D.: Semiclassical Soliton Ensembles for the Focusing Nonlinear Schrödinger Equation. Annals of Mathematics Studies, vol. 154, xii+265 pp. Princeton University Press, Princeton, NJ (2003). ISBN:0-691-11483-8; 0-691-11482-X
37. Khruslov, E.Y.: Decay of initial step-like perturbation of the KdV equation. JETP Lett. **21**, 217–218 (1975)
38. Kotlyarov, V., Minakov, A.: Modulated elliptic wave and asymptotic solitons in a shock problem to the modified Kortweg–de Vries equation. J. Phys. A **48**(30), 305201, 35 pp. (2015)
39. Kruskal, M.D., Zabusky, N.J.: Interaction of solitons in a collisionless plasma and the recurrence of initial states. Phys Rev. Lett. **15**, 240–243 (1965)
40. Lawden, D.F.: Elliptic Functions and Applications. Applied Mathematical Sciences, vol. 80. Springer, New York (1989)
41. Lax, P.D., Levermore, C.D.: The small dispersion limit of the Korteweg de Vries equation, I, II, III. Commun. Pure Appl. Math. **36**, 253–290, 571–593, 809–830 (1983)

42. Levermore, C.D.: The hyperbolic nature of the zero dispersion KdV limit. Commun. Partial Differ. Equa. **13** (4), 495–514 (1988)
43. Leach, J.A., Needham, D.J.: The large-time development of the solution to an initial-value problem for the Korteweg-de Vries equation: I. Initial data has a discontinuous expansive step. Nonlinearity **21**, 2391–2408 (2008)
44. Novikov, S., Manakov, S.V., Pitaevski, L.P., Zakharov, V.E.: Theory of solitons. The inverse scattering method. Translated from the Russian. Contemporary Soviet Mathematics, xi+276 pp. Consultants Bureau [Plenum], New York (1984). ISBN: 0-306-10977-8
45. Sagdeev, R.Z.: Collective processes and shock waves in rarefied plasma. In: Leontovich, M.A. (ed.) Problems in Plasma Theory, vol. 5. Atomizdat, Moscow (1964, in Russian)
46. Schuur, P.C.: Asymptotic Analysis of Soliton Problems. An Inverse Scattering Approach. Lecture Notes in Mathematics, vol. 1232, viii+180 pp. Springer, Berlin (1986). ISBN:3-540-17203-3
47. Segur, H., Ablowitz, M.J.: Asymptotic solutions of nonlinear evolutions equations and Painlevé transcendents. Physica D **3**(1), 165–184 (1981).
48. Tanaka, S.: Korteweg–de Vries equation; asymptotic behavior of solutions. Publ. Res. Inst. Math. Sci. **10**, 367–379 (1975)
49. Tian, F.-R.: Oscillations of the zero dispersion limit of the Korteweg de Vries equations. Commun. Pure App. Math. **46**, 1093–1129 (1993)
50. Tian, F.-R.: The Whitham-type equations and linear overdetermined systems of Euler-Poisson-Darboux type. Duke Math. J. **74** (1), 203–221 (1994)
51. Tian, F.-R.: The initial value problem for the Whitham averaged system. Commun. Math. Phys. **166**(1), 79–115 (1994)
52. Trillo, S., Klein, M., Clauss, G., Onorato, M.: Observation of dispersive shock waves developing from initial depressions in shallow water. Physica D (2016). http://dx.doi.org/10.1016/j.physd.2016.01.007
53. Tsarev, S.P.: Poisson brackets and one-dimensional Hamiltonian systems of hydrodynamic type. Soviet Math. Dokl. **31**, 488–491 (1985)
54. Venakides, S.: Long time asymptotics of the Korteweg–de Vries equation Trans. Am. Math. Soc. **293**, 411–419 (1986)
55. Venakides, V., The zero dispersion limit of the Korteweg de Vries equation for initial potential with nontrivial reflection coefficient. Commun. Pure Appl. Math. **38**, 125–155 (1985)
56. Venakides, S., The Korteweg de Vries equations with small dispersion: higher order Lax-Levermore theory. Commun. Pure Appl. Math. **43**, 335–361 (1990)
57. Whitham, G.B.: Linear and Nonlinear Waves. Wiley, New York (1974)
58. Zakharov, V.E., Manakov, S.V.: Asymptotic behavior of non-linear wave systems integrated by the inverse scattering method. Soviet Phys. JETP **44**(1), 106–112 (1976)

Dispersive Shock Waves: From Water Waves to Nonlinear Optics

Matteo Conforti and Stefano Trillo

Abstract Dispersive shock waves are strongly oscillating wave trains that spontaneously form and expand thanks to the action of weak dispersion, which contrasts the tendency, driven by the nonlinearity, to develop a gradient catastrophe. Here we review the basic concepts and recent progresses made in the description of such nonlinear waves, both in terms of experimental results and modelling. In particular, we discuss the formation of dispersive shocks in shallow water, which can be described in terms of Korteweg-de Vries or Whitham nonlocal equations. We contrast such results with those obtained in the field of nonlinear optics, described in terms of local or nonlocal nonlinear Schrödinger equations. Finally we show that a dispersive shock propagating under the action of small perturbations can radiate. A perturbative approach allows for the accurate prediction of the radiated frequencies.

1 Introduction

Dispersive shock waves (DSWs) are non-stationary wave trains that develop spontaneously in weakly dispersive nonlinear media [1]. The nonlinearity induces front steepening and hence the tendency to develop a gradient catastrophe. A weak dispersion plays a secondary role until steep gradients are eventually formed. At this stage dispersion becomes effective, inducing the onset of strong oscillations which expand in a characteristic fan in the space-time plane. The borders of this fan represent the leading and the trailing edge of the DSW, where the amplitude of the oscillations are largest and vanishingly small, respectively. DSWs constitute the dispersive counterpart of viscous regularization of classical shock waves [2], which occurs when the dissipation dominates over the dispersive effects.

M. Conforti
Univ. Lille, CNRS, UMR 8523 - PhLAM - Physique des Lasers Atomes et Molécules, F-59000 Lille, France
e-mail: matteo.conforti@univ-lille1.fr

S. Trillo (✉)
Dipartimento di Ingegneria, Universitá di Ferrara, Via Saragat 1, 44122 Ferrara, Italy
e-mail: stefano.trillo@unife.it

M. Onorato et al. (eds.), *Rogue and Shock Waves in Nonlinear Dispersive Media*,
Lecture Notes in Physics 926, DOI 10.1007/978-3-319-39214-1_11

The investigation of DSWs has a long history that starts with pioneering contributions in the 60s and the 70s, when DSWs were mainly known as *collisionless shocks*. Indeed Sagdeev and coworkers first predicted the oscillatory nature of the shock occurring in the extremely rarefied (collisionless) plasma [3]. The observation of such dispersive breaking in the lab was reported as early as 1970 [4]. From the theory point of view, the weakly dispersive Korteweg-de Vries (KdV) equation [5–7] have had a pivotal role in the early developments. In 1965 Zabuski and Kruskal [8] investigated soliton-like excitations emerging from the dispersive breaking of a sinusoidal wave. This can be thought of as the periodic analog of smooth waveforms containing a large number of solitons, which start to emerge after a wavebreaking defined in the dispersionless limit. However, more generally DSWs do not require soliton content to develop. A milestone towards a more general description was the solution of the Riemann problem (the evolution of a step initial datum) for the KdV, reported by Gurevich and Pitaeviskii [9], who proposed the first explicit construction of a DSW by exploiting Whitham modulation theory [10]. Later on, the limit of vanishing dispersion was rigorously formulated for the KdV in the framework of the inverse scattering theory [11–15]. On the other hand, the modulation approach was soon extended to the defocusing nonlinear Schrödinger (NLS) equation [16, 17] and then deepened during several decades (see e.g. [18–21], and for more details the chapter by T. Grava and references therein in this book), remaining a powerful technique to describe the long-time asymptotic of the DSW past the breaking point developing in the dispersionless limit. The picture that has globally emerged is that the physical phenomena and the tools employed to analyse such behaviour are common to a wide class of PDE models, both integrable and non-integrable [22, 23].

On the experimental side, many progresses have been made just recently. The purpose of this chapter is to review some recent results that concern the observation of DSW in shallow water and in nonlinear optics. In both areas the dispersive effects on breaking of waves was specifically assessed in the past both theoretically [24–26] and experimentally [27–32] in water waves (where DSW are commonly named as undular bores), as well as in fiber optics [33–37]. However, it is only recently that the renewed interest in DSWs have permitted to explore new regimes, to obtain new data with higher resolution, and to predict new phenomena [38–47]. This also allowed for making more accurate comparisons with the models in order to assess their limit of validity and the importance that previously neglected ingredients can have. For instance, as we will show in the following, nonlocality turns out to be important, though at different levels, both in water waves and optics, where it affects the linear or the nonlinear response, respectively.

The chapter is structured as follows. In Sect. 2 we review the basic concepts of classical shock waves and their dissipative versus dispersive regularisation. In Sect. 3 we present a DSW experiment made in a shallow water tank. In Sect. 4, we discuss optical DSWs. Finally in Sect. 5 we discuss the mechanisms that allows DSWs to resonantly radiate, a phenomenon observed and interpreted just recently. We summarise in Sect. 6.

2 Classical Shock Waves and Regularising Mechanisms

In this section we recall the basic concepts in the theory of shock waves. We privilege the physical intuition rather than aspiring to be mathematically rigorous. In order to understand the basic differences between classical shock waves and DSWs, let us start with the simplest hyperbolic model for *nonlinear* wave propagation, namely the Hopf or inviscid Burgers (or generally nonlinear transport) equation written in conventional variables x (space) and t (time)

$$u_t + uu_x = 0 \qquad \Leftrightarrow \qquad u_t + f_x(u) = 0;\, f(u) = \frac{u^2}{2}, \tag{1}$$

which conveniently generalises the unidirectional *linear* wave (or advection) equation $u_t + cu_x = 0$ to the case where the velocity becomes proportional to the local wave elevation, i.e. $c = c(u) = u$ (the arguments that follow hold true also for more general dependences, e.g. $c(u) = u^n$, n positive integer). The formulation on the right of Eq. (1) is called flux conservative form (or conservation law), $f(u)$ being the flux associated with the wave field u, which usually has the meaning (in fluid dynamics, traffic flow, crowd behavior,...) of a density. In the linear case, the initial disturbance does not change shape and travels with velocity c. Stated differently, we can say that, given any input disturbance, the values $u_0 = u(x_0, t = 0)$ are transported along the characteristic lines $x(t) = x_0 + ct$, which are the oblique parallel lines shown in Fig. 1a. Conversely, in the nonlinear case where the velocity becomes proportional to the wave elevation itself, such characteristics become $x(t) = x_0 + c(u_0(x_0))t$ which are no longer parallel. This reflects the fact that, in particular, along a negative slope front, the higher parts of the wave tends to catch up on the less intense ones, until an infinite gradient is formed at a finite breaking time t_b. In the Hopf equation the breaking time is easily calculated to be $t_b = 1/(-m)$, where m is the maximal negative slope. An example is displayed in Fig. 1b for a Gaussian input.

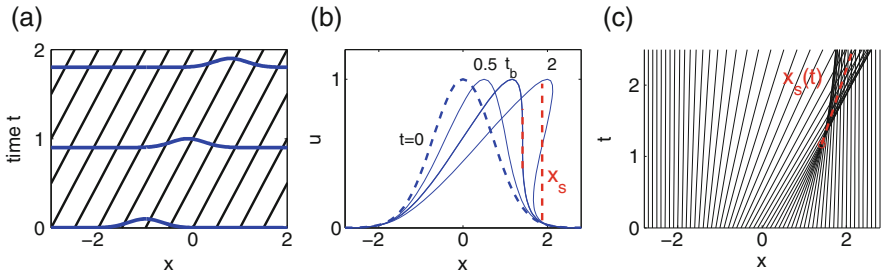

Fig. 1 (**a**) Linear case: transport of a Gaussian field along characteristics (lines at slope $1/c$), ruled by advection equation $u_t + cu_x = 0$; (**b**) nonlinear case: Gaussian developing a gradient catastrophe at time $t = t_b$. The *dashed red line* is the classical shock wave which has location $x_s = x_s(t)$; (**c**) corresponding shock dynamics in the plane (x, t). The first point where characteristic lines intersect stands for the gradient catastrophe point occurring at the breaking time t_b. The *red dashed curve* $x_s(t)$ emanating from this point corresponds to the shock wave evolution

The time t_b is the finite time necessary for the catastrophe to develop and corresponds to the earliest time where the characteristics intersect [see Fig. 1c]. For $t > t_b$ the wave becomes multivalued. A remedy for not dealing with multivalued functions is to introduce a jump [2, 48], as exemplified by the red dashed vertical line in Fig. 1b. This, however, requires to generalise the solution of Eq. (1) for piecewise smooth functions which include a jump. To this end one must resort to the more general integral formulation of the conservation law (from which Eq. (1) derives)

$$\frac{d}{dt}\int_a^b u(x,t)dx = f(a,t) - f(b,t), \tag{2}$$

which states that in the interval (a, b) the rate of change of mass (integral of density) is given by the difference between the incoming and outgoing flux. In general, across a moving discontinuity $x_s(t)$, with $a \leq x_s(t) \leq b$, Eq. (2) reduces to (we omit the proof, which can be found in many textbooks)

$$\mathrm{v}_s = \frac{dx_s(t)}{dt} = \frac{f(x_s^-,t) - f(x_s^+,t)}{u(x_s^-,t) - u(x_s^+,t)} = \frac{[f]}{[u]}, \tag{3}$$

which is known as Rankine-Hugoniot (RH) condition ([...] is the contracted notation for the difference of the quantity inside parenthesis across the jump). Equation (3) gives the instantaneous velocity of the jump v_s for a general one-dimensional conservation law with flux f. A piecewise smooth solution of the conservation law $u_t + f_x = 0$ with a jump that fulfils the RH condition is a classical shock wave of the model with shock path $x_s(t)$.

Returning to the specific example of the Hopf equation (1), one can consider, as a particular case, a step-like initial datum located in $x = 0$, i.e. a jump from $u(x \leq 0, t = 0) = u_L$ to $u(x > 0, t = 0) = u_R$. In this case breaking occurs at $t = 0$ where the characteristic already intersect. The RH condition gives the constant velocity $\mathrm{v}_s = (u_L + u_R)/2$ ($= 1/2$ for a unit amplitude jump to zero), and the shock path is $x_s = \mathrm{v}_s t$. The solution (via characteristics jointed to the RH condition) tells that the jump remain unchanged except for a rigid translation with constant velocity v_s. This is an example of classical shock wave. In the more general case where the initial value is smooth the RH condition is equivalent to select one curve inside the fan of intersecting characteristics [see red curve labeled $x_s(t)$ in Fig. 1c]. Although not explicitly stated so far, the compatibility for a classical shock wave solution requires the so-called entropy condition $u_L > u_R$, implicitly considered to be valid in our example. In the opposite case $u_R > u_L$ the shock is no longer compatible with the conservation law and the relevant solution is a rarefaction wave (see Fig. 2 below for an example) [2, 48].

Although the classical shock waves constitute an important tool in many problems of fluid dynamics, usually in the real world one observes their regularised form, which is due to physical ingredients which are not accounted for in Eq. (1). The phenomena which are relevant can be grouped into two main classes, namely dissipative and dispersive effects. As far as Eq. (1) is concerned, these effects are related (at leading orders) to the lowest-order even and odd spatial derivatives

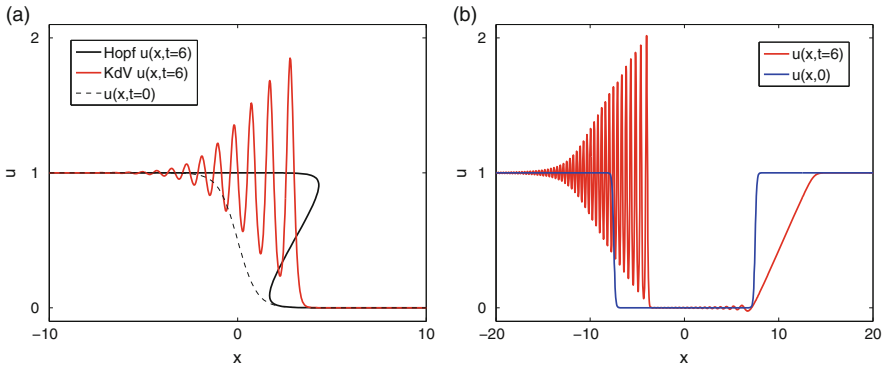

Fig. 2 (**a**) Snapshots comparing the Hopf and weakly dispersing KdV ($\varepsilon^2 = 0.01$) post-breaking evolutions obtained from a negative slope smooth input. Here $u(x, 0) = (1 - \tanh(x))/2$ (*dashed curve*), which yields a breaking time $t_b = 2$. (**b**) Snapshot from KdV integration, with $\varepsilon^2 = 0.002$ and a boxed well as initial value (*blue curve*). The negative slope jump gives rise to a DSW, while the positive slope jump results into a rarefaction wave

in x, respectively. For instance the dissipative generalisation of Eq. (1) leads to the famous Burgers equation

$$u_t + uu_x = \alpha u_{xx}, \tag{4}$$

which has the shock solution of unit amplitude $u = \frac{1}{2}\left\{1 + \tanh\left[\frac{1}{4\alpha}\left(t - \frac{1}{2}x\right)\right]\right\}$. In this case, the shock wave is now smooth, due to dissipation. In the limit $\alpha \to 0$, such solution reduces to the unit jump (classical shock wave) solution of Eq. (1) with the same velocity predicted by the RH condition $v_s = 1/2$. Therefore dissipation does not alter the velocity, but only introduces a characteristic width 4α of the shock, which consistently shrinks to zero in the lossless limit.

Viceversa, by adding to Eq. (1) the lowest-order dispersive contribution u_{xxx} (recall that the first odd derivative u_x is a linear velocity term which is removable by introducing a shifted coordinate), weighted by a coefficient ε^2, one obtains the well known KdV equation

$$u_t + uu_x + \varepsilon^2 u_{xxx} = 0. \tag{5}$$

Let us now compare the solution of the Hopf equation (1) and the weakly dispersing ($\varepsilon \ll 1$) KdV equation (5) when the initial waveform is a smooth negative slope input which undergoes breaking. A typical example is displayed in Fig. 2a. In this case, for $t > t_b$ ($t_b = 2$ in the example), the Hopf equation gives overtaking, i.e. a multivalued field as shown by the black curve. Conversely the KdV does not exhibit any catastrophe and the dynamics remains smooth at all times. The equation reacts to the strong gradient produced by the nonlinearity, with

the onset of spontaneous modulated oscillations. The oscillating field appear on the steepened front at slightly earlier times than the breaking time t_b, and spread afterwards, becoming more pronounced around the front. As shown in Fig. 2a, at a finite time $t = 6$, these oscillations have regularised the pronounced multivalued jump produced by the Hopf equation. Outside the region filled with oscillations the two equations give the same solution. Globally this constitutes a DSW, characterized by a single phase (the phase of the modulated periodic nonlinear wave).

Conversely, if we integrate the KdV with initial value given by a box-shaped well, we obtain the result shown in Fig. 2b. While the negative slope part gives rise to a DSW as discussed before, the positive slope front gives rise to a rarefaction wave, i.e. a front which smooths out as it propagates. At sufficiently large times, the rarefaction wave can interact with the DSW, giving a deformation of the latter. By comparing Fig. 2a and b, it can be noticed that the period of the oscillation decreases for smaller ε. Furthermore, we notice from Fig. 2b that the peak oscillation is twice the jump, as predicted on the basis of the solution of the Riemann problem in the framework of the inverse scattering [49]. In general the region filled with oscillations can be characterised asymptotically in terms of Whitham modulation theory as a $cn-$oidal wave (an invariant periodic wave solution of the KdV) which has slowly varying parameters (amplitude, period, and velocity). In particular, one can show that the modulated periodic wave ranges from a *local* soliton on the leading edge (largest amplitude of the oscillating wavetrain) to linear waves with amplitude tending to zero, on the trailing edge. We point out that the adjective "local" means that the modulus of the modulated Jacobian function m tends to one (as it is for a soliton) only on the leading edge, without implying that the wave contains discrete eigenvalues corresponding to true solitons.

Importantly, for DSWs the single velocity of the classical shock is replaced by the *two characteristic velocities* of the leading and trailing edges of the shock, respectively. Moreover it is important to emphasise that, at variance with the dissipative case, the limit $\varepsilon^2 \to 0$ does not give the corresponding classical shock, since the oscillations become shorter and denser as ε^2 decreases. In other words, the formal position $\varepsilon^2 = 0$ is only useful to determine the dispersionless limit of Eq. (5), i.e. the Hopf equation (1) which governs the breaking mechanism before the dispersion becomes important. Conversely the asymptotic for $\varepsilon^2 \to 0$ should be formulated in the framework of the modulation theory and never gives the classical shock wave.

3 Dispersive Shocks in Shallow Water

It is well known that surface gravity waves with long wavelength, propagating in shallow water, can be modeled in terms of a KdV equation. In dimensional form, calling henceforth z the direction of propagation, the KdV takes the following form:

$$\eta_t + c_0\eta_z + \frac{3}{2}\frac{c_0}{h}\eta\eta_z + \frac{1}{6}c_0h^2\eta_{zzz} = 0, \tag{6}$$

where η is the water elevation over the still water height h, $c_0 = \sqrt{gh}$ is the phase velocity of linear waves. What is less appreciated is that experiments are usually made in a tank by launching waveforms with controlled temporal shape at a fixed ideal plane (the wave maker, $z = 0$) and measuring time series at fixed locations along the tank. Therefore the modeling is more conveniently performed by writing the KdV equation as an evolution equation in space, in such a way that one can directly compare the measured time series with those obtained by solving the Chauchy problem for the KdV, by advancing the solution in space (interestingly enough, as we show below, this is analogous to what is routinely done in optical fibers, and described in terms of NLS model [35, 46]). Therefore one should make use of the following time-like Korteweg-de Vries (T-KdV) equation [50, 51],

$$\eta_z + \frac{1}{c_0}\eta_t - \chi\eta\eta_t - \beta_3\eta_{ttt} = 0;\ \chi = \frac{3}{2}\frac{1}{c_0 h};\ \beta_3 = \frac{1}{6}\frac{h^2}{c_0^3}, \tag{7}$$

where the initial value is in general $\eta(z = 0, t) = \eta_0 f_0(t/t_0)$, η_0 and t_0 being the peak wave amplitude and duration, respectively, and $f_0(t)$ fixes the shape (normalized so to have absolute unit maximum). Equation (7) can be easily derived from Eq. (6) by means of the leading order relation $\eta_z \sim -\eta_t/c_0$. As discussed in [47], Eq. (7) possess a linear dispersion relationship $D(\omega, k) = k - \omega/c_0 - \omega^3 h^2/(6c_0^3) = 0$, which better approximates (at large values of kh) the exact dispersion relationship $\omega(k) = \sqrt{gk\tanh(kh)}$, compared with the dispersion relationship of the standard form of the KdV [Eq. (6)] $D(\omega, k) = \omega - c_0 k + (c_0 h^2/6)k^3 = 0$.

In order to compare with the previous section, and in particular Eq. (5), it is useful to cast the T-KdV equation (7) in dimensionless form

$$u_\zeta - uu_\tau - \varepsilon^2 u_{\tau\tau\tau} = 0, \tag{8}$$

where we introduce the normalized retarded time $\tau = (t - z/c_0)/t_0$ and distance $\zeta = z/L_{nl}$, as well as the normalized elevation $u = \eta/\eta_0$. Here $L_{nl} = t_0/(\chi\eta_0)$ is the nonlinear length, i.e. the characteristic length scale after which the effects due to the nonlinearity become significant. The relative weight of the dispersive effect is measured by the ratio between L_{nl} and the characteristic length scale of the dispersion, namely $L_d = t_0^3/\beta_3$, i.e. by the smallness parameter

$$\varepsilon^2 = \frac{L_{nl}}{L_d} = \frac{\beta_3}{\chi}\frac{1}{\eta_0 t_0^2} = \frac{1}{9}\frac{h^3}{c_0^2}\frac{1}{\eta_0 t_0^2} = \frac{(2\pi)^2}{9}\frac{1}{U}, \tag{9}$$

where the last equality gives the link with the Ursell number $U \equiv (\eta_0/h)(\lambda/h)^2$ [28, 52]. It is important to emphasise that, for a given choice of initial shape, the evolution ruled by Eq. (8) implies that the features of the DSW depend only on the value of ε. However, in a real experiment the real-world length scale of the DSW evolution, depends also on the value of the nonlinear length. In other words what matters are both the ratio L_{nl}/L_d (which mainly affect the period of the DSW oscillations) and the absolute value of nonlinear length L_{nl} (which mainly affects the length scale of the dynamics).

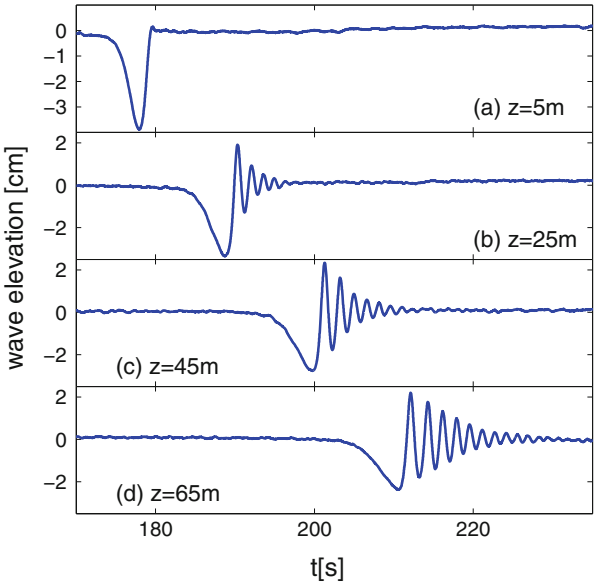

Fig. 3 Surface elevation measured at different distances z from the wave maker ($z = 0$). Here the nominal initial conditions is a depression $\eta(0, t) = -\eta_0 sech^2(t/t_0)$ with amplitude $\eta_0 = 4$ cm and duration $t_0 = 1.27$ s. The dispersion smallness parameter is $\varepsilon^2 = 0.028$ (Ursell number $U = 157$) and the nonlinear length is $L_{nl} = 16.8$ m. One can clearly notice, on top of the rigid translation due to the phase velocity c_0, the different velocities of the leading and trailing edges of the spreading DSW. See also [47]

We show in Fig. 3a typical DSW evolution dynamics recently observed in the sea-keeping basin of the Technical University of Berlin. The basin has a measuring range of $L = 90$ m, a width of 8 m, and the water depth has been adjusted to $h = 40$ cm. The wave elevation is measured by gauges at fixed locations $z = 5 + (k - 1)10$ m, $k = 1, \ldots, 8$, from the wave maker at $z = 0$. At the end of the tank an absorbing beach limits the impact of the reflection. The typical time series generated by a nominal excitation $f(t) = -sech^2(t)$ are shown at distance $z = 5, 25, 45, 65$ in Fig. 3. Since this initial condition contains no solitons, the evolution is dominated by the formation of a DSW. In particular, we notice that one of the initially smooth fronts exhibits a considerable steepening front already at 5 m. Note that, contrary to the case discussed in Fig. 1, it is the positive slope temporal front that steepens consistently with the minus sign in front of the nonlinear term in the T-KdV (7). At longer distances the negative front smooths out generating a rarefaction wave, whereas the steepened front give birth to an expanding modulated train of oscillations. The small (linear) oscillations that arrives later at the end of the tank start to becomes affected by the reflection at the last gauge (data not shown).

A more extended DSW can be observed over the length of the tank, for a shorter nonlinear length even with slightly larger value of ε. This case is displayed in Fig. 4, where the right panel shows the measured elevation at 45 m, obtained for the same

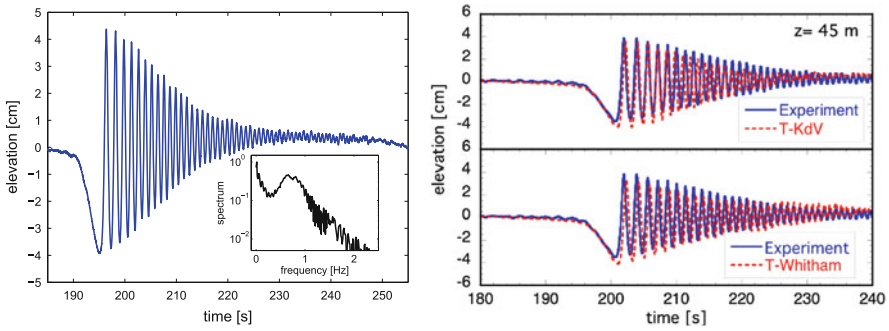

Fig. 4 *Left panel*: Surface elevation measured at 45 m, along with its Fourier spectrum. Here $\eta_0 = 10\,\text{cm}$, $t_0 = 0.64\,\text{s}$, $\varepsilon^2 = 0.045$ ($U = 98$), and $L_{nl} = 3.4\,\text{m}$. *Right double panel*: Data from the *left panel* compared with the elevation computed according to the T-KdV (*upper panel*) or T-Whitham (*lower panel*). In both cases the data at the first gauge are used as the initial value for the computation. See also [47]

initial shape with amplitude and duration resulting in $\varepsilon^2 = 0.045$ ($U = 98$) and $L_{nl} = 3.4\,\text{m}$. As shown a very extended and regular structure is obtained which exhibits > 50 clean oscillations. The DSW continues to expand further but the oscillations on the trailing edge becomes affected by the reflection of the leading edge which arrives earlier at the end of the tank. The spectrum clearly show the non monochromatic character of the DSW with a peak ascribed to the leading edge, followed by a long tail towards high frequencies due to the trailing edge.

In order to assess whether the $T - KdV$ is a good model, we have compared the data with the outcome of the numerical integration of Eq. (7), using the data recorded at the first gauge as initial value. The comparison is shown in the upper right panel in Fig. 4. While the general agreement is satisfactory, some discrepancy can be noticed along the trailing edge. Since this corresponds to the higher frequency tail of the spectrum that challenges the validity of the KdV, better accuracy can be obtained by replacing the term u_{xxx} with a convolution, as suggested by Whitham, which leads to the equation named after him [53, 54]. This allows to account for the full unidirectional dispersion relation of surface gravity waves, at the price of introducing nonlocality (in time) in the model. Consistently with the T-KdV, the nonlocal Whitham equation can be cast as an evolution equation in z, obtaining a T-Whitham equation. The latter, once written in terms of the Fourier Transform operator in time $\mathscr{F}[\ldots]$, reads as

$$\eta_z - \chi\eta\eta_t - \mathscr{F}^{-1}\left[i\,sign(\omega)k(\omega)\mathscr{F}\left[\eta\right]\right] = 0, \tag{10}$$

where $k(\omega)$ results from the inversion of the full linear dispersion relation of surface gravity waves. The comparison of the data with the integration of Eq. (10) gives a better description of the trailing edge of the DSW, as shown in the right bottom panel of Fig. 4.

To summarise this part, we have shown that DSWs in surface gravity waves can be generated, observed, and modelled with high accuracy. This is important also in view of gaining a better understanding of the behaviour of tidal bores [55], the shoaling of tsunamis [56], and atmospheric gravity waves which present similar phenomenologies.

4 Dispersive Shocks in Optics

In optics DSWs can be observed in space during the propagation of a laser beam in a defocusing medium, or in time during the propagation of pulses along fiber optics in the regime of normal dispersion, which is equivalent to the defocusing regime. We warn the reader that, in the latter case, the occurrence of shock waves is often attributed and investigated with reference to higher order cubic terms, which have relevant effect for ultrashort pulses [57]. However, as we show below, it turns out that it is the Kerr effect associated with the standard nonlinear term in the NLS, to be the leading-order effect responsible for wavebreaking (as in the spatial case) under normal experimental conditions that involve pulses with duration in the range from a few *psec* to *nsec*. Below we discuss the relevant NLS-type of models and show a few selected experimental results.

4.1 Temporal DSW in Fibers

In an optical fiber, under common experimental conditions where higher order effects can be safely neglected, the propagation of the electric field envelope $E(Z,T)$ can be described by the following equation

$$iE_Z + ik'E_T - \frac{k''}{2}E_{TT} + \gamma|E|^2E = 0, \tag{11}$$

where $k' = dk/d\omega = 1/V_g$ and $k'' = d^2k/d\omega^2$ are the inverse group-velocity and second-order dispersion, and γ is the nonlinear coefficient (usually measured in (W km)$^{-1}$ with $|E|^2$ giving directly the power in W). It is useful to recall that, unlike the KdV, the NLS equation is an envelope equation where $E(Z,T)$ turns out to slowly modulate a carrier wave $\exp[ik(\omega_0)z - i\omega_0 t]$ at frequency ω_0, where the derivatives k', k'' are calculated.

In the *normal* dispersion regime where $k'' > 0$, by denoting by $P = max(|E(Z = 0,T)|^2)$ and t_0 the peak power and the duration of the input envelope $E(Z = 0,T)$, and introducing the characteristic length scales for the nonlinearity and dispersion, namely $L_{nl} = (\gamma P)^{-1}$ and $L_d = t_0^2/|k''|$, Eq. (11) can be cast in the form

$$i\varepsilon\psi_z - \frac{\varepsilon^2}{2}\psi_{tt} + |\psi|^2\psi = 0, \qquad \varepsilon = \sqrt{\frac{L_{nl}}{L_d}} \tag{12}$$

where $\psi = E/\sqrt{P}$, $t = (T - Z/V_g)/t_0$, and $z = Z/\sqrt{L_{nl}L_d}$. By means of the WKB (or Madelung) transformation $u(t,z) = \sqrt{\rho(t,z)}\exp[iS(t,z)/\varepsilon]$ applied to Eq. (12), at leading order (i.e., neglecting a $O(\varepsilon^2)$ term), we obtain the following dispersionless NLS model [16]

$$\rho_z + (\rho u)_t = 0; \qquad u_z + uu_t + \rho_t = 0, \tag{13}$$

where $u = -S_t$ stands for the chirp. Equations (13) are equivalent to the dispersionless shallow water (or Saint Venant) equations in dimensions 1+1D, where ρ and u stand for the water elevation and the vertically averaged velocity, respectively, or a specific version of the $p-$system of gas dynamics, valid for an isentropic gas with adiabatic index $\gamma = 2$, i.e. pressure law $p = \rho^2/2$. Equations (13) play the same role played by the Hopf equation for the KdV, i.e. Eqs. (13) are dispersionless hyperbolic equations which rule the evolution of the wave up to the catastrophe point where it develops infinite gradients. They are diagonalisable in the form $r_z^{\pm} + [(3r^{\pm} + r^{\mp})/4]r_t^{\pm} = 0$ in terms of the Riemann invariants $r_{\pm} = u \pm 2\sqrt{\rho}$. Although in principle they can be solved in terms of the hodograph transform, in general no simple expressions can be given for the breaking time.

Importantly, the NLS equation exhibits two main different type of breaking depending on the input waveform, as shown in Fig. 5. For a bright bell-shaped (e.g., Gaussian) input on a finite background the effective defocusing action, which is stronger on the top of the pulse, induces the beam to broaden and steepen symmetrically on both fronts, until two symmetric catastrophes occur. As a result the dispersive regularisation exhibits two DSWs expanding in two symmetric fans in the $t - z$ plane [see Fig. 5a and b]. This is the type of breaking observed in fibers [35] (see also [40] for the spatial case and [39] for similar experiments in Bose-Einstein condensates). Note, however, that the role of the background is extremely important in terms of the visibility of the oscillating DSW. Indeed the amplitude of these oscillations greatly reduce in the limit of zero background [16, 17], which is the case considered in [35].

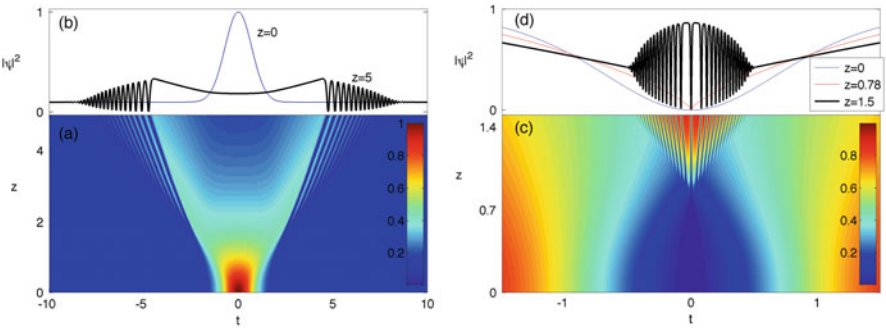

Fig. 5 DSWs ruled by NLS equation: (**a, b**) *colour* level plot (**a**) and snapshot (**b**) from a Gaussian input with 10 % pedestal, with $\varepsilon = 0.05$; (**c, d**) *colour* level plot (**c**) and snapshot (**d**) with input $\psi(t,0) = \tanh(t)$, $\varepsilon = 0.005$

Conversely, when a dark waveform $\psi(t,0) = \tanh(t)$ is launched, the breaking occurs in the null point of the waveform, i.e. in $t = 0$. While in the former case the breaking is generic (only one Riemann invariant develops a singularity at finite distance $z = z_b$), in this case the breaking is non-generic since both Riemann invariants experience simultaneous breaking at the origin $t = 0$ [58] (strictly speaking the analysis in [58] has been carried out by neglecting the phase jump but the numerics suggest that the mechanism ruled by Eqs. (13) remains unchanged in the presence of the phase jump; clearly the asymptotic states differ in the two cases). The emerging DSW exhibits a single fan with a narrower central zero-velocity soliton and symmetric pairs around it [see Fig. 5c, d]. Importantly, while the intermediate stage shown in Fig. 5d shows the typical features of a DSW, the asymptotic state ($z \sim 1/\varepsilon$) in this case turns out to be very different from the previous one, being made by a finite number ($2N - 1$, where $N = Int[1/\varepsilon]$) of asymptotically separated gray solitons living on the same background. Indeed for $\varepsilon = 1/N$, N integer, $\tanh(t)$ is a reflectionless potential in the language of the inverse scattering [59]. Therefore, in this case, we can say that we are in the presence of a purely solitonic DSW (i.e., a multi-soliton solution with a large number of solitons, which behaves as a DSW at intermediate distances).

More recently, it was pointed out that DSWs play a relevant role also in the dynamics of multiple four-wave mixing (mFWM). In optics mFWM indicates the generation of multiple sideband orders at $\omega_0 \pm n\Omega/2$, n odd integer, which is produced via the cubic Kerr term in the NLS by launching two angular frequencies $\omega_0 \pm \Omega/2$ along an optical fiber [60, 61]. When the two frequencies have equal power, the initial waveform is sinusoidal, and the problem of determining the evolution of the field in the regime of weak dispersion becomes the NLS counterpart of the well known problem analysed by Zabusky and Kruskal for the weakly dispersing KdV [8]. In order to unveil the dynamics we consider the dimensionless form of the NLS equation (12) subject to the initial condition $\psi(t,0) = \sqrt{\eta_0}\exp(i\omega t/2) + \sqrt{1-\eta_0}\exp(-i\omega t/2)$, where $\eta_0 = 0.5$ in the balanced case (sinusoidal input) or $\eta_0 \neq 0.5$ for the imbalanced case. Without loss of generality we fix the normalized frequency $\omega = \Omega t_0 = \pi$ by choosing $t_0 = 1/2\Delta f$ as the characteristic time scale of the modulation, $\Delta f = \Omega/2\pi$ being the frequency separation between the two pumps. In this way the dynamics depends only on the parameters ε which reads in this specific case $\varepsilon = \Delta f\sqrt{4k''/(\gamma P)}$ and gives the scale dependence of the problem [62].

At $\varepsilon = O(1)$, only a moderate cyclic (in z) generation of few mFWM orders occurs, which corresponds in time domain to cyclic compression around the minima of the squared cosine. However, when $\varepsilon \ll 1$, the dynamics qualitatively changes as shown in Fig. 6a–c. The cosine exhibits multiple points of breaking at time t corresponding to the nulls of the input power $|\psi(t,0)|^2 = 2\cos^2(\omega t/2)$. The mechanism of breaking is similar to the case of a dark input, except for the fact that, due to the periodic nature of the problem, the points of breaking are infinitely many (in time) and correspond to $t_k = \pm(2k+1)\pi/\omega$, $k = 0, 1, 2, \ldots$. Beyond the breaking point ($z \simeq 0.34$), expanding oscillations appear, similarly to the case shown in Fig. 5c, d. The oscillations fill a fan inside which they appear with decreasing amplitude towards the fan edges. Each oscillation, once formed, clearly

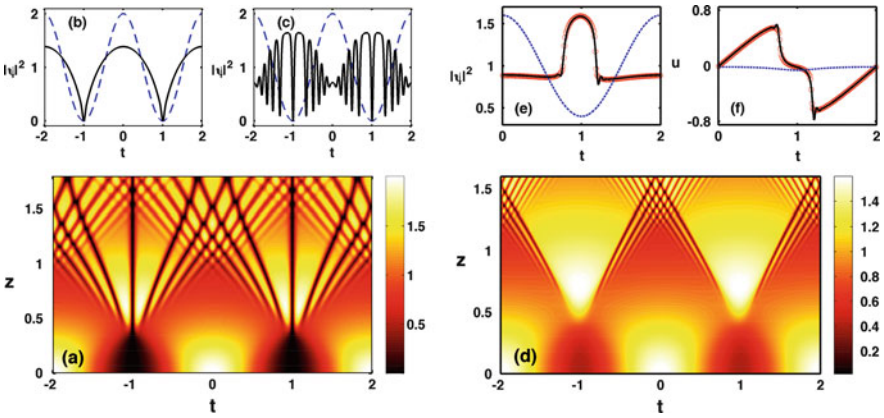

Fig. 6 (**a–c**) Breaking of a cosine (balanced dual-frequency) input according to NLS Eq. (12), $\varepsilon = 0.04$: (**a**) level *colorplot* of power $|\psi|^2$; (**b, c**) snapshots of power $\rho = |\psi|^2$ at breaking distance $z = 0.34$ (**b**) and $z = 0.95$ (**c**) compared with the input (*dashed blue*); (**d–f**) Case of two imbalanced spectral line input, $\eta_0 = 0.9$, $\varepsilon = 0.02$: (**d**) *colorplot* of $|\psi|^2$; (**e, f**) snapshot of power $\rho = |\psi|^2$ (**e**) and chirp $u = -S_t$ (**f**) comparing the outcomes of NLS (*solid lines*) and hydrodynamic limit [Eqs. (13), *red open dots*] at $z = 0.66$; input is *dashed blue*. From [62]

exhibits features of dark solitons (grayness linked to the velocity). They survive the collisions between adjacent DSW fans, which end up forming a multiphase region in the plane (t, z). It is worth emphasising that, strictly speaking, due to the periodic nature of the problem, the inverse scattering is not formulated in terms of solitons, but rather in terms of finite-band solutions. However in the limit $\varepsilon \to 0$, one numerically observes that each band shrinks resembling true solitons of the infinite line problem, while their number grows.

Noteworthy, in the imbalanced case ($\eta_0 \neq 0.5$), the temporal locations of the breaking becomes non-degenerate, and breaking occurs at two distinct instants around all the minima in t_k of the input modulation, as shown in Fig. 6d–f. In this case, two non-symmetric (right and left going) shock fans emerge from each double breaking point around t_k and collide with the adjacent shock fans, as shown in Fig. 6a (right panel). Incidentally the same type of phenomenon occurs also in the infinite line case when the dark input $\psi = \tanh(t)$ is replaced by a dark excitation with finite grayness [63].

The phenomenon of DSW in mFWM was recently observed in a fiber optics experiment, by employing the Picasso platform at Laboratorie Interdisciplinaire Carnot de Bourgogne in Dijon [46]. The setup allows for the full control of the input modulation (either in the presence of the carrier or in carrier suppressed configuration) at the frequency of 28 GHz, and to reach the necessary power of the input under quasi-continuous conditions, i.e. without resorting to pulses, which would hamper the visibility of the DSW. Furthermore, since one cannot easily measure the field along a km-long fiber without destroying it, in the experiment the evolution of the DSW is reconstructed at finite propagation length $L = 6$ km, by increasing the power. Indeed changing the power P at fixed length L amounts at changing the normalized length $z = L\sqrt{k''\gamma P}/t_0$. The results are shown in Fig. 7.

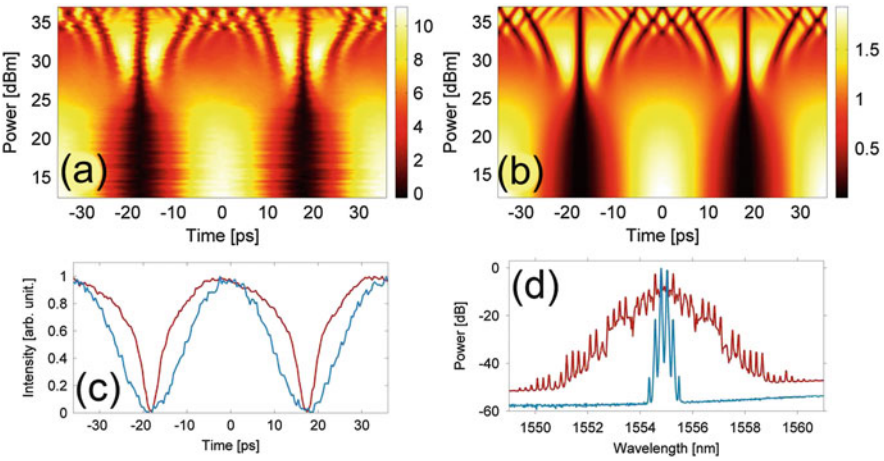

Fig. 7 Measured DSW dynamics due to mFWM with cosine (dual-frequency) input: (**a, b**) *Color*-level plots showing the temporal profiles of the output power obtained at different input powers from measured data (**a**), compared with numerical simulations (**b**), based on NLS Eq. (11); (**c**) temporal traces comparing the input file (*blue curve*) with the output close to the wave-breaking occurring at $P = 25.6$ dBm; (**d**) output spectra in the low-power ($P = 13$ dBm, pre-shock) and high-power ($P = 34.6$ dBm, post-shock) regimes. See also [46]

As shown in Fig. 7a the output temporal traces reported as a function of input power, clearly mimics the longitudinal evolution [compare in particular Fig. 7a, b with Fig. 6a], and turn out to be in excellent agreement with the simulation based on the NLS [see Fig. 7b]. The snapshot at the input power $P = 25.6$ dBm (dBm are logarithmic units such that 0 dBm = 1 mW) displayed in Fig. 7c correspond to the breaking normalized distance, thus being directly comparable with the snapshot in Fig. 6b. In the Fourier domain, the generation of the DSW corresponds to strong spectral broadening, featuring the generation of several generated orders of mFWM, as shown in Fig. 7d. The same setup has permitted to study the imbalanced case as well as input modulations with three-wave spectrum (a carrier plus sidebands), giving a complete picture of the breaking phenomena induced by mFWM [46].

We finish this section by mentioning an important connection between the dispersionless limit of the NLS (13) and the Hopf equation. If we consider pulses where the chirp (equivalent hydrodynamical velocity u) is not arbitrary, but rather linked to the power as $u = \pm\sqrt{2\rho}$, one of the two Riemann invariants identically vanishes. This is a simple wave in the language of the hyperbolic systems, where the evolution is governed by the other Riemann invariant, which obeys indeed a Hopf equation (the same equation can obviously written also for ρ or u). Therefore, by considering pulses with phase initially locked to $\phi(t, z = 0) = 2\varepsilon^{-1}\int_{-\infty}^{t}\sqrt{\rho(t', z = 0)}dt'$, the evolution follows the Hopf dynamics up to the stage where dispersive effects set in. This permits additional freedom to enhancing or suppressing the breaking, as well as a way to control the front where it occurs [64].

Although we have extensively discussed only the defocusing case, we briefly mention that also the *focusing* NLS equation can exhibit the formation of a

singularity. This was predicted on the basis of the dispersionless (or geometric optics) analog of Eq. (13) for the focusing case, which entails a negative pressure term (i.e., in the second of Eq. (13), $\rho_t \rightarrow -\rho_t$) [65]. As a consequence, the dispersionless limit turns out to be elliptic (which reflects the fact that the equation is modulationally unstable) and a different type of catastrophe occurs. For common initial waveforms (bright beams with no background) the catastrophe occurs via the formation of a cusp at the peak, and usually the post-catastrophe dynamics is very complicated with behavior determined by soliton ensembles [66]. Nevertheless, under particular conditions, the observed oscillating structure represents the focusing analog of the DSWs featured by the defocusing case [67].

Finally, we also mention that the defocusing NLS is known to be a valid model also in shallow water as an envelope equation [68]. However, observing the breaking of envelope waves in water wave experiments (as opposed to the non-envelope ones discussed in Sect. 3) is more difficult and was overlooked to date (to the best of our knowledge).

4.2 Spatial DSW in Bulk Materials

The defocusing NLS model (12) with $t \rightarrow x$ (the transverse coordinate x replaces time) and inverted signs between the dispersive and the nonlinear term, describes also the propagation of continuous-wave spatial beams in the paraxial regime (for small spatial frequencies k_x, i.e. small angles with the z-axis) in defocusing media with ideal Kerr response. Although important experiments in photorefractives have been interpreted in the framework of such model [40, 42], in spatial experiments, the nonlinear response can in general deviates from the simple ideal Kerr law, where the refractive index change is $n \propto |\psi|^2$. Depending on the specific material employed, the effects of saturation and nonlocality of the nonlinear response need to be taken into account. The saturation has been discussed in [69], and can be conveniently modelled by the cubic-quintic NLS with nonlinear terms of opposite signs [70–73]. While it is predicted that the quintic term can qualitatively change the wavebreaking scenario, to date there is no experimental evidence of this behavior.

Conversely, the nonlocality has been routinely considered to be important in order to correctly interpret the experiments [41, 43, 44, 74]. In general, it can be accounted for by allowing the nonlinear term to become a convolution, thereby obtaining in dimensionless form

$$i\varepsilon\psi_z + \frac{\varepsilon^2}{2}\nabla^2\psi - \psi\int K(|\mathbf{x}-\mathbf{x'}|)|\psi|^2(\mathbf{x'},z)d\mathbf{x'} = 0, \tag{14}$$

where $K(x)$ is a suitable kernel with normalisation $\int_{-\infty}^{\infty} K(x)dx = 1$, which depends on the material response. Equation (14) involves 1+2D dimensions with $\mathbf{x} \equiv (x, y)$ and $\nabla^2 = \partial_{xx}^2 + \partial_{yy}^2$, which is the most general regime that one deals with in the experiments. We emphasise that, at variance with water waves where the convolution enters at the linear level, in this case the nonlocality is due to the specific

mechanisms of the nonlinear response. A fully differential model which has been widely employed is the paraxial wave equation coupled to a diffusive equation for the normalized refractive index change $n = n(x, y)$, which reads as

$$i\varepsilon\psi_z + \frac{\varepsilon^2}{2}\nabla^2\psi - n(x,y)\,\psi = 0; \qquad n - \sigma^2\nabla^2 n = |\psi|^2, \tag{15}$$

which turns out to be a particular case of Eq. (14) for the kernel choice $K = (1/2\pi\sigma^2)K_0(r/\sigma)$, where K_0 denotes the modified Bessel function of second type and zero-th order, and $r = \sqrt{x^2 + y^2}$, implicitly assuming azimuthal symmetry. Here σ measures the degree of nonlocality (for $\sigma = 0$ the local NLS is recovered). In particular, the model (15) has been shown to constitute a satisfactory description of thermal nonlinearities, where nonlocality arise from heat diffusion.

The shock is a strongly local phenomenon. Therefore one might naively expect that the shock dynamics is strongly modified by the effect of nonlocality and might eventually disappear. However, interestingly enough, it has been shown that DSWs still follow a very similar dynamics compared with the local case, at least for the moderate nonlocality usually observed in experiments carried out, e.g., in thermal media [41, 43, 44, 74]. For instance, thermal samples have permitted to make the first observation of the breaking of a dark stripe (tanh(x) input) [43], the theory of which has been discussed with reference to Fig. 5c and d. The experimental result is displayed in Fig. 8, which shows, at sufficiently high input

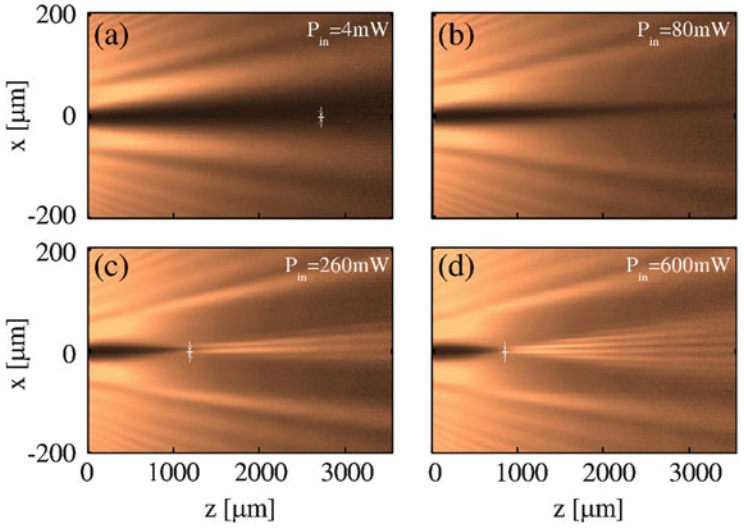

Fig. 8 Observed breaking of a dark beam with zero intensity and π-phase jump at $x = 0$, in a sample with thermal nonlinearity (solution of Rodhamine in methanol). Recorded z-evolution of the transverse (x) profile of the beam, as seen from scattering over the top of the sample, for increasing input power P_{in}: (**a**) quasi linear regime dominated by diffraction; (**b**) overcompensating nonlinearity; (**c**) generation of the DSW fan; (**d**) same as in (**c**) with breaking occurring at shorter distance. Note that the fringes outside the dark beam which remain nearly constant in all panels, are a byproduct of the method used to generate the phase-jump. From [43]

power ($P_{in} = 250$–$600\,\mathrm{mW}$), the formation of a dark focus point from which a characteristic shock fan emanates in the (x, z) plane. The output on the transverse plane $x - y$ is constituted by multiple dark stripes [43]. This is in contrast with a similar experiment in a Bose-Einstein condensate [38], where the generated dark solitons are unstable and are observed to decay into vortices. We attribute the transverse stability of the optical pattern, in our case, to the suppression of the snake instability of the generated dark stripe, owing to the effect of nonlocality [75].

5 Radiating Dispersive Shocks

As we have shown above, the dynamics of DSW is understood in terms of *weakly dispersive formulation* of integrable models (and their non-integrable deformations) such as the KdV or the defocusing NLS equations. However, since the leading order dispersion of such models must be extremely weak for the phenomenon to take place, one is naturally led to wonder about the impact of higher-order dispersion (HOD), which must be accounted for to describe the actual dispersion in many physical situations. The aim of this section is to show that HOD corrections lead DSWs to emit resonant radiation (RR) due to a specific phase-matching with linear waves, that can ultimately alter the shock dynamics itself [76–79].

Perturbed DSWs may emit RR owing to the strong spectral broadening that accompanies wave-breaking, which seeds linear waves that are resonantly amplified thanks to the well defined velocity of the shock front. We specifically formulate our approach with reference to temporal pulse propagation ruled by the defocusing NLS [76], which has immediate application to optical fibers pumped in the normal group-velocity dispersion regime [77, 80]. In this regime recent experiments have pointed out the occurrence of RR phenomena [80], which can also have direct impact over the broadband spectral feature related to the type of supercontinuum developing in the normal dispersion regime [81].

5.1 NLS Equation with HOD in the Semiclassical Regime

We return to the NLS obeyed in the laboratory frame by a slowly-varying envelope $E(Z, T)$ with central frequency ω_0 and wavenumber $k_0 = k(\omega_0)$. Once the NLS equation (11) is generalized to account for the all-order expansion of the wavenumber $k(\omega)$ around ω_0, it can be expressed in terms of the real-world dispersion operator $d_T(i\partial_T) = \sum_{n\geq 1} \partial_\omega^n k\,(i\partial_T)^n/n!$ (all the derivatives being implicitly evaluated at ω_0), reading as

$$iE_Z + d_T(\partial_T)E + \gamma|E|^2E = 0. \tag{16}$$

We recall that the defocusing character of the NLS arises from the assumption $k'' \equiv \partial_\omega^2 k > 0$ (normal dispersion), recalling that $\gamma > 0$. Adopting the same scaling used to obtain Eq. (11), by defining all orders of the dispersion coefficients as $\beta_n = \partial_\omega^n k / \sqrt{(L_{nl})^{n-2}(\partial_\omega^2 k)^n}$ (note that, by definition, $\beta_2 = 1$), we recover the generalized NLS that accounts for HOD, in its weakly dispersing form

$$i\varepsilon\psi_z + d(i\partial_t)\psi + |\psi|^2\psi = 0, \tag{17}$$

$$d(i\partial_t) = \sum_{n\geq 2} \frac{\beta_n}{n!}\varepsilon^n (i\partial_t)^n = -\frac{\varepsilon^2}{2}\partial_t^2 - i\frac{\beta_3\varepsilon^3}{6}\partial_t^3 + \frac{\beta_4\varepsilon^4}{24}\partial_t^4 + \dots$$

Note that the normalized dispersive operator $d(i\partial_t)$ has progressively smaller terms, weighted by powers of the parameter $\varepsilon \ll 1$ and coefficients β_n.

The process of wave-breaking ruled by Eq. (17) can be described by applying, again, the Madelung transformation $\psi = \sqrt{\rho}\exp(iS/\varepsilon)$. At leading-order in ε, we obtain a quasi-linear hydrodynamic reduction, with $\rho = |\psi|^2$ and $u = -S_t$ equivalent density and velocity of the flow,

$$\begin{pmatrix} \rho \\ u \end{pmatrix}_z + A \begin{pmatrix} \rho \\ u \end{pmatrix}_t \; ; \; A = \begin{pmatrix} a_{11} & a_{12} \\ 1 & a_{11} \end{pmatrix} \tag{18}$$

where the matrix elements are $a_{11} = \beta_2 u + \frac{\beta_3}{2}u^2 + \frac{\beta_4}{6}u^3 + \frac{\beta_5}{24}u^4 + \dots = \sum_{n\geq 2}\frac{\beta_n}{(n-1)!}u^{n-1}$, and $a_{12} = \rho\left(\beta_2 + \beta_3 u + \frac{\beta_4}{2}u^2 + \frac{\beta_5}{6}u^3 + \dots\right) = \rho\left(\sum_{n\geq 2}\frac{\beta_n}{(n-2)!}u^{n-2}\right)$. This system can be also conveniently diagonalized to yield

$$r_z^{\pm} + V^{\pm} r_t^{\pm} = 0, \tag{19}$$

by introducing the eigenvelocities (i.e. the eigenvalues of matrix A) $V^{\pm} = a_{11} \pm \sqrt{a_{12}} = \sum_{n\geq 2}\beta_n u^{n-1}/(n-1)! \pm \sqrt{\rho\sum_{n\geq 2}\beta_n u^{n-2}/(n-2)!}$ and the Riemann invariants $r^{\pm} = u \pm 2\frac{\sqrt{\rho}}{\sqrt{\sum_{n\geq 2}\beta_n u^{n-2}/(n-2)!}}$.

By multiplying the first and the second of Eqs. (18), respectively by u and ρ and summing up, we easily recover the equivalent form of a 2×2 conservation law $\mathbf{q}_z + \mathbf{f}_t(\mathbf{q}) = 0$ for $\mathbf{q} = (\rho, \rho u)$

$$\rho_z + \left[\sum_{n\geq 2}\frac{\beta_n}{(n-1)!}(\rho u^{n-1})\right]_t = 0, \tag{20}$$

$$(\rho u)_z + \left[\sum_{n\geq 2}\frac{\beta_n}{(n-1)!}\rho u^n + \frac{1}{2}\rho^2\right]_t = 0. \tag{21}$$

Equations (20) and (21), as far as the HOD terms are such that they remain hyperbolic, admit weak solutions in the form of classical shock waves (SWs), i.e. traveling discontinuity from left (ρ_l, u_l) to right (ρ_r, u_r) values, which constitute the generalization of the scalar case discussed with reference to the Hopf equation. The velocity of such SWs, say V_c, can be found from a generalization of the Rankine-Hugoniot condition (3) to the vectorial case. While the RH condition remains formally the same, i.e. $V_c(\mathbf{q}_l - \mathbf{q}_r) = [\mathbf{f}(\mathbf{q}_l) - \mathbf{f}(\mathbf{q}_r)]$, it should be noticed that the scalar velocity should be the same for the two components of the vectors [48]. In the 2×2 case, the RH equations fix both V_c and the admissible value of one of the parameters of the jump, e.g. u_r given ρ_r, ρ_l, u_l.

For instance, when no HOD is effective (take $\beta_2 = 1$), an admissible right-going shock which satisfies the entropy condition $\rho_l > \rho_r$, can be obtained with

$$u_r = u_l - (\rho_l - \rho_r)\sqrt{\frac{\rho_r + \rho_l}{2\rho_l\rho_r}}; \qquad V_c = u_l + \rho_r\sqrt{\frac{\rho_r + \rho_l}{2\rho_l\rho_r}}. \tag{22}$$

This result can be generalized for HOD, thanks to Eqs. (20) and (21). For instance, if $\beta_3 \neq 0$, the SW velocity becomes

$$V_c = \frac{\beta_2(\rho_l u_l - \rho_r u_r) + \beta_3(\rho_l u_l^2 - \rho_r u_r^2)/2}{(\rho_l - \rho_r)}, \tag{23}$$

where u_r is obtained as the real root of the cubic equation $\beta_3(u_l - u_r)^2(u_l + u_r) + 2\beta_2(u_l - u_r)^2 = g(\rho_l, \rho_r)$, where $g(\rho_l, \rho_r) \equiv (\rho_l - \rho_r)^2(\rho_r + \rho_l)/(\rho_l\rho_r)$ [76].

As described in the previous sections, second-order dispersion regularizes classical SWs by replacing the jump with an expanding fan filled with oscillations described in terms of a modulated nonlinear periodic wave, i.e. a DSW. In this case the SW velocity V_c is replaced by the velocities of the leading V_l and trailing V_t edges (with $V_l < V_c < V_t$), where the periodic wave locally tends to a soliton and a linear wave, respectively. HOD induces this structure to radiate, also altering the dynamics of SW formation. In the following we specifically focus on the effect of two leading HOD, namely third-order (3-HOD) and fourth-order (4-HOD) dispersion, showing how RR is shed with different features depending on the specific dispersive correction.

5.2 *Resonant Radiation Emitted by Dispersive Shocks*

The frequency of the RR can be predicted by applying a perturbation approach which accounts for dispersion at all orders [78]. We start by assuming a radiating shock front $\bar{\psi}$ which travels with invariant profile at definite velocity $V_s = dt/dz$. In other words, we consider the local edge of a solution $\psi(z,t) = \bar{\psi}(\tau)\exp(ik_s z)$ of Eq. (17) with dispersion truncated at second-order, where $\tau = t - V_s z$ and k_s is the

nonlinear wavenumber of the shock. We account for perturbations to this front due to HOD by assuming a perturbed field of the form $\psi = [\bar{\psi}(\tau) + p(z,\tau)]\exp(ik_s z)$. By substituting ψ in Eq. (17), we obtain, after linearization ($|p| \ll |\bar{\psi}|$), the following evolution equation for p

$$i\varepsilon p_z + \hat{d}(i\partial_\tau)p + 2|\bar{\psi}|^2 p + \bar{\psi}^2 p^* = F, \tag{24}$$

where $F = -\left[d(i\partial_\tau) - \beta_2(i\varepsilon\partial_\tau)^2/2\right]\bar{\psi}$ is a forcing term with zero wavenumber, and $\hat{d}(i\partial_\tau) \equiv d(i\partial_\tau) - iV_s\varepsilon\partial_\tau$. Setting $p(z,\tau) = A(z)\exp[i(kz - \omega\tau)] + B^*(z)\exp[-i(kz - \omega\tau)]$, we find that Eq. (24) for $F = 0$ (i.e. for free-running waves) reduces to the following system for the Stokes-antiStokes amplitudes $a(z) = [A(z), B(z)]^T$

$$i\varepsilon\frac{da}{dz} + Ca = 0, \tag{25}$$

$$C = \begin{pmatrix} D(\omega) - \varepsilon k & \bar{\psi}^2 \\ -(\bar{\psi}^*)^2 & -D(-\omega) - \varepsilon k \end{pmatrix}, \tag{26}$$

where $D(\omega) = \tilde{d}(\varepsilon\omega) + 2|\bar{\psi}|^2 - \varepsilon k_s$, and $\tilde{d}(\varepsilon\omega) = \sum_{n\geq 2}\frac{\beta_n}{n!}(\varepsilon\omega)^n - (\varepsilon\omega)V_s$ is the Fourier transform of $\hat{d}(i\partial_\tau)$. The dispersion relation $\kappa = \kappa(\varepsilon\omega)$ of such waves is found by imposing $det(C) = 0$, which yields the following two branches $\kappa = \kappa_\pm(\varepsilon\omega)$

$$\varepsilon\kappa_\pm = \frac{d_{odd}}{2} \pm \frac{1}{2}\sqrt{d_{even}[d_{even} + 4|\psi_0|^2]}, \tag{27}$$

where $d_{odd} \equiv \tilde{d}(\varepsilon\omega) - \tilde{d}(-\varepsilon\omega)$ and $d_{even} \equiv \tilde{d}(\varepsilon\omega) + \tilde{d}(-\varepsilon\omega)$, and we have considered that $k_s = |\psi_0|^2/\varepsilon$ is the Kerr wavenumber shift over the CW plateau (upper state of the shock front) with power $|\psi_0|^2$ where RR is emitted. Frequencies $\omega = \omega_{RR}$ such that $\kappa_\pm = \kappa(\varepsilon\omega_{RR}) = 0$ can grow because they become resonant with the forcing F in Eq. (24). They arise in pairs ($\omega = \pm|\omega_{RR}|$) due to the symmetry of the problem. Note, however, that the wave amplitude that grows at such frequencies is generally very different, being related to the eigenvectors of the matrix.

A sufficiently accurate estimate for ω_{RR} can be obtained by expanding the square root in Eq. (27) under the hypothesis $|\psi_0|^2 \ll |d_{even}|$, which yields

$$\sum_{n\geq 2}\frac{\beta_n}{n!}(\varepsilon\omega)^n - (\varepsilon\omega)V_s + |\psi_0|^2 = 0. \tag{28}$$

In the case of dominant TOD ($\beta_3 \neq 0$, $\beta_n = 0$, $n \geq 4$), Eq. (28) explicitly reads as

$$\left[\beta_3\frac{(\varepsilon\omega)^3}{6} + \beta_2\frac{(\varepsilon\omega)^2}{2} - V_s(\varepsilon\omega)\right] + |\psi_0|^2 = 0. \tag{29}$$

Equation (29) coincides with the condition derived in [76] on simple physical ground. The square bracket represents the wavenumber of linear waves while the remaining term stands for the nonlinear correction induced through cross-phase modulation from the ψ_0 plateau over which radiation is emitted.

In the limit $V_s = 0$, also neglecting the nonlinear correction $|\psi_0|^2$, Eq. (29) gives the approximated result $\varepsilon\omega_{RR} = -3\beta_2/\beta_3$, or $\Omega_{RR} = \omega_{RR}/T_0 = -3\partial_\omega^2 k/\partial_\omega^3 k$ in physical units. This is equivalent to the original result derived for bright soliton [82].

5.2.1 Third-Order Dispersion

When 3-HOD is effective we find a cross-over from a perturbative regime ($|\beta_3| < 0.5$) where the DSW leading edge turns out to be responsible for the RR, to a regime where the 3-HOD is strong enough ($|\beta_3| \sim 1$) to modify the shock formation, leading to enhanced RR produced by a traveling front which is approximated with a classical SW. To show this and verify that Eq. (28) is able to predict the RR frequency in both regimes, we consider first a step initial value that allows us to calculate analytically the velocity. Without loss of generality, we take $\beta_3 < 0$. Specifically, we consider the evolution of an initial jump from the "left" state $\rho_l, u_l = 0$ for $t < 0$ to the "right" state $\rho_r (< \rho_l), u_r = 2(\sqrt{\rho_r} - \sqrt{\rho_l})$ for $t > 0$, which is such to maintain constant $r^-(z = 0, t)$ while $r^+(z = 0, t)$ has step-like variation. In this case, the modulated wavetrain produced upon evolution [see Fig. 9a and c] in the limit $\beta_3 = 0$, is described by a rarefaction wave of the Whitham modulation equations for the unperturbed NLS [16, 17, 39]. Following a modulation approach and exploiting the fact that only one Riemann variable of such Whitham equations changes, one can calculate the edge velocities of the fan [76]. What is relevant for the RR is the leading-edge velocity, which we find to be $V_l = \sqrt{\rho_l} + u_r = 2\sqrt{\rho_r} - \sqrt{\rho_l}$. Given a gray soliton on unchirped background A ($\psi = A[w\tanh(\theta) + iv]\exp(iA^2 z/\varepsilon)$, $\theta = \frac{w}{\varepsilon}(t - Avz)$, $w^2 = 1 - v^2$) V_l turns out to coincide with the soliton velocity $V_{sol} = Av = \sqrt{\rho_{min}}$, with natural position $A = \sqrt{\rho_l}$, $v = (2\sqrt{\rho_r} - \sqrt{\rho_l})/\sqrt{\rho_l}$, and the dip density $\rho_{min} = (2\sqrt{\rho_r} - \sqrt{\rho_l})^2$. We emphasize that the equivalence of the leading edge with a gray soliton holds only locally since the DSW is strictly speaking a modulated nonlinear wave.

In this regime, if we account for $|\psi_0|^2 = \rho_l$, Eq. (28) explicitly reads as

$$\frac{\beta_3}{6}(\varepsilon\omega)^3 + \frac{\beta_2}{2}(\varepsilon\omega)^2 - V_s(\varepsilon\omega) + \rho_l = 0. \tag{30}$$

Real solutions $\omega = \omega_{RR}$ of Eq. (30), with $V_s = V_l \equiv 2\sqrt{\rho_r} - \sqrt{\rho_l}$ correctly predict the RR as long as $|\beta_3| < 0.5$, as shown by the NLS simulation in Fig. 9. The DSW displayed in Fig. 9a clearly exhibits a spectral RR peak besides spectral shoulders due to the oscillating front, as shown by the spectral evolution in Fig. 9b and the output spectrum (compared with unperturbed one) in Fig. 9d. Perfect agreement is

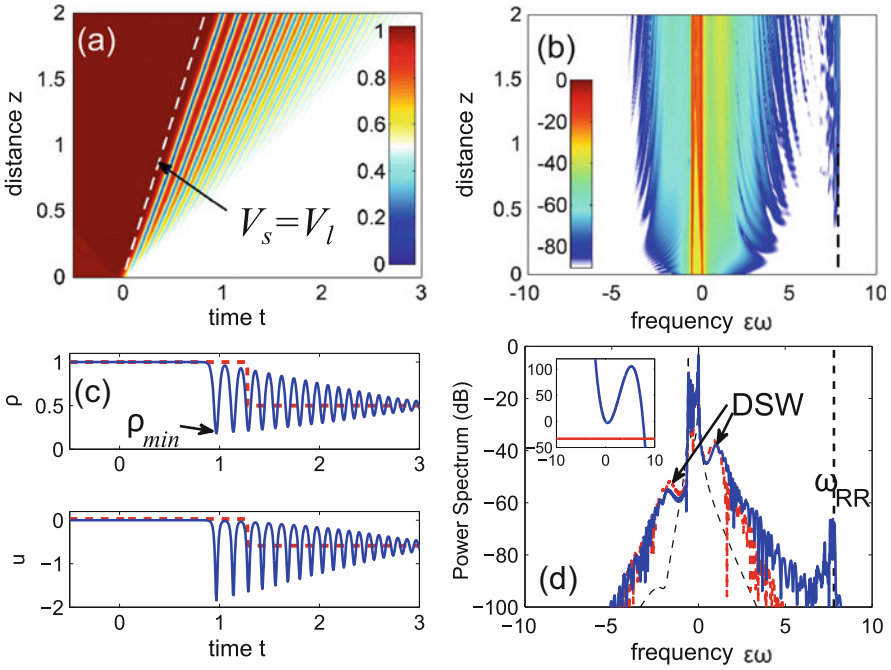

Fig. 9 Radiating DSW from NLS (17) with $\varepsilon = 0.03$, input step $\rho_l, \rho_r = 1, 0.5$, and 3-HOD $\beta_3 = -0.35$: (**a**) *Color* level plot of density $\rho(t, z)$ (the *dashed line* gives the DSW leading edge velocity V_l); (**b**) corresponding spectral evolution; (**c**) snapshots at $z = 2$ of ρ, u of unperturbed case $\beta_3 = 0$ (in *dashed red* the corresponding classical SW); (**d**) comparison of output spectra with (*thick solid blue*) and without (*dashed red*) 3-HOD (input *thin dashed*); inset: graphical solution of Eq. (28). From [76]

found between the RR peak obtained in the numerics and the prediction [dashed vertical line in Fig. 9b and d] from Eq. (30) with velocity $V_s = V_l$ characteristic of the integrable limit ($\beta_3 = 0$, snapshots in Fig. 9c). Indeed, in this regime, the DSW leading edge is nearly unaffected by 3-HOD, whereas using the velocity V_c [Eq. (22)] of the equivalent classical SW [reported for comparison in Fig. 9c] would miss the correct estimate of ω_{RR}. We also point out that k_s represents a small correction, so ω_{RR} can be safely approximated by dropping the last term in Eq. (30) to yield $\varepsilon\omega_{RR} = \frac{3}{2\beta_3}\left(-\beta_2 \pm \sqrt{\beta_2^2 + 8V_s\beta_3/3}\right)$, that can be reduced to the simple formula $\varepsilon\omega_{RR} = -3\beta_2/\beta_3$ [80] only in the limit $\beta_3 V_s \to 0$.

When $|\beta_3|$ grows larger, the aperture of the shock fan reduces (the difference between leading and trailing edge velocities decreases), until quite unexpectedly the DSW resembles a single traveling front, i.e. a classical SW. In this regime, we find that Eq. (30) still gives the correct frequency ω_{RR} provided that V_s is taken as the

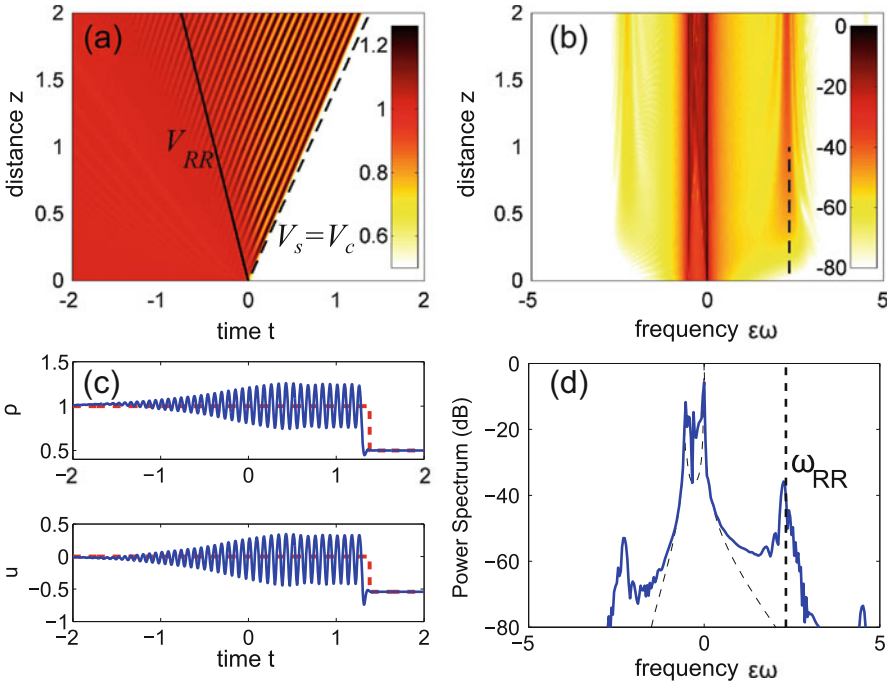

Fig. 10 As in Fig. 9 with larger 3-HOD $\beta_3 = -1$. The *dashed vertical line* in (**b**) and (**d**) gives ω_{RR} from Eq. (30) with velocity $V_s = V_c$ [corresponding to *dashed line* in (**a**)]. Here $V_c = 0.69$ and $u_r = -0.543$ are the parameters of the classical SW [shown in *dashed red* in (**c**)] from Eq. (23). *Solid line* in (**a**) indicates the velocity V_{RR} of the RR. From [76]

Rankine-Hugoniot velocity V_c of the equivalent classical SW calculated for $\beta_3 \neq 0$ [Eq. (23)]. An example of this behavior is illustrated in Fig. 10 for $\beta_3 = -1$. The RR becomes clearly visible in the temporal evolution [Fig. 10a and snapshots in Fig. 10c], and is sufficiently strong to generate also $-\omega_{RR}$ via four-wave mixing, as clear from the spectrum [Fig. 10b–d]. Perfect agreement between the numerics and the value predicted from Eq. (30), once we set $V_s = V_c$, is found also in this case. A physical interpretation of this remarkable transition from dispersive to classical shock is that the emitted radiation behaves as a local loss for the shock front.

The behaviors of step initial data are basically recovered for pulse waveforms that are more manageable in experiments. Figure 11 shows the transition from the perturbative [Fig. 11a] to the non-perturbative [Fig. 11b] regime, for an input gaussian pulse $\psi(z = 0, t) = \nu + (1 - \nu)\exp(-t^2)$ with background to peak density ratio $\nu^2 = 0.09$. As shown in Fig. 11a, for relatively small β_3, two asymmetric DSWs emerge from wave-breaking points on the two pulse edges, which occur at different distances due to broken symmetry in time caused by 3-HOD. Phase-matching is achieved only for the DSW traveling with $V_s > 0$. The corresponding ω_{RR} can be obtained from Eq. (30) provided we set $V_s = V_l$, with the DSW

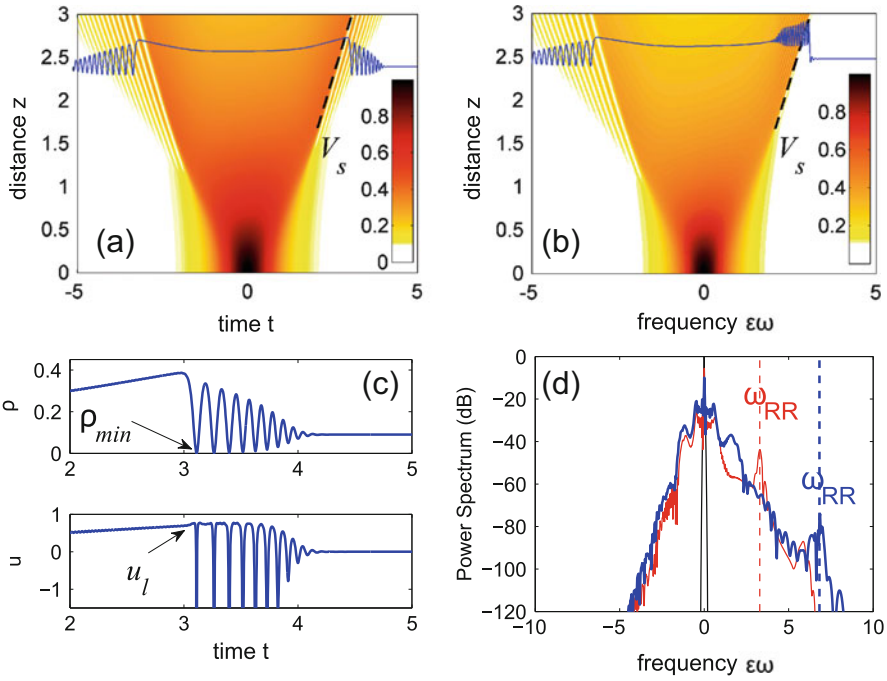

Fig. 11 Radiating DSW from Gaussian pulses with small background $v^2 = 0.09$: (**a**) $\beta_3 = -0.35$; (**b**) $\beta_3 = -0.6$; (**c**) Parameters determining the leading edge velocity $V_s = \sqrt{\rho_{min}} + u_l = \sqrt{10^{-4}} + 0.76 = 0.77$ [*dashed line* in (**a**)], snapshot at $z = 3$; (**d**) Output spectra (*thick blue*, $\beta_3 = -0.35$; *thin red*, $\beta_3 = -0.6$). The *dashed lines* give $\varepsilon\omega_{RR}$ calculated from Eq. (30). Here $\varepsilon = 0.03$; *blue curves* in (**a**), (**b**) depict output snapshots. From [76]

leading edge velocity being (following the discussion of Fig. 9) $V_l = \sqrt{\rho_{min}} + u_l$, where the minimum density and the correction u_l due to the local non-zero chirp are evaluated numerically after wave-breaking as shown in Fig. 11c. Indeed, these parameters cannot be obtained analytically for a generic initial value problem, nor they are strictly constant upon evolution. Also in this case, a larger $|\beta_3|$ results in a narrower fan (and larger shock distance), until eventually a simple front is left which strongly radiates, as shown in Fig. 11b. In this regime, a good approximation of the front velocity is obtained by the approximating classical SW in Eq. (23). In both the regimes shown in Fig. 11a and b, Eq. (30) provides an accurate estimate of the RR frequency, as shown by the dashed lines reported in the output spectra in Fig. 11d. Notice also that, for symmetry reasons, sign reversal of 3-HOD (i.e., $\beta_3 > 0$) simply results into RR with opposite frequency, generated by the DSW with opposite velocity ($V_s < 0$, left DSW).

5.2.2 Fourth-Order Dispersion

A completely different scenario occurs when the dispersive correction is due to 4-HOD. In this case, the shock formation can compete with a different instability mechanism, namely modulational instability (MI). Indeed MI extends to the defocusing regime $\beta_2 = 1$, whenever $\beta_4 < 0$, as proven experimentally [83]. This competition occurs also in different systems [84]. The continuous wave (CW) solution of Eq. (17) reads $\psi(z,t) = \sqrt{P_0}\exp[izP_0/\varepsilon]$. MI arises when periodic perturbations in the form $p(z,t) = a(z)\exp[i\omega t] + b(z)\exp[-i\omega t]$ grow exponentially like $\exp[Gz]$ at the expense of the CW pump. We find that the gain is $G(\varepsilon\omega) = |\Im[\lambda]|/\varepsilon$, where

$$\lambda = \Sigma_o \pm \sqrt{\Sigma_e^2 + 2P_0\Sigma_e} \tag{31}$$

and $\Sigma_e = \sum_{n\geq 1}\beta_{2n}(\varepsilon\omega)^{2n}/(2n)!$, $\Sigma_o = \sum_{n\geq 1}\beta_{2n+1}(\varepsilon\omega)^{2n+1}/(2n+1)!$ are the even and odd parts of dispersion, respectively. It is clear that only even dispersive terms determine the stability properties.

Considering 4-HOD $\beta_4 < 0$ ($\beta_2 = 1$), we have $\max G(\varepsilon\omega) = P_0/\varepsilon$, for $\varepsilon\omega_{peak} = \left[6\left(\beta_2 + \sqrt{\beta_2^2 + 2/3|\beta_4|P_0}\right)/|\beta_4|\right]^{1/2}$. The gain band ranges from $\varepsilon\omega_{min} = \sqrt{12\beta_2/|\beta_4|}$ to $\varepsilon\omega_{max} = \sqrt{6\left(\beta_2 + \sqrt{\beta_2^2 + 4/3|\beta_4|P_0}\right)/|\beta_4|}$ (and symmetric for $\omega \to -\omega$).

Moreover, the phase-matching curve in Eq. (28), involving in this case a fourth order polynomial, leads for the shock with $V_s > 0$ to two possible phase-matching frequencies, ω_{RR1} and $-\omega_{RR2}$ ($\omega_{RR1,2} > 0$), which become four (two symmetric pairs) since opposite frequencies are phase-matched by the shock with opposite velocity $V_s < 0$ according to Eq. (28), as illustrated in Fig. 12a. Our analysis shows that the two frequencies $\omega_{RR1,RR2}$ (arising from shock on opposite edges) lie on the opposite sides of the MI gain curve (calculated for continous waves), which has cut-off frequency $\varepsilon\omega_c = \sqrt{12/|\beta_4|}$ and is narrow bandwidth. For an input pulse MI amplifies frequencies in a larger bandwidth which serve as a seed for the RR. Indeed, as clear from the NLS simulation in Fig. 12b, the twin-band RR starts to grow, triggered by MI, even during the process of pulse steepening [see evolution in Fig. 12c], while becoming prominent as the DSWs start to develop, traveling with definite velocities (here $V_s = \pm 0.77$). The RR frequencies from Fig. 12a fit well those reported in the numerical output spectrum in Fig. 12d. The coexistence of the two wave-breaking phenomena (MI and DSW) is clearly visible in the output snapshot in Fig. 12c.

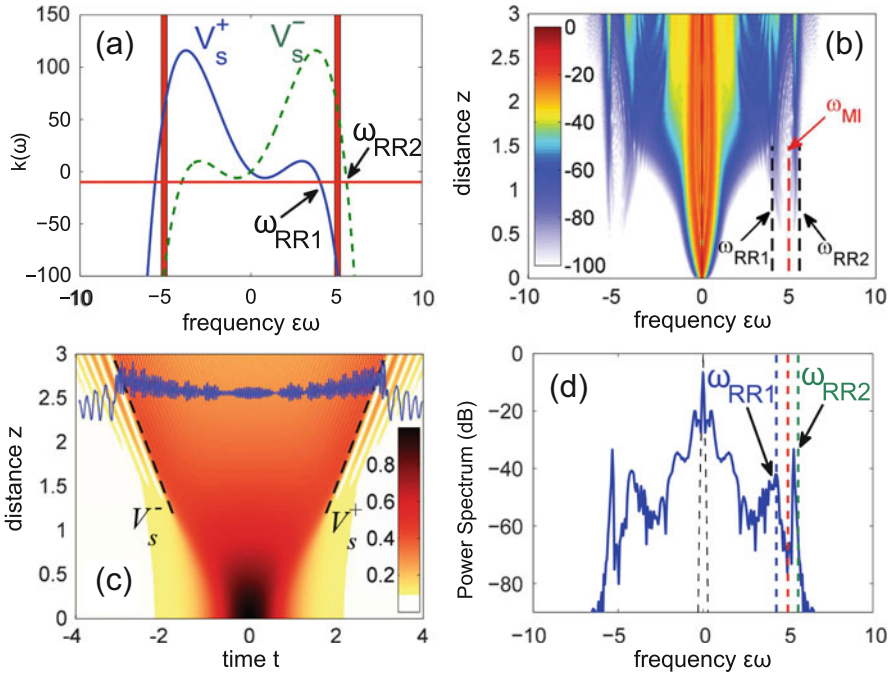

Fig. 12 (RR ruled by 4-HOD ($\beta_3 = 0$, $\beta_4 = -0.5$): (**a**) dispersion curves from Eq. (28) for positive (V_s^+, *solid blue*) and negative (V_s^-, *dashed green*) velocity crossing k_{nl} (*horizontal red line*) in $\pm\omega_{RR1,RR2}$; *vertical stripes* indicate MI gain bands; (**b**) spectral evolution; (**c**) temporal dynamics (*blue curve* depicts output snapshot); (**d**) output spectrum [central *red dashed line* is peak MI gain, *blue and green dashed lines* correspond to RR, arrows in (**a**)]. Here $\varepsilon = 0.05$, input Gaussian pulse with background $\nu^2 = 0.09$. From [76]

6 Conclusions

We have reviewed the area of dispersive hydrodynamics with emphasis on the generation of dispersive shock waves in the field of water waves and nonlinear optics. Experimental evidence of the occurrence of the dispersive shocks have been reported in different regimes that involve initial data with no soliton content, purely solitonic dispersive shocks, or periodic waves. We have discussed the models that allow to describe such phenomenon, i.e. the KdV for surface gravity waves and the NLS in optics. We have emphasised the role of nonlocality which needs to be accounted for, at linear level in water waves (Whitham equation) and at nonlinear level in nonlinear optics (diffusive NLS equation). Furthermore we have demonstrated that dispersive shock waves resulting from the nonlinearity overbalancing a weak leading-order dispersion can emit resonant radiation owing to higher-order dispersive contributions. We have analysed such phenomenon for the defocusing NLS equation, giving criteria for calculating the radiated frequency

based on the estimate of the shock velocity, revealing also a diversity of possible scenarios depending on the order and magnitude of the dispersive corrections.

We point out that the dispersive hydrodynamics is a major area of investigation, and dispersive shocks have been demonstrated to play a substantial role in contexts that we did not have the proper room to discuss in this short survey. They include promising and rapidly developing areas such as the propagation in the presence of material disorder or incoherency of the field [85–87] (see chapter by Picozzi et al.), optical cavities [79, 88], viscous fluid conduits [89], or flow past an obstacle [90], and can be important for several optical applications [91, 92].

Acknowledgements The authors gratefully acknowledge C. Conti, J. Fatome, C. Finot, M. Klein, G. Millot, M. Onorato, M. Peccianti, G. Ruocco, without whom the experiments presented here would have not been possible, as well as fruitful collaboration with A. Armaroli, F. Baronio, G. Bellanca, D. Faccio, A. Fratalocchi, J. Garnier, N. Gofraniha, S. Malaguti, A. Moro, A. Picozzi, A. Valiani, and G. Xu, and enlightening discussions with M. Ablowitz, G. Biondini, B. Dubrovin, G. El, T. Grava, M. Hoefer, A. Kamchatnov, Y. Kodama, P. Miller, and S. Wabnitz. The research was partially supported by IRCICA (USR 3380 Univ. Lille - CNRS), by the ANR NoAWE (ANR-14-ACHN-0014), Labex CEMPI (ANR-11-LABX-0007) and Equipex FLUX (ANR-11-EQPX-0017) projects, by the "Fonds Européen de Développement Economique Régional", and by the grant PRIN 2012BFNWZ2.

References

1. Hoefer, M., Ablowitz, M.: Dispersive shock waves. Scholarpedia **4**(11), 5562 (2009)
2. Whitham, G.B.: Linear and Nonlinear Waves, vol. 42. Wiley, New York (1974)
3. Moiseev, S., Sagdeev, R.: Collisionless shock waves in a plasma in a weak magnetic field. J. Nucl. Energy. Part C: Plasma Phys. Accelerators Thermonuclear Res. **5**(1), 43 (1963)
4. Taylor, R., Baker, D., Ikezi, H.: Observation of collisionless electrostatic shocks. Phys. Rev. Lett. **24**(5), 206 (1970)
5. Korteweg, D.J., De Vries, G.: On the change of form of long waves advancing in a rectangular canal, and on a new type of long stationary waves. Lond. Edinb. Dublin Philos. Mag. J. Sci **39** (240), 422–443 (1895)
6. Boussinesq, J.: Essai sur la théorie des eaux courantes,Mémoires présentés par divers savants a l'Acad. des Sci. Inst. Nat. France, XXIII, pp. 1–680, 1877, vol. 2. Imprimerie nationale (1877)
7. De Jager, E.: On the origin of the Korteweg-de Vries equation. arXiv: preprint math/0602661 (2006)
8. Zabusky, N.J., Kruskal, M.D.: Interaction of "solitons" in a collisionless plasma and the recurrence of initial states. Phys. Rev. Lett. **15**(6), 240 (1965)
9. Gurevich, A., Pitaevskii, L.: Nonstationary structure of a collisionless shock wave. Sov. Phys. JETP **38**, 291 (1974)
10. Whitham, G.: Non-linear dispersive waves. Proc. R. Soc. Lond. A **283**(1393), 238–261 (1965)
11. Flaschka, H., Forest, M., McLaughlin, D.: Multiphase averaging and the inverse spectral solution of the korteweg-de vries equation. Commun. Pure Appl. Math. **33**(6), 739–784 (1980)
12. Lax, P.D., Levermore, C.D.: The small dispersion limit of the korteweg-de vries equation. I. Commun. Pure Appl. Math. **36**(3), 253–290 (1983)
13. Lax, P.D., Levermore, C.D.: The small dispersion limit of the korteweg-de vries equation. II. Commun. Pure Appl. Math. **36**(5), 571–593 (1983)
14. Lax, P.D., Levermore, C.D.: The small dispersion limit of the korteweg-de vries equation. III. Commun. Pure Appl. Math. **36**(6), 809–829 (1983)

15. Lax, P., Levermore, C., Venakides, S.: The generation and propagation of oscillations in dispersive initial value problems and their limiting behavior. In: Fokas, A.S., Zakharov, V.E. (eds) Important Developments in Soliton Theory, pp. 205Ű241. Springer, Berlin (1993)
16. Gurevich, A., Krylov, A.L.: Dissipationless shock waves in media with positive dispersion. Sov. Phys. JETP **65**, 944–953 (1987)
17. El, G.A., Geogjaev, V.V., Gurevich, A.V., Krylov, A.L.: Decay of an initial discontinuity in the defocusing NLS hydrodynamics. Physica D **87**, 186–192 (1995)
18. Dubrovin, B., Novikov, S.: The Hamiltonian formalism of one-dimensional systems of hydrodynamic type and the Bogoliubov-Whitham averaging method. In: Akademiia Nauk SSSR, Doklady, vol. 270, pp. 781–785 (1983)
19. Kamchatnov, A.: Nonlinear Periodic Waves and Their Modulations: An Introductory Course. World Scientific, Singapore (2000)
20. El, G.A.: Resolution of a shock in hyperbolic systems modified by weak dispersion. Chaos: Interdiscip. J. Nonlinear Sci. **15**(3) 037103 (2005)
21. Grava, T., Klein, C.: A numerical study of the small dispersion limit of the KdV equations and asymptotic solutions. Physica D **241**(11), 2246–2264 (2012)
22. Dubrovin, B.: On Hamiltonian perturbations of hyperbolic systems of conservation laws, II: universality of critical behaviour. Commun. Math. Phys. **267**(1), 117–139 (2006)
23. Dubrovin, B., Grava, T., Klein, C., Moro, A.: On critical behaviour in systems of Hamiltonian partial differential equations. J. Nonlinear Sci. **25**(3), 631–707 (2015)
24. Benjamin, T.B., Lighthill, M.: On cnoidal waves and bores. In: Proceedings of the Royal Society of London A, vol. 224, pp. 448–460. The Royal Society, London (1954)
25. Peregrine, D.: Calculations of the development of an undular bore. J. Fluid Mech. **25**(02), 321–330 (1966)
26. Johnson, R.: Shallow water waves on a viscous fluid - the undular bore. Phys. Fluids **15**(10), 1693–1699 (1972)
27. Zabusky, N., Galvin, C.: Shallow-water waves, the Korteweg-deVries equation and solitons. J. Fluid Mech. **47**(04), 811–824 (1971)
28. Hammack, J.L.: A note on tsunamis: their generation and propagation in an ocean of uniform depth. J. Fluid Mech. **60**(04), 769–799 (1973)
29. Segur, H.: The Korteweg-de Vries equation and water waves. Solutions of the equation. Part 1. J. Fluid Mech. **59**(04), 721–736 (1973)
30. Hammack, J.L., Segur, H.: The korteweg-de vries equation and water waves. Part 2. Comparison with experiments. J. Fluid Mech. **65**(02), 289–314 (1974)
31. Hammack, J.L., Segur, H.: The korteweg-de vries equation and water waves. Part 3. Oscillatory waves. J. Fluid Mech. **84**(02), 337–358 (1978)
32. Hammack, J.L., Segur, H.: Modelling criteria for long water waves. J. Fluid Mech. **84**(02), 359–373 (1978)
33. Tomlinson, W.J., Stolen, R.H., Johnson, A.M.: Optical wave breaking of pulses in nonlinear optical fibers. Opt. Lett. **10**, 467–469 (1985)
34. Anderson, D., Desaix, M., Lisak, M., Quiroga-Teixeiro, M.L.: Wave breaking in nonlinear-optical fibers. J. Opt. Soc. Am. B **9**, 1358–1361 (1992)
35. Rothenberg, J.E., Grischkowsky, D.: Observation of the formation of an optical intensity shock and wave breaking in the nonlinear propagation of pulses in optical fibers. Phys. Rev. Lett. **62**(5), 531 (1989)
36. Kodama, Y., Wabnitz, S.: Analytical theory of guiding-center nonreturn-to-zero and return-to-zero signal transmission in normally dispersive nonlinear optical fibers. Opt. Lett. **20**, 2291–2293 (1995)
37. Kodama, Y.: The Whitham equations for optical communications: mathematical theory of NRZ. SIAM J. Appl. Math. **59**(6), 2162–2192 (1999)
38. Dutton, Z., Budde, M., Slowe, C., Hau, L.V.: Observation of quantum shock waves created with ultra-compressed slow light pulses in a Bose-Einstein condensate. Science **293**(5530), 663–668 (2001)

39. Hoefer, M., Ablowitz, M., Coddington, I., Cornell, E., Engels, P., Schweikhard, V.: Dispersive and classical shock waves in Bose-Einstein condensates and gas dynamics. Phys. Rev. A **74** (2), 023623 (2006)
40. Wan, W., Jia, S., Fleischer, J.W.: Dispersive superfluid-like shock waves in nonlinear optics. Nat. Phys. **3**(1), 46–51 (2007)
41. Ghofraniha, N., Conti, C., Ruocco, G., Trillo, S.: Shocks in nonlocal media. Phys. Rev. Lett. **99**(4), 043903 (2007)
42. Jia, S., Wan, W., Fleischer, J.W.: Dispersive shock waves in nonlinear arrays. Phys. Rev. Lett. **99**(22), 223901 (2007)
43. Conti, C., Fratalocchi, A., Peccianti, M., Ruocco, G., Trillo, S.: Observation of a gradient catastrophe generating solitons. Phys. Rev. Lett. **102**(8), 083902 (2009)
44. Ghofraniha, N., Amato, L.S., Folli, V., Trillo, S., DelRe, E., Conti, C.: Measurement of scaling laws for shock waves in thermal nonlocal media. Opt. Lett. **37**(12), 2325–2327 (2012)
45. Ghofraniha, N., Gentilini, S., Folli, V., DelRe, E., Conti, C.: Shock waves in disordered media. Phys. Rev. Lett. **109**(24), 243902 (2012)
46. Fatome, J., Finot, C., Millot, G., Armaroli, A., Trillo, S.: Observation of optical undular bores in multiple four-wave mixing. Phys. Rev. X **4**(2), 021022 (2014)
47. Trillo, S., Klein, M., Clauss, G.F., Onorato, M.: Observation of dispersive shock waves developing from initial depressions in shallow water. Physica D. (2016, in press). doi:10.1016/j.physd.2016.01.007
48. LeVeque, R.J.: Finite-Volume Methods for Hyperbolic Problems. Cambridge University Press, Cambridge (2004)
49. Venakides, S.: Long time asymptotics of the Korteweg-de Vries equation. Trans. Am. Math. Soc. **293**(1), 411–419 (1986)
50. Osborne, A., Petti, M.: Numerical inverse-scattering-transform analysis of laboratory-generated surface wave trains. Phys. Rev. E **47**(2), 1035 (1993)
51. Osborne, A., Petti, M.: Laboratory-generated, shallow-water surface waves: analysis using the periodic, inverse scattering transform. Phys. Fluids **6**(5), 1727–1744 (1994)
52. Ursell, F.: The long-wave paradox in the theory of gravity waves. In: Proceedings of the Cambridge Philosophical Society, vol. 49, pp. 685–694. Cambridge University Press, Cambridge (1953)
53. Whitham, G.: Variational methods and applications to water waves. In: Proceedings of the Royal Society of London, vol. 299, pp. 6–25. The Royal Society, London (1967)
54. Fornberg, B., Whitham, G.B.: A numerical and theoretical study of certain nonlinear wave phenomena. Phil. Trans. R. Soc. A **289**(1361), 373–404 (1978)
55. Chanson, H.: Tidal Bores, Aegir, Eagre, Mascaret, Pororoca: Theory and Observations. World Scientific, Singapore (2011)
56. Arcas, D., Segur, H.: Seismically generated tsunamis. Phil. Trans. R. Soc. A **370**, 1505–1542 (2012)
57. Agrawal, G.P.: Nonlinear Five Optics, 5th edn. Academic, New York (2013)
58. Moro, A., Trillo, S.: Mechanism of wave breaking from a vacuum point in the defocusing nonlinear Schrödinger equation. Phys. Rev. E **89**(2), 023202 (2014)
59. Fratalocchi, A., Conti, C., Ruocco, G., Trillo, S.: Free-energy transition in a gas of noninteracting nonlinear wave particles. Phys. Rev. Lett. **101**, 044101 (2008)
60. Thompson, J.R., Roy, R.: Nonlinear dynamics of multiple four-wave mixing processes in a single-mode fiber. Phys. Rev. A **43**, 4987–4996 (1991)
61. Trillo, S., Wabnitz, S., Kennedy, T.A.B.: Nonlinear dynamics of dual-frequency-pumped multiwave mixing in optical fibers. Phys. Rev. A **50**, 1732–1747 (1994)
62. Trillo, S., Valiani, A.: Hydrodynamic instability of multiple four-wave mixing. Opt. Lett. **35**(23), 3967–3969 (2010)
63. Fratalocchi, A., Armaroli, A., Trillo, S.: Time-reversal focusing of an expanding soliton gas in disordered replicas. Phys. Rev. A **83**, 053846 (2011)
64. Malaguti, S., Corli, A., Trillo, S.: Control of gradient catastrophes developing from dark beams. Opt. Lett. **35**, 4217–4219 (2010)

65. Gurevich, A., Shvartsburg, A.: Exact solutions of the equations of nonlinear geometric optics. Sov. Phys. JETP **31**(6), 1084–1089 (1970)
66. Kamvissis, S., McLaughlin, K.D.T.-R., Miller, P.: Semiclassical Soliton Ensembles for the Focusing Nonlinear Schr ́odinger Equation. Princeton University Press, Princeton (2003)
67. El, G.A., Khamis, E.G., Tovbis, A.: Dam break problem for the focusing nonlinear Schrodinger equation and the generation of rogue waves. arXiv:1505.01785 (2015)
68. Chabchoub, A., Kimmoun, O., Branger, H., Hoffmann, N., Proment, D., Onorato, M., Akhmediev, N.: Experimental observation of dark solitons on the surface of water. Phys. Rev. Lett. **110**, 124101 (2013)
69. El, G.A., Gammal, A., Khamis, E.G., Kraenkel, R.A., Kamchatnov, A.M.: Theory of optical dispersive shock waves in photorefractive media. Phys. Rev. A **76**, 053813 (2007)
70. Crosta, M., Fratalocchi, A., Trillo, S.: Bistability and instability of dark-antidark solitons in the cubic-quintic nonlinear schrödinger equation. Phys. Rev. A **84**, 063809 (2011)
71. Crosta, M., Trillo, S., Fratalocchi, A.: Crossover dynamics of dispersive shocks in Bose-Einstein condensates characterized by two- and three-body interactions. Phys. Rev. A **85**, 043607 (2012)
72. Crosta, M., Trillo, S., Fratalocchi, A.: The whitham approach to dispersive shocks in systems with cubic-quintic nonlinearities. New J. Phys. **14**(9), 093019 (2012)
73. Crosta, M., Fratalocchi, A., Trillo, S.: Double shock dynamics induced by the saturation of defocusing nonlinearities. Opt. Lett. **37**, 1634–1636 (2012)
74. Barsi, C., Wan, W., Sun, C., Fleischer, J.W.: Dispersive shock waves with nonlocal nonlinearity. Opt. Lett. **32**, 2930–2932 (2007)
75. Armaroli, A., Trillo, S., Fratalocchi, A.: Suppression of transverse instabilities of dark solitons and their dispersive shock waves. Phys. Rev. A **80**, 053803 (2009)
76. Conforti, M., Baronio, F., Trillo, S.: Resonant radiation shed by dispersive shock waves. Phys. Rev. A **89**, 013807 (2014)
77. Conforti, M., Trillo, S.: Dispersive wave emission from wave breaking. Opt. Lett. **38**, 3815–3818 (2013)
78. Conforti, M., Trillo, S.: Radiative effects driven by shock waves in cavity-less four-wave mixing combs. Opt. Lett. **39**, 5760–5763 (2014)
79. Malaguti, S., Conforti, M., Trillo, S.: Dispersive radiation induced by shock waves in passive resonators. Opt. Lett. **39**, 5626–5629 (2014)
80. Webb, K.E., Xu, Y.Q., Erkintalo, M., Murdoch, S.G.: Generalized dispersive wave emission in nonlinear fiber optics. Opt. Lett. **38**, 151–153 (2013)
81. Liu, Y., Tu, H., Boppart, S.A.: Wave-breaking-extended fiber supercontinuum generation for high compression ratio transform-limited pulse compression. Opt. Lett. **37**(12), 2172 (2012)
82. Akhmediev, N., Karlsson, M.: Cherenkov radiation emitted by solitons in optical fibers. Phys. Rev. A **51**, 2602–2607 (1995)
83. Cavalcanti, S.B., Cressoni, J.C., da Cruz, H.R., Gouveia-Neto, A.S.: Modulation instability in the region of minimum group-velocity dispersion of single-mode optical fibers via an extended nonlinear Schrödinger equation. Phys. Rev. A **43**, 6162–6165 (1991)
84. Conforti, M., Baronio, F., Trillo, S.: Competing wave-breaking mechanisms in quadratic media. Opt. Lett. **38**, 1648–1650 (2013)
85. Ghofraniha, N., Gentilini, S., Folli, V., DelRe, E., Conti, C.: Shock waves in disordered media. Phys. Rev. Lett. **109**, 243902 (2012)
86. Garnier, J., Xu, G., Trillo, S., Picozzi, A.: Incoherent dispersive shocks in the spectral evolution of random waves. Phys. Rev. Lett. **111**, 113902 (2013)
87. Xu, G., Vocke, D., Faccio, D., Garnier, J., Roger, T., Trillo, S., Picozzi, A.: From coherent shocklets to giant collective incoherent shock waves in nonlocal turbulent flows. Nat. Commun. **6**, 8131 (2015)
88. Malaguti, S., Bellanca, G., Trillo, S.: Dispersive wave-breaking in coherently driven passive cavities. Opt. Lett. **39**, 2475–2478 (2014)
89. Maiden, M., Lowman, N.K., Anderson, D.V., Schubert, M., Hoefer, M.A.: Observation of dispersive shock waves in viscous fluid conduits. Phys. Rev. Lett. **116**, 174501 (2016)

90. Carusotto, I., Hu, S.X., Collins, L.A., Smerzi, A.: Bogoliubov-Cerenkov radiation in a Bose-Einstein condensate flowing against an obstacle. Phys. Rev. Lett. **97**, 260403 (2006)
91. Varlot, B., Wabnitz, S., Fatome, J., Millot, G., Finot, C.: Experimental generation of optical flaticon pulses. Opt. Lett. **38**, 3899–3902 (2013)
92. Millot, G., Pitois, S., Yan, M., Hovhannisyan, T., Bendahmane, A., Hänsch, T., Picquét, N.: Frequency-agile dual-comb spectroscopy. Nat. Photon. **10**, 27–30 (2016)

Acronym Glossary

3WRI Three wave resonant interaction

AB Akhmediev breather

BBO Beta barium borate

BFI Benjamin-Feir index

BO Benjamin-Ono

cmKdV Complex modified Korteweg-de Vries

CW Continuous wave

DNLS Derivative nonlinear Schrödinger

DSW Dispersive shock wave

ECL External cavity laser

ECMWF European centre for medium-range weather forecasts

FROG Frequency resolved optical gating

FT Fourier transform

HOD Higher order dispersion

HOSM Higher order spectral method

h.o.t. Higher order terms

IST Inverse scattering transform

KdV Korteweg-de Vries

KM Kuznetsov-Ma

KMB Kuznetsov-Ma breather

M. Onorato et al. (eds.), *Rogue and Shock Waves in Nonlinear Dispersive Media*,
Lecture Notes in Physics 926, DOI 10.1007/978-3-319-39214-1

KP Kadomptsev-Petviashvilii

LWSH Long-wave-short-wave

mFWM Multiple four-wave mixing

MI Modulational instability

MNLSE Modified nonlinear Schrödinger equation

MTM Massive thirring model

NLS Nonlinear Schrödinger

NLSE Nonlinear Schrödinger equation

PCF Photonic crystal fiber

PDE Partial differential equation

RF Radio frequency

RH Rankine-Hugoniot

RR Resonant radiation

RW Rogue wave

SC Supercontinuum

SG Sine-Gordon

SMF Single-mode fiber

SS Sasa-Satsuma

ST Scattering transform

SW Shock wave

T-KdV Time-like Korteweg-de Vries

VNLS Vector nonlinear Schrödinger

WT Wave turbulence